CASA DIVISION ESPACIO

ALCATEL TELECOM

ECOLE POLYTECHNIQUE FEDERALE DE LAUSANNE

CONFORMAL ARRAY ANTENNA

ESA/ ESTEC Contract 11698/95/NL/SB - Volume 1 / 2

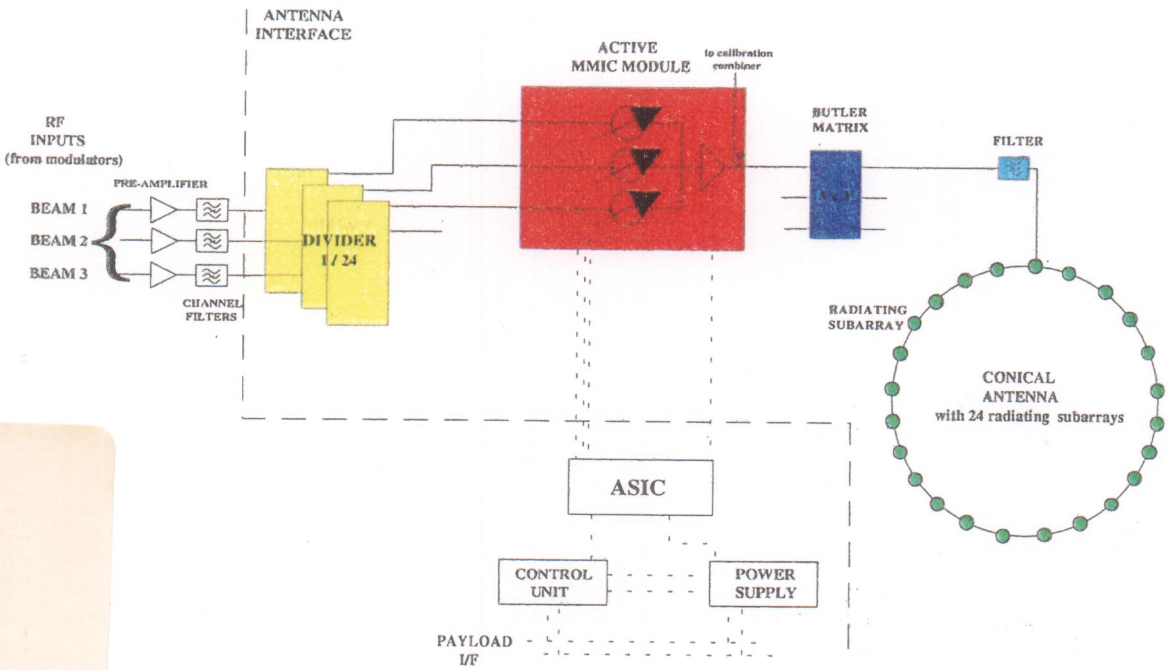

TIDC-CR-6845

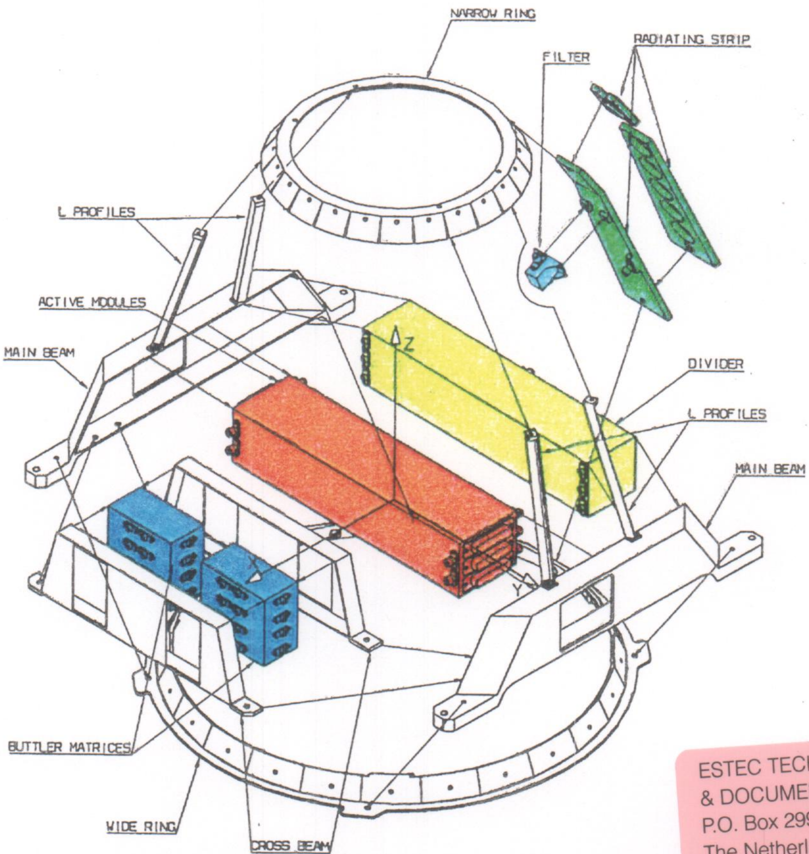

ESTEC TECHNICAL INFORMATION & DOCUMENTATION CENTRE
P.O. Box 299 2200 AG NOORDWIJK
The Netherlands
Tel. 071 565 3015 Fax 071 565 5429

CONFORMAL ARRAY ANTENNA

ESA/ ESTEC Contract 11698/95/NL/SB - Volume 1 / 2

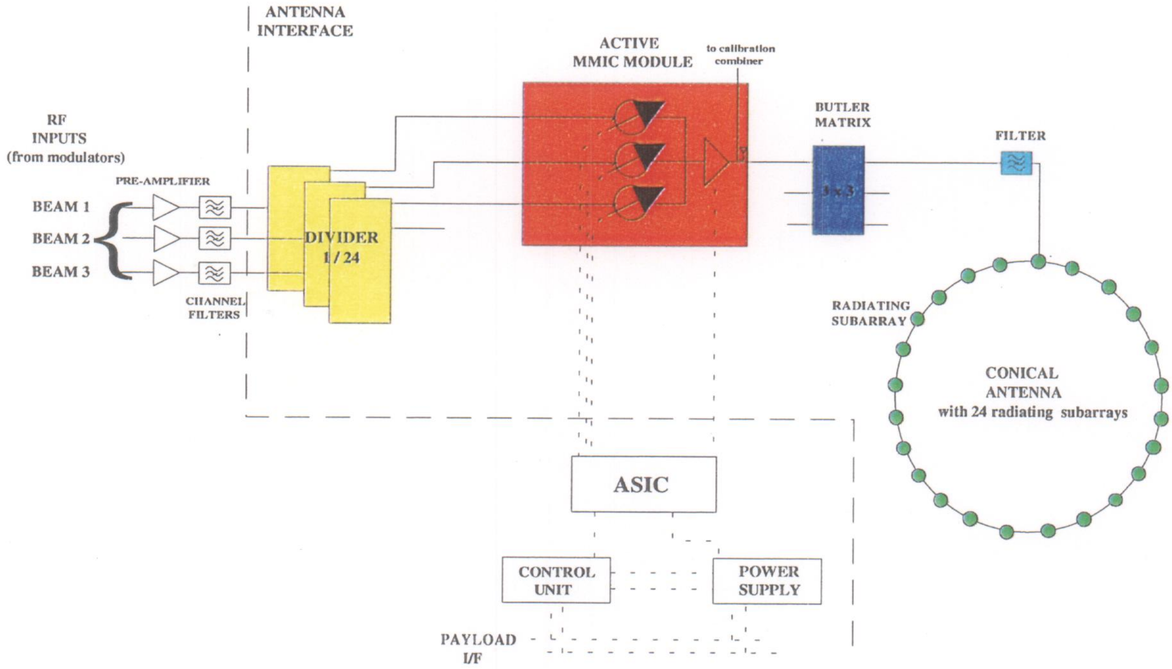

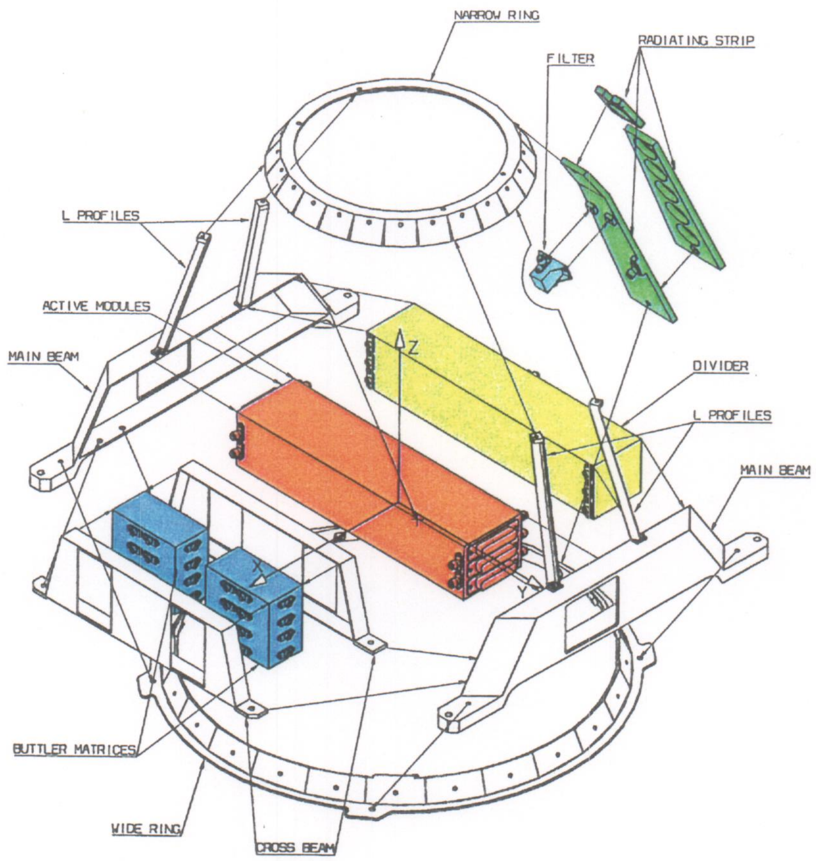

ALCATEL TELECOM	CONFORMAL ARRAY ANTENNA	ESTEC CONTRACT 11698/95/NL/SB	
		AES 960596 / ASP 019	
		DATE : 26/06/96	ED/REV 1/-

CONFORMAL ARRAY ANTENNA

T nation contained in this document is proprietary to ALCATEL ESP shall not be u sed by the recipient to third persons without the written consent of the company

Les info s contenues dans ce document demeurent propriété exclusive d'ALC SPACE et ne do is être divulguées par le destinataire à des tiers sans l'accord écrit de été.

ALCATEL TELECOM	CONFORMAL ARRAY ANTENNA	ESTEC CONTRACT 11698/95/NL/SB	
		AES 960596 / ASP 019	
		DATE : 13/11/97	ED/REV 10/-

OVERALL SUMMARY
Volume 1/2

T mation contained in this document is proprietary to ALCATEL ESP. l shall not be osed by the recipient to third persons without the written consent of the pany

Les info contenues dans ce document demeurent propriété exclusive d'ALC. ESPACE et ne doi s être divulguées par le destinataire à des tiers sans l'accord écrit de la été.

ALCATEL TELECOM	CONFORMAL ARRAY ANTENNA	ESTEC CONTRACT 11698/95/NL/SB	
		AES 960596 / ASP 019	
		DATE : 13/11/97	ED/REV 10/-

PROJECT DIFFUSION LIST

COMPANY	DEPARTMENT	DIF.	RECEIVER NAME
ALCATEL Espace	ASP		G. DURET
			G. CAILLE
			T. DUSSEUX
			E. VOURCH
ESA/ESTEC			A. MARTIN POLLEGRE (5 ex.)
CASA	Div. Espacio		M.J. MARTIN (3 ex.)
EPFL	LEMA		J. MOSIG
			A. ALVAREZ

The information contained in this document is proprietary to ALCATEL ESPACE and shall not be disclosed by the recipient to third persons without the written consent of the company

Les informations contenues dans ce document demeurent propriété exclusive d'ALCATEL ESPACE et ne doivent pas être divulguées par le destinataire à des tiers sans l'accord écrit de la société.

ALCATEL TELECOM	CONFORMAL ARRAY ANTENNA	ESTEC CONTRACT 11698/95/NL/SB		
		AES 960596 / ASP 019		
		DATE : 13/11/97	ED/REV 10/-	

ENREGISTREMENT DES EVOLUTIONS / CHANGE RECORD

ED/REV.	DATE	AUTORISATION AUTHORIZATION	DESCRIPTION DES EVOLUTIONS CHANGE RECORD	REDACTEUR AUTHOR
1/A chap 2	23/02/96		Final issue including ESA comments	J. OSTER
0/- chap 1,3	14/05/96		Draft issue	E. VOURCH
1/- chap 1, 3	26/06/96		Final issue including ESA comments	E. VOURCH
2/- chap 4	14/10/96		Final issue including ESA comments	G. CAILLE
3/- chap 6	30/10/96		Final report	T. ADAM
4/- chap 8	20/12/96		Final report	M.J. MARTIN
5/- chap 9	20/12/96		Final report	M.J. MARTIN
6/- chap 11	20/12/96		Final report	J. NAVARRO J. JIMENEZ A. AGUILAR R. BALANZA M.J. MARTIN
7/- chap 7	15/02/97		Final report	E. VOURCH
8/- chap 10	08/04/97		Final report	E. VOURCH / G. CAILLE
9/- chap 12	27/08/97		Final report	E. VOURCH / G. CAILLE
9/- chap 5	30/06/97		Final report	A. ALVAREZ / J.R. MOSIG
9/- chap 13	01/09/97		Final report	E. VOURCH / G. CAILLE
10/- chap 14	22/10/97		Final report	F. MONJAS Q. GARCIA M.J. MARTIN
10/- chap 15	22/10/97		Final report	M.J. MARTIN
10/- chap 16	22/10/97		Final report	M.J. MARTIN
10/- Exec. Sum.	13/11/97		Final report	G. CAILLE
10/- chap 17	31/10/97		Final report	E. VOURCH / G. CAILLE
10/- chap.10 (annex)	31/10/97		Final report	E. VOURCH / G. CAILLE
10/- chap 18	13/11/97		Final report	E. VOURCH / G. CAILLE

T ...mation contained in this document is proprietary to ALCATEL ESP... ...d shall not be ...osed by the recipient to third persons without the written consent of the ...pany
Les inf... ...s contenues dans ce document demeurent propriété exclusive d'ALC... ESPACE et ne do... ...s être divulguées par le destinataire à des tiers sans l'accord écrit de l... ...été.

CHAPTER 1

INTRODUCTION

Reproduction interdite © ALCATEL ESPACE Reproduction forbidden

The information contained in this document is proprietary to ALCATEL ESPACE and shall not be disclosed by the recipient to third persons without the written consent of the ALCATEL ESPACE.

CHAPTER 1

Titre / Title
INTRODUCTION

Rédigé par / Written by	*Responsabilité / Responsability*	*Date*	*Signature*
CAILLE Gérard	Technical Manager of the study	21/6/96	
Approbation / Approved			
DURET Gilles	Head of Space Antenna Department	24/6/96	

Les informations contenues dans ce document demeurent propriété exclusive d'ALCATEL ESPACE et ne doivent être divulguées par le destinataire à des tiers sans l'accord écrit de l'ALCATEL ESPACE.

a) Current X-Band links from Satellite to Ground for medium data rates are limited in gain and to one beam. In order to increase the potential data rate, the objectives of this study is <u>to design and manufacture a multibeam scanning antenna (up to three beams in three adjacent sub-bands) for a LEO mission (800 Kms).</u> It covers a very promising domain for future performant spaceborne missions.

The concept choosen to satisfy the mission is a Conformal Array Antenna made on a truncated cone.

This concept presents some advantages:

- electronically scanning (no mechanical disturbances during scan operation)
- higher gain than conventionnal antenna (due to its interesting geometry, particularly well suited to a large field of view as required in LEO mission)

A Conformal Array Antenna (with a single beam) had been developed by ALCATEL during a similar CNES study (SPOT mission with an altitude between 680 and 800 Kms). This antenna was built in a truncated cone of 60 columns and an active concept was choosen to form the beam: the electronically scanning consisted in switching ON/OFF columns around the circonference of the cone.

In this study, the same concept will be extended to three beams generation and the passive and semi-active options will then be studied.

b) The study has been carried on by an international team lead by ALCATEL Espace, with CASA, and LEMA / EPFL as subcontractors.

c) As recalled on the WBS next page (fig. I-a), the study is divided in three phases:

PHASE 1

- a system analysis
- a trade-off between active, semi-active and passive concepts
- preliminary design and performances computations for these concepts

PHASE 2

- detailed design of all parts of the antenna

PHASE 3

- manufacturing and test of an elegant breadboard of the antenna

The information contained in this document is proprietary to ALCATEL ESPACE and shall not be disclosed by the recipient to third persons without the written consent of the company.

Les informations contenues dans ce document demeurent propriété exclusive d'ALCATEL ESPACE et ne doivent être divulguées par le destinataire à des tiers sans l'accord écrit de la société.

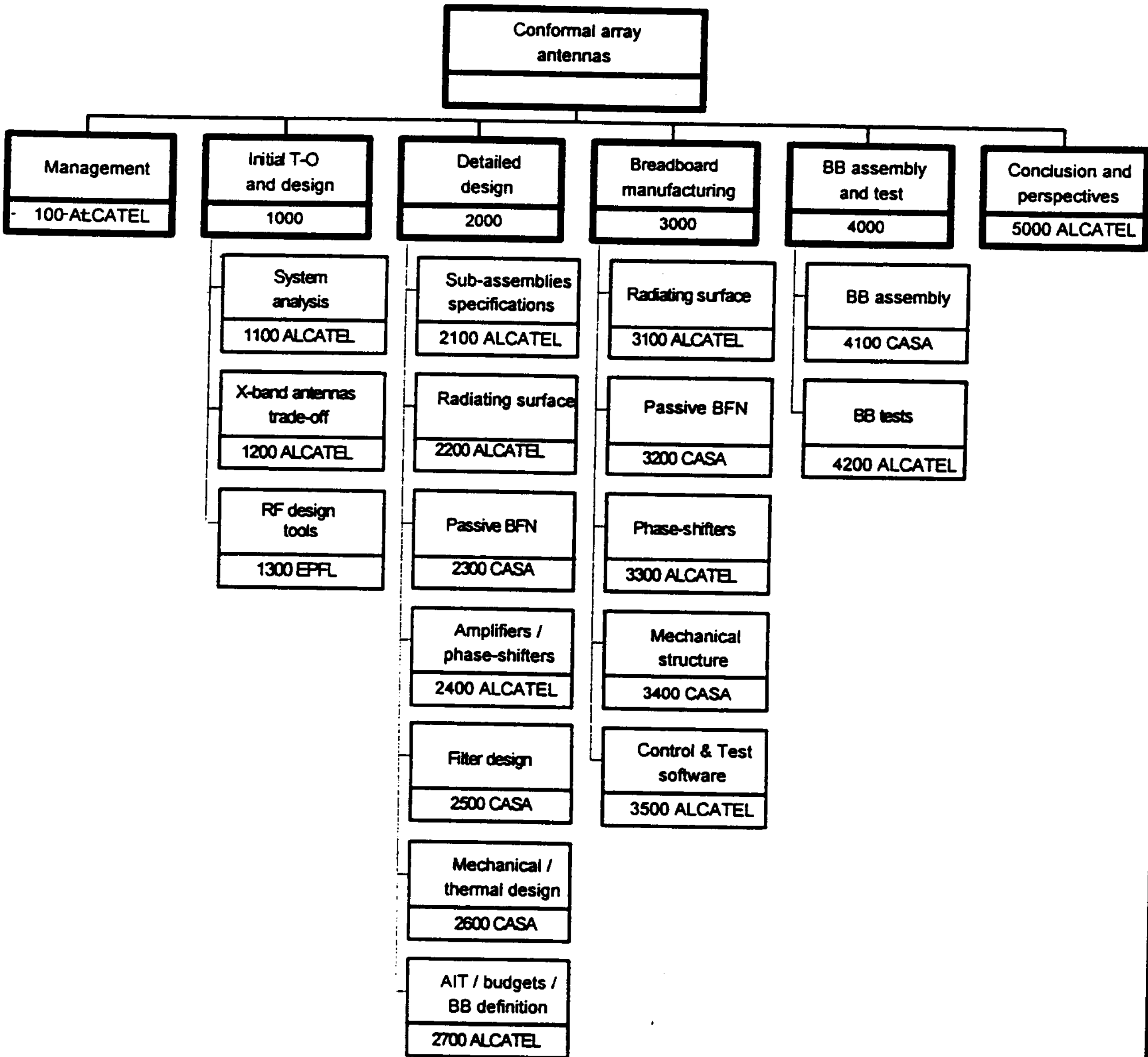

Fig. I-a: *Work Breakdown Structure*

Th... ...ation contained in this document is proprietary to ALCATEL ESPA... shall not be ...d by the recipient to third persons without the written consent of the ...SPACE

Les infor... ...s contenues dans ce document demeurent propriété exclusive d'ALCA... et ne doi... être divulguées par le destinataire à des tiers sans l'accord écrit de l...

ALCATEL TELECOM	CONFORMAL ARRAY ANTENNA	ESTEC CONTRACT 11698/95/NL/SB		
		AES 960596 / ASP 019		
		DATE : 26/06/96	ED/REV 1/-	1- 4

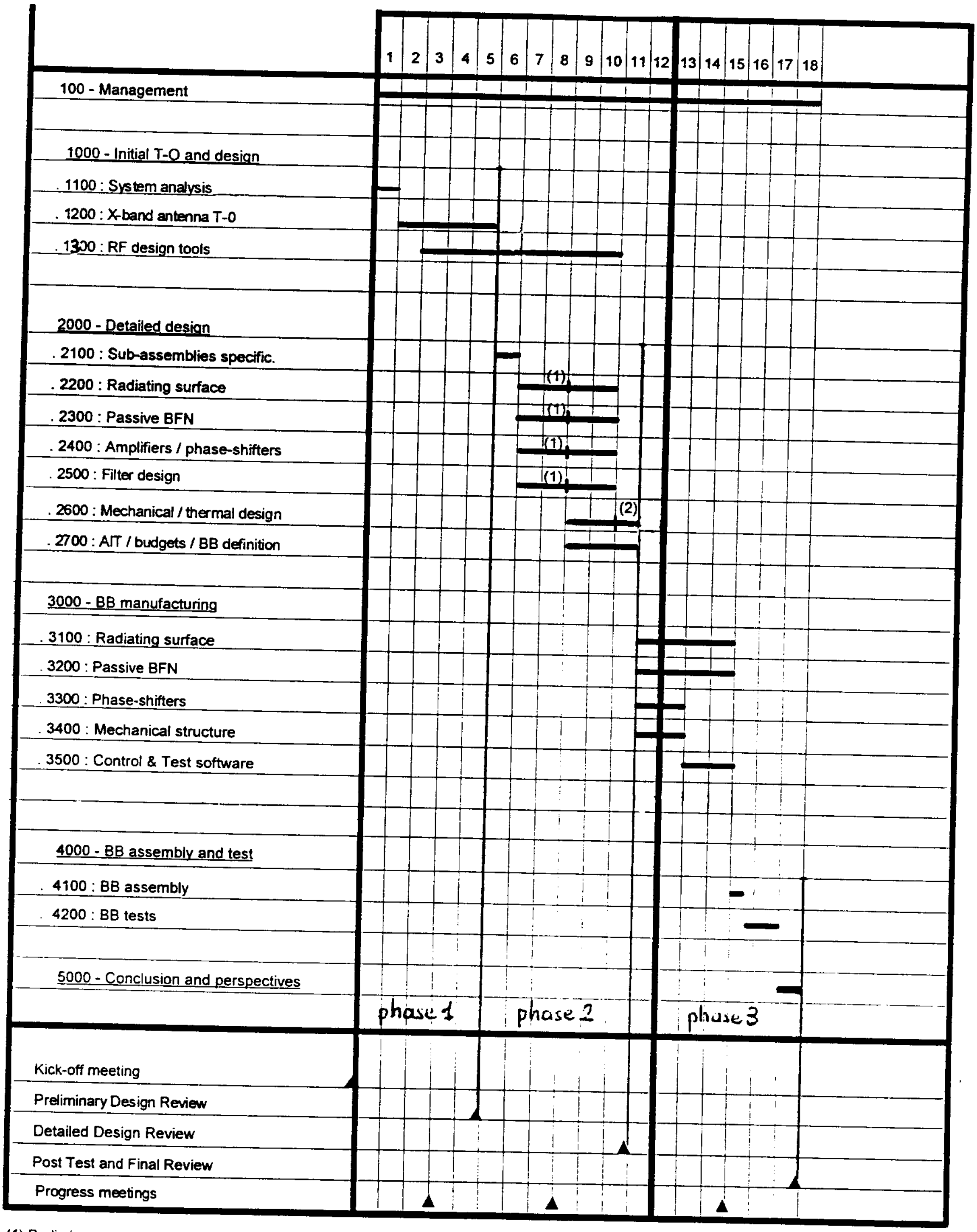

(1) Preliminary outputs for WP 2600 and 2700.

(2) Last month of 2600: drawings for BB manufacturing.

Fig. I-b: Schedule

The information contained in this document is proprietary to ALCATEL ESPACE and shall not be disclosed by the recipient to third persons without the written consent of the ALCATEL ESPACE company.
Les informations contenues dans ce document demeurent propriété exclusive d'ALCATEL ESPACE et ne doivent pas être divulguées par le destinataire à des tiers sans l'accord écrit de l'ALCATEL ESPACE société.

CONFORMAL ARRAY

CHAPTER 2

SYSTEM ANALYSIS

(WP 1100)

Reproduction interdite © ALCATEL ESPACE Reproduction forbidden

ALCATEL ESPACE	**Conformal array Antenna**	REF: ATES 96 005003SCS0017 Chapter 1		
		DATE : 23/02/96	ED / REV : 1/A	PAGE : 1

Titre / Title

RF SYSTEM ANALYSIS :

TECHNICAL REPORT

Rédigé par / Written by	Responsabilité / Responsibility	Date	Signature
J. OSTER	RF System Engineer	23/02/96	
Approbation/Approved			
P.KAROUBY	Satellite Control Department Manager	23/02/96	
G.CAILLE	Active Antenna Department Manager	23/2/96	

Les informations contenues dans ce document demeurent la propriété exclusive d'ALCATEL ESPACE et ne doivent pas être divulguées par le destinataire à des tiers, sans l'accord de la société.

The information contained in this document is proprietary to ALCATEL ESPACE and shall not be disclosed by the recipient to third persons without the written consent of the company.

ALCATEL ESPACE	Conformal array Antenna	REF: ATES 96 005003SCS0017		
		DATE : 23/02/96	ED / REV : 1/A	PAGE : 2

PROJECT DIFFUSION LIST

COMPANY	DEPARTMENT	DIF.	RECEIVER NAME
ALCATEL-ESPACE	ASP		G.DURET
			G. CAILLE
			E. VOURCH
	~~DTT~~		~~P. KAROUBY~~
	DTT		J.OSTER
	DOBS		L. DIDEROT
	DCTC		M. CHAINE
ESA/ESTEC			G. VAN DOOREN (5 ex)
			~~T. JONES~~
			A. ~~ROEDERER~~
			S. ~~BENETTI~~
CASA	Div. Espacio		~~M. LANCHO~~
			M.J. MARTIN (3 ex)
EPFL	LEMA		J. Mosig
			A. Alvarez

The information contained in this ...nt is proprietary to ALCATEL ESPACE and shall not be disclosed by the recipient to thi... ...sons without the written consent of the company.

...ormations contenues dans ce document demeurent la propriété exclu... ALCATEL ESPACE ...oivent pas être divulguées par le destinataire à des tiers, sans l'accord ...ociété.

The information contained in this document is proprietary to ALCATEL ESPACE and shall not be disclosed by the recipient to third persons without the written consent of the company.

Les informations contenues dans ce document demeurent la propriété exclusive de ALCATEL ESPACE et ne doivent pas être divulguées par le destinataire à des tiers, sans l'accord de la société.

ENREGISTREMENT DES EVOLUTIONS / CHANGE RECORD

ED./REV.	DATE	AUTORISATION AUTHORIZATION	§: DESCRIPTION DES EVOLUTIONS §: CHANGE RECORD	REDACTEUR AUTHOR
0/-	31.01.96		Draft Issue	J.OSTER
1/A	23.02.96		Issue 1/A following TSA comments	

LISTE DE REVISION DES PAGES / PAGE REVISION LETTER LIST

DATES													DATES												
	INDICES													INDICES											
Pages	-	A	B	C	D	E	F	G	H	I	J	K	Pages	-	A	B	C	D	E	F	G	H	I	J	K
1	X																								
2	X																								
3	X																								
4	X																								
5	X																								
6	X																								
7	X																								
8	X																								
9	X																								
10	X	X																							
11	X																								
12	X																								
13	X																								
14	X	X																							
15	X	X																							
16	X	X																							
17	X	X																							
18	X	X																							
19	X	X																							
20	X	X																							
21	X	X																							
22	X	X																							
23	X	X																							
24	X	X																							
25	X	X																							
26	X	X																							
27	X	X																							
28	X	X																							
29	X	X																							
30	X	X																							
31	X	X																							
32	X	X																							
33	X	X																							
34	X	X																							
35	X	X																							
36	X	X																							
37	X	X																							
38	X	X																							
39	X	X																							
40	X	X																							
41		X																							
42		X																							
43																									

The information contained in this ...nt is proprietary to ALCATEL ESPACE and shall not be disclosed by the recipient to thi... ...ons without the written consent of the company.

...rmations contenues dans ce document demeurent la propriété exclu... ...LCATEL ESPACE ...oivent pas être divulguées par le destinataire à des tiers, sans l'accord ...ociété.

The information contained in this document is proprietary to ALCATEL ESPACE and shall not be disclosed by the recipient to third persons without the written consent of the company.
Les informations contenues dans ce document demeurent la propriété exclusive d'ALCATEL ESPACE et ne doivent pas être divulguées par le destinataire à des tiers, sans l'accord de la société.

TABLE OF CONTENTS

The information contained in this document is proprietary to ALCATEL ESPACE and shall not be disclosed by the recipient to third persons without the written consent of the company.

Les informations contenues dans ce document demeurent la propriété exclusive d'ALCATEL ESPACE et ne doivent pas être divulguées par le destinataire à des tiers, sans l'accord de la société.

The information contained in this document is proprietary to ALCATEL ESPACE and shall not be disclosed by the recipient to third persons without the written consent of the company.

Les informations contenues dans ce document demeurent la propriété exclusive d'ALCATEL ESPACE et ne doivent pas être divulguées par le destinataire à des tiers, sans l'accord de la société.

1. SCOPE

The aim of this document is to define the best configuration for the payload telemetry transmitter, taking into account :

1 - The spectral allocation constraints at X-band (8025-8400 MHz) and ;

2 - The degradation not to be exceeded for the link quality losses (ACI and IMP) of the 3-carriers multiplex.

The output of the document is a proposal for an updated requirement specification of the conformal array antenna.

The information contained in this document is proprietary to ALCATEL ESPACE and shall not be disclosed by the recipient to third persons without the written consent of the company.

Les informations contenues dans ce document demeurent la propriété exclusive d'ALCATEL ESPACE et ne doivent pas être divulguées par le destinataire à des tiers, sans l'accord de la société.

2. APPLICABLE AND REFERENCE DOCUMENTS

2.1. Applicable documents

[AD1] : Negociation Meeting DOTT 95058 at ESTEC on 25/10/95.

[AD2] : Conformal array antenna proposal in response to ESA-AO 2816 (P627E, from June 1995).

[AD3] : Conformal array antenna : Answers to ESA questions and updating of P627E proposal (P627E, Rev. A from October 1995).

2.2. Reference documents

[RD1] : UIT/CCIR Regulation of Radio-Communications RR8-137/139.

[RD2] : UIT/CCIR Rapport 687-1 : règles de partage SFS (7-8 GHz) et Espace lointain.

[RD3] : UIT/CCIR Recommandation 358-3 : Flux max. admissibles au sol produits par satellites.

[RD4] : UIT/CCIR Rapport 685-3 : Protections de l'Espace lointain.

[RD5] : UIT/CCIR Recommandation 328-7 : Spectres et largeur de bande d'émission.

The information contained in this document is proprietary to ALCATEL ESPACE and shall not be disclosed by the recipient to third persons without the written consent of the company.
Les informations contenues dans ce document demeurent la propriété exclusive de ALCATEL ESPACE et ne doivent pas être divulguées par le destinataire à des tiers, sans l'accord de la société.

3. MAIN SYSTEM HYPOTHESIS

3.1. X-Band Link Hypothesis

- Orbit geometry : the assumption is an heliosynchronous orbit at 800 Km altitude. The mission type is considered similar to ERS or ENVISAT systems.

- Operational conditions : the transmission system is designed in order to be able to send data from satellite to earth as soon as the elevation angle is equal or higher than 5°. The link budgets are defined for Kiruna 1 earth station [AD1].

- Multiplex definition : up to three QPSK or BPSK-modulated carriers can be transmitted. In case of BPSK modem, the data rate on one carrier is 50 Mb/s, and for QPSK modem the data rate becomes 2*50 Mb/s. The 3 carriers frequencies are 8100, 8200 and 8300 MHz. This frequency plan can be reviewed in the course of this study.

- Telecommunication characteristics : the BER requirement is 10^{-7} for BPSK modulation and 10^{-5} for QPSK modulation. The link availability requirement is 99%.

The information contained in this document is proprietary to ALCATEL ESPACE and shall not be disclosed by the recipient to third persons without the written consent of the company.
Les informations contenues dans ce document demeurent la propriété exclusive de ALCATEL ESPACE et ne doivent pas être divulguées par le destinataire à des tiers, sans l'accord préalable écrit de la société.

3.2. Frequency Allocation Constraints

The frequency bandwidth within the range 8025-8400 MHz is allocated by UIT/CCIR to the earth exploration service (EEX), as reported in document [RD1].

3.2.1. Compatibility with Satellite Services below 8.025 GHz and within 8.025-8.4 GHz range.

It is required by UIT/CCIR that space agencies and space operators insure the compatibility between the Earth Exploration Service (EEX) and the Fixed/Mobile Satellite Services (FFS/MSS). This is ruled by the report [RD2] and the recommendation [RD3] from CCIR and also confirmed by the final acts of WARC-92 and WARC-95 (Genève).

Below 8025 MHz, the maximum power flux at earth level shall not exceed the following values, θ being the earth station elevation angle :

- -152 db(W/m²) pour $\theta \le 5°$
- $-152 + 0.5 * (\theta - 5)$ db(W/m²) pour $5° < \theta \le 25°$
- -142 db(W/m²) pour $25° < \theta \le 90°$

Power flux density limits are integrated in any 4 KHz bandwidth.

Within the 8.025-8.4 GHz range, the levels are quite similar to the previous ones (-150 and -140 instead of -152 and -142 are given in WARC-95 document).

...nt is proprietary to ALCATEL ESPACE and shall not ...ons without the written consent of the company. The information contained in this ...be disclosed by the recipient to thi...

...rmations contenues dans ce document demeurent la propriété exclu... ALCATEL ESPACE ...ivent pas être divulguées par le destinataire à des tiers, sans l'accord ...ociété.

3.2.2. Compatibility with the Satellite Services above 8.4 GHz

It concerns the sharing conditions between the Earth Exploration Service and the Space Research Service (Deep Space). The regulation rules are given in report [RD4].

This report defines that the maximum admissible Power Flux Density at earth level shall not exceed - 255 dbW/m²/Hz within the frequency range 8.4-8.45 GHz.

3.2.3. Occupancy of the allocated frequency channel.

CCIR define as follows the signal frequency bandwidth [RD5] :

It is the bandwidth in which 99% of the total transmitted power is concentrated.

This definition applies to the allocated bandwidth 8.025-8.4 GHz.

The signal here is the 3-carriers multiplex.

The information contained in this ...nt is proprietary to ALCATEL ESPACE and shall not be disclosed by the recipient to thi... ...sons without the written consent of the company.
...formations contenues dans ce document demeurent la propriété exclu... ALCATEL ESPACE ...oivent pas être divulguées par le destinataire à des tiers, sans l'accord ...société.

4. RF SYSTEM ANALYSIS

4.1. UIT/CCIR Constraints Analysis

4.1.1. Occupancy of the allocated frequency channel

The PSK spectra of the three modulated carriers are given on figures 4.1.1/A, 4.1.1/B and 4.1.1/C.

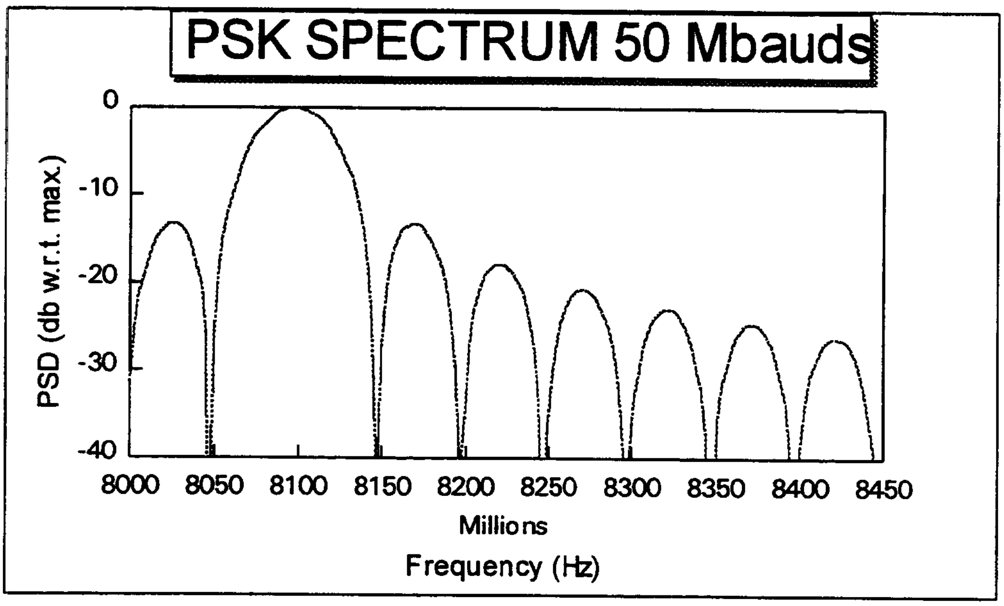

Figure 4.1.1/A : Channel 1 spectrum (8.1 GHz).

The information contained in this document is proprietary to ALCATEL ESPACE and shall not be disclosed by the recipient to third persons without the written consent of the company.

Les informations contenues dans ce document demeurent la propriété exclusive d'ALCATEL ESPACE et ne doivent pas être divulguées par le destinataire à des tiers, sans l'accord de la société.

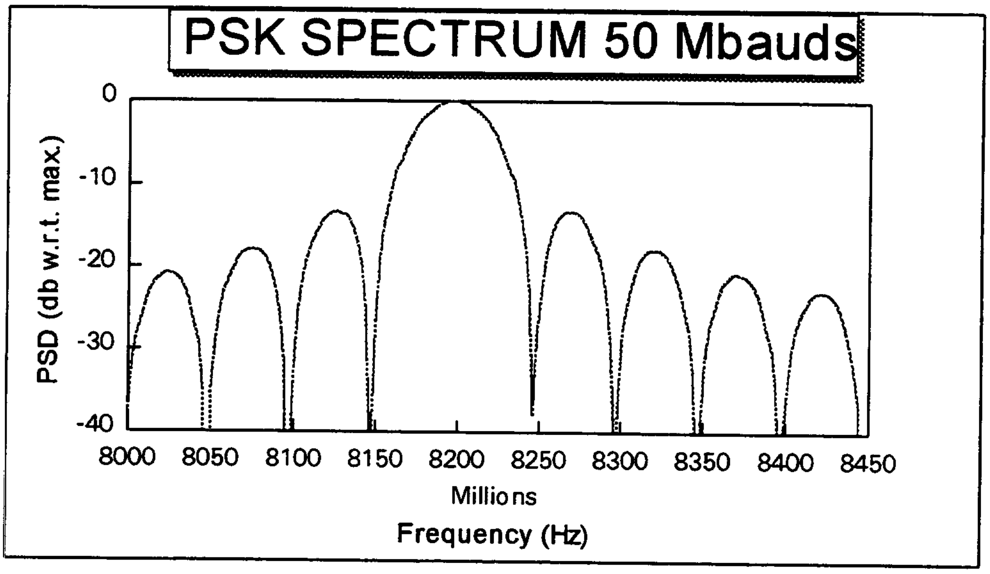

Figure 4.1.1/B : Channel 2 spectrum (8.2 GHz).

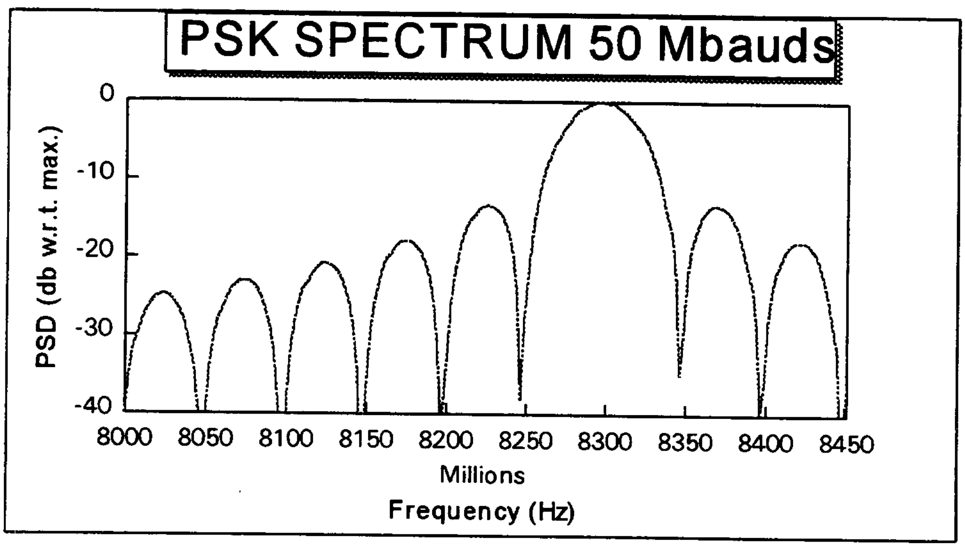

Figure 4.1.1/C : Channel 3 spectrum (8.3 Ghz).

The information contained in this document is proprietary to ALCATEL ESPACE and shall not be disclosed by the recipient to third persons without the written consent of the company.

Les informations contenues dans ce document demeurent la propriété exclusive d'ALCATEL ESPACE et ne doivent pas être divulguées par le destinataire à des tiers, sans l'accord de la société.

The required filtering attenuation depends on the channel linearity.

When it is linear, the analysis is detailed in annex 1 and the conclusion is that a smooth pass-band filter (6 dB attenuation at 8025 and 8400 MHz) is sufficient.

In case the channel is non-linear, we have to consider a power rise of PSK spectrum secondary lobes. As computed in annex 2.1, an extra-dB attenuation (total 7 dB) has to be added for the filter out-of-band attenuation.

4.1.2. Out-of-band Power Flux Density

4.1.2.1. Linear channel

We have to deal with power flux below 8025 MHz and power flux above 8400 MHz.

- Below 8025 MHz, the worst case is obtained for channel 1 (8100 Mhz). The computed Power Flux within 4 KHz bandwidth is shown on figure 4.1.2/A.

The margin w.r.t. the requirement is higher than 20 dB and there is no need of filter for that.

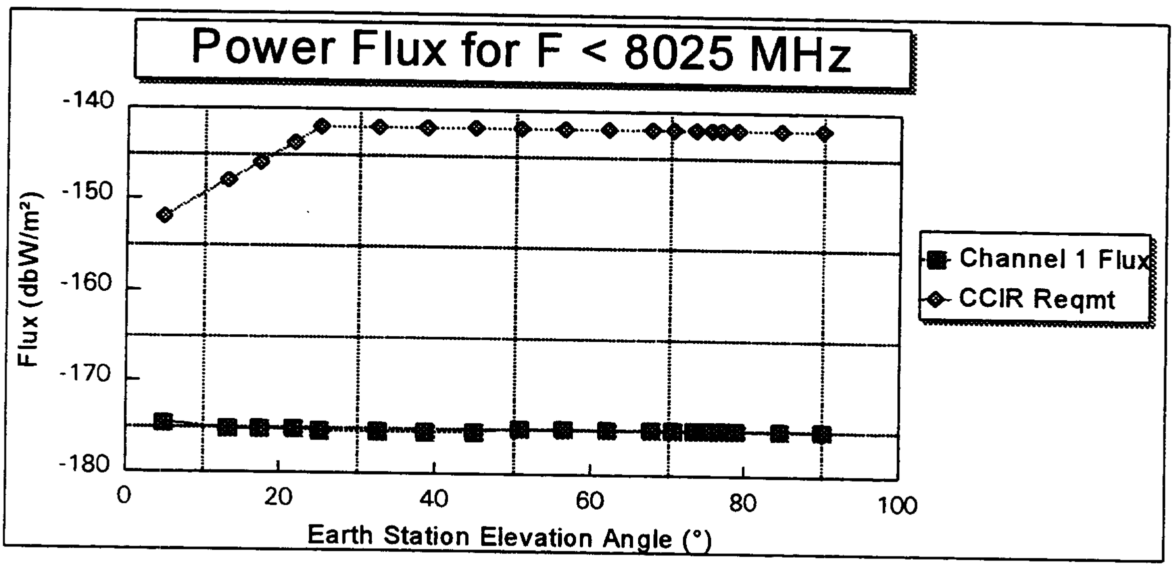

Figure 4.1.2/A : Channel 1 power flux

The information contained in this document is proprietary to ALCATEL ESPACE and shall not be disclosed by the recipient to third persons without the written consent of the company.
Les informations contenues dans ce document demeurent la propriété exclusive d'ALCATEL ESPACE et ne doivent pas être divulguées par le destinataire à des tiers, sans l'accord de la société.

- Above 8400 Mhz, the worst case condition is for channel 3. The computed Power Flux Density (PFD) is shown on figure 4.1.2/B.

There is no margin and the out-of-spec. is around 38 dB. As a worst case, the contributions of channel 2 (5 dB below) and of channel 1 (8 dB below) can increase the total out-of-spec value to 40 dB (when r.m.s. summed).

Computation of power fluxes is given in annex 3.

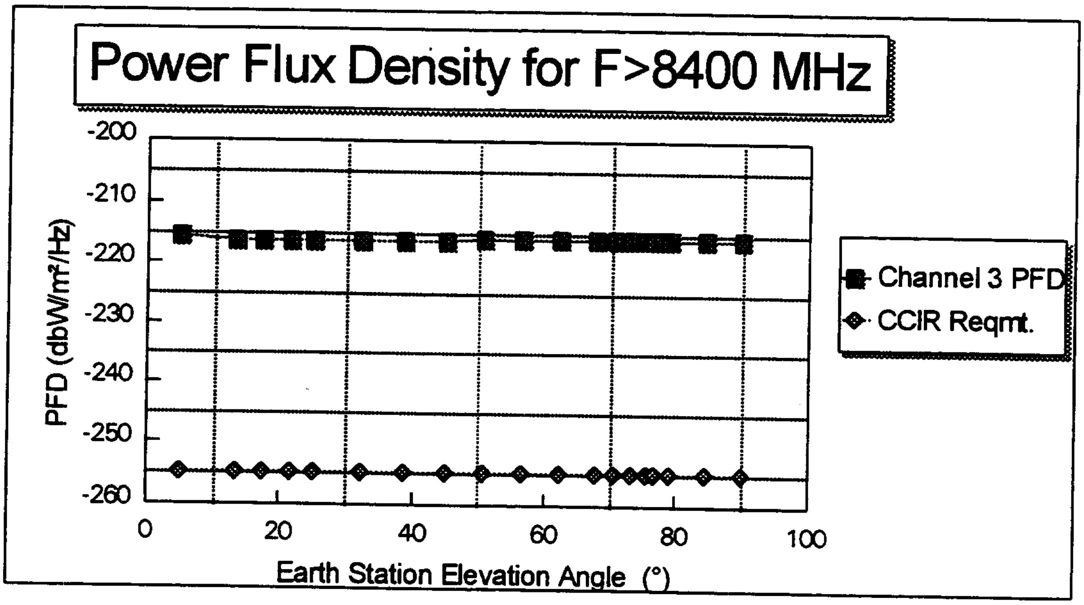

Figure 4.1.2/B : Channel 3 PFD

4.1.2.2. Non-linear channel

When the RF channel is affected by a non-linearity, two effects have to be analysed :

1 - The occurence of InterModulation Products (IMP) between the 3 carriers.

2 - The reduction of the filters efficiency when these filters are located in front of the N-L. It is due to the Intermodulation Products within the PSK spectrum creating power rise of the secondary lobes.

4.1.2.2.1. IMP between the 3 carriers.

The IMP analysis is performed in annex 7.4.1.

Taking into account the percentage of IMP falling within the 8400-8450 MHz range, the spectrum widening and the C/I$_3$ level (11dB is the figure achieved for nearly-saturated amplifier), we obtain without filtering at SSPA output the levels of figure 4.1.2/C.

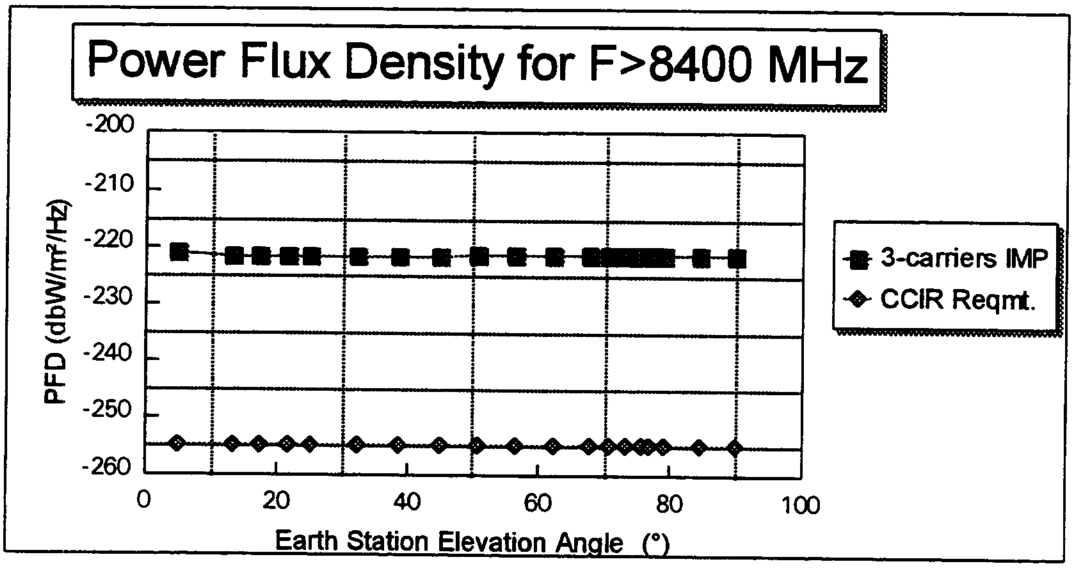

Figure 4.1.2/C : 3-carriers multiplex IMP

The out-of specification is around 34 dB regarding the level required by CCIR.

The compliance could be achieved :

* Either by increasing the C/I$_3$ ratio up to 45 dB;
* Or by putting a 34 dB attenuation filter at SSPA output;
* Or by changing the frequency plan to remove IMP's out of the 8400-8450 MHz band.

The information contained in this document is proprietary to ALCATEL ESPACE and shall not be disclosed by the recipient to third persons without the written consent of the company.
Les informations contenues dans ce document demeurent la propriété exclusive de ALCATEL ESPACE et ne doivent pas être divulguées par le destinataire à des tiers, sans l'accord de la société.

The information contained in thi) ent is proprietary to ALCATEL ESPACE and shall not be disclosed by the recipient to th. .rsons without the written consent of the company.

formations contenues dans ce document demeurent la propriété excl ALCATEL ESPACE doivent pas être divulguées par le destinataire à des tiers, sans l'accor. société.

4.1.2.2.2.Effects of IMP from PSK spectrum power components

This effect, analysed in annex 2.2, is produced when filter exists in front of the non-linearity.

Even with high attenuation filters, the out-of-spec remains around 20 dB (the secondary lobe is risen by 20 dB).

The compliance could be achieved :

* Either by increasing the C/I_3 ratio to cancel the IMP effect;
* Or by filtering at SSPA's output;
* Or by both actions.

A frequency plan shift towards lower frequencies gives some advantage by combining PSK spectrum components with lower RF powers (at least one component belonging to first secondary lobes).

4.1.2.2.3.On-board configurations

Five configurations are analysed more in detail :

- The first one consists in putting a band-pass filter (BPF) in front of each of the 3 BFN's, without aiming at CCIR conformity. These filters will be smooth ones (15 dB attenuation) in order to prevent from secondary lobes rise. In this case, there is an out-of spec. of around 28 dB w.r.t. CCIR recommendation for spectrum and 34 dB for IMP's (with C/I_3=11 dB). The harware impact is limited and simple since only a filter at each output of the 3 PSK modulators is needed.

- A second configuration has the same design as the first one except that the conformity to CCIR requirements is now guaranteed. It is done by operating the amplifiers in the linear zone with a high C/I_3 requirement (45 dB), and by using BPF's with 40 dB-attenuation at 8400 MHz and steep amplitude slope between 8325 and 8400 MHz.

- A third configuration uses also high attenuation filters located in front of the SSPA's . It is based on a C/I_3 ratio of 32 dB which is an intermediate value between the two previous ones and uses a modified frequency plan giving some improvement on IMP's (4 dB) . The proposed plan is 8100 MHz for channel 1, 8175 for channel 2 and 8250 for channel 3.

There is a reduced CCIR out-of-spec (around 16 dB) compared to config 1.

The information contained in this document is proprietary to ALCATEL ESPACE and shall not be disclosed by the recipient to third persons without the written consent of the company.

Les informations contenues dans ce document demeurent la propriété exclusive d'ALCATEL ESPACE et ne doivent pas être divulguées par le destinataire à des tiers, sans l'accord de la société.

The implemention of config. 1, 2 and 3 are shown on figure 4.1.2/D.

- The fourth and fifth configurations are based on implementation of a rejection filters at the output of each SSPA, along with three BPF's at the input of each BFN (to prevent from ACI degradations). They both guarantee the compliance with CCIR requirement.

For configuration 4, the modified frequency plan is proposed. The filtering function is shared : 24 dB in front of the BFN's and 13 dB behind the SSPA's; indeed 37 db is now required for spectrum filtering instead of 40 dB, the secondary lobes level being at -21 dB instead of -18 dB. A 28 dB C/I_3 ratio (17 dB improvement w.r.t. figure 4.1.2/C) is required to remove the 30-dB out-of-spec .

For configuration 5, we stick to the initial frequency plan. A 28 dB C/I_3 ratio (17 dB improvement w.r.t. figure 4.1.2/C) allows to remove the 34-dB out-of-spec. when associated with a a 17-dB rejection filter at SSPA's outputs. A 23 dB BPF is still needed at BFN's inputs.

Implementation of config. 4 and 5 is shown on figure 4.1.2/E

Remarks :

* Solution with Nyquist filters (or sub-optimal base-band filters) and adjacent channels should allow to satisfy CCIR requirements without extra-filtering within the 8400-8450 MHz range by removing the all the 3-carriers IMP's out of this band.

Nevertheless, we disregard this channel scheme since ESA do not intend to implement base-band filters.

* Solution with high rejection filters (40 dB) at SSPA's outputs is not considered for the design would be complex, the losses high and the accomodation difficult.

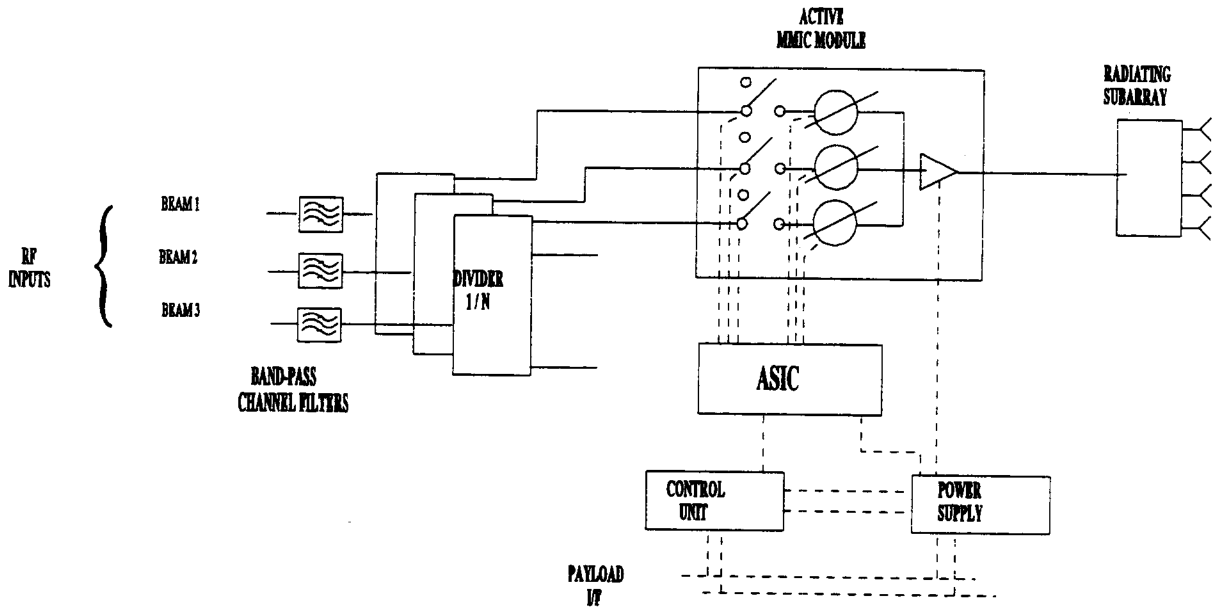

Figure 4.1.2/D : Configurations1, 2 and 3

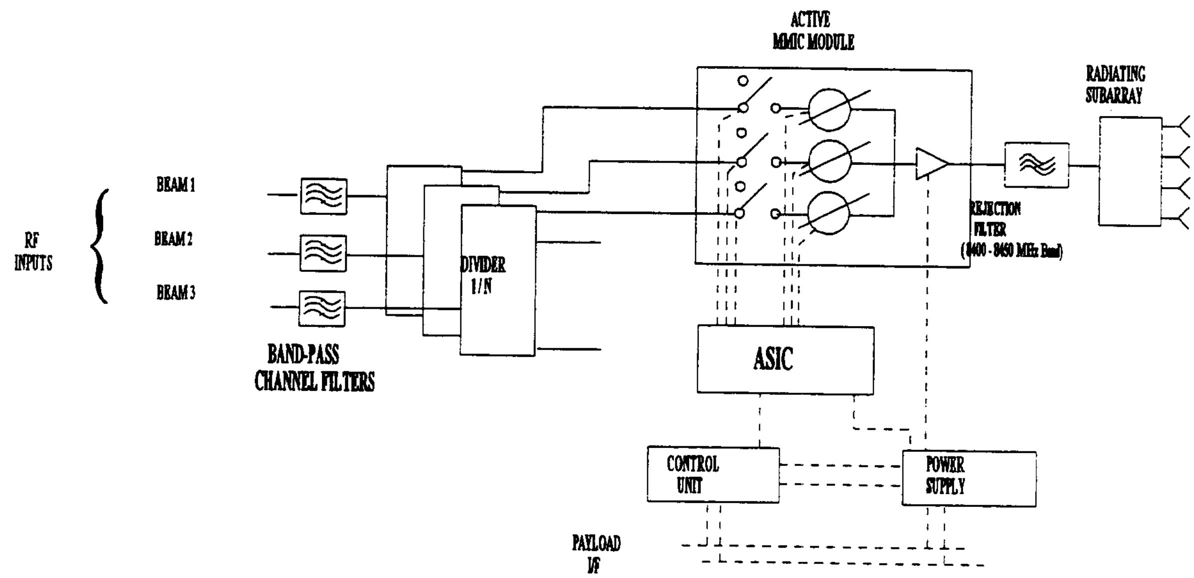

Figure 4.1.2/E : Configurations 4 and 5

The information contained in this document is proprietary to ALCATEL ESPACE and shall not be disclosed by the recipient to third persons without the written consent of the company.
Informations contenues dans ce document demeurent la propriété exclusive d'ALCATEL ESPACE. Elles ne doivent pas être divulguées par le destinataire à des tiers, sans l'accord de la société.

The information contained in this document is proprietary to ALCATEL ESPACE and shall not be disclosed by the recipient to third persons without the written consent of the company.
Les informations contenues dans ce document demeurent la propriété exclusive d'ALCATEL ESPACE et ne doivent pas être divulguées par le destinataire à des tiers, sans l'accord de la société.

4.2. Design trade-off

4.2.1. Definition of criteria

The following criteria are choosen in order to compare the different configurations :

- CCIR/UIT conformity;
- RF and link quality losses;
- Design complexity;
- Mass and on-board accomodation;
- Power consumption and dissipation;
- Frequency plan impact.

4.2.2. CCIR Conformity

Configurations 2, 4 and 5 are fully compliant while configurations 1 and 3 are not. It depends on mission analysis to judge if the non-conformance is really unacceptable.

4.2.3. RF and link quality losses

The best solution occurs when the following conditions are fullfilled :

* Absence of filters after the SSPA's and then no additional RF losses;
* Existence of a sufficiently stong channel filter in front of the BFN 's and then no truncation losses;
* Very low level of IMP and ACI falling in the adjacent channels and then reduction of link quality losses.

On the contrary, if one or several out of these conditions are not satisfied, the solutions are considered as less favourable.

The information contained in this document is proprietary to ALCATEL ESPACE and shall not be disclosed by the recipient to third persons without the written consent of the company.

Les informations contenues dans ce document demeurent la propriété exclusive d'ALCATEL ESPACE et ne peuvent pas être divulguées par le destinataire à des tiers, sans l'accord de la société.

The worst cases are obtained for configuration 4 with around 1.5 dB E_b/N_0 losses (ACI) and for configuration 5 with 0.5 dB minimum additional RF losses (with DRO or cavity filters technology) . The other three configurations have similar E_b/N_0 losses (< 1 dB) and negligible additional RF losses.

Principles for losses computation are given in annex 4.

4.2.4. Design complexity

Configurations without high attenuation filters and/or without large bandwidth filters and/or without significative on-ground impact are considered better than the others from design point of view.

Configurations with amplitude linearisers in front of the SSPA's are regarded as more complex.

4.2.5. Mass and on-board accomodation

The number of filters (32 for configurations 4 and 5, 3 for the others) along with the required technologies define the more or less favourable evaluation of the solutions.

Wide-band BPF's with 40 dB attenuation close to the RF channel typically have a mass of 0.1 Kg in « comb-line » or interdigital technology and 0.4 Kg with Invar cavity.

4.2.6. Power consumption and dissipation

As preliminary analysis, we take the assumptions of 30-35% efficiency of SSPA's when operating at compression and 10% when operating in linear zone ($C/I_3 \sim 45$ dB) [AD2] [AD3].

With an active antenna, the overall power consumption of typically 8 SSPA's is around 10 W at compression (0 dB Output Back-Off or OBO). For a semi-active one, this figure becomes around 13 W, assuming 32 SSPA's (*) operating in linear area (6 dB OBO).

The information contained in this document is proprietary to ALCATEL ESPACE and shall not be disclosed by the recipient to third persons without the written consent of the company.

Les informations contenues dans ce document demeurent la propriété exclusive d'ALCATEL ESPACE et ne doivent pas être divulguées par le destinataire à des tiers, sans l'accord de la société.

For an active antenna, the maximum power dissipation is around 6 W, concentrated on 8 among 32 SSPA's and then on 8 hot spots. For a semi-active one, the max. dissipated power is 11.5 W but splitted over 32 SSPA's.

For high C/I (40 dB or more) the benefit from lineariser is questionable but for C/I ratios around 25-30 dB, a significant improvement in term of efficiency can be expected.

We can obtain thanks to a lineariser a good C/I with a limited OBO (3 dB) and then still a high efficiency (25-30%). Such a circuit can be interesting for configurations 3, 4 and 5.

As an example, simulations were performed with COSSAP software in the frame of the french telecom. technological satellite, and gave an improvement of 10.5 dB on the C/I_3 ratio of a linearized-11Ghz-CAMP (from 18.7 dB to 29.2 dB with 3-dB OBO).

(*) The figure of 32 comes from Alcatel-Espace proposal [AD 2], but can be reviewed and decreased during the course of the study.

4.2.7. Frequency plan impact

Configurations without change on frequency plan are considered better as the others.

4.3. Trade-off results

The comparaison between the different configurations is shown on table 4.3.

The information contained in this document is proprietary to ALCATEL ESPACE and shall not be disclosed by the recipient to third persons without the written consent of the company.
Les informations contenues dans ce document demeurent la propriété exclusive de ALCATEL ESPACE et ne doivent pas être divulguées par le desinataire à des tiers, sans l'accord de la société.

	CCIR	Losses	Design	Mass Accomodation	Power Cons/Diss	Freq. Plan	Total
WEIGHT	2	1	1	1	1	1	
CONFIG. 1	– –	+	+	+	+	+	+ 1
CONFIG. 2	+	+	– –	+	– –	+	+ 1
CONFIG. 3	–	+	=	+	=	–	- 1
CONFIG. 4	+	=	–	–	+	–	0
CONFIG 5	+	=	–	–	+	+	+ 2

Table 4.3 : Trade-off results

The configuration 5 appears to be ahead and is considered as the baseline solution. It is based on three filters in front of the BFN's and extra rejection filters are added at SSPA's outputs. This rejection filter will be designed by CASA during WP 2500 activities.

Among the configurations 1 and 2, the solution 2 is preferred as an option for two reasons :

1- It allows to meet the CCIR requirements even if the design feasibility has to be checked more in detail.

2- In case of 5-10 dB relaxation of these requirements this solution becomes more attractive since it can reduce the design constraints on C/I level, main drawback of this solution.

The information contained in this document is proprietary to ALCATEL ESPACE and shall not be disclosed by the recipient to third persons without the written consent of the company.

...rmations contenues dans ce document demeurent la propriété exclusive d'ALCATEL ESPACE et ne doivent pas être divulguées par le destinataire à des tiers, sans l'accord de la société.

5. ANTENNA REQUIREMENTS SPECIFICATION

5.1. Antenna modes

The antenna shall transmit, from LEO satellites to the ground, three simultaneously beams carrying high rate digital data provided by earth observation instruments.

There is no receive mode for the antenna.

5.2. Frequency band

The allocated frequency bandwidth shall be the X-band within the 8025-8400 MHz range.

Each beam takes one channel and the three carriers frequencies are :

* 8100, 8200 and 8300 MHz.

Each carrier is PSK-modulated and the information rate is 50 Mbauds. The relevant channel bandwidth (Nyquist one) is 50 MHz.

5.3. Polarisation

The antenna polarisation shall be RHCP (Refer to « IEEE Standard Definition of Terms for Antennas » : IEEE Standard 145).

The maximum axial ratio over the whole antenna coverage shall be less than 1.5 (or 3.5 dB).

5.4. Field of view

The antenna field of view shall be :

* 0-360° in azimut (ϕ angle);
* 0-63° in elevation (θ angle).

The 0° antenna reference angle is defined as the antenna axis of revolution for each beam.

The information contained in this document is proprietary to ALCATEL ESPACE and shall not be disclosed by the recipient to third persons without the written consent of the company.
Les informations contenues dans ce document demeurent la propriété exclusive d'ALCATEL ESPACE et ne doivent pas être divulguées par le destinataire à des tiers, sans l'accord de la société.

The requirement is for continuous beam while scanning.

5.5. Minimum Gain

The minimum gain at 62.3° elevation shall be higher than 20 dBi.

5.6. EIRP

The minimum and maximum EIRP per channel versus the off-nadir antenna angle is given on figure 5.6/A. It is computed according to the document [AD1] and it takes into account the assumptions of paragraph 3.1.

The requirement is for uniform power flux density on earth's surface in the beam pointing direction within the coverage area.

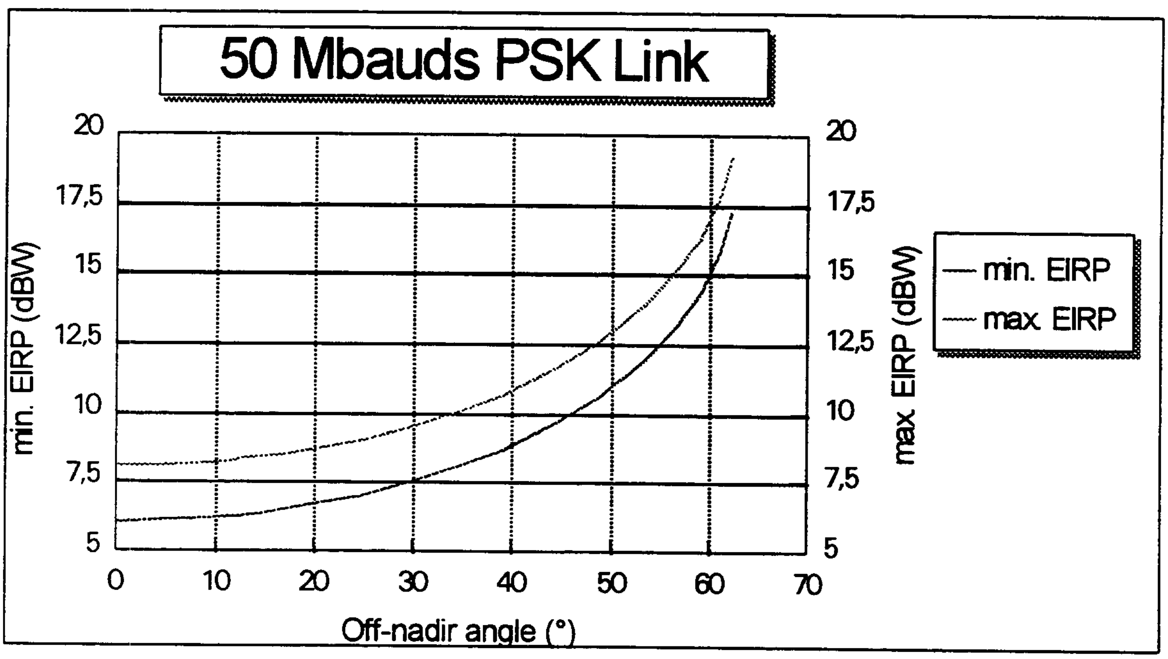

Figure 5.6/A : EIRP per Channel

The information contained in this document is proprietary to ALCATEL ESPACE and shall not be disclosed by the recipient to third persons without the written consent of the company.

Les informations contenues dans ce document demeurent la propriété exclusive d'ALCATEL ESPACE et ne doivent pas être divulguées par le destinataire à des tiers, sans l'accord de la société.

5.7. Link quality requirements

5.7.1. Phase and amplitude jumps during scanning

The maximum phase and amplitude jumps are 3° and ± 0.3 dB. These figures shall be considered as design goals, but higher figures could be proposed by Alcatel-Espace (typically 10° and ± 1 dB) without significant BER performances degradation.

The scan rate of the antenna is 1°/sec.

5.7.2. IMP effects

The C/I_3 ratio shall be higher than 28 dB for the baseline configuration (typical OBO of 3 dB).

The C/I_3 ratio shall be within the 35-45 dB range for the optional configuration (typical OBO between 6 and 8 dB).

5.8. Out-of-band filtering requirements

5.8.1. Baseline configuration

Each channel filter shall have a 3-dB bandwidth of 100 Mhz.

The amplitude losses, within ± 25 MHz around each carrier frequency, shall be lower than 0.4 dB. The group delay variation shall be lower than 3 ns within ± 25 MHz around each carrier frequency.

The information contained in this document is proprietary to ALCATEL ESPACE and shall not be disclosed by the recipient to third persons without the written consent of the company.
Les informations contenues dans ce document demeurent la propriété exclusive de ALCATEL ESPACE et ne doivent pas être divulguées par le destinataire à des tiers, sans l'accord de la société.

The global amplitude attenuation of the filter between 8400 and 8450 MHz shall be higher than 37 dB. This filtering scheme will be shared between BPF's in front of the BFN's and rejection filters behind each SSPA.

The filters masks are shown on figures 5.8/A and 5.8/B.

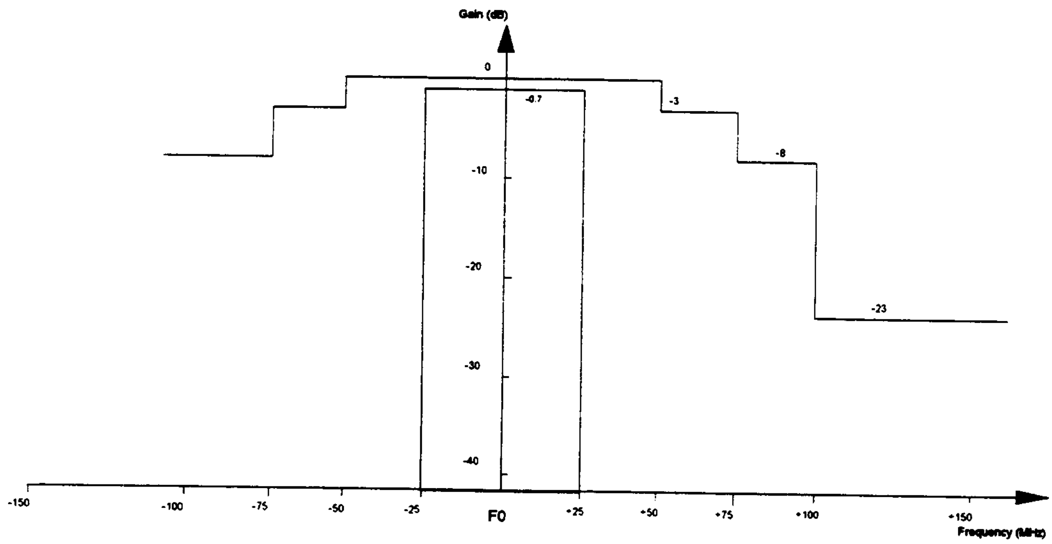

Figure 5.8/A : BPF amplitude mask

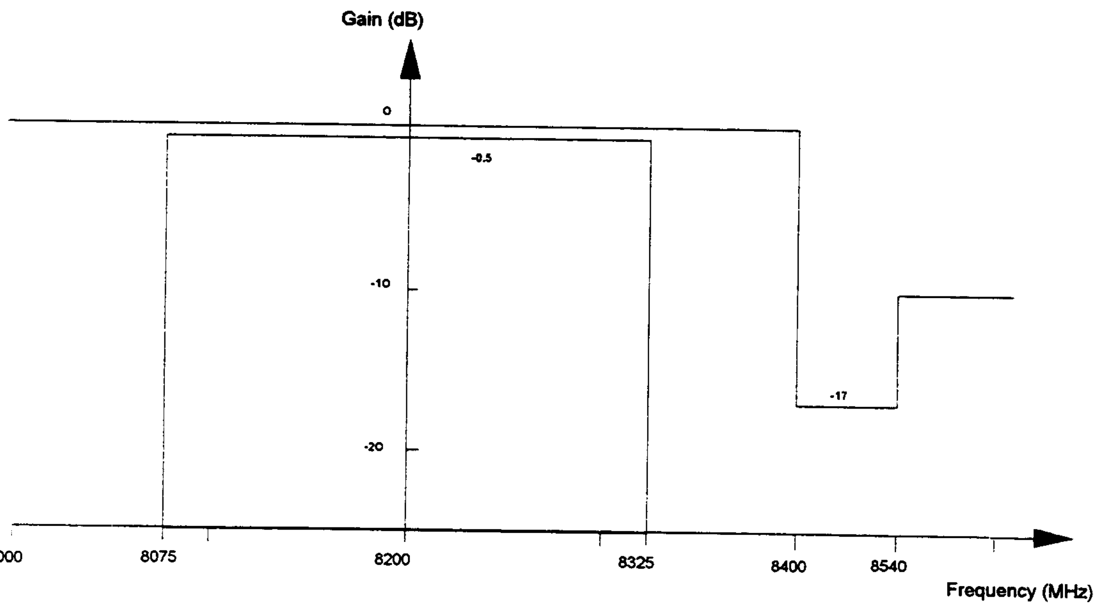

Figure 5.8/B : Rejection filter amplitude mask

The information contained in this document is proprietary to ALCATEL ESPACE and shall not be disclosed by the recipient to third persons without the written consent of the company.
Les informations contenues dans ce document demeurent la propriété exclusive d'ALCATEL ESPACE et ne doivent pas être divulguées par le destinataire à des tiers, sans l'accord de la société.

5.8.2. Optional configuration

Each channel filter shall have a 3-dB bandwidth of 100 Mhz.

The amplitude losses, within ± 25 MHz around each carrier frequency, shall be lower than 0.4 dB. The group delay variation shall be lower than 3 ns within ± 25 MHz around each carrier frequency.

The amplitude attenuation mask is given on figure 5.8/C.

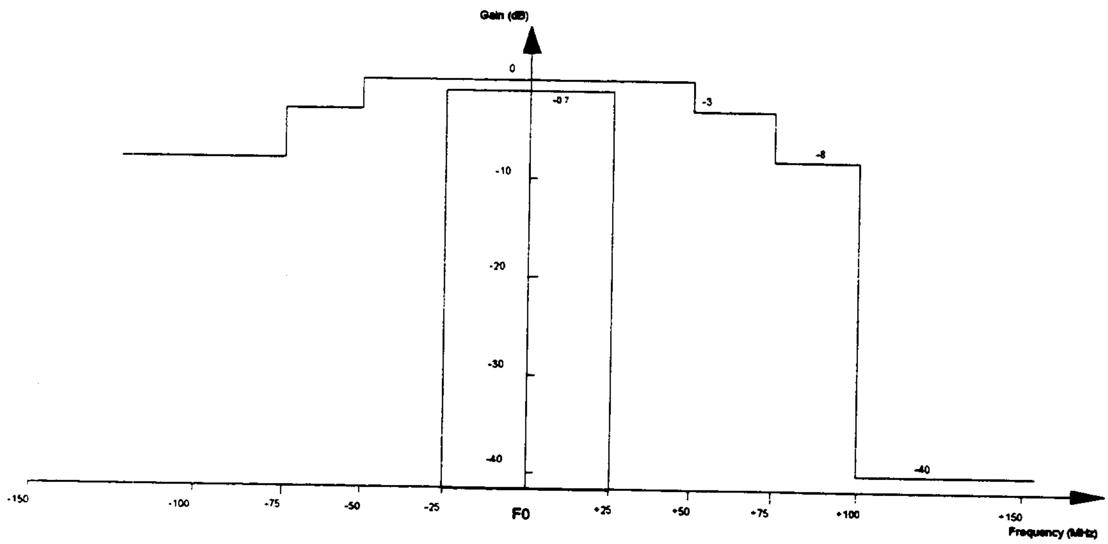

Figure 5.8/C : BPF amplitude mask

5.9. Other specifications

- The input V.S.W.R. at the antenna interface shall be less than 1.5.
- The overall antenna mass shall be less than 20 Kg.
- Thermal conditions : -150°/+150° for the external equipment (TBC by thermal analysis in WP 2600);

  -20°/+40° for the internal equipment.
- Environmental conditions : ESD free (all the exposed surfaces are conductive).

The information contained in this document is proprietary to ALCATEL ESPACE and shall not be disclosed by the recipient to third persons without the written consent of the company.
Les informations contenues dans ce document demeurent la propriété exclusive de ALCATEL ESPACE et ne doivent pas être divulguées par le destinataire à des tiers, sans l'accord de la société.

6. CONCLUSION

The main conclusions of the RF system analysis are :

1- With the current frequency plan, i.e. channel 1 at 8100 MHz, channel 2 at 8200 and channel 3 at 8300, it is not easy for the active or semi-active antenna to meet the UIT/CCIR out-of-band requirements. Solutions would induce more complex design either with steep band-pass filters and linearizers before the amplifiers, or with a great number of high rejection filters at SSPA's outputs.

2- By slight modification of the frequency plan, i.e. channel 1 at 8100 MHz, channel 2 at 8175 and channel 3 at 8250, the filtering constraints could be released and it could make easier the conformity status regarding the UIT/CCIR requirements. Nevertheless, such a design is not proposed in this study since ESA/ESTEC prefer to keep the current frequency plan in order not to restrict the allocated band utilization.

3- A third frequency plan with Nyquist adjacent channels (8050, 8118.5 and 8187 Mhz) would be interesting to investigate since both IMP's and ACI's could be removed by using only base-band Nyquist filters. However, mismatch losses between on-board and on-ground filters can increase with such non-linear channels and it is out of scope of this study to cover this channel filtering concept whose performances can only be assessed by simulation.

The information contained in this document is proprietary to ALCATEL ESPACE and shall not be disclosed by the recipient to third persons without the written consent of the company.

Les informations contenues dans ce document demeurent la propriété exclusive d'ALCATEL ESPACE et ne doivent pas être divulguées par le destinataire à des tiers, sans l'accord de la société.

7. ANNEX

7.1. Annex 1 : RF Power Computations with NRZ/PSK spectrum

The power spectrum of a NRZ/PSK modulated signal is a square cardinal sine function centered on the carrier frequency. Its form is $[\sin(\pi*x)/(\pi*x)]^2$, x being the variable, product of the frequency f by the inverse of the information rate 1/R.

On figures 7.1/A, 7.1/B and 7.1/C, is computed the percentage of power versus the variable x.

Without any filtering, concentration of 99% of the power is achieved for x=10 i.e. f/R = 10; then the total occupied frequency band is equal to 2*f.

The allocated channel bandwidth being 2*f, a 50 Mbauds information rate would require $2*10*50*10^6$ = 1000 MHz bandwidth; on other words, a maximum allocated band of 375 Mhz as it is at X-band allows a maximum rate of 18.75 Mbauds.

We conclude that filtering is required when information rate is higher than 18.75 Mbauds.

Here we have three channels, 50 Mbauds each.

For channel 1 at 8100 Mhz, about 3.5% of the power is located below 8025 Mhz and then a filter with 6 dB attenuation at the corner frequency is sufficient to comply with CCIR spectral occupancy rules. Indeed we have the result $(0.965*P)/(0.035*P/10^{6/10})$ > required 99%.

For channel 2, 3 dB attenuation on both limits (8025 and 8400 Mhz) is enough and for channel 3, 5 dB attenuation at 8400 Mhz corner frequency is required.

To summarize, a gauge as shown here-below (figure 7.1/0) has to be applied on each channel in order to satisfy the bandwidth occupancy requirement (99% of total power).

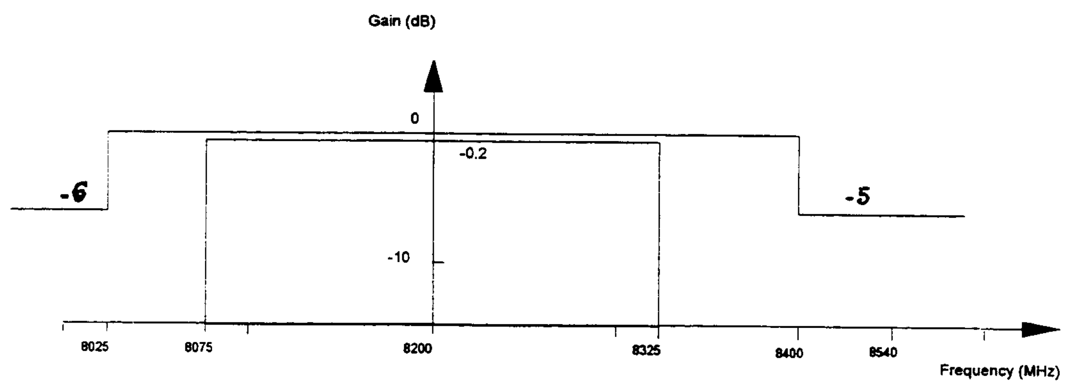

Figure 7.1/0 : bandwidth occupancy requirement

ALCATEL ESPACE	Conformal array Antenna	REF: ATES 96 005003SCS0017		
		DATE : 23/02/96	ED / REV : 1/A	PAGE : 31

The information contained in t ument is proprietary to ALCATEL ESPACE and shall not be disclosed by the recipient t persons without the written consent of the company.

Les informations contenues dans ce document demeurent la propriété exc d'ALCATEL ESPACE doivent pas être divulguées par le destinataire à des tiers, sans l'ac la société.

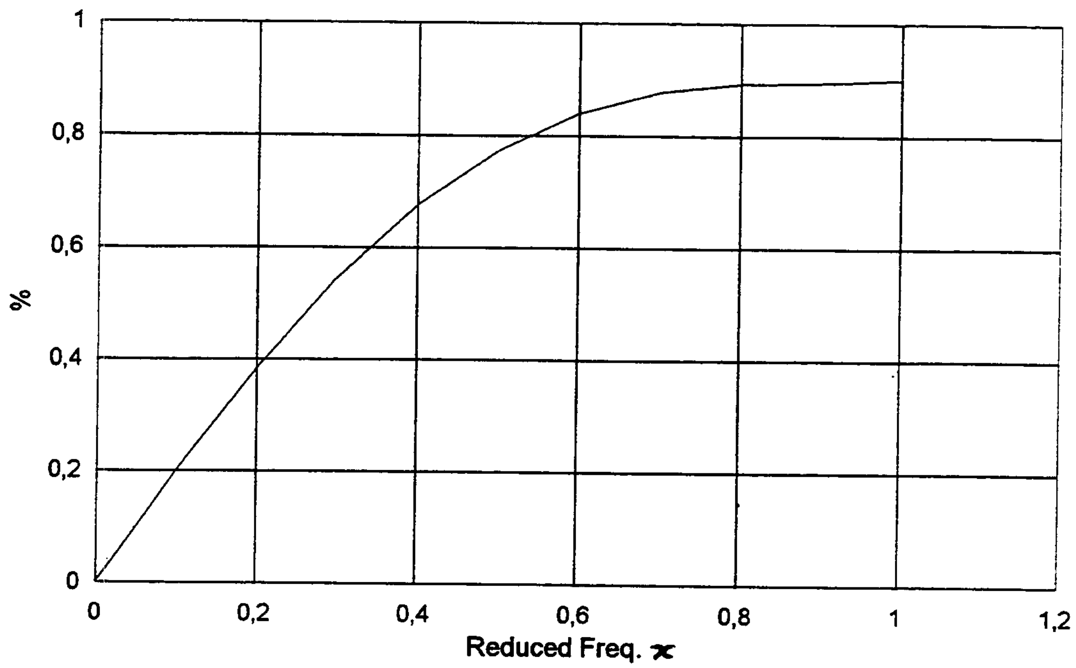

Figure 7.1/A : power integrated within [-x,+x] upon total power versus x

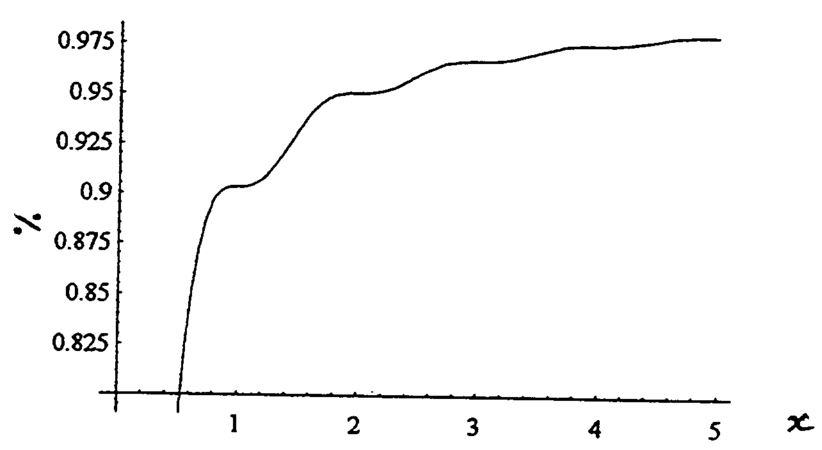

Figure 7.1/B : power integrated within [-x,+x] upon total power versus x

The information contained in this document is proprietary to ALCATEL ESPACE and shall not be disclosed by the recipient to persons without the written consent of the company.

Les informations contenues dans ce document demeurent la propriété exclusive d'ALCATEL ESPACE et ne doivent pas être divulguées par le destinataire à des tiers, sans l'accord de la société.

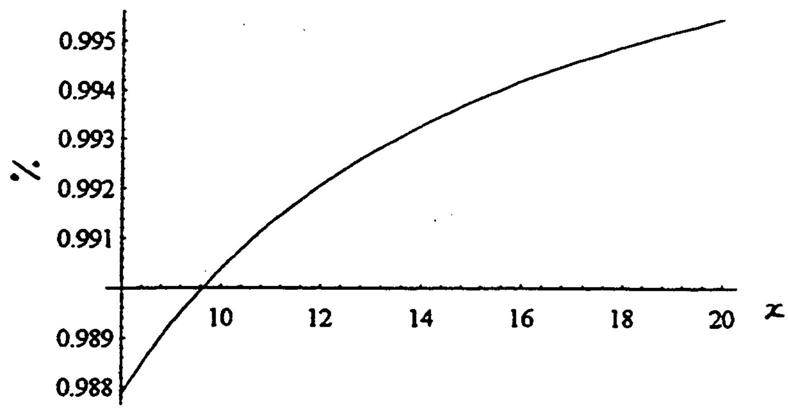

Figure 7.1/C : power integrated within [-x,+x] upon total power versus x

The information contained in this document is proprietary to ALCATEL ESPACE and shall not be disclosed by the recipient to third persons without the written consent of the company.

Les informations contenues dans ce document demeurent la propriété exclusive d'ALCATEL ESPACE et ne doivent pas être divulguées par le destinataire à des tiers, sans l'accord de la société.

7.2. Annex 2

7.2.1. Annex 2.1 : non-linear effects computation

On figure 7.2/A, we represent the PSK spectrum for one channel. We can see that the -6dB attenuation required without non-linearity takes place at different frequencies according to the channel number.

The most critical impact of non-linearity is obviously on the channel 1, the closest from 8025 MHz, lower limit of the frequency band. Indeed, it is only for this channel that we can have IMP's between spectral components of the main lobe. For the other 2 channels, the IMP's are very low since they result from combination of secondary lobes with a very little percentage of power.

So, for channel 1, we have the following combinations of powers components falling in the first secondary lobe below -75 MHz :

- one combination within the main lobe (2 parts accounting each for 10/15% of total power);
- combinations between main lobe and first secondary lobes.

With a C/I_3 ratio of 11 dB, we obtain for these combinations a level of - 33 dB. When combining this level with the power within the secondary lobe attenuated by 6 dB, we have to sum up - 33 dB and -20-6 = -26 dB; it gives a resulting level of -25 and then an extra attenuation of 1 dB is required for the filter.

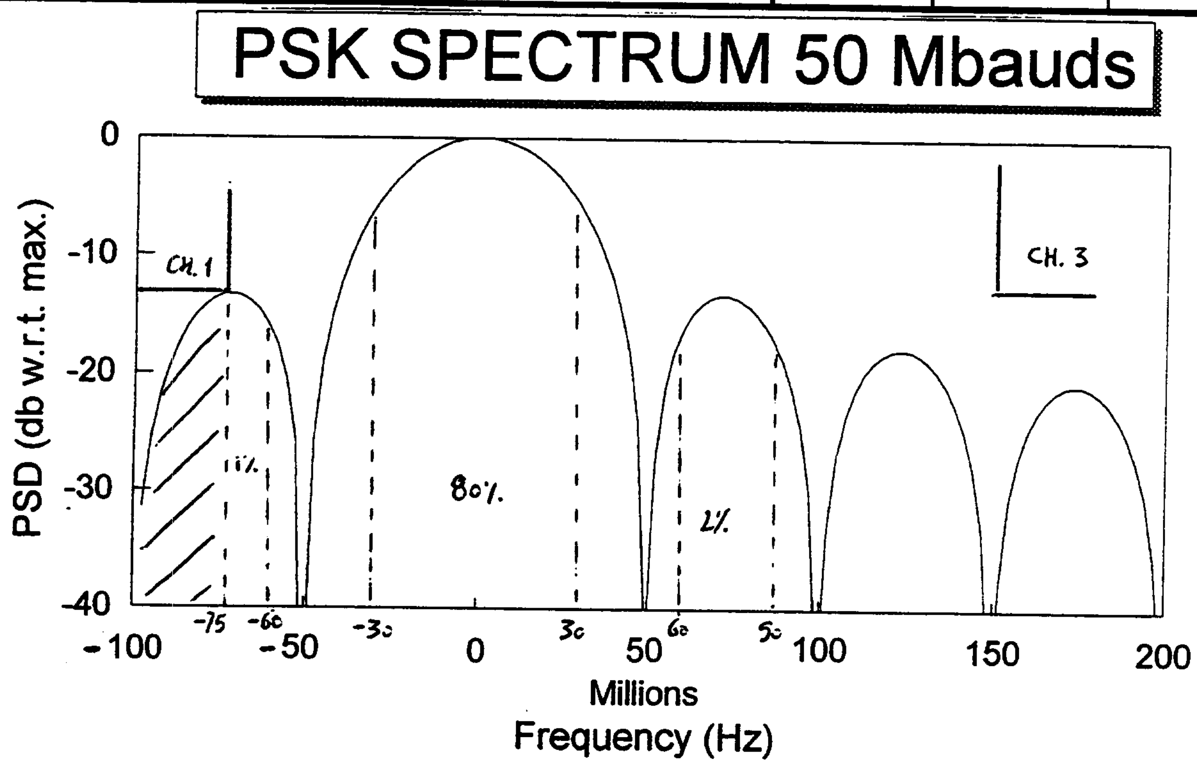

Figure 7.2/A : IMP on first secondary lobe

7.2.2. Annex 2.2 : analysis and simulations results

As an example of N-L effects, we show on figures 7.2/B and 7.2/C simulation results giving the secondary lobes level increase when a PSK-modulated-filtered signal go through an amplitude non-linearity. These simulations demonstrated that the pre-amplification filters become less and less efficient when their out-of-band attenuation increases.

Indeed, on figure 7.2/B, the spectrum is centered on 8250 MHz, and the information rate is the same as for our application. It can be seen that the filter efficiency, when this filter is located in front of the N-L, is reduced by some tens of dB. On the contrary, with a filter whose attenuation is now 20 dB at 8400 MHz (figure 7.2/C), the non-linearity does not degrade more than 3-6 dB the efficiency.

In our application, the centre frequency is 8300 MHz and we can estimate on figure 7.2/B that, by using a high attenuation filter, its efficiency decreases from 40 to 20 dB in the 100-150 MHz range far from the carrier (relevant to DSN band).

The information contained in this document is proprietary to ALCATEL ESPACE and shall not be disclosed by the recipient to third persons without the written consent of the company.
Les informations contenues dans ce document demeurent la propriété exclusive d'ALCATEL ESPACE et ne peuvent pas être divulguées par le destinataire à des tiers, sans l'accord préalable de la société.

The information contained in this document is proprietary to ALCATEL ESPACE and shall not be disclosed by the recipient to persons without the written consent of the company.

Informations contenues dans ce document demeurent la propriété exclusive d'ALCATEL ESPACE doivent pas être divulguées par le destinataire à des tiers, sans l'accord de la société.

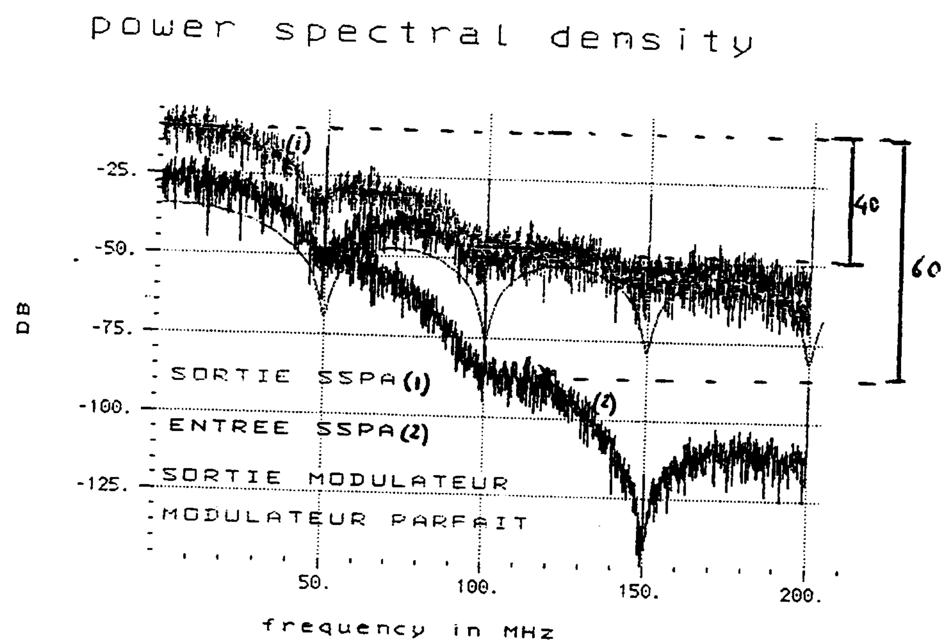

Figure 7.2/B : Simulation for high attenuation BPF

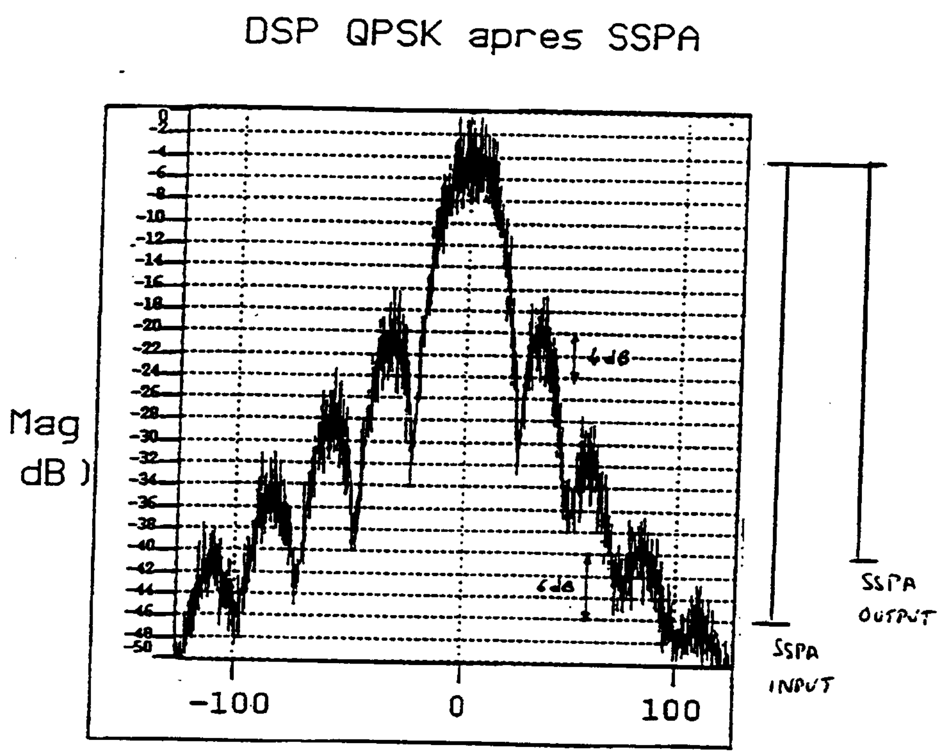

Figure 7.2/C : simulation for low attenuation BPF

The information contained in this document is proprietary to ALCATEL ESPACE and shall not be disclosed by the recipient to third persons without the written consent of the company.
Les informations contenues dans ce document demeurent la propriété exclusive d'ALCATEL ESPACE. Elles ne doivent pas être divulguées par le destinataire à des tiers, sans l'accord de la société.

By rough computations, we can get figures whose range of magnitude is quite similar to the one provided by simulations. It can also explain the differences regarding the BPF's out-of-band attenuation.

Indeed, if we analyse the spectrum components combination, we have different spectral components falling within the 8400-8450 MHz band :

- one IMP due to main lobe frequencies ($2*f_1-f_2$ form);
- two IMP's due to main lobe and first secondary lobe mixing ($2*f_1-f_2$ form);
- four IMP's due main lobe and first secondary lobe mixing ($f_1+f_2-f_3$ form).

Schemas and computations here-below (figure 7.2/D) show examples of these IMP power combinations.

In case of strong filters ($A_1 \approx 10$ dB), it can be seen that individual levels for each IMP is around -50 dB; rms summed it gives around -40 dB higher by 20 dB than the filtered power.

In case of smooth filters ($A_1 \approx 5$ dB), the individual levels of each IMP is around -45 dB or -36 dB rms summed, and the filtered power is at -36 dB.

If we change the frequency plan, as proposed, we can remove some IMP's and a filter having 40 dB attenuation becomes 30 dB after passing through the N-L.

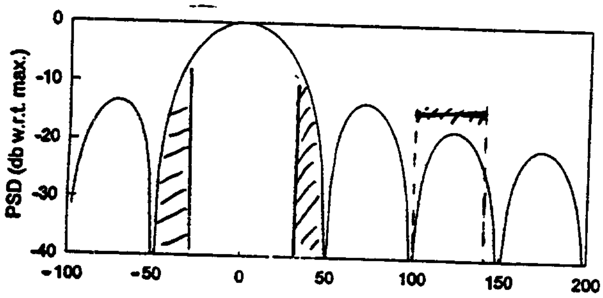

IMP level ~ -47-A_0 dB

A = Filter attenuation

* A_0= main lobe (0 dB)
* A_1= first secondary lobe

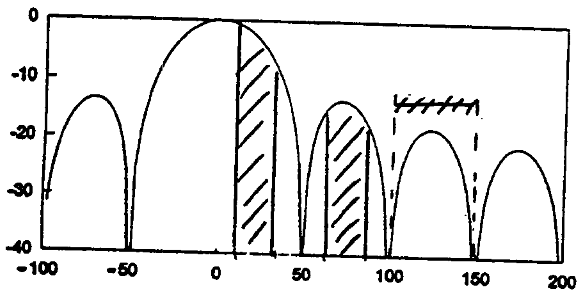

IMP level ~ -36-A_1 dB

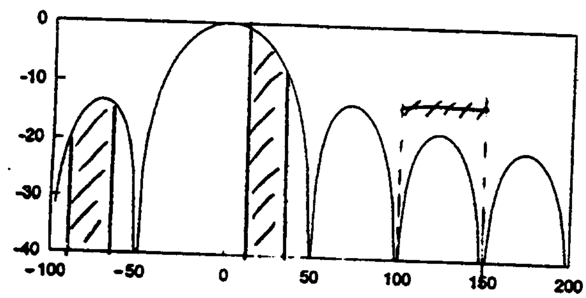

IMP level ~ -37.5-A_1 dB

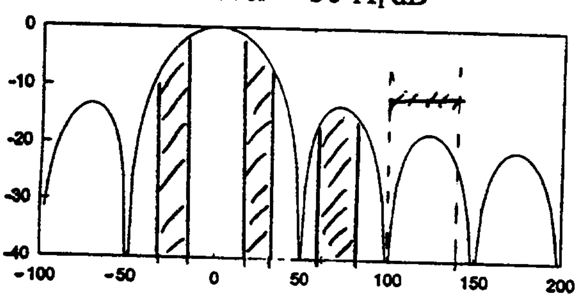

IMP level ~ -48-A_1 dB

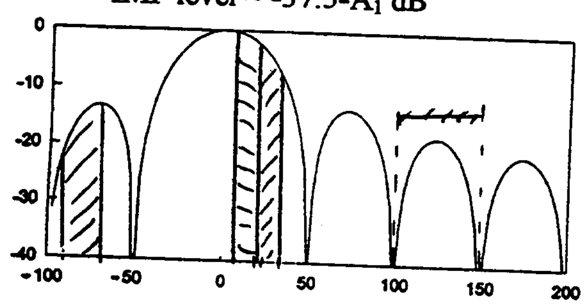

IMP level ~ -46-A_1 dB

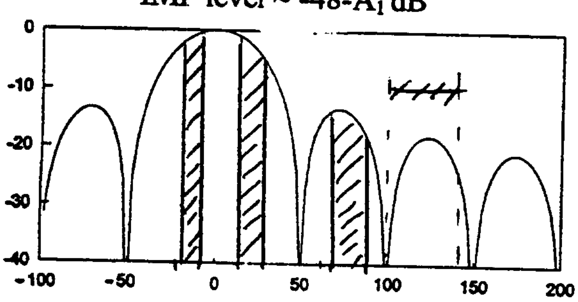

IMP level ~ -46-A_1 dB

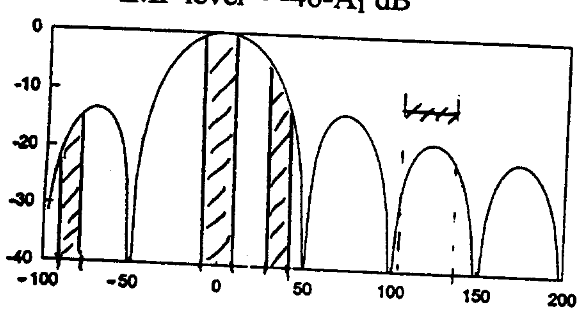

IMP level ~ -49-A_1 dB

Figure 7.2/D : power contributions producing IMP within 8400-8450 MHz band

The information contained in th[is doc]ument is proprietary to ALCATEL ESPACE and shall not be disclosed by the recipient to [p]ersons without the written consent of the company.

Les informations contenues dans ce document demeurent la propriété exclusive d'ALCATEL ESPACE [et ne] doivent pas être divulguées par le destinataire à des tiers, sans l'acco[rd de] la société.

The information contained in this document is proprietary to ALCATEL ESPACE and shall not be disclosed by the recipient to third persons without the written consent of the company.

Les informations contenues dans ce document demeurent la propriété exclusive d'ALCATEL ESPACE et ne doivent pas être divulguées par le destinataire à des tiers, sans l'accord de la société.

7.3. Annex 3 : Power Flux Computations

NRZ/QPSK-modulated carrier exhibits a power spectral density whose expression is as follows :

$PSD(f - f_0) = (A^2/2) * T_s * (\sin u/u)^2$, with $u = \pi * (f - f_0) * T_s$

A amplitude of transmitted signal;

T_s symbol duration (= inverse of information rate in Mbauds).

f_0 carrier frequency.

The EIRP is the intégral of the PSD over the whole signal spectrum :

$EIRP = \int PSD(f - f_0)\, df = A^2/2$ and then $PSD(f - f_0) = (EIRP) * T_s * (\sin u/u)^2$

The RF transmitted power integrated within a frequency band B, at $f_1 - f_0$ from the carrier, has the following expression :

$Pe = (EIRP) * T_s * (\sin u_1/u_1)^2$, avec $u_1 = \pi * (f_1 - f_0) * T_s$

The surfacic power on-ground Ps integrated in B, with atmospheric attenuation aqual to zero (worst case) is :

$Ps = Pe * B / 4 / \pi / D^2$, D earth to satellite range.

And considering the real satellite EIRP, we get :

$Ps = (EIRP)_{real.} * T_s * B * (\sin u_1/u_1)^2 / (4 * \pi * D^2)$

$(\sin u_1/u_1)^2$ accounts for the attenuation in B (around f_1) w.r.t. the maximum power density at f_0.

With on-board filtering, the previous expression has to be multiplied by the transfer function of the filter $TF(f_1 - f_0)$.

The information contained in this document is proprietary to ALCATEL ESPACE and shall not be disclosed by the recipient to third persons without the written consent of the company.
Les informations contenues dans ce document demeurent la propriété exclusive d'ALCATEL ESPACE. Elles ne doivent pas être divulguées par le destinataire à des tiers, sans l'accord de la société.

7.4. Annex 4 : link quality effects

7.4.1. IMP analysis

The computation of the IMP's power is performed by taking into account :

- The percentage of power concentrated within the Nyquist bandwidth of each channel (worst case channel).
- The frequency spreading of the IMP's power (=3 times the Nyquist channel bandwidth for third-order products).
- The C/I_3 ratio.

Nine third-order IMP's are spurring both DSN band and comms adjacent channels :
$2*f_2-f_3$ (1) ; $2*f_3-f_2$ (2) ; $2*f_1-f_2$ (3) ; $2*f_2-f_1$ (4) ; $2*f_1-f_3$ (5) ; $2*f_3-f_1$ (6) ;
$f_1+f_2-f_3$ (7) ; $f_1+f_3-f_2$ (8) ; $f_2+f_3-f_1$ (9).

Figure 7.4/A describes the spectral occupancy of the 3-carriers third-order IMP's for the current frequency plan (so-called P_0) : 8100, 8200, 8300 MHz.

On figures 7.4/B, IMP's description is given for proposed modified frequency plan (so-called P_1), i.e. 8100, 8175, 8250 MHz.

Finally figure 7.4/C shows a frequency plan (P_2 for 8050, 8118.75, 8187.5 MHz) with quite-adjacent channels, but without any interference within the DSN bandwidth.

With P_0 , there are 3 IMP's, (2), (6), (9), spurring the DSN band; for 2 of them only 1/3 of their power falls in this band, and for 1 of them only 1/6. So, 5/54 of the total IMP power is located inside the DSN band. Concerning IMP within adjacent channels, in worst case 2/54 of the total IMP power is concentrated in the DSN band.

With P_1, the ratios are 1/27 within DSN band and 5/54 in worst case within adjacent channels.

The information contained in this document is proprietary to ALCATEL ESPACE and shall not be disclosed by the recipient to third persons without the written consent of the company.
Les informations contenues dans ce document demeurent la propriété exclusive d'ALCATEL ESPACE et ne doivent pas être divulguées par le destinataire à des tiers, sans l'accord de la société.

With P2, there are only interferences within adjacen channels (1/9 ratio in worst case).

Then the degradation affecting the E_b/N_0 ratio is computed by adding the thermal noise PSD and the IMP PSD. E_b/N_0 = 17 dB in our case :

$$(E_b/N_0)_{Total} = 1/[10^{-(C/I)/10} + 10^{-(Eb/N0)/10}]$$

Baseline : 0.6 dB.

Option : 0.1 dB.

7.4.2. ACI analysis

The ACI's are computed by taking in account :

1 - The percentage of adjacent channel falling in the considered channel (its Nyquist bandwidth) : worst case is channel 2. With current freq. plan this power accounts for 2% (1% from each adjacent channel).

2 - The BPF attenuation at the edge of Nyquist bandwidth.

Then the degradation affecting the E_b/N_0 ratio is computed by adding the thermal noise PSD and the ACI PSD.

Baseline : 0.6 dB (8 dB filter).

Option : 0.6 dB.

7.4.3. Summation IMP+ACI

We perform a rms sum between IMP, ACI and on-ground thermal noise.

For the baseline, we get 0.84 dB and for the option 0.6 dB.

ALCATEL ESPACE	Conformal array Antenna	REF: ATES 96 005003SCS0017		
		DATE : 23/02/96	ED / REV : 1/A	PAGE : 41

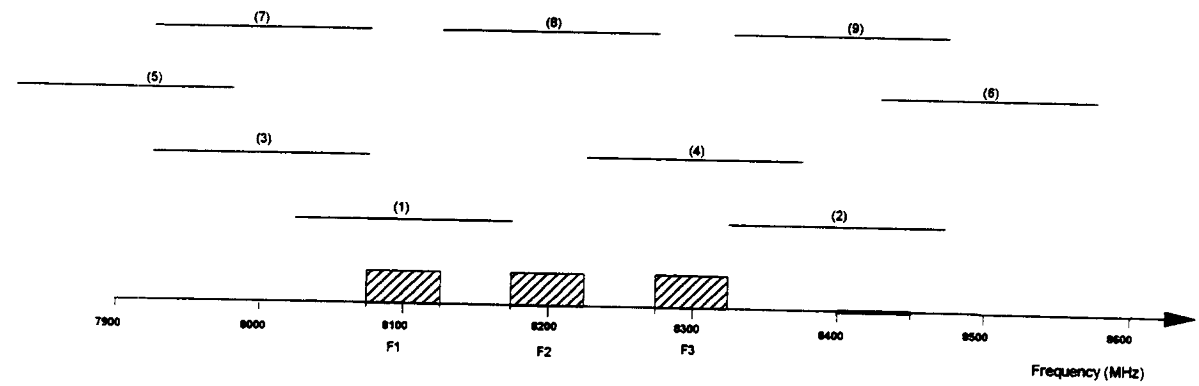

Figure 7.4/A : IMP's description with P_0 current frequency plan

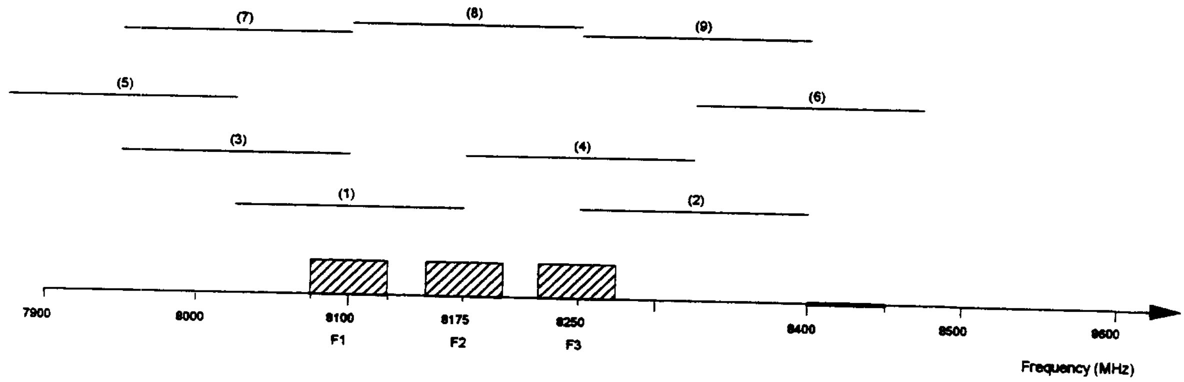

Figure 7.4/B : IMP's description with P_1 modified frequency plan

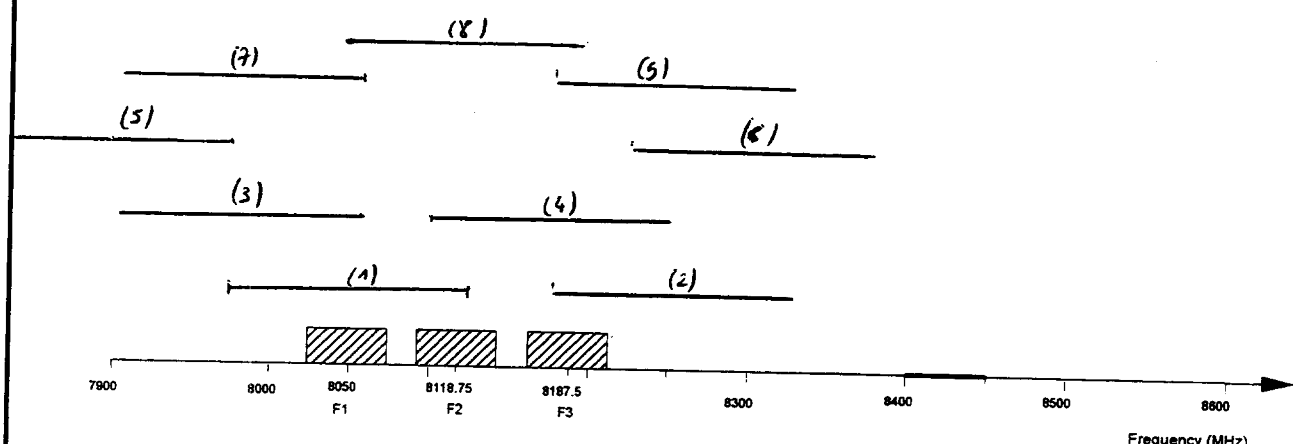

Figure 7.4/C : IMP's description with P_2 modified frequency plan

The information contained in this ...ent is proprietary to ALCATEL ESPACE and shall not be disclosed by the recipient to th... ...rsons without the written consent of the company.
...formations contenues dans ce document demeurent la propriété excl... ALCATEL ESPACE ...doivent pas être divulguées par le destinataire à des tiers, sans l'accor... société.

The information contained in this document is proprietary to ALCATEL ESPACE and shall not be disclosed by the recipient to third persons without the written consent of the company.
Les informations contenues dans ce document demeurent la propriété exclusive d'ALCATEL ESPACE. Elles ne doivent pas être divulguées par le destinataire à des tiers, sans l'accord de la société.

7.4.4. Transmitter thermal noise

The transmitter thermal noise includes :
- The contribution from PSK modulator;
- The contribution of SSPA noise figure.

Assuming a noise power spectral density of -160 dBm/Hz at modulator output, and RF losses of 30 dB between the modulator output and the SSPA input (RF splitter, cables, atten., phase shifters, etc), we have a level of noise PSD equal to -190 dbm/Hz at SSPA input.
Concerning the SSPA itself (noise figure 10 dB), we get -164 dBm/Hz noise PSD.

With a typical modulator output level of 0 dBm, the S/N ratio at SSPA output is 40 dB within 2 GHz bandwidth (SSPA pass-band), imputable to the SSPA noise. In order to make totally negligible the transmitter noise contribution to the link degradation, a way to improve this ratio is to put a 20 dB amplifier at the BFN input. Then the signal to noise ratio at SSPA output becomes around 60 dB.

CONFORMAL ARRAY

CHAPTER 3

TRADE-OFF BETWEEN CONCEPTS AND PRELIMINARY RF DESIGN

(WP 1200)

Reproduction interdite © ALCATEL ESPACE Reproduction forbidden

CHAPTER 3

Titre / Title
TRADE-OFF BETWEEN CONCEPTS **AND** **PRELIMINARY RF DESIGN (WP 1200)**

Rédigé par / Written by	*Responsabilité / Responsability*	*Date*	*Signature*
VOURCH Eric	Antenna Study Engineer	19/06/96	
Approbation / Approved			
CAILLE Gérard	Technical Manager of the study	21/6/96	
DURET Gilles	Head of Space Antenna Department	24/6/96	

The ...mation contained in this document is proprietary to ALCATEL ESPA... shall not be ...ed by the recipient to third persons without the written consent of the ...y

Les info... ...s contenues dans ce document demeurent propriété exclusive d'ALCA... ESPACE et ne d... être divulguées par le destinataire à des tiers sans l'accord écrit de ...

The information contained in this document is proprietary to ALCATEL ESPACE, shall not be disclosed by the recipient to third persons without the written consent of the company

Les informations contenues dans ce document demeurent propriété exclusive d'ALCATEL ESPACE et ne doivent pas être divulguées par le destinataire à des tiers sans l'accord écrit de la société.

TABLE OF CONTENTS

I INTRODUCTION

The objectives of this preliminary study (WP1200) are to determine the complete geometry of the truncated conical antenna and then to analyse which concept (among passive, active and semi-active concepts) is more suited to reach the specifications of the mission.

A preliminary trade-off has been made in our proposal, which have shown that the passive concept has main drawbacks. So in the following analysis, only active and semi-active concepts will be detailed.

The outputs of task 1200 will be:

- the geometry of the antenna (cone angle, elementary radiator, number of patches in a column, number of total column in the whole antenna)
- a trade-off between <u>the active concept</u> developed for CNES contract (and extended to a three beam generation) and <u>a semi-active concept</u> based on the use of BUTLER matrixes.

II TECHNICAL SPECIFICATIONS

The technical specifications of the antenna are summarised in the table of fig. II-a.

Parameter	*Specifications*
Orbit	800 Kms
Antenna modes	Tx only 3 simultaneous beams
Frequency band	8025 - 8400 MHz (each beam has a 3-dB bandwidth of 100 Mhz) The three carriers frequency are 8100, 8200 and 8300 MHz
Polarisation / Axial Ratio (within 5° of the pointing direction)	Circular (right hand); A.R < 1.5 (3.5 dB)
Field of view	360° in azimuth (ϕ angle) 0 - 62.3° in elevation (θ angle) Continuous beam while scanning
Minimum gain	20 dBi at 62.3° in elevation
EIRP	* minimum = 17.23 dBW at 62.3° elevation angle and uniform power flux density on the earth's surface from 0° to 62.3°. * maximum = minimum + 2 dB for any angle (See figure II-b)

The ...ation contained in this document is proprietary to ALCATEL ESPA... shall not be ...ed by the recipient to third persons without the written consent of the ...ny

Les info... contenues dans ce document demeurent propriété exclusive d'ALCA... ...SPACE et ne de... être divulguées par le destinataire à des tiers sans l'accord écrit de ...é.

Maximum amplitude / phase jumps when scanning	± 0.3 dB / ± 3°
Scan rate	1°/second
Antenna VSWR	< 1.5 (14 dB return loss)
Mass	10 to 20 kg
Thermal Conditions	external equipment: -150° / +150° covered equipment: -20° / +40° internal dissipation of the generated heat
Environmental conditions	ESD free (all exposed surfaces should avoid electric charges storage)

Fig. II-a: Technical specifications

The EIRP per channel versus the off-nadir antenna angle had been determined in the System Analysis task (WP1100 see CHAPTER 2) and is given on fig. II-b.

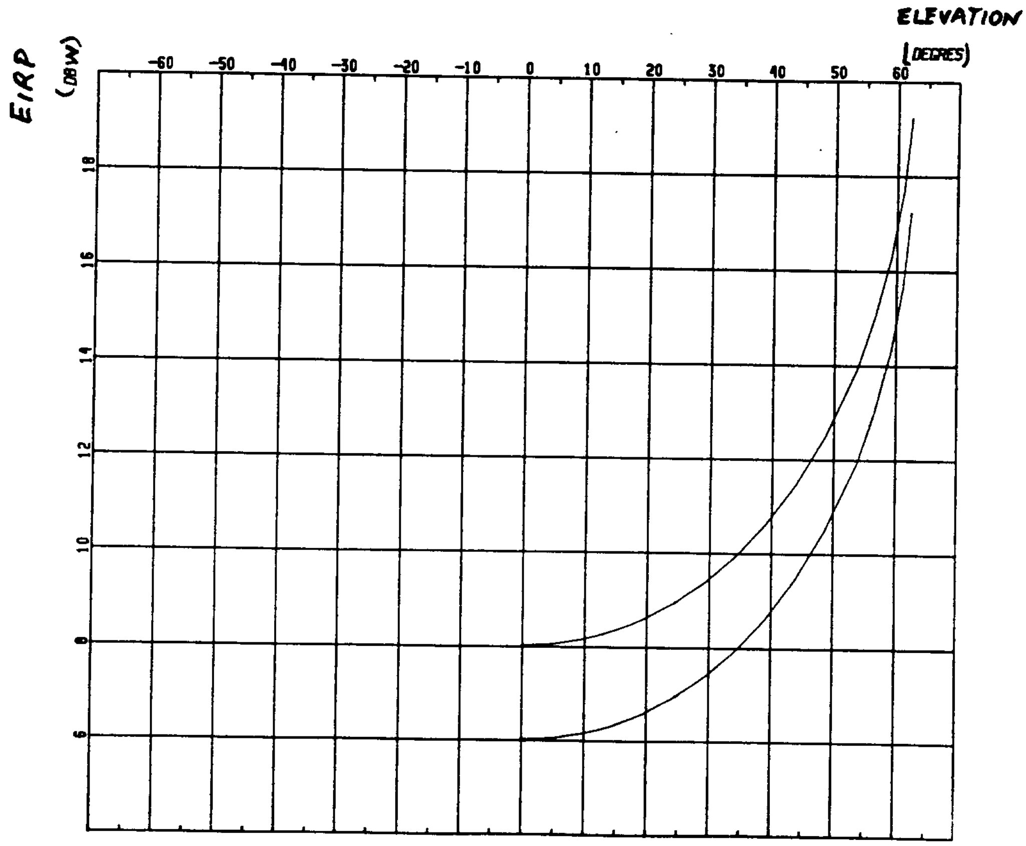

Fig. II-b: EIRP specifications

The information contained in this document is proprietary to ALCATEL ESPACE and shall not be disclosed by the recipient to third persons without the written consent of the company

Les informations contenues dans ce document demeurent propriété exclusive d'ALCATEL ESPACE et ne doivent pas être divulguées par le destinataire à des tiers sans l'accord écrit de la société.

III THE CONICAL ANTENNA

There are two main reasons for choosing a conical antenna:

- first, the required coverage is a revolution coverage (ϕ=0 to 360°) which implies that the antenna must have a revolution axis,

- then, the particular pattern of the EIRP specification (maximum radiation at 62.3° in elevation and uniform power density elsewhere) leads to the choice of an antenna in which the elementary radiators are tilted in order to have their maximum radiating axis at 62.3° in elevation.

That's why, a truncated cone of angle β as shown in figure III-a is an antenna well suited to the mission. The nadir direction is chosen as the revolution axis of the antenna. In this figure, the notion of azimuth (θ angle) and elevation (ϕ angle) are also clarified.

If the normal of each generatrix points towards around 60° from the nadir: so half angle of the cone would be about 30°. The cone can be folded with a lower part pointing towards an elevation angle lower than 60° to improve the gain around nadir, if necessary.

To comply the EIRP specification (or Elevation mask), an original concept, assuming both elevation and azimuth scanning, with a minimum number of phase controls, has been patented by ALCATEL:

- along each generatrix (N_{tot} generatrixes on the circonference of the cone), the N_{ER} radiating patches are fed from a single port with a matched amplitude and phase distribution: the pattern of such a subarray approaches the elevation mask.

- phase control of each columns insures both:
    * azimuth scanning by collimation of the useful part of the array towards the desired ϕ angle (for maximal gain at 62.3°)
    * elevation scanning from 62.3° to 0° by suited phase shifts between the columns

So one dimensionnal set of phase shifters (around the circonference of the cone) provides two dimensionnal scanning (azimuth / elevation) thanks to Conjugate Matching in a virtual Rx mode to the phases induced at each subarray port. If N patches are necessary in each column, this concept divides by N the number of phase-shifters, compared to a conventional two dimensional phased array.

This concept is compatible to active or semi-active option.

The information contained in this document is proprietary to ALCATEL ESPACE and shall not be disclosed by the recipient to third persons without the written consent of the ALCATEL ESPACE.
Les informations contenues dans ce document demeurent propriété exclusive d'ALCATEL ESPACE et ne doivent être divulguées par le destinataire à des tiers sans l'accord écrit de ALCATEL ESPACE.

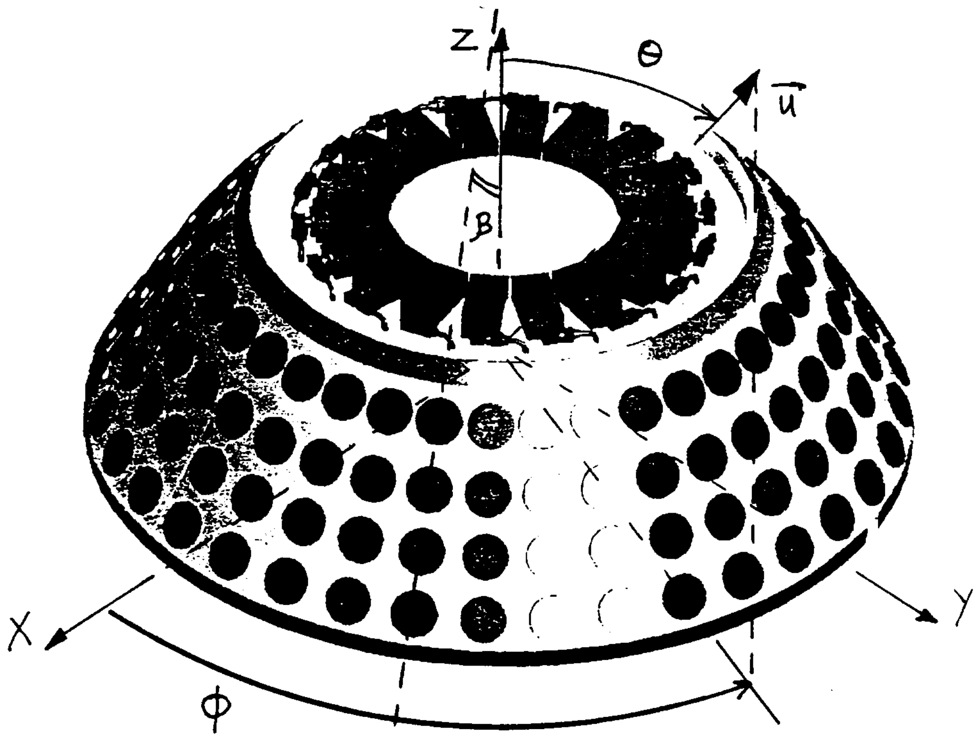

1)

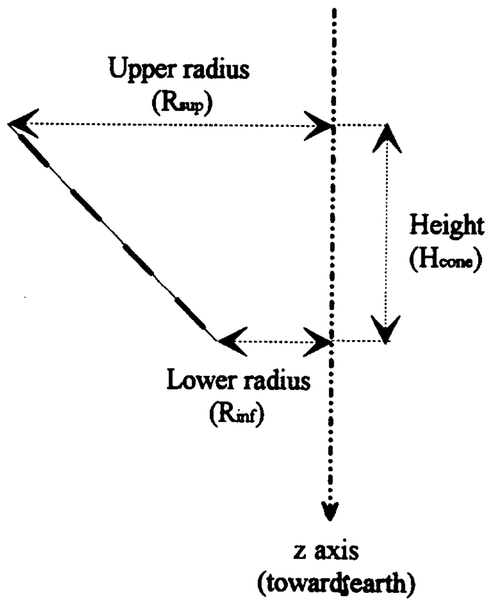

2)

Fig. III-a: The Conformal Array Antenna:
1) Truncated cone with N_{ER}=4
2) Cross section of the cone

The information contained in this document is proprietary to ALCATEL ESPACE and shall not be disclosed by the recipient to third persons without the written consent of the ...
Les informations contenues dans ce document demeurent propriété exclusive d'ALCATEL ESPACE et ne doivent pas être divulguées par le destinataire à des tiers sans l'accord écrit de ...

IV PRINCIPLES OF ACTIVE AND SEMI-ACTIVE CONCEPTS

IV-1 THE ACTIVE CONCEPT

The design of a Conformal Active Antenna is shown in figure IV-a as the result of WP 1100.

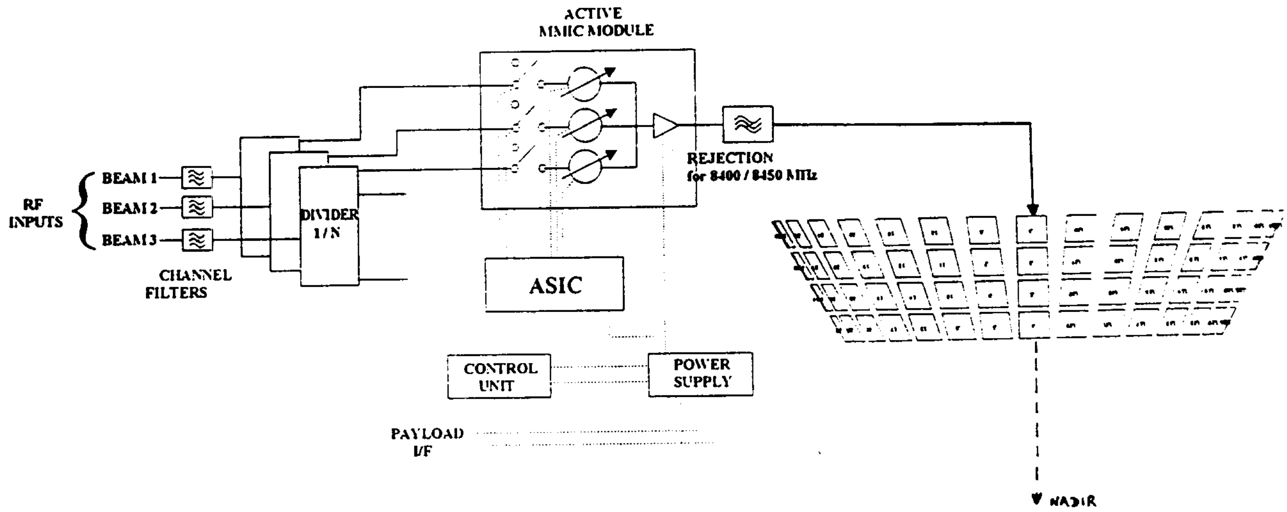

Fig. IV-a: The active concept

There are three RF dividers connected to "a three way active modules" and three phase-shifters are obviously necessary, one being associated to each beam. An absorptive switch must be put on each of the three ways (possibly integrated on the same MMIC chip as the phase-shifter), such as to supress signals corresponding to the beams which do not use this radiating subarray. If the output of a divider is not connected to a phase-shifter, it is equivalent to a connection to a load; this avoids bad VSWR at the beam inputs, and loosen power is low because it is at low level, before the amplifiers.

The main drawback of this solution is the output power of the amplifier. It varies from 1 to 3 according to 1, 2 or 3 channels are active on a given module (i.e: 1, 2 or 3 beams can use the corresponding radiating subarray). So, these amplifiers will be oversized: they should be able to remain linear for 3 more watts than necessary if the beams are spread regularly.

Their Power Added Efficiency will be very bad: unless complicate adaptive biaising would be used, the DC power consumption will remain the same even if RF power is 1/3 or 2/3 of the maximum operating point compliant with C/I specification.

When one or two of the other beams goes through the same amplifier, intermodulation products would occur from the 2 or 3 channels simultenously present in the same amplifier. That's why filtering is required at the output of the amplifier (see WP 1100 - Chapter 2).

Th…mation contained in this document is proprietary to ALCATEL ESPA… shall not be …sed by the recipient to third persons without the written consent of the …ly

Les infor…ns contenues dans ce document demeurent propriété exclusive d'ALCA…ESPACE et ne do…être divulguées par le destinataire à des tiers sans l'accord écrit de …é.

The information contained in this document is proprietary to ALCATEL ESPACE and shall not be disclosed by the recipient to third persons without the written consent of the ALCATEL ESPACE
Les informations contenues dans ce document demeurent propriété exclusive d'ALCATEL ESPACE et ne doivent être divulguées par le destinataire à des tiers sans l'accord écrit de

IV-2 THE SEMI-ACTIVE CONCEPT

The high losses in the passive concept and the bad efficiency of the amplifiers in the active concept lead to assess deeply a semi-active concept where distributed amplifiers are placed at the middle of the BFN (ie: after power dividers and phase-shifters, and 3→1 combiners, all lossy components, but before several Butler matrixes which can transform equal amplitude inputs to a suited amplitude / phase distribution for feeding the radiating subarray).

Such concept has been proposed by M. ROEDERER for multi-beam antennas, either for a Focal Array Fed Reflector (FAFR), or for a cylindrical antenna, alternative to the Electronically Despun Antenna (EDA) for spinned Meteosat Satellites.

The principle is applied to an array with a symmetry of revolution (fig. IV-b). This figure is for a two beams case with 16 subarrays.

If we want that the outputs A_1, B_1, C_1 and D_1 would be fully excited, the phase distributions at the input of each Butler matrix are linear, with total shift even or odd multiple of π radians (according to using 180° or 90° hybrids in the matrices); by discrete Fourier Transform, the energy is concentrated to only one of the four outputs of each matrix.

If it is better for pattern shaping to excite at half level D_1 and D_4, the appropriate phase distribution is applied at the input of the Butler matrix D, without changing phase-shifters at the input of the three other Butler matrixes.

The critical electrical points will be the computation of the suited phases for each beam provided for a conical geometry, limiting the amplitude and phase errors after the amplifiers (dispersions in the Butler matrixes and the cables towards the subarrays), and checking that equal amplitude on all amplifiers (all loaded by the various beams) do not degrade beam forming capability.

If these points are solved, this concept is very attractive because it could use all amplifiers at equal and constant power to transmit three independent beams, so minimizing the global consumption of the amplifiers.

The information contained in this document is proprietary to ALCATEL ESPACE and shall not be disclosed by the recipient to third persons without the written consent of the ALCATEL ESPACE.

Les informations contenues dans ce document demeurent propriété exclusive d'ALCATEL ESPACE et ne doivent pas être divulguées par le destinataire à des tiers sans l'accord écrit de ALCATEL ESPACE.

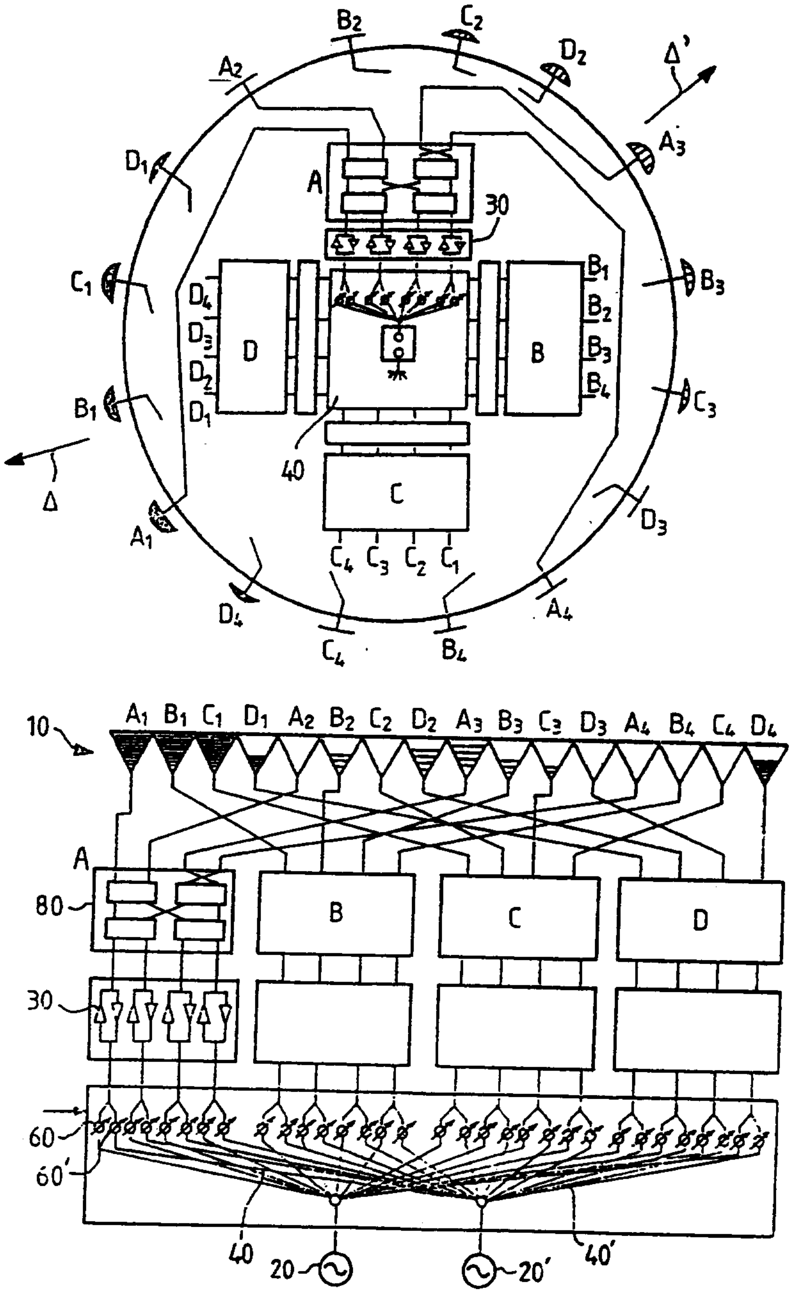

Fig. IV-b: Semi-active conformal antenna with 2 beams and 16 subarrays

The information contained in this document is proprietary to ALCATEL ESPACE and shall not be disclosed by the recipient to third persons without the written consent of the ALCATEL ESPACE.
Les informations contenues dans ce document demeurent propriété exclusive d'ALCATEL ESPACE et ne doivent pas être divulguées par le destinataire à des tiers sans l'accord écrit de ALCATEL ESPACE.

V LOGIC FOR OPTIMIZING THE CONICAL ANTENNA

V-1 DETAILING THE SOFTWARE TOOLS

All the software packages necessary to optimise the profile of the antenna will be reviewed:

- **SYRLC** optimises complex excitations and patches orientation along a subarray w.r.t. the elevation mask (in relative dB, which means that the maximum value of the mask will be equal to 0), with amplitude range limitation for excitations.

  * input parameters:
    - radiated pattern of the elementary radiator and number of radiators
    - frequency, polarisation, Axial Ratio
    - elevation mask (in relative dB)

  * output parameters:
    - complex excitations of each radiator
    - orientation of each radiator
    - geometrical description of the conical antenna
    - RI File (including geometry and excitations)

- **GECRI** optimises complex excitations among the radiating columns by amplitude / phase conjugate matching or phase only conjugate matching. This software is used only for the *active concept*.

  * input parameters:
    - RI file issued from SYRLC
    - radiating pattern of each elementary radiator
    - Frequency, polarisation
    - Description of the cone (N_{tot}, N_{act})
    - pointed direction (in θ, ϕ coordinates)

  * output parameters:
    - RI File (including geometry and excitations) in the pointed direction

- **RIASA** computes far field pattern of the antenna (in the pointed direction specified in GECRI software) in (θ, ϕ) coordinates.

  * input parameters:
    - RI file issued from GECRI
    - radiating pattern of each elementary radiator
    - Frequency, polarisation

  * output parameters:
    - SA File (radiated pattern of the whole antenna in (θ, ϕ) coordinates)

- **SYCOB** optimises complex excitations at the inputs of Butler matrixes for the *semi-active concept.* In this software, the Butler matrix is equivalent to its tranfer function given in page 3-35.

* <u>input parameters</u>:
- Geometrical characteristics of the cone (R_{sup}, β_i, H_{cone}, N_{tot})
- complex excitation of a subarray (issued from SYRLC)
- radiating pattern of each elementary radiator
- Butler's configuration (Number N_B, order N and connexion to the conical antenna)
- Polarisation

* <u>output parameters</u>:
- CO file (including EIRP performances for each elevation point)
- BUT file (including the optimal excitations at the input of the Butler's for each elevation point, *this is the result of the optimisation*)

- **BUTRI** describes both geometry and excitations of the columns as a RI standard file; computation of far-field radiated pattern for the semi-active concept is given by using RIASA software.

* <u>input parameters</u>:
- RI file (issued from SYRLC)
- BUT file (issued from SYCOB)
- complex excitation of a subarray (issued from SYRLC)
- pointed direction (θ, ϕ)
- Butler's configuration (Number N_B, order N and connexion to the conical antenna)

* <u>output parameters</u>:
- BUT file (including the optimal excitations at the outputs of the Butler's for each elevation point)
- RI file (including geometry and excitations of the columns of the antenna in the specified (θ, ϕ) pointed direction)

<u>Remark</u>: in the BUTRI software, BUT file is both an input and an output parameter for the reason that BUTRI uses the BUT file generated by SYCOB and the transfer function of a Butler to give another BUT file which contains the amplitudes and phases at the output of the Butlers (excitations applied to the subarrays).

The information contained in this document is proprietary to ALCATEL ESPACE and shall not be disclosed by the recipient to third persons without the written consent of the ALCATEL ESPACE.
Les informations contenues dans ce document demeurent propriété exclusive d'ALCATEL ESPACE et ne doivent pas être divulguées par le destinataire à des tiers sans l'accord écrit de l'ALCATEL ESPACE.

V-2 PROCEDURE FOR OPTIMISATION

The complete procedure of optimisation is given in the following algorithm (figure V-a).

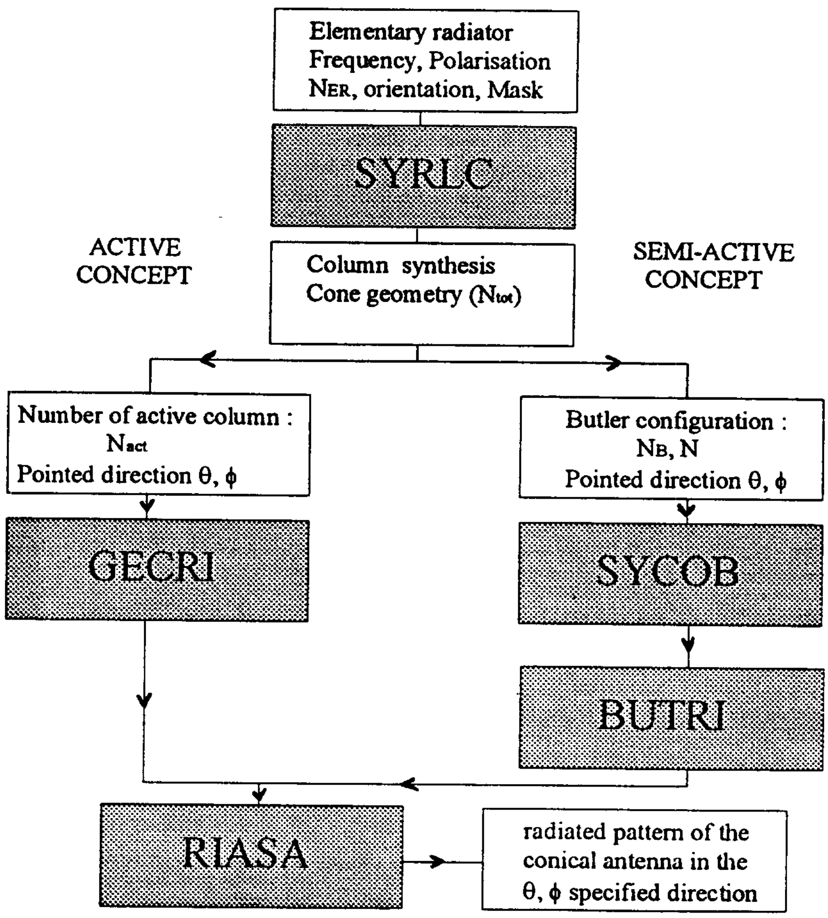

Fig. V-a: Optimisation of the conical antenna for active and semi-active concept

The information contained in this document is proprietary to ALCATEL ESPACE and shall not be disclosed by the recipient to third persons without the written consent of the company.
Les informations contenues dans ce document demeurent propriété exclusive d'ALCATEL ESPACE et ne doivent pas être divulguées par le destinataire à des tiers sans l'accord écrit de la société.

VI THE ELEMENTARY RADIATOR

For the purpose of the study, the radiator must have the following constraints:

- Bandwidth: 8025 - 8400 Mhz (4.6 %).
- Axial Ratio: A specification of 3.5 dB is required for the antenna; so for the element, a similar value on the whole bandwidth for θ angle up to about 60°.
- Polarisation: RHCP
- Directivity: from 7 to 8 dBi, to be suited to the area of the array cell.

ALCATEL had developed several kind of radiating elements from L-Band to Ku Band. The reasons for development of such element are the following:

- minimization of mass and volume (by using printed antenna technology)
- increase of the bandwidth (by stacked resonators of different widths)
- limitation of the electromagnetic coupling (by inserting the resonators in cavities for better antenna pattern control)
- reduction of ohmic losses and surface waves (by the use of low permittivity substrate)
- one access circular polarization (fed by only one stripline, special shape of the resonators)

A priori the elementary radiator developed for CNES contract will be re-used in this study (See figure VI-a). No software is able to predict the radiated patterns of such kind of elements: Presently, waiting the work to be performed by LEMA-EPFL in WP 1300, optimisation has been made by "cut and try" on the different parameters (diameters and height of cavities, deep and width of the slots, position of patches...), and measuring the VSWR, the Axial Ratio and directivity in the whole bandwidth.

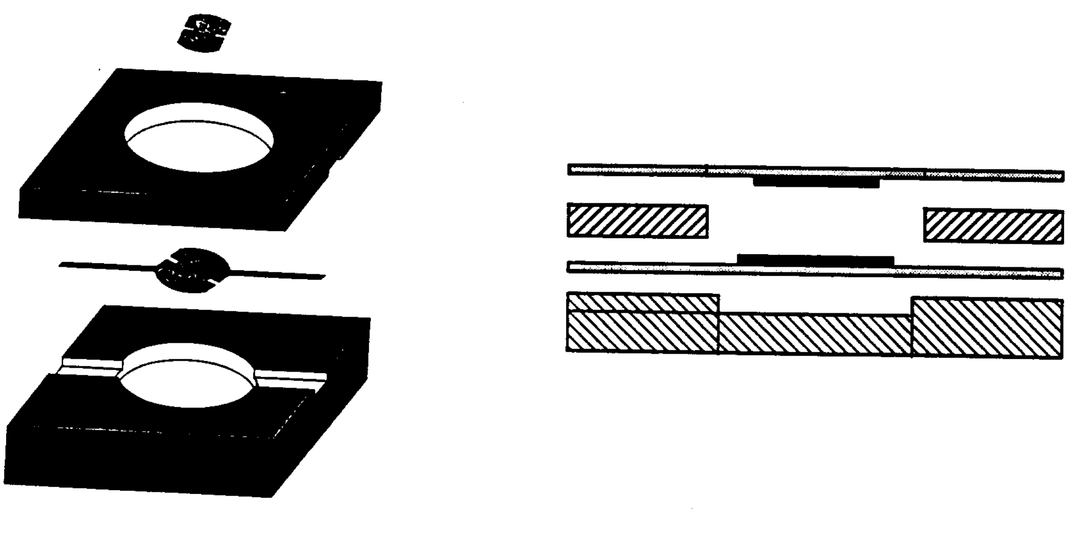

Fig. VI-a: Geometrical characteristics of elementary radiator

The information contained in this document is proprietary to ALCATEL ESPACE and shall not be disclosed by the recipient to third persons without the written consent of the ALCATEL ESPACE.
Les informations contenues dans ce document demeurent propriété exclusive d'ALCATEL ESPACE et ne doivent pas être divulguées par le destinataire à des tiers sans l'accord écrit de l'ALCATEL ESPACE.

ALCATEL TELECOM	CONFORMAL ARRAY ANTENNA	ESTEC CONTRACT 11698/95/NL/SB		
		AES 960596 / ASP 019		
		DATE : 26/06/96	ED/REV 1/-	3- 14

The obtained electrical performances are the following:

- Axial Ratio: under 1 dB on the Bandwidth (see figure VI-b)
- Directivity: about 7.7 dBi (see fig. VI-c)

The effect of the ground plane is observed with a diminution of directivity in 0° axis. If we would simulate with the measured pattern, there would be a false drop of the directivity near 0°; it has been proved, during the CNES study, that this problem does not appear in the final breadboard. That's why, a theoretical model best suited for simulations. The simulations will be made with a theoretical pattern of 7.7 dBi directivity with a zero at +120° and -120°. A comparison between measured and theoretical patterns is proposed at 8200 MHz in figure VI-c.

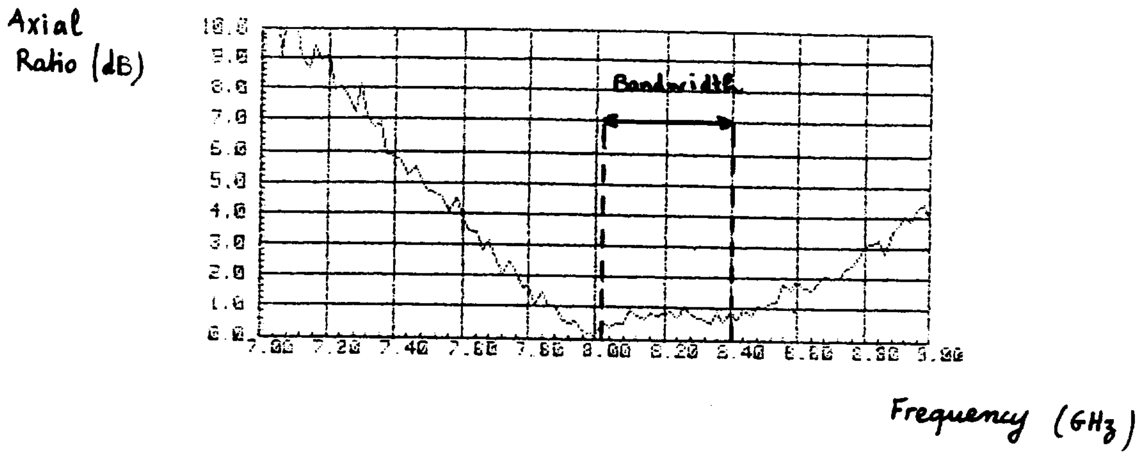

Fig. VI-b: Axial Ratio of the elementary radiator

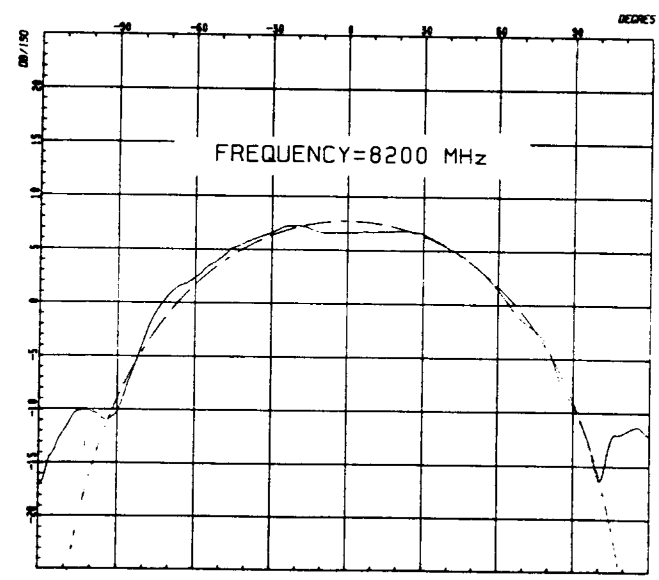

Fig. VI-c: Radiating pattern of the elementary radiator
Measurement and theoretical modelisation

The ...ation contained in this document is proprietary to ALCATEL ESPA... shall not be ...d by the recipient to third persons without the written consent of the ...
Les infor... contenues dans ce document demeurent propriété exclusive d'ALCA... SPACE et ne doi... être divulguées par le destinataire à des tiers sans l'accord écrit de l...

The information contained in this document is proprietary to ALCATEL ESPACE and shall not be disclosed by the recipient to third persons without the written consent of the ALCATEL ESPACE.

Les informations contenues dans ce document demeurent propriété exclusive d'ALCATEL ESPACE et ne doivent pas être divulguées par le destinataire à des tiers sans l'accord écrit de ALCATEL ESPACE.

VII DETERMINATION OF THE GENERATRIX PROFILE

VII-1 ANTENNA LOSS BUDGET

In order to take enough margin in the synthesis of the subarray, an antenna loss budget is done. The values considered in this budget come from ALCATEL experience during other studies in the same frequency bandwidth or in the same concept. The antenna loss budget will depend essentially on one parameter: the number of patches in a subarray, N_{ER}.

* Difference between (fitted on previous breadboard measurements) and actual patch pattern, on the whole bandwidth: - 0.20 dB

* Return loss (< 14 dB): - 0.15 dB
(worst case over whole bandwidth and all pointing directions)

* ohmic losses on the subarray (estimation for parallel repartitor)	4 patches:	- 0.30 dB
	6 patches:	- 0.50 dB
	8 patches:	- 0.80 dB

* amplitude and phase errors from ideal values within a subarray	4 patches:	- 0.05 dB
	6 patches:	- 0.10 dB
	8 patches:	- 0.20 dB

* amplitude and phase errors from ideal values among various subarrays: - 0.05 dB
(corresponding to standard deviations: gaussian error function with 0.5 dB / 5°)

TOTAL LOSSES:
4 patches subarray: 0.75 dB
6 patches subarray: 1.00 dB
8 patches subarray: 1.40 dB

Remark: ESA mask will now be drawn including the budget loss.

VII-2 PARAMETRICAL STUDY

The generatrix of the antenna has a profile presented on figure VII-a. Each radiating element lies on a plane and centers within a subarray is in a meridian. The orientation of the patch number i is described by an angle β_i between the nadir of the antenna and the line which contained the patch. In order to limit mutual coupling between the patches of the same subarray, by widening the elevation field of view of the antenna, the angles (β_i) must increase from i=1 to N_{ER}.

This constraint is not taken into consideration in SYRLC software. That's why it is really difficult to optimise the orientation of the patches with SYRLC. An example of SYRLC output, when an optimization of the generatrix profile is required, is proposed in figure VII-b for N_{ER}=4 and N_{ER}=6.

ALCATEL TELECOM	CONFORMAL ARRAY ANTENNA	ESTEC CONTRACT 11698/95/NL/SB		
		AES 960596 / ASP 019		
		DATE : 26/06/96	ED/REV 1/-	3- 16

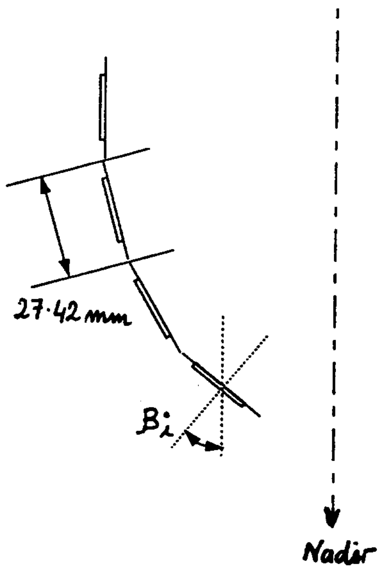

Fig. VII-a: Generatrix profile

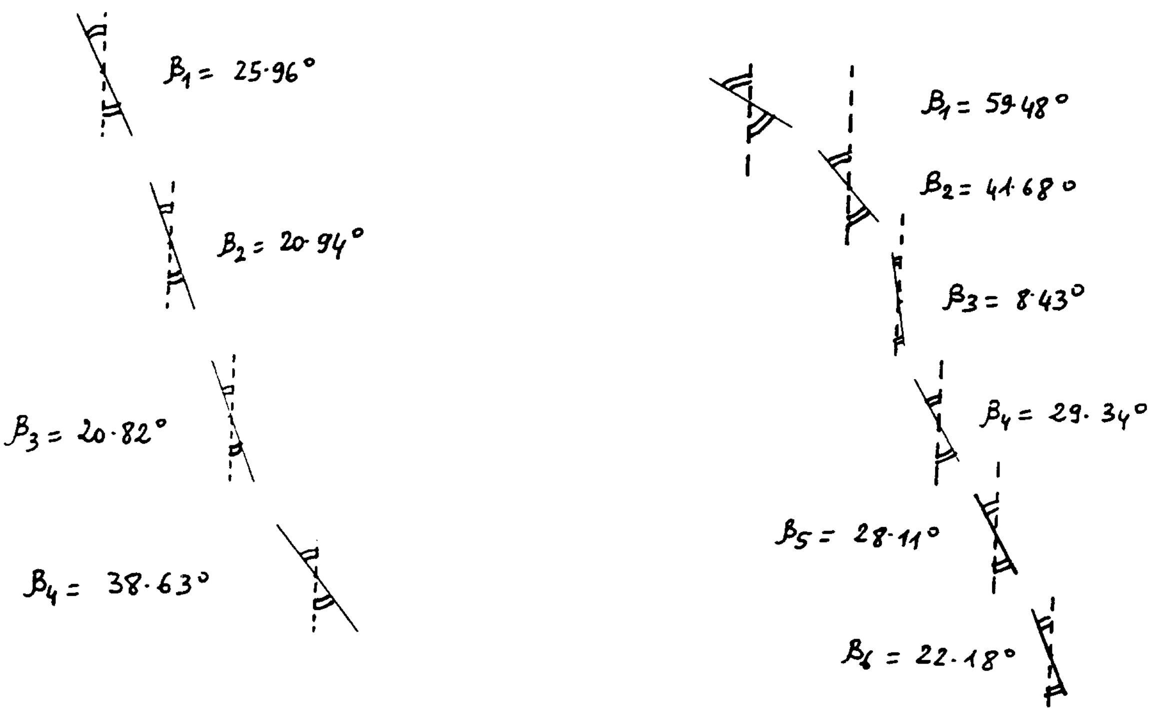

Fig. VII-b: Optimisation of the patches orientation using SYRLC

The information contained in this document is proprietary to ALCATEL ESPACE and shall not be disclosed by the recipient to third persons without the written consent of the ALCATEL ESPACE.
Les informations contenues dans ce document demeurent propriété exclusive d'ALCATEL ESPACE et ne doivent pas être divulguées par le destinataire à des tiers sans l'accord écrit de l'ALCATEL ESPACE.

The information contained in this document is proprietary to ALCATEL ESPACE, shall not be disclosed by the recipient to third persons without the written consent of the company

It is evident, especially when N_{ER} is higher than 4, that SYRLC can not be used for optimising the generatrix profile. That's why, a parametrical study will be lead in order to see the best suited profile (in terms of number of patches and orientation of patches).

The number of patches in a same subarray, N_{ER}, is limited to 8 and the number of brisures will be limited to: 1 for N_{ER} =4
2 for N_{ER} =6 and 8

Several sets of values of β_i (for i=1 to N_{ER}) (with the constraint that $\beta_1 \leq \beta_2 \leq .. \beta_{NER}$) have been computed in SYRLC software. For each profile, optimisation of complex excitations is done with the only constraint of 6 dB range in the amplitude control of each elementary radiator. The conjugate matching in a specified direction is done by phase control only, which means that each active column has the same RF power.

In the following studies:

N_{tot} is the total number of columns in the cone
N_{ER} is the number of elementary radiators in a column
H_{cone} is the height of the cone
R_{sup} is the upper radius of the cone
β_i are the orientations of the elementary radiators
margin=computed performance - total loss - specified value
(for the worst case in elevation from 0° to 62.3°)
D_{min} 62.3 is the directivity obtained at 62.3° in elevation

(so, if we analyse the first line of the following table, we can conclude that the worst case is obtained at 62.3° in elevation because the directivity is equal to 20.76 dBi which gives a margin of: 20.76 - 0.75 - 20 = +0.01 dB)

* <u>first parametrical study:</u> N_{ER} =4, N_{tot}=29 and N_{act}=11 (see figure VII-c)

Ntot	*Ner*	*Hcone (in mm)*	*Rsup (in mm)*	*β_1 (in °)*	*β_2 (in °)*	*β_3 (in °)*	*β_4 (in °)*	*margin (in dB)*	*D_{min} 62.3 (in dBi)*
29	4	99.40	150.90	25	25	25	25	+0.01	20.76
29	**4**	**94.99**	**158.32**	**30**	**30**	**30**	**30**	**+0.11**	**20.89**
29	4	89.84	165.38	35	35	35	35	+0.04	20.85
29	4	98.30	153.02	25	25	25	30	+0.02	20.77
29	4	97.01	155.04	25	25	25	35	+0.01	20.76
29	4	93.70	160.34	30	30	30	35	+0.10	20.87
29	4	90.63	164.00	30	30	30	45	+0.01	20.78
29	**4**	**94.62**	**159.18**	**25**	**25**	**35**	**35**	**+0.14**	**20.92**
29	4	92.42	162.36	30	30	35	35	+0.12	20.90
29	4	89.50	166.15	30	30	40	40	+0.08	20.88
29	4	92.23	163.31	25	35	35	35	-0.02	20.77
29	4	86.76	170.07	30	40	40	40	-0.12	20.68

Fig. VII-c: Parametrical study for the generatrix profile for N_{ER}=4

Les informations contenues dans ce document demeurent propriété exclusive d'ALCATEL ESPACE et ne doivent être divulguées par le destinataire à des tiers sans l'accord écrit de la société.

The table of figure VII-c leads to the conclusion that a folded subarray of (25°/25°/35°/35°) is the best solution. But, if we compared this solution with a straight subarray of angle 30°, a gain of only 0.03 dB is obtained. We can not consider that this gain is sufficient to justify the use of a folded subarray for N_{ER}=4 patches. That's why, for the following simulations with N_{ER}=4, only a straight subarray will be taken into account.

<u>* second parametrical study:</u> N_{ER} =6, N_{tot}=24 and N_{act}=9 (see figure VII-d)

Ntot	*Ner*	*Hcone*	*Rsup*	β_1	β_2	β_3	β_4	β_5	β_6	*margin*	*D_{min} 62.3*
24	**6**	**142.48**	**166.55**	**30**	**30**	**30**	**30**	**30**	**30**	**-0.44**	**20.65**
24	6	134.77	177.65	35	35	35	35	35	35	-0.66	20.43
24	6	148.00	157.01	25	25	25	25	25	30	-0.32	20.75
24	**6**	**146.72**	**159.02**	**25**	**25**	**25**	**25**	**25**	**35**	**-0.30**	**20.76**
24	6	145.26	160.92	25	25	25	25	25	40	-0.30	20.75
24	6	143.64	162.68	25	25	25	25	25	45	-0.65	20.43
24	6	141.19	168.57	30	30	30	30	30	35	-0.65	20.35
24	6	139.74	170.47	30	30	30	30	30	40	-0.42	20.66
24	6	133.31	179.55	35	35	35	35	35	40	-0.67	20.42
24	6	131.69	181.31	35	35	35	35	35	45	-0.96	20.19
24	6	146.90	159.13	25	25	25	25	30	30	-0.36	20.72
24	6	144.33	163.16	25	25	25	25	35	35	-0.40	20.70
24	6	139.90	170.59	30	30	30	30	35	35	-0.52	20.58
24	6	145.79	161.25	25	25	25	30	30	30	-0.38	20.69
24	6	141.94	167.30	25	25	25	35	35	35	-0.48	20.59
24	6	138.62	172.61	30	30	30	35	35	35	-0.56	20.54
24	6	134.25	178.30	30	30	30	40	40	40	-1.17	19.83
24	6	142.12	167.41	25	25	30	30	35	35	-0.45	20.63
24	6	144.51	163.27	25	25	25	30	30	35	-0.36	20.71

Fig. VII-d: Parametrical study for the generatrix profile for N_{ER}=6

A few sets of profiles have been computed and the conclusion is that a folded profile is really interesting in this case because a gain of 0.14 dB is obtained if we compared a folded profile (25°/25°/25°/25°/25°/35°) with a straight one (30°). The second remark, analysing the results of figure VII-d, is that a profile with two brisures does not give better results. For the following simulations, two solutions will be retained: a straight subarray of angle β=30° and a folded one with the following profile (25°/25°/25°/25°/25°/35°)

The ...ation contained in this document is proprietary to ALCATEL ESPA... shall not be ...d by the recipient to third persons without the written consent of the ...y ESPACE

Les infor...ns contenues dans ce document demeurent propriété exclusive d'ALCA... et ne doi... être divulguées par le destinataire à des tiers sans l'accord écrit de ...

Th... ration contained in this document is proprietary to ALCATEL ESPA... shall not be ...ed by the recipient to third persons without the written consent of the ...ny
Les infor... ons contenues dans ce document demeurent propriété exclusive d'ALCA... ESPACE et ne do... être divulguées par le destinataire à des tiers sans l'accord écrit de ...é.

<u>* third parametrical study:</u> N_{ER} =8, N_{tot}=24 and N_{act}=9 (see figure VII-e)

Ntot	*Ner*	*Hcone*	*Rsup*	β_1	β_2	β_3	β_4	β_5	β_6	β_7	β_8	*margin*	D_{min} *62.3*
24	8	198.81	178.06	25	25	25	25	25	25	25	25	-0.74	20.66
24	**8**	**189.97**	**193.97**	**30**	**30**	**30**	**30**	**30**	**30**	**30**	**30**	**-0.56**	**20.84**
24	8	179.69	209.11	35	35	35	35	35	35	35	35	-0.56	20.86
24	8	191.82	190.58	25	25	25	25	30	30	35	35	-0.50	20.90
24	8	188.91	194.38	25	25	25	25	30	30	40	40	-0.46	20.94
24	8	183.10	201.94	25	25	25	25	35	35	45	45	-0.70	20.70
24	8	185.67	197.91	25	25	25	25	30	30	45	45	-0.46	20.94
24	8	188.69	195.99	30	30	30	30	30	30	30	35	-0.51	20.89
24	**8**	**187.23**	**197.89**	**30**	**30**	**30**	**30**	**30**	**30**	**30**	**40**	**-0.47**	**20.94**
24	8	185.61	199.65	30	30	30	30	30	30	30	45	-0.54	20.86
24	8	187.40	198.01	30	30	30	30	30	30	35	35	-0.51	20.89
24	8	184.49	201.80	30	30	30	30	30	30	40	40	-0.47	20.93
24	**8**	**180.63**	**207.86**	**30**	**30**	**30**	**30**	**35**	**35**	**40**	**40**	**-0.43**	**20.97**
24	8	177.89	211.77	30	30	35	35	35	40	40	40	-0.44	20.97

Fig. VII-e: Parametrical study for the generatrix profile for N_{ER}=8

The analysis of the simulated results of figure VII-e leads to the following comments:

- first, a folded profile with two brisures is the best solution because a gain of 0.13 dB is obtained compared to the straight one,

- and then, if we compare the results of figure VII-e with the ones of figure VII-d, we can see that for the same antenna configuration, a gain of 0.27 dB is obtained with N_{ER}=8 compared to N_{ER}=6. But as the losses are 0.4 dB higher for the column of 8 patches, it is not interesting to consider a subarray with 8 patches.

The conclusion of this parametrical study on the generatrix profile is:

- for 4 patches, straight subarrays (β=30°) will be considered
- for 6 patches, two kinds of subarrays will be analysed: -folded one (25°/.../25°/35°)
- straight one (30°)
- no 8 patches subarray will be considered

The information contained in this document is proprietary to ALCATEL ESPACE and shall not be disclosed by the recipient to third persons without the written consent of the ALCATEL ESPACE.

Les informations contenues dans ce document demeurent propriété exclusive d'ALCATEL ESPACE et ne doivent être divulguées par le destinataire à des tiers sans l'accord écrit de ALCATEL ESPACE.

VIII THE ACTIVE CONCEPT: PROPOSITION OF A SOLUTION

VIII-1 UNDERSTANDING THE CONCEPT

If the station is located at an azimuth ϕ_0, an odd number of columns -from 1 to N_{act} will be active (the other columns are switched off - i.e.: only N_{act} of the N_{tot} amplifiers are working for an azimuth ϕ_0) and the azimuth ϕ_0 corresponds to the one of the central column as shown in figure VIII-a (N_{act}=11, N_{tot}=32). The phase and amplitude control on the N_{act} columns is made by conjugate matching.

The cone is divided in N_S angular areas of 360 / N_{tot} degrees. The scanning outside the angular area [ϕ_0 - 360 / N_{tot} , ϕ_0 + 360 / N_{tot}] is achieved by commutation of the beam around the revolution axis: *switching on* the N_{act}+1 column and then *switching off* the first column. Inside the angular area, the phase and modulus control of the columns are optimized for each elevation angle.

The major problem of this solution is the amplitude and phase jumps during the commutation. When the N_{act}+1 column is switching on, the amplitude jump can be, in the worst case, equal to 20 log (N_{act} / N_{act} +1) if the contribution of all columns are equal (which is the worst case on the nadir).

During the CNES contract, a cone of 60 columns (19 columns active) was built and the amplitude jumps was about 0.5 dB, coherent with the previous formula.

It is quite evident that the objective of the study is to minimize the cost of the antenna by reducing the number of column. The parametrical study will be done with N_{tot} max = 32 and if we considerer that 1/3 of the cone will be active N_{act}=11 and the worst case amplitude jump will be about 0.7 dB. However, this value is not so critical because ALCATEL had demonstrated that value of amplitude or phase jumps up to 1 dB does not create significant BER performances degradation.

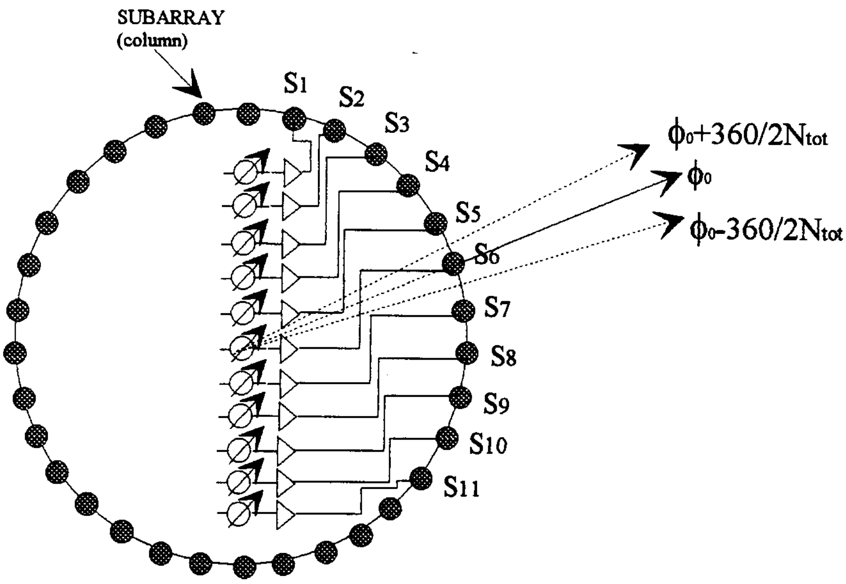

Fig. VIII-a: Understanding the Active solution

VIII-2 PARAMETRICAL STUDY

The parametrical study will be limited to the profiles selected in §VII.

The global notations (figure VIII-b) used during the parametrical optimisation will be:

- A_K and ϕ_K are respectively the amplitude and phase controls for the subarray (or column) number K (K varying from 1 to N_{act})
- a_i and ζ_i are respectively the amplitude and phase control of each elementary radiator (i varying from 1 to N_{ER})

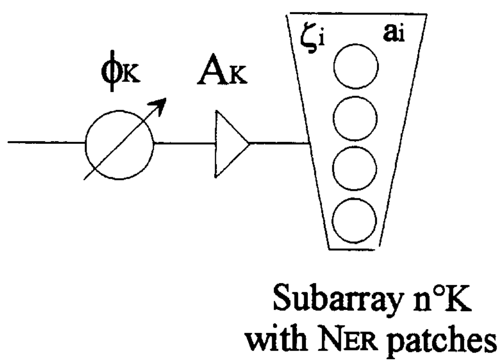

Fig. VIII-b: Amplitude and phase control of each subarray

The information contained in this document is proprietary to ALCATEL ESPA[CE and] shall not be used by the recipient to third persons without the written consent of the company
Les informations contenues dans ce document demeurent propriété exclusive d'ALCATEL ESPACE et ne doivent être divulguées par le destinataire à des tiers sans l'accord écrit de la [société].

Les informations contenues dans ce document demeurent propriété exclusive d'ALCATEL ESPACE et ne doivent être divulguées par le destinataire à des tiers sans l'accord écrit de la société.
The information contained in this document is proprietary to ALCATEL ESPACE, shall not be disclosed by the recipient to third persons without the written consent of the company

The parametrical study will be lead in three steps:

-at first, the performance without any constraint (apart from the dynamic range limitation to 6 dB of A_K and a_i) will be obtained (column called margin 1 in the table of figure VIII-c; margin 1 = D_{min} (the worst obtained for the 20 elevation samples from 0 to 62.3°) - specified value - total loss (0.75 dB and 1 dB for 4 and 6 patches), **for the worst case of elevation among 20 samples from 0° to 62.3° in elevation.**

-then, the performance, with an equal power feeding of the columns (A_K is constant for K=1 to N_{act}) and a dynamic range limitation of 6 dB for a_i, will be obtained (column called margin 2 in the table of figure VIII-c).

-Finally, the performance with the same constraints than in step 2 and with a constraint of feasibility of the repartitor (the a_i must decrease from the middle to the extremity of the subarray) are reported in the column called margin 3.

The results of the optimisation are proposed in the table of figure VIII-c.

N_{tot}	N_{ER}	N_{act}	Beta (°)	margin 1	margin 2	margin 3
24	4	9	30	-0.51 dB	-0.71 dB	-0.81 dB
26	4	11	30	-0.04 dB	-0.43 dB	-0.51 dB
28	4	11	30	0.21 dB	-0.05 dB	-0.14 dB
30	**4**	**11**	**30**	**0.43 dB**	**0.25 dB**	**0.14 dB**
32	4	13	30	0.82 dB	0.51 dB	0.42 dB
32	4	16	30	0.96 dB	0.14 dB	0.07 dB
24	6	9	30	-0.15 dB	-0.44 dB	-1.14 dB
26	6	11	30	0.34 dB	-0.20 dB	-0.75 dB
28	6	11	30	0.58 dB	0.19 dB	-0.45 dB
30	6	11	30	0.79 dB	0.54 dB	-0.20 dB
32	**6**	**13**	**30**	**1.19 dB**	**0.74 dB**	**0.14 dB**
32	**6**	**16**	**30**	**0.95 dB**	**0.32 dB**	**0.00 dB**
24	6	11	25/.../25/35	-0.06 dB	-0.30 dB	-1.01 dB
26	6	11	25/.../25/35	0.42 dB	-0.05 dB	-0.64 dB
28	6	11	25/.../25/35	0.66 dB	0.34 dB	-0.32 dB
30	**6**	**11**	**25/.../25/35**	**0.88 dB**	**0.72 dB**	**0.15 dB**
32	6	11	25/.../25/35	1.28 dB	0.89 dB	0.26 dB
32	6	16	25/.../25/35	1.47 dB	0.57 dB	0.07 dB

Fig. VIII-c: optimisation for active concept

Les informations contenues dans ce document demeurent propriété exclusive d'ALCATEL ESPACE et ne doivent pas être divulguées par le destinataire à des tiers sans l'accord écrit de la société.
The information contained in this document is proprietary to ALCATEL ESPACE and shall not be disclosed by the recipient to third persons without the written consent of the company

Several remarks can be made, analysing the table of figure VIII-c:

- In the hypothesis of equal power feeding in the columns, the results for N_{tot}=32 and N_{act}=13 or 16 confirm that the optimal number of active column is approximatively $N_{act}=N_{tot}/3$. This is comprehensive because if we use half of a cone, at the edges, patch radiation is very low (pattern for θ=90° is about -17 dB versus maximum). So power feeding these patches is rather wasted. As directivity is proportional to the power of the global radiated field, divided by total excitation power, patches which have very low contribution in the pointing direction lowers the global directivity.

- the obtained performances, with the only constraint of dynamic range, permit to show that the number of total column N_{tot} can not be lower than 25. Increasing the number of patches (from 4 to 6) permits, with the same profile, to increase margin of 0.4 dB or to reduce the number of column from 27 to 25. A folded profile permits to increase margin of approximately 0.1 dB compared to the straight one.

- the loss induced by a equal power feeding of the column are respectively 0.27 dB for a 4-patches subarray and 0.38 dB for a 6-patches subarray. We can see that this loss can be compensated by increasing the number of column by 2 for both 4 or 6 patches-subarrays. Equal RF power in the columns (i.e.: conjugate matching with only phase control) means better EIRP (i.e.: for maximal given power p_{max} for MMIC-HPA's, or for given power consumption. In this case, $p_{rad}=N_{act} \times p_{max}$; with tapered amplitude, $p_{rad} << N_{act} \times p_{max}$). Moreover, equal power avoids variable attenuators. <u>That's why, an equal power feeding of the active columns will be chosen.</u>

The EIRP and directivity specifications at 62.3° (i.e.: D_{min}=20 dBi and 17.23 dBW ≤ EIRP ≤ 19.23 dBW) impose a total RF power bounded by -2.77 dBW and -0.77 dBW.

- the loss due to the feasibility of the subarray can be explained by the type of the chosen repartitor. Several kinds of repartitor can be selected: serial repartitor, parallel one or a combination of serial and parallel feeding (see figure VIII-d).

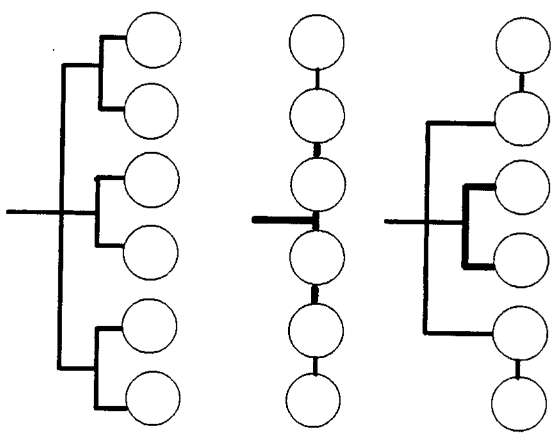

Fig. VIII-d: Several kinds of repartitors parallel, serial and combined serial / parallel

The serial repartitor is the most interesting for the purpose of our study because the feeding lines are going through the patches, so reducing the width of a column and consequently the mass of the breadboard. Also, lenght of lines is reduced, so ohmic losses lower. But the main drawback of this solution is the stringent constraints in the phase and amplitude controls; that's why the feasibility of a serial repartitor will not taken as a criteria to cancel a solution.

The parallel repartitor has less constraints in the realisation of the phase and amplitude controls but if we want to minimise the mass of a column, the transmission lines width must be small (which could be a drawback for the precision of the printed circuits: a precision of 20 μm is obtained on the printed circuits which oblige to work with width larger than 0.4 mm) and go very near from the cavities.

The only constraint imposed for all kinds of repartitors is to have constant or decreasing amplitude from the middle to the extremities.

The total losses introduced by this feasibility constraints are approximately 0.10 dB for 4 patches-subarray and 0.60 dB for 6 patches-subarray.

It leads to the conclusion that a 4-patches subarray is more interesting that a 6-patches one, folded or not folded. A total number of 29 columns is necessary to be compliant whereas 30 columns are necessary with the 6-patches folded subarray.

That's why, the retained solution for the active concept will be : $N_{tot}=29$, $N_{act}=11$ and $N_{ER}=4$. This solution will be detailed in next part of the chapter.

VIII-3 THE CHOSEN SOLUTION

Geometrical characteristics

The chosen solution is proposed in figure VIII-e. The truncated cone is characterised by the following parameters:

- H_{cone}, the height of the cone (94.99 mm)
- R_{sup}, the upper radius of the cone (158.32 mm)
- R_{inf}, the lower radius of the cone (103.48 mm)

In the truncated cone, the elementary radiators (or patches) are arranged in 29 columns of $N_{ER}=4$. A constant elevation spacing is chosen: 27.42 mm (i.e.: 0.75 λ at 8.2 GHz). Concerning the azimuth spacing, it varies according to the crown of the cone from 24 mm (0.66 λ at 8.2 GHz) to 32.95 mm (0.90 λ at 8.2 GHz):

$d_{az1}=32.95$ mm
$d_{az1}=29.96$ mm
$d_{az1}=26.98$ mm
$d_{az4}=24.00$ mm

Th... ...nation contained in this document is proprietary to ALCATEL ESPA... shall not be di...osed by the recipient to third persons without the written consent of the company
Les inf... contenues dans ce document demeurent propriété exclusive d'ALC... ESPACE et ne do... être divulguées par le destinataire à des tiers sans l'accord écrit de la ...té.

The information contained in this document is proprietary to ALCATEL ESPACE and shall not be disclosed by the recipient to third persons without the written consent of the
Les informations contenues dans ce document demeurent propriété exclusive d'ALCATEL ESPACE et ne doivent pas être divulguées par le destinataire à des tiers sans l'accord écrit de

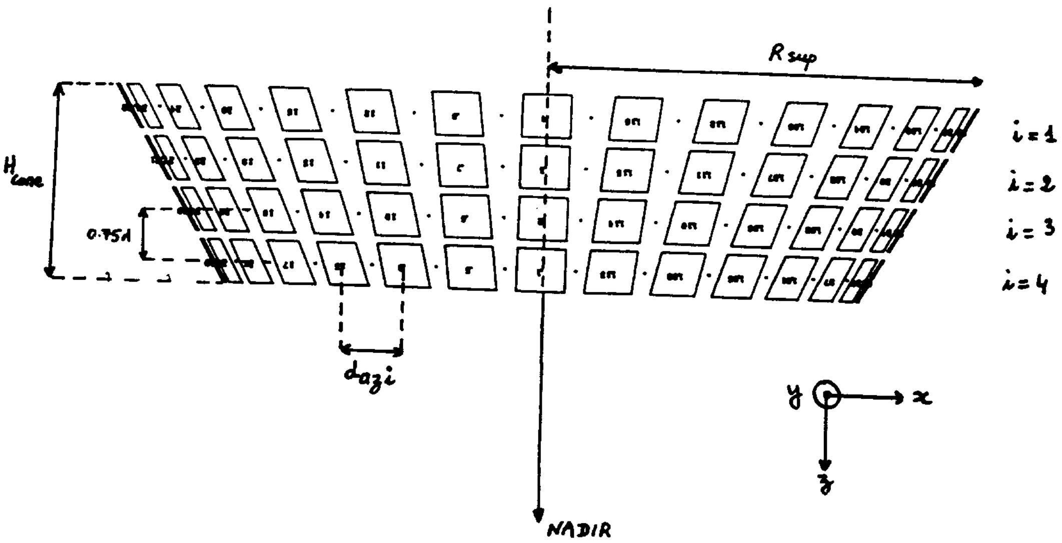

Fig. VIII-e: Geometrical characteristics of the active solution

Electrical characteristics

The feeding law of the subarray is proposed in the table of figure VIII-f.

i	*a_i (en dB)*	*ζ_i (en °)*
1	*-3.35*	*0*
2	*-2.16*	*48*
3	*0*	*0*
4	*-5.04*	*348*

Fig. VIII-f: feeding law of the 4-patches subarray

The information contained in this document is proprietary to ALCATEL ESPACE and shall not be disclosed by the recipient to third persons without the written consent of the company

Les informations contenues dans ce document demeurent propriété exclusive d'ALCATEL ESPACE et ne doivent pas être divulguées par le destinataire à des tiers sans l'accord écrit de la Société.

The radiated pattern of the subarray is given in figure VIII-g. The pattern is rather similar to EIRP mask.

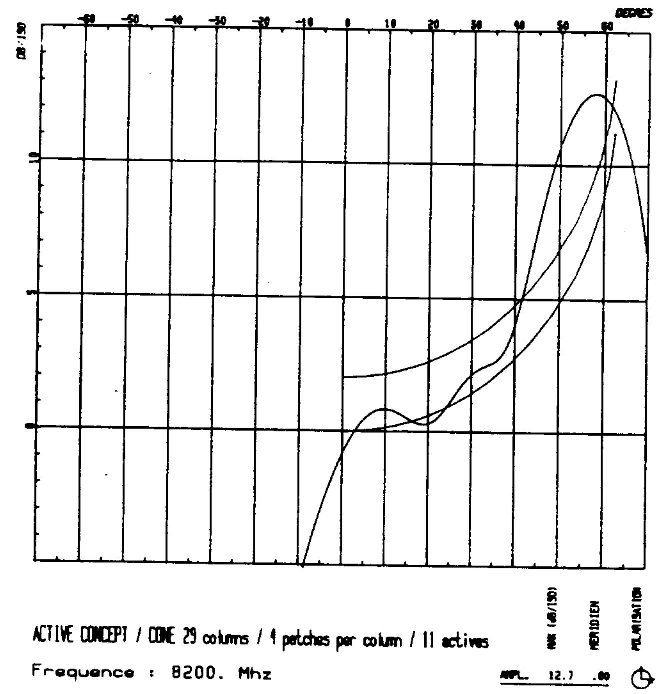

Fig. VIII-g: Radiated pattern of the 4-patches subarray

The EIRP performances of the antenna, when 11 columns are active, are given in figure VIII-h, with a RF power of -2.18 dBW. ESA mask is represented including a margin of 0.75 dB, which represents the total losses of a 4-patches subarray (see the antenna loss budget). The numerical values of EIRP are proposed in annex 1 and the radiated pattern of the antenna for several elevation samples too. The objective of 20.75 dBi directivity is reached with a margin of 0.05 dB, whereas a margin of 0.64 dBW is taken on the EIRP specifications. We can notice that the mask is overshot from 50° to 60°; it could become compliant by mismatching somewhat the phases.

For a single beam, each column is fed with a RF power of 55 mW (-12.6 dBW). So, <u>for three beams</u>, the RF power per column will be -12.6 + 10 log 3 = -7.83 dBW.

The amplifiers are connected to the columns via a filter which permits to reduce the intermodulation effects (see chapter 1 - System Analysis). The losses introduced by this connection must be taken into account for determining the RF power of a single SSPA. Presently, we take as hypothesis 1 dB losses (0.8 dB for the filter and 0.2 dB for the connections). A RF power of -6.83 dBW (210 mW) per amplifier is required. As eleven amplifiers are working at the same time, <u>a total RF power of 2.28 W is obtained for the antenna.</u>

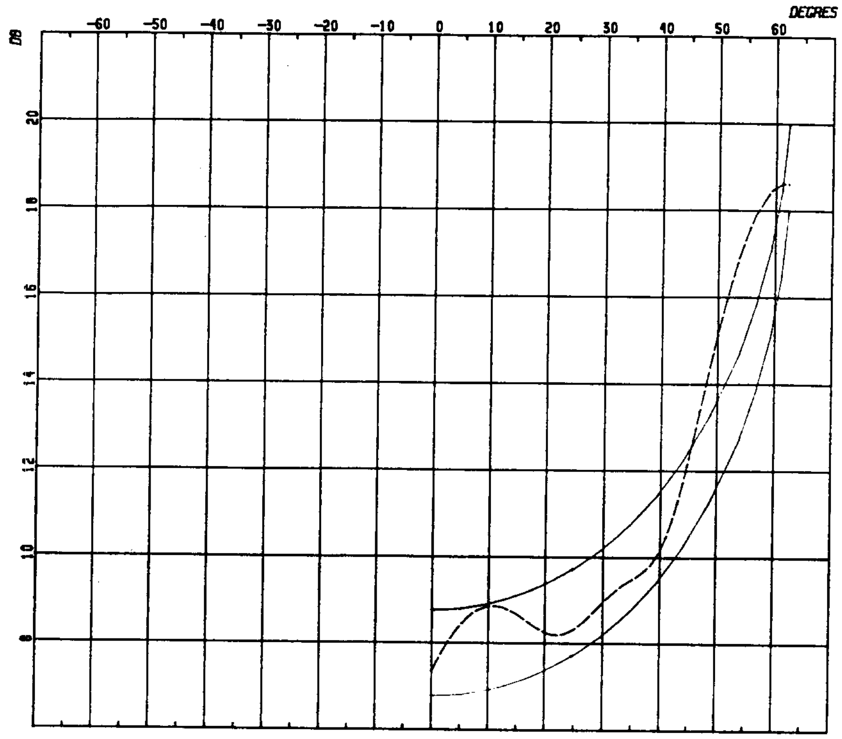

Fig. VIII-h: EIRP performances for the active antenna

The dynamical behaviour of the antenna must now be studied. It consists in demonstrating its capability to follow a ground station being compliant with required specifications (0.3 dB amplitude jump and 0.3° phase jump).

We have used a software developped for CNES, which computes all the commands necessary to follow a ground station according to three typical trajectories and to verify that the amplitude and phase variations do not exceed specified values. The typical trajectories (proposed in figure VIII-i) represent three typical passings of SPOT 1 from the ground station of Aussaguel (near Toulouse - 43.4 N latitude). The characteristics of these trajectories are described in the table of figure VIII-i.

The information contained in this document is proprietary to ALCATEL ESPACE and shall not be disclosed by the recipient to third persons without the written consent of the ALCATEL ESPACE.

Les informations contenues dans ce document demeurent propriété exclusive d'ALCATEL ESPACE et ne doivent être divulguées par le destinataire à des tiers sans l'accord écrit de ALCATEL ESPACE.

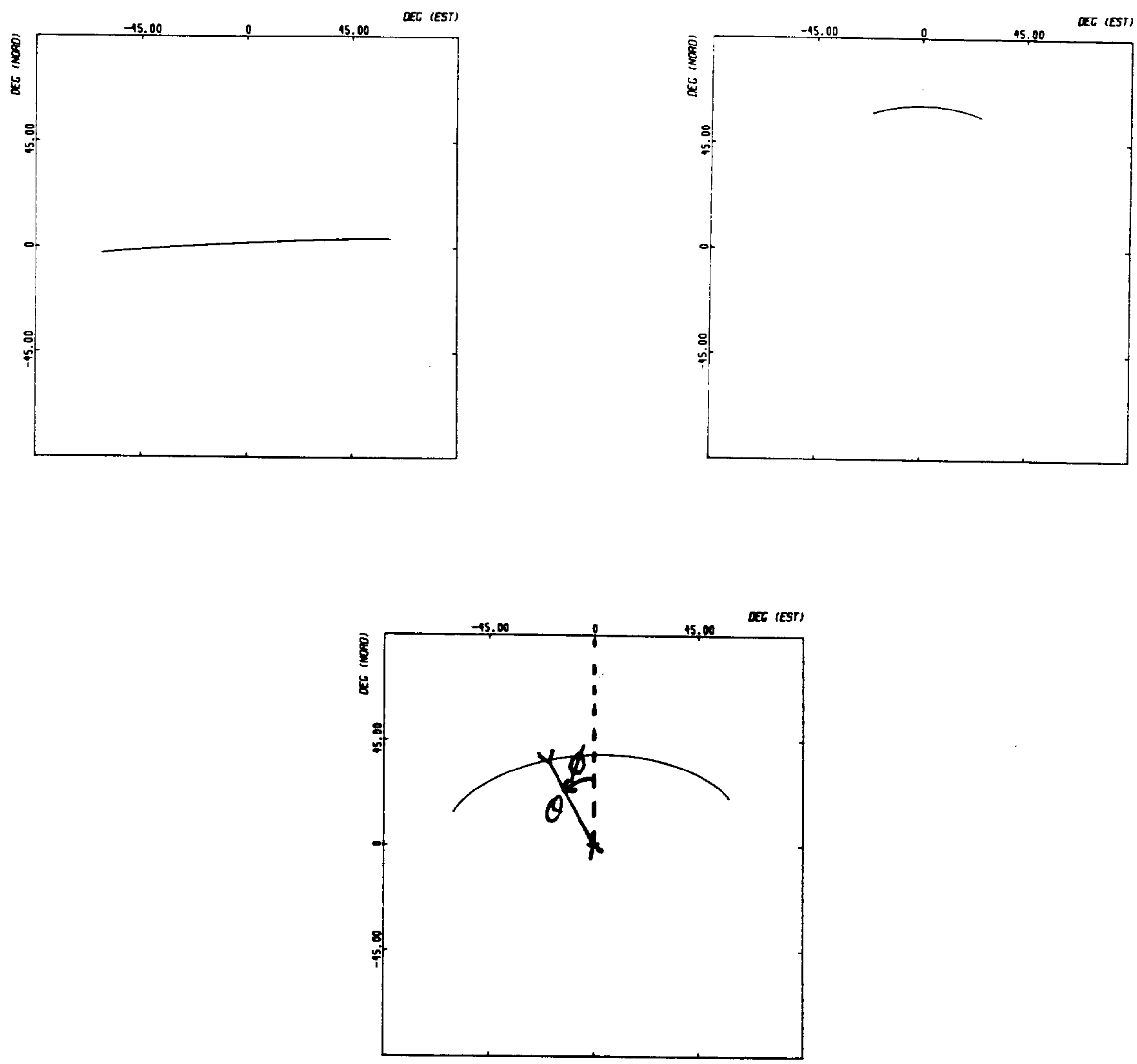

Type	QUASI NADIR	MEDIUM	HORIZON
duration	771 s	741 s	110 s
azimuth coverage	[-92.3°, 86.4°]	[-92.3°, 86.4°]	[-92.3°, 86.4°]
elevation coverage	[1.9°, 61.8°]	[-38.9°, 61.8°]	[-61.77°, 61.85°]
Clock	77 ms	150 ms	370 ms
P_{RF} (per column)	55 mW	55 mW	55 mW

Fig. VIII-i: Three typical trajectories of SPOT from Aussaguel (43.4 N latitude) and characterisation of these trajectories

The ...ation contained in this document is proprietary to ALCATEL ESPA... ...all not be ...d by the recipient to third persons without the written consent of the ... ...y

Les infor... contenues dans ce document demeurent propriété exclusive d'ALCA... ...SPACE et ne do... être divulguées par le destinataire à des tiers sans l'accord écrit de l'...

The information contained in this document is proprietary to ALCATEL ESPACE and shall not be disclosed by the recipient to third persons without the written consent of the company

Les informations contenues dans ce document demeurent propriété exclusive d'ALCATEL ESPACE et ne doivent être divulguées par le destinataire à des tiers sans l'accord écrit de la société.

The hypothesis of five bits phase-shifters is made. So the Lest Significant Bit (LSB) of a phase-shifter is 11.25°. The results of these simulations are reported in the table of figure VIII-j and the amplitude and phase jumps versus to time are given for each trajectory in figures VIII-k to VIII-m.

Trajectory	*Quasi Nadir*	*Medium*	*Horizon*
RF power (1 col)	*55 mW*	*55 mW*	*55 mW*
clock	*77ms*	*150 ms*	*370 ms*
Amplitude jumps	0.5 dB	0.4 dB	0.3 dB
Phase jumps	5°	4°	3°
Commutations	303	573	239

Fig. VIII-j: Amplitude and phase jumps performances

The most critical trajectory is the quasi-nadir one. This trajectory does not require a lot of commutations during initial and final parts because in these regions, the azimuth of the station is quasi constant and equal to -90° in the initial part and +90° in the final part. When the station is over nadir, a shift of almost 180° in azimuth is required which explain the high number of commutations obtained during time 4800 to 5300 (see figure VIII-k).

An important parameter for commutation is the clock. Figure VIII-n represents the amplitude and phase jumps obtained for the quasi-nadir trajectory when the clock is 154 ms. It is clear that the time for commutation is too long and the antenna has not the time to activate the suited column with the same constraints than for a 77 ms-clock (0.5 dB / 5°). A compromise must be found for the clock value:

- a too slow value does not permit to follow the ground station
- a too fast value means a lot of commands for the antenna, so it increases the complexity of the management unit. Moreover, the consumption of the ASIC's increase with the velocity of commutation.

The amplitude / phase jumps performances are not compliant with the required specifications (0.5 dB / 5° obtained against 0.3 dB / 3° required). These excessive values are essentially due to the switching of the columns. The worst case of amplitude jump is given by : 20 log (N_{act}+1 / N_{act}) which is equal to 0.7 dB if N_{act}=11.

During the CNES study (cone of 60 columns, 19 active), the performances were the following:

- theoretical simulation 1 (simulation of the column pattern): 0.3 dB / 3°
- theoretical simulation 2 (including measurement of the column pattern): 0.5 dB / 5°
- measurement (adding specific test error) 0.7 dB / 4.5°

That's why, if the same hypothesis are made for this study, <u>the final amplitude and phase jumps will certainly be about 0.9 dB / 7°.</u>

The only way to be compliant with the 0.3 dB / 3° specifications is to increase the number of active columns and consequently N_{tot}, but it will increase considerably the number of active modules, so the cost of the antenna... That's why, if we want to design an active antenna with a competitive cost, a solution could be to modify the specifications. An increment of amplitude and phase jumps up to 1 dB / 1° does not degrade significantly the performances of the antenna (see System Analysis).

Th[illegible] [illegible]nation contained in this document is proprietary to ALCATEL ESPA[illegible] shall not be [illegible]osed by the recipient to third persons without the written consent of the company

Les inf[illegible] [illegible]s contenues dans ce document demeurent propriété exclusive d'ALC[illegible] [illegible]SPACE et ne do[illegible] [illegible]s être divulguées par le destinataire à des tiers sans l'accord écrit de l[illegible] [illegible]té.

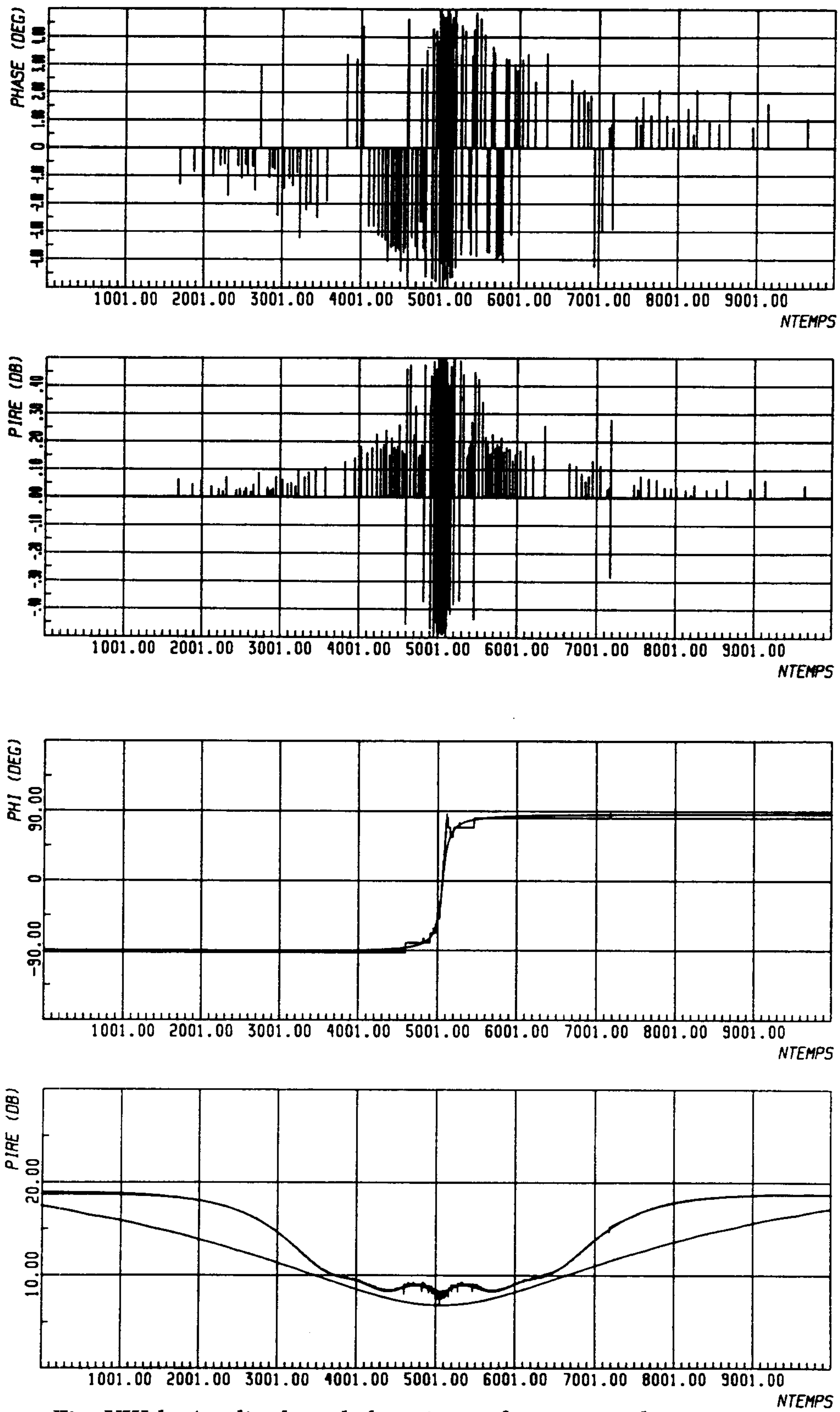

Fig. VIII-k: Amplitude and phase jumps for quasi-nadir trajectory

The information contained in this document is proprietary to ALCATEL ESPACE and shall not be disclosed by the recipient to third persons without the written consent of the ALCATEL ESPACE

Les informations contenues dans ce document demeurent propriété exclusive d'ALCATEL ESPACE et ne doivent pas être divulguées par le destinataire à des tiers sans l'accord écrit de l'ALCATEL ESPACE

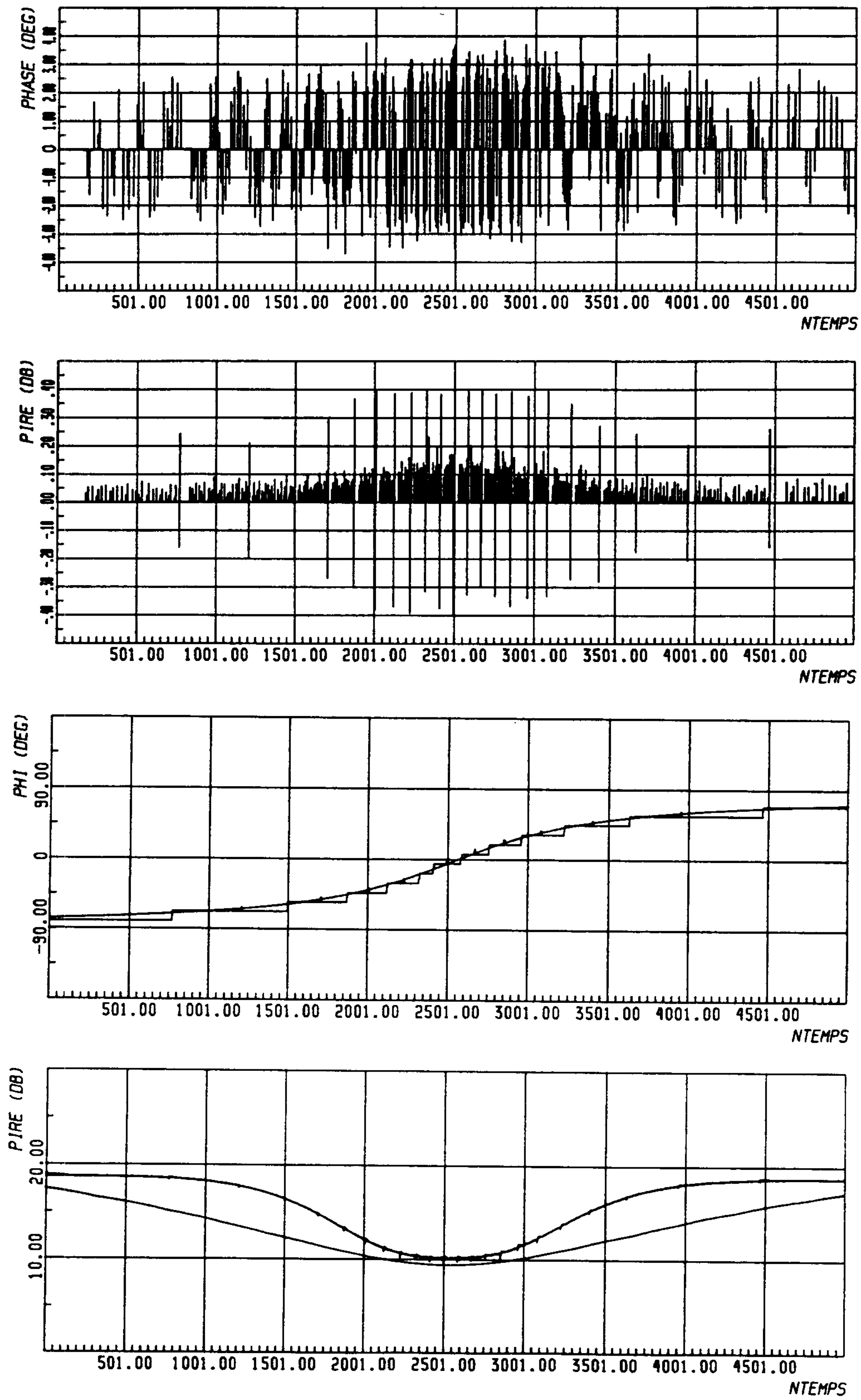

Fig. VIII-l: Amplitude and phase jumps for medium trajectory

The information contained in this document is proprietary to ALCATEL ESPACE and shall not be disclosed by the recipient to third persons without the written consent of the [...]

Les informations contenues dans ce document demeurent propriété exclusive d'ALCATEL ESPACE et ne doivent être divulguées par le destinataire à des tiers sans l'accord écrit de l'[...]

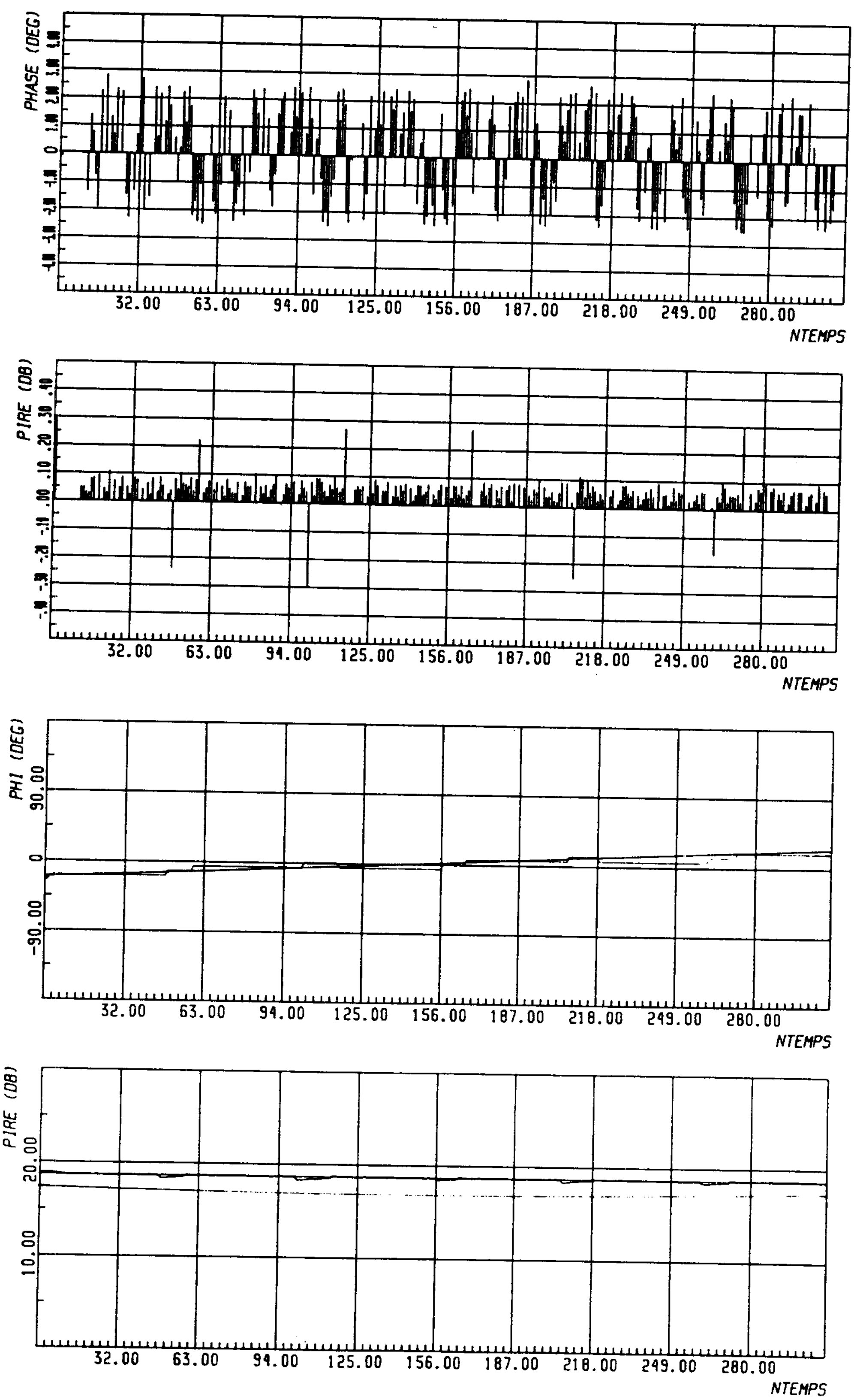

Fig. VIII-m: Amplitude and phase jumps for horizon trajectory

The ...ation contained in this document is proprietary to ALCATEL ESPA... shall not be ...d by the recipient to third persons without the written consent of the ...

Les infor... contenues dans ce document demeurent propriété exclusive d'ALCA... SPACE et ne doi... être divulguées par le destinataire à des tiers sans l'accord écrit de l...

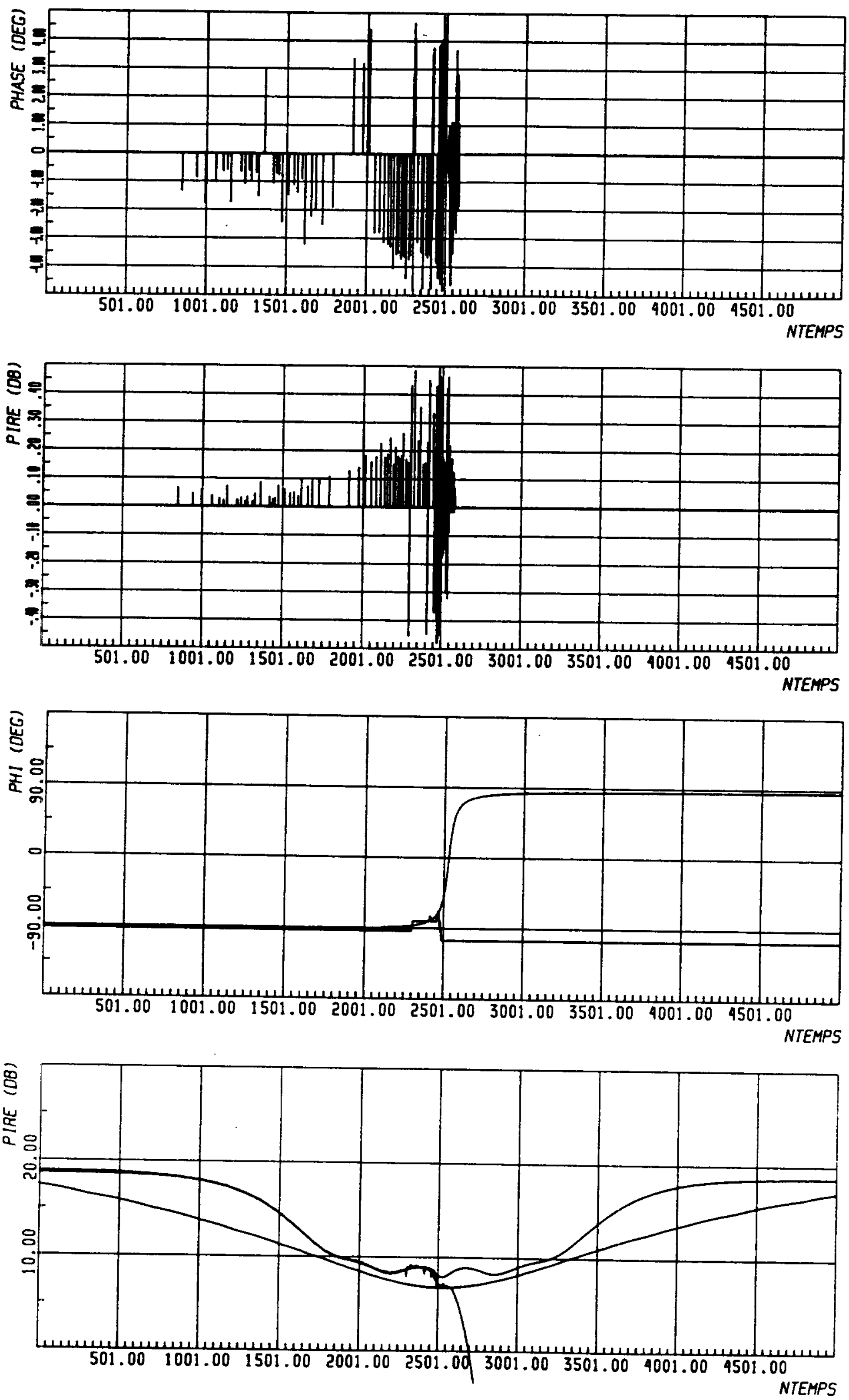

Fig. VIII-n: Amplitude and phase jumps for quasi-nadir trajectory (clock=154ms)

The information contained in this document is proprietary to ALCATEL ESPACE and shall not be disclosed by the recipient to third persons without the written consent of the company.

Les informations contenues dans ce document demeurent propriété exclusive d'ALCATEL ESPACE et ne doivent pas être divulguées par le destinataire à des tiers sans l'accord écrit de l'entreprise.

IX THE SEMI-ACTIVE CONCEPT: PROPOSITION OF A SOLUTION

IX-1 PRINCIPLE OF A BUTLER MATRIX

The semi-active concept is based on the use of Butler matrixes.

A Bulter matrix N x N (ie: with N inputs and N outputs) is a 2N-port network, where $N=2^p$ (p is an integer). All ports are matched and the N ports of the input side are mutually isolated, as are the N ports on the output side.

It can be defined by a transferring matrix Bn as shown in figure IX-a.

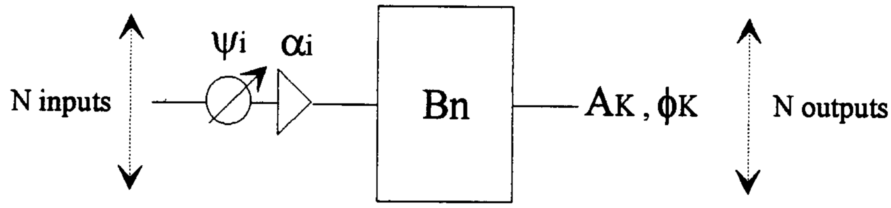

Fig. IX-a: Representation of a Butler matrix

with the following relation

$$\langle A_K, \phi_K \rangle = \sum_{i=1}^{N} \left(\frac{\alpha_i}{\alpha} \exp j(\phi + \psi_i + (K-1)(\phi_0 + \frac{2i\pi}{N})) \right)$$

where α is the amplitude loss through the matrix
ϕ is the insertion phasis of the matrix

It means that a linear phase distribution is induced by the excitation of input i (see figure IX-b).

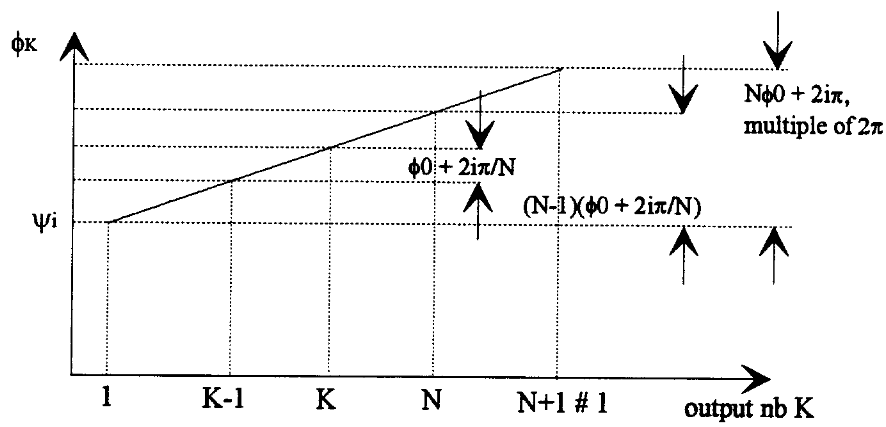

Fig. IX-b: Phase distribution induced by excitation of input i

The information contained in this document is proprietary to ALCATEL ESPACE and shall not be disclosed by the recipient to third persons without the written consent of the company.
Les informations contenues dans ce document demeurent propriété exclusive d'ALCATEL ESPACE et ne doivent pas être divulguées par le destinataire à des tiers sans l'accord écrit de la société.

The information contained in this document is proprietary to ALCATEL ESPACE and shall not be disclosed by the recipient to third persons without the written consent of the company
Les informations contenues dans ce document demeurent propriété exclusive d'ALCATEL ESPACE et ne doivent pas être divulguées par le destinataire à des tiers sans l'accord écrit de la société.

A Butler matrix is finally, an implementation of the Fourier transform. The signal combinations (sums, differences) is achieved by a set of hybrids couplers.

For the purpose of our study, the outputs of the Butler matrixes will be connected to the columns of the conical antenna as shown in figure IX-c.

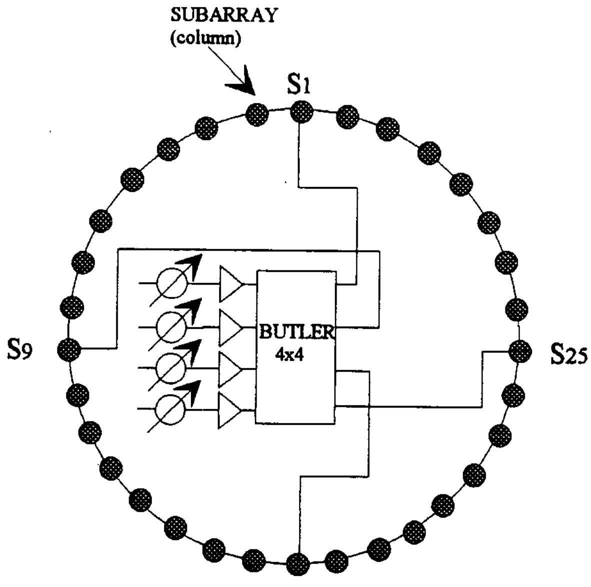

Fig. IX-c: Semi-active concept in a cone of 32 columns (N=4 and N_B=8)

Let us consider the case of a conical antenna of N_{tot} columns fed by N_B Butler matrixes with N inputs and N outputs (figure IX-c). During the active concept, it has been demonstrated that the optimum radiation is obtained when one third of the cone is switching on. The capability of a Butler matrix to concentrate energy to one output means that a particular connection of the outputs of the matrixes must be done in order to be able to concentrate energy to a number of N_B columns.

The order of connection of the outputs round a circle will be:

- column 1: output 1 of matrix 1
- column 2: output 1 of matrix 2
-......
- column N_B: output 1 of matrix N_B
- column N_B +1: output 2 of matrix 1
-.....
- column 2 N_B: output 2 of matrix N_B
-....
- column N_{tot}=N$\times$$N_B$: output N of matrix N_B

The information contained in this document is proprietary to ALCATEL ESPACE and shall not be disclosed by the recipient to third persons without the written consent of the company

Les informations contenues dans ce document demeurent propriété exclusive d'ALCATEL ESPACE et ne doivent être divulguées par le destinataire à des tiers sans l'accord écrit de la société.

In order to turn regularly the beam around the cone, a constant phase difference between two consecutive outputs must be induced by the excitation of an input. It is easy to demonstrate that the only way to reach this constraint (see figure IX-b, ϕ_0 multiple of 2π) is by the use of 180°-hybrids (see annex A to chapter 3).

The azimuth control is achieved by according the phase and amplitude of all the inputs of the Butler matrixes (ie: all the amplifiers are working at the same time). The amplifiers are introduced at the inputs of the Butler matrixes as shown in figure IX-c and all amplifiers are working all the time which permits to reduce DC and RF power compared to active option.

A circular permutation of the Butler matrixes (ie: matrix 1 $\rightarrow$ matrix 2,...matrix N_B $\rightarrow$ matrix 1) permits to turn the beam of an angle equal to 360° / N_{tot}, whereas a circular permutation of the outputs of the Butler (ie: output 1 of matrix 1 $\rightarrow$ output 2 of matrix 1, ..., output N of matrix 1 $\rightarrow$ output 1 of matrix 2, ..., output N of matrix N_B $\rightarrow$ output 1 of matrix 1) permits to turn the beam of an angle equal to 360° x N_B / N.

From our knowledge of antenna litterature (see annex A to chapter 3), Butler matrixes are the best way to make multiple well decoupled beams «turn around» a circular array, with limited loss, and equal amplitude excitation at the inputs of the matrixes (so better efficiency of the amplifiers).

The critical point in the use of a Butler matrix for a conical antenna is the level of the far field at the nadir. It is easy to demonstrate (detail of the calculation is proposed in annex number 2) that, if N_B is the number of Butler matrixes connected to a conical antenna and if D is the dynamique range of the α_i in dB, this level is equal to:

$$20\log\left(N_B\sqrt{N}\,\alpha_{\max}E_1\right)$$

where

E_1 is the level of a single column at the nadir

and $$\alpha_{\max}=\sqrt{\frac{X^2}{X^2N_B+(N-1))N_B}}\quad \text{(with}\quad X=10^{\frac{D}{20}}\text{)}$$

The level at the nadir is then about proportionnal to the number of Butler matrixes N_B. In case of equal power feeding of the Butler's inputs (D=0, so X=1), this level becomes equal to $20\log\left(\sqrt{N_B}\right)+20\log(E_1)$.

For example, if we consider a conical antenna of N_{tot}=32 columns, it is preferable to use 8 4x4 Butler matrixes in place of 4 matrixes 8x8 because for a same level of a single column at the nadir, 3 dB more is obtained with 8 matrixes 4x4.

The information contained in this document is proprietary to ALCATEL ESPACE and shall not be divulged by the recipient to third persons without the written consent of the ALCATEL ESPACE.
Les informations contenues dans ce document demeurent propriété exclusive d'ALCATEL ESPACE et ne doivent pas être divulguées par le destinataire à des tiers sans l'accord écrit de ALCATEL ESPACE.

For example, if we consider a conical antenna of N_{tot}=32 columns, it is preferable to use 8 4x4 Butler matrixes in place of 4 matrixes 8x8 because for a same level of a single column at the nadir, 3 dB more is obtained with 8 matrixes 4x4.

IX-2 PARAMETRICAL STUDY

A parametrical study in the semi-active concept will be lead assuming that the same level of RF power is given in each input of the Butler; which gives better efficiency of the amplifiers as shown in the active concept. The optimisation will be done only on a straight generatrix (with β=30°). If a six patches subarray is selected as the best solution, a comparison between the folded profile selected in the active concept and a straight profile of 30° will be proposed.

The parameters will be:

- N_{tot} (varying from 24 to 32)
- N : 2, 3, 4 and 8
- N_B depending on N_{tot} and N ($N_B=N_{tot}/N$)
- N_{ER} : 4 or 6

The results of the optimization are reported in the table of figure IX-d.

N_{tot}	N_{ER}	N_B	N	margin for Dir 62.3°	P_{RF} total
30	4	15	2	-0.71 dB	-2.01 dBW
30	4	10	3	-0.08 dB	-2.69 dBW
32	4	16	2	-0.44 dB	-2.32 dBW
32	4	8	4	+0.16 dB	-2.30 dBW
32	4	4	8	-0.69 dB	+0.72 dBW
33	4	11	3	+0.40 dB	-3.17 dBW
24	**6**	**12**	**2**	**-1.79 dB**	**-1.17 dBW**
24	**6**	**8**	**3**	**-1.06 dB**	**-1.38 dBW**
24	**6**	**6**	**4**	**-1.15 dB**	**-0.13 dBW**
24	**6**	**3**	**8**	**-1.64 dB**	**+2.88 dBW**
27	6	9	3	-0.46 dB	-1.89 dBW
28	6	14	2	-1.10 dB	-1.66 dBW
28	6	7	4	-0.47 dB	-0.80 dBW
30	6	15	2	-0.80 dB	-1.97 dBW
30	6	10	3	-0.07 dB	-2.35 dBW
32	6	16	2	-0.53 dB	-2.24 dBW
32	6	8	4	+0.13 dB	-1.38 dBW

Fig. IX-d: Parametrical study in the active concept

The information contained in this document is proprietary to ALCATEL ESPACE, shall not be disclosed by the recipient to third persons without the written consent of the company

Les informations contenues dans ce document demeurent propriété exclusive d'ALCATEL ESPACE et ne doivent pas être divulguées par le destinataire à des tiers sans l'accord écrit de la société.

Several remarks can be made on the results of the parametrical study:

- a maximum RF power of -0.77 dBW is required in the specifications, and all the configurations with N=8 are not compliant because of the nadir level.

- all the configurations with N=2 have an excellent level at the nadir but the directivity at 62.3° in elevation is critical. That's why a compromise must be realise in the order of the Butler matrixes It leads to the conclusion that that N=3 or 4.

- if we analyse the different results obtained for N_{tot}=24 and N_{ER}=6, we can deduce that the best configuration will be obtained with Butler matrixes 3x3. This is normal because with 3x3 matrixes, the beam will be formed with 8 columns which correponds to one third of the cone.

- if we focus on the EIRP performances of a solution (N_{tot}=30, N_{ER}=6, N_B=10 and N=3) as shown in figure IX-e, it is clear that we have a minimum margin of about 1 dB from 2° in elevation to 55°; and no margin at the two extremities. That's why the radiated pattern of a single column must be re-optimised by modifying the mask (increasing the levels at the extremities and decreasing the level between the extremities). A new optimisation of this solution lead to the pattern reported in figure IX-f. The obtained performances with this new radiated pattern is considerably better because a total number of columns of 24 (8 matrixes 3x3) gives compliant results for both directivity at 62.3° in elevation and total RF power (figure IX-f). A second step optimisation is then necessary. It will be lead only with N=3 and N=4.

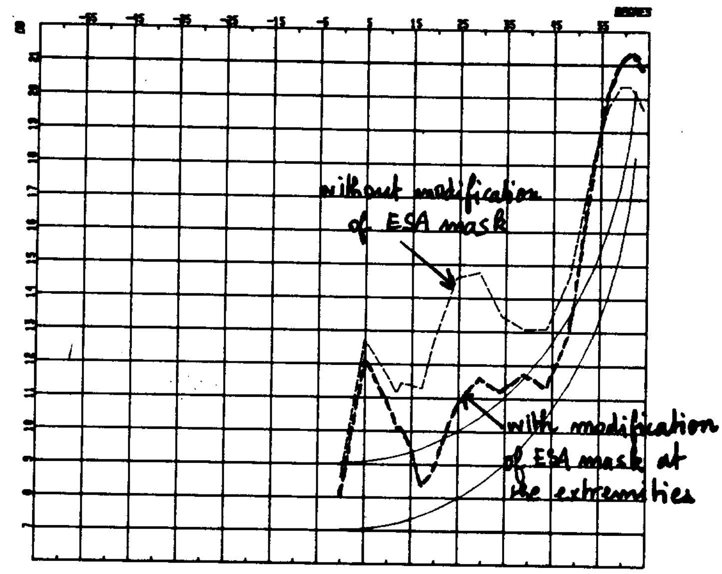

Fig. IX-e: EIRP performances (N_{ER}=6, N_{tot}=30, N_B=10 and N=3)

The information contained in this document is proprietary to ALCATEL ESPACE ... shall not be disclosed by the recipient to third persons without the written consent of the ...

Les informations contenues dans ce document demeurent propriété exclusive d'ALCATEL ESPACE et ne doivent pas être divulguées par le destinataire à des tiers sans l'accord écrit de ...

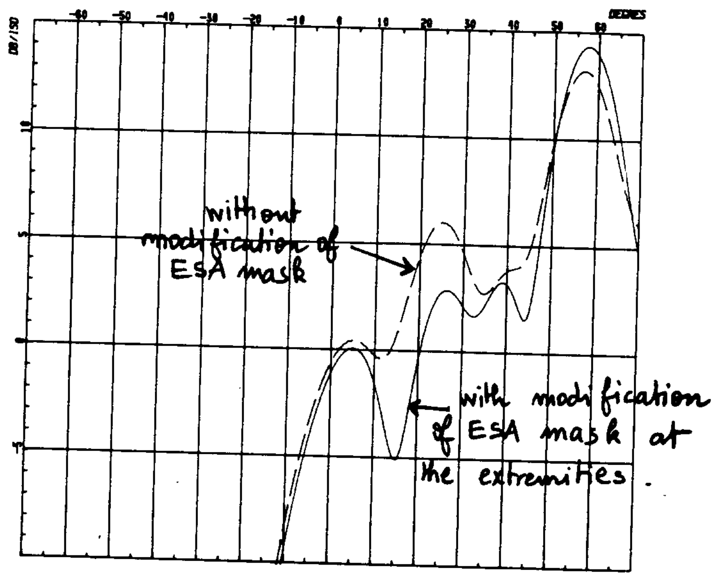

Fig. IX-f: Subarray radiated pattern (N_{ER}=6)

Final optimisation give the results reported in table of figure IX-g. A trade-off is made according to the feasibility of a 6-patches subarray and the feasibility of a 3x3 Butler matrix. The alternative to the feasibility of a 3x3 Butler matrix is a 4x4 Butler matrix and the alternative to the feasibility of a 6-patches subarray is a 4-patches subarray.

Moreover, for the solutions with 6-patches subarray, a comparison between folded and straight subarrays will be made.

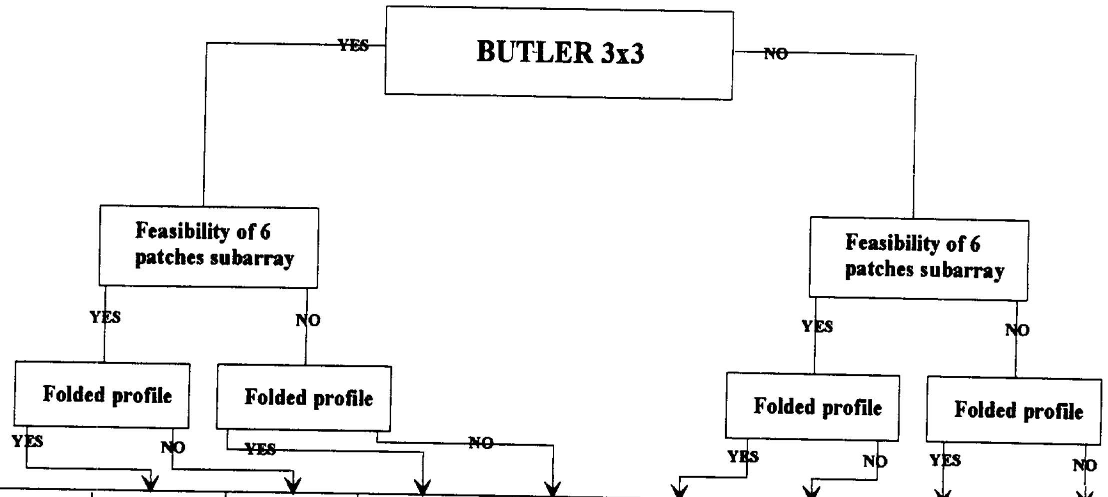

Ntot / NER	24 / 6	24 / 6	27 / 4	27 / 4	28 / 6	28 / 6	28 / 4	28 / 4
Cone profile	25/.../25/35	30	30	30	25/.../25/35	30	30	30
Butler	8 3x3	8 3x3	9 3x3	9 3x3	7 4x4	7 4x4	7 4x4	7 4x4
Dmin 62.3°	21.08 dBi	21.05 dBi	20.92 dBi	20.92 dBi	21.43 dBi	21.28 dBi	20.80 dBi	20.80 dBi
Margin for Dmin	0.08 dB	0.05 dB	0.17 dB	0.17 dB	0.43 dB	0.28 dB	0.05 dB	0.05 dB
Margin for RF power	0.22 dBW	0.00 dBW	0.22 dBW	0.22 dBW	0.40 dBW	0.35 dBW	0.05 dBW	0.05 dBW

Fig. IX-g: Trade-off in the semi-active concept

<u>If we consider that the main criterium to compare the solutions is the number of total columns</u> (in order to reduce the complexity, the mass and so the cost of the antenna), the best solution is a cone of 24 columns with a 6-patches folded subarray. Margins of 0.08 dB and 0.22 dB are obtained for respectively directivity at 62.3° and RF power. The results are significatively increased with a folded profile: 0.22 dB more margin for RF power and 0.03 dB for directivity.

However, the proposed solution had several drawbacks:
- the feasibility of a Butler 3x3
- the feasibility of a 6-patches subarray (loss in the bandwidth expected higher on longer subarrays - to be assessed in WP 2200)
- the folded subarray which induces some risks in the fabrication

<u>That's why, alternatives are proposed with 4x4 Butler matrixes and 4-patches subarray</u>. The solutions will be classified from 1 to 4. The best solution will be more detailed in next part and EIRP performances of the other solutions will be proposed in annex 3. The proposed solution are:

1-	$N_{tot}=24$	$N_B=8$	$N=3$	$N_{ER}=6$
2-	$N_{tot}=27$	$N_B=9$	$N=3$	$N_{ER}=4$
3-	$N_{tot}=28$	$N_B=7$	$N=4$	$N_{ER}=6$
4-	$N_{tot}=28$	$N_B=7$	$N=4$	$N_{ER}=4$

The information contained in this document is proprietary to ALCATEL ESPACE and shall not be disclosed by the recipient to third persons without the written consent of the company.
Les informations contenues dans ce document demeurent propriété exclusive d'ALCATEL ESPACE et ne doivent pas être divulguées par le destinataire à des tiers sans l'accord écrit de la société.

The information contained in this document is proprietary to ALCATEL ESPACE and shall not be disclosed by the recipient to third persons without the written consent of the company
Les informations contenues dans ce document demeurent propriété exclusive d'ALCATEL ESPACE et ne doivent pas être divulguées par le destinataire à des tiers sans l'accord écrit de la société.

IX-3 THE CHOSEN SOLUTIONS

The parametrical study has led to the choice of a 6 patches folded subarray fed by a serial repartitor. The complete feasibility of the serial repartitor for the 6 patches subarray has not been already demonstrated. That's why, two solutions will be retained and presented in §IX:

- a 24 column antenna with 6 patches folded subarray fed by a serial repartitor
- a 24 column antenna with 6 patches folded subarray fed by a parallel repartitor

The performances obtained with the two configurations of repartitors are quasi equivalent. Final choice between the two solutions will be made during WP 2200.

Geometrical characteristics

The geometrical characteristics of the retained solutions are proposed in figure IX-h.

The truncated cone is characterised by the following parameters:

H_{cone}, the height of the cone (SERIAL: 146.72 mm, PARALLEL: 146.72 mm)
R_{sup}, the upper radius of the cone (SERIAL: 159.02 mm, PARALLEL: 174.21 mm)
R_{inf}, the lower radius of the cone (SERIAL: 83.29 mm, PARALLEL: 98.48 mm))

In the truncated cone, the elementary radiators (or patches) are arranged in 24 folded columns of N_{ER}=6. A constant elevation spacing is chosen: 27.42 mm (i.e.: 0.75 λ at 8.2 GHz).

Concerning the azimuth spacing d_{az}, it varies according to the crown of the cone from:
-24 mm (0.66 λ at 8.2 GHz) to 39.80 mm (1.09 λ at 8.2 GHz) (SERIAL REPARTITOR)
-28 mm (0.77 λ at 8.2 GHz) to 43.80 mm (1.20 λ at 8.2 GHz) (PARALLEL REPARTITOR)

A minimum azimuth spacing of 24 mm is taken on the first crown because the diameter of the lower cavity of the elementary radiator is equal to 23 mm. This is the shortest value which could be taken only if a serial repartitor is chosen because no space is needed for the feeding lines (they pass through the patches). If a parallel or combined serial / parallel repartitor is chosen, this value must be greater due to the feeding lines and be equal at minimum to 28mm.

The exact azimuth spacing values are the following:

Azimuth spacing	*SERIAL*	*PARALLEL*
d_{az1}	39.80 mm	43.80 mm
d_{az2}	36.75 mm	40.75 mm
d_{az3}	33.70 mm	37.70 mm
d_{az4}	30.65 mm	34.65 mm
d_{az5}	27.60 mm	31.60 mm
d_{az6}	24.00 mm	28.00 mm

Th ...mation contained in this document is proprietary to ALCATEL ESPA... ESPACE ... shall not be ...ed by the recipient to third persons without the written consent of the ...hy

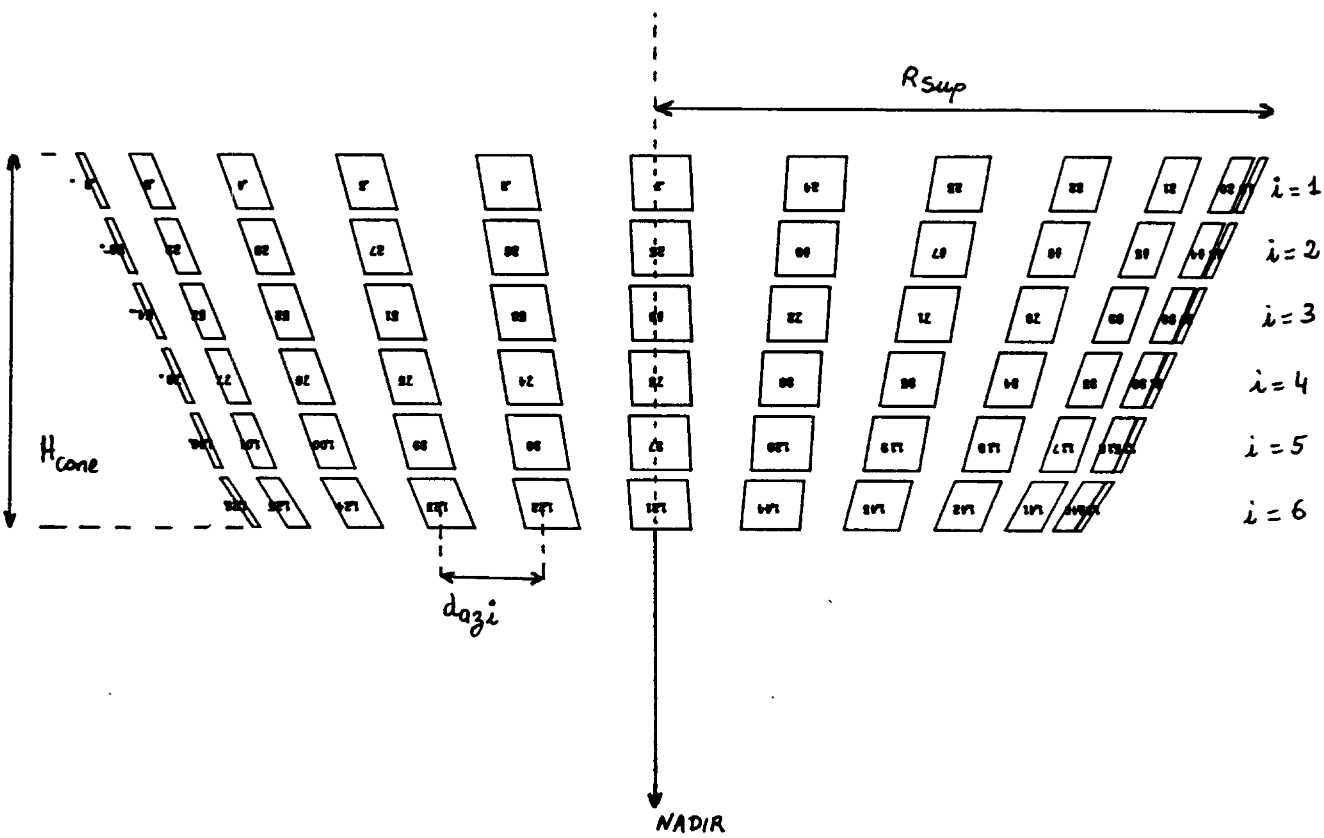

Fig. IX-h: Geometrical characteristics of the semi-active solution

Les infor...s contenues dans ce document demeurent propriété exclusive d'ALCA... et ne dc... être divulguées par le destinataire à des tiers sans l'accord écrit de ...

Electrical characteristics

The feeding law of the subarray is proposed in the tables of figure IX-i-1 and IX-i-2.

i	*SERIAL REPARTITOR*		
i	a_i *(in dB)*	ζ_i *(in °)*	β *(in °)*
1	*-2.00*	*0*	*25*
2	*-1.00*	*20*	*25*
3	*0.00*	*322*	*25*
4	*0.00*	*348*	*25*
5	*-1.00*	*265*	*25*
6	*-2.00*	*219*	*35*

Fig. IX-i-1: feeding law of the 6-patches folded subarray fed by a serial repartitor

i	*PARALLEL REPARTITOR*		
i	a_i *(in dB)*	ζ_i *(in °)*	β *(in °)*
1	*-0.23*	*0*	*25*
2	*-0.27*	*43*	*25*
3	*0*	*346*	*25*
4	*-0.13*	*11*	*25*
5	*-0.23*	*291*	*25*
6	*-0.27*	*255*	*35*

Fig. IX-i-2: feeding law of the 6-patches folded subarray fed by a parallel repartitor

The radiated pattern of the subarrays is given in figure IX-i-3.

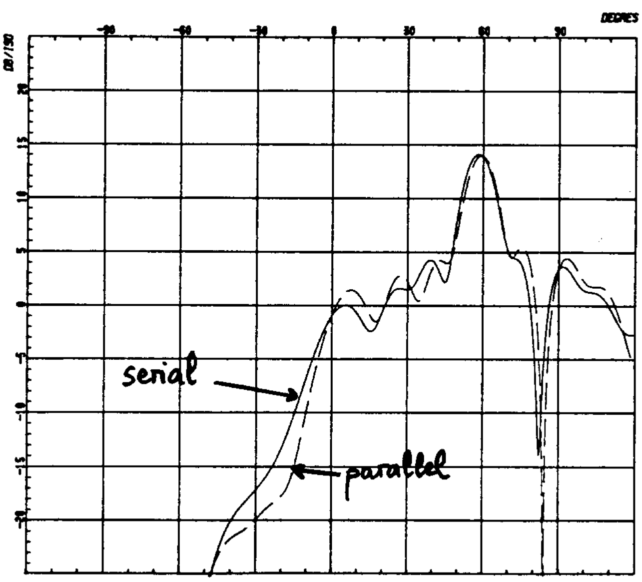

Fig. IX-i-3: Radiated pattern of the folded 6-patches subarrays
(fed by serial or parallel repartitors)

The information contained in this document is proprietary to ALCATEL ESPACE and shall not be disclosed by the recipient to third persons without the written consent of the ...
Les informations contenues dans ce document demeurent propriété exclusive d'ALCATEL ESPACE et ne doivent pas être divulguées par le destinataire à des tiers sans l'accord écrit de ...

The EIRP performances of the antenna are given in figure IX-j, with a RF power of -0.77 dBW, which corresponds to maximum RF power possible for the antenna. ESA mask is represented including a margin of 1.00 dB, which represents the total losses of a 6-patches subarray (see the antenna loss budget). The numerical values of EIRP are proposed in annex 3 for the two configurations and the radiated pattern of the antenna (with the serial repartitor) for several elevation samples too.

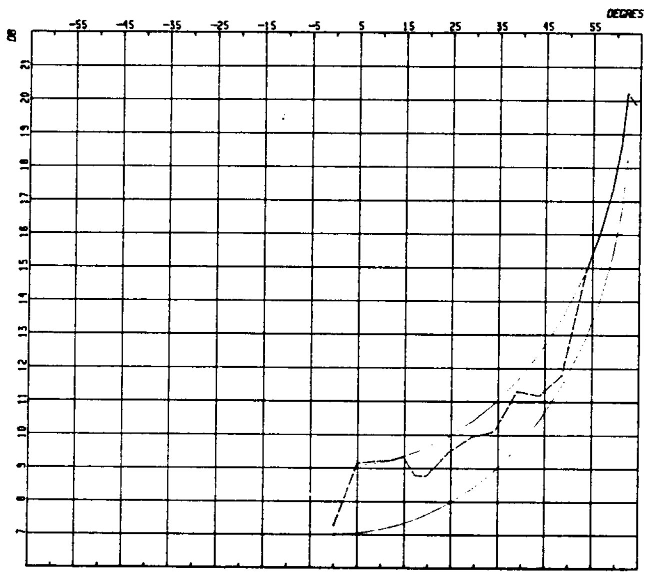

Fig. IX-j-1: EIRP pattern for the semi-active antenna with serial feeding

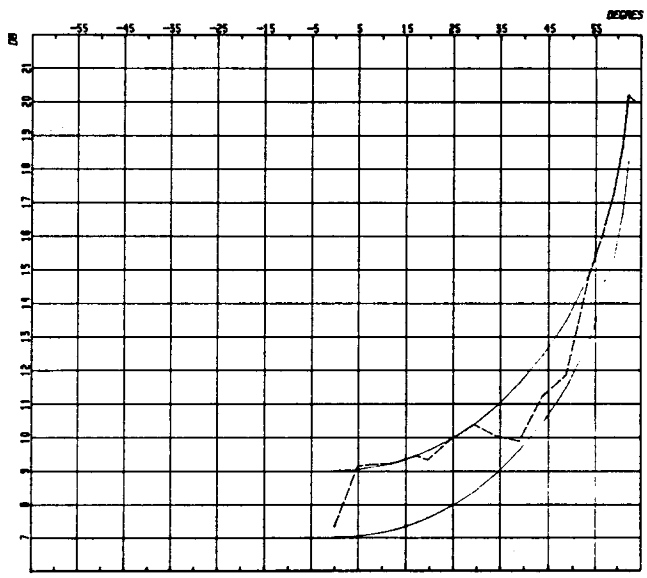

Fig. IX-j-2: EIRP pattern for the semi-active antenna with parallel feeding

Th· ·ration contained in this document is proprietary to ALCATEL ESPA· shall not be ·:d by the recipient to third persons without the written consent of the ·y
Les infor· ·ns contenues dans ce document demeurent propriété exclusive d'ALCA· ·SPACE et ne do· ·être divulguées par le destinataire à des tiers sans l'accord écrit de· ·é.

The information contained in this document is proprietary to ALCATEL ESPACE and shall not be disclosed by the recipient to third persons without the written consent of the ALCATEL ESPACE.
Les informations contenues dans ce document demeurent propriété exclusive d'ALCATEL ESPACE et ne doivent pas être divulguées par le destinataire à des tiers sans l'accord écrit de ALCATEL ESPACE.

The objective of 21.00 dBi directivity is reached with a margin of 0.08 dB for the serial repartitor and a margin of 0.00 dB with the parallel one. Concerning the RF power a margin of approximately 0.2 dBW is obtained for both cases.

The EIRP characteristics are fully compliant with ESA specifications (RF input power=-0.77 dBW and EIRP values don't exceed 2 dB more than minimum required values for all the elevation samples comprise between 0 to 62.3°).

For a single beam, each column is feeding with a RF power of 35 mW (-14.57 dBW). So, for three beams, the RF power will be -14.57 + 10 log 3 = -9.80 dBW. The amplifiers are connected to the columns via a Butler matrix and filter. The losses introduced by this connection must be taken into account for determining the RF power of a single SSPA. These losses are approximately 2.0 dB (1 dB for the Butler, 0.8 dB for the filter and 0.2 dB for the connections). A RF power of -7.80 dBW (166 mW) per amplifier is required.

As 24 amplifiers are working at the same time, a total RF power of 3.98 W is obtained for the antenna.

The EIRP performances are obtained for ϕ=0° (taken at the center of a column as shown in figure IX-k). Due to its revolution geometry, we must analyse the performances of the antenna for the azimuth sector [$-360/(2\ N_{tot})$; $+\ 360/(2\ N_{tot})$]. This analysis will be proposed only for the antenna with a serial repartitor because the conclusions will be the same for the antenna with the serial repartitor.

Figure IX-l shows the RF power on each column for both cases ϕ=0° and ϕ=7.5° =360/(2x24) when a RF input level of 1 is taken in each input.

Thanks to the properties of the Butler matrix, we can see that energy is concentrated on one output because a level of quasi 3 in RF power is obtained on eight columns. For the case where ϕ=7.5°, a symmetrical distribution of energy (with a short taperisation) is obtained whereas unsymmetrical distribution is obtained for ϕ=0°, which corresponds to the worst case and gives some backward radiations. We can conclude that the performances proposed in figure IX-j are the worst performances obtained in a [-7.5°, 7.5°] azimuth sector.

As a comparison, if the same configuration is taken with the active concept (in which 9 columns will be active), a level of 20.97 dBi is obtained at 62.3° in elevation (approximately 0.1 dB less than the semi-active concept). In the active concept, the same performance can be obtained by a short taperisation of the column level. This taperisation is naturally induced in the semi-active concept by the phase distribution of the inputs.

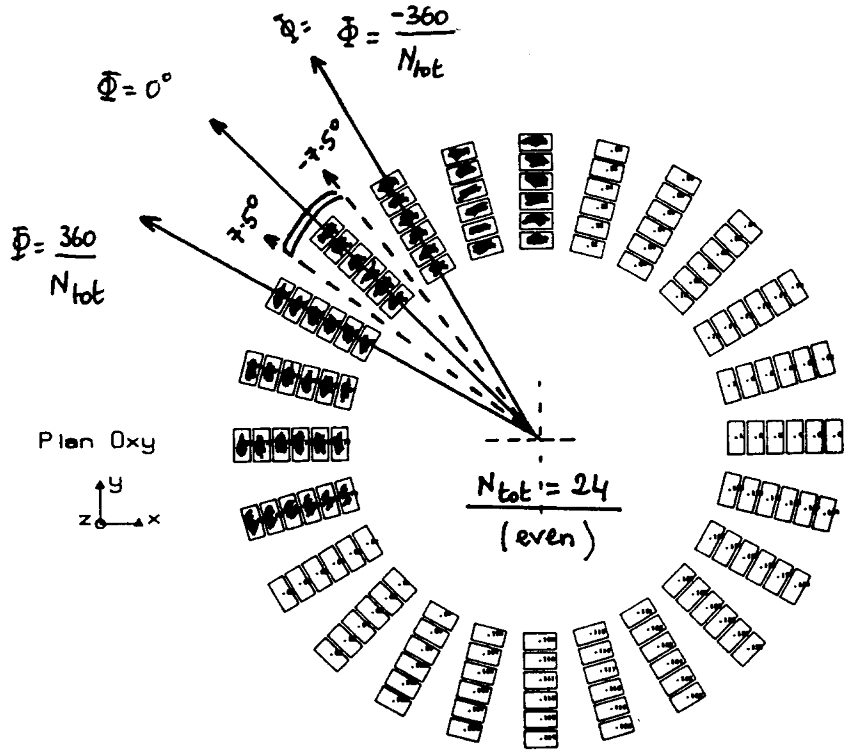

Fig. IX-k: the azimuth sector [-360/(2 N_{tot}); + 360/(2 N_{tot})].

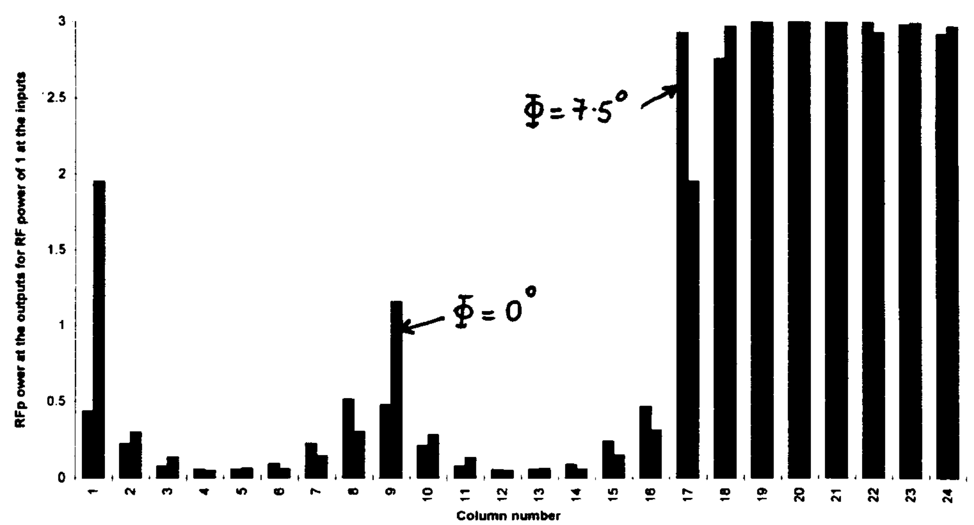

Fig. IX-l: Focus on the Butler matrixes output for optimisation at 62.3° (ϕ=0° and 7.5°)

The information contained in this document is proprietary to ALCATEL ESPACE and shall not be ...ed by the recipient to third persons without the written consent of the ...ly
Les informations contenues dans ce document demeurent propriété exclusive d'ALCATEL ESPACE et ne doivent être divulguées par le destinataire à des tiers sans l'accord écrit de ...é

The dynamical behaviour of the semi-active antenna has not been evaluated during this work package. However, the principle of turning the beam around the cone, by shifting the phases at the inputs of each Butler, does not require to switch on or off amplifiers. That's why better results are expected concerning amplitude and phase jumps.

The principle of calculation of amplitude and phase jumps for a semi-active antenna which follows a ground station between position 1 (given by elevation angle θ_1 and azimuth angle ϕ_1) and position 2 (given by θ_2 and ϕ_2) will be the following:

step 1: optimisation of the Butler's inputs for position 1
which gives the law : $(\psi_{11}, \psi_{21}, \psi_{31}, \ldots, \psi_{N\alpha 1})$

step 2: optimisation of the Butler's inputs for position 2
which gives the law : $(\psi_{12}, \psi_{22}, \psi_{32}, \ldots, \psi_{N\alpha 2})$
$(\psi_{12}, \psi_{22}, \psi_{32}, \ldots, \psi_{N\alpha 2}) - (\psi_{2m} - \psi_{1m})$
(ψ_{2m} and ψ_{1m} are respectively the averages of the law 2 and 1)

step 3: from the initial law $(\psi_{11}, \psi_{21}, \psi_{31}, \ldots, \psi_{N\alpha 1})$ to final law $(\psi_{12}, \psi_{22}, \psi_{32}, \ldots, \psi_{N\alpha 2}) - (\psi_{2m} - \psi_{1m})$ one LSB per one LSB incrementation (LSB depending on the number of bits chosen for each phase-shifter) and comparison of far field value with the far field value obtained with previous law.

The bits number of each phase-shifter will certainly be an important parameter in the amplitude and phase jumps. A parametrical study in the number of bits will be lead in order to determine the best compromise.

Th[...]ation contained in this document is proprietary to ALCATEL ESPA[...] shall not be [...]sed by the recipient to third persons without the written consent of the company

Les info[...] contenues dans ce document demeurent propriété exclusive d'ALC[...]SPACE et ne do[...] être divulguées par le destinataire à des tiers sans l'accord écrit de [...]é.

The information contained in this document is proprietary to ALCATEL ESPACE, shall not be disclosed by the recipient to third persons without the written consent of the company.
Les informations contenues dans ce document demeurent propriété exclusive d'ALCATEL ESPACE et ne doivent être divulguées par le destinataire à des tiers sans l'accord écrit de la société.

X TRADE-OFF BETWEEN THE CONCEPTS

X-1 MECHANICAL CHARACTERISTICS, PASSIVE EQUIPMENTS AND COST

The mechanical characteristics are summarized in the table of figure X-a.

	SEMI-ACTIVE	*ACTIVE*
Height of the cone	*146.72 mm*	*94.99 mm*
Upper radius	*159.02 mm*	*158.32 mm*
Lower radius	*83.29 mm*	*103.48 mm*
Number of columns	*24*	*29*
Type of subarray	*folded (25°/25°/25°/25°/25°/35°)*	*straight (30°)*
Patches per column	*6*	*4*
Number of active columns / Butler	*8 BUTLER 3x3*	*11 active columns*
Design simplicity	*Butler matrixes dispersion effects + 6 patches subarrays*	*Experience of CNES study + 4 patches subarray*
Beam shaping quality	*dispersion on matrixes TBV*	*good results (c.f. CNES)*
Equipment	*Butler + cables added to active concept but 5 modules less without bias switching*	*29 distributed active modules including HPA's (with bias switching) and phase-shifters*
TRADE-OFF	-	+

Fig. X-a: Mechanical characteristics of the different solutions

<u>The mechanical trade-off is more favourable to the active concept for two main reasons:</u>

- the active conical antenna is more lighter than the semi-active one:
  * 29x4=116 elementary radiators against 24x6=144 for the semi-active concept
  * a lower volume of the cone due to the 4-patches subarray configuration against a 6-patches one for the semi-active concept

- the fabrication of a 4-patches straight subarray is very easy compared to a folded 6-patches one, because there is no risk in breaking the substrate by the brisure of 10° between patch number 5 and patch number 6.

It is then obvious that the experience of precedent study concerning the active concept and the use of a 4-patches subarray minimises the risks in the final breadboard performances compared to the semi-active solution in which:
- a complex subarray of 6 patches must be fabricated
- the dispersion of a Butler matrix could induce graceful degradations on EIRP performances

The information contained in this document is proprietary to ALCATEL ESPACE and shall not be disclosed by the recipient to third persons without the written consent of the company
Les informations contenues dans ce document demeurent propriété exclusive d'ALCATEL ESPACE et ne doivent pas être divulguées par le destinataire à des tiers sans l'accord écrit de la société.

X-2 ELECTRICAL CHARACTERISTICS

The electrical characteristics are summarized in the table of figure X-b.

	SEMI-ACTIVE	*ACTIVE*
D_{min} 62.3° / margin	*21.08 dBi / +0.08 dB compliant*	*20.80 dBi / +0.05 dB compliant*
EIRP margin	*+0.22 dBW compliant and $\Delta < 2$ dB*	*+0.64 dBW compliant but $\Delta > 2$ dB (could be compliant by mismatching)*
Amplitude and phase jumps	*1.4° / 0.13 dB analytically calculated*	*0.90 dB / 7° (ON/OFF switching) No compliant*
TRADE-OFF	+	-

Fig. X-b: Electrical characteristics of the different solutions

The electrical trade-off is more favourable for the semi-active concept for the following reasons:

- the results are fully compliant with the technical specifications (D_{min} at 62.3° in elevation is equal to 21.0 dBi -20 dBi specified - 1 dB (loss budget)-; the EIRP values are verifying both minimum and maximum masks)

- the amplitude and phase jumps have not been computes; but an analytical calculation shows that there will be about 1.4° and 0.13 dB (see annex B to chapter 3). It is evident that the result is better than for active concept because no switching is needed to turn the beam in azimuth. The control of the antenna in azimuth is achieved by selecting the proper phase at the inputs of the Butlers by incrementing bit by bit each phase shifter. This is the great interest of this antenna to be able to follow a ground station without significative amplitude and phase jumps. If semi-active concept is chosen, a software will be developed in order to compute the amplitude and phase jumps by the principle explained in page 3-48.

The information contained in this document is proprietary to ALCATEL ESPACE and shall not be disclosed by the recipient to third persons without the written consent of the company

Les informations contenues dans ce document demeurent propriété exclusive d'ALCATEL ESPACE et ne doivent pas être divulguées par le destinataire à des tiers sans l'accord écrit de la société.

X-3 ACTIVE MODULES

The active modules trade-off is proposed in the table of figure X-c.

	SEMI-ACTIVE	*ACTIVE*
Efficiency of HPAs	*Equal and constant power*	*three levels of power*
possible degradation	*less degradation with one failure over 24 active amplifiers instead of 1 / 11 for active concept*	*graceful degradation*
losses between HPAs and subarrays	*# 2 dB (Butler matrixes + cables+filter)*	*# 1 dB (filter+connection)*
P_{RF} per amplifier (for three beams)	*166 mW for the three beams*	*210 mW for the three beams*
total RF power	*3.98 W*	*2.28 W*
DC power	*good efficiency of the amplifiers*	*poor efficiency of the amplifiers*
TRADE-OFF	*+*	*0*

Fig. X-c: Active modules of the different solutions

The main drawbacks of the active concept (compared to the semi-active one) appear in two points:

- at first, a failure in one amplifier will induce more degradation in the EIRP specifications because 10 amplifiers over 11 will work, which gives a loss of about 10 percent of the power compared to 1 over 24 for the semi-active concept (4 % of the power lost)

- then, three levels of power are necessary because for the worst case in which the azimuth of the three beams will be closer whereas a constant power is required for the Butlers, which increases considerably the efficiency of the amplifiers.

The needed RF power (at the output of the amplifiers) of the semi-active antenna is equal to 3.98 W compared to 2.28 W for the active antenna. This phenomenon is due to the supplementary losses induced by the use of a Butler matrix (1 dB more). But no specifications is given for maximum RF consumption.

Therefore, it is obvious that the total power consumption (DC power) will be more important in the active concept than in the semi-active one, due to the efficiency of the amplifiers.

The information contained in this document is proprietary to ALCATEL ESPACE shall not be disclosed by the recipient to third persons without the written consent of the company

Les informations contenues dans ce document demeurent propriété exclusive d'ALCATEL ESPACE et ne doivent être divulguées par le destinataire à des tiers sans l'accord écrit de la société.

XI CONCLUSION

A complete summary of the trade-off is proposed, included global notations, in the table of figure XI-a.

	SEMI-ACTIVE	*ACTIVE*
mechanical, passive equip. and cost	-	+
electrical	+	-
active modules	+	*0*
GLOBAL NOTATION	*+1*	*0*

Fig. XI-a: Final trade-off

Main drawback of the active concept is the value of amplitude and phase jumps during commutation. The modification of amplitude and phase jumps specifications, as suggested during WP1100, were the only possibility if the active concept was chosen.

The above global notation leads to the choice of the semi-active concept to comply with the specification of this three beams LEO mission.

ALCATEL TELECOM	**CONFORMAL ARRAY ANTENNA**	ESTEC CONTRACT 11698/95/NL/SB
		AES 960596 / ASP 019
		DATE : 26/6/96 — ED/REV 1/-

The information contained in this document is proprietary to ALCATEL ESPACE and shall not be disclosed by the recipient to third persons without the written consent of the company.

Les informations contenues dans ce document demeurent propriété exclusive d'ALCATEL ESPACE et ne doivent pas être divulguées par le destinataire à des tiers sans l'accord écrit de la société.

ANNEX 1

CONFORMAL ARRAY
****
ACTIVE CONCEPT
CONICAL ANTENNA
Ntot=29
Ner=4
Nact=11
****
Frequency=8.2 GHz
Prf=0. dBW
****
PHI=0o

Elevation (o)	EIRP (dBW)
.0000000E+00	.9558376E+01
.1000000E+01	.9819535E+01
.2000000E+01	.1005873E+02
.3000000E+01	.1027478E+02
.4000000E+01	.1046661E+02
.4900001E+01	.1061776E+02
.6000000E+01	.1077392E+02
.7000000E+01	.1088796E+02
.8000000E+01	.1097499E+02
.9800001E+01	.1106332E+02
.1050000E+02	.1107436E+02
.1180000E+02	.1106192E+02
.1280000E+02	.1102519E+02
.1470000E+02	.1090139E+02
.1550000E+02	.1083345E+02
.1720000E+02	.1067508E+02
.1800000E+02	.1060140E+02
.1880000E+02	.1053351E+02
.1960000E+02	.1047523E+02
.2100000E+02	.1040712E+02
.2200000E+02	.1039189E+02
.2300000E+02	.1040818E+02
.2450000E+02	.1049175E+02
.2550000E+02	.1058294E+02
.2650000E+02	.1069640E+02
.2850000E+02	.1096214E+02
.2940000E+02	.1108638E+02
.3040000E+02	.1121976E+02
.3140000E+02	.1134332E+02
.3240000E+02	.1145400E+02
.3340000E+02	.1155141E+02
.3420000E+02	.1162122E+02
.3520000E+02	.1170318E+02
.3620000E+02	.1178779E+02
.3720000E+02	.1188740E+02
.3820000E+02	.1201700E+02
.3900000E+02	.1215270E+02
.4000000E+02	.1237363E+02
.4100000E+02	.1266068E+02
.4200000E+02	.1301748E+02
.4300000E+02	.1344126E+02
.4380000E+02	.1382306E+02
.4480000E+02	.1434346E+02
.4580000E+02	.1489886E+02
.4680000E+02	.1547497E+02
.4780000E+02	.1605824E+02
.4860000E+02	.1652184E+02
.4960000E+02	.1708849E+02
.5060000E+02	.1763298E+02
.5160000E+02	.1814794E+02
.5260000E+02	.1862746E+02
.5370000E+02	.1910854E+02
.5470000E+02	.1949960E+02
.5570000E+02	.1984360E+02
.5660000E+02	.2011106E+02
.5920000E+02	.2064705E+02
.6109999E+02	.2080640E+02
.6230000E+02	.2080179E+02

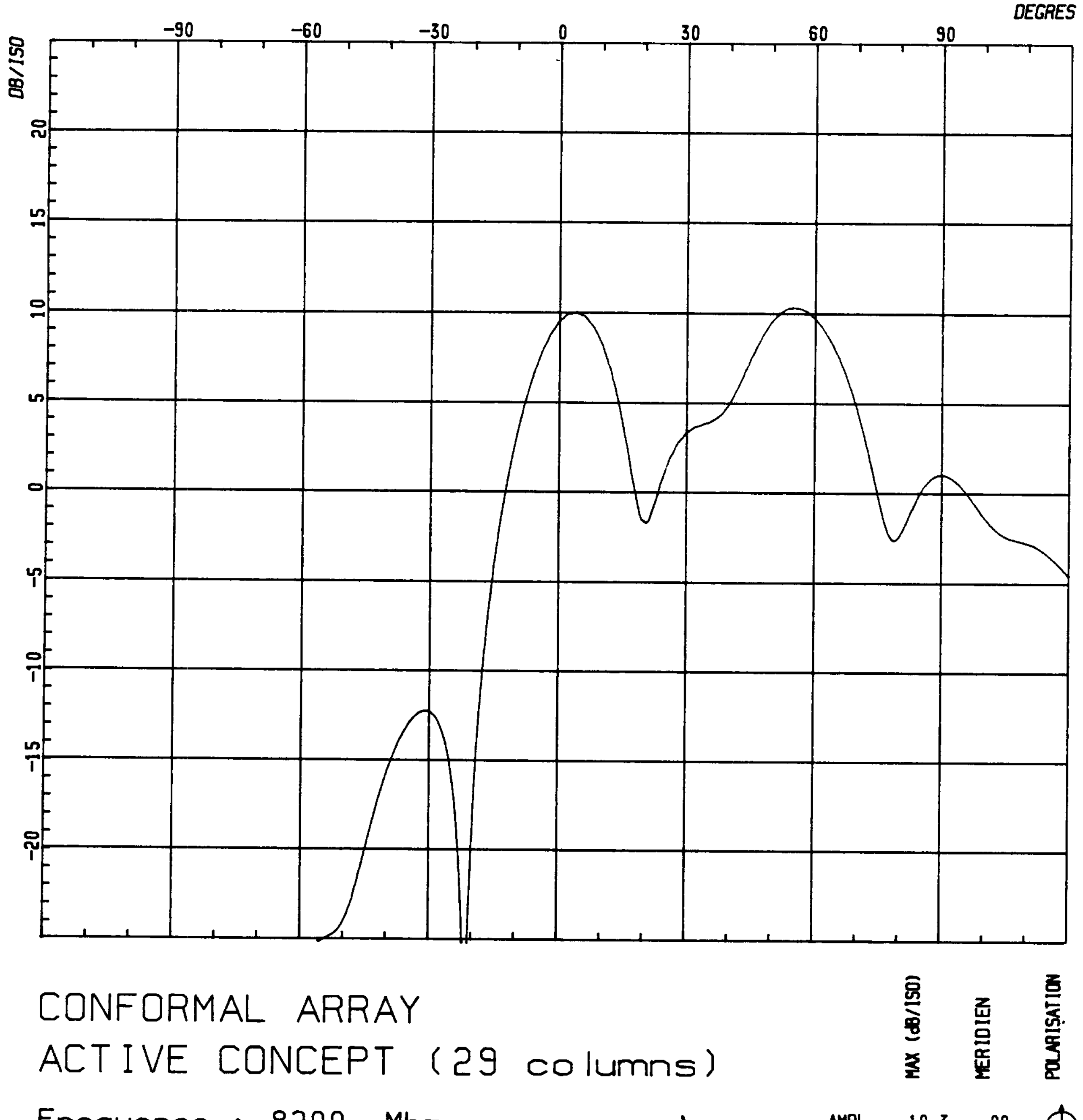

CONFORMAL ARRAY
ACTIVE CONCEPT (29 columns)

Frequence : 8200. Mhz
Fichier sasome 16 Plans
Rayon : 1000.00 mm

($\theta = 0°$)

ATES le 17 JUIN 1996

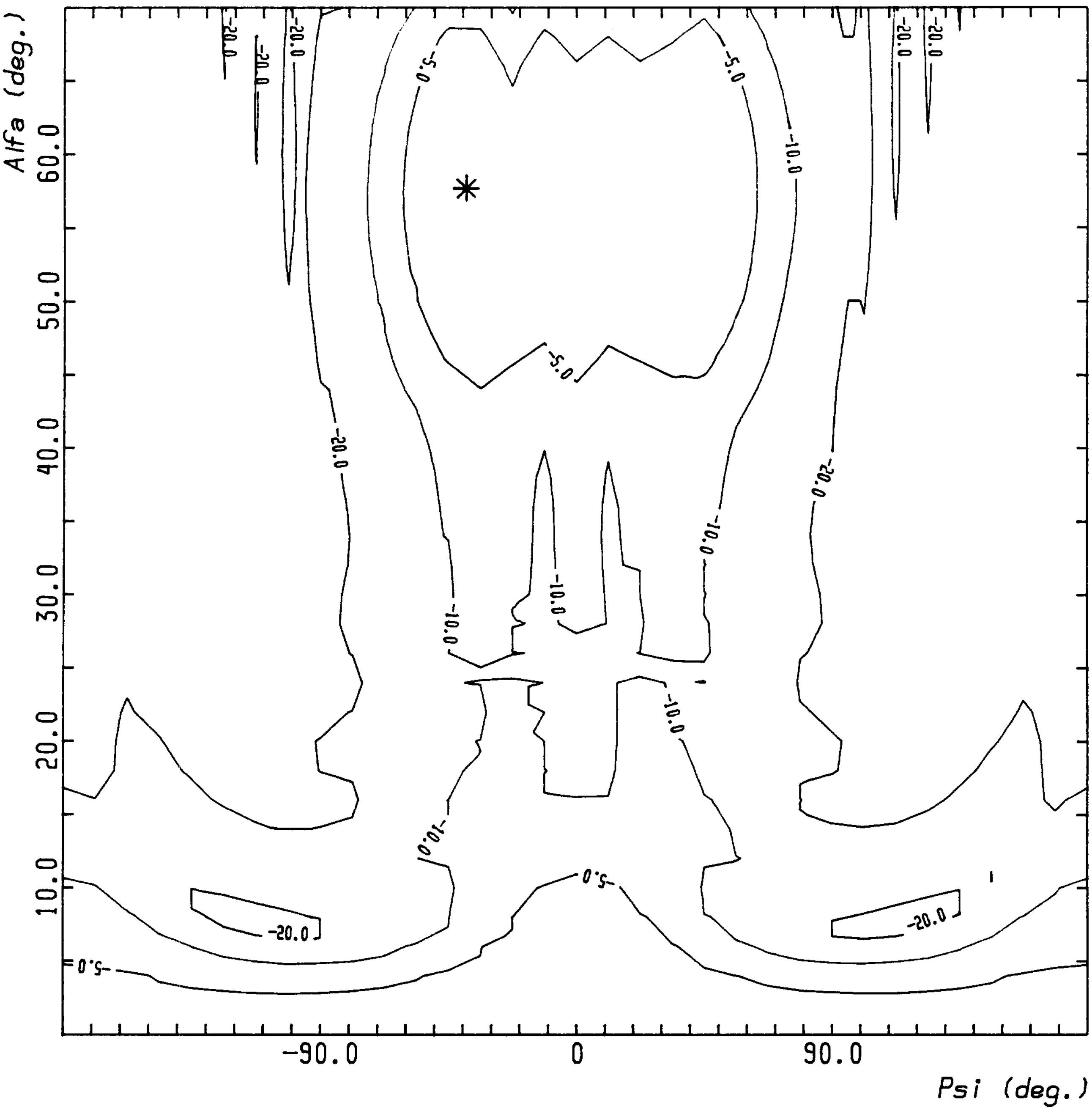

ACCES 1
Niveau (dB/Max)
Polar. circ. droite
Frequence 8200. Mhz
CONFORMAL ARRAY

MAX : .46 dB

($\theta = 0°$)

Alcatel le 17 JUIN 1996
a 18 h. 29 min.
sesome Acces 1.

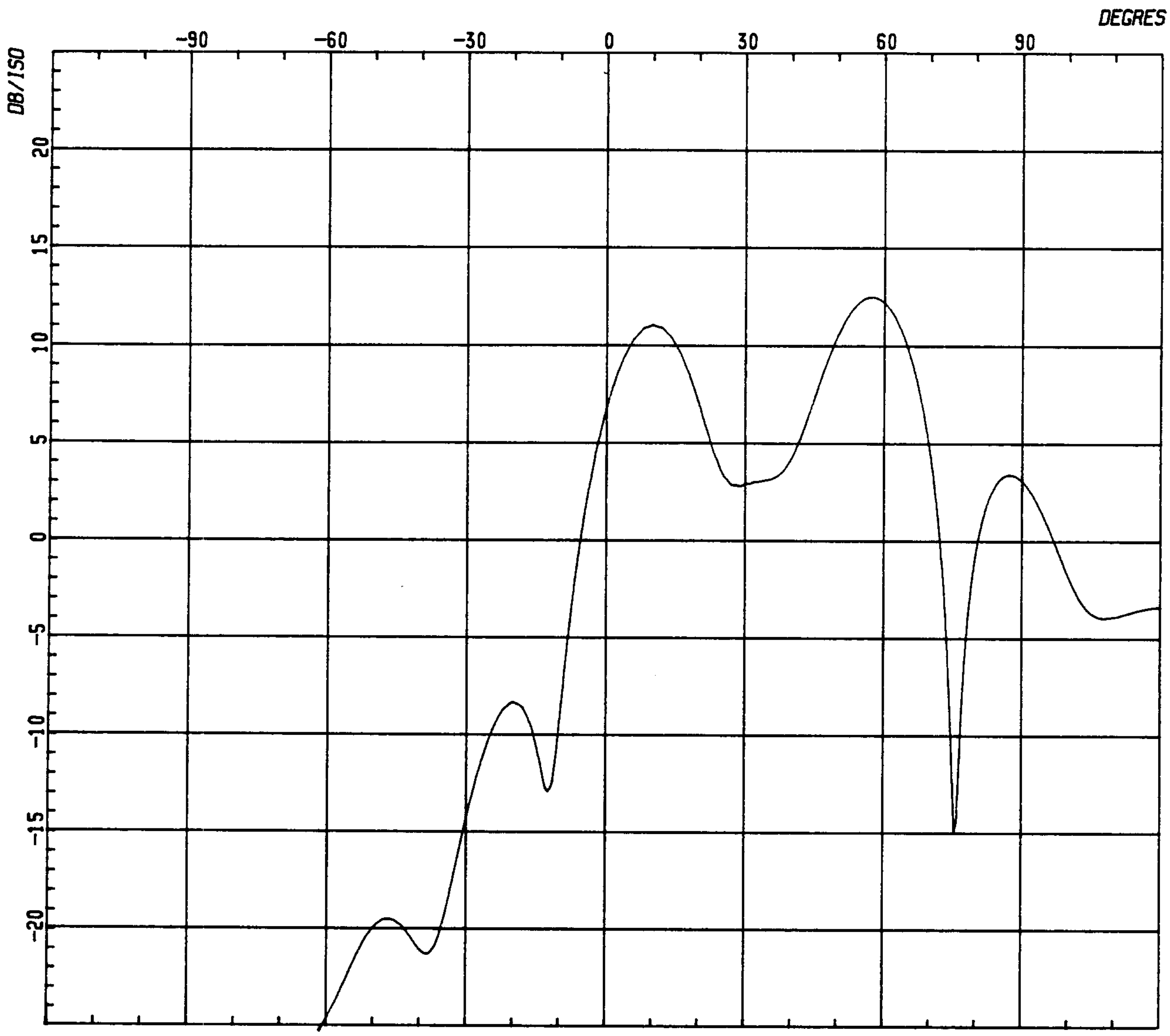

CONFORMAL ARRAY
ACTIVE CONCEPT (29 columns)

MAX (dB/ISO) MERIDIEN POLARISATION

Frequence : 8200. Mhz ($\theta = 9.8°$)

AMPL. 12.5 .00

Fichier sasome 16 Plans
Rayon : 1000.00 mm

ATES le 17 JUIN 1996

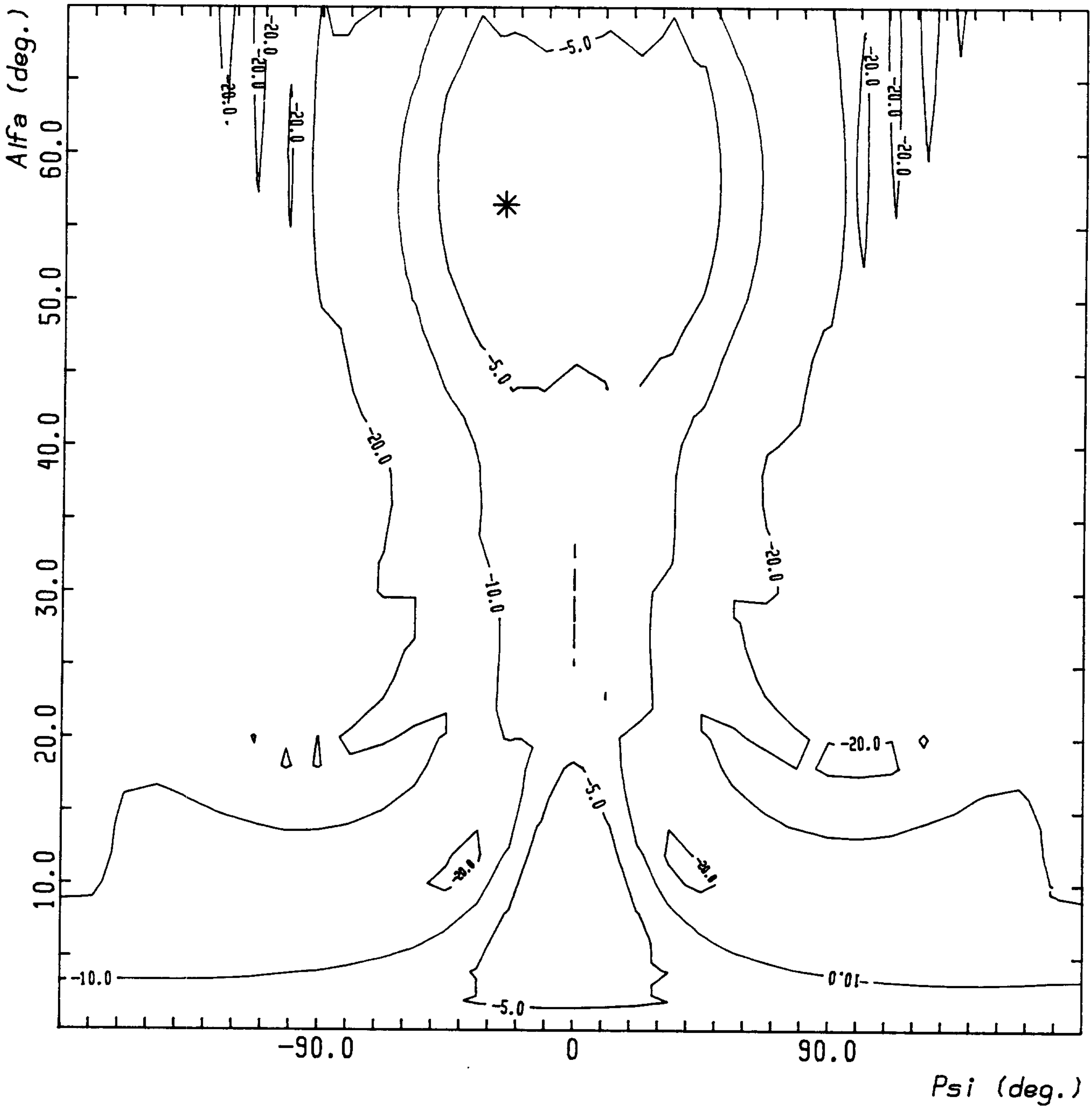

ACCES 1
Niveau (dB/Max)
Polar. circ. droite
Frequence 8200. Mhz
CONFORMAL ARRAY

MAX : .09 dB

($\theta = 9.8°$)

Alcatel le 17 JUIN 1996
a 18 h. 29 min.
sesome Acces 1.

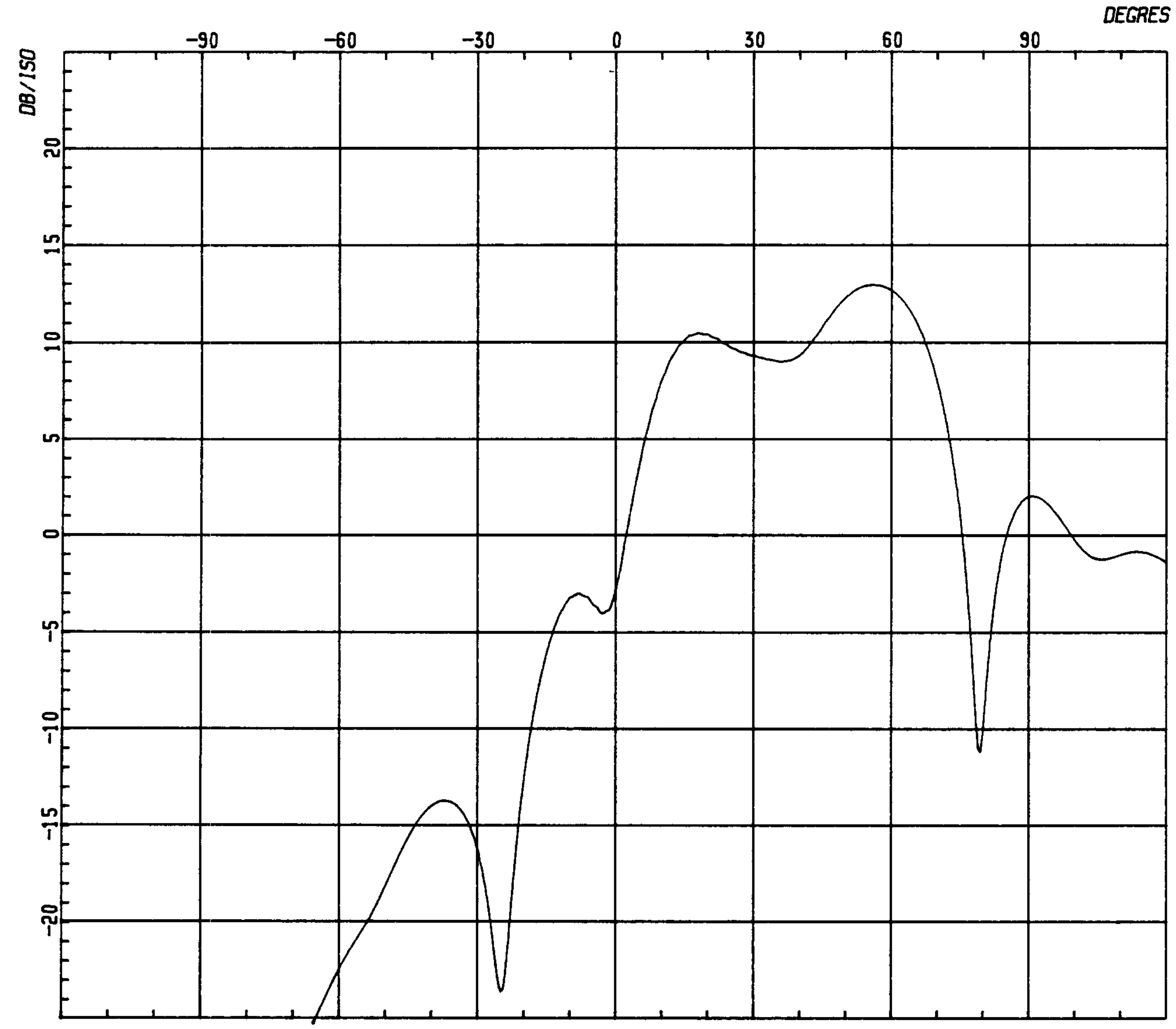

CONFORMAL ARRAY
ACTIVE CONCEPT (29 columns)

MAX (dB/ISO)	MERIDIEN	POLARISATION
AMPL. 13.0	.00	

Frequence : 8200. Mhz
Fichier sasome 16 Plans
Rayon : 1000.00 mm

($\theta = 19.6°$)

ATES le 17 JUIN 1996

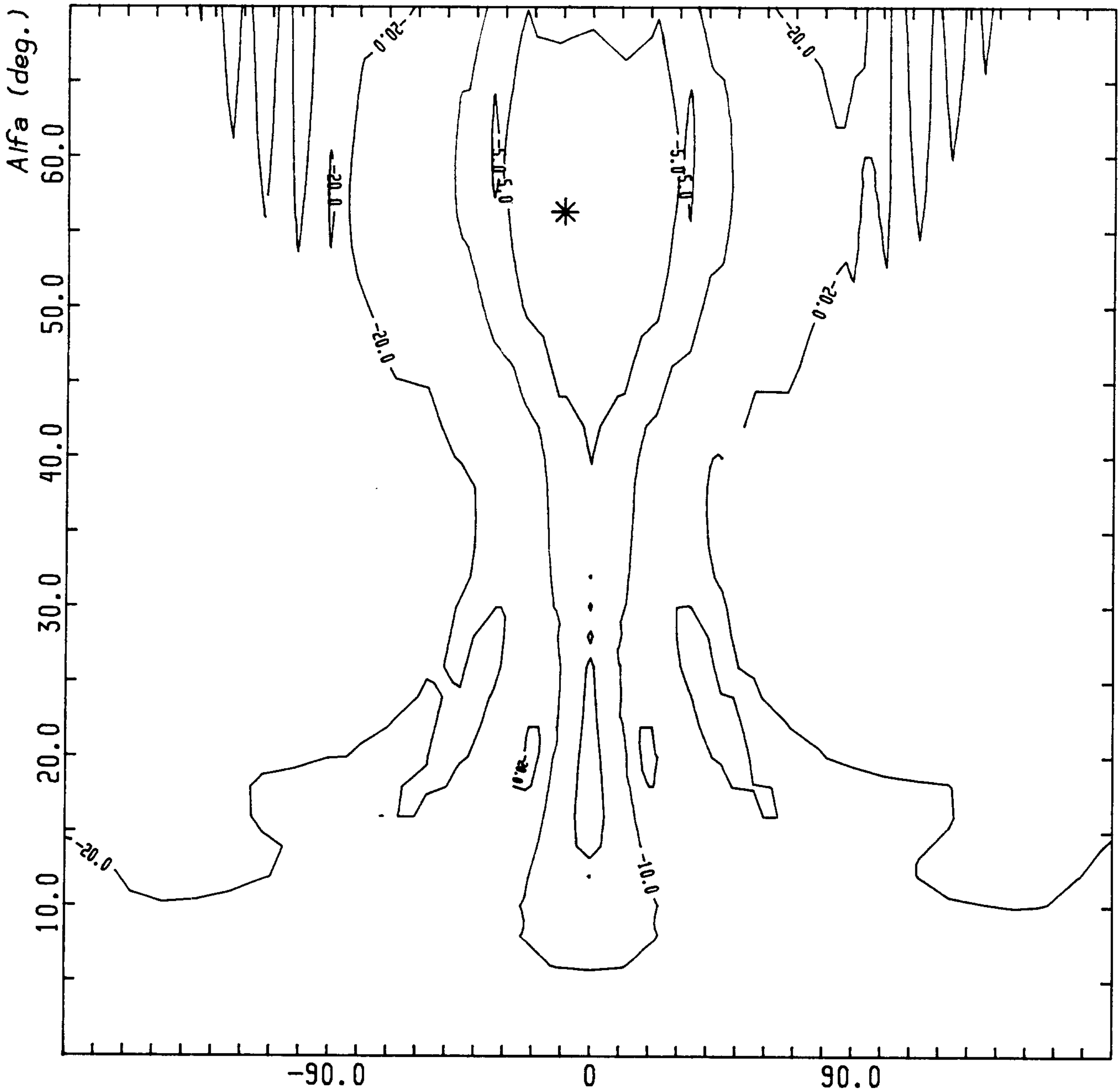

ACCES 1
Niveau (dB/Max)
Polar. circ. droite
Frequence 8200. Mhz
CONFORMAL ARRAY

MAX : .00 dB

($\theta = 19.6°$)

Alcatel le 17 JUIN 1996
a 18 h. 31 min.
sasome Acces 1.

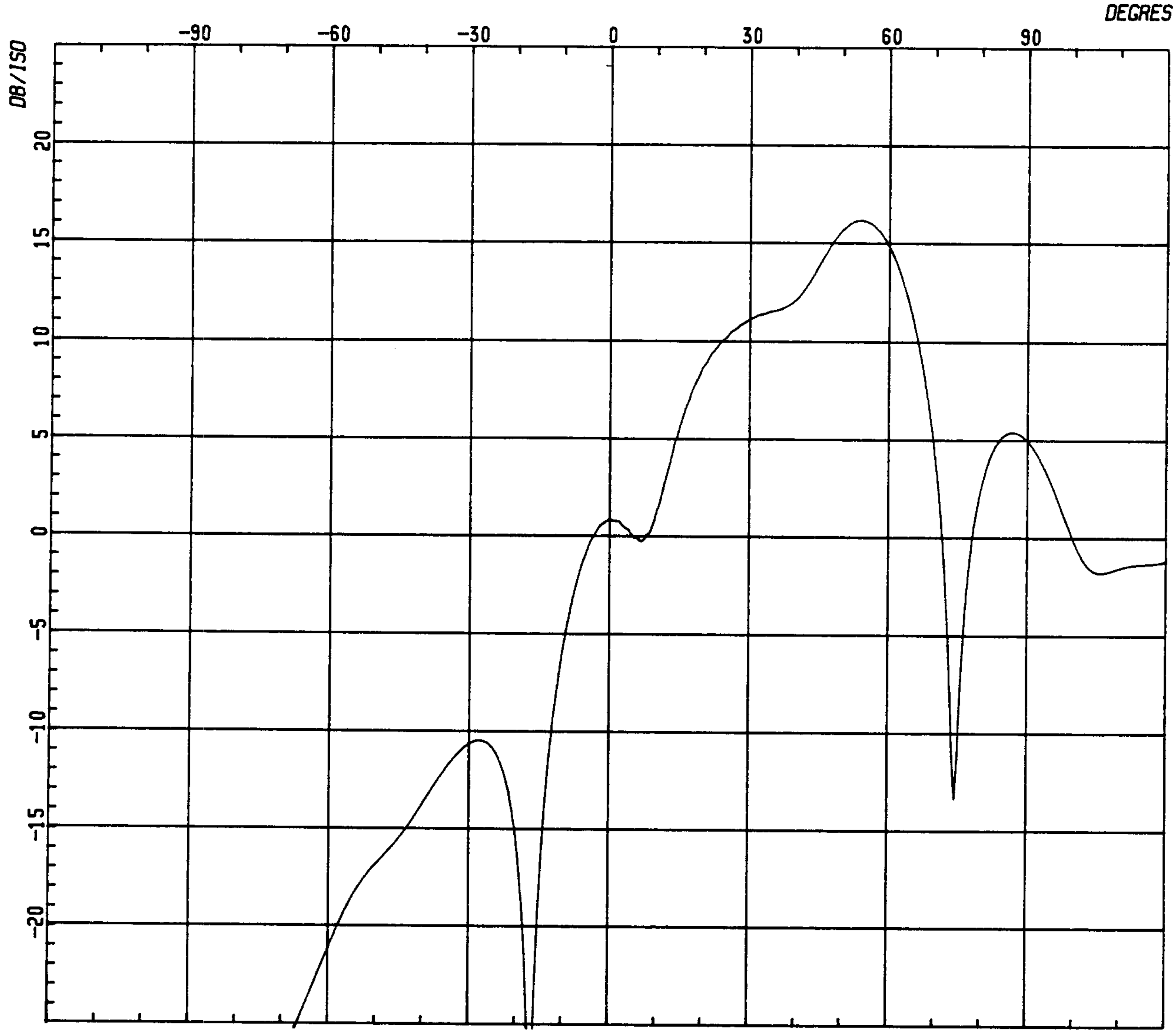

CONFORMAL ARRAY
ACTIVE CONCEPT (29 columns)

MAX (dB/ISO)	MERIDIEN	POLARISATION
AMPL. 16.2	.00	

Frequence : 8200. Mhz
Fichier sasome 16 Plans
Rayon : 1000.00 mm

(θ = 29.4°)

ATES le 17 JUIN 1996

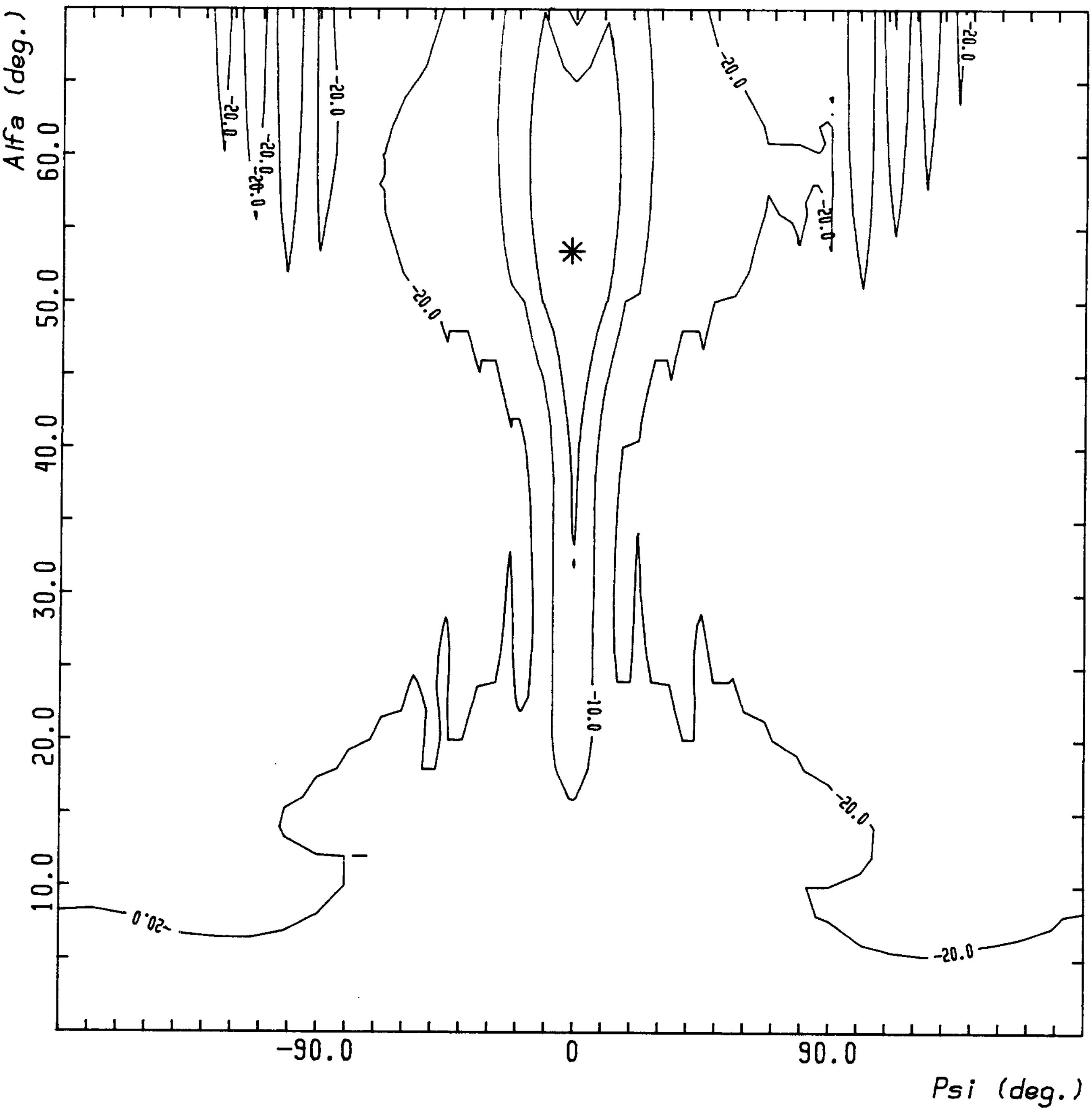

ACCES 1
Niveau (dB/Max)
Polar. circ. droite
Frequence 8200. Mhz
CONFORMAL ARRAY

MAX : .06 dB

(θ = 29.4°)

Alcatel le 17 JUIN 1996
a 18 h. 31 min.
sasome Acces 1.

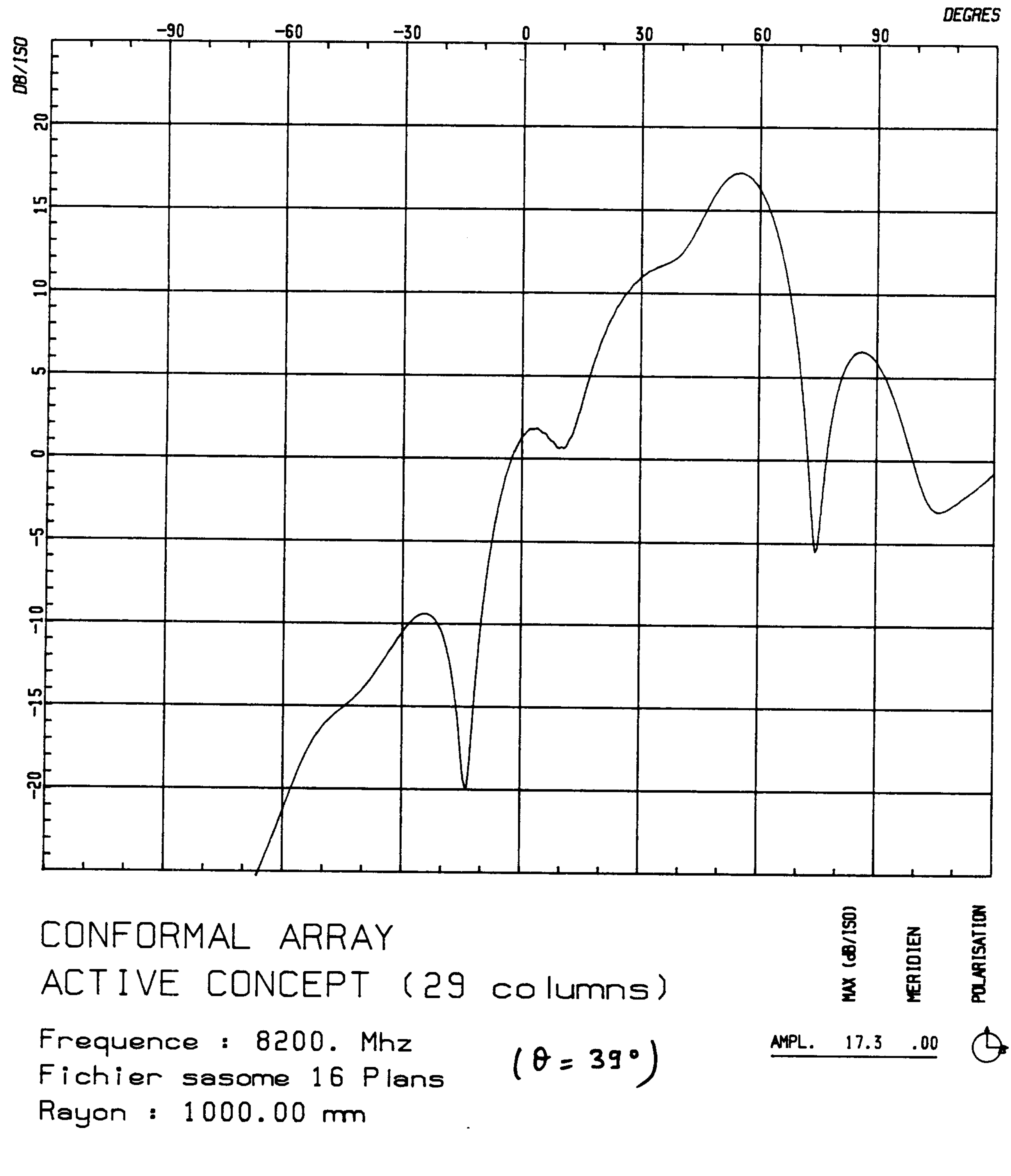

CONFORMAL ARRAY
ACTIVE CONCEPT (29 columns)

Frequence : 8200. Mhz
Fichier sasome 16 Plans
Rayon : 1000.00 mm

($\theta = 39°$)

ATES le 17 JUIN 1996

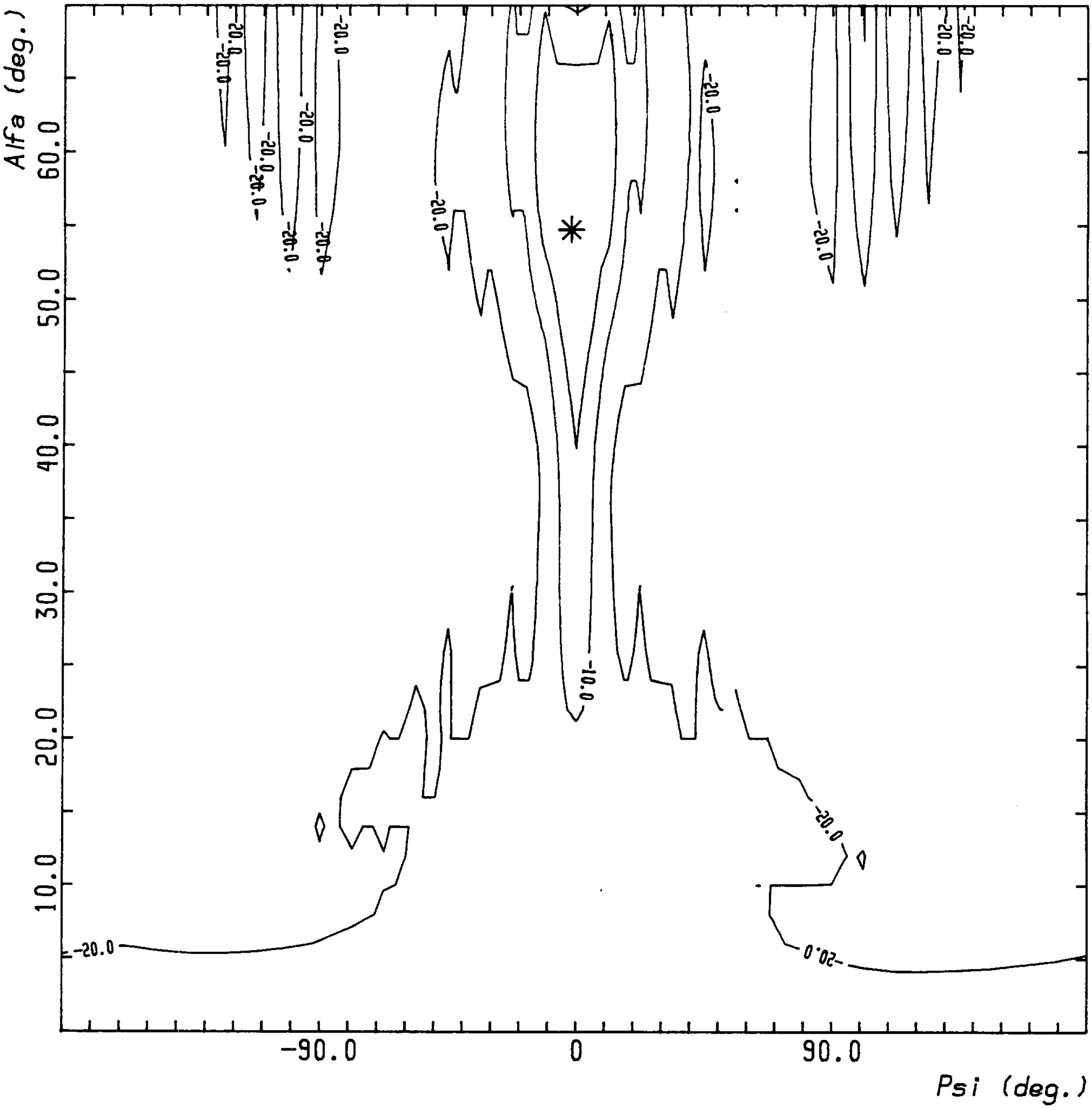

ACCES 1
Niveau (dB/Max)
Polar. circ. droite
Frequence 8200. Mhz
CONFORMAL ARRAY

MAX : .18 dB

($\theta = 39°$)

Alcatel le 17 JUIN 1996
a 18 h. 32 min.
sesome Acces 1.

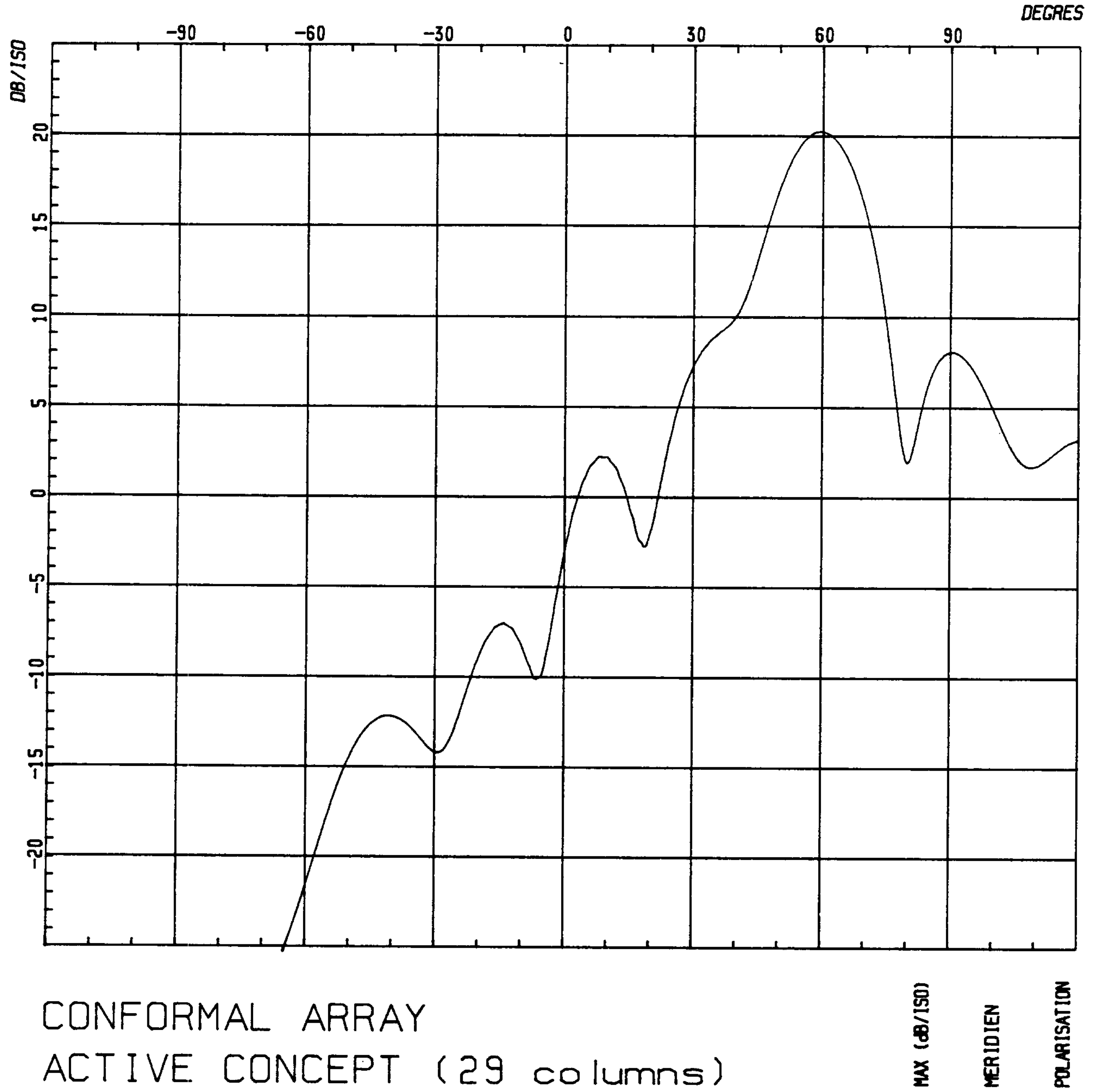

CONFORMAL ARRAY
ACTIVE CONCEPT (29 columns)

Frequence : 8200. Mhz
Fichier sasome 16 Plans ($\theta = 53.7°$)
Rayon : 1000.00 mm

ATES le 17 JUIN 1996

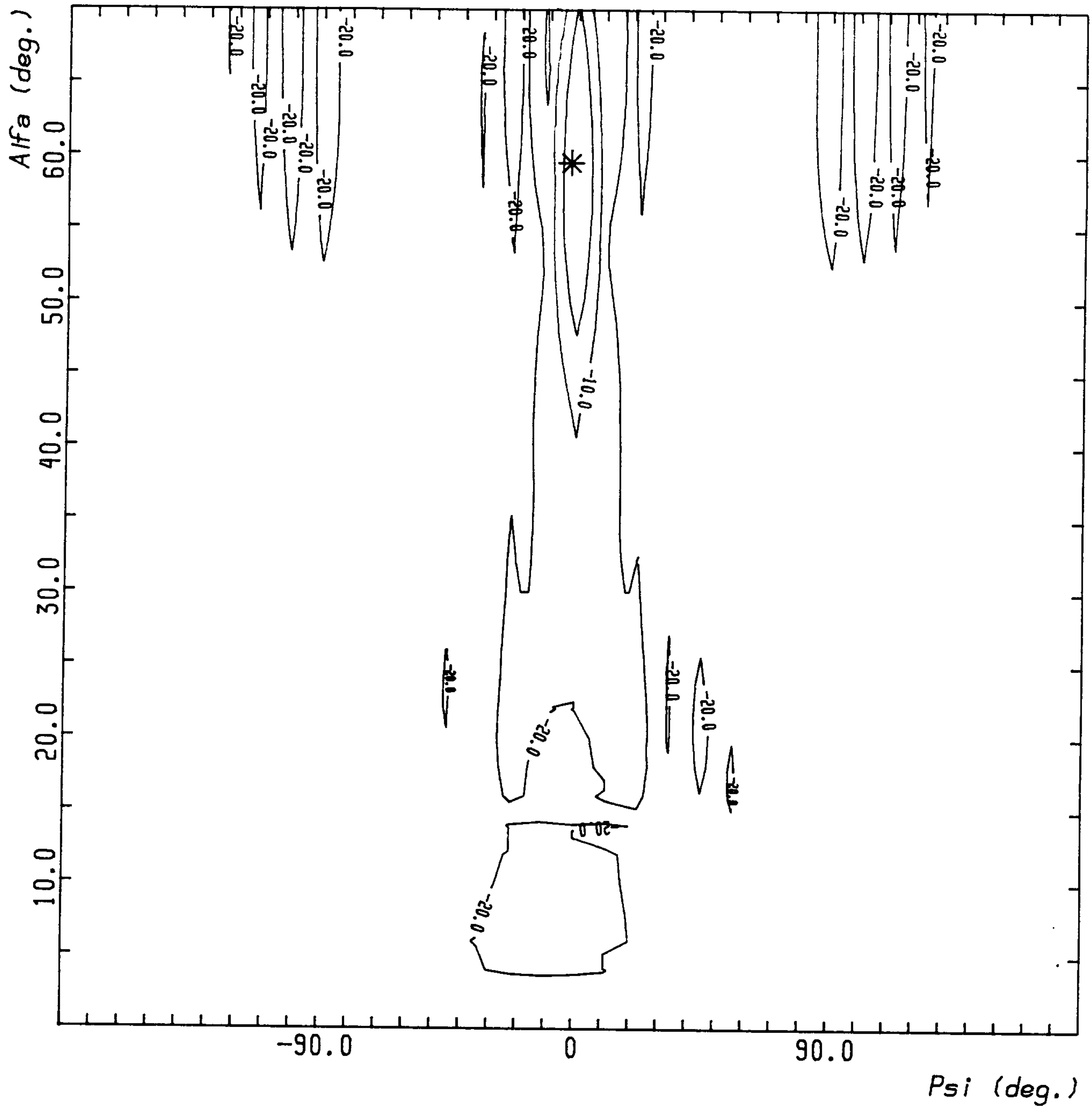

ACCES 1
Niveau (dB/Max)
Polar. circ. droite
Frequence 8200. Mhz
CONFORMAL ARRAY

MAX : .48 dB

($\theta = 53.7°$)

Alcatel le 17 JUIN 1996
a 18 h. 32 min.
sasome Acces 1.

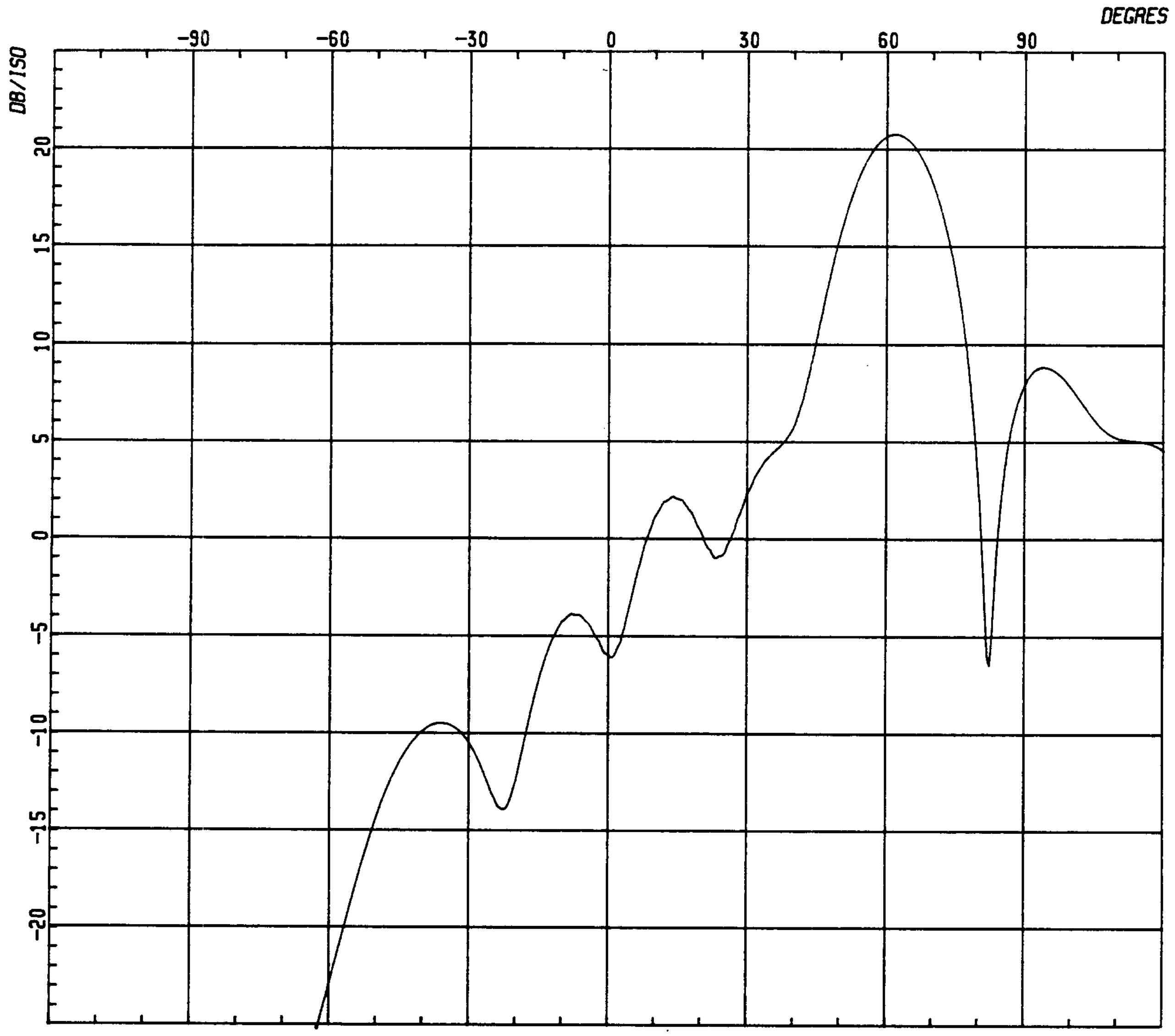

CONFORMAL ARRAY
ACTIVE CONCEPT (29 columns)

Frequence : 8200. Mhz
Fichier sasome 16 Plans
Rayon : 1000.00 mm

($\theta = 62.3°$)

MAX (dB/ISO)	MERIDIEN	POLARISATION
AMPL. 20.8	.00	

ATES le 17 JUIN 1996

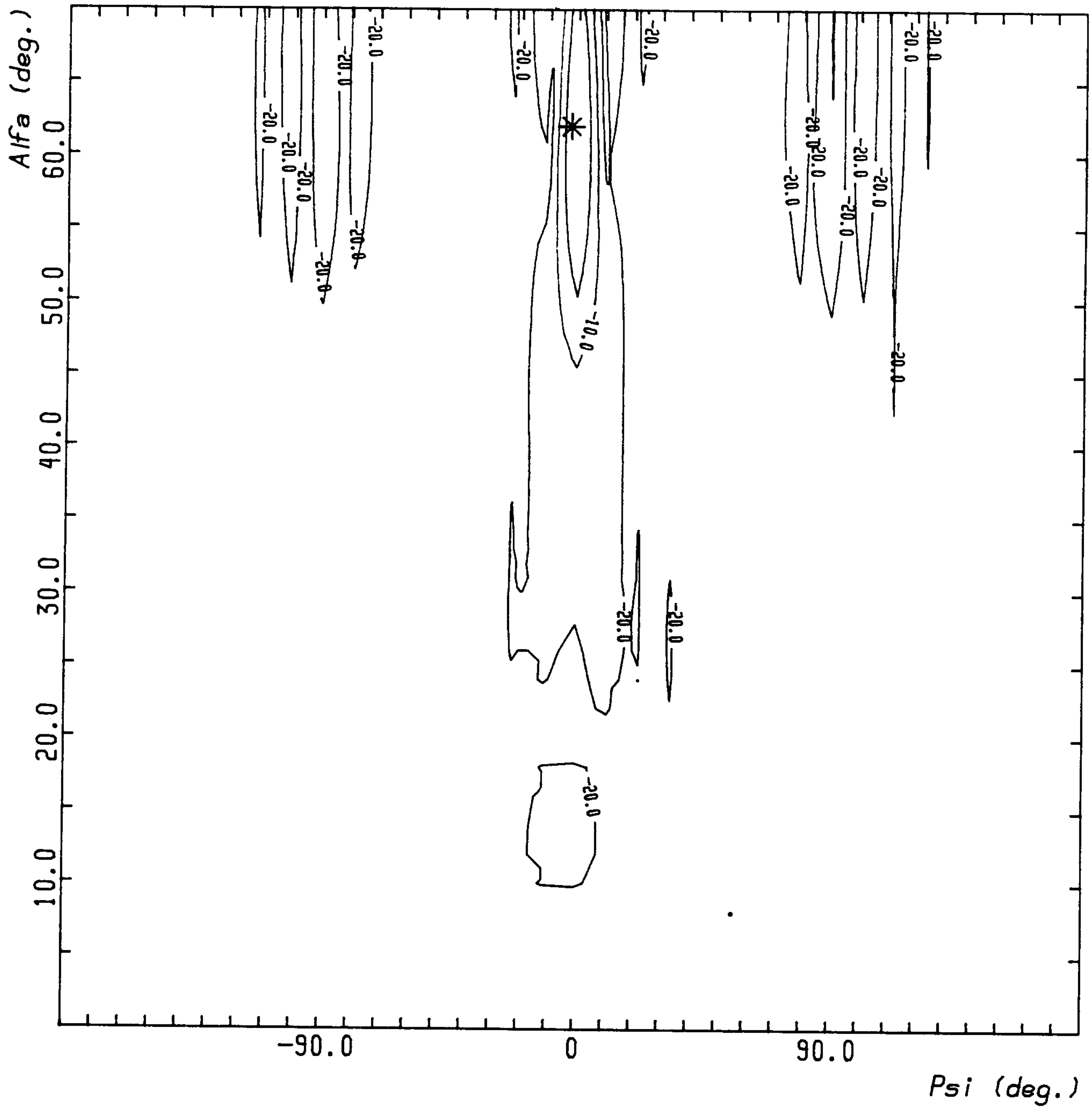

ACCES 1
Niveau (dB/Max)
Polar. circ. droite
Frequence 8200. Mhz
CONFORMAL ARRAY

MAX : .59 dB

$(\theta = 62.3°)$

Alcatel le 17 JUIN 1996
a 18 h. 32 min.
sesome Acces 1.

...nation contained in this document is proprietary to ALCATEL ESPA... shall not ...ed by the recipient to third persons without the written consent of the ...y

Th... be

...ESPACE ...é

Les infor...ns contenues dans ce document demeurent propriété exclusive d'ALCA... et ne d...être divulguées par le destinataire à des tiers sans l'accord écrit de...

ANNEX 2

The information contained in this document is proprietary to ALCATEL ESPACE and shall not be disclosed by the recipient to third persons without the written consent of the company

Les informations contenues dans ce document demeurent propriété exclusive d'ALCATEL ESPACE et ne doivent être divulguées par le destinataire à des tiers sans l'accord écrit de la société.

Let us consider a NxN Butler matrix. As shown in § IX-1 (page 3-35 of this document), we have the following relation:

$$\left\langle A_K, \phi_K \right\rangle = \sum_{i=1,N} \left(\frac{\alpha_i}{\alpha} \exp j[\phi + \psi_i + (K-1)(\phi_0 + \frac{2i\pi}{N})] \right)$$

where $\phi_0 = 0$ (180° hybrids)

At the nadir, with a circular polarisation, the far field created by the N columns connected to a single Butler matrix is:

$$E_1(\text{nadir}) = \sum_{K=1,N} \left\langle A_K, \phi_K \right\rangle \varepsilon_1(\text{nadir}) \exp[j\frac{2\pi}{N}(K-1)]\frac{1}{\sqrt{N}}$$

where $\varepsilon_1(\text{nadir})$ is the far field at the nadir created by a single column

The contribution of input number i could be written as:

$$\sum_{K=1,N} \frac{\alpha_i}{\alpha} \exp j[\phi + \psi_i + (K-1)\frac{2i\pi}{N}] \exp j[(K-1)\frac{2\pi}{N}] \varepsilon_1(\text{nadir}) \frac{1}{\sqrt{N}}$$

$$= \frac{\alpha_i}{\alpha} \frac{\varepsilon_1(\text{nadir})}{\sqrt{N}} \exp j[\phi + \psi_i] \sum_{K=1,N} \left(\exp j\frac{2\pi}{N}(i+1) \right)^{K-1}$$

$$= \frac{\alpha_i}{\alpha} \frac{\varepsilon_1(\text{nadir})}{\sqrt{N}} \exp j[\phi + \psi_i] \frac{\left(\exp j\frac{2\pi}{N}(i+1)N \right) - 1}{\left(\exp j\frac{2\pi}{N}(i+1) \right) - 1}$$

This expression is equal to zero unless i=N-1.

If i=N-1, the contribution of the input is:

$$\frac{\alpha_{N-1}}{\alpha} \frac{\varepsilon_1(\text{nadir})}{\sqrt{N}} \exp j[\phi + \psi_{N-1}] \sum_{K=1,N} (1)^{K-1} = \frac{\alpha_{N-1}}{\alpha} \varepsilon_1(\text{nadir}) \exp j[\phi + \psi_{N-1}] \sqrt{N}$$

For the purpose of the theoretical study, equal power is given on each input; which means that for a total power of 1:

$\sum_{i=1}^{NN_B} \alpha_i^2 = 1$ which implies that $\alpha_i = \frac{1}{\sqrt{NN_B}}$ for each input of the Butler.

If we suppose that α =1 (no loss in the Butler), the modulus of the far field at the nadir (including the N_B Butler matrixes) becomes equal to:

$$\boxed{\begin{gathered}\frac{1}{\sqrt{N N_B}} N_B \sqrt{N} \left|\varepsilon_1(\text{nadir})\right| = \\ \sqrt{N_B} \left|\varepsilon_1(\text{nadir})\right|\end{gathered}}$$

so directly proportional to the number of Butler matrixes N_B.

The information contained in this document is proprietary to ALCATEL ESPACE and shall not be disclosed by the recipient to third persons without the written consent of the company

Les informations contenues dans ce document demeurent propriété exclusive d'ALCATEL ESPACE et ne doivent pas être divulguées par le destinataire à des tiers sans l'accord écrit de la société.

ANNEX 3

The information contained in this document is proprietary to ALCATEL ESPACE and shall not be disclosed by the recipient to third persons without the written consent of the ALCATEL ESPACE company.

Les informations contenues dans ce document demeurent propriété exclusive d'ALCATEL ESPACE et ne doivent pas être divulguées par le destinataire à des tiers sans l'accord écrit de la société.

```
CONFORMAL ARRAY
****************
SEMI-ACTIVE CONCEPT
CONICAL ANTENNA
Ntot=24
Ner=6
Nb=8
N=3
folded subarray (beta=25/25/25/25/25/35)
serial repartitor
******************************
Frequency=8.2 GHz
Prf=-0.77 dBW
******************************
PHI=-7.5o

   Elevation (o)  EIRP (dBW)
   -------------------------
   .0000000E+00, .7296994E+01,
   .4900001E+01, .9172892E+01,
   .9800001E+01, .9239302E+01,
   .1180000E+02, .9239302E+01,
   .1280000E+02, .9275618E+01,
   .1470000E+02, .9357183E+01,
   .1720000E+02, .8743603E+01,
   .1960000E+02, .8909016E+01,
   .2450000E+02, .9725931E+01,
   .2940000E+02, .9699458E+01,
   .3420000E+02, .1033676E+02,
   .3900000E+02, .1133029E+02,
   .4380000E+02, .1110571E+02,
   .4860000E+02, .1190046E+02,
   .5370000E+02, .1492647E+02,
   .5660000E+02, .1604661E+02,
   .5920000E+02, .1732779E+02,
   .6109999E+02, .1870070E+02,
   .6230000E+02, .2023256E+02,

PHI=-3.75o

   Elevation (o)  EIRP (dBW)
   -------------------------
   .0000000E+00, .7296994E+01,
   .4900001E+01, .9172892E+01,
   .9800001E+01, .9239302E+01,
   .1180000E+02, .9239302E+01,
   .1280000E+02, .9275618E+01,
   .1470000E+02, .9357183E+01,
   .1720000E+02, .8765968E+01,
   .1960000E+02, .8901796E+01,
   .2450000E+02, .9682491E+01,
   .2940000E+02, .9726081E+01,
   .3420000E+02, .1032129E+02,
   .3900000E+02, .1133925E+02,
   .4380000E+02, .1110989E+02,
   .4860000E+02, .1191033E+02,
```



```
   .5370000E+02, .1492562E+02,
   .5660000E+02, .1604661E+02,
   .5920000E+02, .1732779E+02,
   .6109999E+02, .1870070E+02,
   .6230000E+02, .2023256E+02,

PHI=0o

   Elevation (o)  EIRP (dBW)
   -------------------------
   .0000000E+00, .7296994E+01,
   .4900001E+01, .9172892E+01,
   .9800001E+01, .9239302E+01,
   .1180000E+02, .9239302E+01,
   .1280000E+02, .9275618E+01,
   .1470000E+02, .9357183E+01,
   .1720000E+02, .8804497E+01,
   .1960000E+02, .8783934E+01,
   .2450000E+02, .9506775E+01,
   .2940000E+02, .9950648E+01,
   .3420000E+02, .1013094E+02,
   .3900000E+02, .1132633E+02,
   .4380000E+02, .1119111E+02,
   .4860000E+02, .1180226E+02,
   .5370000E+02, .1492562E+02,
   .5660000E+02, .1604661E+02,
   .5920000E+02, .1732779E+02,
   .6109999E+02, .1870070E+02,
   .6230000E+02, .2023256E+02,

PHI=3.75o

   Elevation (o)  EIRP (dBW)
   -------------------------
   .0000000E+00, .7296994E+01,
   .4900001E+01, .9172892E+01,
   .9800001E+01, .9239410E+01,
   .1180000E+02, .9239302E+01,
   .1280000E+02, .9275618E+01,
   .1470000E+02, .9357183E+01,
   .1720000E+02, .8800627E+01,
   .1960000E+02, .8768826E+01,
   .2450000E+02, .9542282E+01,
   .2940000E+02, .9929721E+01,
   .3420000E+02, .1012992E+02,
   .3900000E+02, .1133926E+02,
   .4380000E+02, .1120442E+02,
   .4860000E+02, .1181257E+02,
   .5370000E+02, .1492562E+02,
   .5660000E+02, .1604661E+02,
   .5920000E+02, .1732779E+02,
   .6109999E+02, .1870070E+02,
   .6230000E+02, .2023256E+02,

PHI=7.5o
```



```
   Elevation (o)  EIRP (dBW)
   -------------------------
   .0000000E+00, .7296994E+01,
   .4900001E+01, .9172892E+01,
   .9800001E+01, .9239300E+01,
   .1180000E+02, .9239302E+01,
   .1280000E+02, .9275618E+01,
   .1470000E+02, .9357183E+01,
   .1720000E+02, .8743603E+01,
   .1960000E+02, .8908767E+01,
   .2450000E+02, .9725935E+01,
   .2940000E+02, .9699475E+01,
   .3420000E+02, .1033676E+02,
   .3900000E+02, .1133029E+02,
   .4380000E+02, .1110571E+02,
   .4860000E+02, .1190046E+02,
   .5370000E+02, .1492562E+02,
   .5660000E+02, .1604661E+02,
   .5920000E+02, .1732779E+02,
   .6109999E+02, .1870070E+02,
   .6230000E+02, .2023256E+02,
```

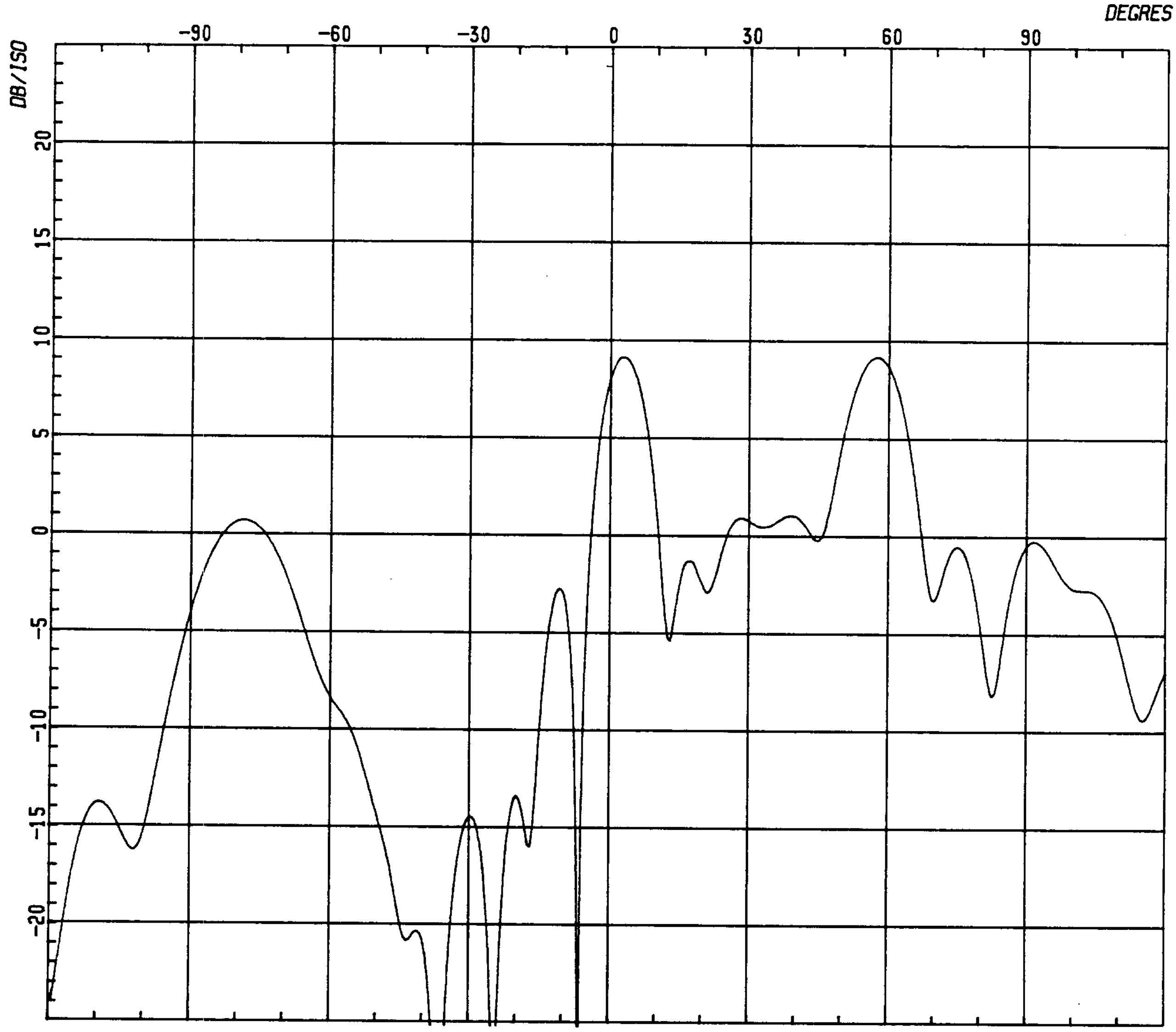

CONFORMAL ARRAY

SEMI-ACTIVE CONCEPT (folded subarray - serial rep)

MAX (dB/ISO)	MERIDIEN	POLARISATION
AMPL. 9.2	.00	

Frequence : 8200. Mhz

($\vartheta = 0°$)

Fichier sasom.da 16 Plans

Rayon : 1000.00 mm

ATES le 13 JUIN 1996

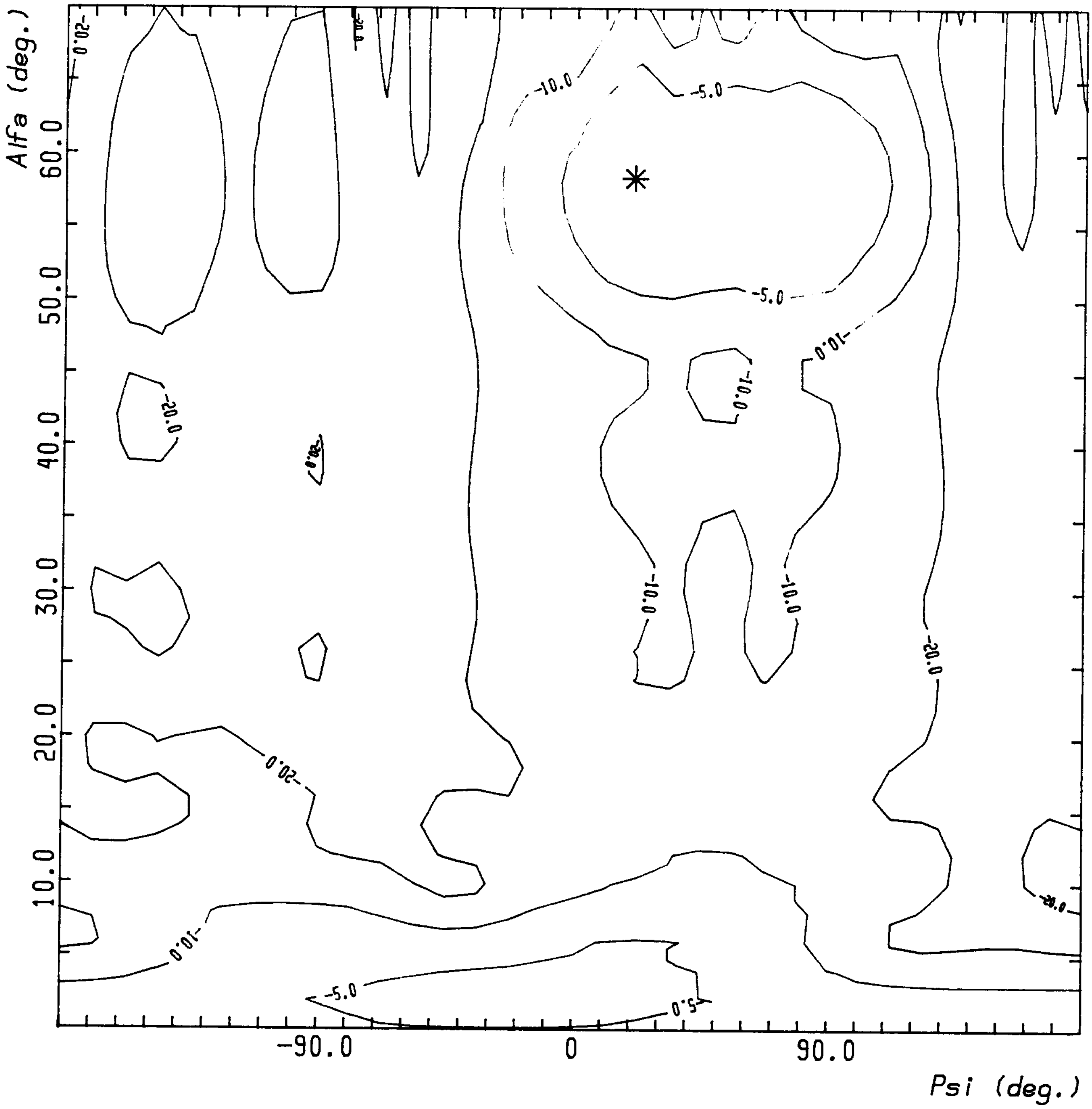

ACCES 1
Niveau (dB/Max)
Polar. circ. droite
Frequence 8200. Mhz
CONFORMAL ARRAY

($\theta = 0°$)

Alcatel le 13 JUIN 1996
a 19 h. 57 min.
sesom Acces 1.

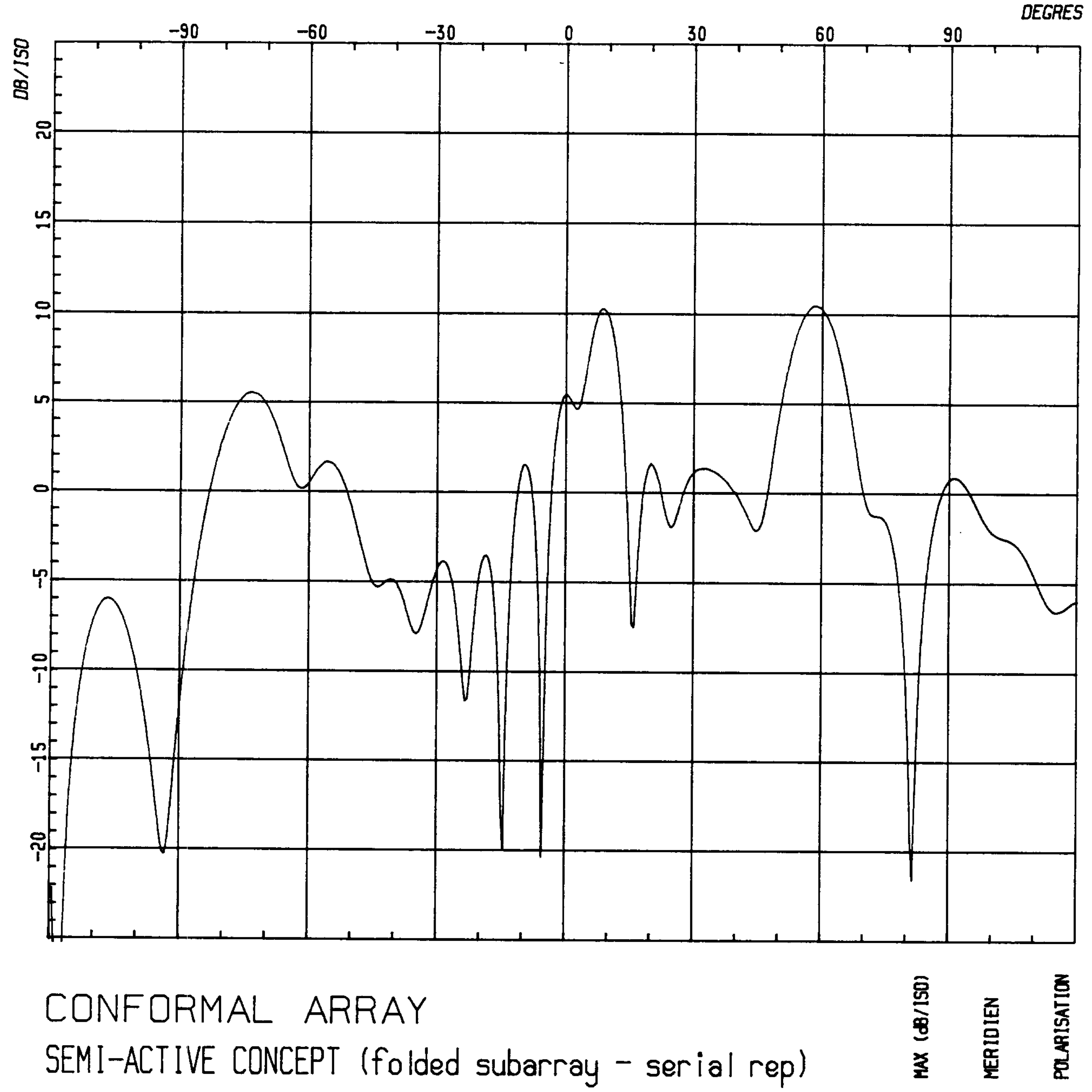

CONFORMAL ARRAY

SEMI-ACTIVE CONCEPT (folded subarray - serial rep)

Frequence : 8200. Mhz

Fichier sasom.da 16 Plans $(\theta = 9.8°)$

Rayon : 1000.00 mm

ATES le 13 JUIN 1996

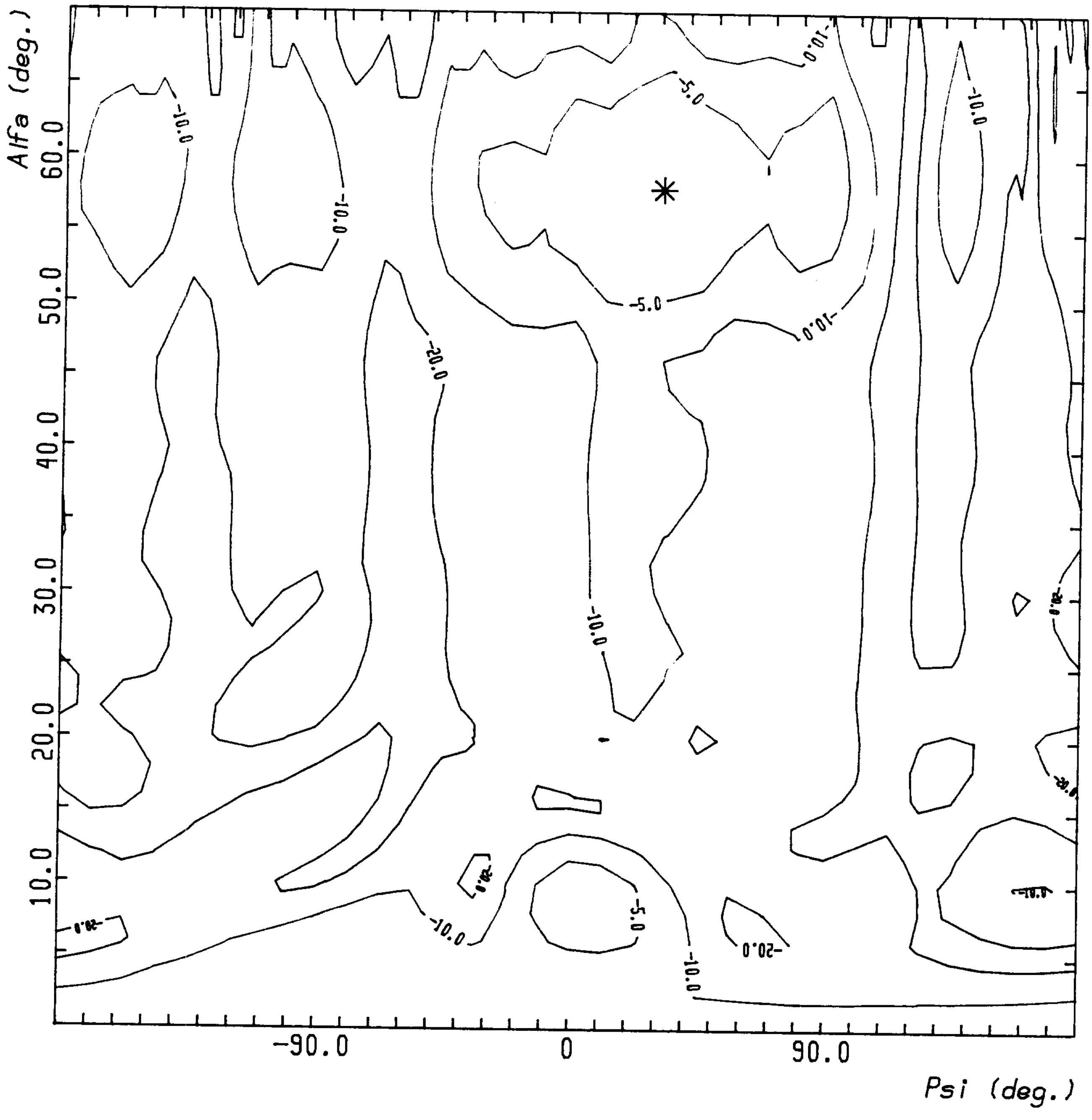

ACCES 1
Niveau (dB/Max)
Polar. circ. droite
Frequence 8200. Mhz
CONFORMAL ARRAY

$(\theta = 9.8°)$

Alcatel le 13 JUIN 1996
a 19 h. 58 min.
sasom Acces 1.

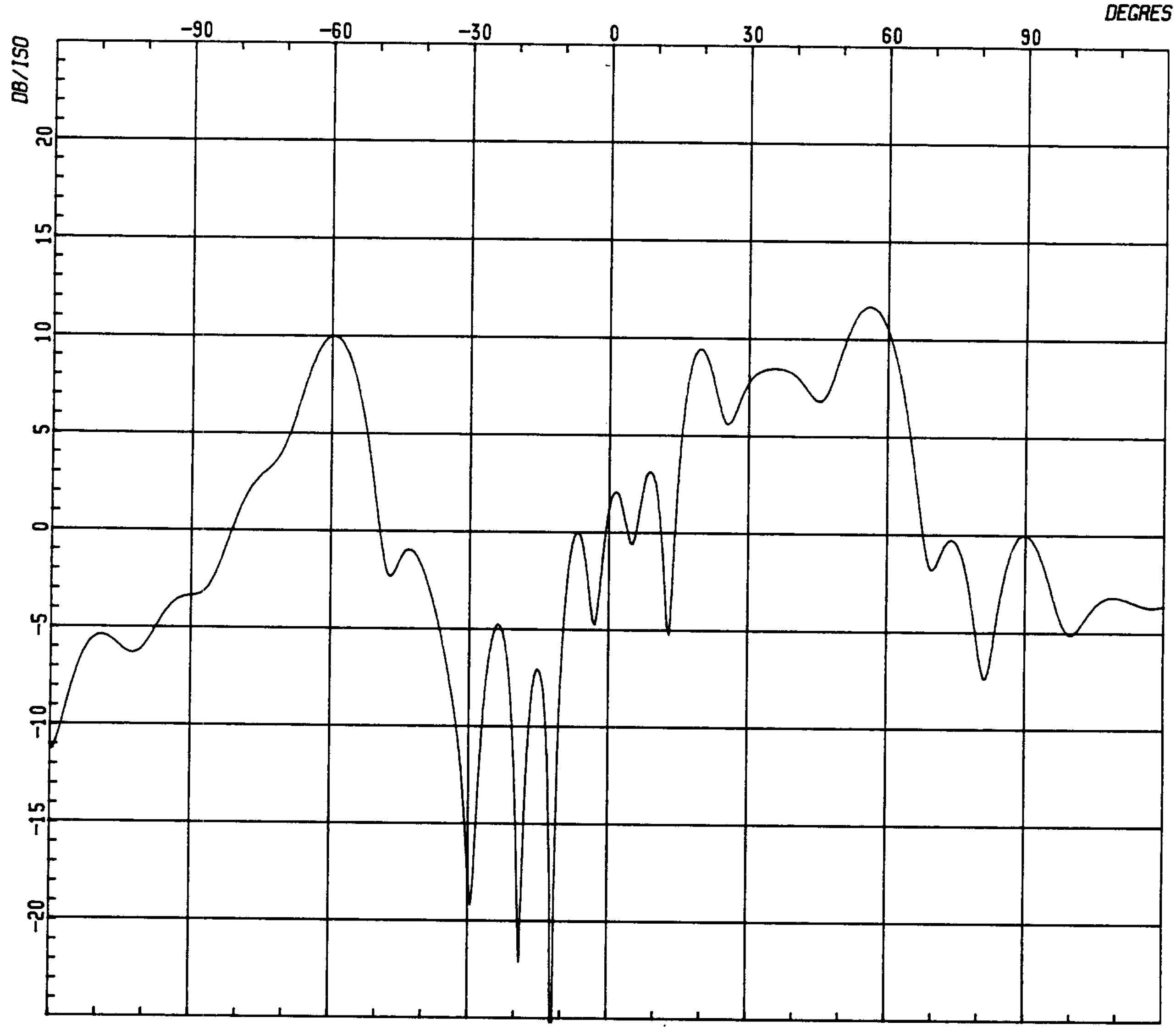

CONFORMAL ARRAY

SEMI-ACTIVE CONCEPT (folded subarray - serial rep)

MAX (dB/ISO)	MERIDIEN	POLARISATION
AMPL. 11.7	.00	

Frequence : 8200. Mhz
Fichier sasom.da 16 Plans
Rayon : 1000.00 mm

($\theta = 19.6°$)

ATES le 13 JUIN 1996

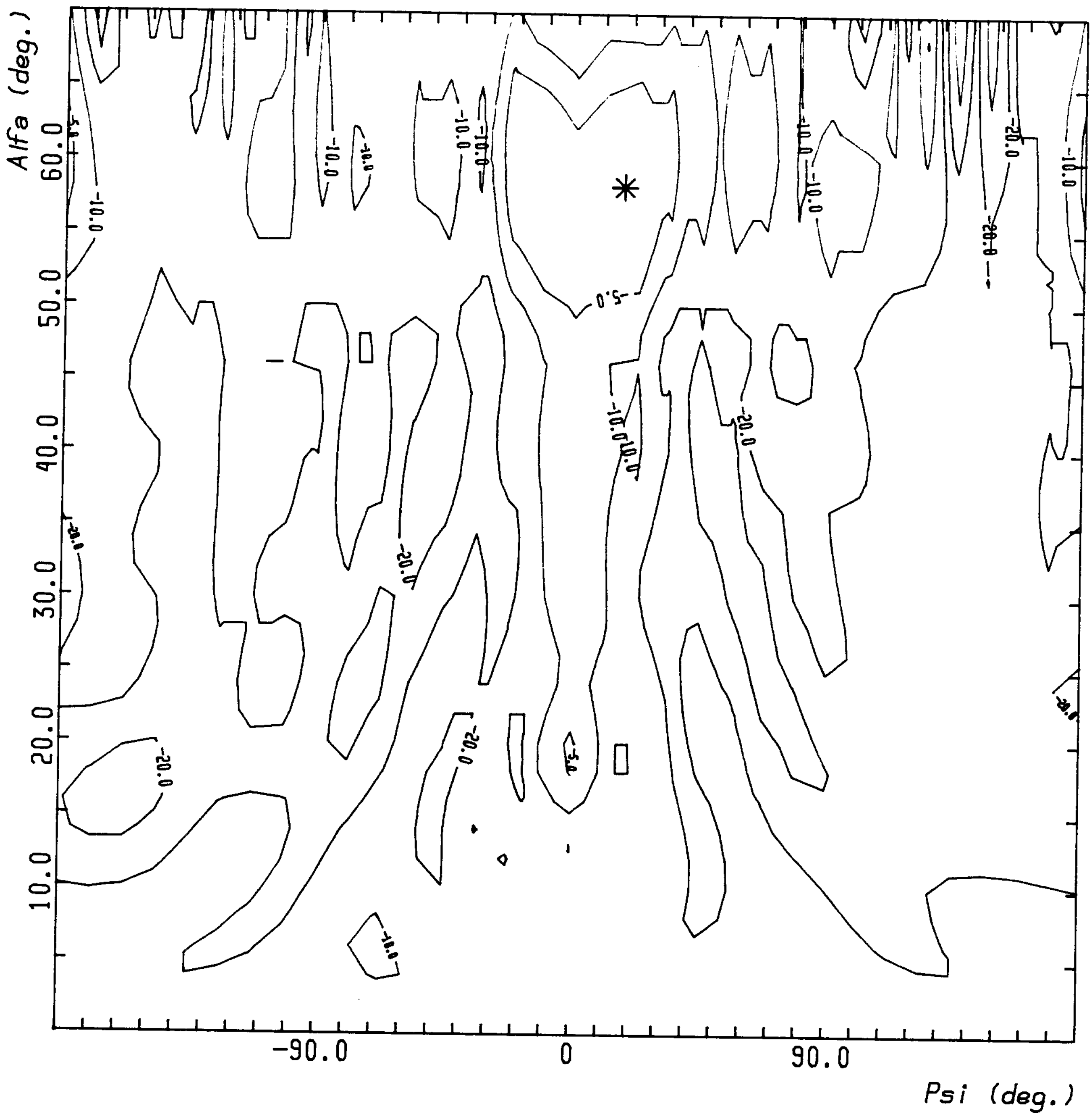

ACCES 1
Niveau (dB/Max)
Polar. circ. droite
Frequence 8200. Mhz
CONFORMAL ARRAY

($\theta = 19.6°$)

Alcatel le 13 JUIN 1996
a 19 h. 59 min.
sasom Acces 1.

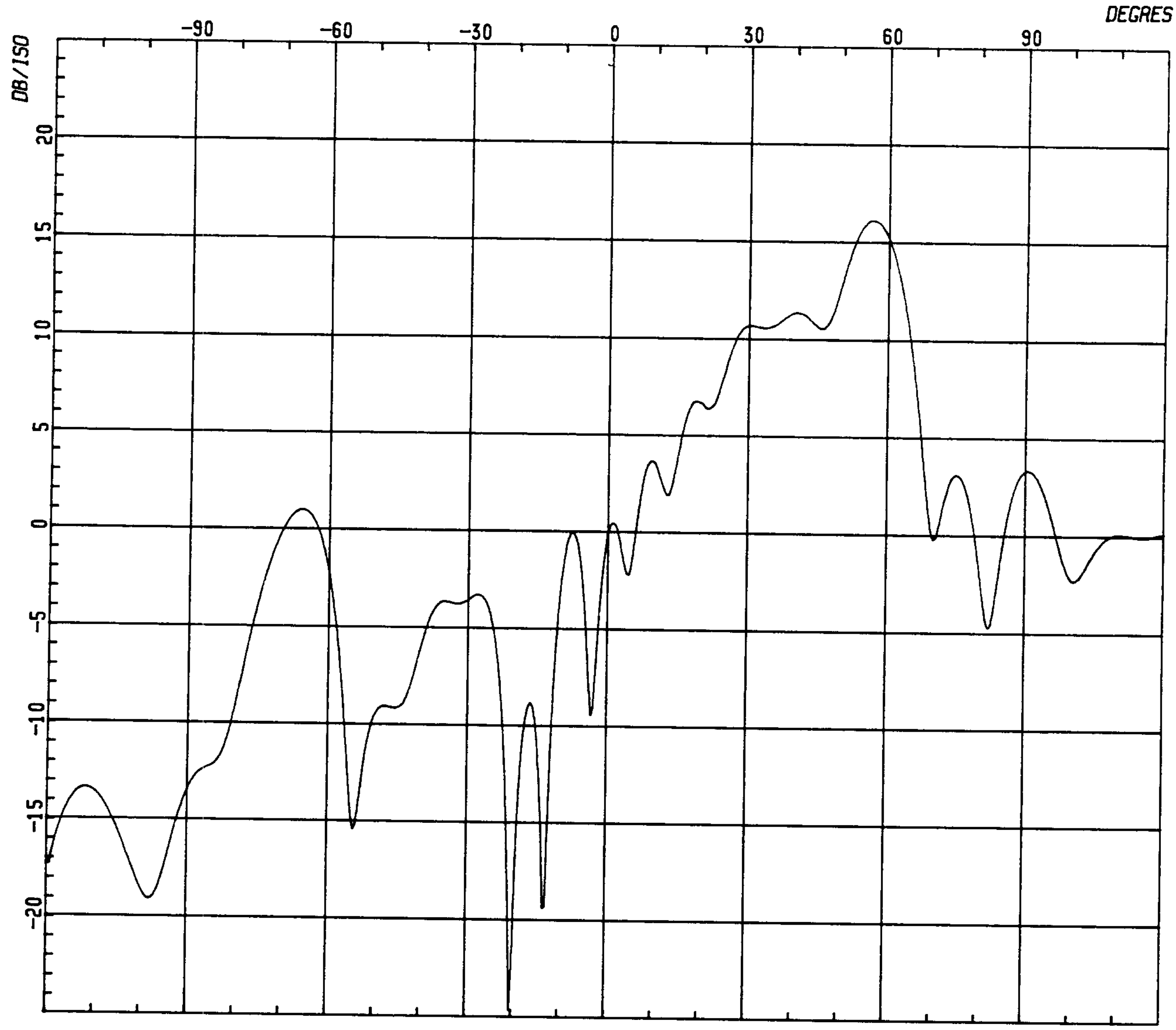

CONFORMAL ARRAY

SEMI-ACTIVE CONCEPT (folded subarray - serial rep)

MAX (dB/ISO) MERIDIEN POLARISATION

AMPL. 16.1 .00

Frequence : 8200. Mhz

Fichier sasom.da 16 Plans ($\theta = 29.4°$)

Rayon : 1000.00 mm

ATES le 13 JUIN 1996

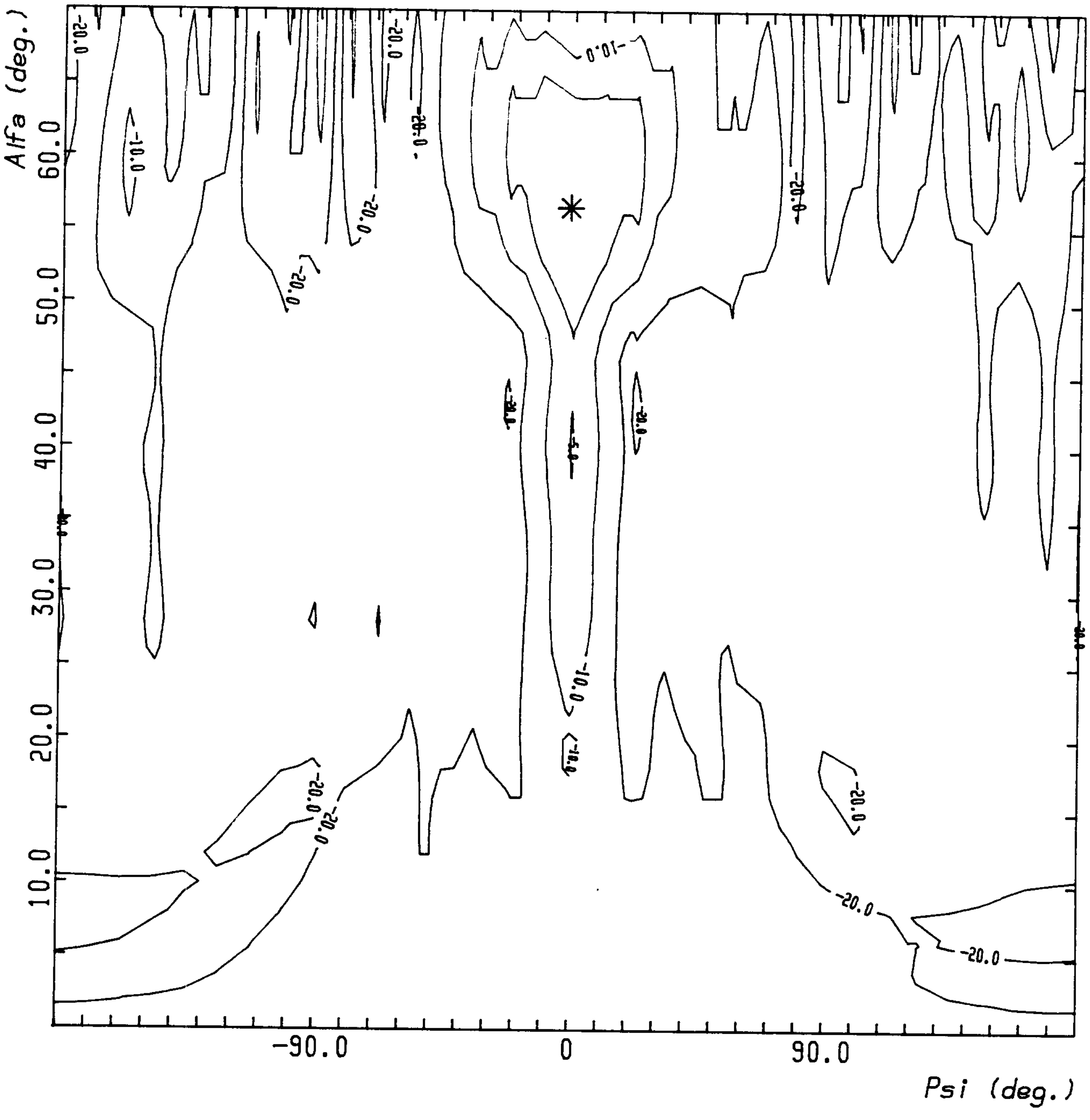

ACCES 1
Niveau (dB/Max)
Polar. circ. droite
Frequence 8200. Mhz
CONFORMAL ARRAY

($\theta = 29.4°$)

Alcatel le 13 JUIN 1996
a 19 h. 59 min.
sesom Acces 1.

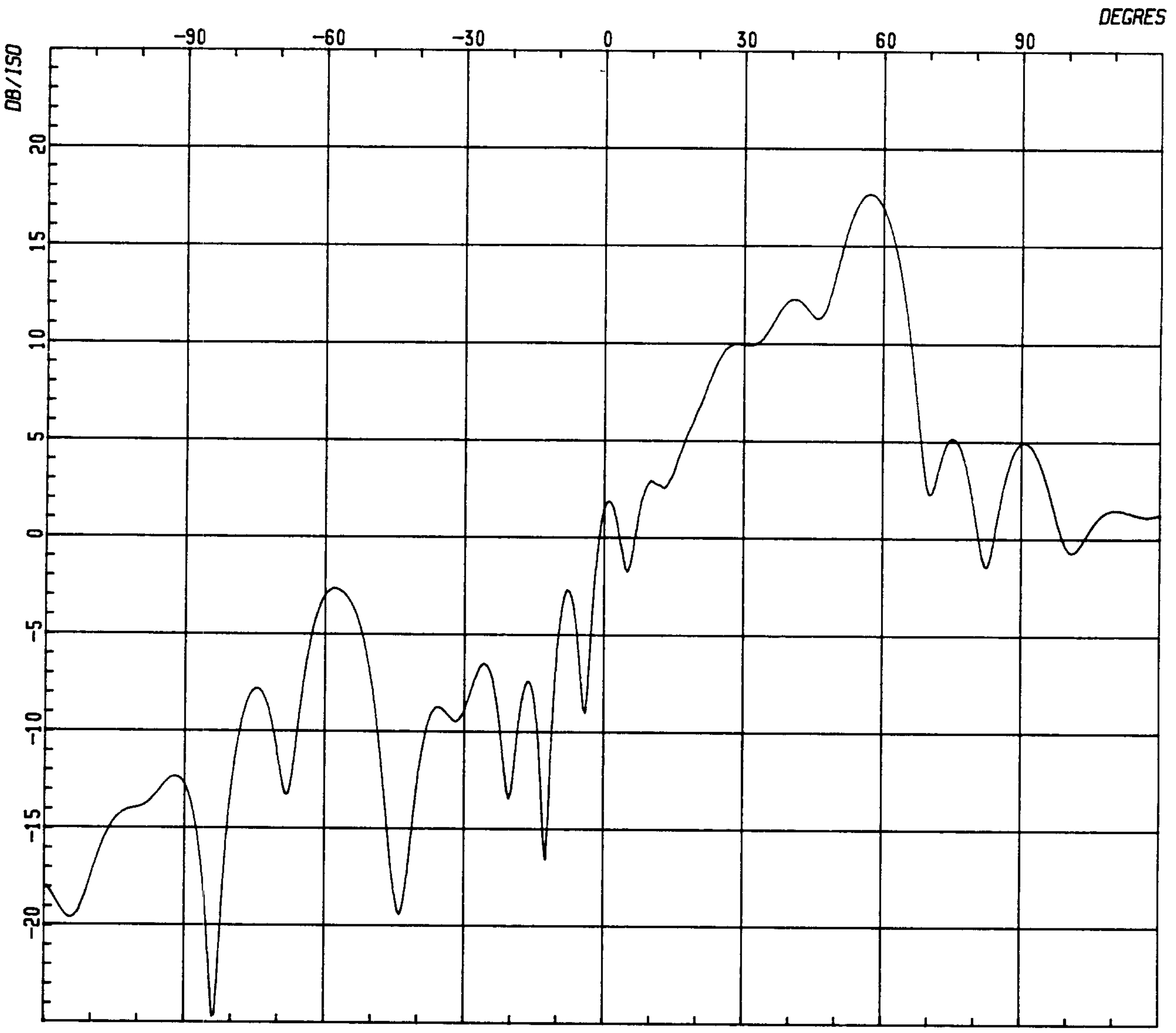

CONFORMAL ARRAY

SEMI-ACTIVE CONCEPT (folded subarray - serial rep)

Frequence : 8200. Mhz

Fichier sasom.da 16 Plans ($\theta = 39°$)

Rayon : 1000.00 mm

ATES le 13 JUIN 1996

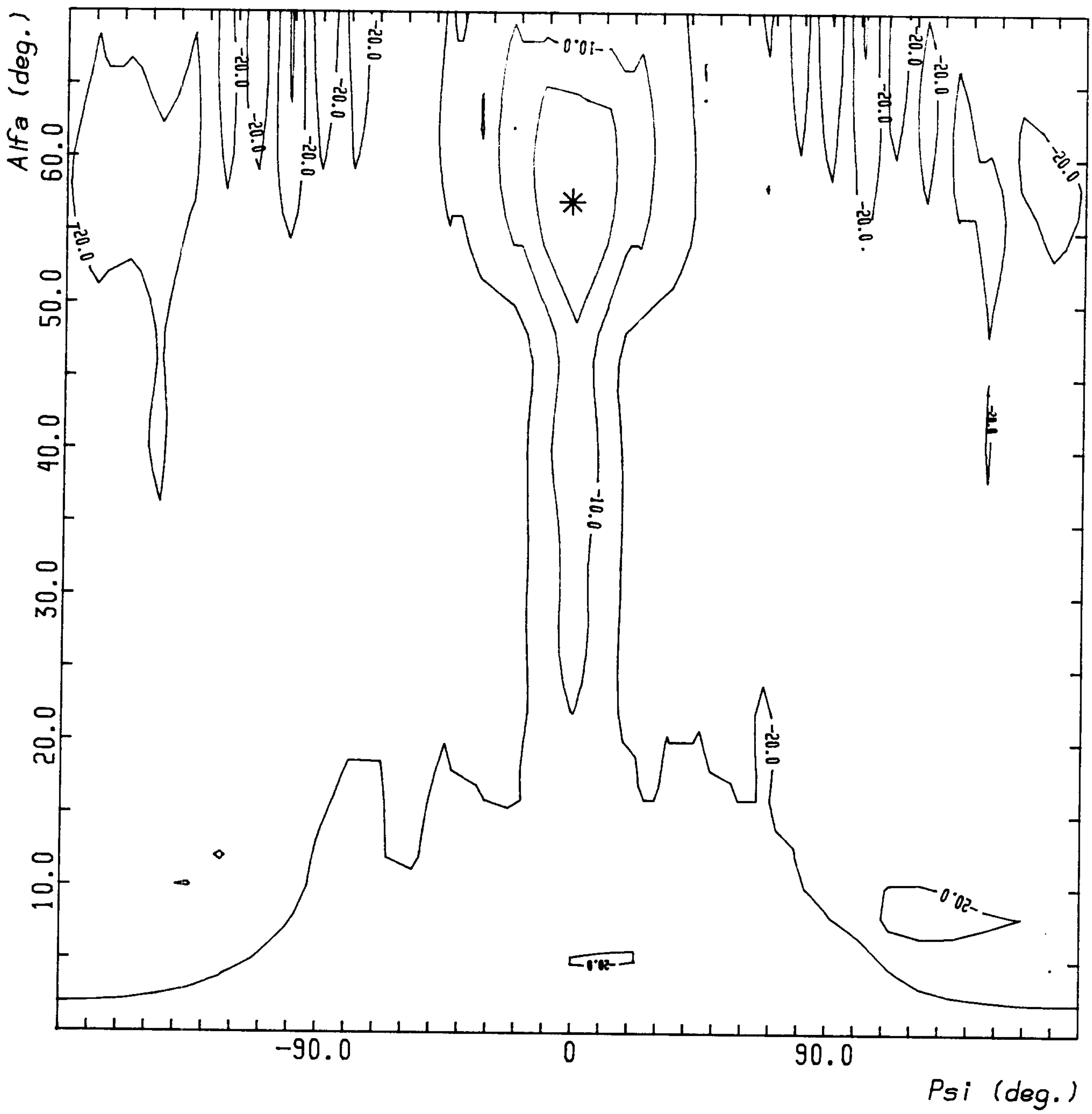

ACCES 1
Niveau (dB/Max)
Polar. circ. droite
Frequence 8200. Mhz
CONFORMAL ARRAY

($\theta = 39°$)

Alcatel le 13 JUIN 1996
a 20 h. 0 min.
sesom Acces 1.

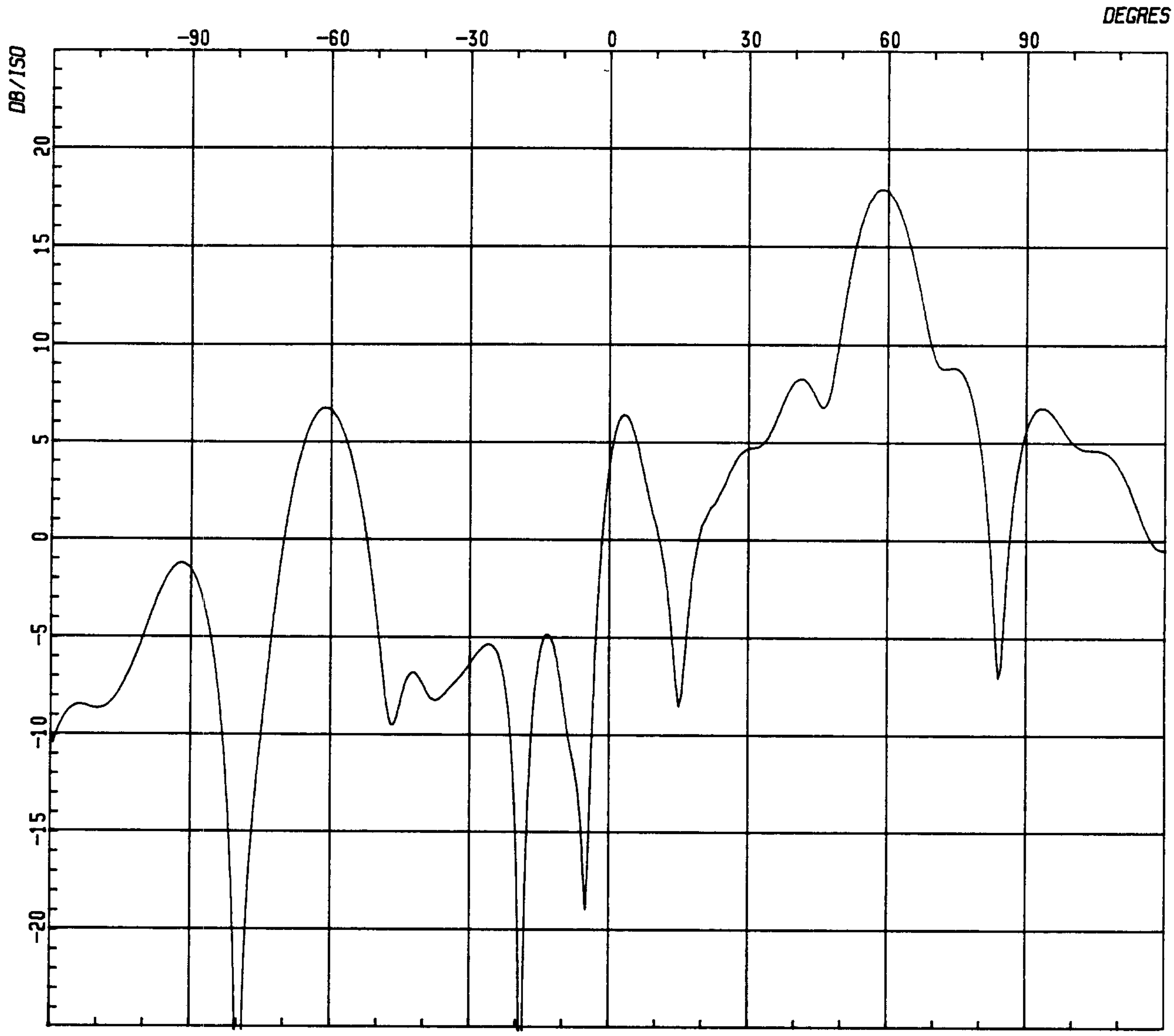

CONFORMAL ARRAY

SEMI-ACTIVE CONCEPT (folded subarray - serial rep)

MAX (dB/ISO)	MERIDIEN	POLARISATION
AMPL. 17.9	.00	

Frequence : 8200. Mhz

Fichier sasom.da 16 Plans ($\vartheta = 53.7°$)

Rayon : 1000.00 mm

ATES le 13 JUIN 1996

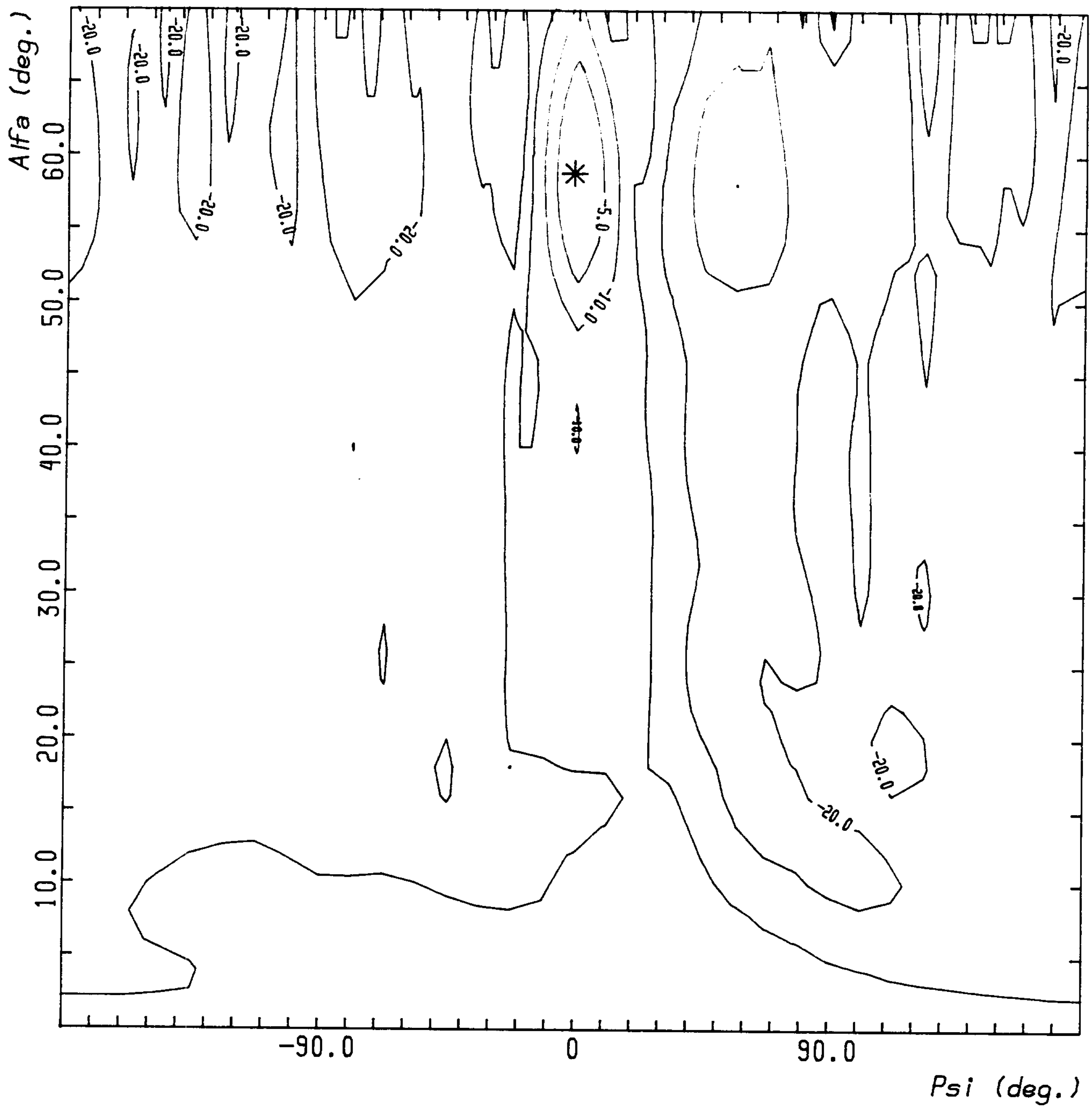

ACCES 1
Niveau (dB/Max)
Polar. circ. droite
Frequence 8200. Mhz
CONFORMAL ARRAY

(θ = 53.7°)

Alcatel le 13 JUIN 1996
a 20 h. 1 min.
sasom Acces 1.

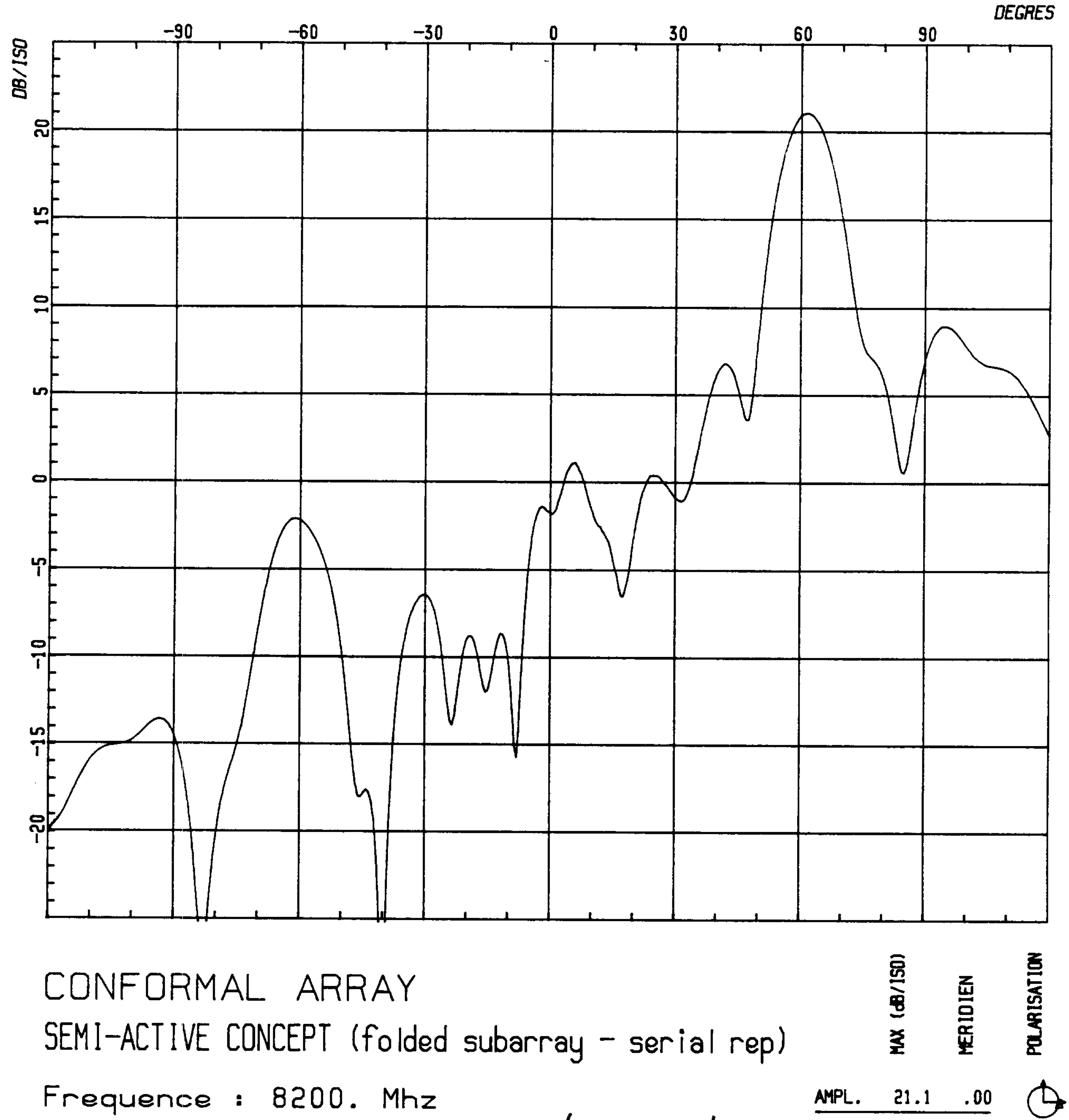

CONFORMAL ARRAY

SEMI-ACTIVE CONCEPT (folded subarray - serial rep)

Frequence : 8200. Mhz

Fichier sasom.da 16 Plans (θ = 62.3°)

Rayon : 1000.00 mm

ATES le 13 JUIN 1996

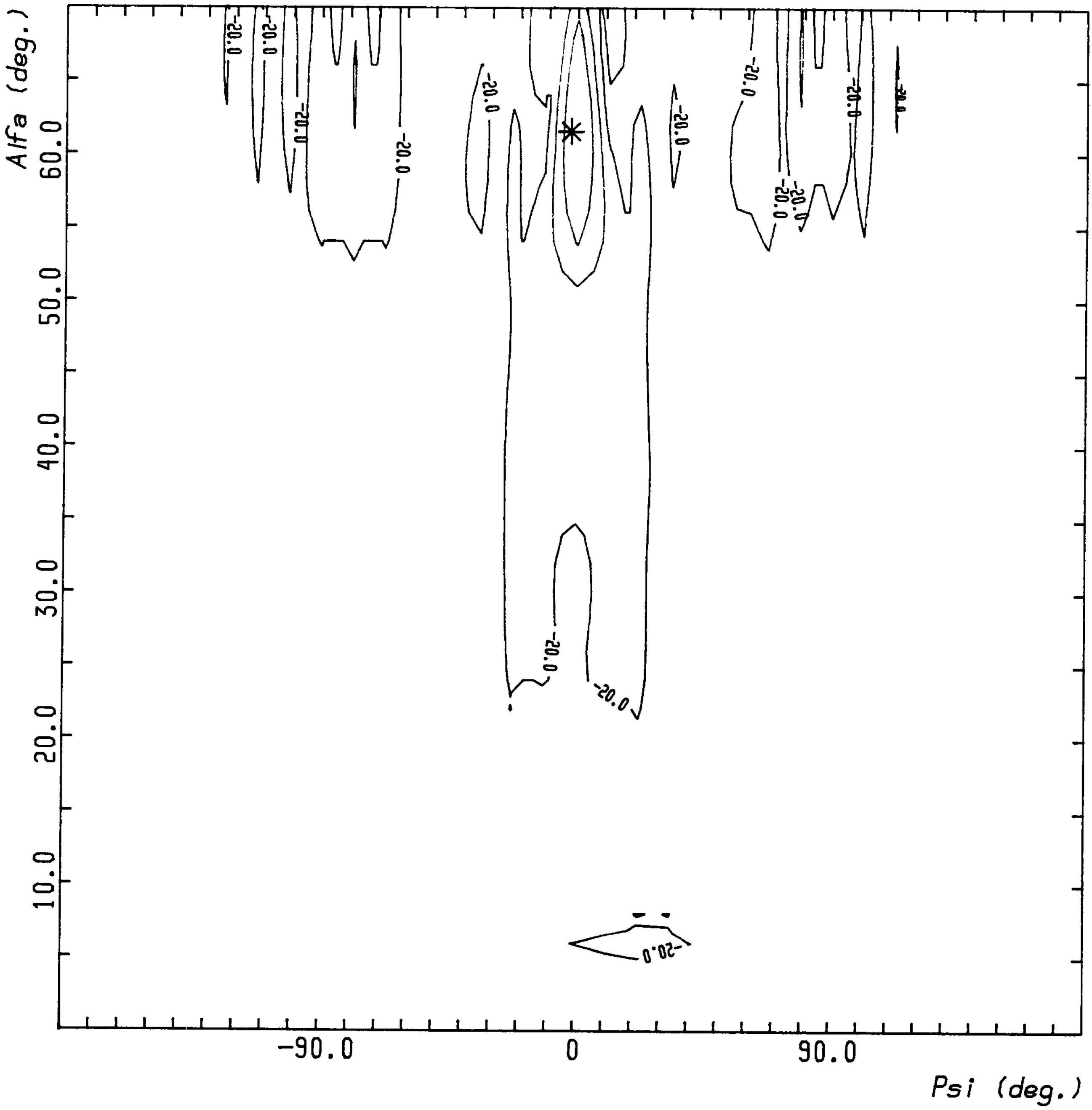

ACCES 1
Niveau (dB/Max)
Polar. circ. droite
Frequence 8200. Mhz
CONFORMAL ARRAY

(θ = 62.3°)

Alcatel le 13 JUIN 1996
a 20 h. 1 min.
sesom Acces 1.

```
CONFORMAL ARRAY
***************
SEMI-ACTIVE CONCEPT
CONICAL ANTENNA
Ntot=24
Ner=6
Nb=8
N=3
folded subarray (beta=25/25/25/25/25/35)
parallel repartitor
******************************
Frequency=8.2 GHz
Prf=-0.77 dBW
******************************
PHI=-7.5o

   Elevation (o)  EIRP (dBW)
   -------------------------
   .0000000E+00, .7371598E+01,
   .4900001E+01, .9173271E+01,
   .9800001E+01, .9239302E+01,
   .1180000E+02, .9239302E+01,
   .1280000E+02, .9275618E+01,
   .1470000E+02, .9357183E+01,
   .1720000E+02, .9478460E+01,
   .1960000E+02, .9422502E+01,
   .2450000E+02, .9854271E+01,
   .2940000E+02, .1040354E+02,
   .3420000E+02, .9939784E+01,
   .3900000E+02, .1009174E+02,
   .4380000E+02, .1132266E+02,
   .4860000E+02, .1191149E+02,
   .5370000E+02, .1492594E+02,
   .5660000E+02, .1604661E+02,
   .5920000E+02, .1732779E+02,
   .6109999E+02, .1870070E+02,
   .6230000E+02, .2023256E+02,

PHI=-3.75o

   Elevation (o)  EIRP (dBW)
   -------------------------
   .0000000E+00, .7371598E+01,
   .4900001E+01, .9172892E+01,
   .9800001E+01, .9239330E+01,
   .1180000E+02, .9239302E+01,
   .1280000E+02, .9275618E+01,
   .1470000E+02, .9357183E+01,
   .1720000E+02, .9478460E+01,
   .1960000E+02, .9330235E+01,
   .2450000E+02, .9964006E+01,
   .2940000E+02, .1040354E+02,
   .3420000E+02, .1000819E+02,
   .3900000E+02, .1011558E+02,
   .4380000E+02, .1131088E+02,
   .4860000E+02, .1192010E+02,
```



```
   .5370000E+02, .1492562E+02,
   .5660000E+02, .1604661E+02,
   .5920000E+02, .1732779E+02,
   .6109999E+02, .1870070E+02,
   .6230000E+02, .2023256E+02,

PHI=0o

   Elevation (o)  EIRP (dBW)
   -------------------------
   .0000000E+00, .7371598E+01,
   .4900001E+01, .9172892E+01,
   .9800001E+01, .9239302E+01,
   .1180000E+02, .9239302E+01,
   .1280000E+02, .9275618E+01,
   .1470000E+02, .9357183E+01,
   .1720000E+02, .9478460E+01,
   .1960000E+02, .9344858E+01,
   .2450000E+02, .9964006E+01,
   .2940000E+02, .1040354E+02,
   .3420000E+02, .1005555E+02,
   .3900000E+02, .9894252E+01,
   .4380000E+02, .1125212E+02,
   .4860000E+02, .1187740E+02,
   .5370000E+02, .1492639E+02,
   .5660000E+02, .1604661E+02,
   .5920000E+02, .1732779E+02,
   .6109999E+02, .1870070E+02,
   .6230000E+02, .2022703E+02,

PHI=3.75o

   Elevation (o)  EIRP (dBW)
   -------------------------
   .0000000E+00, .7371598E+01,
   .4900001E+01, .9172892E+01,
   .9800001E+01, .9239302E+01,
   .1180000E+02, .9239302E+01,
   .1280000E+02, .9275618E+01,
   .1470000E+02, .9357183E+01,
   .1720000E+02, .9478460E+01,
   .1960000E+02, .9217776E+01,
   .2450000E+02, .9964006E+01,
   .2940000E+02, .1040354E+02,
   .3420000E+02, .9938571E+01,
   .3900000E+02, .9897969E+01,
   .4380000E+02, .1127602E+02,
   .4860000E+02, .1188297E+02,
   .5370000E+02, .1492593E+02,
   .5660000E+02, .1604687E+02,
   .5920000E+02, .1732779E+02,
   .6109999E+02, .1870070E+02,
   .6230000E+02, .2023256E+02,

PHI=7.5o
```



```
   Elevation (o)  EIRP (dBW)
   -------------------------
   .0000000E+00, .7371598E+01,
   .4900001E+01, .9172892E+01,
   .9800001E+01, .9239302E+01,
   .1180000E+02, .9239302E+01,
   .1280000E+02, .9275618E+01,
   .1470000E+02, .9357183E+01,
   .1720000E+02, .9478460E+01,
   .1960000E+02, .9422500E+01,
   .2450000E+02, .9854273E+01,
   .2940000E+02, .1040354E+02,
   .3420000E+02, .9939986E+01,
   .3900000E+02, .1009175E+02,
   .4380000E+02, .1132266E+02,
   .4860000E+02, .1191118E+02,
   .5370000E+02, .1492594E+02,
   .5660000E+02, .1604661E+02,
   .5920000E+02, .1732779E+02,
   .6109999E+02, .1870070E+02,
   .6230000E+02, .2023256E+02,
```

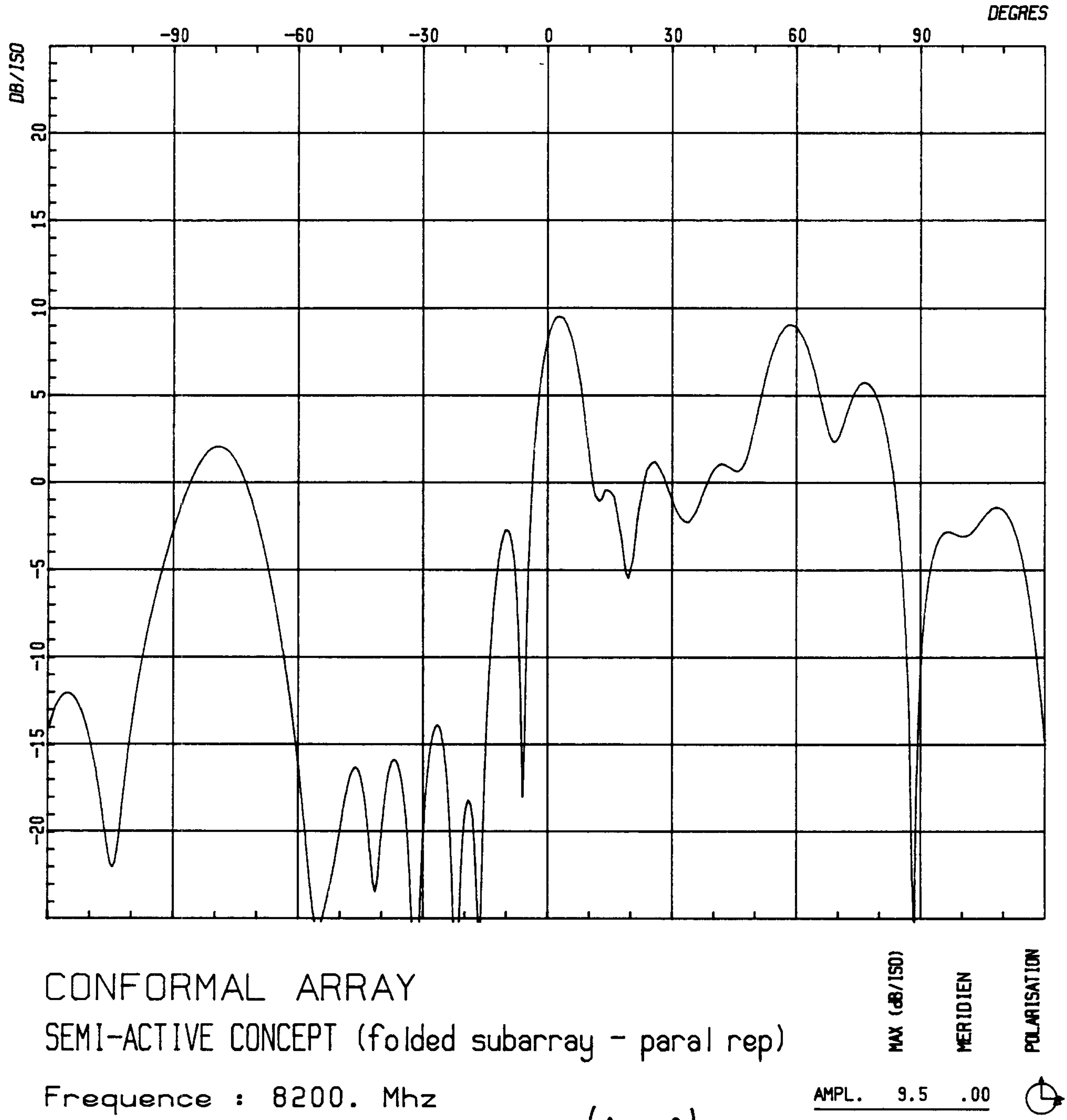

CONFORMAL ARRAY

SEMI-ACTIVE CONCEPT (folded subarray - paral rep)

Frequence : 8200. Mhz

Fichier sasom.da 16 Plans (ϑ = 0°)

Rayon : 1000.00 mm

ATES le 13 JUIN 1996

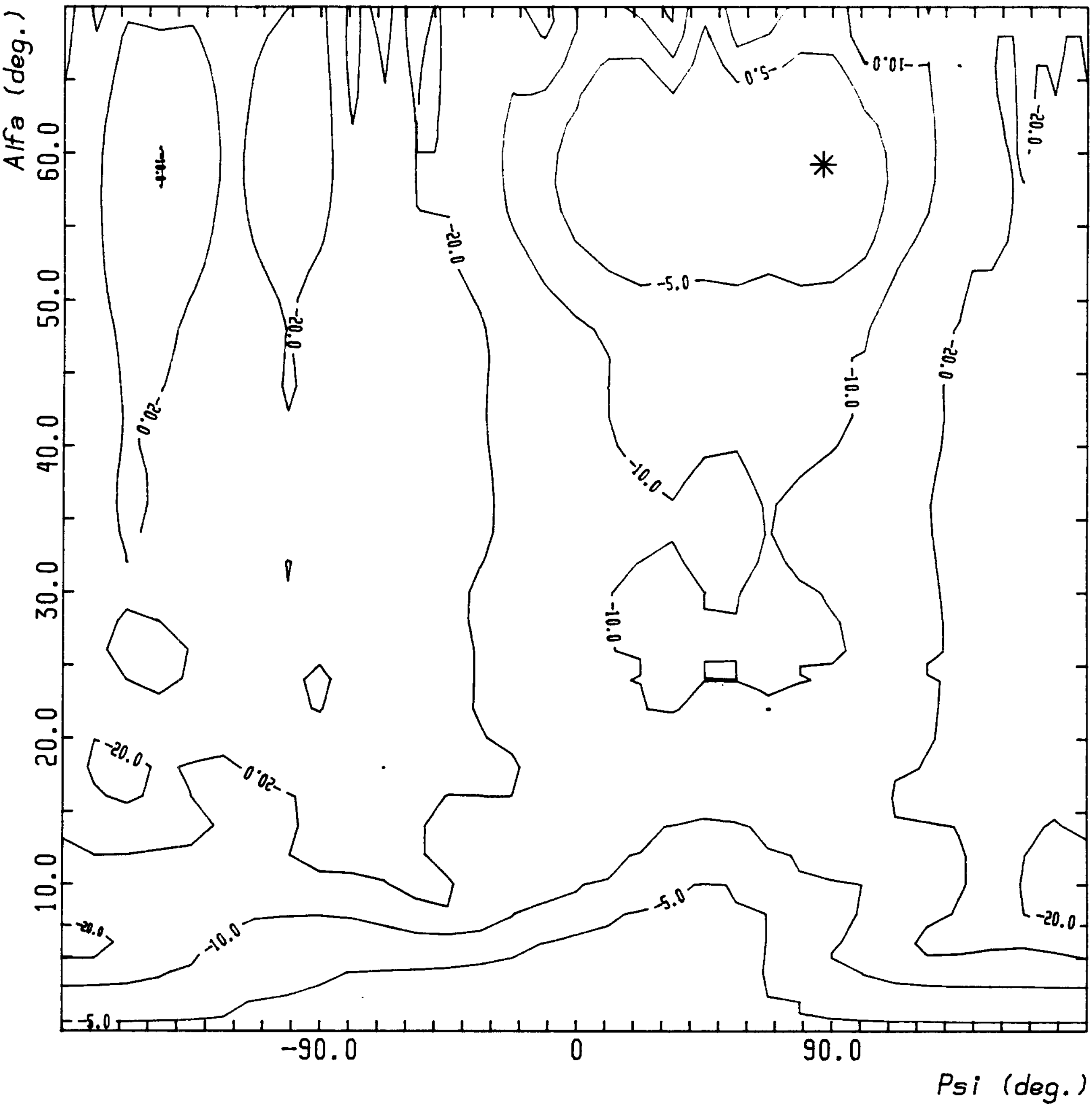

ACCES 1
Niveau (dB/Max)
Polar. circ. droite
Frequence 8200. Mhz
CONFORMAL ARRAY

($\theta = 0°$)

Alcatel le 13 JUIN 1996
a 20 h. 57 min.
sasom Acces 1.

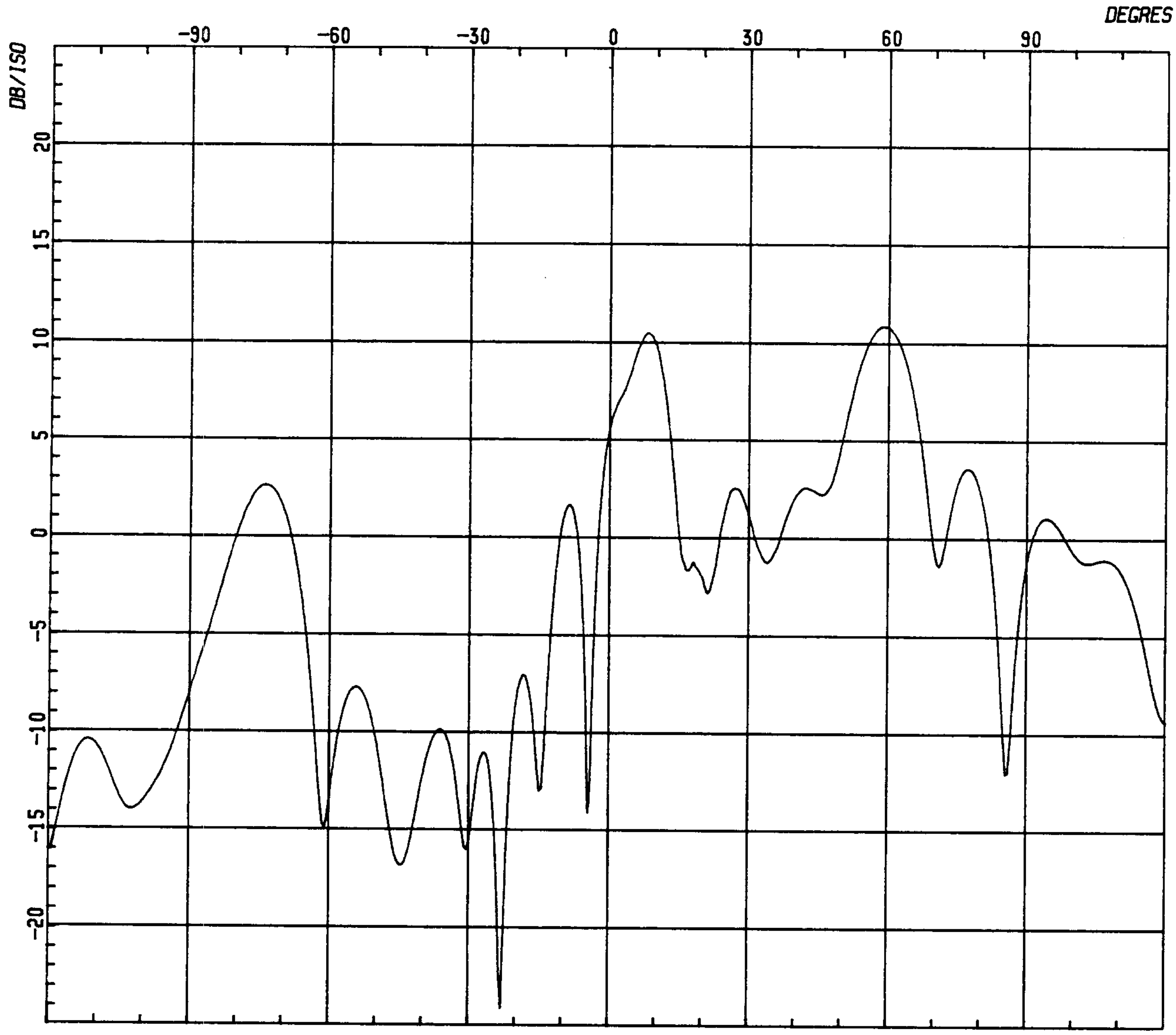

CONFORMAL ARRAY

SEMI-ACTIVE CONCEPT (folded subarray - paral rep)

MAX (dB/ISO)	MERIDIEN	POLARISATION
AMPL. 10.9	.00	

Frequence : 8200. Mhz ($\theta = 9.8°$)

Fichier sasom.da 16 Plans

Rayon : 1000.00 mm

ATES le 13 JUIN 1996

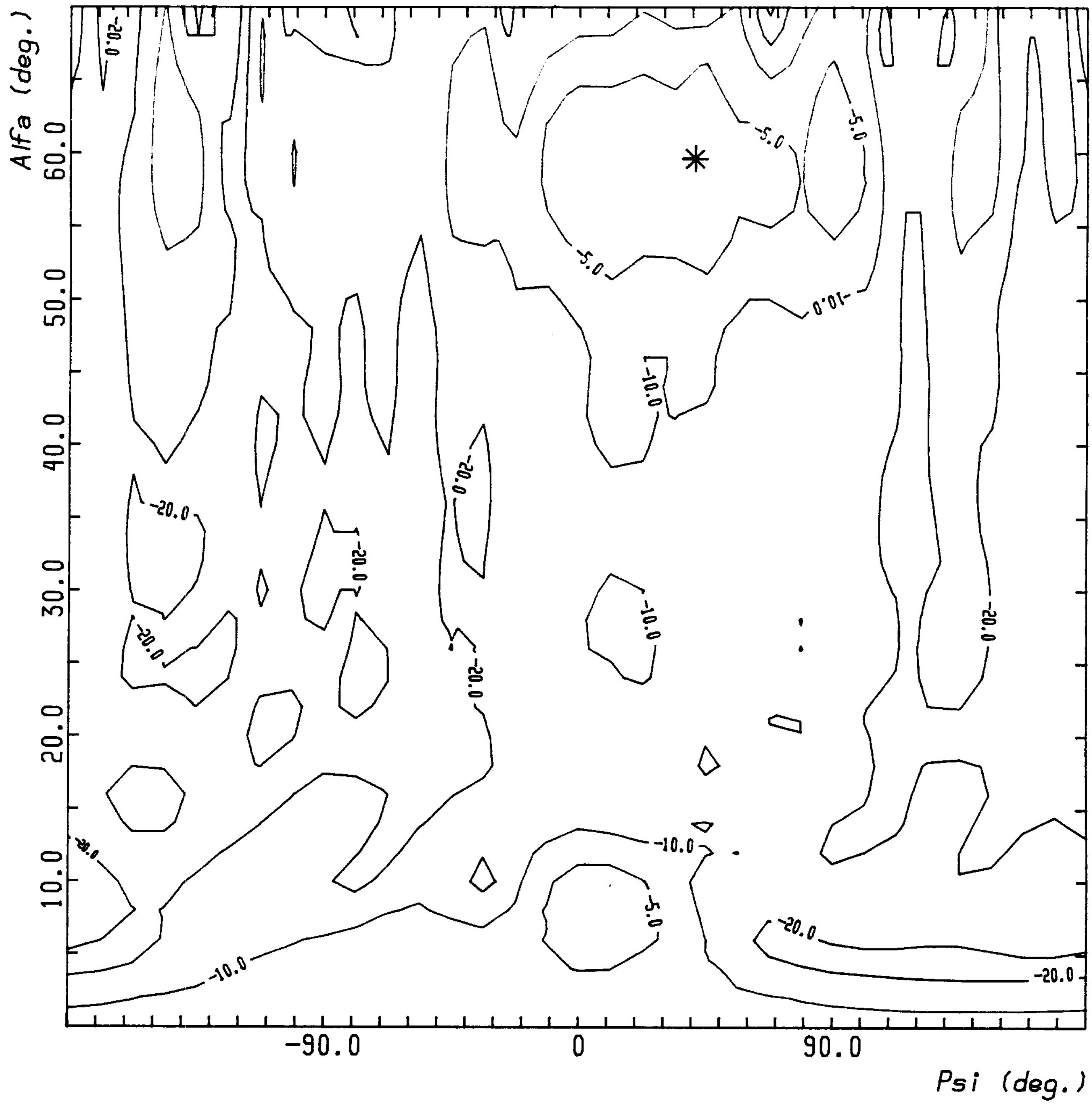

ACCES 1
Niveau (dB/Max)
Polar. circ. droite
Frequence 8200. Mhz
CONFORMAL ARRAY

($\theta = 9.8°$)

Alcatel le 13 JUIN 1996
a 20 h. 58 min.
sesom Acces 1.

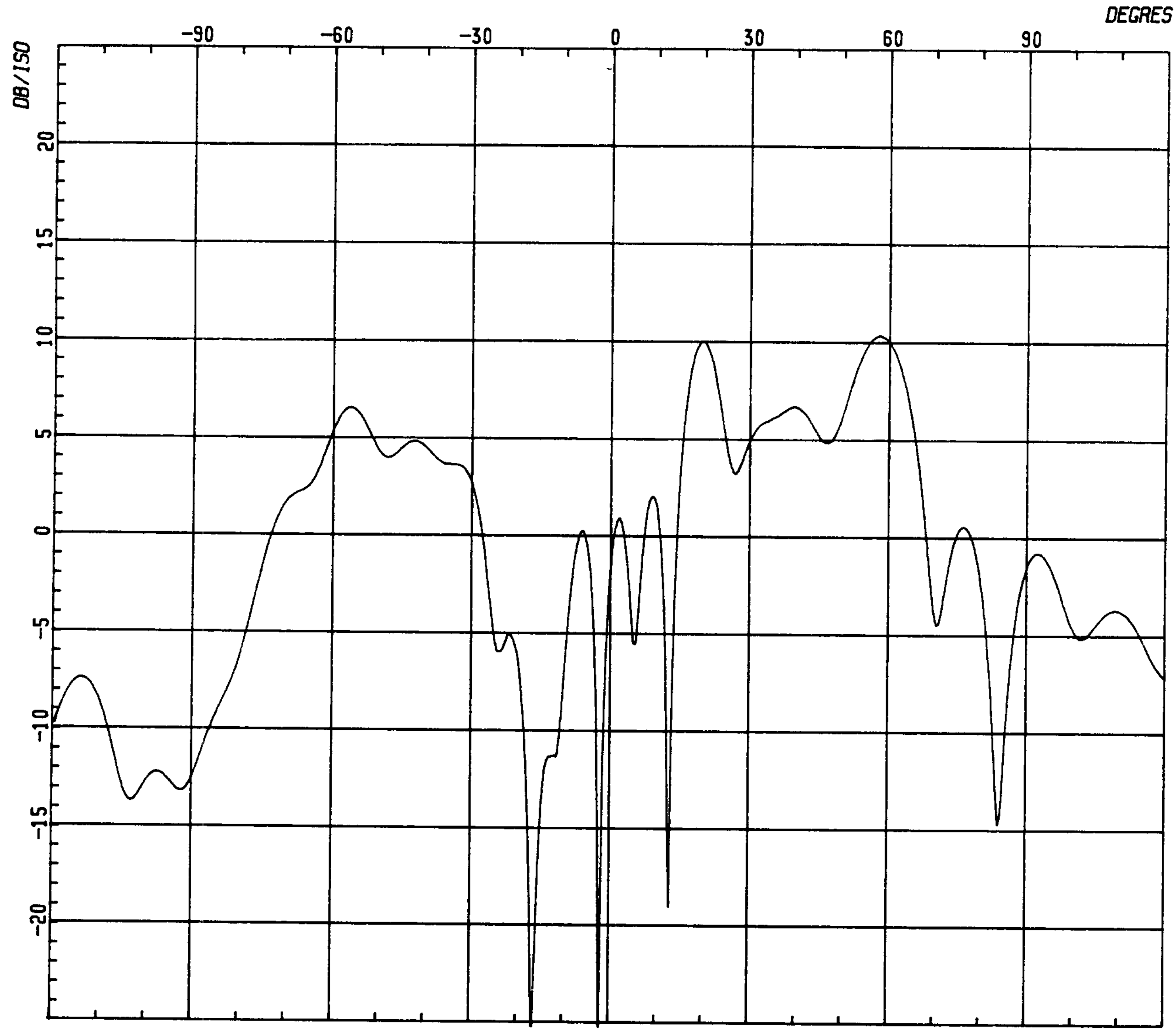

CONFORMAL ARRAY

SEMI-ACTIVE CONCEPT (folded subarray - paral rep)

Frequence : 8200. Mhz ($\vartheta = 19.6°$)

Fichier sasom.da 16 Plans

Rayon : 1000.00 mm

ATES le 13 JUIN 1996

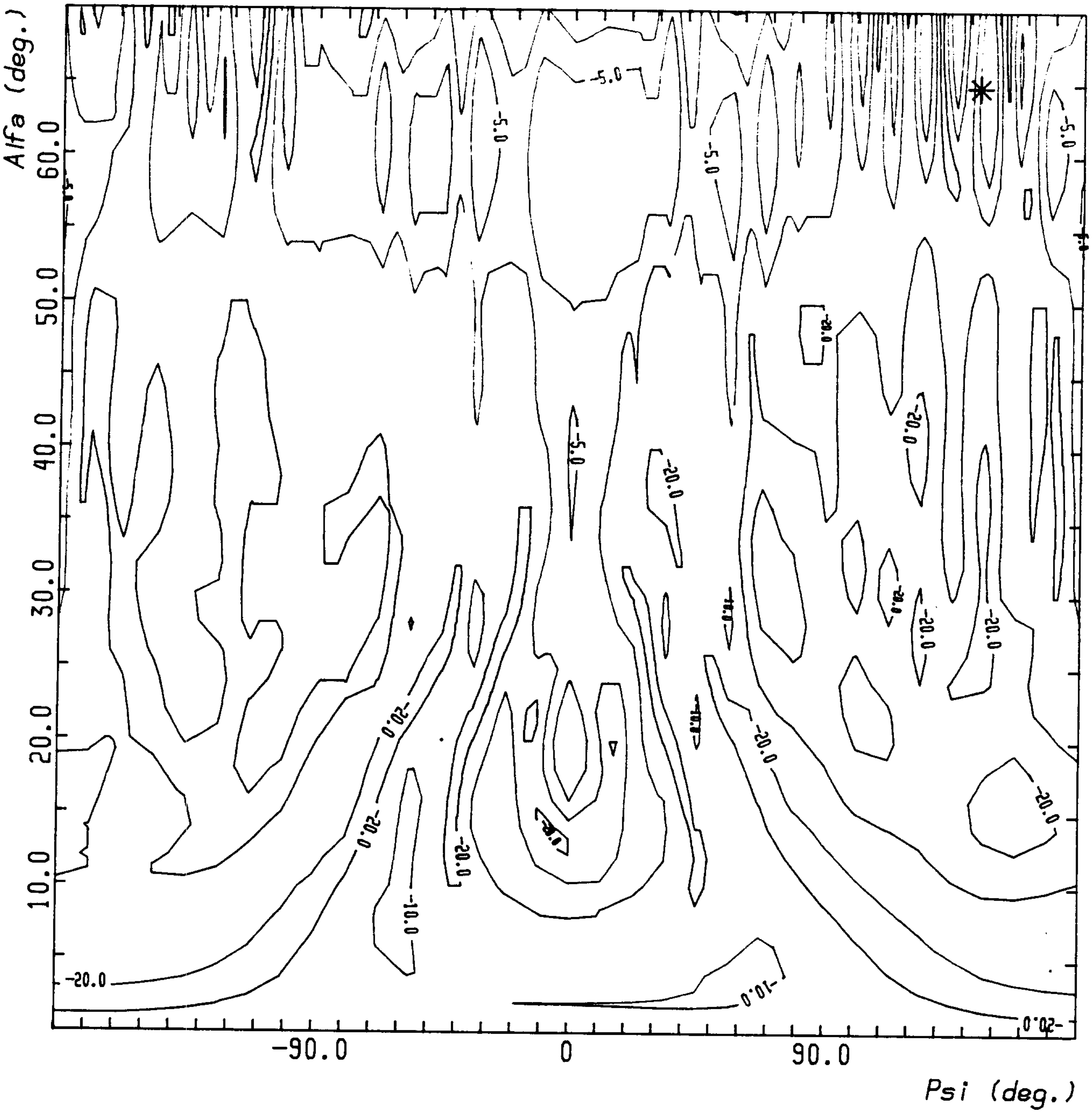

ACCES 1
Niveau (dB/Max)
Polar. circ. droite
Frequence 8200. Mhz
CONFORMAL ARRAY

(θ = 19.6°)

Alcatel le 13 JUIN 1996
a 20 h. 58 min.
sasom Acces 1.

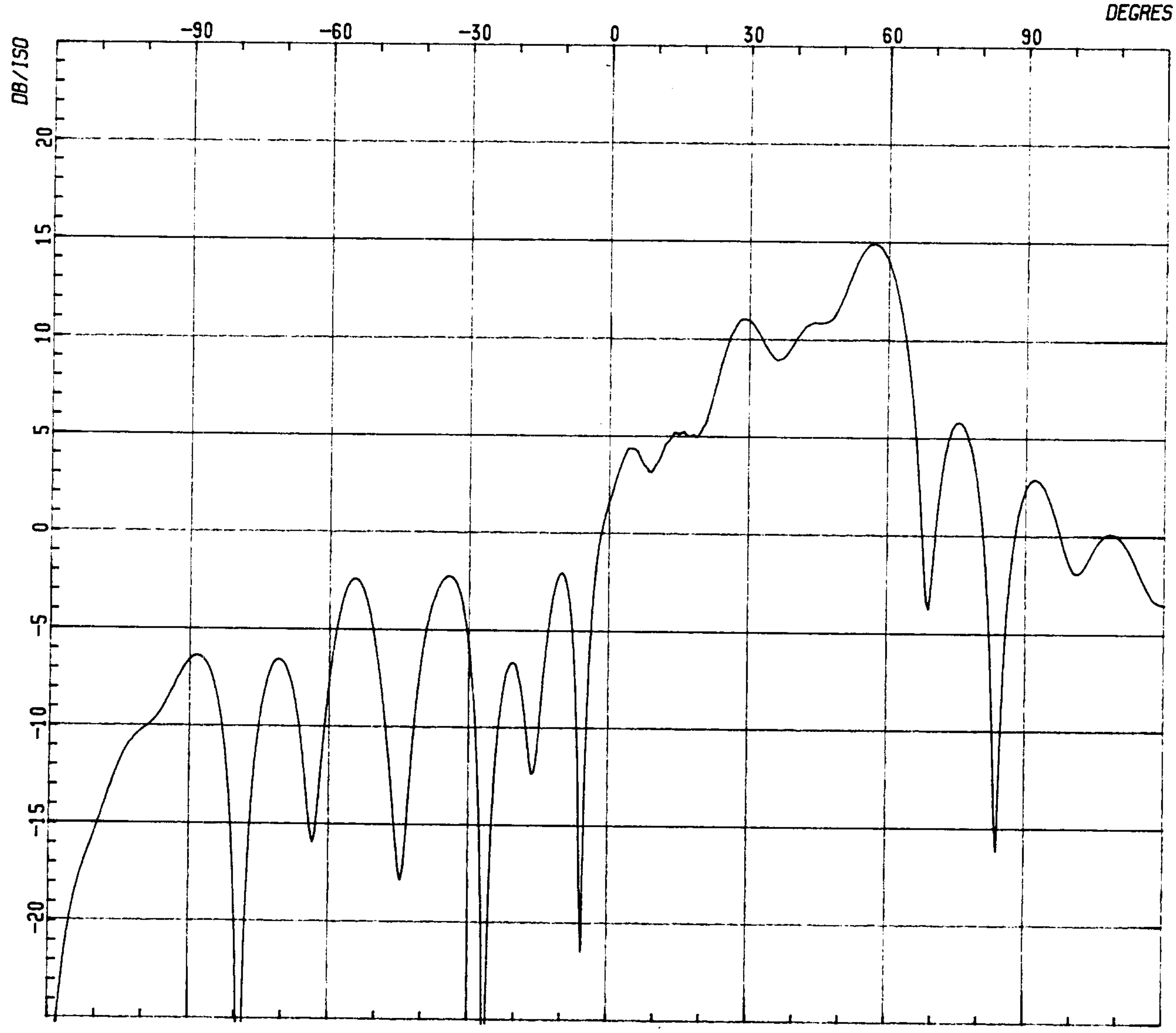

CONFORMAL ARRAY

SEMI-ACTIVE CONCEPT (folded subarray - paral rep)

Frequence : 8200. Mhz

Fichier sasom.da 16 Plans

Rayon : 1000.00 mm

($\theta = 29.4°$)

MAX (dB/ISO)	MERIDIEN	POLARISATION
AMPL. 14.9	.00	

ATES le 13 JUIN 1996

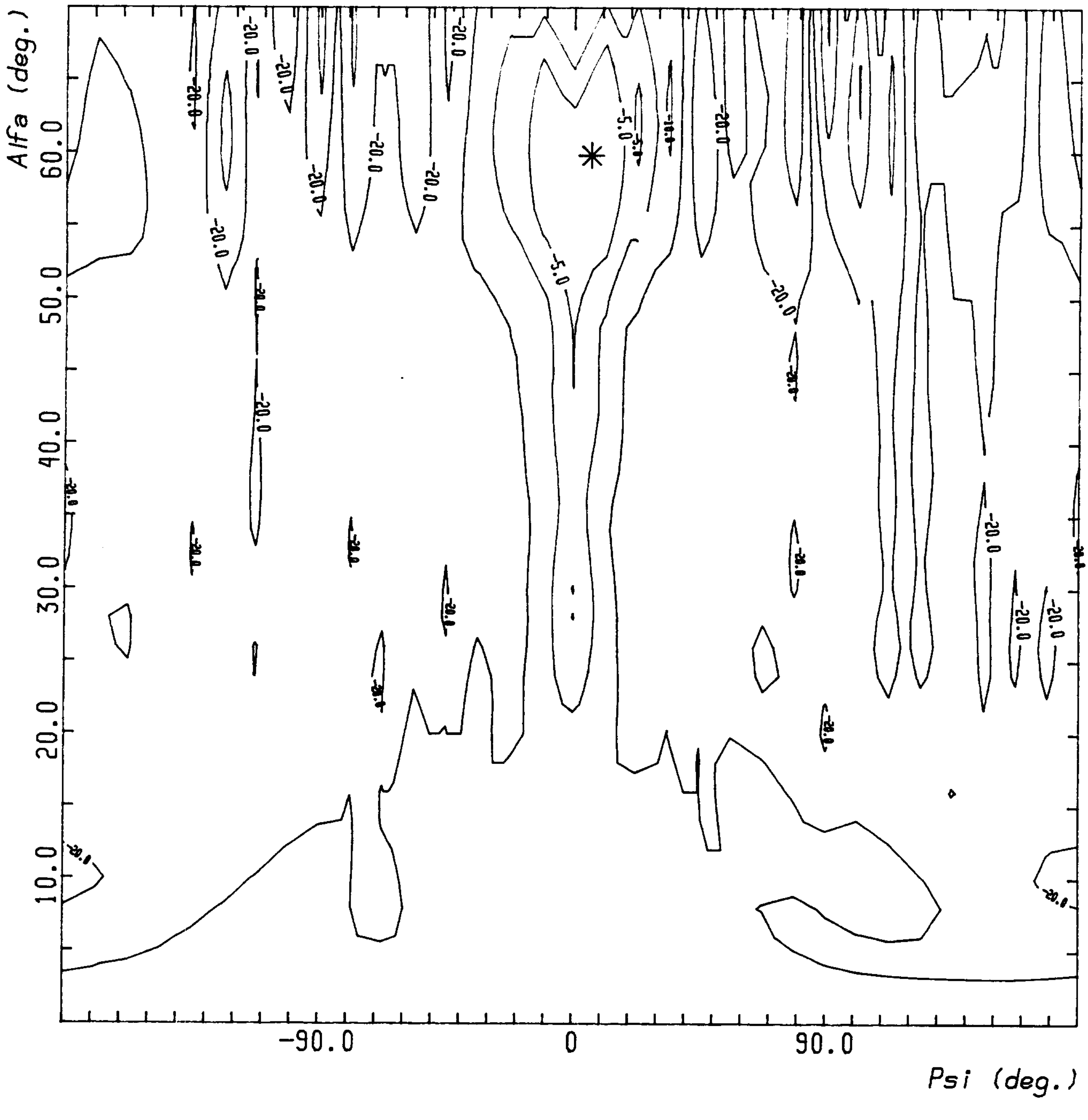

ACCES 1
Niveau (dB/Max)
Polar. circ. droite
Frequence 8200. Mhz
CONFORMAL ARRAY

$(\theta = 29.4°)$

Alcatel le 13 JUIN 1996
a 20 h. 59 min.
sesom Acces 1.

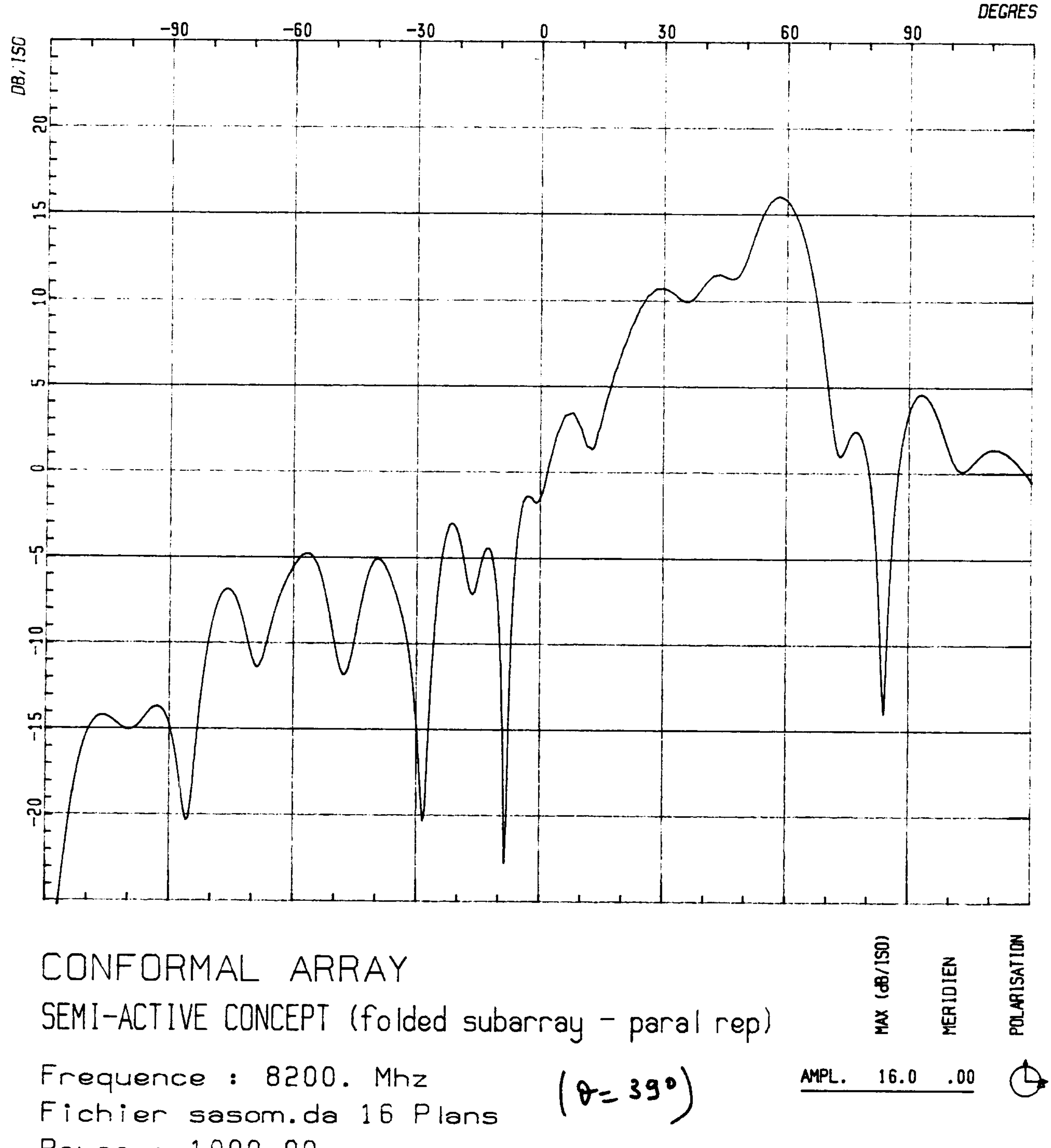

CONFORMAL ARRAY

SEMI-ACTIVE CONCEPT (folded subarray - paral rep)

Frequence : 8200. Mhz (θ = 39°)

Fichier sasom.da 16 Plans

Rayon : 1000.00 mm

ATES le 13 JUIN 1996

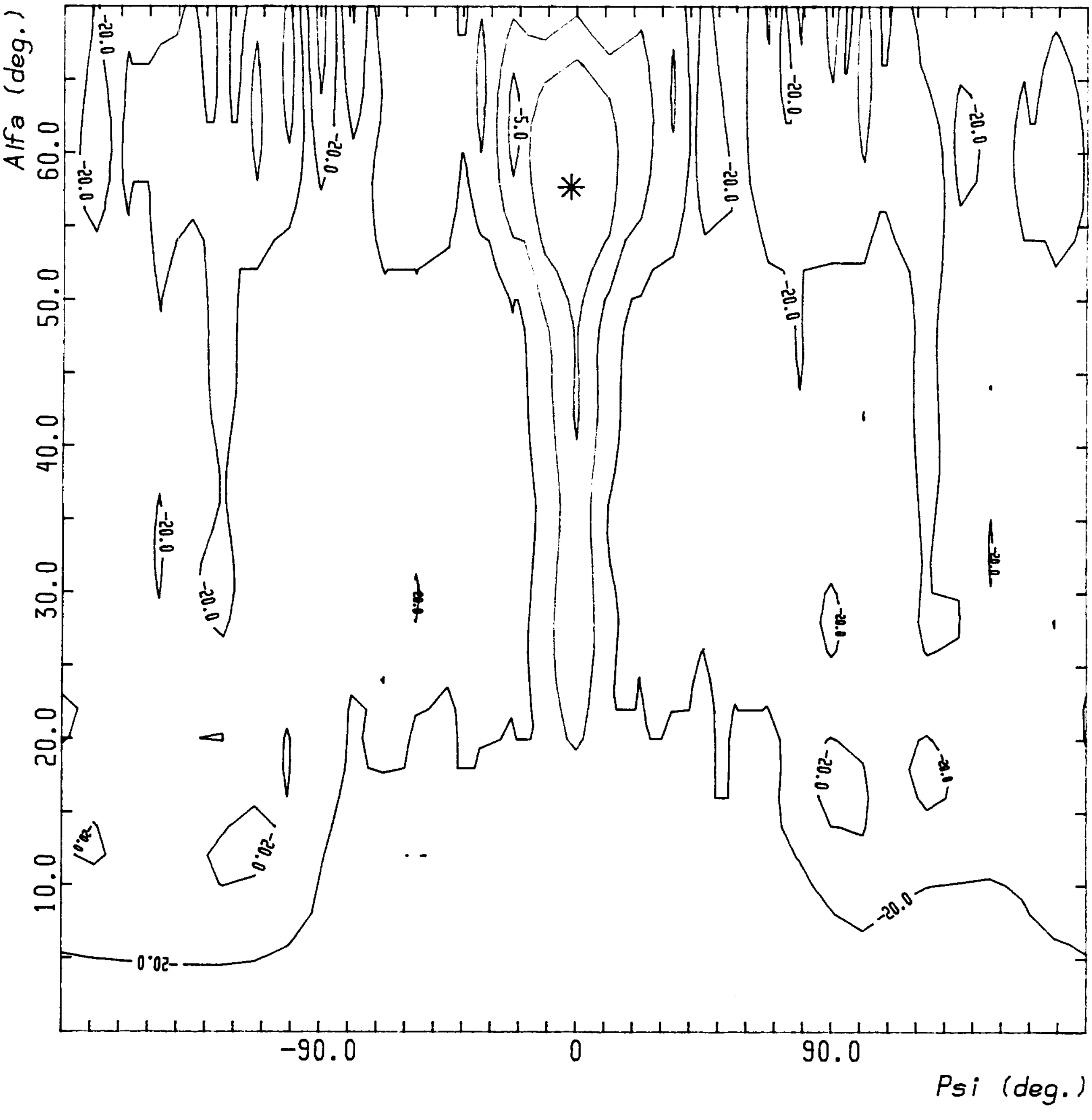

ACCES 1
Niveau (dB/Max)
Polar. circ. droite
Frequence 8200. Mhz
CONFORMAL ARRAY

($\vartheta = 39°$)

Alcatel le 13 JUIN 1996
a 21 h. 0 min.
sesom Acces 1.

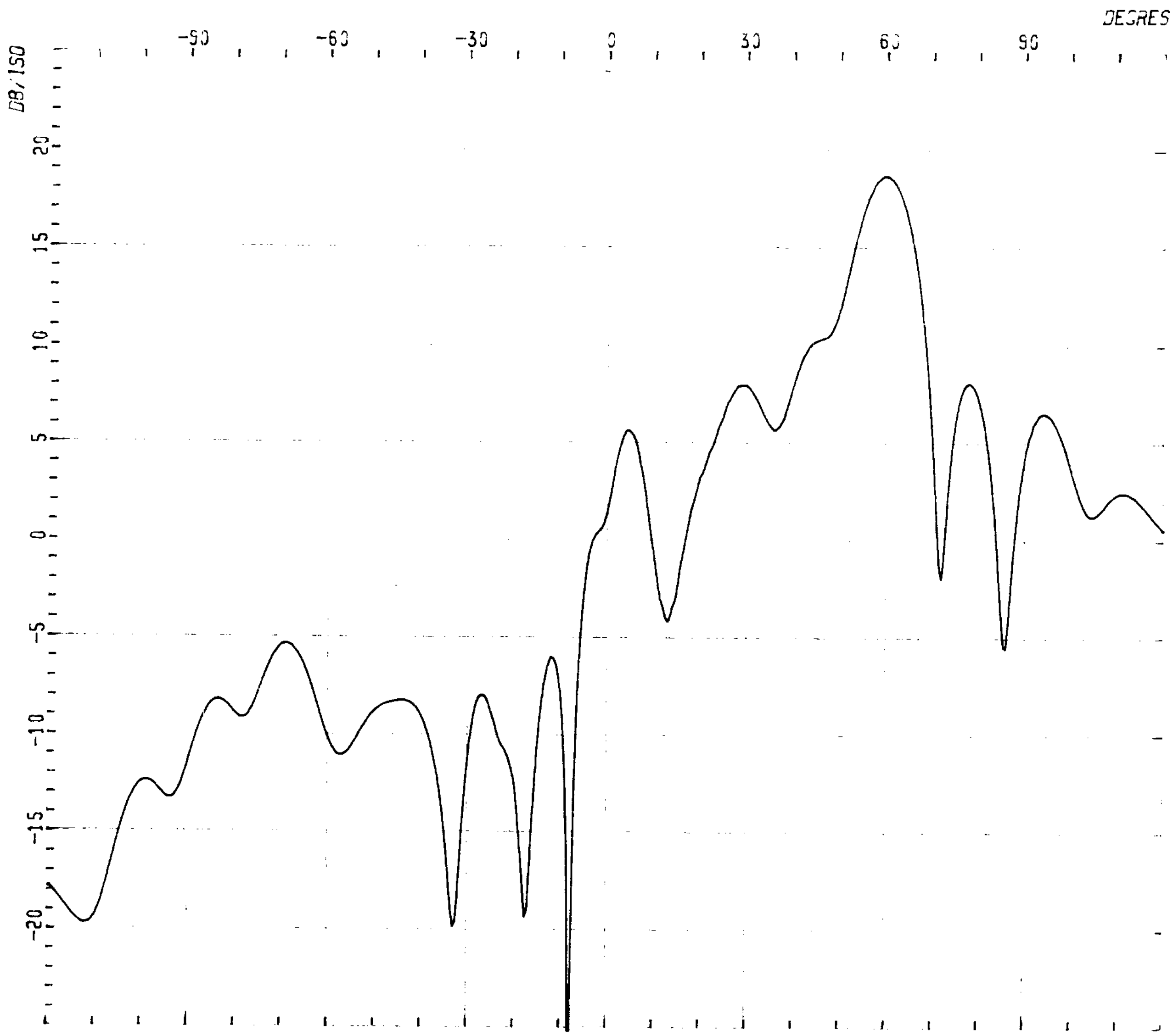

CONFORMAL ARRAY

SEMI-ACTIVE CONCEPT (folded subarray - paral rep)

MAX (dB/ISO) MERIDIEN POLARISATION

AMPL. 18.7 .00

Frequence : 8200. Mhz

Fichier sasom.da 16 Plans

Rayon : 1000.00 mm

(θ = 53.70)

ATES le 13 JUIN 1996

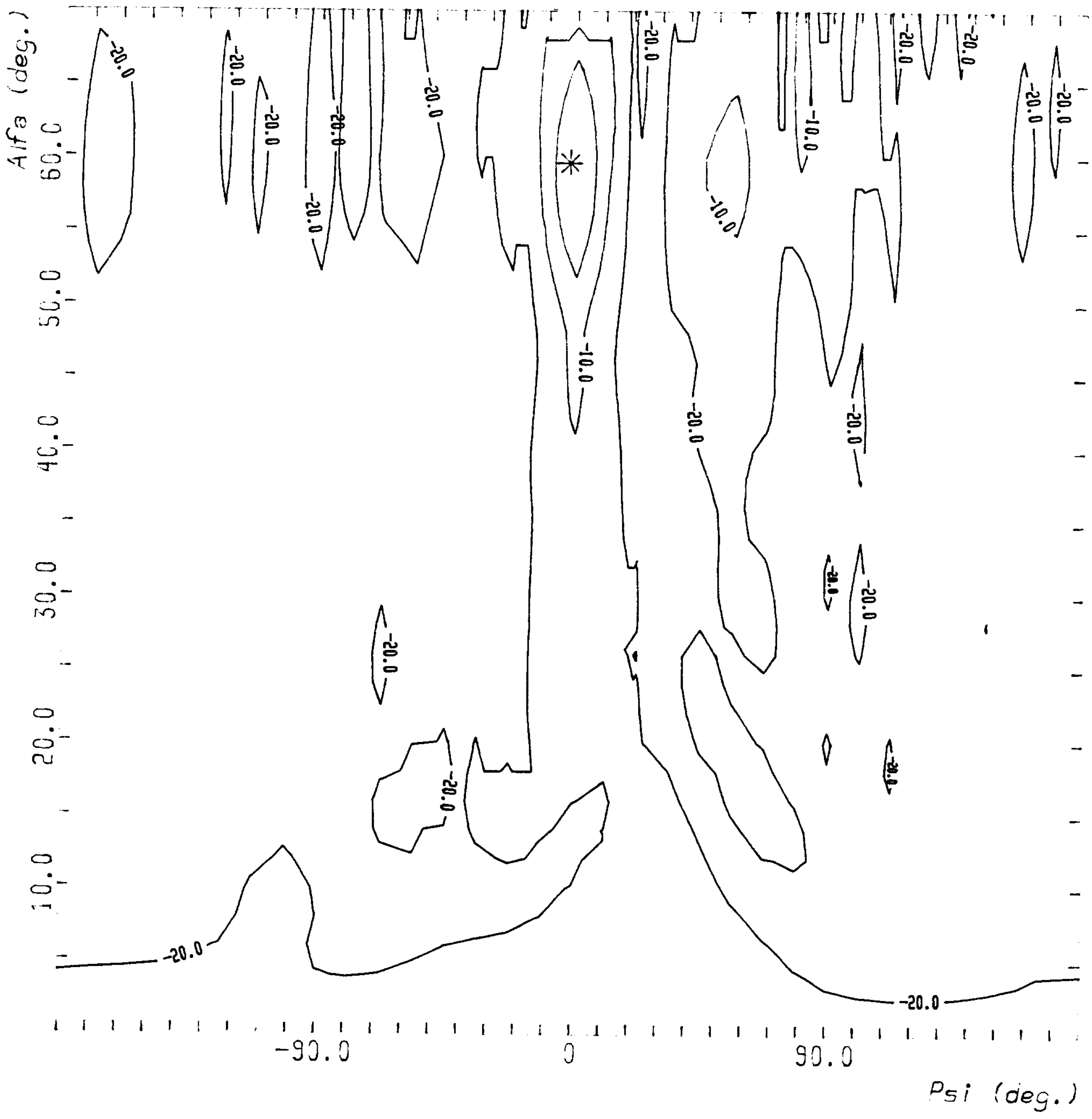

ACCES 1
Niveau (dB/Max)
Polar. circ. droite
Frequence 8200. Mhz
CONFORMAL ARRAY

$\cdot\,(\theta = 53.7^\circ)$

Alcatel le 13 JUIN 1996
a 21 h. 1 min.
sesom Acces 1.

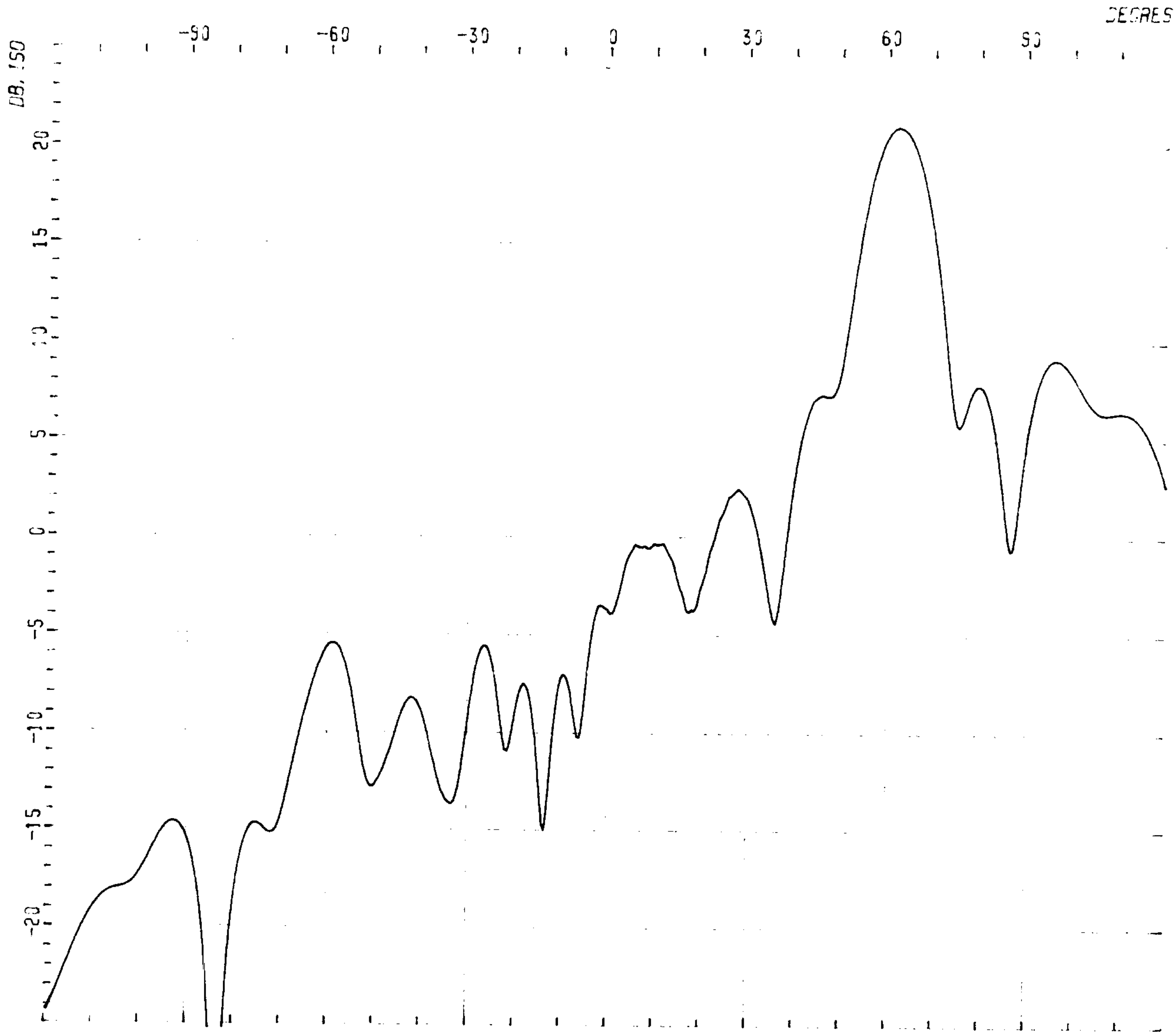

CONFORMAL ARRAY

SEMI-ACTIVE CONCEPT (folded subarray - paral rep)

Frecuence : 8200. Mhz

Fichier sasnm.da 16 Plans

Rayon : 1000.00 mm

(θ = 62.3°)

MAX (dB/ISO) MERIDIEN POLARISATION

AMPL. 21.0 .00

ATES le 13 JUIN 1996

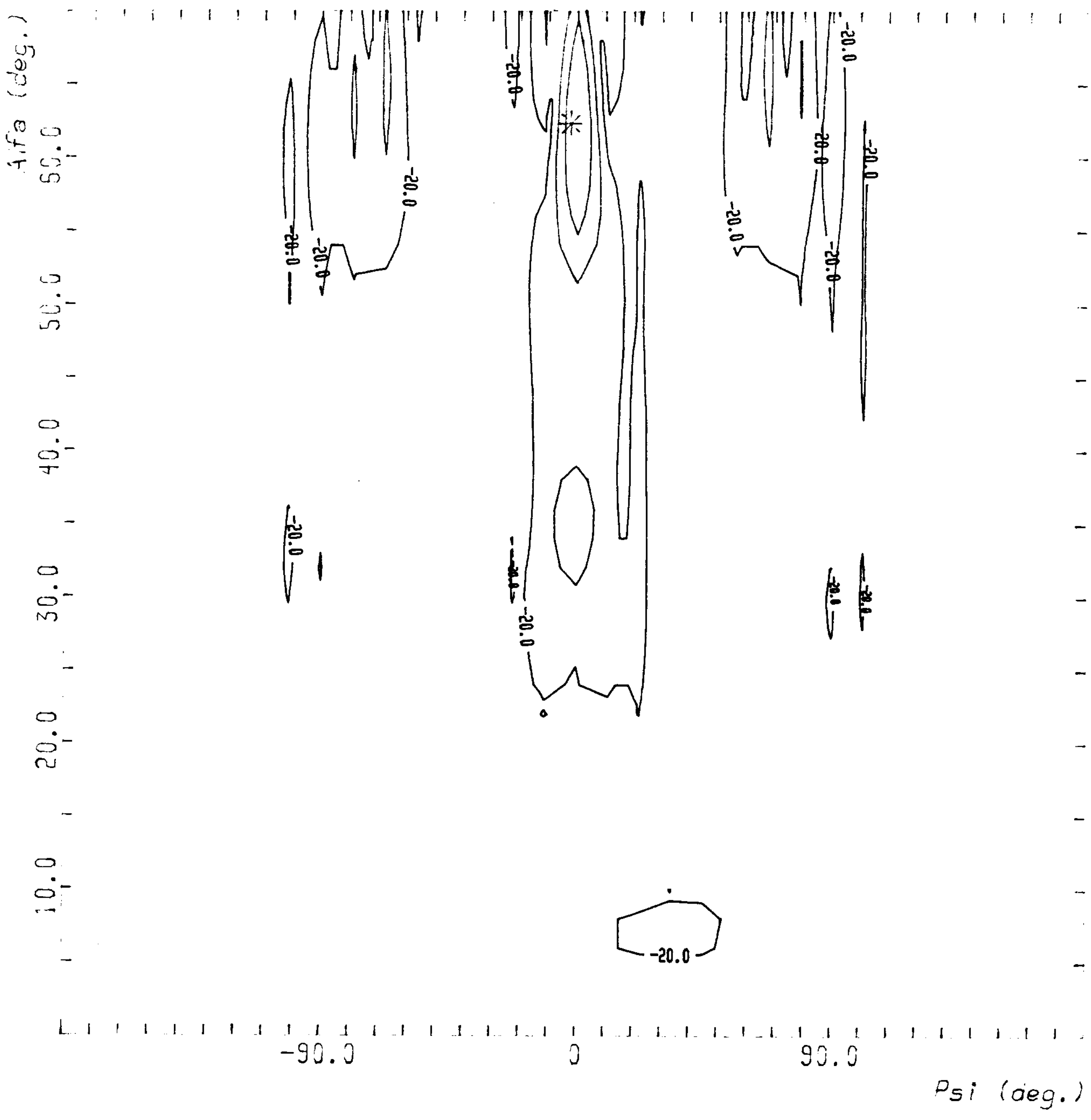

ACCES 1
Niveau (dB/Max)
Polar. circ. droite
Frequence 8200. Mhz
CONFORMAL ARRAY

($\theta = 62.30$)

Alcatel le 13 JUIN 1996
a 21 h. 1 min.
sasom Acces 1.

```
CONFORMAL ARRAY
***************
SEMI-ACTIVE CONCEPT
CONICAL ANTENNA
Ntot=24
Ner=6
Nb=8
N=3
non folded subarray (beta=30o)
******************************
Frequency=8.2 GHz
Prf=-0.77 dBW
******************************
PHI=0o

   Elevation (o)  EIRP (dBW)
   -------------------------
   .0000000E+00 .7095831E+01
   .4900001E+01 .9172892E+01
   .9800001E+01 .9239304E+01
   .1180000E+02 .9239302E+01
   .1280000E+02 .9107910E+01
   .1470000E+02 .8035112E+01
   .1720000E+02 .7704394E+01
   .1960000E+02 .7628924E+01
   .2450000E+02 .9637423E+01
   .2940000E+02 .1040354E+02
   .3420000E+02 .1022050E+02
   .3900000E+02 .1095971E+02
   .4380000E+02 .1039646E+02
   .4860000E+02 .1197682E+02
   .5370000E+02 .1492660E+02
   .5660000E+02 .1604661E+02
   .5920000E+02 .1732779E+02
   .6109999E+02 .1870070E+02
   .6230000E+02 .2023256E+02
```

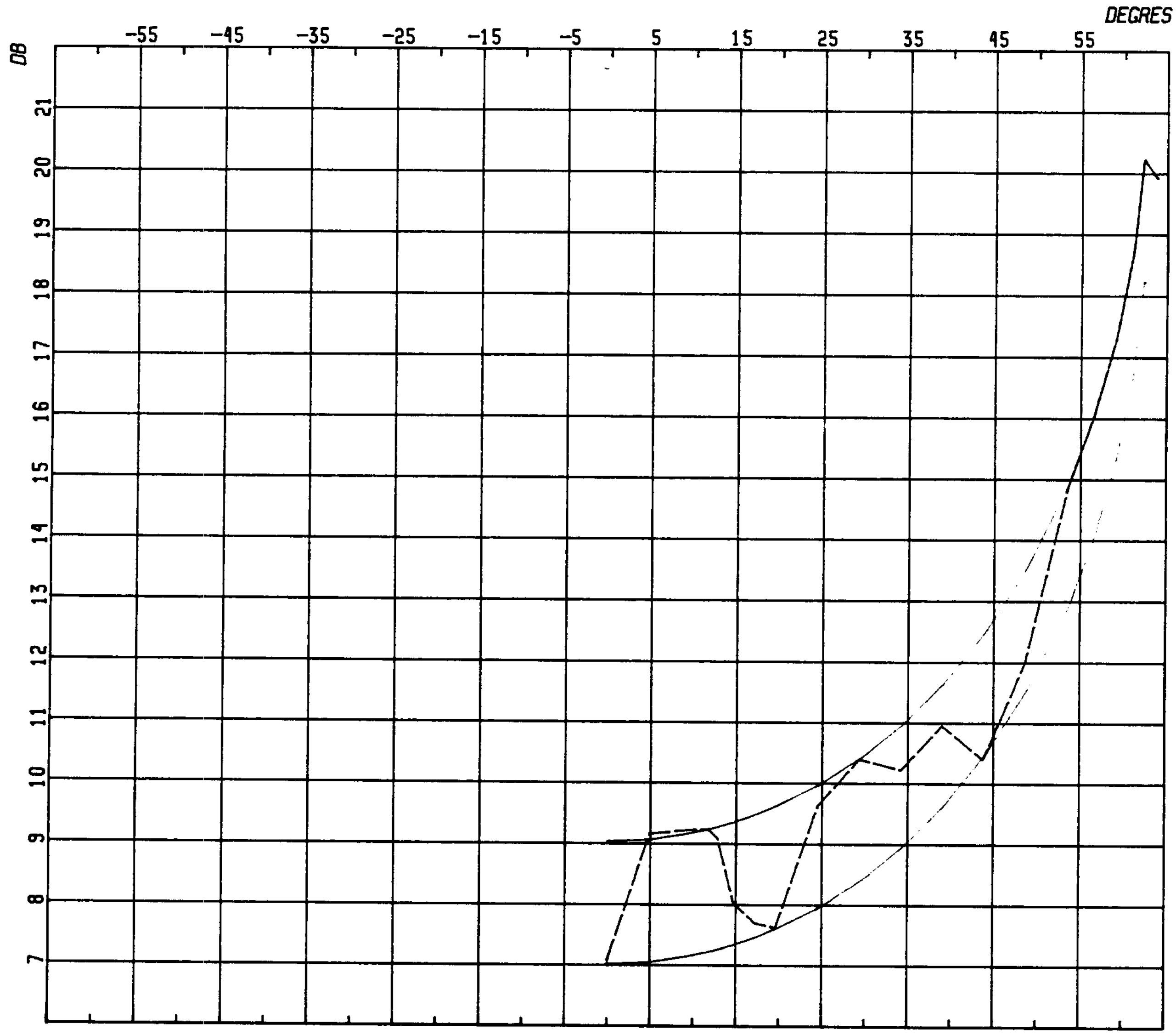

24 col 6 p/col - non Folded subarray (30o) 8 BUTLER 3x3 Dyn=0dB PHI=0o

ATES le 13 JUIN 1996

CONFORMAL ARRAY
****
SEMI-ACTIVE CONCEPT
CONICAL ANTENNA
Ntot=28
Ner=6
Nb=7
N=4
folded subarray (beta=25/25/25/25/25/35)
serial repartitor
****
Frequency=8.2 GHz
Prf=-0.77 dBW
****
PHI=0o

Elevation (o)	EIRP (dBW)
0000000E+00,	.7509946E+01,
.4900001E+01,	.9172890E+01,
.9800001E+01,	.9239302E+01,
.1180000E+02,	.9239666E+01,
.1280000E+02,	.9275618E+01,
.1470000E+02,	.9357183E+01,
.1720000E+02,	.9478596E+01,
.1960000E+02,	.9619684E+01,
.2450000E+02,	.9964006E+01,
.2940000E+02,	.1040354E+02,
.3420000E+02,	.1094951E+02,
.3900000E+02,	.1162473E+02,
.4380000E+02,	.1087403E+02,
.4860000E+02,	.1254332E+02,
.5370000E+02,	.1492562E+02,
.5660000E+02,	.1604661E+02,
.5920000E+02,	.1732779E+02,
.6109999E+02,	.1870070E+02,
.6230000E+02,	.2023256E+02,

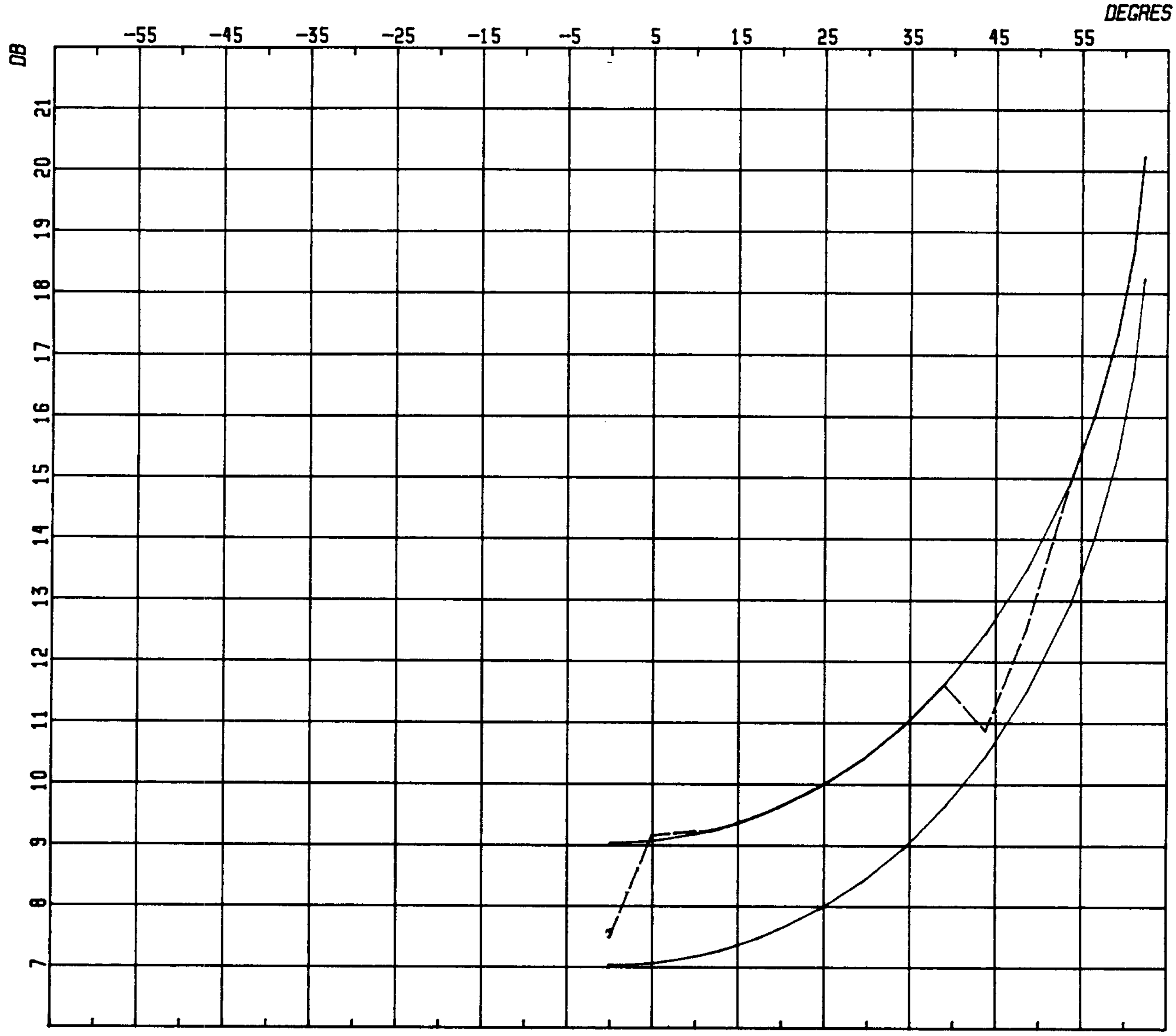

28 col 6 p/col - Folded subar. (25/../25/35)- 7 BUTLER 4x4 Dyn=0dB PHI=0

ATES le 14 JUIN 1996

CONFORMAL ARRAY
****
SEMI-ACTIVE CONCEPT
CONICAL ANTENNA
Ntot=28
Ner=6
Nb=7
N=4
non folded subarray (beta=30)
serial repartitor
****
Frequency=8.2 GHz
Prf=-0.77 dBW
****
PHI=0o

Elevation (o)	EIRP (dBW)
0000000E+00,	.7401068E+01,
.4900001E+01,	.9172892E+01,
.9800001E+01,	.9239302E+01,
.1180000E+02,	.9239302E+01,
.1280000E+02,	.9275618E+01,
.1470000E+02,	.9298313E+01,
.1720000E+02,	.9478460E+01,
.1960000E+02,	.9619684E+01,
.2450000E+02,	.9964006E+01,
.2940000E+02,	.1040354E+02,
.3420000E+02,	.1091897E+02,
.3900000E+02,	.1098533E+02,
.4380000E+02,	.1108960E+02,
.4860000E+02,	.1349781E+02,
.5370000E+02,	.1492592E+02,
.5660000E+02,	.1604661E+02,
.5920000E+02,	.1732779E+02,
.6109999E+02,	.1870070E+02,
.6230000E+02,	.2023256E+02,

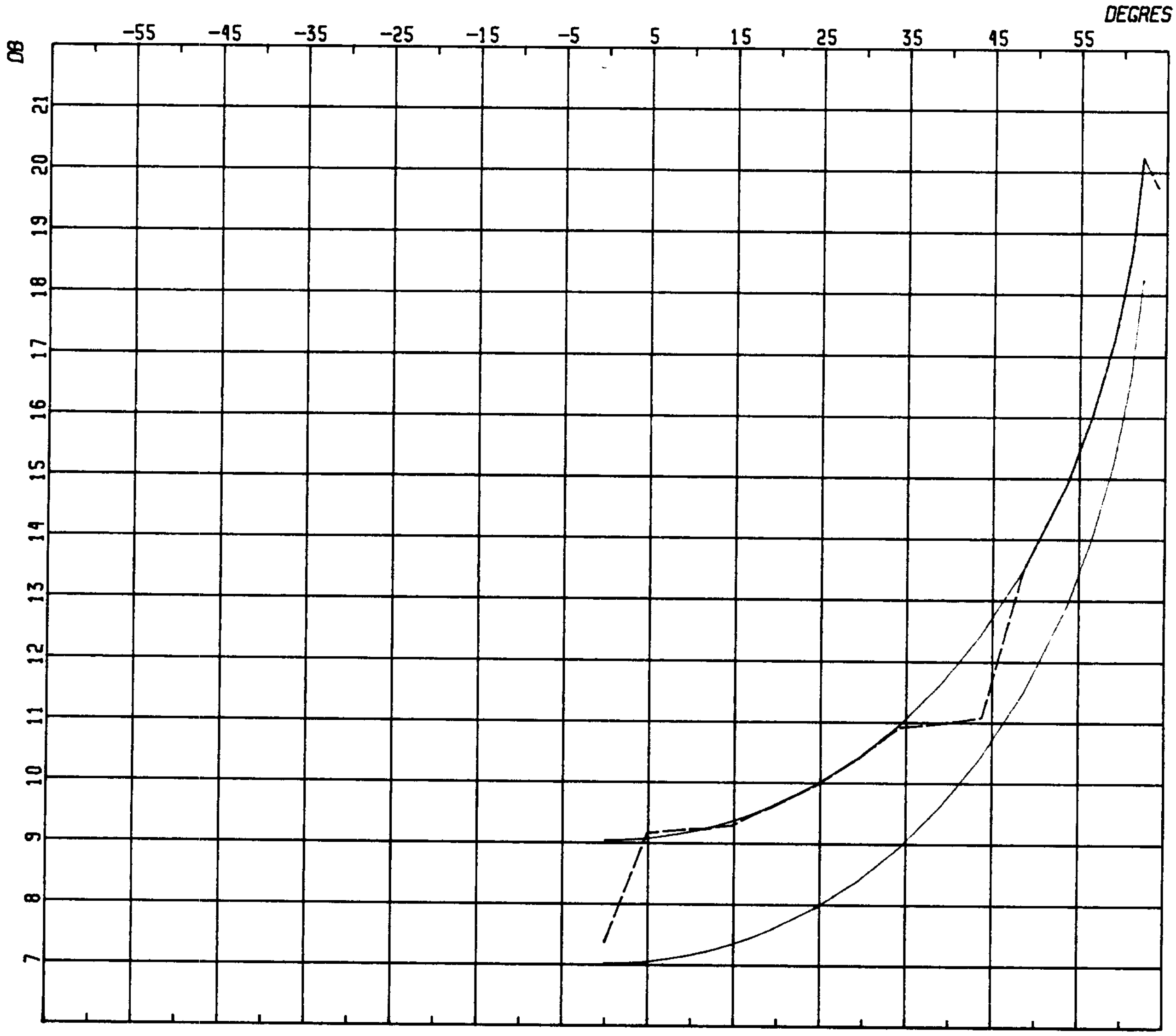

28 col 6 p/col - non Folded subarray- 7 BUTLER 4x4 Dyn=0dB PHI=0o

ATES le 14 JUIN 1996

```
CONFORMAL ARRAY
***************
SEMI-ACTIVE CONCEPT
CONICAL ANTENNA
Ntot=27
Ner=4
Nb=9
N=3
non folded subarray (beta=30)
serial repartitor
******************************
Frequency=8.2 GHz
Prf=-0.77 dBW
******************************
PHI=0o

   Elevation (o)  EIRP (dBW)
   -------------------------
   .0000000E+00, .6987087E+01,
   .4900001E+01, .8923122E+01,
   .9800001E+01, .8989398E+01,
   .1180000E+02, .8989299E+01,
   .1280000E+02, .9025718E+01,
   .1470000E+02, .9107407E+01,
   .1720000E+02, .9228456E+01,
   .1960000E+02, .9369684E+01,
   .2450000E+02, .9429995E+01,
   .2940000E+02, .9241349E+01,
   .3420000E+02, .9120666E+01,
   .3900000E+02, .9690539E+01,
   .4380000E+02, .1180852E+02,
   .4860000E+02, .1324808E+02,
   .5370000E+02, .1467588E+02,
   .5660000E+02, .1579661E+02,
   .5920000E+02, .1707798E+02,
   .6109999E+02, .1845070E+02,
   .6230000E+02, .1998256E+02,
```

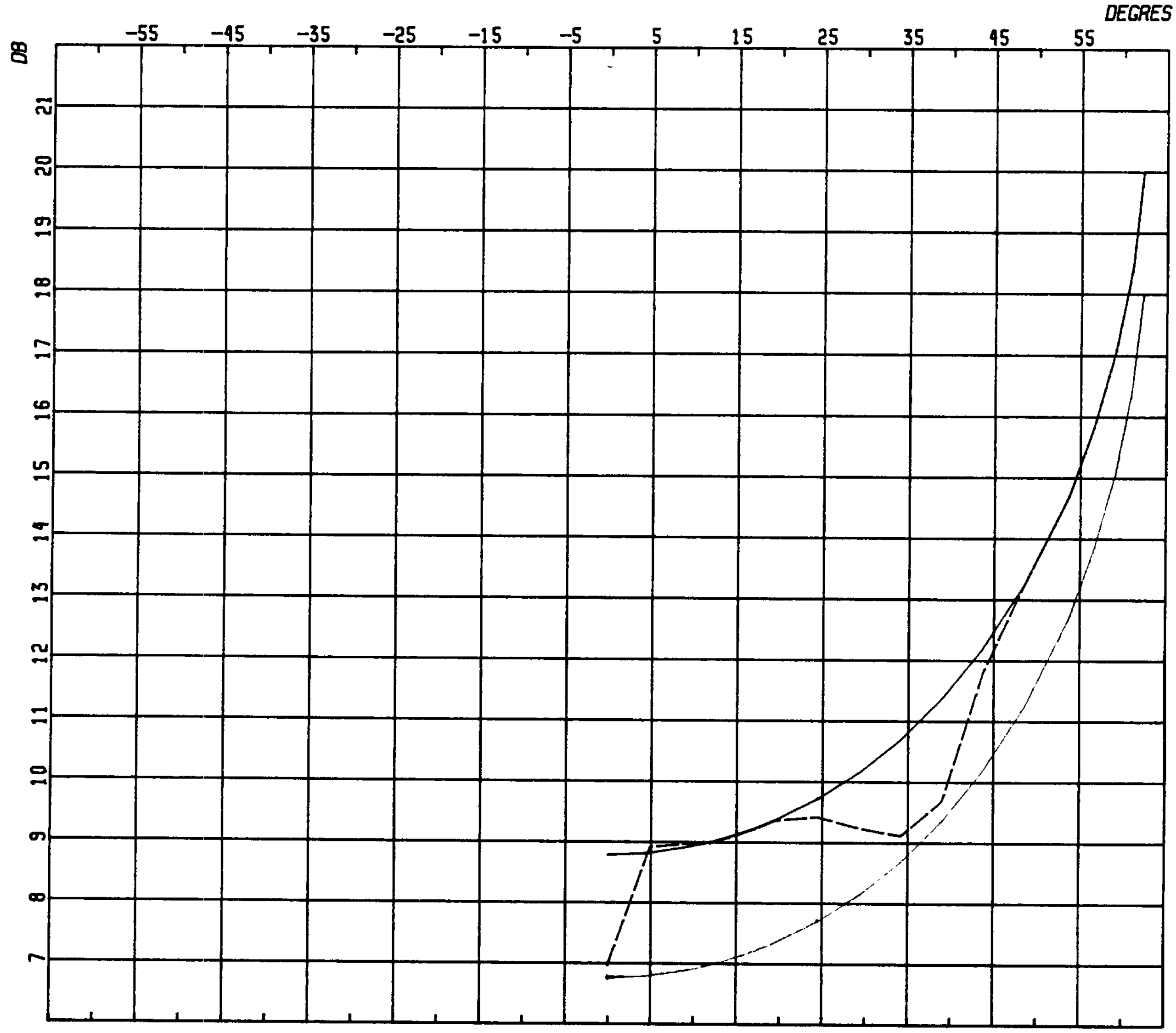

27 col 4 p/col - non Folded subarray- 9 BUTLER 3x3 Dyn=0dB PHI=0o

ATES le 17 JUIN 1996

```
CONFORMAL ARRAY
***************
SEMI-ACTIVE CONCEPT
CONICAL ANTENNA
Ntot=28
Ner=4
Nb=7
N=4
non folded subarray (beta=30)
serial repartitor
******************************
Frequency=8.2 GHz
Prf=-0.77 dBW
******************************
PHI=0o

   Elevation (o)  EIRP (dBW)
   -------------------------
   .0000000E+00, .6858913E+01,
   .4900001E+01, .8923100E+01,
   .9800001E+01, .8989302E+01,
   .1180000E+02, .8989503E+01,
   .1280000E+02, .9025616E+01,
   .1470000E+02, .9107241E+01,
   .1720000E+02, .9228491E+01,
   .1960000E+02, .9369686E+01,
   .2450000E+02, .8843721E+01,
   .2940000E+02, .8573909E+01,
   .3420000E+02, .8833711E+01,
   .3900000E+02, .1046997E+02,
   .4380000E+02, .1218260E+02,
   .4860000E+02, .1324810E+02,
   .5370000E+02, .1467589E+02,
   .5660000E+02, .1579681E+02,
   .5920000E+02, .1707795E+02,
   .6109999E+02, .1845070E+02,
   .6230000E+02, .1998256E+02,
```

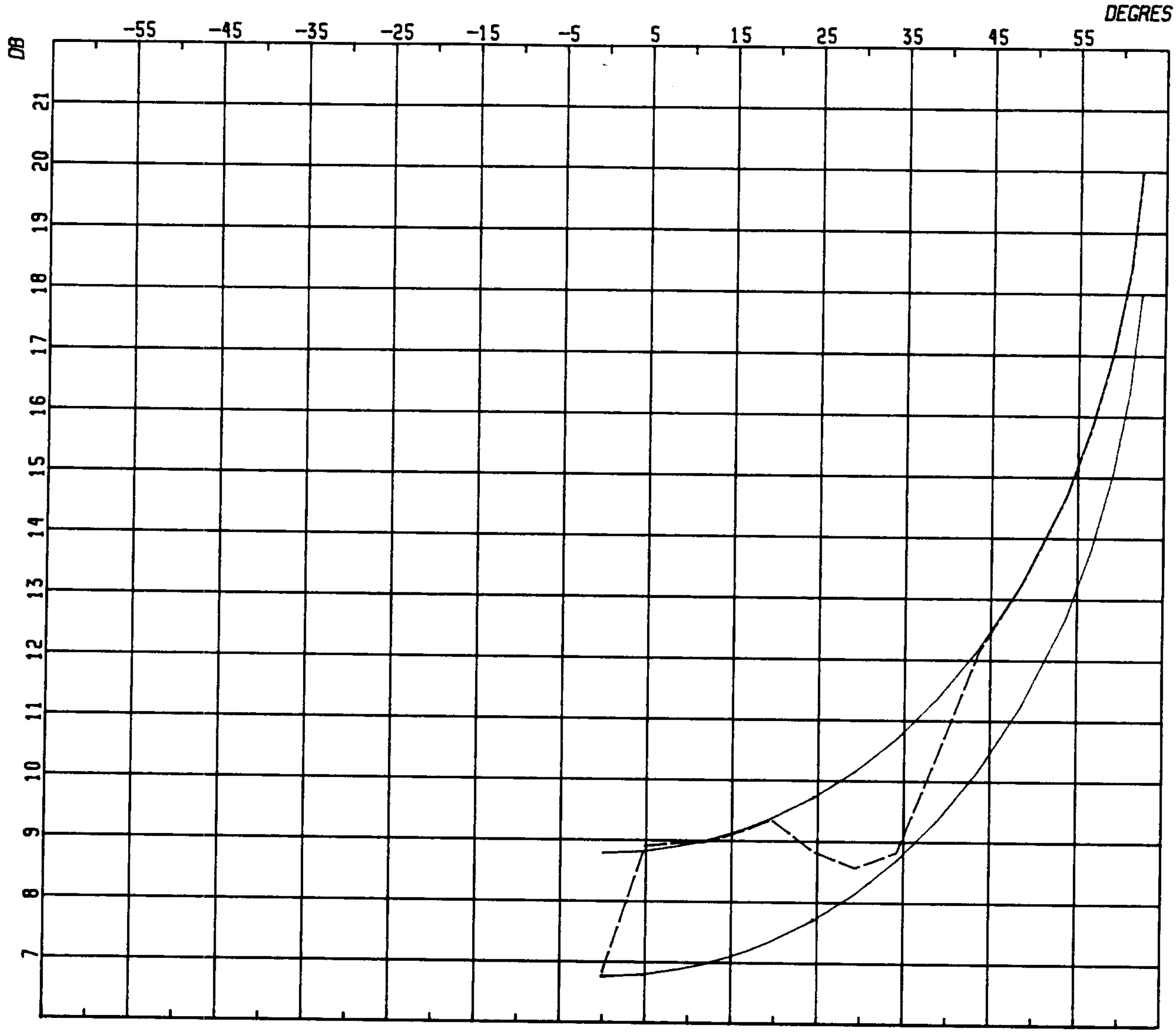

28 col 4 p/col - non Folded subarray- 7 BUTLER 4x4 Dyn=0dB PHI=0o

ATES le 14 JUIN 1996

ALCATEL TELECOM	CONFORMAL ARRAY ANTENNA	ESTEC CONTRACT 11698/95/NL/SB		
		AES 960596 / ASP 019		
		DATE : 26/6/96	ED/REV 1/-	

ANNEX A TO CHAPTER 3

Analysis of bibliography about «matrix fed circular array»

Th...mation contained in this document is proprietary to ALCATEL ESPACE ... shall not be ...ed by the recipient to third persons without the written consent of the ...hy ...é.

Les infor...ns contenues dans ce document demeurent propriété exclusive d'ALC... et ne d... être divulguées par le destinataire à des tiers sans l'accord écrit de ...

1) Lo and Lee : Antenna Handbook [ref A1 photocopied at the end of this annex]

Pages 19 / 101 to 105 explain clearly the basic principle of moving smoothly a narrow beam around a circular array by changing slowly the slope of the phase excitations, linearly distributed over the inputs of a Butler matrix: so output excitations are samples of a (sin x)/x, which reduce to focused power on only one output in the best case where one sample is at the peak of (sin x) / x, and others at nulls.

2) A. Roederer/ C. Van't Klooster : french patent 91/01086

The principle of Ref. A1 is applied after replacing one large Butler matrix N_{tot} x N_{tot} (bulky and difficult to manufacture) by N_B small matrixes NxN, with N_B x N = N_{tot} . Emphasis is put on the advantages to use equal amplitude signals at the inputs of the matrixes, especially if SSPAs are placed just after the phase-shifters.

3) Verification of such principle by our software

In figures A-3-c and d, are given excitations sets computed for eight 3x3 matrixes and various azimuth pointing directions û:

a) fig. A-3-c in the case where û comes from the center of the array O to the middle point M between two radiating elements (R.E, which are for the pseudo-conical antenna the inputs to almost a column subarray): it appears clearly that each matrix « focuse » the power from all the inputs to a single output: 8 R.E. (one per matrix) receive nearly maximal amplitude, and the others are very weakly excited.

This correspond to the top part of figure 84 in ref. [A1] - except that for us there is no amplitude taper between output excitations-, for maximizing amplifiers efficiency.

b) in fig. A-3-d, the pointing direction û comes from the center of the circular array to one R.E. M' . The matrix, the outputs of which are columns S1 and S17 has to share its power between and, so that the global excitation of the array should be symmetrical with respect to M'.

Here, we are in the case of the bottom part of fig. 84 in ref [A1]: the (sin x) / x desired excitation on the R.E is sampled at -3.9 dB points in the main lobe (equally spaced from its peak to the first nulls) and near the peak of the sidelobes. That's why we cannot avoid spurious back radiation from the R.E nb 9 (the third output of the same matrix).

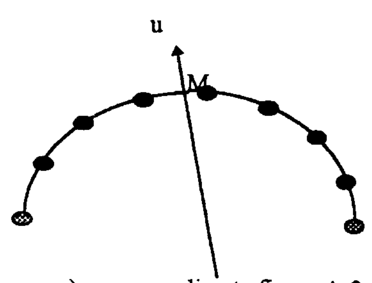

case a) corresponding to figure A-3-c
(for case b, see figure A-3-b)

Th…nation contained in this document is proprietary to ALCATEL ESPA… shall not be d…osed by the recipient to third persons without the written consent of the company
Les inf… contenues dans ce document demeurent propriété exclusive d'ALC… SPACE et ne do… être divulguées par le destinataire à des tiers sans l'accord écrit de l… …té.

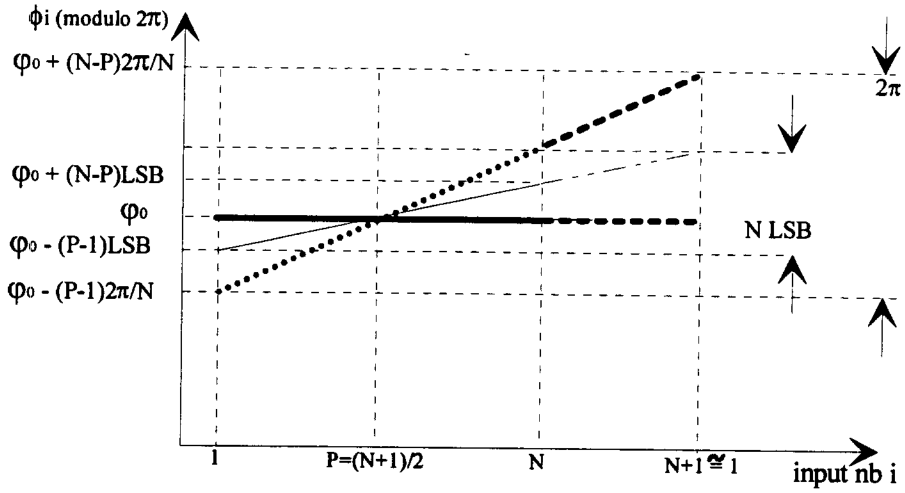

Figure A-3-a:
input phase-shifts to move smoothly the power focused on one output to the next (example for the case where N is odd); φ_0 is the reference insertion phase of the matrix (corresponding to the shortest path)

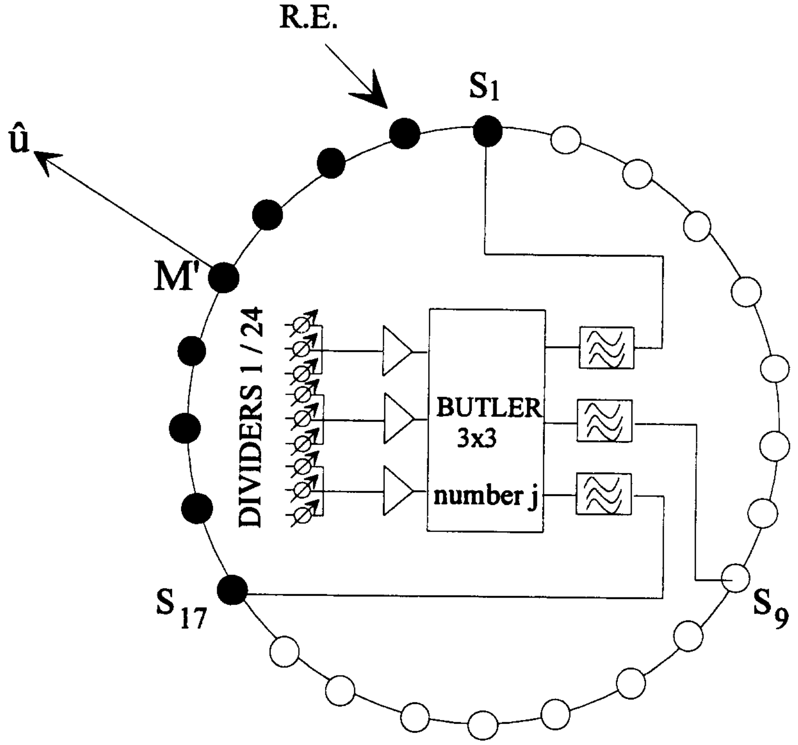

Figure A-3-b:
How to point in û direction, by sharing excitation of the drawn matrix (number j) between S_1 and S_{17} (+ small spurious radiation on S_9): example of the semi-active array proposed in the study
(N_{tot}=24 with N_B=8 Butlers and N=3 inputs and outputs each)

The information contained in this document is proprietary to ALCATEL ESPACE ... shall not be ... by ... ed by the recipient to third persons without the written consent of the ... ESPACE
Les informations contenues dans ce document demeurent propriété exclusive d'ALCA... et ne d... être divulguées par le destinataire à des tiers sans l'accord écrit de ...

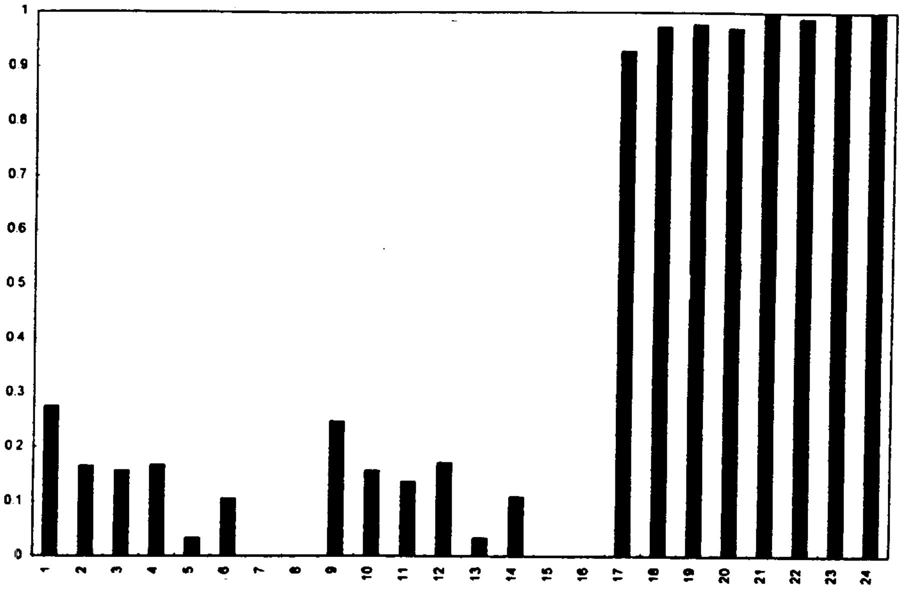

Figure A-3-c:
Computed excitations for eight 3x3 Butler matrixes
(the pointing direction comes from the center of the circular array to the middle of two R.E)

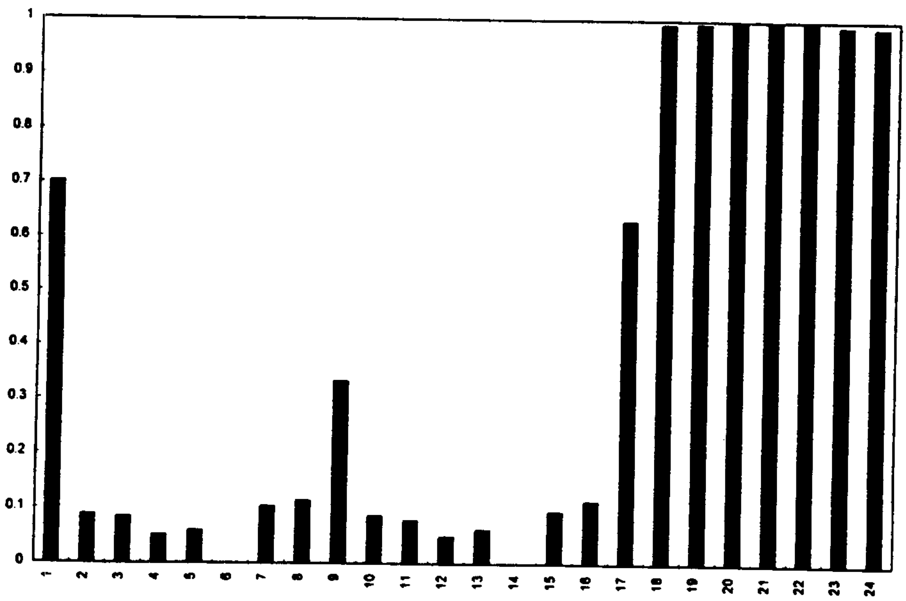

Figure A-3-d:
Computed excitations for eight 3x3 Butler matrixes
(the pointing direction comes from the center of the circular array to one R.E)

The information contained in this document is proprietary to ALCATEL ESPACE and shall not be disclosed by the recipient to third persons without the written consent of the company.
Les informations contenues dans ce document demeurent propriété exclusive d'ALCATEL ESPACE et ne doivent pas être divulguées par le destinataire à des tiers sans l'accord écrit de la société.

Les informations contenues dans ce document demeurent propriété exclusive d'ALCATEL ESPACE et ne doivent pas être divulguées par le destinataire à des tiers sans l'accord écrit de la société.
The information contained in this document is proprietary to ALCATEL ESPACE and shall not be disclosed by the recipient to third persons without the written consent of the company

4) Choice of Butler architectures

There are three kinds of such matrixes:

a) *one's built with 90° hybrids*: if we connect such a matrix to N points equally spaced on a circle, the total phase-shift around it, when any input i is excited above is: $\phi_i = (2\ k_i + 1)\ \pi$, where k_i are successive integers (with suited numbering of the inputs)

b) *other's built with 180° hybrids*: with similar connection and rotation, $\phi_i = 2\ k_i\ \pi$.

c) *simpler matrixes «Butler-like»* in multiport amplifier have the only constraint that output excitations corresponding to each input are orthogonal:

$$\sum_{m,n} E_m E_n^* = \delta_{m,n}$$

(Kronecker symbol: 0 if m not equal to n, 1 if m=n)

They don't provide linear phase-shifts, multiples of π, at the output.But it is not necessary when inverse matrixes are used in front and after the amplifiers. The orthogonality condition is sufficient to provide power exchange between amplifiers and find the same signal on the output nb i of the global MPA (e.g. M matrix / HPAs / M^{-1} matrix) than on the input nb i.

<u>To feed a circular array, references [A1], [A4] and [A5] say clearly that *b-type* of Butler matrixes are the best for following fundamental reasons:</u>

1- when one input is excited, the phase-shift between whatever two outputs is always the same, even between the last and the first, with «modulo 2π» computation: because the total phase-shift ϕ_i is always an integer multiple of 2π radians. That is what various authors and us call «rotational symmetry».

2- if we want to focuse the energy on one output, and then the next, we add on any input *i* a phase-shift computed by the very simple formula: $\Delta\phi_i=(i-P)2\pi/N$, with P=N/2 if N is even and P=N+1 / 2 if N is odd (see figure A-3-a). On a physical antenna, with dispersion between HPA's and phase-shifters, we have to add a «compensation phase» issued from measurement of these equipments; and also a compensation of various path lengths in free space to the selected column of the concerned matrix (conjugate matching). The computation to be made in the control unity, or in the ASICs of the active modules (if their dispersions are put in a PROM, for example) to rotate the beam by $2\pi/N_{tot}$ is very simple: add $2\pi(i-P)/N$ to the input nb *i*, take the result modulo 2π between 0 and 2π, and sample it to the nearest bit of the phase-shifter (LSB resolution).

3- with *b-type* matrixes, to move the beam a little bit in azimuth, we have to move the global excitations of outputs a little bit around the array. The simplest way to induce a very low amplitude and phase jump in the radiated field, is to add *(i-P) LSB* to the inputs of matrix nb *j* (that which outputs are connected to the edges of the active part). This operation keeps always the ideal linear phase at the inputs of this matrix, because there is no phase discontinuity between input nb N and input nb 1 (see figure A-3-a): that will not the case with a-type or c-type of matrixes.

Moreover, the global radiated field, as complex sum of the fields radiated by each R.E. will change very little:

- R.E. from other matrixes will keep the same excitations

- the mean of the phases at the inputs of matrix j will keep the same if N is odd (for example, if N=3, phase-shifts will be: -LSB, 0, +LSB) and change by only LSB/N if N is even. So, the excitations around the array will move a little bit (following principle of figure 84 in ref. A1), with very little amplitude and phase variation of the global radiated field : in the worst case LSB/N_{tot} in phase; for example if 24 R.E and 5 bits phase-shifter, this phase jump will be 0.5°.

REFERENCES

[A1] : Lo, Lee: Antenna Handbook (ed. VNR), chapter 19 §6: cylindrical array feeds.

[A2] : A. Roederer, C. Van't Klooster: French patent 91/01086.

[A3] : Sheleg: A matrix-fed-circular array for continuous scanning (especially last § of first column, p. 2018). Proceedings of IEEE, November 1968.

[A4] : Shelton, Hsiao: Reflective Butler Matrices (especially second § of second column, p. 652). IEEE A.P. Transactions, Sept. 1979.

[A5] : Macnamara: Simplified procedures for Butler matrices incorporating 90°-hybrids or 180°-hybrids. IEE proceedings 134H1, February 1987.

[A6] : Rudge and al: Handbook of Antenna design (ed. Peter Peregrinus): chapters 11 and 12.

The information contained in this document is proprietary to ALCATEL ESPACE and shall not be disclosed by the recipient to third persons without the written consent of the company.

Les informations contenues dans ce document demeurent propriété exclusive d'ALCATEL ESPACE et ne doivent être divulguées par le destinataire à des tiers sans l'accord écrit de la société.

Th… …ation contained in this document is proprietary to ALCATEL ESPA… shall not be …ed by the recipient to third persons without the written consent of the …ay

Les info… …ns contenues dans ce document demeurent propriété exclusive d'ALC… et ne do… être divulguées par le destinataire à des tiers sans l'accord écrit de… …SPACE …é.

Selection of most important pages from reference [A1]

Matrix-Fed Cylindrical Arrays

The various matrix-fed arrays can be readily understood by use of the following tutorial model.

Consider two back-to-back Butler matrices with controllable phase shifters in between them as shown in Fig. 84a. If an input port a_n of Butler matrix A is excited with any amplitude and phase, a corresponding port b_n of Butler matrix B will be excited with equal amplitude and phase when the phase shifters are all set equal. If the a_ns are weighted in amplitude and phase to any desired distribution, a corresponding distribution is achieved at the outputs b_n. Now if a linear phase distribution with a total phase of $\boxed{m2\pi \text{ } (m \text{ an integer})}$ is applied across the array of phase shifters, the entire distribution over b_n will translate across the output in increments of one element spacing for each successive value of m. The translation of the output distribution by an increment less than one element spacing requires a total phase that is a nonintegral multiple K of 2π. That is, $|m| < |K| < |m| + 1$. In these cases there is no longer a one-to-one correspondence between an input port excitation and an output port excitation. Instead, if one input port is excited, not one but all output ports are excited to some extent. However, as would be expected the two adjacent ports corresponding to phases of $m2\pi$ and $(m + 1)2\pi$ are excited most strongly since they straddle the "phantom" element corresponding to the phase of $K2\pi$. In fact, the output distribution is a discrete sampling of a sharp $(\sin x)/x$ distribution as shown in Fig. 84b. The width of the "main lobe" of the

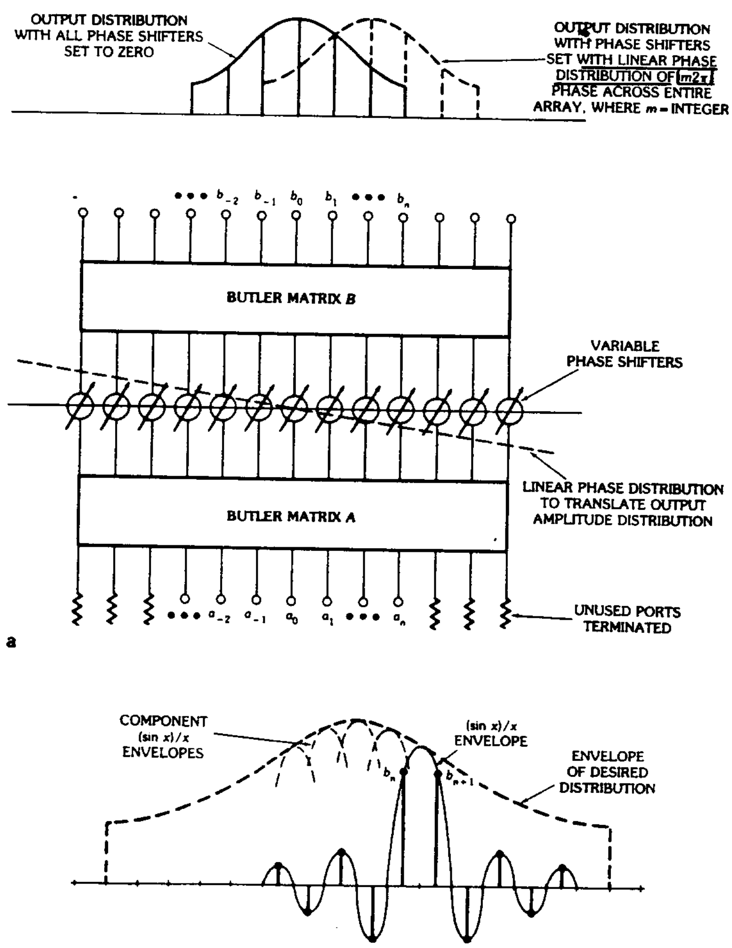

Fig. 84. Back-to-back Butler matrix feeding technique. (*a*) Tutorial model of matrix feeding. (*b*) Output excitation when only one input is excited and linear phase across bank of phase shifters is not an integral multiple of 2π. (*Courtesy Hughes Aircraft Co., Fullerton, Calif.*)

The information contained in this document is proprietary to ALCATEL ESPACE and shall not be disclosed by the recipient to third persons without the written consent of the company
Les informations contenues dans ce document demeurent propriété exclusive d'ALCATEL ESPACE et ne doivent pas être divulguées par le destinataire à des tiers sans l'accord écrit de la société.

envelope $(\sin x)/x$ is two elements and the side lobe width is one element. The output distribution corresponding to phases of integral multiples of 2π consists of discrete values identical with those at the input to the first Butler matrix A because of the one-to-one correspondence between a_ns and b_ns. This is consistent with the sampled $(\sin x)/x$ output in these special cases; the sampling points are all at the nulls of the $(\sin x)/x$ function except at the peak of the main lobe, hence only that element is excited. For intermediate cases corresponding to nonintegral multiples of 2π, the output distribution is a superposition of sampled $(\sin x)/x$ functions of the kind just described. The net result is that the envelope of this output distribution is almost identical with that of the envelope of the designed output distribution, which is identical with the input distribution of matrix A.

Now, if the output ports b_n are connected by equal line lengths to a similar number of elements arranged uniformly along a circle of radius R, linear phase shifter adjustments will cause the distribution over the b_ns to move along the periphery of the circular array. If the phase distribution is such as to radiate a plane wavefront from the circular array, a directive beam is formed from the circular array that can be steered by means of changing the linear progressive phase of the phase shifters. It is obvious that this peripherally scanned distribution should not extend more than a semicircle because elements to the rear should not be excited. The input ports corresponding to these rearward-looking elements are shown terminated in Fig. 84a. In practice, less than 180° of the circular (or cylindrical) array is excited for one beam direction because of active element patterns, local grating lobe formation, and aperture matching problems associated with the edge elements that are locally phased for near end-fire. Also, for intermediate phasing, the elements near the edge of the active portion of the cylinder may have their corresponding sampled $(\sin x)/x$ lobes to the rear that are greater than desired for low side lobe and rear lobe patterns.

Collimation of the beam from the circular array requires a phase distribution of $\phi_n = kR(1 - \cos n\Delta\theta)$, where $\Delta\theta$ is the angle subtended by one-element spacing, R is the radius of the cylinder, and $k = 2\pi/\lambda$. This phase is easily incorporated in the weighting of the a_ns.

It is interesting to note that the amount of beam scan in terms of antenna beamwidths for each 2π of total phase change is equal to one beamwidth if the element spacing Δs is $\lambda/2$:

$$\Delta s = R\,\Delta\theta = \frac{\lambda}{2}, \qquad \Delta\theta = \frac{\lambda}{2R}$$

This is also the beamwidth for a uniform array of aperture $2R$.

The foregoing serves as a tutorial basis for describing some of the feeding techniques for cylindrical arrays to be discussed.

Sheleg Method—In the preceding discussion it is readily seen that the output of the first Butler matrix A (input to the bank of phase shifters) has an amplitude and phase distribution that is fixed (independent of beam steering); therefore it can be replaced by a passive feed network that produces that same distribution. This reduces to the Sheleg approach. A simplified schematic diagram of the approach

The information contained in this document is proprietary to ALCATEL ESPACE and shall not be disclosed by the recipient to third persons without the written consent of the ALCATEL ESPACE.

Les informations contenues dans ce document demeurent propriété exclusive d'ALCATEL ESPACE et ne doivent pas être divulguées par le destinataire à des tiers sans l'accord écrit de ALCATEL ESPACE.

for an eight-element array is shown in Fig. 85. Sheleg arrived at this solution from a different point of view. He expressed the far-field pattern in cylindrical modes in the form

$$E(\phi) = \sum_{-N}^{N} C_m e^{jm\phi}$$

where the number of elements is $2N$, and

$$C_m = 2\pi K j^m I_m J_m(ka)$$
$$K = \text{constant}$$

Sheleg made the observation that it is not necessary or even desirable to use all the *m* modes of the Butler matrix. This concurs with the foregoing tutorial discussion in that modes that excite elements to the rearward direction of the cylinder should not be used. As stated earlier, in practice less than half the number of available modes should be used to avoid local end-fire radiation at the extremes of the active semicircle. The Sheleg scheme is depicted for an eight-element array in Fig. 85.

This technique can be used to produce uniform or tapered illuminations for the cylindrical array. Sheleg gives computed and measured results for uniform, cosine, and cosine-squared array distributions with quite close correlation between

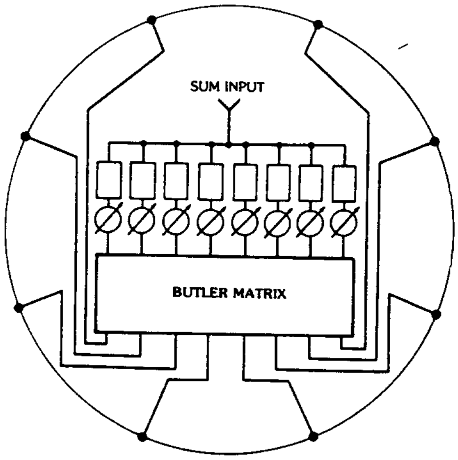

Fig. 85. Sheleg's approach. (*Courtesy Hughes Aircraft Co., Fullerton, Calif.*)

measurement and theory except in the remote side lobe region. He shows the patterns as a function of the number of modes used. Up to a point the patterns improve as more modes are used; then, beyond this point, the radiation pattern degrades somewhat. This has been explained by use of the tutorial model previously discussed.

For uniform distribution the azimuth pattern shape as a function of azimuth scanning of the main beam is shown to be reasonably invariant, i.e., it makes little difference whether the peak of the array distribution falls on an element, midway between two elements, or any fractional part thereof. This is also explained by use of the tutorial model. For more details the reader is referred to Sheleg's paper [56].

[The infor]mation contained in this document is proprietary to ALCATEL ESPA[CE and shall not] be [disclos]ed by the recipient to third persons without the written consent of the [compan]y.

Les info[rmati]ons contenues dans ce document demeurent propriété exclusive d'ALC[ATEL ESPACE] et ne d[oivent pa]s être divulguées par le destinataire à des tiers sans l'accord écrit de [la société].

ANNEX B TO CHAPTER 3

Analytic analysis of amplitude and phase jumps

The information contained in this document is proprietary to ALCATEL ESPACE and shall not be disclosed by the recipient to third persons without the written consent of the company

Les informations contenues dans ce document demeurent propriété exclusive d'ALCATEL ESPACE et ne doivent être divulguées par le destinataire à des tiers sans l'accord écrit de la société.

As shown by active concept simulations, amplitude and phase jumps are the most critical when the beam turns around the nadir. Suppose for example a little rotation in azimuth from the direction OM^- to OM^+, where M^- and M^+ are points on the circle, a little before and after a R.E. M (see figure B-3-b).

* *for the active concept*, we put ON one HPA, so one R.E. (M^+4 on the figure B-3-a), and then put OFF one R.E. on the opposite side of the active part of the array subarray (M^-4 on the figure).

In each case, we can compensate with the phase-shifters for the pointing direction jump $2\pi / N_{tot}$. But for each of this two operations, the amplitude jump is, in the worst case near nadir, where side columns radiation is not lowered by the element pattern (near nadir, angle viewed by each column is about the same): 20 log ($N_{act}+1 / N_{act}$), so 1 dB if $N_{act}=8$ (see figure B-3-a).

* *for the semi-active concept*, we can proceed as described in annex A-3 (see § 4-c-3) : shift the input phases of the Butler matrix connected to M^-4 and M^+4 by (i-2) LSB at each step. We need 2π / N LSB = 2^b / N such steps, to switch off M^-4 and switch on M^+4 (b is the number of bits of the phase-shifter).

Recall: a total phase-shift of 2π over all the inputs +1 is necessary to move the energy focused on one output to the next (see figure A-3-a, or fig. 84 from reference A1).

So, for each step, the beam moves in azimuth by $\delta\theta=(360/N_{tot}) / (2^b/N) = 360 / (2^b N_B)$

Example

$N_B=8$ (3x3 matrixes; $N_{tot}=24$, b=5 bits) gives $\delta\theta = 1.4°$

The azimuth 3 dB beamwidth is about $50.8\ \lambda / D_{mid} = 6.8°$ (D_{mid}=271 mm)

If the top of the main beam is approximated as gaussian $G_{dB} = G_0-3(2\theta/\theta_3)^2$

It is optimal to switch the beam when the station has turned from $\delta\theta/2=0.7°$. In that case, we find 0.13 dB amplitude jump.

Phase jump will be also very low because radiated phase is constant at the top of the main beam ($\delta\theta \# \theta_3/10$), and global phase offset has been computed in annex A as LSB / N_{tot} = 0.5°.

Remark: we find the same jumps (1.4° and 0.13 dB) by complex summation of vectors representing radiation of each active column, near nadir (see figure B-3-a).

In conclusion, for this typical azimuth small rotation and same number of columns (24) for each concept, semi-active one shows 7.7 times lower amplitude jump.

Remark: with such a step by step azimuth phase shifting [*(i-2) LSB* on the input 3x3 matrix], computations of commands are very simple: there is no need for compensation by phases of too high angle jump when ON / OFF switching of a column in the active concept.

The elevation phases are computed apart by conjugate matching: the same value is added at all inputs of a given matrix, because there are mainly 1 or 2 outputs of this matrix which contribute to the beam (in the case of 2 outputs, they are symmetrical w.r.t the pointing direction, which induce same phase by conjugate matching).

After that, and before sending commands, a general phase offset, common for all phase-shifters, is computed to keep the same average phase over all inputs: so that elevation scanning will be provided with very low phase jump: at last, the clock intervals at which phases will be modified to follow a given earth station will be computed so that the amplitude jump (mainly due to the elevation scanning) remain less than the specified one.

Such separable (azimuth / elevation) computation will be implemented in a specific software as told at the beginning of the answer.

But we are already sure that amplitude / phase jumps will be lower for the semi-active concept; we think we have explain why hereabove, for the most critical case of near nadir azimuth rotation.

Th[illegible]mation contained in this document is proprietary to ALCATEL ESPA[illegible] shall not be d[illegible]osed by the recipient to third persons without the written consent of the company

Les inf[illegible]s contenues dans ce document demeurent propriété exclusive d'ALC[illegible]SPACE et ne do[illegible]être divulguées par le destinataire à des tiers sans l'accord écrit de l[illegible]été.

a) active concept

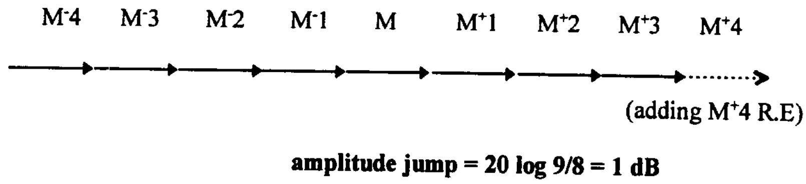

b) semi-active concept

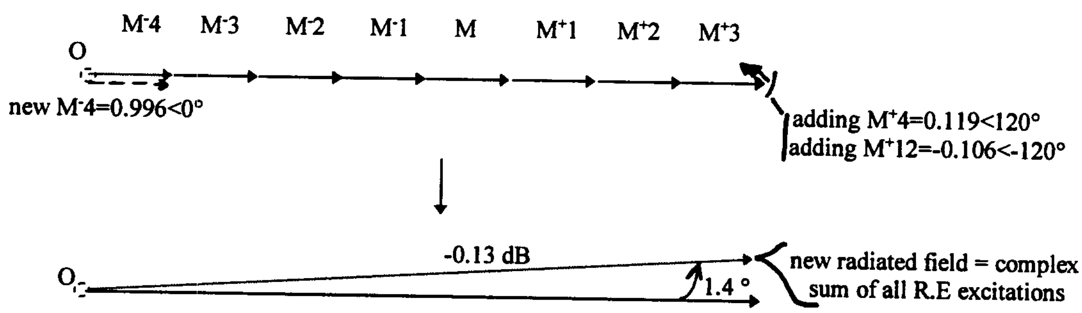

Figure B-3-a:
Presentation in the complex plane of worst case amplitude / phase jump (for 24 columns subarray) of the radiated field, sum of contribution of 8 R.E (coherent phase summation without weighting by the element pattern: near nadir, its effect is the same for all R.E; offsets in the input phases of various matrixes compensate for the rotation of the elementary pattern (equivalent to a phase-shift in circular polarization)

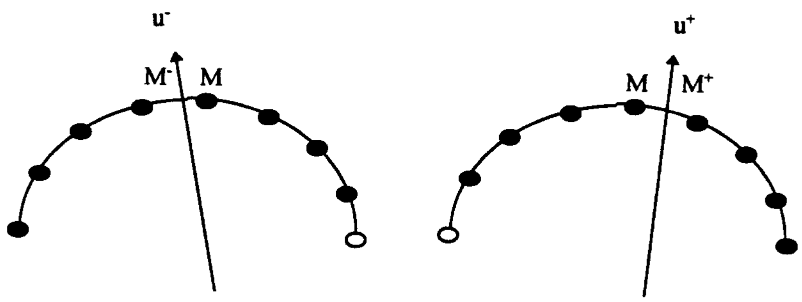

Figure B-3-b:
Small rotation of the beam in azimuth: example for 24 R.E., 8 or 9 of them active.

...rmation contained in this document is proprietary to ALCATEL ESPA... shall not ...ed by the recipient to third persons without the written consent of the ...
Les inf...ons contenues dans ce document demeurent propriété exclusive d'ALC... ESPACE ...
et ne ...s être divulguées par le destinataire à des tiers sans l'accord écrit de ...

CHAPTER 4

SUB-ASSEMBLIES SPECIFICATIONS

(WP 2100)

Reproduction interdite © ALCATEL ESPACE Reproduction forbidden

# CONFORMAL ARRAY ANTENNA	AES 96-29460/ASP-394		
	Estec Contract 11698/95/NL/SB		
	DATE : 14/10/96	**ED/REV :** 1/A	

Titre / Title
CHAPTER 4 (WP 2100) **SUB-ASSEMBLIES** **SPECIFICATIONS**

Rédigé par / Written by	**Responsabilité / responsibility**	**Date**	**Signature**
G. CAILLE	Technical Manager of the Contract	14/10/96	
Vérifié par / Verified by			
Approbation / Approved			

Reproduction interdite © ALCATEL ESPACE Reproduction forbidden

CONFORMAL ARRAY ANTENNA	AES 96-29460/ASP-394	
	Estec Contract 11698/95/NL/SB	
	DATE : 14/10/96	ED/REV : 1/A

ENREGISTREMENT DES EVOLUTIONS / CHANGE RECORD

ED./ REV.	DATE	§ CONCERNES CONCERNED §	§: DESCRIPTION DES EVOLUTIONS §: CHANGE RECORD	REDACTEUR AUTHOR
1/-	19/09/96		First Issue	G. CAILLE
1/A	14/10/96		Final issue including ESA comments on first issue	G. CAILLE

Reproduction interdite © ALCATEL ESPACE Reproduction forbidden

CONFORMAL ARRAY ANTENNA	AES 96-29460/ASP-394		
	Estec Contract 11698/95/NL/SB		
	DATE : 14/10/96	**ED/REV :** 1/A	

PROJECT DIFFUSION LIST

COMPANY	DEPARTMENT	DIF.	RECEIVER NAME
ALCATEL Espace	ASP		G. DURET → armoire G.C F. CROQ
			G. CAILLE
			E. VOURCH
	REP		~~B. COGO~~
			T. ADAM
	DTT		J. OSTER
	DOBS		~~L. DIDEROT~~
	DCTC		~~M. CHAINE~~
ESA/ESTEC			G. VAN DOOREN (5 ex.)
CASA	Div. Espacio		M.J. MARTIN (3 ex.)
EPFL	LEMA		J. MOSIG
			A. ALVAREZ

Reproduction interdite © ALCATEL ESPACE Reproduction forbidden

CONFORMAL ARRAY ANTENNA	AES 96-29460/ASP-394		
	Estec Contract 11698/95/NL/SB		
	DATE : 14/10/96	ED/REV : 1/A	

CONTENTS

GENERAL REMARK

Waiting thermal analysis (previewed in WP 2600), for these "first run" specifications, we have taken following hypothesis concerning the temperature ranges (issued from a past study for CNES on a similar antenna and of ALCATEL experience in passive thermal control of active antennas, with suited coatings or radomes):

- radiating surface and passive BFN (including Butler matrices) : -50°,+50°C

- active modules (gathered at the bottom and about center of the antenna; if necessary connected to the heatpipes of the platform): -5°,+40°C, with no more than 5° difference between the 6 packages, each including 4 front-end modules.

Titre / Title

SPECIFICATIONS FOR THE PASSIVE BFN (DIVIDERS, CABLES, MEASUREMENTS OF THE WHOLE BFN)

Rédigé par / Written by	Responsabilité / responsibility	Date	Signature
G. CAILLE	Technical Manager of the Contract	19/9/96	
Vérifié par / Verified by			
Approbation / Approved			

ALCATEL TELECOM

Reproduction interdite © ALCATEL ESPACE Reproduction forbidden

ENREGISTREMENT DES EVOLUTIONS / CHANGE RECORD

ED./ REV.	DATE	§ CONCERNES CONCERNED §	§: DESCRIPTION DES EVOLUTIONS §: CHANGE RECORD	REDACTEUR AUTHOR
1/-	02/07/96		First Issue	G. CAILLE
1/A	19/09/96		Modification of § 3-3-c	G. CAILLE

Reproduction interdite © ALCATEL ESPACE Reproduction forbidden

SUMMARY

Reproduction interdite © ALCATEL ESPACE Reproduction forbidden

1. COMPOSITION OF A FLIGHT ANTENNA BFN

See figure 1-a next page.

2. COMPOSITION OF THE BREADBOARD BFN

Interactions from the 3 beams could be measured only on a full model with amplifiers (non-linearity, IMP...)

As they will not be present on the BB of this contract, "one-channel BFN" will be implemented (see figure 2-a), but linear performances of the 3 channels will be measured by shifting the frequency of the input signal to the antenna.

a) In front of the "control modules"

- One divider 1/24 (decomposed as chosen by CASA), the input of which (female SMA connectors) should be accessible, to be connected to the test bench of the whole antenna for radiating measurements.
- 24 cables 50 cm long (TBC by mechanical lay-out of the breadboard in WP 2600) for connection to the commercial phase-shifters located on a specific support close to the antenna.

b) After the "control modules"

- 24 cables for connection to the eight 3 x 3 Butler matrices integrated in the antenna (about 50 cm long, TBC in WP 2600).
- Eight 3 x 3 Butler matrices.
- 24 cables connecting to the radiating elements (rejection filters are not implemented). Their length should be suited to the mechanical lay-out (WP 2600), according to the radiating surface geometry described in WP 1200 ALCATEL report: typically 20 to 25 cm.

c) Connectors

All equipment will use SMA female connectors; all cables will use SMA male connectors.

Reproduction interdite © ALCATEL ESPACE Reproduction forbidden

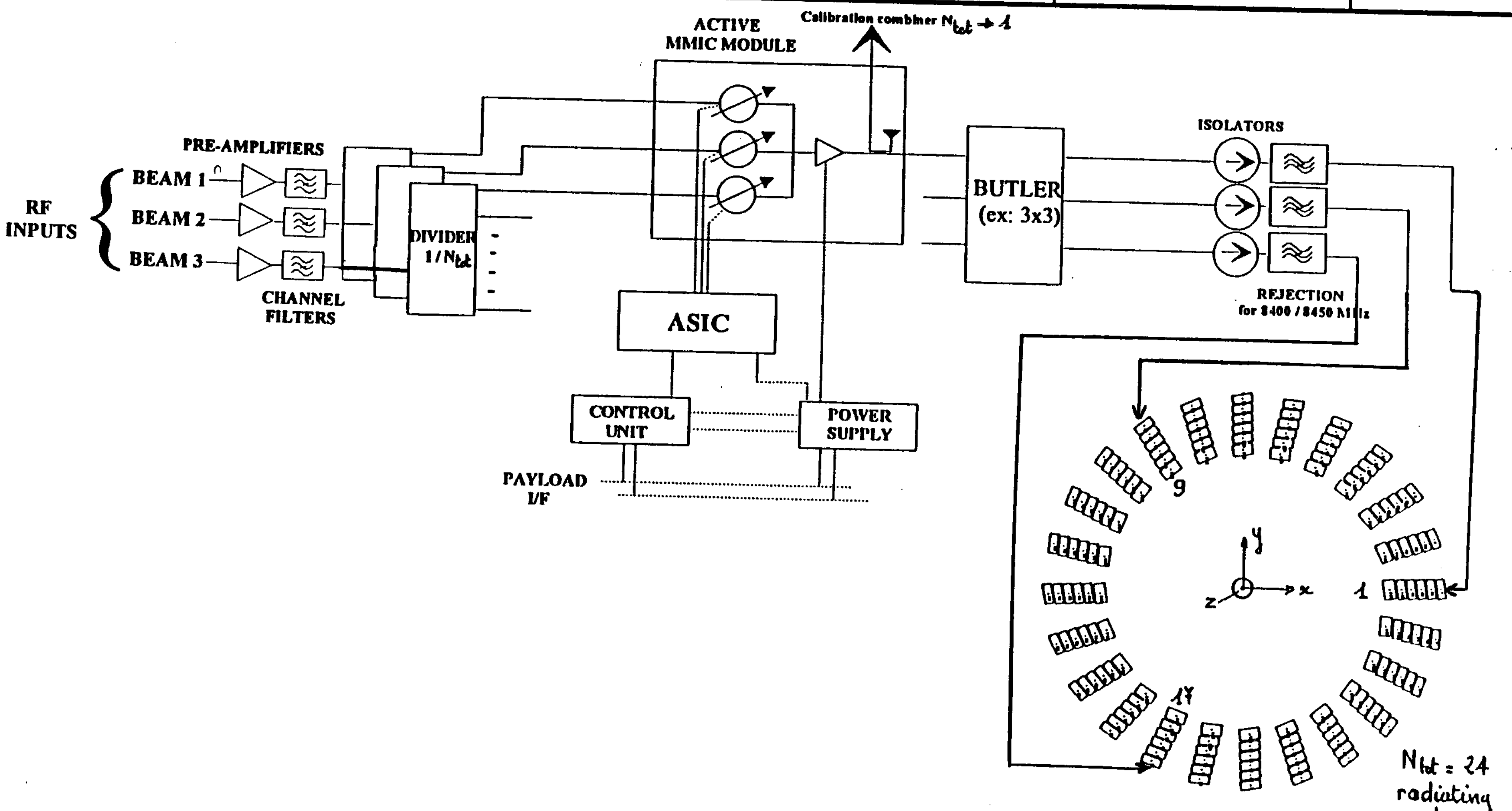

Figure 1-a: Semi-active antenna architecture, for a flight-type full antenna, showing two BFN parts, before and after the active modules

Reproduction interdite © ALCATEL ESPACE Reproduction forbidden

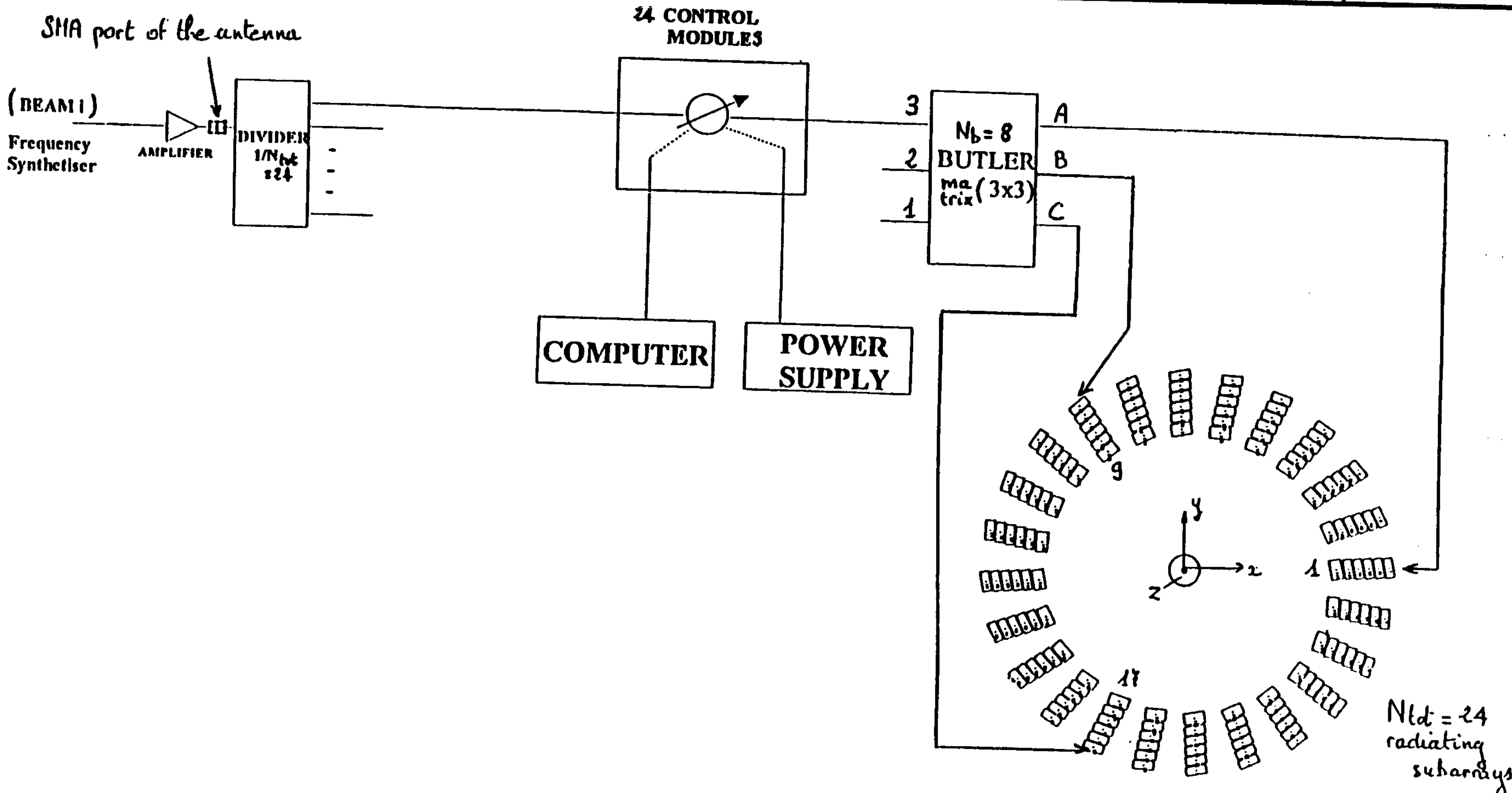

Figure 2-a: Architecture of the "one simultaneous channel" breadboard, without distributed amplifiers, neither filters, the 3 channels are measured one after each other, through the same BFN

Reproduction interdite © ALCATEL ESPACE Reproduction forbidden

3. SPECIFICATIONS FOR ONE-CHANNEL BFN

3.1 GENERAL

Specifications are identical for a flight-type full antenna than for the breadboard:

- in the first case, they apply to the three channel-BFN's for the part a) in front of the active or control modules;
- in the second case, they apply to the "one-channel BFN" implemented;
- the 3 → 1 combiners are part of the active modules; so they are not included in this specification.
- the part b) after the active or control modules is identical for flight-type full antenna and for the breadboard.

The whole allocated bandwidth is 8025 - 8400 MHz.

3.2 ELECTRICAL SPECIFICATIONS FOR THE PART OF THE BFN IN FRONT OF THE ACTIVE MODULES (DIVIDERS + CABLES)

a) matching: input and outputs return-loss < -18 dB on the whole bandwidth.

b) insertion loss: from the antenna port(s) to the active or control module:

- < 2 dB for a flight-type full antenna (active modules located around the center of the antenna);
- < 2.5 dB for the breadboard, due to the longer cables to the control modules placed on a specific support.

c) amplitude unbalance: < 0.2 dB peak-peak, at a given frequency.

d) phase unbalance: < 50° peak-peak (can be compensated by the phase-shifters).

e) amplitude variation within each channel < 0.2 dB peak-peak.

f) group-delay variation within each channel: < 2 ns peak-peak.

* isolation < -18 dB (non spec)

Reproduction interdite © ALCATEL ESPACE Reproduction forbidden

3.3 ELECTRICAL SPECIFICATIONS FOR THE PART OF THE BFN AFTER THE ACTIVE OR CONTROL MODULES (BUTLER MATRICES + CABLES)

Appairment of cables with Butler matrices already measured (as specified in AES.96-0602/ASP-025), explained below in § 4, can allow to minimize unbalances, and to reach following specifications for the whole part of the BFN located between control modules and radiating subarrays.

a) matching: input and outputs return-loss < -18 dB on the whole bandwidth.

b) insertion loss:

- less than 1.1 dB (including Butler matrices) for a flight-type antenna where modules and matrices would be located around the center of the antenna, with direct connection from modules to matrices and then 20 to 25 cm cables to the radiating elements.
- < 1.6 dB for the breadboard, due to longer cables coming from the control modules placed on a specific support.

c) amplitude unbalance at a given frequency, over all the 24 cables and for any path through the Butler matrixes: 0.4 dB peak-peak for a flight-type antenna; 0.6 dB for the breadboard.

d) phase unbalance: < 5° peak-peak (cannot be compensated by the phase-shifters) for a flight-type antenna, 10° for the breadboard.

e) amplitude variation within each channel: < 0.5 dB peak-peak.

f) group-delay variation within each channel: < 6 ns peak-peak.

3.4 THERMAL SPECIFICATIONS

a) Temperature range in flight: -50, +50°C (TBC by WP 2600).

b) All electrical specifications of § 3.2 and 3.3 should be met on the whole temperature range.

c) For a flight-antenna, they should be verified for all paths at the extreme and ambient temperature.

d) For the breadboard, only S_{21} temperature variations for the 3 first paths of the first part (divider + cables) and for 3 first cables of the second part (after the first matrix), from ambient to the extreme temperatures, will be checked. It will be used to define if temperature compensation would be necessary inside the active modules for a flight model: indeed, this compensation could include divider, cables and Butler matrix variations (the last measured during the test of the matrices, according to their own specification), likely far smaller than that of the SSPA (gain and phase).
For minimizing such variations, materials with low ε_r temperature variation should be chosen for the dividers (such as Duroïd 6002) and for the cables.

Reproduction interdite © ALCATEL ESPACE Reproduction forbidden

3.5 MECHANICAL SPECIFICATIONS

a) Mass

The mass of the whole passive BFN, excluding Butler matrices specified elsewhere (so for dividers and cables, before and after the active and control modules), should not be higher than:

- 2.2 kg for a FM-type 3-beams full antenna.
- 1.2 kg for the breadboard "one-channel" BFN.

b) Vibration

For a flight model, typical vibration levels will be deduced from mechanical analysis (WP 2600).

Vibrating tests are not required for the breadboard, but the design should be made in order to comply with usual levels, to avoid new design in further study or program phases.

Reproduction interdite © ALCATEL ESPACE Reproduction forbidden

4. APPAIRMENT AND MEASUREMENTS OF THE PASSIVE BFN TO BE DELIVERED FOR THE BREADBOARD

a) From the S_{21} amplitude and phase of the cables, given by the supplier, or measured by CASA, appairment should be made for minimizing:

- amplitude unbalance of dividers + cables before the control modules;
- amplitude and phase unbalance among all the Butler matrix outputs, added to that of the corresponding cables. "Among all Butler matrix outputs" means that, for each output, will be averaged the errors from the mean insertion loss of all matrices ($\bar{L}=\frac{1}{N_b}\Sigma L_n$) and from the ideal transmission phase - this averaging being over the 3 paths through the matrix leading to the concerned output. This will make easier to reach the unbalance specifications; and in all cases, improve the antenna gain by minimizing errors.

b) After these appairments, S_{11}, S_{21} and S_{22} of the two parts of the BFN should be measured, with delivering:

- curves over the whole bandwidth for the S_{21} amplitude and phase of the 24 shortest paths obtained by following association of matrices ports: 3 $\rightarrow$ A; 2 $\rightarrow$ B; 1 $\rightarrow$ C), and same for the 3 paths of the first matrix in temperature, with markers at 8.1, 8.2 and 8.3 GHz;
- all S-parameters: 24 S_{11} and S_{22}, 72 S_{21} corresponding to the various associations of input/output matrix ports, sampled with 25 MHz steps, on a diskette formatted as a "CS" file described in Annex A.

c) A table of compliance will be set-up, comparing with the specifications of § 3 and 4:

- the part of the BFN before the control modules, on one hand;
- the part of the BFN after the control modules, on the other hand.

Due to the large number of paths (72 S_{21} for the second part of the BFN), will be given in this table:

- the min, mid, max values and standard deviation of $|S_{11}|$, $|S_{22}|$, $|S_{21}|$ and Arg (S_{21}) among all the paths; each at 8.1, 8.2 and 8.3 GHz.
- the min and max values of $|S_{11}|$, $|S_{22}|$, $|S_{21}|$ and Arg (S_{21}) among the 24 shortest paths over the whole bandwidth.
- the maximal frequency variation of $|S_{21}|$ and of the group-delay among these 24 shortest paths within each channel.

Reproduction interdite © ALCATEL ESPACE Reproduction forbidden

5. OTHER DELIVERING REQUIREMENTS

5.1 EXTERNAL PLATING

The metallic parts of the dividers and cables should be plated (for example chemical oxydation) such as to avoid any surface aspect degradation during 5 years.

5.2 INSPECTION AND REVIEW OF SPECIFICATIONS COMPLIANCE

Before integration in the breadboard, ALCATEL should be called, and ESA notified, to a MTR (Manufacturing and Test Review):

- Visual inspection of the divider 1/24 and the 3 times 24 cables to be delivered,
- Review of the table of compliance prepared by CASA, as defined in § 4.c.

5.3 MARKING

- A serial number should be marked on each cable and possible part of the divider.
- Each port of the divider must be marked with nb. 1 for the input and 2 to 25 for the outputs (to comply with the CS format: see first page of Annex A).
- Each cable appaired with the divider should be marked by number 2 to 25 corresponding to the associated output of the divider.
- The cables appaired with the Butler matrices should be marked by numbers: J.4, J.5 and J.6, if J is the number of the associated matrix and 4, 5, 6 the number of its output port.

All these markings should remain readable during 5 years in the temperature range -50, +50°C.

Reproduction interdite © ALCATEL ESPACE Reproduction forbidden

ANNEX A
CS FORMAT FOR DELIVERING S-PARAMETERS FILES ON DISQUETTES

Numbering of the ports, compliant with the line NU of the CS file (see next page):

a) For the first part of the BFN before the control modules (divider + cables):

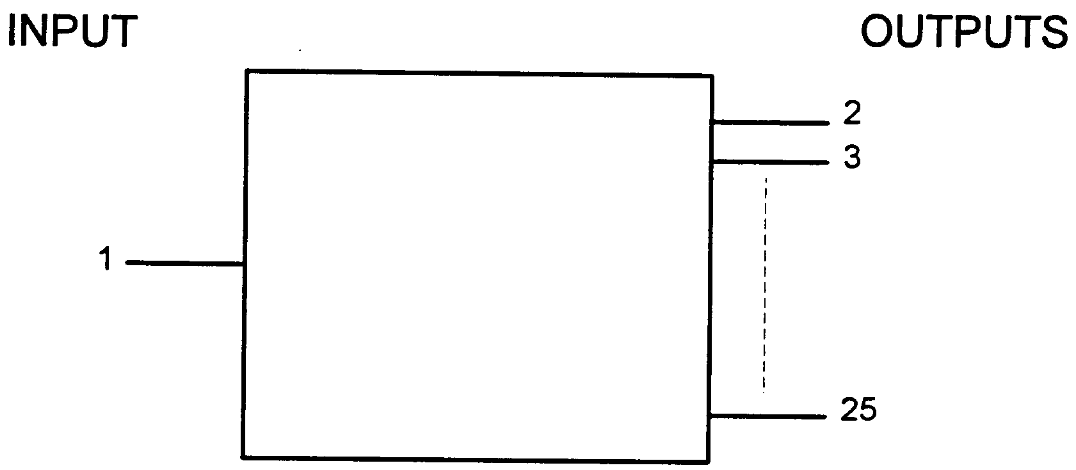

b) for the second part of the BFN after the control modules (shortest paths of the Butler matrices + cables):

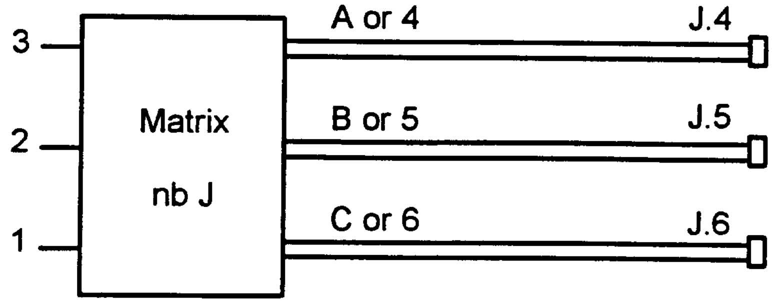

Reproduction interdite © ALCATEL ESPACE Reproduction forbidden

Notice explaining CS norm (only main passages are translated ; other French terms are easy to understand)

Jul 09 15:17 1996 normecs.doc Page 1

as "Coefficient [S]"

```
cs . . . .
==========

fichier question : cs.....fq

  Ce FICHIER prepare les donnees du fichier cs....
  Le fichier CS contient la matrice des parametres S d'un multipole.

  Si on considere un multipole a N portes,
  pour chaque frequence de calcul, on retrouve dans le fichier
  cs.... la valeur des coefficients de la matrice S comme suit :

       QS11, QS12, .... , QS1N
       QS21, QS22, .... , QS2N
       ....
       QSN1, QSN2, .... , QSNN

  avec :
       QSij nombre complexe
       i,j  numerotation des portes du multipole


       SUITE  ??
 > SI OUI Aller en   1.
 . . . . . . . . . . . . . . . . . . . . . . . . . . . . . . . . . . . .

  1.

       ENTREE DES DONNEES DU FICHIER :
       -----------------------------


TI    titre du fichier CS.... ??
 . . . . . . . . . . . . . . . . . . . . . . . . . . . . . . . . . . . .


       DONNEES DESCRIPTIVES
       --------------------


NP    Nombre de portes du multipole  ??
 . . . . . . . . . . . . . . . . . . . . . . . . . . . . . . . . . . . .


       Numerotation des portes du multipole
       ------------------------------------
```

N (or N_p) ports

Jul 09 15:17 1996 normecs.doc Page 2

Numbering the ports begins at left-bottom corner, and turns as the watch

avoids 2 kinds of numbers, "user number" and "CS format numbering"

```
On donne ici la liste des portes du multipole en commencant par le coin
bas gauche et en se deplacant dans le sens des aiguilles d'une montre
  ex :
               n3=4      n4=3
                |         |
                |         |
          *****************
   n2=1-----*               *-------- n5=7        *NB :les numéros se
            *               *                          rapportent a
   n1=2-----*               *-------- n6=8             la numerotation
          *****************                            utilisateur.
                |      |
                |      |
              n8=5   n7=6

  Ici les numeros des portes sont 2,1,4,3,7,8,6,5

NU       numeros des portes ?
 . . . . . . . . . . . . . . . . . . . . . . . . . . . . . . . . . . . .

      Orientation des portes du multipole :
      -----------------------------------

   par convention   ouest=1 , nord=2 , est=3 , sud=4

   de meme que precedement on donne l'orientation des portes
   en commencant par le coin bas gauche et en se deplacant dans
   le sens des aiguilles d'une montre .

   ex :
                 2      2
                 |      |
           *****************
     1 -----*               *-------- 3
            *               *
     1 -----*               *-------- 3
           *****************
                    |
                    4

OP       orientations des portes ?
 . . . . . . . . . . . . . . . . . . . . . . . . . . . . . . . . . . . .

NC    Nom du multipole (8 caracteres max) ??
 . . . . . . . . . . . . . . . . . . . . . . . . . . . . . . . . . . . .
```

← figure A

← figure B

Jul 09 15:17 1996 normecs.doc Page 3

DONNEES MATRICE S :

2.

ATTENTION : Les lignes FR , MS doivent se trouver par ordre croissant en frequence . increasing frequency points

FR Frequence (MHz) ??
. . . .

valeurs des coefficients de la matrice S

Np lignes de 2*Np valeurs (complexes : real part, imaginary part for S_{11} , real part, imaginary part for S_{12} , etc - - - -

```
QS11 , QS12 ,        ,QS1n
QS21 , QS22 , ........ ,QS2n
..........................
QSn1 , QSn2 ,        ,QSnn
```

MS MATRICE S ?
Reponse multiligne (Attention aux 2 blancs)
. . . .

AUTRE FREQUENCE (OUI/NON ??)
> Si OUI Aller en 2.
. . . .

Reproduction interdite © ALCATEL ESPACE Reproduction forbidden

Exemple of presentation (long because 2.5 MHz steps)

```
Jul 09 15:17 1996  csexemple.da Page 1

GA  cs0100.da     28--09--93  12::23::34                      see fig. A.p.13
    fsacs         30-08-89  12::00::00
    fsacs5.pt
TIKUDRI SUP M.CONT. EL.DEL.=-733PS   (title)
NP .2000000E+01,        (how many ports? : 2 here)
NU .1000000E+01, .2000000E+01, (numbering ports : 1,2,3, ---- Np)
OP .1000000E+01, .3000000E+01  (orientation of ports -> see fig. B p 13)
NCRX01 (name of the multipole)
FR .1400000E+05,
MS-.1436234E-01,-.5509949E-01, .7275772E-01,-.5626678E-02,   Re(S11), Im(S11) ---
   .7188797E-01,-.5882263E-02,-.3644562E-01,-.9993744E-01,   Re(S21), Im(S21) ---
FR .1400250E+05,
MS-.2393723E-02,-.5330276E-01, .7297134E-01,-.5626678E-02,
   .7172394E-01,-.6011963E-02,-.3705597E-01,-.9906006E-01,
FR .1400500E+05,
MS .8045200E-02,-.4890060E-01, .7249832E-01,-.5462646E-02,
   .7143402E-01,-.5744934E-02,-.3687286E-01,-.9835815E-01,
FR .1400750E+05,
MS .8186340E-02,-.3849411E-01, .7260513E-01,-.5218506E-02,
   .7174301E-01,-.5336761E-02,-.3672791E-01,-.9750366E-01,
FR .1401000E+05,
MS .4615780E-02,-.3127098E-01, .7318878E-01,-.5142212E-02,
   .7143402E-01,-.5603790E-02,-.3662109E-01,-.9634399E-01,
FR .1401250E+05,
MS-.4322052E-02,-.2958488E-01, .7274246E-01,-.4699707E-02,
   .7158279E-01,-.4673004E-02,-.3686523E-01,-.9529877E-01,
FR .1401500E+05,
MS-.1160431E-01,-.3326607E-01, .7271576E-01,-.4878998E-02,
   .7166672E-01,-.4558563E-02,-.3668976E-01,-.9430695E-01,
FR .1401750E+05,
MS-.1031113E-01,-.3723907E-01, .7340240E-01,-.4993439E-02,
   .7206345E-01,-.4814148E-02,-.3674316E-01,-.9286499E-01,
FR .1402000E+05,
MS-.7619858E-02,-.4148865E-01, .7300949E-01,-.4531860E-02,
   .7186508E-01,-.4440308E-02,-.3678894E-01,-.9147644E-01,
FR .1402250E+05,
MS-.2759933E-02,-.4274750E-01, .7332993E-01,-.4386902E-02,
   .7180786E-01,-.3715515E-02,-.3687286E-01,-.9054565E-01,
FR .1402500E+05,
MS-.3376007E-03,-.3922653E-01, .7323074E-01,-.4283905E-02,
   .7231522E-01,-.4047394E-02,-.3684998E-01,-.8940887E-01,
FR .1402750E+05,
MS-.2403259E-03,-.3585052E-01, .7367325E-01,-.4119873E-02,
   .7231140E-01,-.3883362E-02,-.3736115E-01,-.8861542E-01,
FR .1403000E+05,
MS-.4766464E-02,-.3195000E-01, .7376480E-01,-.4531860E-02,
   .7237244E-01,-.3372192E-02,-.3768921E-01,-.8815002E-01,
FR .1403250E+05,
MS-.5302429E-02,-.2874947E-01, .7380676E-01,-.5050659E-02,
   .7271957E-01,-.3978729E-02,-.3787994E-01,-.8799744E-01,
FR .1403500E+05,
MS-.8008957E-02,-.2979279E-01, .7420349E-01,-.4589081E-02,
   .7244110E-01,-.3650665E-02,-.3873444E-01,-.8840942E-01,
FR .1403750E+05,
MS-.8419037E-02,-.2924538E-01, .7332230E-01,-.4791260E-02,
   .7289505E-01,-.3513336E-02,-.3987122E-01,-.8896637E-01,
```

for each frequency

```
Jul 09 15:17 1996  csexemple.da Page 2

FR .1404000E+05,
MS-.1436234E-01,-.2999115E-01, .7360077E-01,-.5363464E-02,
   .7304382E-01,-.3841400E-02,-.4176331E-01,-.8921051E-01,
FR .1404250E+05,
MS-.1587677E-01,-.3268814E-01, .7369995E-01,-.5325317E-02,
   .7292557E-01,-.4280090E-02,-.4383850E-01,-.8971405E-01,
FR .1404500E+05,
MS-.1940155E-01,-.3295326E-01, .7312393E-01,-.5062103E-02,
   .7330704E-01,-.3841400E-02,-.4559326E-01,-.8941650E-01,
FR .1404750E+05,
MS-.2150726E-01,-.3169060E-01, .7330322E-01,-.5172729E-02,
   .7326889E-01,-.4055023E-02,-.4763031E-01,-.8908081E-01,
FR .1405000E+05,
MS-.2389908E-01,-.2980423E-01, .7329559E-01,-.4516602E-02,
   .7302856E-01,-.3295898E-02,-.4919434E-01,-.8815765E-01,
FR .1405250E+05,
MS-.2872086E-01,-.2735519E-01, .7295227E-01,-.4207611E-02,
   .7274246E-01,-.3787994E-02,-.5056000E-01,-.8712006E-01,
FR .1405500E+05,
MS-.3372192E-01,-.3664017E-01, .7301331E-01,-.4234314E-02,
   .7259369E-01,-.3551483E-02,-.5194855E-01,-.8578491E-01,
FR .1405750E+05,
MS-.3906250E-01,-.4356766E-01, .7274628E-01,-.3868103E-02,
   .7289886E-01,-.3288269E-02,-.5268860E-01,-.8393097E-01,
FR .1406000E+05,
MS-.3361511E-01,-.5730820E-01, .7312012E-01,-.3856659E-02,
   .7290268E-01,-.3337860E-02,-.5326080E-01,-.8195496E-01,
FR .1406250E+05,
MS-.2080917E-01,-.6109238E-01, .7325363E-01,-.3761292E-02,
   .7245255E-01,-.3284454E-02,-.5351257E-01,-.8010101E-01,
FR .1406500E+05,
MS-.7568359E-02,-.6178665E-01, .7307816E-01,-.3726959E-02,
   .7260513E-01,-.2994537E-02,-.5361176E-01,-.7806396E-01,
FR .1406750E+05,
MS .1289370E-02,-.5265236E-01, .7302475E-01,-.3574371E-02,
   .7288361E-01,-.2849579E-02,-.5367279E-01,-.7608032E-01,
FR .1407000E+05,
MS .3376010E-02,-.4003525E-01, .7282257E-01,-.3147125E-02,
   .7312012E-01,-.2391815E-02,-.5381775E-01,-.7406616E-01,
FR .1407250E+05,
MS-.2241135E-02,-.3058624E-01, .7318115E-01,-.3738403E-02,
   .7341003E-01,-.2334595E-02,-.5410004E-01,-.7220459E-01,
FR .1407500E+05,
MS-.9119034E-02,-.2991295E-01, .7375336E-01,-.3383636E-02,
   .7368851E-01,-.2487183E-02,-.5420685E-01,-.6983566E-01,
FR .1407750E+05,
MS-.1733017E-01,-.3627396E-01, .7381058E-01,-.3192902E-02,
   .7379532E-01,-.2861023E-02,-.5455017E-01,-.6813431E-01,
FR .1408000E+05,
MS-.1752663E-01,-.3975487E-01, .7373047E-01,-.3726959E-02,
   .7385635E-01,-.3341675E-02,-.5453110E-01,-.6630707E-01,
FR .1408250E+05,
MS-.1186562E-01,-.4331017E-01, .7328033E-01,-.3505707E-02,
   .7408905E-01,-.3349304E-02,-.5435562E-01,-.6422043E-01,
FR .1408500E+05,
MS-.8516312E-02,-.4075623E-01, .7400894E-01,-.3471375E-02,
```

Reproduction interdite © ALCATEL ESPACE Reproduction forbidden

```
Jul 09 15:17 1996  csexemple.da Page 3

    .7349777E-01,-.3608704E-02,-.5435944E-01,-.6243515E-01,
 FR .1408750E+05,
 MS-.8420944E-02,-.3292847E-01, .7366180E-01,-.3475189E-02,
    .7368851E-01,-.3658295E-02,-.5409241E-01,-.6096268E-01,
 FR .1409000E+05,
 MS-.1199913E-01,-.2952003E-01, .7357407E-01,-.3543854E-02,
    .7352066E-01,-.3116608E-02,-.5339050E-01,-.5923080E-01,
 FR .1409250E+05,
 MS-.1730728E-01,-.2626228E-01, .7316589E-01,-.3875732E-02,
    .7330704E-01,-.3757477E-02,-.5258942E-01,-.5868912E-01,
 FR .1409500E+05,
 MS-.2009964E-01,-.2949333E-01, .7280731E-01,-.3295898E-02,
    .7357788E-01,-.2929688E-02,-.5131149E-01,-.5767441E-01,
 FR .1409750E+05,
 MS-.2052116E-01,-.3480721E-01, .7340240E-01,-.3170013E-02,
    .7371521E-01,-.3116608E-02,-.5030823E-01,-.5726624E-01,
 FR .1410000E+05,
 MS-.2057266E-01,-.3775406E-01, .7352448E-01,-.3597260E-02,
    .7394791E-01,-.3299713E-02,-.4962158E-01,-.5714417E-01,
 FR .1410250E+05,
 MS-.1807785E-01,-.3890800E-01, .7334137E-01,-.3334045E-02,
    .7371902E-01,-.3433228E-02,-.4842758E-01,-.5709839E-01,
 FR .1410500E+05,
 MS-.1634789E-01,-.3920174E-01, .7332230E-01,-.3215790E-02,
    .7349777E-01,-.2822876E-02,-.4760742E-01,-.5785751E-01,
 FR .1410750E+05,
 MS-.1768684E-01,-.3495789E-01, .7337189E-01,-.2819061E-02,
    .7302094E-01,-.3273010E-02,-.4704666E-01,-.5820465E-01,
 FR .1411000E+05,
 MS-.1971054E-01,-.3178406E-01, .7331085E-01,-.3189087E-02,
    .7357788E-01,-.2830505E-02,-.4734039E-01,-.5926514E-01,
 FR .1411250E+05,
 MS-.2680206E-01,-.3284836E-01, .7334518E-01,-.2735138E-02,
    .7366943E-01,-.3070831E-02,-.4761124E-01,-.5921936E-01,
 FR .1411500E+05,
 MS-.3720856E-01,-.3425217E-01, .7348633E-01,-.2059937E-02,
    .7354355E-01,-.2861023E-02,-.4820633E-01,-.5943298E-01,
 FR .1411750E+05,
 MS-.4231262E-01,-.4219055E-01, .7332230E-01,-.2155304E-02,
    .7270432E-01,-.2811432E-02,-.4894638E-01,-.5878448E-01,
 FR .1412000E+05,
 MS-.4267883E-01,-.5455399E-01, .7356644E-01,-.2357483E-02,
    .7346344E-01,-.2376556E-02,-.4984665E-01,-.5788422E-01,
 FR .1412250E+05,
 MS-.3796387E-01,-.6104660E-01, .7378387E-01,-.2502441E-02,
    .7367706E-01,-.1956940E-02,-.5089951E-01,-.5699158E-01,
 FR .1412500E+05,
 MS-.2594757E-01,-.6492615E-01, .7368088E-01,-.2670288E-02,
    .7344818E-01,-.2712250E-02,-.5149078E-01,-.5577469E-01,
 FR .1412750E+05,
 MS-.1521301E-01,-.5892181E-01, .7350540E-01,-.2403259E-02,
    .7335281E-01,-.2368927E-02,-.5239105E-01,-.5437469E-01,
 FR .1413000E+05,
 MS-.5287170E-02,-.4963684E-01, .7318878E-01,-.2559662E-02,
    .7326889E-01,-.2403259E-02,-.5309296E-01,-.5248260E-01,
 FR .1413250E+05,
```

```
Jul 09 15:17 1996  csexemple.da Page 4

MS-.6660461E-02,-.4044342E-01, .7309723E-01,-.2323151E-02,
   .7334518E-01,-.2494812E-02,-.5382538E-01,-.5042267E-01,
FR .1413500E+05,
MS-.1105118E-01,-.3639984E-01, .7339096E-01,-.2269745E-02,
   .7366180E-01,-.2613068E-02,-.5389404E-01,-.4888153E-01,
FR .1413750E+05,
MS-.1546097E-01,-.3588104E-01, .7303619E-01,-.2155304E-02,
   .7334518E-01,-.2437592E-02,-.5393982E-01,-.4668427E-01,
FR .1414000E+05,
MS-.1716614E-01,-.3980637E-01, .7334900E-01,-.2304077E-02,
   .7362747E-01,-.2788544E-02,-.5418396E-01,-.4454041E-01,
FR .1414250E+05,
MS-.1462555E-01,-.3942108E-01, .7320786E-01,-.1953125E-02,
   .7265472E-01,-.2628326E-02,-.5346680E-01,-.4288483E-01,
FR .1414500E+05,
MS-.9246826E-02,-.3602982E-01, .7342529E-01,-.1800537E-02,
   .7314301E-01,-.2643585E-02,-.5309296E-01,-.4087830E-01,
FR .1414750E+05,
MS-.1250267E-01,-.2960014E-01, .7346344E-01,-.1914978E-02,
   .7302475E-01,-.2311707E-02,-.5236435E-01,-.3886032E-01,
FR .1415000E+05,
MS-.1688576E-01,-.2434349E-01, .7369614E-01,-.2075195E-02,
   .7321930E-01,-.2342224E-02,-.5147552E-01,-.3713608E-01,
FR .1415250E+05,
MS-.2598572E-01,-.2268982E-01, .7304764E-01,-.1903534E-02,
   .7287598E-01,-.2532959E-02,-.5043030E-01,-.3527451E-01,
FR .1415500E+05,
MS-.3220558E-01,-.2728081E-01, .7304764E-01,-.2506256E-02,
   .7268524E-01,-.2727509E-02,-.4901886E-01,-.3377914E-01,
FR .1415750E+05,
MS-.3233337E-01,-.3157806E-01, .7302475E-01,-.1598358E-02,
   .7257462E-01,-.2437592E-02,-.4724121E-01,-.3174591E-01,
FR .1416000E+05,
MS-.2785492E-01,-.3860474E-01, .7342529E-01,-.1766205E-02,
   .7238388E-01,-.2288818E-02,-.4548645E-01,-.3142548E-01,
FR .1416250E+05,
MS-.2412415E-01,-.4030609E-01, .7362366E-01,-.1731873E-02,
   .7262421E-01,-.1949310E-02,-.4375458E-01,-.3048706E-01,
FR .1416500E+05,
MS-.1842880E-01,-.3504562E-01, .7334518E-01,-.1403809E-02,
   .7239914E-01,-.1266479E-02,-.4178619E-01,-.3005219E-01,
FR .1416750E+05,
MS-.1597595E-01,-.3100204E-01, .7314682E-01,-.1338959E-02,
   .7257462E-01,-.1186371E-02,-.4003906E-01,-.3002930E-01,
FR .1417000E+05,
MS-.2071381E-01,-.2719498E-01, .7323074E-01,-.1689911E-02,
   .7229614E-01,-.1583099E-02,-.3844452E-01,-.3018188E-01,
FR .1417250E+05,
MS-.2448654E-01,-.2531815E-01, .7357025E-01,-.1499176E-02,
   .7284164E-01,-.1621246E-02,-.3691864E-01,-.3076172E-01,
FR .1417500E+05,
MS-.3094864E-01,-.2922821E-01, .7313919E-01,-.1483917E-02,
   .7265091E-01,-.1384735E-02,-.3542328E-01,-.3145599E-01,
FR .1417750E+05,
MS-.3829193E-01,-.3427887E-01, .7275009E-01,-.1384735E-02,
   .7277298E-01,-.1281738E-02,-.3449249E-01,-.3259277E-01,
```

file end (always a complete MS = $Re(S_{ij})$, $Im(S_{ij})$ set)

Reproduction interdite © ALCATEL ESPACE Reproduction forbidden

CONFORMAL ARRAY ANTENNA	AES 96-29461/ASP-395		
	Estec Contract 11698/95/NL/SB		
	DATE : 16/09/96	ED/REV : 1/A	PAGE : 1 / 11

Titre / Title

SPECIFICATIONS FOR THE ACTIVE MODULES AND PREAMPLIFIER OF A FLIGHT-TYPE ANTENNA

Rédigé par / Written by	Responsabilité / responsibility	Date	Signature
G. CAILLE	Technical Manager of the Contract	18/9/96	G. Caille
Vérifié par / Verified by			
Approbation / Approved			

ALCATEL
TELECOM

Reproduction interdite © ALCATEL ESPACE Reproduction forbidden

ENREGISTREMENT DES EVOLUTIONS / CHANGE RECORD

ED./ REV.	DATE	§ CONCERNES CONCERNED §	§: DESCRIPTION DES EVOLUTIONS §: CHANGE RECORD	REDACTEUR AUTHOR
1/-	02/07/96		First Issue	G. CAILLE
1/A	16/09/96		• Updating of gain and ouptut power specifications, according to first simulations of various equipments • Correction of an error in the total power computation	G. CAILLE

Reproduction interdite © ALCATEL ESPACE Reproduction forbidden

SUMMARY

Reproduction interdite © ALCATEL ESPACE Reproduction forbidden

1. FUNCTIONALITIES

According to the electrical diagram of the "semi-active" three-beams conformal antenna presented in figure 1-a, an active module should perform following functions:

a) Phase control over 360° of each of the 3 input-signals (each beam corresponds to a 50 MHz wide channel, centered at $f_1 = 8100$, $f_2 = 8200$, $f_3 = 8300$ MHz).

The desired phase-shifts are computed by the control unit, including:

- beam scanning phase (simultaneously in azimuth and elevation, thanks to conjugate matching at the input of a feeding network based on eight 3 x 3 Butler matrices);
- compensation of phase dispersions between the various BFN paths, located before the Butler matrices, including the active modules themselves (phase-shifter at 0° reference state);
- possibly, if the thermal analysis shows that it is necessary, phase dispersion due to temperature differences between various active modules. This needs temperature measurement inside each module.

b) Combining the three channels, with equal amplitude transmission from each of them.

c) Amplifying the signal to the desired level, to comply with specified EIRP, taking into account losses of passive equipment, and maximal level at the phase-shifters input. As the necessary active gain is about 48 dB (see precise specification § 2-c)), a pre-amplifier can be put after the modulator and channel filter to decrease the necessary gain of the 24 SSPA's, and minimize the overall power consumption. In that case, the architecture, gain and consumption of this preamplifier will be given, as for the active module itself.

d) Auto-compensating gain dispersions between the SSPA's, and of the phase-shifters for various commands, if it appears necessary to comply with the specifications.

e) Providing a very good C/I3 ≥ 28 dB: because of stringent limitation of power radiated in the Deep Space Network Band (8400 - 8450): this can require internal linearizer.

f) Providing a calibration signal, by the way of a -20 dB directive coupler, at the output of the SSPA. This signal will go through a passive and particularly stable combiner, to a calibration receiver.

Reproduction interdite © ALCATEL ESPACE Reproduction forbidden

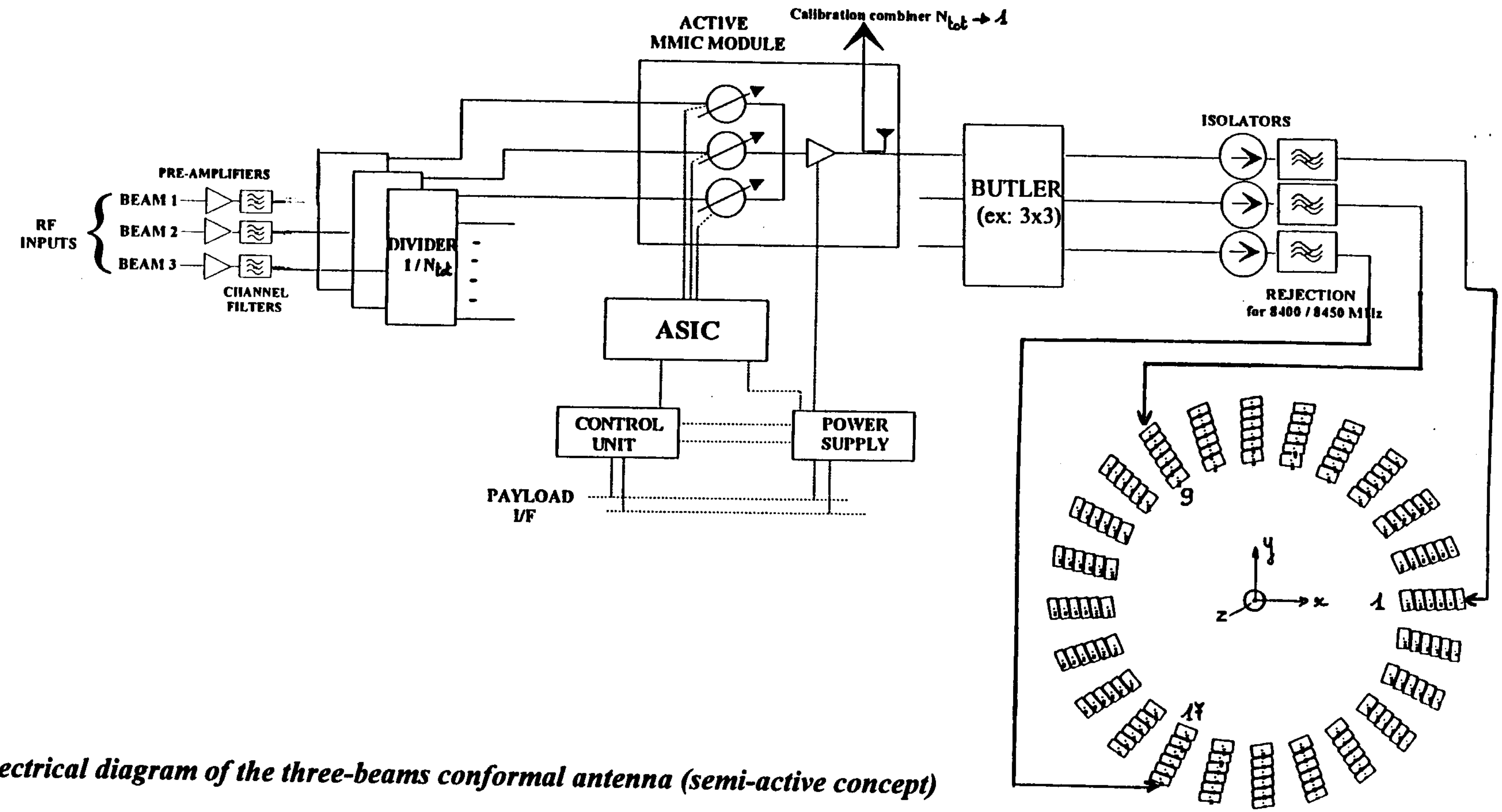

Figure 1-a: Electrical diagram of the three-beams conformal antenna (semi-active concept)

N_{tot} = 24 radiating subarrays

Reproduction interdite © ALCATEL ESPACE Reproduction forbidden

A suited calibration algorithm should then monitor the amplitude and phase of the signal issued of each path, such as:

- to know possible failures or gain loss with ageing, and re-optimize the excitation sets taking them into account;
- to measure possible phase ageing, and compensate them by controlling the phase-shifter.

Several algorithms for such a calibration have been proposed in the litterature, and are not the subject of this study. For example:

- putting all paths except nb *n* in phase opposition (shifted one from each other by $360°/(N_{tot} - 1)$);
- sending the various possible commands to the phase-shifter of the calibrated path number *n*.
- So, in the complex plane, the extremity of the vector representing the contribution of this path number *n* describes approximately a circle: its center can be found as barycenter of all measured points; then the amplitude and phase errors corresponding to each phase-state are deduced.

g) Remark: no gain control is required for beam forming; only a limited unbalance between gain of various modules is required (see § 2.e).

Reproduction interdite © ALCATEL ESPACE Reproduction forbidden

2. ELECTRICAL SPECIFICATIONS OF THE "ACTIVE SUB-ASSEMBLY"

"Active sub-assembly" means: an active module + possible preamplifier. All equipment should be provided with female SMA connector.

a) Bandwidth:

- whole allocated to the mission: 8025/8400 MHz
- 3 useful channels, 50 MHz wide, centered around: f_1 = 8100, f_2 = 8200, f_3 = 8300 MHz.

b) Matching:

- Return loss < -18 dB on the whole bandwidth for all inputs and outputs,
- except active modules output, where -14 dB can be tolerated, as the electrical length until the next equipment (Butler matrix) is very short.

c) Gain:

35.5 dB overall: possible preamplifier + active module (including phase-shifter combiner and calibration coupler losses: attention to the 10 log 3 minimal loss through the 3 → 1 combiner, because its 3 inputs are fed by different frequency channels).

This figure is derived from the following preliminary gain/levels budgets:

Output of the modulator	0	dBm
Channel filter loss	-0.7	dB
Divider 1/24 and cables insertion loss	- 2	dB
1/24 division loss	-13.8	dB
Butler matrix loss	-1	dB
Loss of cables before and after the matrices	-0.3	dB
Isolator	-0.4	dB
Rejection filter loss (worst case over the 3 channels)	-1.2	dB
Overall provision for mismatching between equipments	-0.6	dB
Level at subarray input without active sub-assembly	-20	dBm
Level at subarray input required	15.5	dBm
REQUIRED GAIN (for any of the three channels):	35.5	dB

Reproduction interdite © ALCATEL ESPACE Reproduction forbidden

d) Output power for each channel (from above estimations): 19 dBm (80 mW). Don't forget that there are 3 simultaneous channels at different frequencies.

e) Phase control:

6 digital bits (LSB = 5.625°).

RMS phase error over all the 64 states (after possible reading of a calibration table for each module) ≤ 3° for each module.

Worst case phase error over all the 64 states < 9° for each module.

f) Gain unbalance:

- For a given module, over all 64 phase states : ≤ 1.2 dB peak-peak
- for a given module, RMS over all the 64 phase states: ≤ 0.4 dB
- among all modules, for the reference 0° command and maximal 5°C temperature difference between them: ≤ 1 dB peak-peak
- RMS among all modules for the reference 0° command and maximal 5°C temperature difference between them: ≤ 0.4 dB

g) Variations within each 50 MHz channel:

- amplitude: ≤ 0.3 dB peak-peak
- time-delay: ≤ 2 ns

h) Linearity:

C/I3 ≥ 28 dB for three carriers with C = output power C specified in § 2-d); I3 being anyone of the third order intermodulation products.

i) Power consumption:

To be minimized; in all cases, not higher than 50 W (DC) for the whole active sub-assembly, corresponding to 11.4 % overall efficiency versus the total output power delivered simultaneously by the 24 modules (37.6 dBm = 5.7 W) in the 3 channels.

The power supply consumption is not included in this figure, but should be indicated roughly.

j) Switching time:

≤ 150 ns (ASIC included)

Reproduction interdite © ALCATEL ESPACE Reproduction forbidden

3. THERMAL SPECIFICATIONS

a) Temperature range of the base plate (thanks to appropriate thermal control of the antenna): -5°, +40°C.

b) All electrical specifications should be met within this temperature range.

c) The output power from the active modules can vary, above the minimum value of 19 dBm, by no more than 2 dB over the whole temperature range - providing that the amplitude control specifications 2.e and 2.f would be met.

Reproduction interdite © ALCATEL ESPACE Reproduction forbidden

4. MECHANICAL SPECIFICATIONS

a) Mass

The mass of each distributed active module, and of the pre-amplifier, including packages and one ASIC for 1 to 4 modules, should be less than 60 g per module (possibly gathered) and for the pre-amplifier.

b) Vibration

No detailed study of the vibrating level accepted by the active modules will be made in this contract. But the mass should be confirmed with technologies taking into account usual requirements for modules in active antennas.

Reproduction interdite © ALCATEL ESPACE Reproduction forbidden

5. OUTPUTS OF W.P. 2400

- Detailed electrical diagram of the active modules, and possible pre-amplifier.
- Technology proposed for the amplifiers, number of stages expected.
- Technology proposed for the phase-shifters.
- Technology proposed for the combiner and the coupler.
- Necessary voltages and power consumtions.
- Evaluation of mass and volume.
- Table of compliance with the present specifications.

Reproduction interdite © ALCATEL ESPACE Reproduction forbidden

CONFORMAL ARRAY ANTENNA

AES 96-0602/ASP-025		
Estec Contract 11698/95/NL/SB		
DATE : 13/09/96	**ED/REV :** 1/C	**PAGE :** 1 / 24

Titre / Title

SPECIFICATIONS FOR

3 X 3 BUTLER MATRICES

Rédigé par / Written by	Responsabilité / responsibility	Date	Signature
G. CAILLE	Technical Manager of the Contract	18/9/96	
Vérifié par / Verified by			
Approbation / Approved			

ALCATEL
TELECOM

Reproduction interdite © ALCATEL ESPACE Reproduction forbidden

ENREGISTREMENT DES EVOLUTIONS / CHANGE RECORD

ED./ REV.	DATE	§ CONCERNES CONCERNED §	§: DESCRIPTION DES EVOLUTIONS §: CHANGE RECORD	REDACTEUR AUTHOR
1/-	18/03/96		First Issue	G. CAILLE
1/A	10/04/96			G. CAILLE
1/B	11/08/96	§ 3	– Clearer redaction of accuracy specifications (unbalance/frequency variations)	G. CAILLE
		end of § 3	– Added remark	
		§ 4 and 5	– Added thermal and mechanical specifications	
		§ 6	– Added delivering requirements	
		Annex A	– Format for delivering S-parameters on files	
1/C	13/09/96	§ 3	Correcton of missing $1/\sqrt{3}$ p 13, and amplitude unbalance added	G. CAILLE

Reproduction interdite © ALCATEL ESPACE Reproduction forbidden

SUMMARY

Reproduction interdite © ALCATEL ESPACE Reproduction forbidden

1. SUBJECT

This document specifies the Butler matrices necessary for the *semi-active concept* of the "Conformal array antenna" contract.

In § 2, choice of the Butler type (kind of hybrids and number of ports) is justified, to be suited to the antenna specifications.

In § 3, detailed specifications are settled for the eight 3 x 3 matrices to be integrated in the breadboard.

Reproduction interdite © ALCATEL ESPACE Reproduction forbidden

2. ELECTRICAL CONSTRAINTS FOR FEEDING A CIRCULAR ARRAY

2.1 PRINCIPLES

Principle for feeding a circular array by means of phase-shifters control at the input of a set of Nb Butler matrices, each with Np input and output ports, is described on figures 2.1-a and 2.1-b.

N = Nb x Np is the total number of subarrays inputs, equally spaced around a circle.

- Fig. 2-a shows the general principle for generating M = 2 independent beams in different azimuth directions (drawing is made with Nb = 4 and Np = 8).
- Fig. 2-b is suited to the conformal array optimal configuration, as issued from numerous simulations made by ALCATEL during W.P. 1200: Nb = 8 and Np = 3.

Reproduction interdite © ALCATEL ESPACE Reproduction forbidden

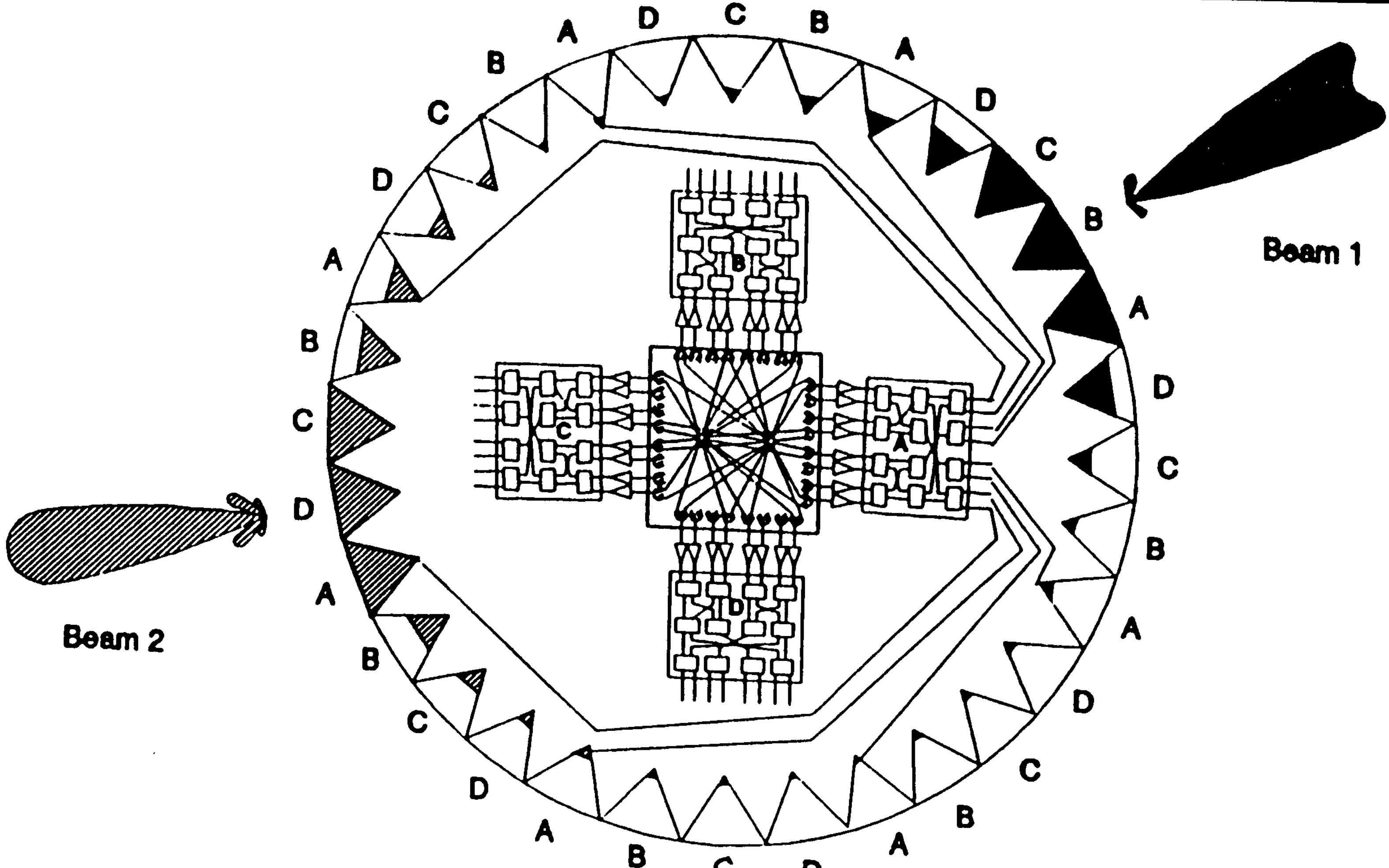

Figure 2.1-a: Principle of semi-active multibeam circular array (here $M = 2$ beams, $N = 32$ radiating subarrays)

Reproduction interdite © ALCATEL ESPACE Reproduction forbidden

Optimally, energy is concentrated on one output of each Butler, but can be moved slowly around the cone by driving phase-shifters

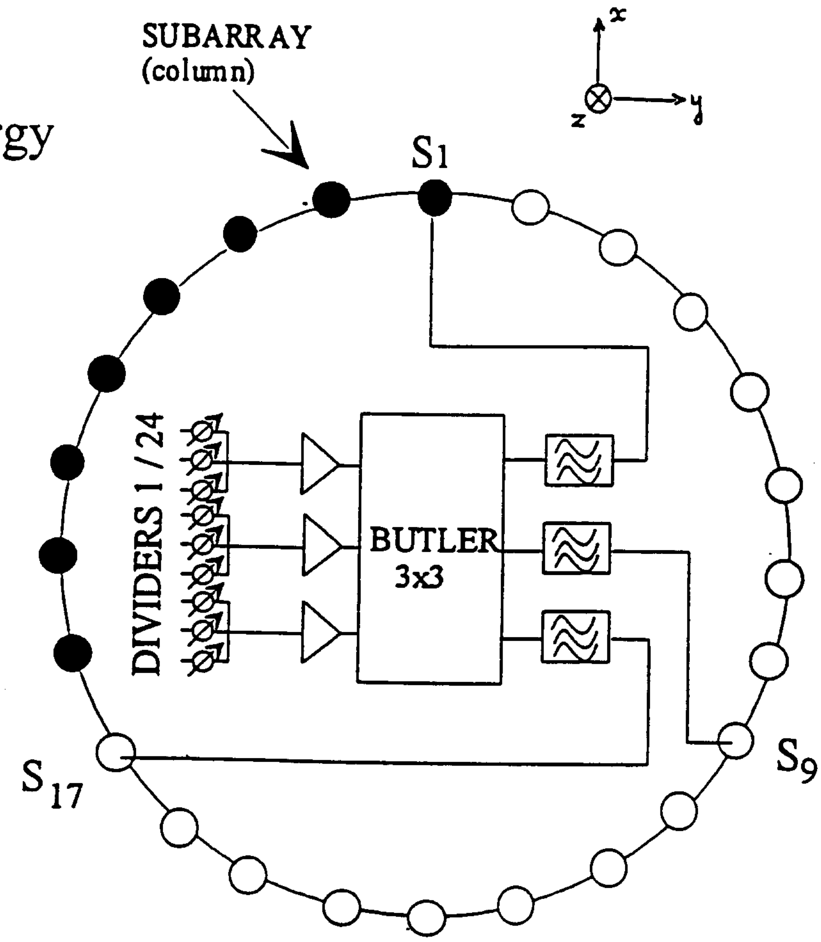

Figure 2.1-b: Semi-active circular array suited to this study (M = 3, N = 24 with Nb = 8 Butlers and Np = 3 inputs and outputs each)

Reproduction interdite © ALCATEL ESPACE Reproduction forbidden

2.2 BUTLER-TYPE SUITED TO SMOOTH ROTATION OF THE BEAM

One of the most stringent specification of the mission is low amplitude and phase jumps for the electric field radiated towards an earth station direction, moving around the antenna revolution axis.

This can be achieved far better with Butler matrices made with 180° - hybrids (waveguide magic tees, planar rat-races ...) than with 90° - hybrids (parallel waveguides coupled by holes, branch-line planar couplers), for following reasons:

a) As it is explained in references [1][2][3], *a Butler matrix built with 180° hybrids*, when its outputs are connected to radiating elements (R.E.) equally spaced along a circle, provides phase-shifts along one turn, which are always *integer multiples of 2π radians* (see figure 2.2-a). In the example of a classical 4 x 4 matrix shown on the figure, if we add respectively (thanks to variable phase-shifters) 0°, 90°, 180°, 270° to the inputs numbered 1, 2, 3, 4 of the matrix, the excitations corresponding to any combination of input signals will move by 90° on the circle:

- if we add the above phase-shifts at the inputs of all the Butler matrices, the beam will turn by 90° around the array axis.
- if we have an optimized excitation where all the energy is concentrated on Nb adjacent R.E., i.e. for example A_1, B_1, C_1, D_1, to turn the beam by $\frac{2\pi}{N}$, the phase-shifts explained before, applied only to matrix A inputs, move the energy from A_1 to A_2 (figure 2.2-c). Then we apply the same phase-shifts to matrix B, which moves the output energy from B_1 to B_2 ... and so on.

b) On the opposite, *a Butler matrix built with 90° hybrids* (as shown on figure 2.2-b for the classical 4 x 4 case), when connected to a circular array, provide non regular phase-shifts along one turn, because phase-difference along one turn is an *odd multiple of π radians*. This is far worse suited to smooth rotation of the beam around the array axis.

N.B.: It would be possible to have the same output phase distribution than on figure 2.2-a with a Butler built with 90°, by adding 90° phase-shifts at one input and one output of each hybrid coupler (but this would make it more difficult to build with good phase stability over the bandwidth).

Reproduction interdite © ALCATEL ESPACE Reproduction forbidden

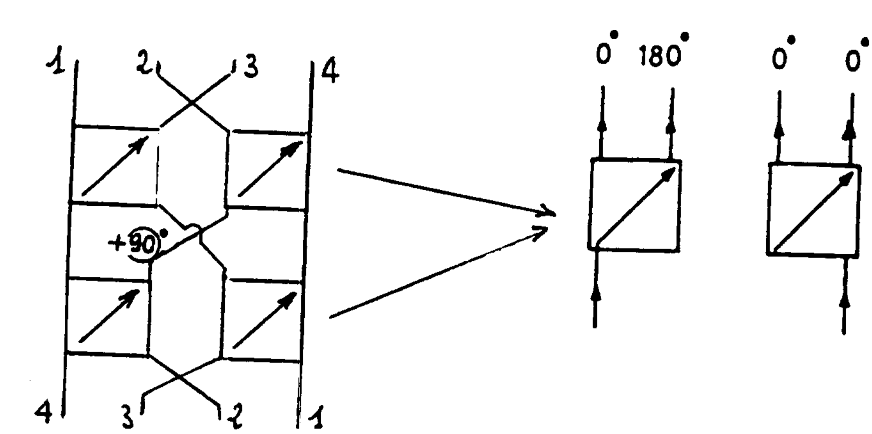

(numbering inputs and outputs has been chosen so that the matrix is unvariant by 180° rotation around Oz perpendicular to the sheet plane).

1) **4 x 4 Butler matrix built with 180° - hybrids**

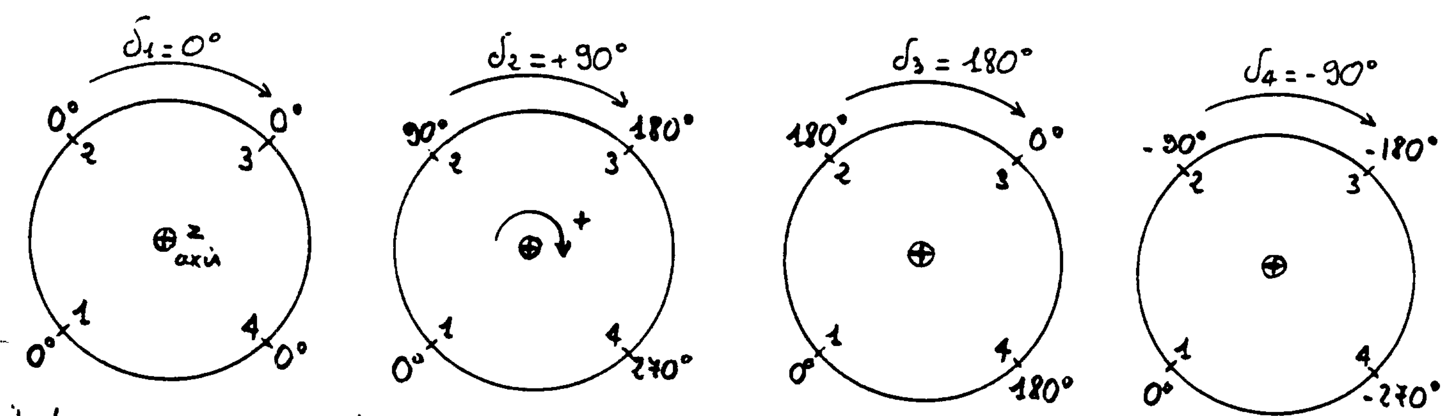

excited input i	1	2	3	4
δ_i	0°	+90°	+180°	270° = -90°

2) **Outputs regularly connected to a circular array (insertion phase of the shortest path 1 ⇆ 4 must be added to all output phases, written around the circles)**

Figure 2.2-a: 4 x 4 Butler matrix built with 180° - hybrids (1), providing equal phase-shifts δ_i on outputs regularly connected to 1, 2, 3, 4 on a circular array

Reproduction interdite © ALCATEL ESPACE Reproduction forbidden

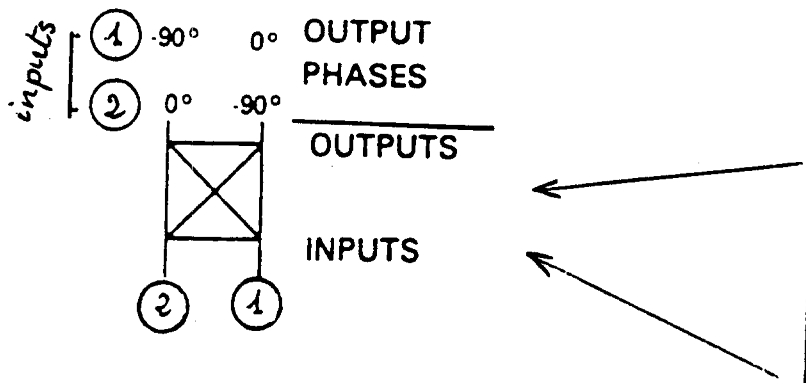

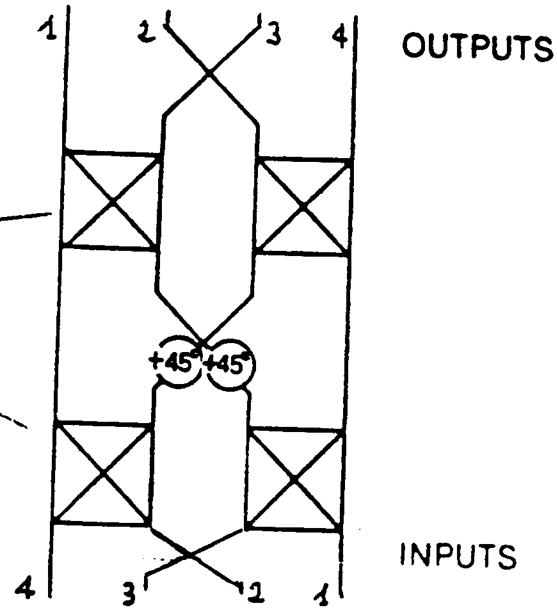

1) 4 x 4 Butler matrix built with 90° - hybrids

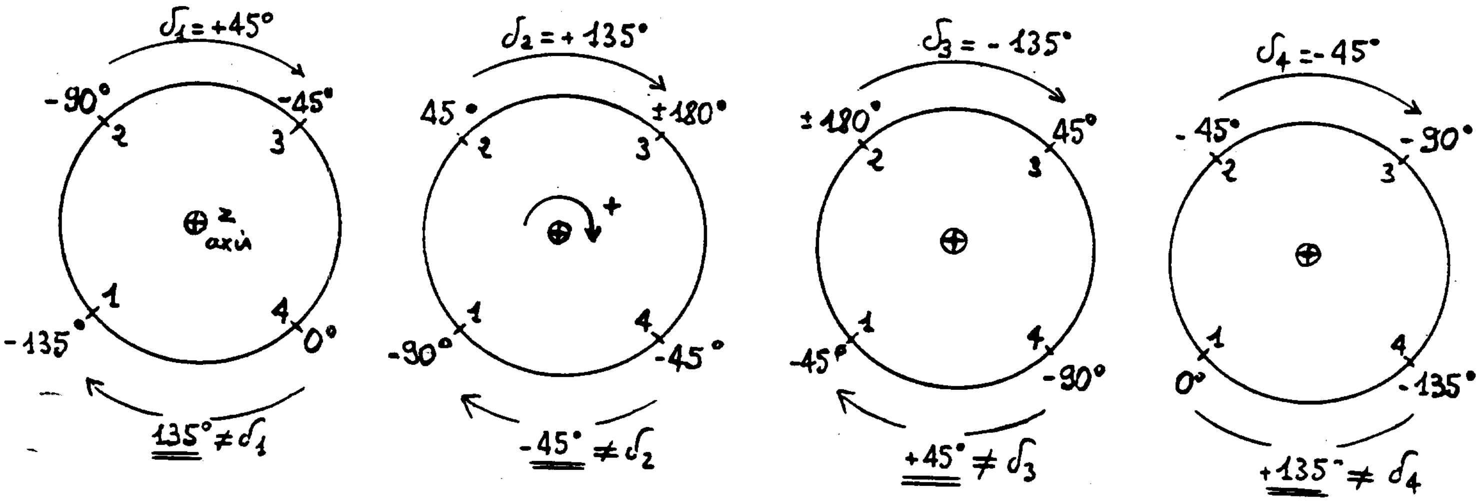

excited input i	1	2	3	4
δ_i	+45°	+135°	+225° = -135°	315° = -45°

2) Outputs regularly connected to a circular array (same remark as in the last page)

Figure 2.2-b: 4 x 4 Butler matrix built with 90° - hybrids (1), providing non equal phase-shifts δ_i between the outputs connected to the circular array (2)

Reproduction interdite © ALCATEL ESPACE Reproduction forbidden

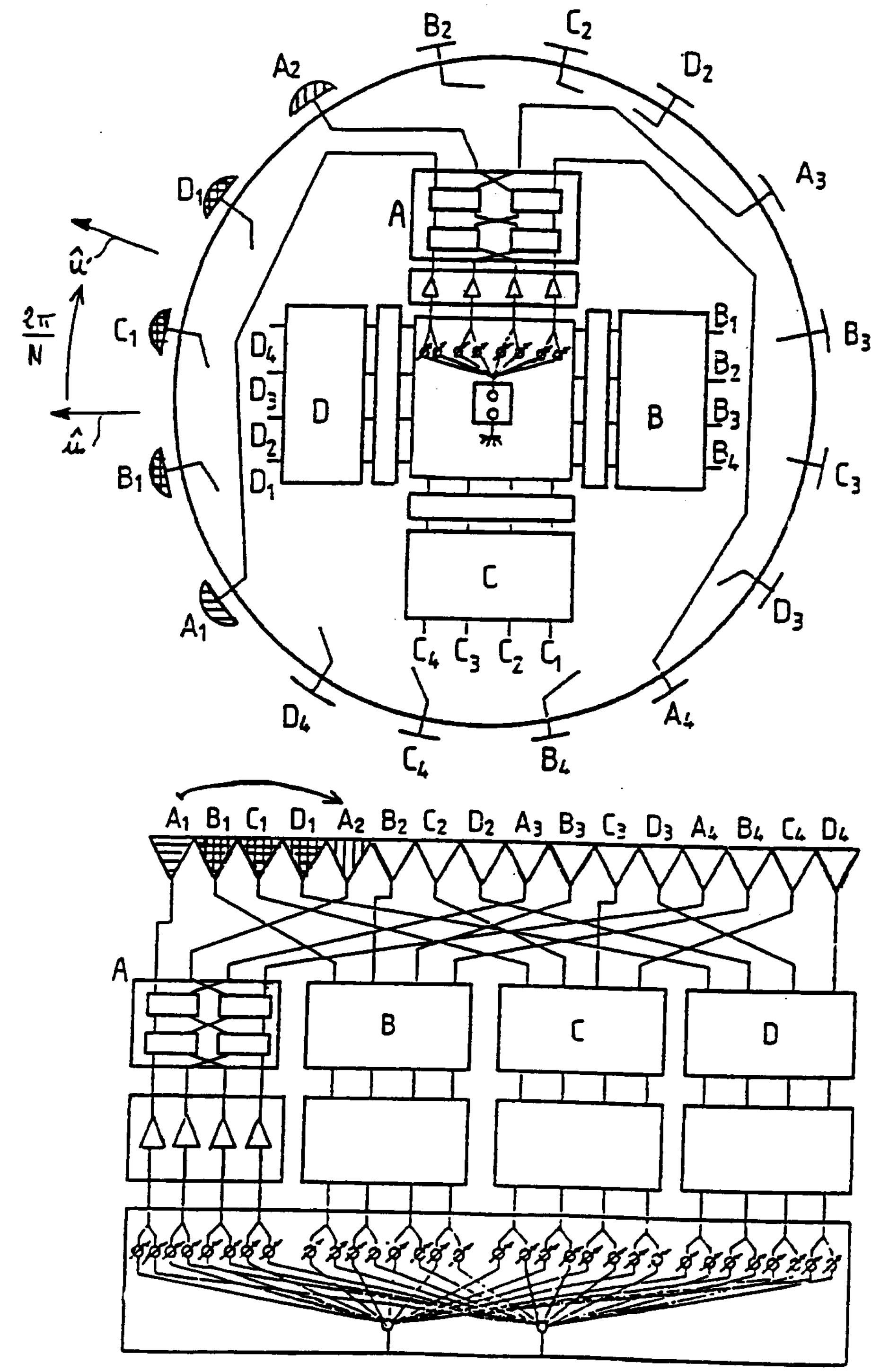

Figure 2.2-c: moving the beam by $\frac{2\pi}{N}$, thanks to phase-shifts δ_i applied on the i = 1 to 4 inputs of the matrix A

Reproduction interdite © ALCATEL ESPACE Reproduction forbidden

2.3 ADVANTAGES OF 3 X 3 MATRICES

It is well known in the literature ([6]), that nearly *uniform excitation of about one third of an array with circular symmetry* (circular, cylindrical, or conical array) *gives the best directivity.*

This can be achieved easily with an array fed by Nb (8 for example) Butler 3 x 3: by proper phase slope at the Butler inputs, we can concentrate the energy on one output for each Butler. By choosing properly these outputs, the power can be concentrated on Nb = N/3 adjacent R.E.

This is compliant with equal and constant amplitudes at the input of the Butler matrices, which allows to optimize the SSPAs' efficiency for the required output level.

Moreover, numerous computations made by ALCATEL ESPACE during W.P. 1200 has shown that the best gain and the lower P_{RF} to the radiating columns, compliant with EIRP are provided by 3 x 3 matrices, for a given total number of subarrays: for example, if N = 24n after the first optimisation run:

- Eight 3 x 3 matrices gives **19.94 dBi** gain, and P_{RF} = **-1.38 dBW**,
- Six 4 x 4 matrices gives 19.85 dBi gain, and P_{RF} = -0.13 dBW,
- Three 8 x 8 matrices gives 19.36 dBi gain, and P_{RF} = +2.88 dBW,
- Twelve 2 x 2 matrices gives 19.21 dBi gain, and P_{RF} = -0.98 dBW.

N.B.: The above gain is the most critical, for 62.3° elevation angle. It is specified to 20 dBi: a second optimisation run has given some tenths of dB more gain, **compliant only for eight 3 x 3 matrices.**

En if 3 x 3 matrices are less classical than 4 x 4 ones, designs have been already proposed (see reference 8), and measured (reference 7).

Reproduction interdite © ALCATEL ESPACE Reproduction forbidden

3. ELECTRICAL SPECIFICATIONS FOR THE 3 X 3 MATRICES

◊ whole specified bandwidth: 8025/8400 MHz

◊ Useful channels: 50 MHz centered around $f_1 = 8100$, $f_2 = 8200$, $f_3 = 8300$ MHz.

a) When feeding successively one of the three inputs:

- *The output amplitudes* must be theoretically equal; in fact, unbalance between the 3 x 3 = 9 paths of a given matrix *i*, and over all 8 matrices delivered, can be tolerated no more than ± 0.2 dB at a given frequency within the X whole bandwidth, w.r.t. the mean insertion loss $\bar{L} = (\Sigma L_n / N_b)$($L_n$ insertion loss averaged on the 9 paths of the matrix $_n$).
- *The transmission phases* towards outputs named A, B, C must be ideally:
  - $\varphi_o, \varphi_o, \varphi_o$ when input numbered 1 is excited,
  - $\varphi_o, \varphi_o + 120°, \varphi_o - 120°$ when input numbered 2 is excited,
  - $\varphi_o, \varphi_o - 120°, \varphi_o + 120°$ when input numbered 3 is excited.

φ_o is a fixed value (*reference* insertion phase) for a given frequency. Errors from these values must be no more than ± 5° at a given frequency over the whole bandwidth.

This is equivalent to specify the following transfer matrix [T]:

$$[T] = \begin{bmatrix} 1 & 1 & 1 \\ 1 & e^{j\frac{2\pi}{3}} & e^{-j\frac{2\pi}{3}} \\ 1 & e^{-j\frac{2\pi}{3}} & e^{j\frac{2\pi}{3}} \end{bmatrix} \cdot \frac{e^{j\varphi_o}}{\sqrt{3}}$$ Recall that [T] is defined by:

$$\begin{bmatrix} Sa \\ Sb \\ Sc \end{bmatrix} = [T] \begin{bmatrix} e1 \\ e2 \\ e3 \end{bmatrix}$$ with

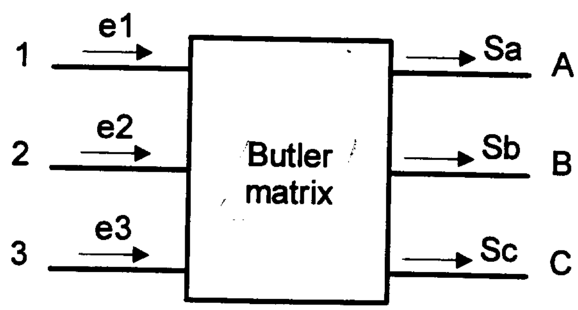

A, B, C is proposed for numbering the outputs, so that is separates clearly ports to be used as inputs or outputs (dispersion specifications are not the same).

b) φ_o can vary over all matrices by less than 50° peak-peak (these φ_o values should be measured with ± 1° accuracy, and will be compensated by ALCATEL in the phase-shifters commands).

Reproduction interdite © ALCATEL ESPACE Reproduction forbidden

c) **Mean insertion loss L_n** (over the 9 paths corresponding to any input and any output) must be less than 0.8 dB* over the whole bandwidth.

Amplitude unbalance: between |Sij| of the 9 paths < 0.4 dB peak-peak, within in each channel for a given frequency.

Frequency variation within each of the 3 channels, for any of the 9 paths of each matrix: less than 0.4 dB peak-peak.

d) **Group-delay variation** over each channel shall not vary by more than 6 ns peak-peak for each path of the 8 delivered matrices.

We recall that the group delay can be, either measured with a modern network analyser, or computed as $Tg = -\frac{1}{2\pi}\frac{d(\varphi_0)}{df}$.

e) **Interfaces**: For the breadboard of this contract, interfaces of the matrices must be SMA (or SSMA) female coaxial connectors.
For a FM type design, waveguide flanges could be accepted (which would mean active modules with waveguide interfaces, and connection to the radiating elements by means of flexible waveguides).

f) **Mass**: For one matrix, it should be less than 50 g*, excluding possible waveguide to coaxial transitions, specific for the breadboard.

g) **Matching**:

- Return loss < -14 dB at the inputs,
- Return loss < -18 dB at the outputs (because of the long cable lengths to the radiating rows, and system specification to avoid ripple within the useful band).

*** Remark:**

0.8 dB insertion loss and 50 g mass are worst case requirements, corresponding in fact not to the same technology (0.8 dB for microstrip; 50 g for waveguide). According to the chosen technology, one of these two parameters should provide an important margin versus the specification.

For coherence with SSPA's and proposed filters technology, matrices made from printed-circuits are preferred.

Reproduction interdite © ALCATEL ESPACE Reproduction forbidden

4. THERMAL SPECIFICATIONS

a) Temperature range in flight: -50, +50°C (TBC by WP 2600).

b) All electrical specifications of § 3 should be met on the whole temperature range.

c) For a flight-antenna, they should be verified for all matrices at the extreme and ambient temperature.

d) For the breadboard, only S_{21} temperature variations for the 9 paths of one matrix from ambient to the extreme temperatures, will be checked. It will be used to settle a typical error budget for a FM-type antenna, including temperature variations.
For minimizing such variations, substrates with low ε_r temperature variation should be chosen (such as Duroïd 6002) in the case of a planar technology.

Reproduction interdite © ALCATEL ESPACE Reproduction forbidden

5. MECHANICAL SPECIFICATIONS

For a flight model, typical vibrating levels will be deduced from mechanical analysis (WP 2600).

Vibrating tests are not required for the breadboard, but the design should be made in order to comply with usual levels for space equipment, to avoid new design in further study or program phases.

Reproduction interdite © ALCATEL ESPACE Reproduction forbidden

6. DELIVERING REQUIREMENTS

6.1 EXTERNAL PLATING

The metallic parts of the matrices should be plated (for example chemical oxydation) such as to avoid any surface aspect degradation during 5 years.

6.2 INSPECTION AND REVIEW OF SPECIFICATIONS COMPLIANCE

Before integration in the breadboard, ALCATEL should be called to a MTR (Manufacturing and Test Review), with notification to ESA:

- Visual inspection of the 8 matrices to be delivered,
- Review of the compliance matrix prepared by CASA, comparing measures made on all the Butler's with the specifications from § 3 to 5. For all quantitative specified parameters, this matrix will include min, mid, max values and standard deviation over the 8 Butler's.

6.3 MEASUREMENTS TO BE DELIVERED

a) **Amplitude and phase of S_{11}, S_{21} and S_{22}, and time-delays**, should be measured at ambient for the 9 paths of each matrix, and S_{21} at extreme temperatures for one matrix, with 3 markers at 8.1, 8.2, 8.3 GHz :

- curves over the whole bandwidth will be delivered in the report for the three first matrices (including probable first-run breadboard) and for that measured in temperature.
- for all matrices to avoid too many full pages in the report, the specified parameters will be delivered on a diskette, according to the "CS" format described in Annex A. For each parameter, values will be given with 25 MHz stepsfrom 8025 to 8400 (so 16 points).

b) One phase-shifter per channel is placed before each Butler input and can be used to compensate possible phase errors S_{ik} (for various i = input number), averaged over all outputs k. The matrices would probably present symmetry allowing exchange between "inputs" named i = 1, 2, 3 and "outputs" named k = A, B, C (according to the sense for the Tx mode of the antenna). In that case, for assembling the whole BFN, **the orientation of each matrix will be chosen** so that the 0°, +120° or -120° phase-shifts between outputs (when one input is excited) will be the most accurate.

Reproduction interdite © ALCATEL ESPACE Reproduction forbidden

6.4 MARKING

- A serial number should be marked on each Butler matrix: J = 1 to 8.
- Each port must be identified by: 1, 2, 3, A, B, C.

All these markings should remain readable during 5 years in the temperature range -50, +50°C.

Reproduction interdite © ALCATEL ESPACE Reproduction forbidden

7. BIBLIOGRAPHY (REFERENCES)

[1] Sheleg: A matrix-fed-circular array for continuous scanning (especially last § of first column, P. 2018). Proceedings of the IEEE, November 1968.

[2] Shelton, Hsiao: Reflective Butler Matrices (especially second § of second column, P. 652). IEEE A.P. Transactions, Sept 1979.

[3] Macnamara: Simplified procedures for Butler matrices incorporating 90° - hybrids or 180° - hybrids. IEE proceedings 134H1, February 1987.

[4] Lo, Lee: Antenna handbook (ed. VNR), chapter 19 § 6: cylindrical array feeds.

[5] Rudge and al: Handbook of antenna design (ed. Peter Perigrinus): chapters 11 and 12.

[6] Mailloux: Phased array antenna handbook (ed. Artech House): chapter 4 (especially figure 4.14).

[7] Roederer, Garcia, ML. Hernanz, Martin-Pascual: Six ports couplers for generalized Butler-like matrices (ESA workshop on advanced BFN - Nov. 1991).

[8] Roederer, Martin-Pascual: European patent 0.189 632.B1 (demand registration 91403242.0)

Reproduction interdite © ALCATEL ESPACE Reproduction forbidden

ANNEX A
CS FORMAT FOR DELIVERING
S-PARAMETERS FILES ON DISQUETTES

Proposed numbering of the ports of a 3 x 3 Butler matrix, compliant with the line NU of the CS file (see next page):

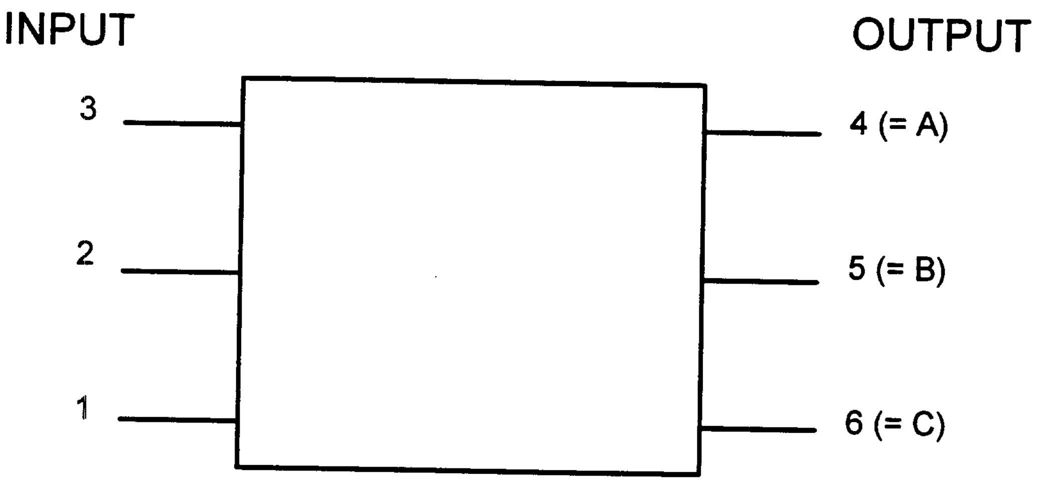

Reproduction interdite © ALCATEL ESPACE Reproduction forbidden

Notice explaining CS norm (only main passages are translated; other French terms are easy to understand)

Jul 09 15:17 1996 normecs.doc Page 1

```
c s . . .  -- as "Coefficient [S]"
==========

fichier question : cs.....fq

  Ce FICHIER prepare les donnees du fichier cs....
  Le fichier CS contient la matrice des parametres S d'un multipole.

  Si on considere un multipole a N portes,  -- N (or Np) ports
  pour chaque frequence de calcul, on retrouve dans le fichier
  cs.... la valeur des coefficients de la matrice S comme suit :

      QS11, QS12, .... , QS1N
      QS21, QS22, .... , QS2N
      ....
      QSN1, QSN2, .... , QSNN

  avec :
      QSij nombre complexe
      i,j  numerotation des portes du multipole


       SUITE  ??
  > SI OUI Aller en   1.
. . . . . . . . . . . . . . . . . . . . . . . . . . . . . . . . .

 1.

    ENTREE DES DONNEES DU FICHIER :
    -------------------------------

TI    titre du fichier CS.... ??
. . . . . . . . . . . . . . . . . . . . . . . . . . . . . . . . .

    DONNEES DESCRIPTIVES
    --------------------

NP    Nombre de portes du multipole  ??
. . . . . . . . . . . . . . . . . . . . . . . . . . . . . . . . .

    Numerotation des portes du multipole
    ------------------------------------
```

Jul 09 15:17 1996 normecs.doc Page 2

Numbering the ports begins at left-bottom corner and turns as the watch

avoids 2 kinds of numbers, "user number" ("nug") and "CS format numbering"

```
On donne ici la liste des portes du multipole en commencant par le coin
bas gauche et en se deplacant dans le sens des aiguilles d'une montre
   ex :
              n3=4     n4=3
               |        |
               |        |
         ******************
  n2=1------*                *-------- n5=7       *NB :les numeros se
            *                *                         rapportent a
  n1=2------*                *-------- n6=8            la numerotation
         ******************                             utilisateur.
                |      |                 <- figure A
                |      |
              n8=5   n7=6

  Ici les numeros des portes sont 2,1,4,3,7,8,6,5

NU      numeros des portes ?
. . . . . . . . . . . . . . . . . . . . . . . . . . . . . . . . .

    Orientation des portes du multipole :
    -------------------------------------

    par convention   ouest=1 , nord=2 , est=3 , sud=4

    de meme que precedement on donne l'orientation des portes
    en commencant par le coin bas gauche et en se deplacant dans
    le sens des aiguilles d'une montre .

    ex :
              2        2
              |        |
         ******************
  1 -----*                *-------- 3
         *                *                  <- figure B
  1 -----*                *-------- 3
         ******************
                  |
                  4

OP      orientations des portes ?
. . . . . . . . . . . . . . . . . . . . . . . . . . . . . . . . .

NC    Nom du multipole (8 caracteres max) ??
. . . . . . . . . . . . . . . . . . . . . . . . . . . . . . . . .
```

Reproduction interdite © ALCATEL ESPACE Reproduction forbidden

```
Jul 09 15:17 1996  normecs.doc Page 3


        DONNEES MATRICE S :
        -----------------

  2.

       ATTENTION : Les lignes FR , NS doivent se trouver par ordre
       croissant en frequence .
```

increasing frequency points

```
FR    Frequence  (MHz)  ??
. . . . . . . . . . . . . . . . . . . . . . . . .

       valeurs des coefficients de la matrice S

       Np lignes de 2*Np valeurs (complexes :
       QS11 , QS12 ,        ,QS1n
       QS21 , QS22 ,........,QS2n
       .........................
       QSn1 , QSn2 ,        ,QSnn
```

real part, imaginary part (for S_{11}), real part, imaginary part (for S_{12}), etc ...

```
NS        MATRICE S  ?
Reponse multiligne (Attention aux 2 blancs)
. . . . . . . . . . . . . . . . . . . . . . . . .

         AUTRE FREQUENCE (OUI/NON ??)
 > Si OUI Aller en   2.
. . . . . . . . . . . . . . . . . . . . . . . . .
```

Exemple of presentation (long because 2.5 MHz steps)

```
Jul 09 15:17 1996  csexemple.da Page 1

GA  cs0100.da        28--09--93  12::23::34
    fsacs            30-08-89  12::00::00
    fsacs5.pt
TIKUDRI SUP M.CONT. EL.DEL.=-733PS   (title)
NP .2000000E+01,              (how many ports? : 2 here)
NU .1000000E+01, .2000000E+01, (numbering ports : 1, 2, 3, .... Np)
OP .1000000E+01, .3000000E+01 (orientation of ports -> see fig. B p.21)
NCRX01 (name of the multipole)
FR .1400000E+05,
MS-.1436234E-01,-.5509949E-01, .7275772E-01,-.5626678E-02,   Re(S11), Im(S11) ---
   .7188797E-01,-.5882263E-02,-.3644562E-01,-.9993744E-01    Re(S21), Im(S21) ---
FR .1400250E+05,
MS-.2393723E-02,-.5330276E-01, .7297134E-01,-.5626678E-02,
   .7172394E-01,-.6011963E-02,-.3705597E-01,-.9906006E-01,
FR .1400500E+05,
MS .8045200E-02,-.4890060E-01, .7249832E-01,-.5462646E-02,
   .7143402E-01,-.5744934E-02,-.3687286E-01,-.9835815E-01,
FR .1400750E+05,
MS .8186340E-02,-.3849411E-01, .7260513E-01,-.5218506E-02,
   .7174301E-01,-.5336761E-02,-.3672791E-01,-.9750366E-01,
FR .1401000E+05,
MS .4615780E-02,-.3127098E-01, .7318878E-01,-.5142212E-02,
   .7143402E-01,-.5603790E-02,-.3662109E-01,-.9634399E-01,
FR .1401250E+05,
MS-.4322052E-02,-.2958488E-01, .7274246E-01,-.4699707E-02,
   .7158279E-01,-.4673004E-02,-.3686523E-01,-.9529877E-01,
FR .1401500E+05,
MS-.1160431E-01,-.3326607E-01, .7271576E-01,-.4878998E-02,
   .7166672E-01,-.4558563E-02,-.3668976E-01,-.9430695E-01,
FR .1401750E+05,
MS-.1031113E-01,-.3723907E-01, .7340240E-01,-.4993439E-02,
   .7206345E-01,-.4814148E-02,-.3674316E-01,-.9286499E-01,
FR .1402000E+05,
MS-.7619858E-02,-.4148865E-01, .7300949E-01,-.4531860E-02,
   .7186508E-01,-.4440308E-02,-.3678894E-01,-.9147644E-01,
FR .1402250E+05,
MS-.2759933E-02,-.4274750E-01, .7332993E-01,-.4386902E-02,
   .7180786E-01,-.3715515E-02,-.3687286E-01,-.9054565E-01,
FR .1402500E+05,
MS-.3376007E-03,-.3922653E-01, .7323074E-01,-.4283905E-02,
   .7231522E-01,-.4047394E-02,-.3684998E-01,-.8940887E-01,
FR .1402750E+05,
MS-.2403259E-03,-.3585052E-01, .7367325E-01,-.4119873E-02,
   .7231140E-01,-.3883362E-02,-.3736115E-01,-.8861542E-01,
FR .1403000E+05,
MS-.4766464E-02,-.3195000E-01, .7376480E-01,-.4531860E-02,
   .7237244E-01,-.3372192E-02,-.3768921E-01,-.8815002E-01,
FR .1403250E+05,
MS-.5302429E-02,-.2874947E-01, .7380676E-01,-.5050659E-02,
   .7271957E-01,-.3978729E-02,-.3787994E-01,-.8799744E-01,
FR .1403500E+05,
MS-.8008957E-02,-.2979279E-01, .7420349E-01,-.4589081E-02,
   .7244110E-01,-.3650665E-02,-.3873444E-01,-.8840942E-01,
FR .1403750E+05,
MS-.8419037E-02,-.2924538E-01, .7332230E-01,-.4791260E-02,
   .7289505E-01,-.3513336E-02,-.3987122E-01,-.8896637E-01,
```

for each frequency

see fig. A p.21

```
Jul 09 15:17 1996  csexemple.da Page 2

FR .1404000E+05,
MS-.1436234E-01,-.2999115E-01, .7360077E-01,-.5363464E-02,
   .7304382E-01,-.3841400E-02,-.4176331E-01,-.8921051E-01,
FR .1404250E+05,
MS-.1587677E-01,-.3268814E-01, .7369995E-01,-.5325317E-02,
   .7292557E-01,-.4280090E-02,-.4383850E-01,-.8971405E-01,
FR .1404500E+05,
MS-.1940155E-01,-.3295326E-01, .7312393E-01,-.5062103E-02,
   .7330704E-01,-.3841400E-02,-.4559326E-01,-.8941650E-01,
FR .1404750E+05,
MS-.2150726E-01,-.3169060E-01, .7330322E-01,-.5172729E-02,
   .7326889E-01,-.4055023E-02,-.4763031E-01,-.8908081E-01,
FR .1405000E+05,
MS-.2389908E-01,-.2980423E-01, .7329559E-01,-.4516602E-02,
   .7302856E-01,-.3295898E-02,-.4919434E-01,-.8815765E-01,
FR .1405250E+05,
MS-.2872086E-01,-.2735519E-01, .7295227E-01,-.4207611E-02,
   .7274246E-01,-.3787994E-02,-.5056000E-01,-.8712006E-01,
FR .1405500E+05,
MS-.3372192E-01,-.3664017E-01, .7301331E-01,-.4234314E-02,
   .7259369E-01,-.3551483E-02,-.5194855E-01,-.8578491E-01,
FR .1405750E+05,
MS-.3906250E-01,-.4356766E-01, .7274628E-01,-.3868103E-02,
   .7289886E-01,-.3288269E-02,-.5268860E-01,-.8393097E-01,
FR .1406000E+05,
MS-.3361511E-01,-.5730820E-01, .7312012E-01,-.3856659E-02,
   .7290268E-01,-.3337860E-02,-.5326080E-01,-.8195496E-01,
FR .1406250E+05,
MS-.2080917E-01,-.6109238E-01, .7325363E-01,-.3761292E-02,
   .7245255E-01,-.3284454E-02,-.5351257E-01,-.8010101E-01,
FR .1406500E+05,
MS-.7568359E-02,-.6178665E-01, .7307816E-01,-.3726959E-02,
   .7260513E-01,-.2994537E-02,-.5361176E-01,-.7806396E-01,
FR .1406750E+05,
MS .1289370E-02,-.5265236E-01, .7302475E-01,-.3574371E-02,
   .7288361E-01,-.2849579E-02,-.5367279E-01,-.7608032E-01,
FR .1407000E+05,
MS .3376010E-02,-.4003525E-01, .7282257E-01,-.3147125E-02,
   .7312012E-01,-.2391815E-02,-.5381775E-01,-.7406616E-01,
FR .1407250E+05,
MS-.2241135E-02,-.3058624E-01, .7318115E-01,-.3738403E-02,
   .7341003E-01,-.2334595E-02,-.5410004E-01,-.7220459E-01,
FR .1407500E+05,
MS-.9119034E-02,-.2991295E-01, .7375336E-01,-.3383636E-02,
   .7368851E-01,-.2487183E-02,-.5420685E-01,-.6983566E-01,
FR .1407750E+05,
MS-.1733017E-01,-.3627396E-01, .7381058E-01,-.3192902E-02,
   .7379532E-01,-.2861023E-02,-.5455017E-01,-.6813431E-01,
FR .1408000E+05,
MS-.1752663E-01,-.3975487E-01, .7373047E-01,-.3726959E-02,
   .7385635E-01,-.3341675E-02,-.5453110E-01,-.6630707E-01,
FR .1408250E+05,
MS-.1186562E-01,-.4331017E-01, .7328033E-01,-.3505707E-02,
   .7408905E-01,-.3349304E-02,-.5435562E-01,-.6422043E-01,
FR .1408500E+05,
MS-.8516312E-02,-.4075623E-01, .7400894E-01,-.3471375E-02,
```

Reproduction interdite © ALCATEL ESPACE Reproduction forbidden

```
Jul 09 15:17 1996  csexemple.da Page 3

    .7349777E-01,-.3608704E-02,-.5435944E-01,-.6243515E-01,
 FR .1408750E+05,
 MS-.8420944E-02,-.3292847E-01, .7366180E-01,-.3475189E-02,
    .7368851E-01,-.3658295E-02,-.5409241E-01,-.6096268E-01,
 FR .1409000E+05,
 MS-.1199913E-01,-.2952003E-01, .7357407E-01,-.3543854E-02,
    .7352066E-01,-.3116608E-02,-.5339050E-01,-.5923080E-01,
 FR .1409250E+05,
 MS-.1730728E-01,-.2626228E-01, .7316589E-01,-.3875732E-02,
    .7330704E-01,-.3757477E-02,-.5258942E-01,-.5868912E-01,
 FR .1409500E+05,
 MS-.2009964E-01,-.2949333E-01, .7280731E-01,-.3295898E-02,
    .7357788E-01,-.2929688E-02,-.5131149E-01,-.5767441E-01,
 FR .1409750E+05,
 MS-.2052116E-01,-.3480721E-01, .7340240E-01,-.3170013E-02,
    .7371521E-01,-.3116608E-02,-.5030823E-01,-.5726624E-01,
 FR .1410000E+05,
 MS-.2057266E-01,-.3775406E-01, .7352448E-01,-.3597260E-02,
    .7394791E-01,-.3299713E-02,-.4962158E-01,-.5714417E-01,
 FR .1410250E+05,
 MS-.1807785E-01,-.3890800E-01, .7334137E-01,-.3334045E-02,
    .7371902E-01,-.3433228E-02,-.4842758E-01,-.5709839E-01,
 FR .1410500E+05,
 MS-.1634789E-01,-.3920174E-01, .7332230E-01,-.3215790E-02,
    .7349777E-01,-.2822876E-02,-.4760742E-01,-.5785751E-01,
 FR .1410750E+05,
 MS-.1768684E-01,-.3495789E-01, .7337189E-01,-.2819061E-02,
    .7302094E-01,-.3273010E-02,-.4704666E-01,-.5820465E-01,
 FR .1411000E+05,
 MS-.1971054E-01,-.3178406E-01, .7331085E-01,-.3189087E-02,
    .7357788E-01,-.2830505E-02,-.4734039E-01,-.5926514E-01,
 FR .1411250E+05,
 MS-.2680206E-01,-.3284836E-01, .7334518E-01,-.2735138E-02,
    .7366943E-01,-.3070831E-02,-.4761124E-01,-.5921936E-01,
 FR .1411500E+05,
 MS-.3720856E-01,-.3425217E-01, .7348633E-01,-.2059937E-02,
    .7354355E-01,-.2861023E-02,-.4820633E-01,-.5943298E-01,
 FR .1411750E+05,
 MS-.4231262E-01,-.4219055E-01, .7332230E-01,-.2155304E-02,
    .7270432E-01,-.2811432E-02,-.4894638E-01,-.5878448E-01,
 FR .1412000E+05,
 MS-.4267883E-01,-.5455399E-01, .7356644E-01,-.2357483E-02,
    .7346344E-01,-.2376556E-02,-.4984665E-01,-.5788422E-01,
 FR .1412250E+05,
 MS-.3796387E-01,-.6104660E-01, .7378387E-01,-.2502441E-02,
    .7367706E-01,-.1956940E-02,-.5089951E-01,-.5699158E-01,
 FR .1412500E+05,
 MS-.2594757E-01,-.6492615E-01, .7368088E-01,-.2670288E-02,
    .7344818E-01,-.2712250E-02,-.5149078E-01,-.5577469E-01,
 FR .1412750E+05,
 MS-.1521301E-01,-.5892181E-01, .7350540E-01,-.2403259E-02,
    .7335281E-01,-.2368927E-02,-.5239105E-01,-.5437469E-01,
 FR .1413000E+05,
 MS-.5287170E-02,-.4963684E-01, .7318878E-01,-.2559662E-02,
    .7326889E-01,-.2403259E-02,-.5309296E-01,-.5248260E-01,
 FR .1413250E+05,
```

```
Jul 09 15:17 1996  csexemple.da Page 4

MS-.6660461E-02,-.4044342E-01, .7309723E-01,-.2323151E-02,
   .7334518E-01,-.2494812E-02,-.5382538E-01,-.5042267E-01,
FR .1413500E+05,
MS-.1105118E-01,-.3639984E-01, .7339096E-01,-.2269745E-02,
   .7366180E-01,-.2613068E-02,-.5389404E-01,-.4888153E-01,
FR .1413750E+05,
MS-.1546097E-01,-.3588104E-01, .7303619E-01,-.2155304E-02,
   .7334518E-01,-.2437592E-02,-.5393982E-01,-.4668427E-01,
FR .1414000E+05,
MS-.1716614E-01,-.3980637E-01, .7334900E-01,-.2304077E-02,
   .7362747E-01,-.2788544E-02,-.5418396E-01,-.4454041E-01,
FR .1414250E+05,
MS-.1462555E-01,-.3942108E-01, .7320786E-01,-.1953125E-02,
   .7265472E-01,-.2628326E-02,-.5346680E-01,-.4288483E-01,
FR .1414500E+05,
MS-.9246826E-02,-.3602982E-01, .7342529E-01,-.1800537E-02,
   .7314301E-01,-.2643585E-02,-.5309296E-01,-.4087830E-01,
FR .1414750E+05,
MS-.1250267E-01,-.2960014E-01, .7346344E-01,-.1914978E-02,
   .7302475E-01,-.2311707E-02,-.5236435E-01,-.3886032E-01,
FR .1415000E+05,
MS-.1688576E-01,-.2434349E-01, .7369614E-01,-.2075195E-02,
   .7321930E-01,-.2342224E-02,-.5147552E-01,-.3713608E-01,
FR .1415250E+05,
MS-.2598572E-01,-.2268982E-01, .7304764E-01,-.1903534E-02,
   .7287598E-01,-.2532959E-02,-.5043030E-01,-.3527451E-01,
FR .1415500E+05,
MS-.3220558E-01,-.2728081E-01, .7304764E-01,-.2506256E-02,
   .7268524E-01,-.2727509E-02,-.4901886E-01,-.3377914E-01,
FR .1415750E+05,
MS-.3233337E-01,-.3157806E-01, .7302475E-01,-.1598358E-02,
   .7257462E-01,-.2437592E-02,-.4724121E-01,-.3174591E-01,
FR .1416000E+05,
MS-.2785492E-01,-.3860474E-01, .7342529E-01,-.1766205E-02,
   .7238388E-01,-.2288818E-02,-.4548645E-01,-.3142548E-01,
FR .1416250E+05,
MS-.2412415E-01,-.4030609E-01, .7362366E-01,-.1731873E-02,
   .7262421E-01,-.1949310E-02,-.4375458E-01,-.3048706E-01,
FR .1416500E+05,
MS-.1842880E-01,-.3504562E-01, .7334518E-01,-.1403809E-02,
   .7239914E-01,-.1266479E-02,-.4178619E-01,-.3005219E-01,
FR .1416750E+05,
MS-.1597595E-01,-.3100204E-01, .7314682E-01,-.1338959E-02,
   .7257462E-01,-.1186371E-02,-.4003906E-01,-.3002930E-01,
FR .1417000E+05,
MS-.2071381E-01,-.2719498E-01, .7323074E-01,-.1689911E-02,
   .7229614E-01,-.1583099E-02,-.3844452E-01,-.3018188E-01,
FR .1417250E+05,
MS-.2448654E-01,-.2531815E-01, .7357025E-01,-.1499176E-02,
   .7284164E-01,-.1621246E-02,-.3691864E-01,-.3076172E-01,
FR .1417500E+05,
MS-.3094864E-01,-.2922821E-01, .7313919E-01,-.1483917E-02,
   .7265091E-01,-.1384735E-02,-.3542328E-01,-.3145599E-01,
FR .1417750E+05,
MS-.3829193E-01,-.3427887E-01, .7275009E-01,-.1384735E-02,
   .7277298E-01,-.1281738E-02,-.3449249E-01,-.3259277E-01,
```

file end (always a complete $MS = \mathrm{Re}(S_{ij}), \mathrm{Im}(S_{ij})$ set)

Reproduction interdite © ALCATEL ESPACE Reproduction forbidden

CONFORMAL ARRAY ANTENNA	AES 96-32058/ASP-139		
	Estec Contract 11698/95NL/SB		
	DATE : 11/09/96	ED/REV : 1/-	PAGE : 1 / 10

Titre / Title

SPECIFICATIONS FOR THE DSN BAND REJECTION FILTERS

Rédigé par / Written by	Responsabilité / responsibility	Date	Signature
G. CAILLE	Technical Manager of the Contract	17/9/96	GCaille
Vérifié par / Verified by			
Approbation / Approved			

ALCATEL
TELECOM

Reproduction interdite © ALCATEL ESPACE Reproduction forbidden

ENREGISTREMENT DES EVOLUTIONS / CHANGE RECORD

ED./ REV.	DATE	AUTORISATION AUTHORIZATION	§: DESCRIPTION DES EVOLUTIONS §: CHANGE RECORD	REDACTEUR AUTHOR
1/-	11/09/96		First Issue	G. CAILLE

Reproduction interdite © ALCATEL ESPACE Reproduction forbidden

TABLE OF CONTENTS

Reproduction interdite © ALCATEL ESPACE Reproduction forbidden

1. FILTERING REQUIREMENTS FOR THE FM-TYPE CONFORMAL ANTENNA

a) **The antenna mission** is to radiate three independently electronically steerable beams from LEO observation platforms to three ground stations, which will process the data gathered on-board.

The overall bandwidth allocated for this mission is 8025 - 8400 MHz.

As specified in the chapter 1 of this report (RF System analysis), for each beam is allocated a 50 MHz channel, centered respectively around following carriers:

- 8100 MHz for beam number 1
- 8200 MHz for beam number 2
- 8300 MHz for beam number 3

The Power Flux Density (PFD) on earth must comply with UIT-R requirements. As result of the RF system analysis, this is possible with following filtering (see figure 1-a):

- **3 Band-Pass Filters (BPF),** one for each channel, at the output of the carrier modulators; in fact, they are not part of the semi-active antenna, so not specified in this document,
- **24 Band-Stop Filters (BSF),** in front of each radiating subarray, to reject the 8400-8450 MHz band, allocated to Deep Space Network (DSN) ground stations, which could be located near to those receiving the data from the LEO platforms.

The DSN stations must not at all be perturbated by the antenna radiation. As it is close to the three carriers, intermodulation products (IMP) generated by the 24 SSPA's located inside the antenna, could fall in this band.

b) As a compromise with lowering the amplifiers efficiency with too stringent linearity requirements, **the C/I of the amplifiers has been specified at 28 dB, and the rejection of the BSF at -17 dB.**

However the last value has been computed with the minimum transmitted power from the amplifiers; this one can vary somewhat, due to dispersions between them, even after adjustment and to variation with antenna temperature.

Reproduction interdite © ALCATEL ESPACE Reproduction forbidden

At the beginning of the amplifiers study, two options are considered concerning the power control of the amplifiers:

1. Either precise thermal compensation is provided inside the active modules or by means of the controller: that means amplitude and phase control devices, commanded from temperature. In that case, transmitted power can be kept constant within 1 dB range over all the 24 amplifiers and the whole temperature range. **So the filter rejection must be 18 dB** = 17 dB for minimum transmitted power + 1 dB possible variation of this power.
2. Or the thermal design insures that temperatures are kept very similar over all the amplifiers, and the electrical design using MMIC technology guaranties quasi identical ΔG/ΔT (gain variation coefficient, with temperature) over all SSPA's. So no thermal compensation is necessary (which induces cheaper antenna), but transmitted power can vary by up to 3 dB within the temperature range (and over all amplifiers), added to 1 dB maximum dispersion between modules at ambient

   Then, to keep the same PFD on ground, **the filter rejection must be increased to 21 dB** = 17 dB for minimum transmitted power +1 dB dispersion, +3 dB possible variation of this power within the temperature range.

c) **Remark**: Inside this limited funding contract, only design and simulation of the BSF filter is provided, compatible with its implementation behing the 24 radiating columns of the truncated conical antenna.

Reproduction interdite © ALCATEL ESPACE Reproduction forbidden

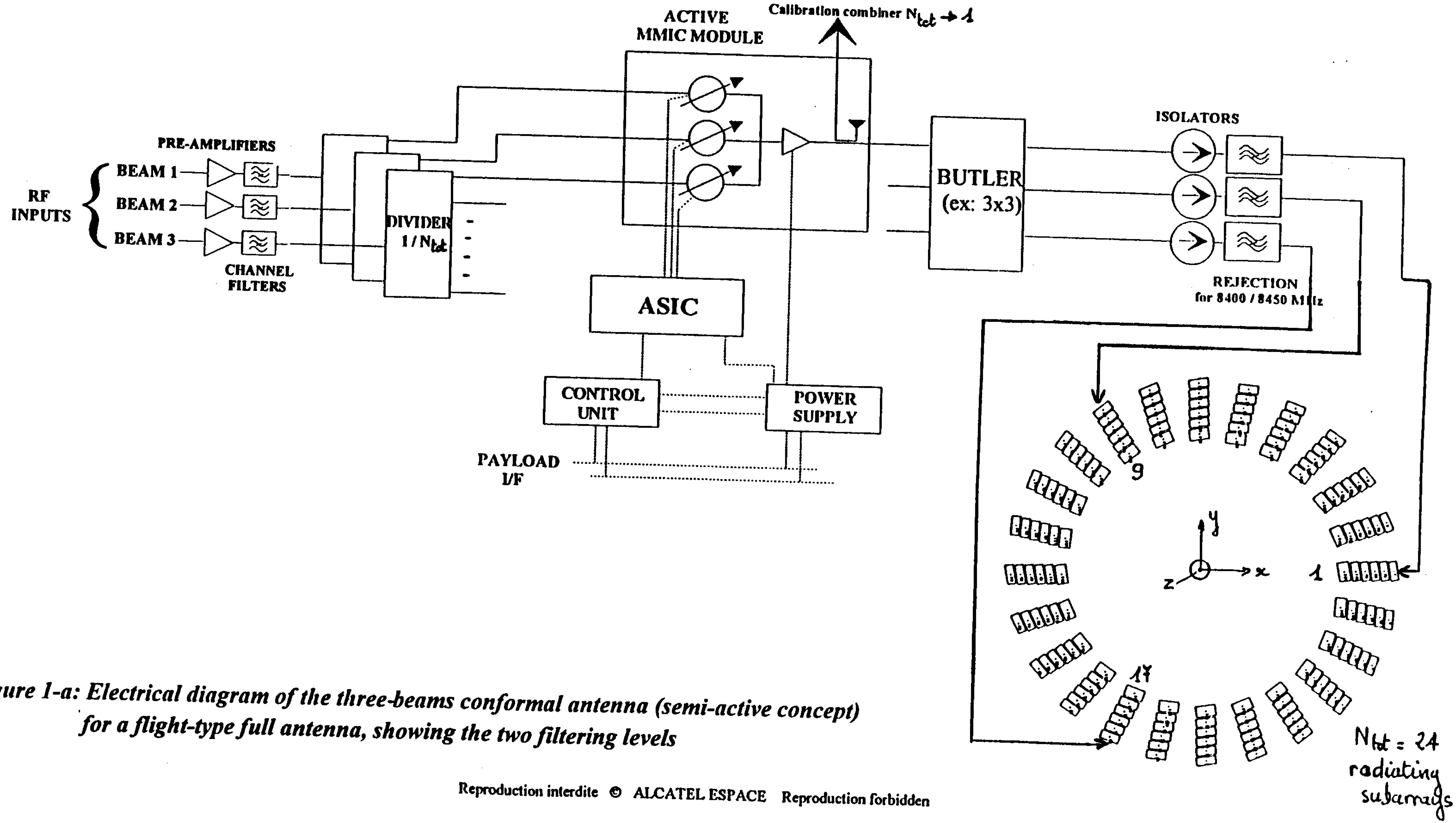

Figure 1-a: Electrical diagram of the three-beams conformal antenna (semi-active concept) for a flight-type full antenna, showing the two filtering levels

Reproduction interdite © ALCATEL ESPACE Reproduction forbidden

2. ELECTRICAL SPECIFICATIONS FOR THE 24 BAND STOP FILTERS

2.1 AMPLITUDE TRANSFER FUNCTION

$|S_{21}|$ (f) must comply with the following mask, where RL = rejection level, relative to maximum level "0 dB", must be equal to:

- 18 dB as a minimum;
- 21 dB as a goal, to comply with the second option of § 1-b (no thermal compensation inside the active modules). It will be checked by simulation of perturbation due to manufacturing tolerances, if this value is reachable without adding new poles, so increasing significantly the filter loss.

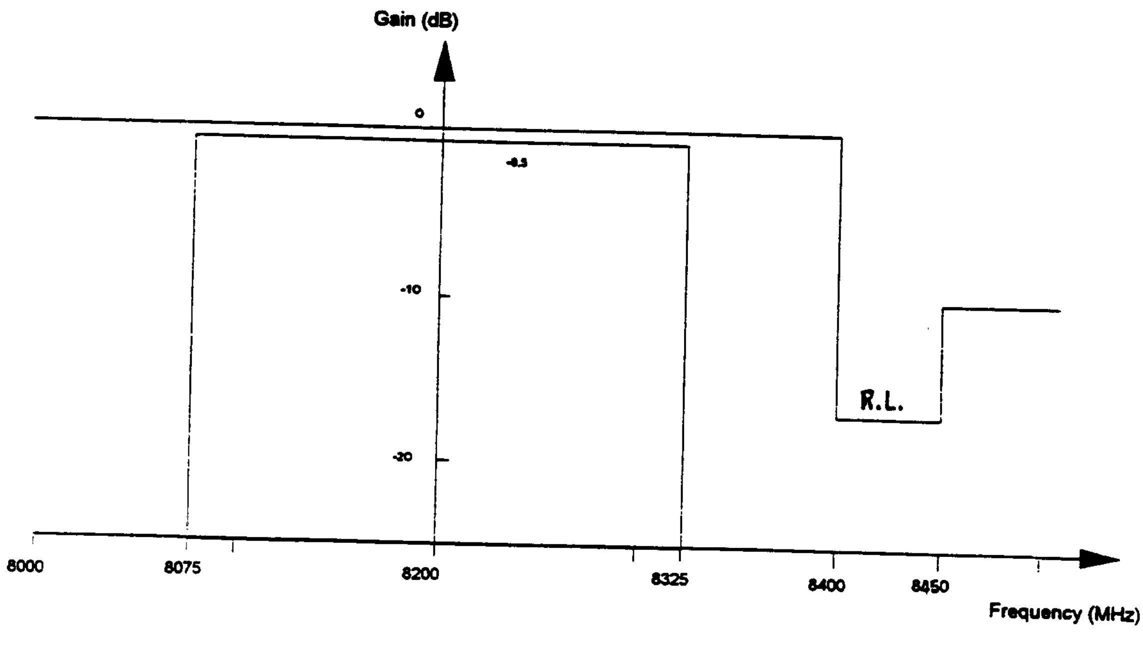

Figure 2.1-a: Rejection filter amplitude mask

Reproduction interdite © ALCATEL ESPACE Reproduction forbidden

2.2 In-band insertion loss

The 0 dB level of the previous mask must correspond to a loss lower than 0.7 dB, for all filters.

Remark: mask + specification 2.2 $\Leftrightarrow$ L - 0.5 dB < $|S_{21}|$ < L, with L > -0.7 dB

2.3 Amplitude ripple

Within each useful channel, 50 MHz wide (see § 1-a), $|S_{21}|$ should not vary by more than 0.3 dB peak-peak for all filters.

2.4 Matching

On the whole bandwidth and for all filters:

- $|S_{11}| \leq -14$ dB (isolators at the input), $|S_{22}| \leq -18$ dB at outputs connected to the radiating columns.

2.5 Group-delay variation

Within each useful channel, 50 MHz wide, the group-delay through the filter must not vary by more than 3 ns peak-peak.

2.6 Amplitude unbalance

Over the 24 filters to be integrated on a FM-type antenna, the $|S_{21}|$ must not vary, for any given frequency within the three useful channels, by more than 0.4 dB peak-peak.

2.7 Phase unbalance

In the same conditions than § 2.6, phase unbalance must not be more than 5° peak-peak: as they are after the Butler matrices, they cannot be compensated by the phase shifters control. If dispersions were larger, they should be compensated by adjustement of the lengths of the various coaxial cables connecting the outputs of the Butler matrices to the isolators/filters/radiating columns.

Reproduction interdite © ALCATEL ESPACE Reproduction forbidden

3. THERMAL SPECIFICATIONS

a) Temperature range in flight: -50, +50° C (TBC by WP 2600).

b) All electrical specifications of § 2 should be met on the whole temperature range.

c) For a flight-antenna, they should be verified for all paths at the extreme and ambient temperature.

d) For minimizing temperature variations, if the filters are implemented in microstrip technology, a substrate with low ε_r temperature variation should be chosen (such as Duroïd 6002 or TMM 10i from Rogers Corporation).

Reproduction interdite © ALCATEL ESPACE Reproduction forbidden

4. MECHANICAL SPECIFICATIONS

a) Mass

To minimize the mass of the FM-type antenna, preferential option is to implement the filters in microtrip technology, just behind the radiating subarrays, with direct connection to them (by means of a short coaxial pin, or coupling through a slot).

In that case, mass of each filter should be less than 3g, excluding that of the support: this would be the same that the radiating column support, so included in the radiating surface mass budget.

b) Vibration

For a flight model, typical vibration levels will be deduced from mechanical analysis (WP 2600).

No filter will be included in the breadboard, but the design should be made in order to comply with usual levels, to avoid new design in further study or program phases.

Reproduction interdite © ALCATEL ESPACE Reproduction forbidden

Titre / Title

SPECIFICATIONS FOR THE RADIATING SUBARRAYS

Rédigé par / Written by	Responsabilité / responsibility	Date	Signature
G. CAILLE	Technical Manager of the Contract		
Vérifié par / Verified by			
Approbation / Approved			

ALCATEL TELECOM

Reproduction interdite © ALCATEL ESPACE Reproduction forbidden

ENREGISTREMENT DES EVOLUTIONS / CHANGE RECORD

ED./ REV.	DATE	§ CONCERNES CONCERNED §	§: DESCRIPTION DES EVOLUTIONS §: CHANGE RECORD	REDACTEUR AUTHOR
1/-	14/08/96		First Issue	G. CAILLE

Reproduction interdite © ALCATEL ESPACE Reproduction forbidden

SUMMARY

Reproduction interdite © ALCATEL ESPACE Reproduction forbidden

1. GENERAL

a) The unit radiator is a double patch inside a double level cavity, providing good circular polarization over a wide range, with only one feeding link.

It has already been described in Chapter 3 (p. 3.13 and 3.14).

b) The architecture of the subarray has been chosen after numerous optimizations and comparison between the performances of the whole pseudo-conical antenna with various parameters:

- straight of folded subarrays,
- made of 4, 6 or 8 patches.

This analysis made during W.P. 1200 has led to choose the subarray described in § 2.

Reproduction interdite © ALCATEL ESPACE Reproduction forbidden

2. DESCRIPTION OF THE SUBARRAY

It is fitted to the truncated conical profile described in figure 2-a:

- It is made of 6 unit radiators.
- Starting from larger diameter of the truncated cone, the 5 first patches are inclined by 25° from the 2 axis (pointing towards nadir), and the last by 35°.

- To provide good stability over the 8025 - 8400 bandwidth, a parallel feeding with nearly equal length lines has been chosen (see example figure 2-b).
- The relative excitations of the patches can be optimized thanks to following parameters:
  - impedances of the lines derive the amplitude law: uniform excitation is easier, because all lines located after the dividing tees have the same width.
  - lengths of feeding lines from the port of the subarray derive the phase law, taking into account possible rotations of the patches, as compromise between sequential rotation which improves the pattern symmetry and the cross-polarization ratio on one hand, lay-out and phasing constraints on the other hand.

Reproduction interdite © ALCATEL ESPACE Reproduction forbidden

H_{cone}= 146.72 mm
R_{sup}= 175.94 mm
N_{tot}= 24
N_{ER}= 6
N_B = 8
N=3
β=25°/25°/25°/25°/25°/35°
d_{elev}= 27.42 mm (0.75 λ)
d_{az1}= 44.80 mm (1.23 λ)
d_{az2}= 41.75 mm (1.14 λ)
d_{az3}= 38.70 mm (1.06 λ)
d_{az4}= 35.65 mm (0.98 λ)
d_{az5}= 32.60 mm (0.89 λ)
d_{az6}= 29.00 mm (0.79 λ)

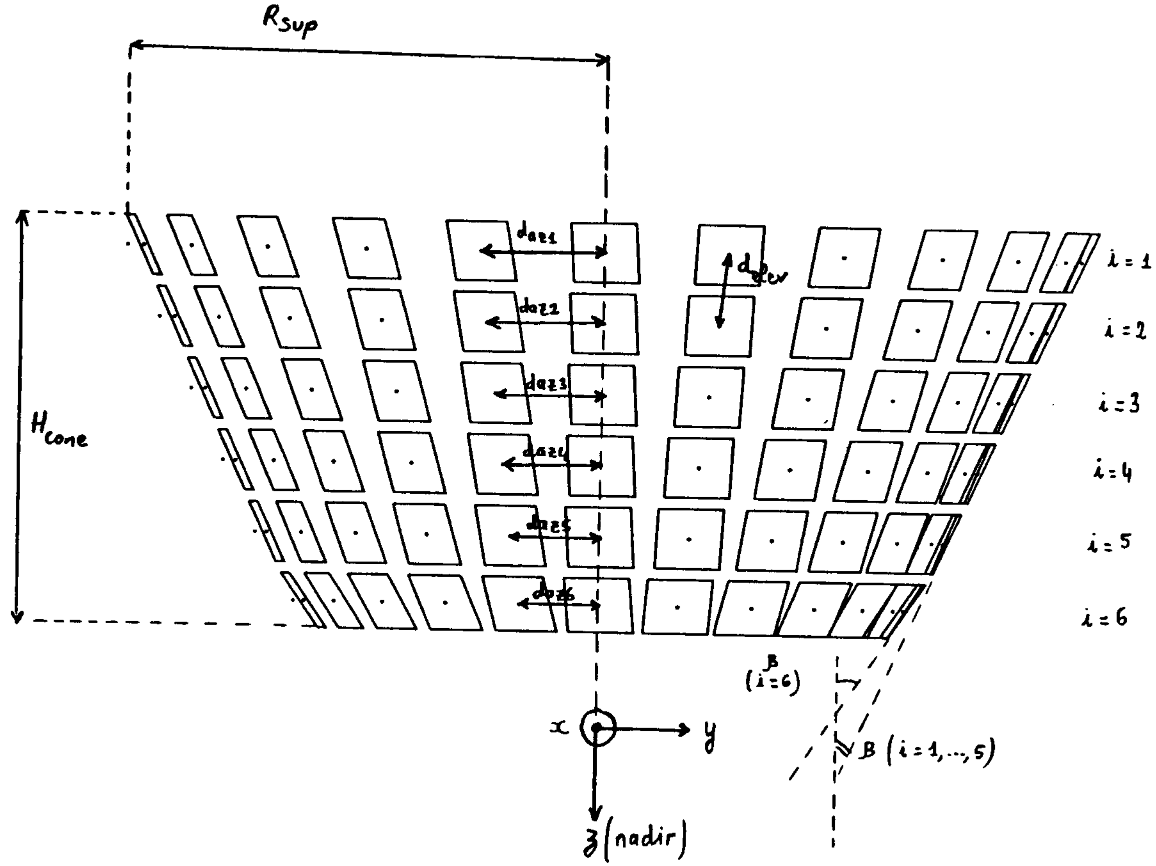

Figure 2-a: Geometry of the truncated cone made of 24 subarrays

Reproduction interdite © ALCATEL ESPACE Reproduction forbidden

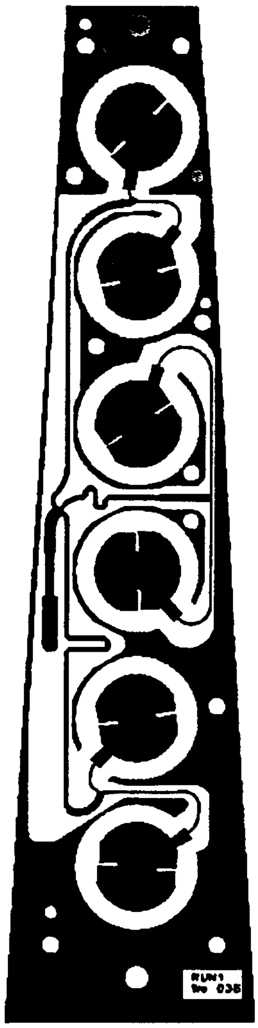

Figure 2-b: Typical implementation of a radiating subarray: feeding lines and driving patches in the lower triplate level

Reproduction interdite © ALCATEL ESPACE Reproduction forbidden

3. ELECTRICAL SPECIFICATIONS

a) **Matching:** S_{11} < -14 dB from 8025 to 8400 MHz

b) As a result of the optimization of the gain of the pseudo-conical antenna over the coverage, the ideal relative excitations between the 6 patches are given in the following table, including phase-shift induced by the patch rotation:

i	Ai (dB)	φi (degree)	β (in °)
1	-0.23	-10	25
2	-0.27	32	25
3	0	-25	25
4	-0.13	0	25
5	-0.23	-80	25
6	-0.27	-116	35

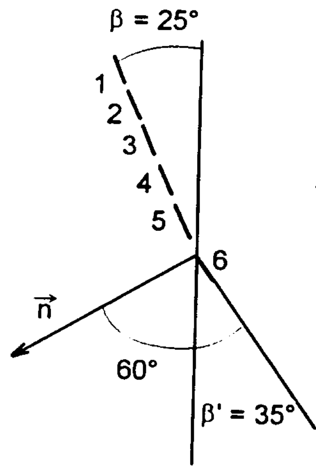

c) Difference between ideal excitations and the ones provided by the feeding lines, simulated by Academy, should not be more than ± 0.7 dB and ± 10° within the whole bandwidth.

d) As measurement of actual excitation of the patches is not precise, the elevation cut of the pattern E(θ') (measured at 8100, 8200 and 8300 MHz) of a subarray should be close to the theoretical value $E_{th}(\theta')$, computed from the ideal excitations:

$\| E(\theta')| - | E_{th}(\theta') \| < +1$ dB, for each critical θ' ,if |E| are directivities in dBi;

$|\text{ang}\,[E(\theta')] - \text{ang}\,[E_{th}(\theta')]| < 20°$, for each critical θ'

Remark: θ' and Ø are the classical angles in spherical coordinates, but referred to the subarray normal, which is inclined by 60° from the nadir direction.

e) **Dispersions**

* The gain of each subarray will be measured by comparison with a standard horn, in 2 most critical directions θ' = 0° and -60° in the longitudinal plane of the subarray: it should be comprised between G_{th} - 0.3 dB and G_{th} + 0.6 dB, if G_{th} is the theoretical gain, computed from:

  - the directivity of the pattern computed from the ideal excitations
  - decreased by 0.95 dB loss predicted (effect of the dispersion between columns is not taken into account in this measurement).

Reproduction interdite © ALCATEL ESPACE Reproduction forbidden

* The elevation and azimuth cuts of 4 subarrays will be measured and should vary from the theoretical computed pattern by no more than ± 1 dB, for critical θ', for -60° < θ' < +2.3° for the elevation cut and |Ø'| < 30° in the plane normal to the previous.
  The amplitude and phase requirement can be multiplied by 1.5 for 30° < Ø' < 60°, and multiplied by 2 for 60° < Ø' < 90°.

f) **Frequency variation :** The gain variation (measured for θ' = 0° and -60°) must not vary by more than 0.3 dB peak peak within each 50 MHz wide-channel.

* The transmission phases for the same angles should not vary by more than 10° peak-peak among the various subarrays.

Reproduction interdite © ALCATEL ESPACE Reproduction forbidden

4. THERMAL SPECIFICATIONS

g) Temperature range in flight: -50, +50°C (TBC by W.P. 2600).

h) Electrical specifications of § 3-a) and 3-c) should be met on the whole temperature range (pattern and gain measurement in temperature are too difficult).

i) For a flight-antenna, matching specification should be checked for all subarrays at the extreme and ambient temperature.

j) For the breadboard, it will be checked for only 3 of them, because of the difficulty of matching measurements in temperature and good reproducibility guaranteed by compliance to dispersion specifications § 3-e.
For minimizing such variations, substrates with low ε_r, temperature variation should be chosen.

Reproduction interdite © ALCATEL ESPACE Reproduction forbidden

5. MECHANICAL SPECIFICATIONS

a) Mass

The mass of a radiating subarray, self-supporting, should be less than 90 g.

b) Vibration

For a flight model, typical vibrating levels will be deduced from mechanical analysis (W.P. 2600).

Vibrating tests are not required for the breadboard, but the design should be made in order to comply with usual level, to avoid new design in further study or program phases.

Reproduction interdite © ALCATEL ESPACE Reproduction forbidden

6. TABLE OF COMPLIANCE

It will sum up the test results compared with the above specifications.

Reproduction interdite © ALCATEL ESPACE Reproduction forbidden

A Software Tool for the Analysis and Design of the Conformal Array Single Elementary Radiator

Final Report - WP1300

LEMA-RTAA-97-01
Prepared for ESTEC/Contract No. 11698/95/NL/SB
June 1997

by A. Álvarez-Melcón and Juan R. Mosig

Laboratoire d'Electromagnétisme et d'Acoustique.
Department d'Electricité-Ecublens.
Ecole Polytechnique Fédérale de Lausanne.
CH-1015, Lausanne, Suisse.

ÉCOLE POLYTECHNIQUE FÉDÉRALE DE LAUSANNE

EPFL REPRO 1997

A Software Tool for the Analysis and Design of the Conformal Array Single Elementary Radiator

Final Report - WP1300

LEMA-RTAA-97-01
Prepared for ESTEC/Contract No. 11698/95/NL/SB
June 1997

by A. Álvarez-Melcón and Juan R. Mosig

Laboratoire d'Electromagnétisme et d'Acoustique.
Department d'Electricité-Ecublens.
Ecole Polytechnique Fédérale de Lausanne.
CH-1015, Lausanne, Suisse.

ÉCOLE POLYTECHNIQUE
FÉDÉRALE DE LAUSANNE

EPFL ~~REPRO~~ 1997

Abstract

This report reflects the activities carried out for the work package WP-1300 *Design Tools Developments* of the ESA/ESTEC contract No. 11698/95/NL/SB. The main activity of this contract concerns the optimization, analysis, design and fabrication of an active conformal array antenna intended for satellite communication applications. Within the frame of this contract, the activity WP-1300 *Design Tools Developments*, subject of this report, concentrates in the development of a dedicated software tool for the accurate characterization of the single elementary radiator to be incorporated in the final conformal array antenna.

The theoretical developments have followed two main directions towards the rigorous full-wave analysis of the structure. The first one is the derivation of general algorithms for the analysis of multilayered infinite planar printed antennas of complex geometries as required by the conformal array single elementary radiator. For this purpose an integral equation method has been proposed and developed combined with a Galerkin Method of Moments algorithm based on triangular cells. The use of triangular cells for the geometry discretization has proved to suit well to the complex patch shapes used in the conformal array antenna. The second research line is the development of algorithms to take into account the presence of lateral cylindrical walls. For this purpose two techniques have been thoroughly investigated, namely the image approach and the modal expansion approach. In this document both approaches are presented but in the final form of the software only the modal expansion approach has been retained. In consequence, the software developed accommodates the analysis of the conformal array radiator considering infinite transverse dimensions with the analysis including the effects of the shielding cavity. These two types of analysis gives enough flexibility to study many electromagnetic coupling phenomena occurring in the structure, including the effects of the metallic cavity on the overall performance of the antenna.

In this document a detailed description of all the techniques developed is exposed. Some results and validation examples are given both with measurements on real manufactured hardware and in the case of no lateral walls with other commercial software packages. The results have shown that the accuracy achieved is suitable for engineering purposes and the computational times suggest that the software tool is valuable as a real engineering tool for the optimization of this type of antenna. In a separate document a User Manual of the software tool is included, showing all the steps needed for the optimization of the structure and all its computational capabilities are brought to understanding.

Contents

List of Figures

List of Tables

Chapter 1

Basic Ideas

1.1 Introduction

Planar antennas operating at microwave frequencies have rapidly become very interesting candidates in many satellite communication applications [1]. Traditionally, printed antennas have been designed using quasi-static approaches, but these techniques can only be used for rather simple antenna configurations [2]. More recently, the antenna elements to be incorporated into satellite communication systems have become more and more complex, and the quasi-static based design techniques already developed can no longer be used because of their limited accuracy [3]. In the absence of efficient design techniques, many of the actual antenna sub-systems are designed by characterizing experimentally all the parts constituent of the antenna. While these experimental techniques are indeed possible, they are usually expensive and time consuming because they require the bread-boarding of several prototypes until the final hardware, matching the desired specifications, is obtained. What it would be therefore desired, is the development of efficient software tools that could at the same time be fast and accurate, so that the hardware manufacturing phases of the design processes could be substituted by *soft* design in the computer of the different parts of the antenna. In this context, the WP1300 activity of the ESA/ESTEC contract No. 11698/95/NL/SB was launched. The main goal of this activity is the development of an accurate software tool for the electromagnetic characterization of an elementary radiator to be incorporated into the conformal array antenna, thus eliminating the need of its experimental characterization.

1.2 Description of the Geometry

The basic conformal array's elementary radiator proposed by ALCATEL is a rather complex multilayered antenna structure composed of basically two metallic printed radiating patches stacked together as shown in Fig. 1.1. In Fig. 1.1, the lower patch has also been called the active patch, because input and output lines are attached to it in order to feed the antenna. The patch placed just above it has also been called the passive patch since no direct excitation is fed into it. In order to reduce the mutual coupling between single elementary radiators when combined in an array configuration, a cylindrical cavity is used to house the active patch as also shown in Fig. 1.1. Covering the cylindrical cavity, the passive patch is used to increase the axial ratio performance of the antenna.

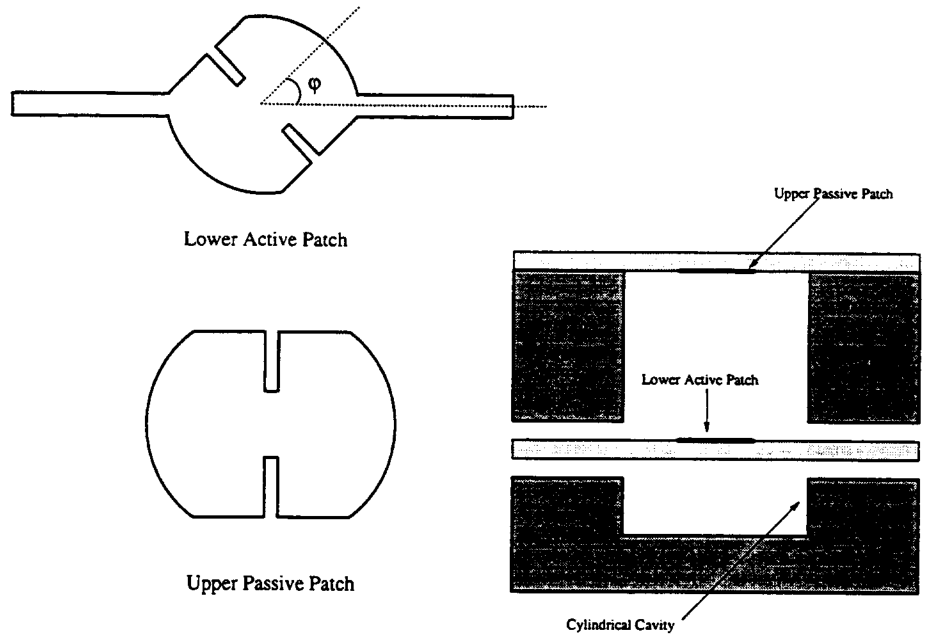

Figure 1.1: General form of the conformal array elementary radiator structure subject of this work.

The global antenna topology can be seen in Fig. 1.1 and several variants concerning the position and form of the patches can be envisaged. In Fig. 1.2 we show all the different configurations that will be the subject of our analysis. As shown, we will consider the lower active patch with one or two ports in order to cover all the possible feeding alternatives that can be used in the final assembly of the elementary radiator into the conformal array antenna. In addition, we can consider the upper active patch at the upper ground plane level or above it, with a circular aperture as the coupling element between the two patches. In this last situation the upper passive patch is placed outside the metallic cavity and the analysis techniques will have to be modified accordingly. All these variants are shown in Fig. 1.2 and the developed software tool is designed with enough flexibility to allow for the analysis of all of them.

1.3 Description of the Work

For the analysis of the structure presented in the previous section, a rigorous full-wave technique based on an integral equation approach formulated in the space domain is proposed and developed. A key element in the integral equation formulation is the derivation of the dyadic spatial Green's functions. In the present work, the Green's functions are first derived for multilayered media of infinite transverse dimensions and then, the cylindrical cavity walls are incorporated. The resulting integral equation is solved with a Galerkin Method of Moments algorithm formulated with subsectional basis functions defined on triangular cells. The use of triangular cells is imposed by the complex geometries of the patches used in the conformal array elementary radiator. Finally, a software tool based on the proposed approach is developed and validation results are given including measurements on real manufactured hardware. The organization of the document is as follows:

In Chapter 2 we show the techniques used to derive the multilayered media spatial Green's func-

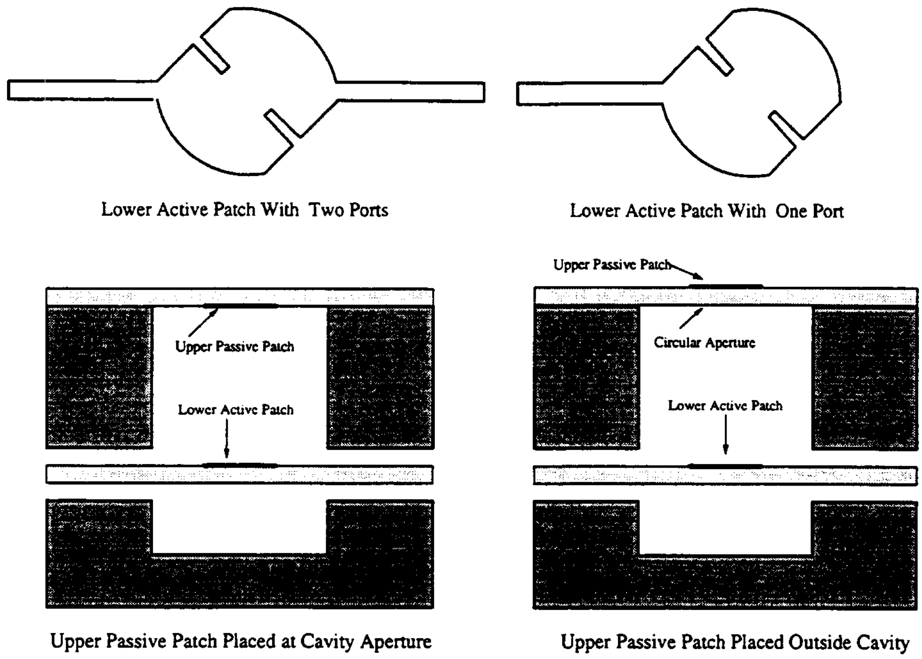

Figure 1.2: Typical variants of the conformal array elementary radiator to be analyzed.

tions needed in the integral equation formulation when infinite transverse dimensions are considered. In Chapter 3 the techniques used in the modelization of the lateral cavity walls are presented including the image approach and the expansion of the spatial domain Green's functions in cavity modes. Chapter 4 is dedicated to the solution of the system of integral equations using a Galerkin Method of Moments (MoM) procedure based on triangular cell discretization. In this context, the mesh strategy followed to discretize the complex geometries of the conformal array radiator is briefly presented. Chapter 5 is dedicated to the computation of the electrical characteristics of the antenna using the information extracted from the MoM algorithm. Two basic electrical quantities are investigated, namely the input impedance with full scattering matrix for the two ports configuration, and the radiation properties or radiated far field of the antenna. Finally, in Chapter 6 some results and validation examples are included for both the non-cavity and the cavity situations, and comparisons with real manufactured hardware are also presented. For the non-cavity case, comparisons with the `HP-MOMEMTUM` commercial software package are in addition shown for several test cases.

Chapter 2

Green's Functions in Layered Media of Infinite Transverse Dimensions

2.1 Introduction

The first key element in the integral equation formulation that we want to derive for the analysis of the elementary radiator in the non-cavity situation, is the so-called Green's functions defined as the fields and potentials produced by a unitary dipole embedded in a multilayered medium of infinite transverse dimensions. The techniques to be described in this chapter have been developed in the past, are well known and extensive information can be found in the specialized technical literature. Here we just present the basic ideas related to multilayered media Green's functions and derive step by step all the Green's functions that we will need in subsequent chapters to perform the analysis of the conformal array elementary radiator. The chapter covers two main aspects of the Green's functions theory in layered media. First we show how the Green's functions can be computed in the spectral domain by using simple equivalent transmission line networks. Finally, the numerical techniques used to evaluate the so-called Sommerfeld integrals in order to transform the spectral domain Green's functions to the spatial domain are also discussed.

2.2 Spectral Domain Green's Functions

Consider a unitary electric dipole embedded in the multilayered environment of Fig. 2.1. It is well known that the fields and potentials produced by this unitary dipole can be derived, in the spectral domain, from an equivalent transmission line network representing the dependence of the structure along the axis of the stratification (z-axis in Fig. 2.1) [4], [5]. If one introduces a double spatial Fourier transformation into the original Maxwell equations governing the behavior of the fields in our antenna structure, the following expressions are obtained for the spectral domain electric and magnetic dyadic field Green's functions respectively:

$$
\begin{array}{ll}
\tilde{G}_{E_J}^{xx} = -\frac{k_x^2}{k_\rho^2} V_J^{TM} - \frac{k_y^2}{k_\rho^2} V_J^{TE} & \tilde{G}_{E_J}^{xy} = \frac{k_x k_y}{k_\rho^2}\left(-V_J^{TM} + V_J^{TE}\right) \\
\tilde{G}_{E_J}^{yx} = \frac{k_y k_x}{k_\rho^2}\left(-V_J^{TM} + V_J^{TE}\right) & \tilde{G}_{E_J}^{yy} = -\frac{k_y^2}{k_\rho^2} V_J^{TM} - \frac{k_x^2}{k_\rho^2} V_J^{TE} \\
\tilde{G}_{E_J}^{zx} = -\frac{k_x}{\omega \epsilon} I_J^{TM} & \tilde{G}_{E_J}^{zy} = -\frac{k_y}{\omega \epsilon} I_J^{TM}
\end{array}
\tag{2.1}
$$

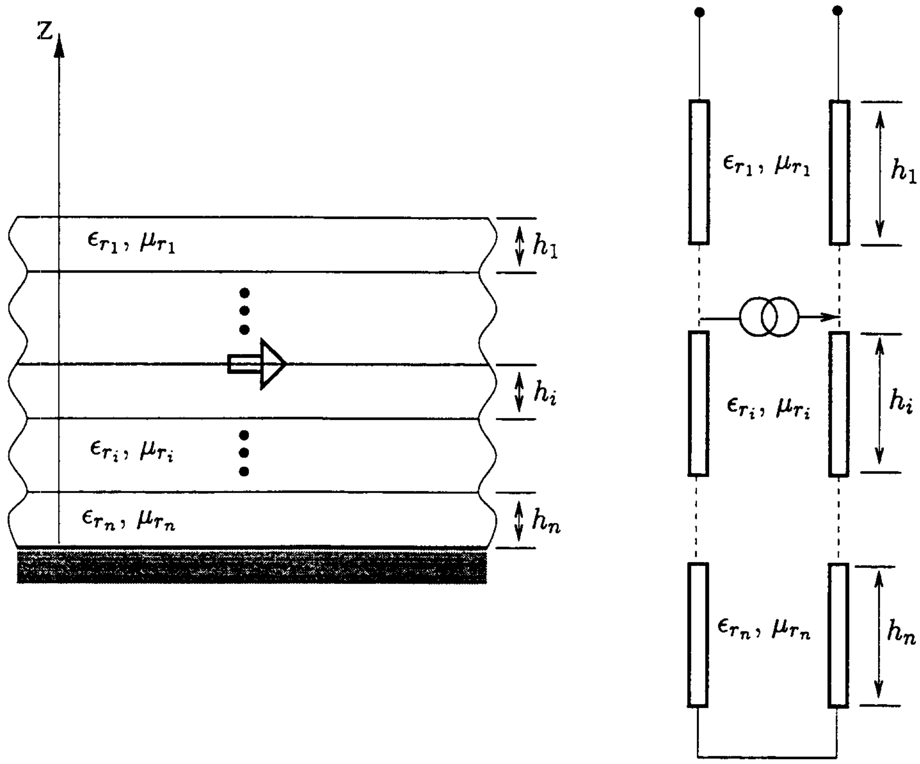

Figure 2.1: Unitary electric dipole embedded in a multilayered medium and its equivalent transmission line network.

$$
\begin{array}{ll}
\tilde{G}^{xx}_{H_J} = \frac{k_x k_y}{k_\rho^2}\left(I_J^{TM} - I_J^{TE}\right) & \tilde{G}^{xy}_{H_J} = \frac{k_y^2}{k_\rho^2} I_J^{TM} + \frac{k_x^2}{k_\rho^2} I_J^{TE} \\
\tilde{G}^{yx}_{H_J} = -\frac{k_x^2}{k_\rho^2} I_J^{TM} - \frac{k_y^2}{k_\rho^2} I_J^{TE} & \tilde{G}^{yy}_{H_J} = -\frac{k_x k_y}{k_\rho^2}\left(-I_J^{TM} + I_J^{TE}\right) \\
\tilde{G}^{zx}_{H_J} = -\frac{k_y}{\omega \mu} V_J^{TE} & \tilde{G}^{zy}_{H_J} = \frac{k_x}{\omega \mu} V_J^{TE}
\end{array}
\tag{2.2}
$$

where V and I are voltages and currents in the equivalent transmission line network of the structure shown in Fig. 2.1 and only horizontal dipoles are considered because of the planar nature of the structure under analysis. Moreover, the superscripts TE and TM are used to indicate that the associated voltages or currents are measured under TE or TM wave excitation respectively. In addition, the spectral variables defined in above equation k_x, k_y and k_ρ are related to the spatial derivatives through the following standard Fourier transform relations.

$$
\begin{array}{l}
\frac{\partial}{\partial x} = j\, k_x \\
\frac{\partial}{\partial y} = j\, k_y \\
k_\rho^2 = k_x^2 + k_y^2
\end{array}
\tag{2.3}
$$

Each transmission line section of the equivalent circuit shown in Fig. 2.1 is now characterized by its characteristic impedance and propagation constant. They are defined in the usual way for both TE or TM wave, namely:

$$
\begin{array}{l}
Z_c^{TM} = \frac{\beta}{\omega \epsilon} \\
Z_c^{TE} = \frac{\omega \mu}{\beta}
\end{array}
\tag{2.4}
$$

where the propagation constant β has been defined in this study as.

$$\begin{aligned} \beta &= \sqrt{k^2 - k_\rho^2} \\ k &= \omega\,\sqrt{\mu\,\epsilon} \end{aligned} \tag{2.5}$$

Once the basic field Green's functions have been computed, the potential Green's functions can be easily expressed as a function of the normal components of the fields as shown in [6]. Using the expressions for the normal components of the fields above, the electric vector potential and scalar magnetic potential Green's functions can also be easily expressed in terms of the voltages and currents in the equivalent transmission line network of Fig. 2.1. Using the Sommerfeld choice for the potentials described in [6] one easily finds.

$$\begin{aligned} &\tilde{G}_A^{xx} = \tfrac{V_J^{TE}}{j\,\omega} \quad \tilde{G}_A^{xy} = 0 \\ &\tilde{G}_A^{yx} = 0 \quad\quad \tilde{G}_A^{yy} = \tfrac{V_J^{TE}}{j\,\omega} \\ &\tilde{G}_A^{xx} = \tilde{G}_A^{yy} = \tilde{G}_A \end{aligned} \tag{2.6}$$

$$\tilde{G}_v = \frac{\omega}{k_\rho^2}\left[j\,V_J^{TM} + \frac{V_J^{TE}}{j}\right] \tag{2.7}$$

This step completes all the required derivations in the spectral domain concerning electric dipoles. In our antenna structure however, the radiation through apertures will be modeled with the aid of equivalent magnetic currents, and the associated Green's functions must therefore be computed also in this case. For this purpose we first take a magnetic unitary dipole embedded in a multilayered medium of infinite transverse dimensions as shown in Fig. 2.2. Similar considerations as in the case of electric currents can now be made, and the dyadic field Green's functions can be derived from the equivalent transmission line network shown in Fig. 2.2. As seen in Fig. 2.2, the only difference to remark is that the equivalent transmission line network is now excited by a voltage generator instead of the current generator of Fig. 2.1. Following a dual formulation as for electric currents, the electric and magnetic dyadic field Green's functions can be written, in the spectral domain, as:

$$\begin{aligned} \tilde{G}_{E_M}^{xx} &= -\tfrac{k_x\,k_y}{k_\rho^2}\left(V_M^{TE} - V_M^{TM}\right) & \tilde{G}_{E_M}^{xy} &= -\tfrac{k_y^2}{k_\rho^2}V_M^{TE} - \tfrac{k_x^2}{k_\rho^2}V_M^{TM} \\ \tilde{G}_{E_M}^{yx} &= \tfrac{k_x^2}{k_\rho^2}V_M^{TE} + \tfrac{k_y^2}{k_\rho^2}V_M^{TM} & \tilde{G}_{E_M}^{yy} &= +\tfrac{k_x\,k_y}{k_\rho^2}\left(V_M^{TE} + V_M^{TM}\right) \\ \tilde{G}_{E_M}^{zx} &= \tfrac{k_y}{\omega\,\epsilon}I_M^{TM} & \tilde{G}_{E_M}^{zy} &= -\tfrac{k_x}{\omega\,\epsilon}I_M^{TM} \end{aligned} \tag{2.8}$$

$$\begin{aligned} \tilde{G}_{H_M}^{xx} &= -\tfrac{k_x^2}{k_\rho^2}I_M^{TE} - \tfrac{k_y^2}{k_\rho^2}I_M^{TM} & \tilde{G}_{H_M}^{xy} &= -\tfrac{k_x\,k_y}{k_\rho^2}\left(I_M^{TE} - I_M^{TM}\right) \\ \tilde{G}_{H_M}^{yx} &= -\tfrac{k_y\,k_x}{k_\rho^2}\left(I_M^{TE} - I_M^{TM}\right) & \tilde{G}_{H_M}^{yy} &= -\tfrac{k_y^2}{k_\rho^2}I_M^{TE} - \tfrac{k_x^2}{k_\rho^2}I_M^{TM} \\ \tilde{G}_{H_M}^{zx} &= -\tfrac{k_x}{\omega\,\mu}V_M^{TE} & \tilde{G}_{H_M}^{zy} &= -\tfrac{k_y}{\omega\,\mu}V_M^{TE} \end{aligned} \tag{2.9}$$

where now V and I are voltages and currents computed in the equivalent transmission line network of Fig. 2.2 and the transmission line sections are characterized by the same parameters as in equations (2.4,2.5). Again by duality we can directly write the form of the electric vector potential and scalar magnetic potential Green's functions, namely.

$$\begin{aligned} &\tilde{G}_F^{xx} = \tfrac{I_M^{TM}}{j\,\omega} \quad \tilde{G}_F^{xy} = 0 \\ &\tilde{G}_F^{yx} = 0 \quad\quad \tilde{G}_F^{yy} = \tfrac{I_M^{TM}}{j\,\omega} \end{aligned} \tag{2.10}$$

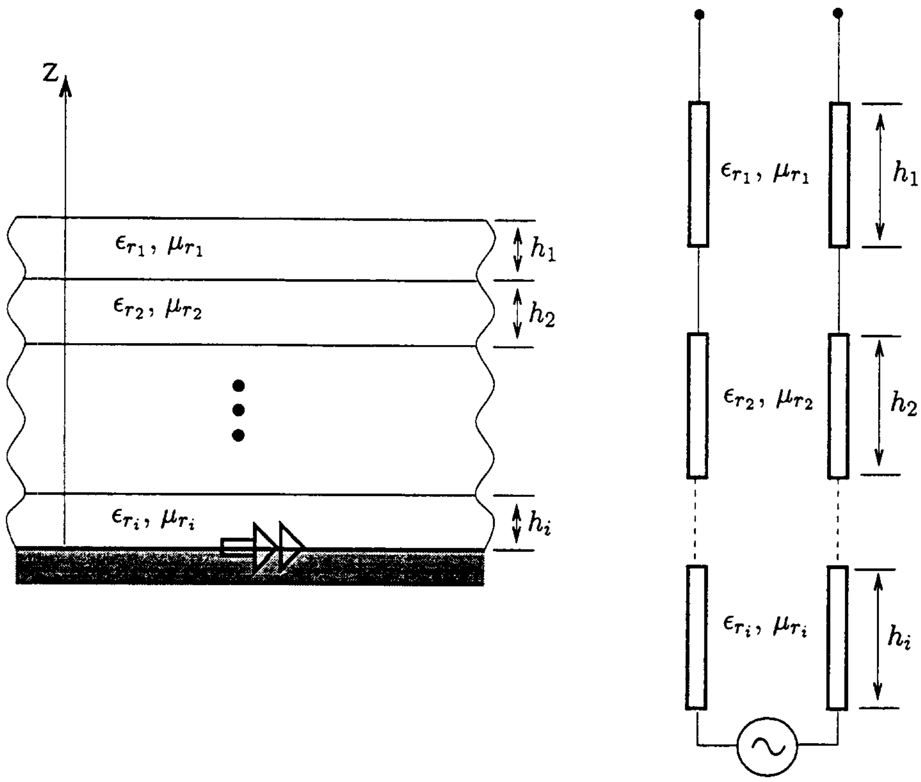

Figure 2.2: Magnetic dipole embedded in a multilayered medium and its equivalent transmission line network.

$$\tilde{G}_w = \frac{\omega}{k_\rho^2}\left[j\, I_M^{TE} + \frac{I_M^{TM}}{j}\right] \tag{2.11}$$

Using this formalism, the computation of the spectral domain Green's functions is greatly simplified. Indeed, only the equivalent transmission line networks representing the variation of the structure along the stratification axis need to be built as shown in Fig. 2.1 and 2.2. Next, these networks are easily analyzed using standard transmission line theory in order to compute all the required currents and voltages. Finally, the spectral domain Green's functions are computed by direct application of equations (2.1) to (2.11).

It is interesting to observe that for the analysis of the structure of interest presented in chapter 1, all the Green's functions derived in this section will be utilized. In fact the interactions of the same nature (*electric-electric* or *magnetic-magnetic*) are solved using a Mixed Potential formulation (MPIE) while the interactions of different nature are solved using a Field formulation (FIE). This choice is very convenient from the numerical point of view since the self interactions are treated with an MPIE formulation which best treats the singular behavior of the Green's functions [6]. The result is that both the potential Green's functions and the field Green's functions will intervene at certain moments along the integral formulation process.

2.3 Spatial Domain Green's Functions

Once the spectral domain Green's functions are computed, they must be transformed into the spatial domain, so that they can be used in the integral equation formulation needed for the analysis of the structure. For this purpose, the well known inverse Sommerfeld transformation need to be applied to each one of the spectral functions evaluated in the previous section. By definition, the inverse Sommerfeld transformation of order n is expressed with the following improper integral [7]:

$$G(\rho) = S_n\left[\tilde{G}(k_\rho)\right] = \int_0^\infty J_n(k_\rho\,\rho)\; k_\rho^{n+1}\,\tilde{G}(k_\rho)\; dk_\rho \tag{2.12}$$

Using equation (2.12), any function of the spectral variable k_ρ is converted into a function of the radial space distance ρ. Extensive effort has been devoted in the past to develop numerical methods for the efficient evaluation of the inverse Sommerfeld transformation [8]. Traditionally, two main problems for the numerical evaluation of the integral have been reported. The first one is due to the nature of the spectral domain Green's functions, which present in the complex k_ρ plane branch cuts and poles closed to the integration path. The other main difficulty is due to the oscillatory behavior associated to the Bessel function $J_n(k_\rho\,\rho)$ and to the k_ρ^{n+1} term which might render the whole integrand divergent in many situations. Mathematically, both difficulties are explicitly shown by splitting the integration interval in the following two regions.

$$G(\rho) = S_n\left[\tilde{G}(k_\rho)\right] = \int_0^{k_0} J_n(k_\rho\,\rho)\; k_\rho^{n+1}\,\tilde{G}(k_\rho)\; dk_\rho + \int_{k_0}^\infty J_n(k_\rho\,\rho)\; k_\rho^{n+1}\,\tilde{G}(k_\rho)\; dk_\rho = T_1 + T_2 \tag{2.13}$$

In this equation T_1 is an integral over the bounded interval $[0,k_0]$, of a function containing poles in the integration path. On the contrary, the function to be integrated for T_2 does not contain poles, but the integral itself is extended to the unbounded interval $[k_0,\infty]$ and the function to the integrated might diverge in many situations.

In the present work, the integration technique used to evaluate the first integral T_1 is the one described in [9]. Using this method the integral is evaluated by deforming the integration path, originally in the real axis, through an elliptic contour which avoids all the poles of the spectral functions. The final integration path selected is shown in Fig. 2.3 where the elliptic contour chosen to avoid the poles is clearly indicated. The technique has been implemented in a way that allows the computation of the spatial Green's functions in a wide range of spatial distances. To avoid lossing precision when the spatial distance increases, the whole range of spatial distances has been divided into a number of sub-regions and in each sub-region the original minor semiaxis of the ellipse is decreased following a linear rule. This method has been tested with spatial distances of the order of $\rho = 500\,k_0$ and even greater obtaining very good accuracy. This range should be more that enough to cover all practical operational cases of the antenna. As regard the second integral T_2, a specially tailored numerical method to integrate divergence functions over improper intervals, known as the weighted average method, has been implemented. Extensive results and convergence behavior of the technique when applied to microstrip antennas can be found in [6] or [8] for instance.

Once a numerical procedure is established for the evaluation of the inverse Sommerfeld transformation, all desired spatial domain Green's functions need to be formulated in terms of Sommerfeld

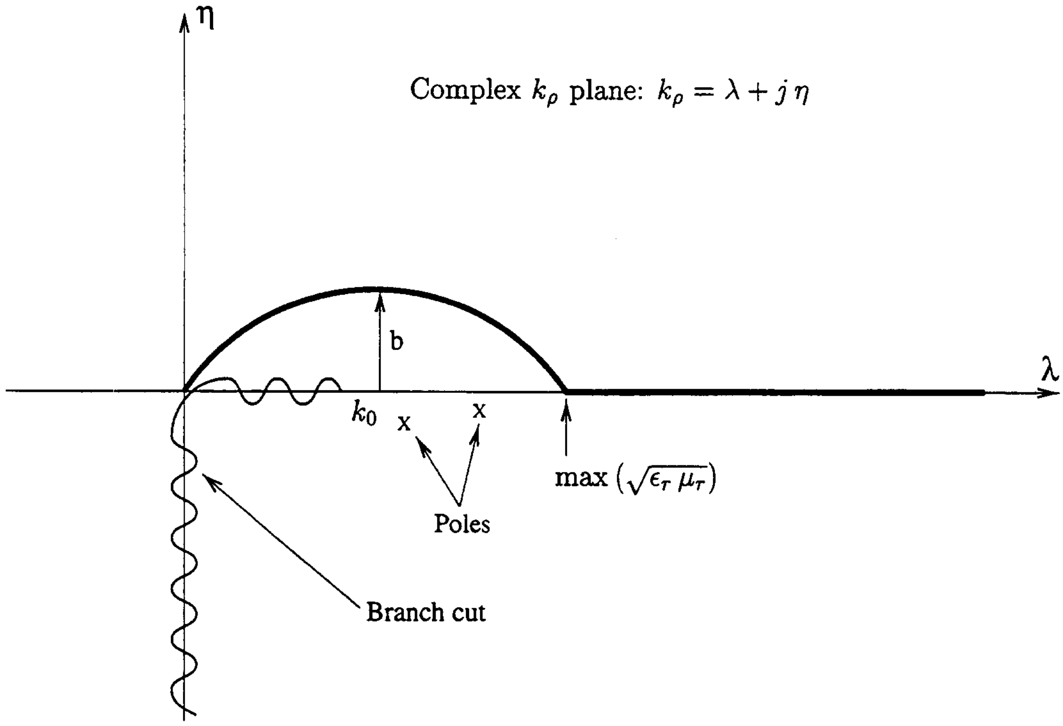

Figure 2.3: Complex k_ρ plane showing the poles and branch cut of the spectral domain functions.

integrals of the type shown in equation (2.12). For the case of the potentials (functions of only the radial spectral variable k_ρ) this is a very simple task since we can directly write.

$$G_A^{xx}(\rho) = G_A^{yy}(\rho) = S_0\left[\tilde{G}_A^{xx}(k_\rho)\right] = S_0\left[\tilde{G}_A^{yy}(k_\rho)\right] \tag{2.14}$$

$$G_F^{xx}(\rho) = G_F^{yy}(\rho) = S_0\left[\tilde{G}_F^{xx}(k_\rho)\right] = S_0\left[\tilde{G}_F^{yy}(k_\rho)\right] \tag{2.15}$$

$$G_v(\rho) = S_0\left[\tilde{G}_v(k_\rho)\right] \tag{2.16}$$

$$G_w(\rho) = S_0\left[\tilde{G}_w(k_\rho)\right] \tag{2.17}$$

For the electric and magnetic fields Green's functions however, the radial symmetry is lost and first the spatial derivatives shown in equation (2.3) must be evaluated. After cumbersome but straightforward manipulations on equation (2.12) one obtains the following relations:

$$\tilde{G} = j\,k_x\,j\,k_x\,\tilde{A} \mapsto G = \frac{\cos(2\,\varphi)}{\rho} S_1\left[\tilde{A}\right] - \cos^2\varphi\,S_0\left[k_\rho^2\,\tilde{A}\right] \tag{2.18}$$

$$\tilde{G} = j\,k_y\,j\,k_y\,\tilde{A} \mapsto G = -\frac{\cos(2\,\varphi)}{\rho} S_1\left[\tilde{A}\right] - \sin^2\varphi\,S_0\left[k_\rho^2\,\tilde{A}\right] \tag{2.19}$$

$$\tilde{G} = j\,k_x\,j\,k_x\,\tilde{A} \mapsto G = \frac{\sin(2\,\varphi)}{\rho} S_1\left[\tilde{A}\right] - \frac{1}{2}\sin(2\,\varphi)\;S_0\left[k_\rho^2\,\tilde{A}\right] \tag{2.20}$$

where $\tilde{A}$ is a spectral quantity with radial symmetry (function of only k_ρ) and φ is the standard angle of cylindrical coordinates. With above equations, the spatial domain magnetic field Green's function produced by electric currents can finally be written as:

$$G^{xx}_{H_J} = -\frac{\sin(2\varphi)}{\rho} S_1 \left[\frac{I_J^{TM} - I_J^{TE}}{k_\rho^2}\right] + \frac{1}{2}\sin(2\varphi)\ S_0\left[I_J^{TM}\right] - \frac{1}{2}\sin(2\varphi)\ S_0\left[I_J^{TE}\right] \tag{2.21}$$

$$G^{xy}_{H_J} = -\frac{\cos(2\varphi)}{\rho} S_1 \left[\frac{I_J^{TM} - I_J^{TE}}{k_\rho^2}\right] + \sin^2(\varphi)\, S_0\left[I_J^{TM}\right] + \cos^2(\varphi)\, S_0\left[I_J^{TE}\right] \tag{2.22}$$

$$G^{yx}_{H_J} = \frac{\cos(2\varphi)}{\rho} S_1 \left[\frac{I_J^{TM} - I_J^{TE}}{k_\rho^2}\right] - \cos^2(\varphi)\, S_0\left[I_J^{TM}\right] - \sin^2(\varphi)\, S_0\left[I_J^{TE}\right] \tag{2.23}$$

$$G^{yy}_{H_J} = -G^{xx}_{H_J} \tag{2.24}$$

and the electric field Green's function due to magnetic currents as:

$$G^{xx}_{E_M} = \frac{\sin(2\varphi)}{\rho} S_1 \left[\frac{V_M^{TE} - V_M^{TM}}{k_\rho^2}\right] - \frac{1}{2}\sin(2\varphi)\ S_0\left[V_M^{TE}\right] + \frac{1}{2}\sin(2\varphi)\ S_0\left[V_M^{TM}\right] \tag{2.25}$$

$$G^{xy}_{H_J} = -\frac{\cos(2\varphi)}{\rho} S_1 \left[\frac{V_M^{TE} - V_M^{TM}}{k_\rho^2}\right] - \sin^2(\varphi)\, S_0\left[V_M^{TE}\right] - \cos^2(\varphi)\, S_0\left[V_M^{TM}\right] \tag{2.26}$$

$$G^{yx}_{E_M} = -\frac{\cos(2\varphi)}{\rho} S_1 \left[\frac{V_M^{TE} - V_M^{TM}}{k_\rho^2}\right] + \cos^2(\varphi)\, S_0\left[V_M^{TE}\right] + \sin^2(\varphi)\, S_0\left[V_M^{TM}\right] \tag{2.27}$$

$$G^{yy}_{E_M} = -G^{xx}_{EM} \tag{2.28}$$

This last step completes all operations in the spatial domain required for the evaluation of all spatial domain Green's functions needed in the integral equation formulation of the elementary radiator antenna structure. It should be pointed out however, that up to now all derivations are valid considering the transverse dimensions of the dielectrics infinite. In the next chapter we will present the theoretical developments undertaken in this contract, in order to account for the presence of the lateral cavity walls used to house the conformal array elementary radiator.

Chapter 3

Boxed Green's Functions

3.1 Introduction

As shown in chapter 1, the conformal array elementary radiator subject of the present study is shielded in a cylindrical cavity used to give rigidity to the structure and to reduce the parasitic coupling between elements when disposed in array configuration. The present chapter is dedicated to detail the theoretical efforts put towards the inclusion, in the analysis algorithms, of the effects of the lateral cavity walls in the final performance of the antenna. Two main techniques have been developed, namely the image approach and the modal expansion approach. In this chapter we review both techniques including some results obtained and emphasizing the difficulties encountered. As we will see through out the chapter, the implementation of the image approach poses many practical difficulties related to the slow convergence of the series involved. This is the main reason why in the final analysis software tool the modal expansion approach has been adopted.

3.2 The image Approach

In chapter 2 we developed a powerful tool to compute the fields and potentials produced by unitary electric and magnetic dipoles embedded in a multilayered medium. The first straightforward way of accounting for the presence of lateral cavity walls in the analysis, is by replacing the metallic walls by the images of the radiating unitary dipoles. In this study several image configurations have been developed in order to take into account the cylindrical cavity walls of the conformal array single elementary radiator. The strategy followed is to start from rather simple image configurations to account first for the walls at the ports positions. The initial rearrangements are then complicated in order to try to account for the whole cylindrical shape. In the next subsections we detail all the image rearrangements developed in this study.

3.2.1 One image to the closest input port

In this arrangement, the two metallic walls placed at the ports positions are substituted by a single image taken with respect the closest wall to the electric source dipole. The situation is shown in Fig. 3.1. The Green's functions for the potentials can now be derived from the Green's functions of

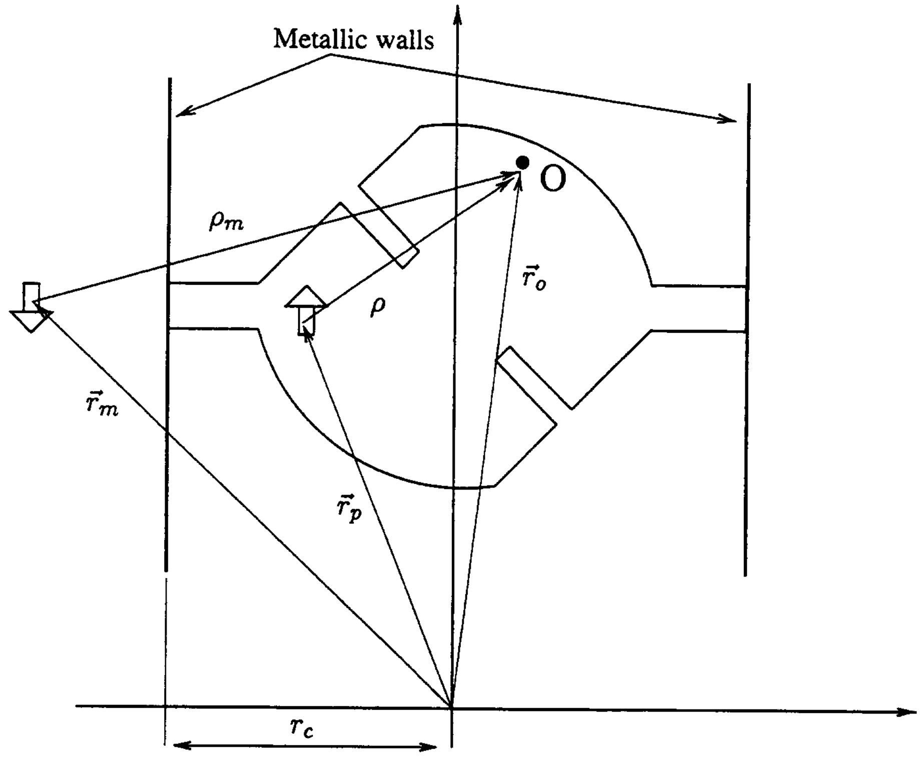

Figure 3.1: Spatial image situation when one image is taken with respect the closest wall to the electric source dipole.

the original source plus its image. It is straightforward to write:

$$\begin{aligned} G_{A_T}^{xx} &= G_A(\rho) + G_A(\rho_m) \\ G_{A_T}^{yy} &= G_A(\rho) - G_A(\rho_m) \\ G_{v_T} &= G_v(\rho) - G_v(\rho_m) \end{aligned} \tag{3.1}$$

where G_{A_T}, G_{v_T} are the total new Green's functions in the structure with the lateral walls, G_A, G_v are the Green's function of a single electric unitary dipole as derived in chapter 2, ρ is the distance from the original source to the observation point and ρ_m the distance from the image to the observation point. If r_c is the distance from the origin to the closest port as shown in Fig. 3.1, the following vector relations complete the formulation:

$$\begin{array}{ll} \vec{r}_p = x_p\,\hat{e}_x + y_p\,\hat{e}_y & \vec{r}_m = x_m\,\hat{e}_x + y_m\,\hat{e}_y \\ \vec{r}_o = x_o\,\hat{e}_x + y_o\,\hat{e}_y & \\ \rho = sqrt(x_o - x_p)^2 + (y_o - y_p)^2 & \rho_m = sqrt(x_o - x_m)^2 + (y_o - y_m)^2 \\ x_m = 2\,r_c - x_p & y_m = y_p \end{array} \tag{3.2}$$

In Fig. 3.2 we show the simulated results computed when this correction is applied to the conformal array lower active patch. In the same graphic we show the results when the pure laterally opened model is used and also measurements obtained when the lower active patch is backed by a cylindrical cavity and radiation is produced through a circular aperture opened at 8.0 mm distance from the lower active patch. As we can see, the results obtained applying the correction are better than if only the laterally opened model is used.

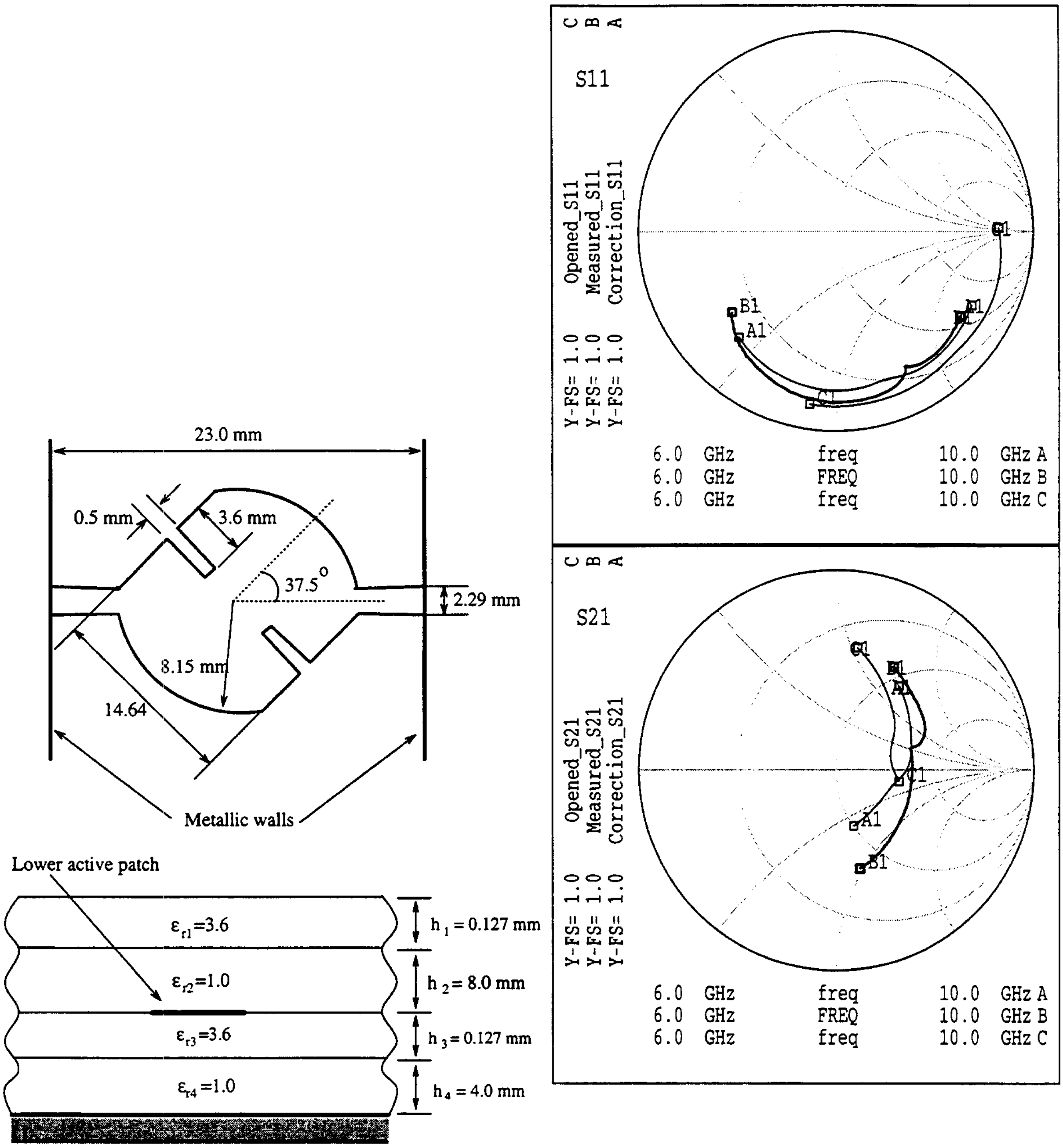

Figure 3.2: Comparison between the results obtained applying the correction, results obtained using the laterally opened model and measurements. Measured results correpond to thick line.

3.2.2 Infinite images with respect input and output ports

A more accurate modelization of the excitation can be obtained if the two metallic walls placed at the ports positions are taken into account at the same time. For this purpose an infinite number of images need to be included if the boundary conditions for the fields are to be satisfied at the two parallel metallic walls. What remains to be discussed is the convergence rate of the resulting series of images. The situation is shown in Fig. 3.3. In this case the total Green's functions are computed

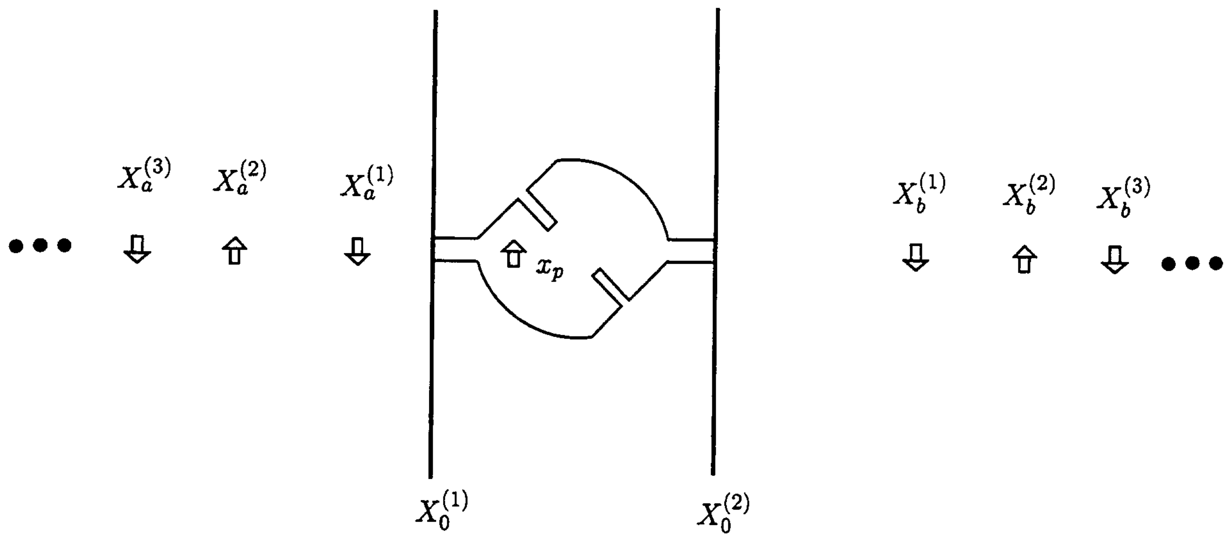

Figure 3.3: Spatial image situation when an arbitrary number of images is taken with respect two metallic walls placed at the ports positions.

through the following infinite series.

$$
\begin{aligned}
G_{A_T}^{xx} &= G_A(\rho) + \sum_{s=1}^{\infty} \left[G_A\left(\rho_a(s)\right) + G_A\left(\rho_b(s)\right)\right] \\
G_{A_T}^{yy} &= G_A(\rho) + \sum_{s=1}^{\infty} (-1)^s \left[G_A\left(\rho_a(s)\right) + G_A\left(\rho_b(s)\right)\right] \\
G_{v_T} &= G_v(\rho) + \sum_{s=1}^{\infty} (-1)^s \left[G_v\left(\rho_a(s)\right) + G_v\left(\rho_a(s)\right)\right]
\end{aligned} \tag{3.3}
$$

and according to figure 3.1.2.1, the distances of all the images $\rho_a(s)$, $\rho_b(s)$ to a generic observation point are found through the following recurrent relations.

$$
\begin{aligned}
&\left.\begin{aligned} X_a^{(1)} &= 2\,X_0^{(1)} - x_p \\ X_b^{(1)} &= 2\,X_0^{(2)} - x_p \end{aligned}\right\} \text{ Driven quantities} \\
&X_a^{(s)} = 2\,X_0^{(1)} - X_b^{(s-1)} \quad X_b^{(s)} = 2\,X_0^{(2)} - X_a^{(s-1)} \\
&s = 2, 3, \cdots, \infty
\end{aligned} \tag{3.4}
$$

$$
\begin{aligned}
\rho(s) &= \sqrt{(x_o - x_p)^2 - (y_o - y_p)^2} \\
\rho_a(s) &= \sqrt{\left(x_o - X_a^{(s)}\right)^2 - (y_o - y_p)^2} \\
\rho_b(s) &= \sqrt{\left(x_o - X_b^{(s)}\right)^2 - (y_o - y_p)^2} \\
s &= 1, 2, \cdots, \infty
\end{aligned} \tag{3.5}
$$

where (x_o, y_o) are the coordinates of the observation point, (x_p, y_p) the coordinates of the source point and $X_0^{(1)}$, $X_0^{(2)}$ the abscissa of the two lateral metallic walls as shown in Fig. 3.3. As in the previous section, in Fig. 3.4 we show the simulated results computed when this correction is applied to the conformal array lower active patch. In the same graphic we show the results when the pure laterally opened model is used and also measurements obtained when the lower active patch is backed by a cylindrical cavity and radiation is produced through a circular aperture opened at 8.0 mm distance from the lower active patch. As we can see the results are very similar to those obtained in the previous case.

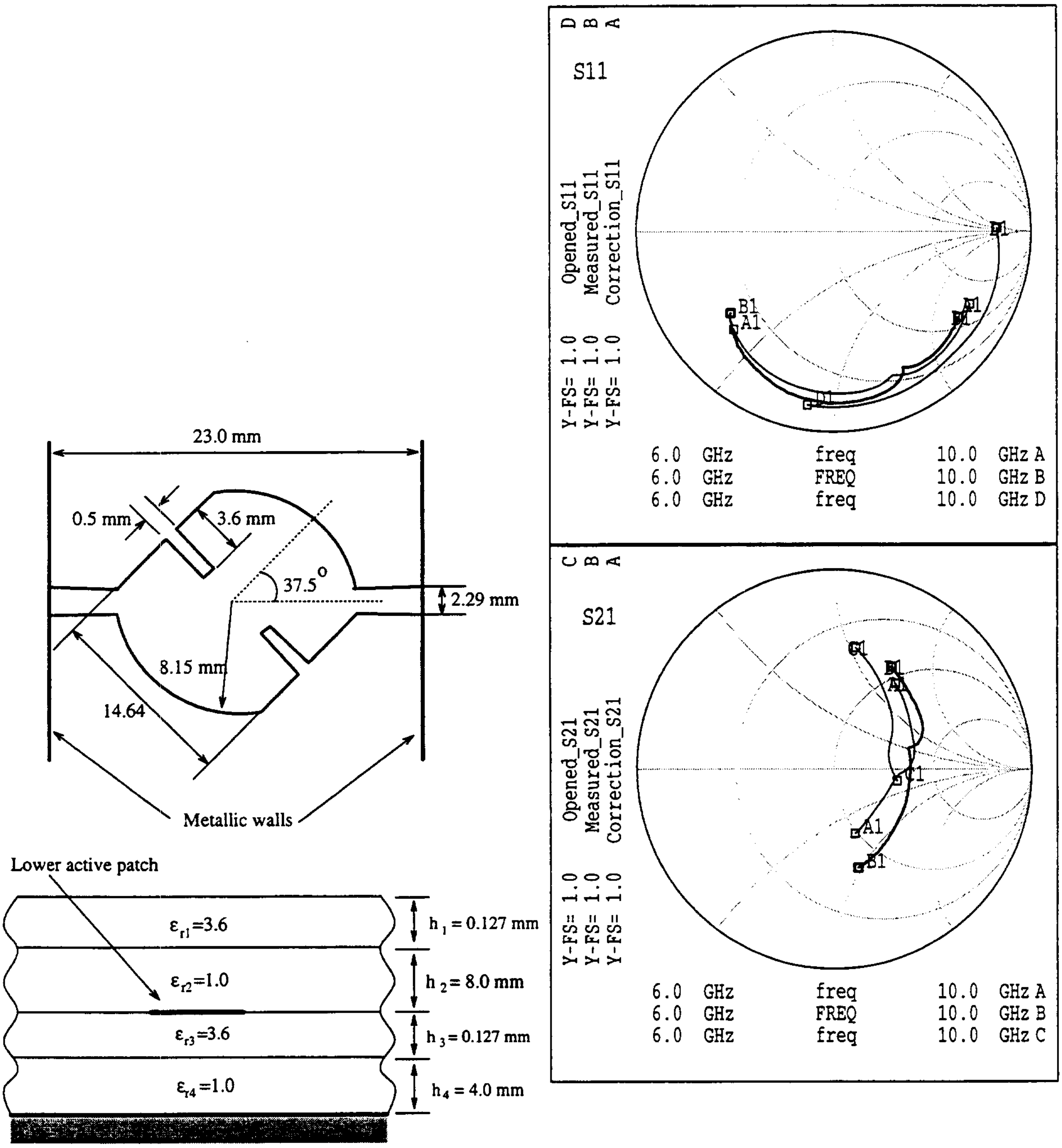

Figure 3.4: Comparison between the results obtained applying the correction, results obtained using the laterally opened model and measurements. Measured results correspond to thick line.

3.2.3 One image with respect closest tangent plane to cylindrical cavity

This is the first step towards the inclusion of the whole cylindrical cavity in the analysis algorithms. If we consider the situation shown in Fig. 3.5, then the total Green's functions in the cavity situation can be written as:

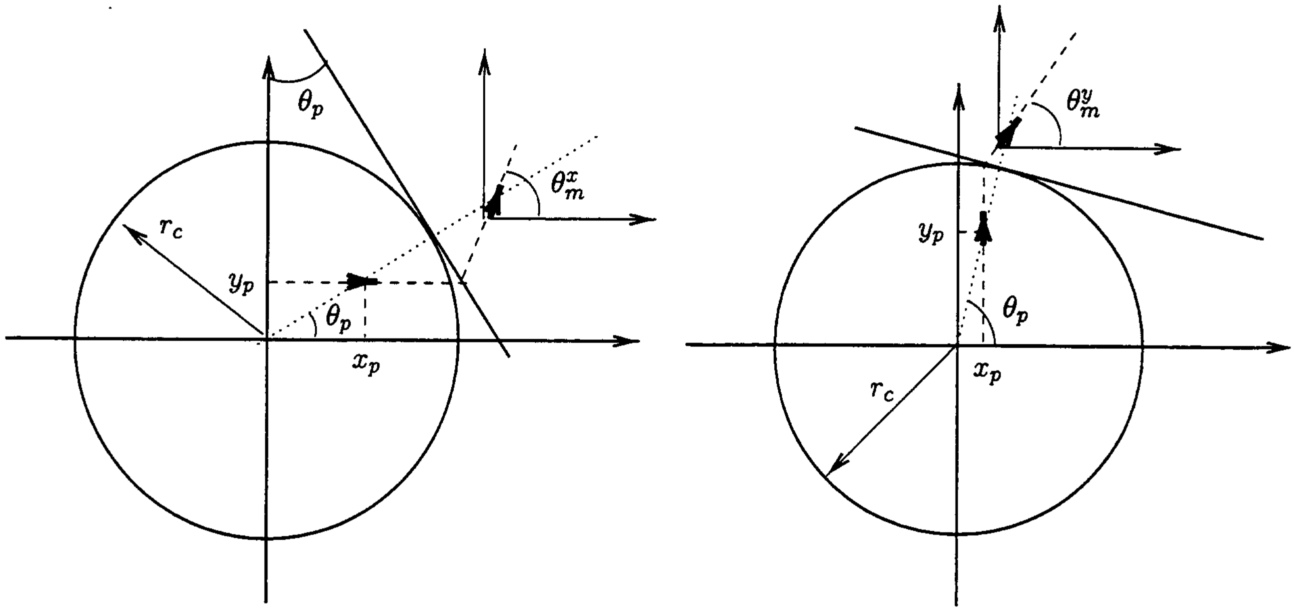

Figure 3.5: Spatial image situation when one image is taken with respect the closest tangent plane to the cylindrical cavity.

$$
\begin{aligned}
G_{A_T}^{xx} &= G_A(\rho) + \cos\left(\theta_m^x\right)\, G_A\left(\rho_m\right) \\
G_{A_T}^{yx} &= \sin\left(\theta_m^x\right)\, G_A\left(\rho_m\right) \\
G_{A_T}^{xy} &= \cos\left(\theta_m^y\right)\, G_A\left(\rho_m\right) \\
G_{A_T}^{yy} &= G_A(\rho) + \sin\left(\theta_m^y\right)\, G_A\left(\rho_m\right) \\
G_{v_T} &= G_v(\rho) - G_v\left(\rho_m\right)
\end{aligned}
\tag{3.6}
$$

and the following auxiliary geometrical parameters are defined according to Fig. 3.5:

$$
\begin{aligned}
r_p &= \sqrt{x_p^2 + y_p^2} \qquad \theta_p = \arctan\left(\tfrac{y_p}{x_p}\right) \\
r_m &= 2\, r_c - r_p \\
x_m &= r_m \cos\left(\theta_p\right) \quad y_m = r_m \sin\left(\theta_p\right) \\
\theta_m^x &= 2\,\theta_p \qquad\qquad \theta_m^y = 2\,\theta_p - \tfrac{\pi}{2}
\end{aligned}
\tag{3.7}
$$

where r_c is the radius of the cylindrical cavity, (x_p, y_p) the coordinates of the source point, (x_m, y_m) the coordinates of the image, ρ the distance from the source to the observer point and ρ_m the distance from the image to the observer point. It is interesting to note that in this case, the presence of the cylindrical cavity couples all possible orientations of the dipole and therefore none of the four components of the magnetic vector potential dyadic Green's function are zero. This is clearly shown in equation (3.6) where the analytic expressions of all four components of the dyadic are given. As before, in Fig. 3.6 we show the simulated results computed when this correction is applied to the conformal array lower active patch. In the same graphic we show the results when the pure laterally opened model is used and also measurements obtained when the lower active patch is backed by a cylindrical cavity and radiation is produced through a circular aperture opened at 8.0 mm distance from the lower active patch. As we see, no special accuracy improvements are obtained with respect the previous models.

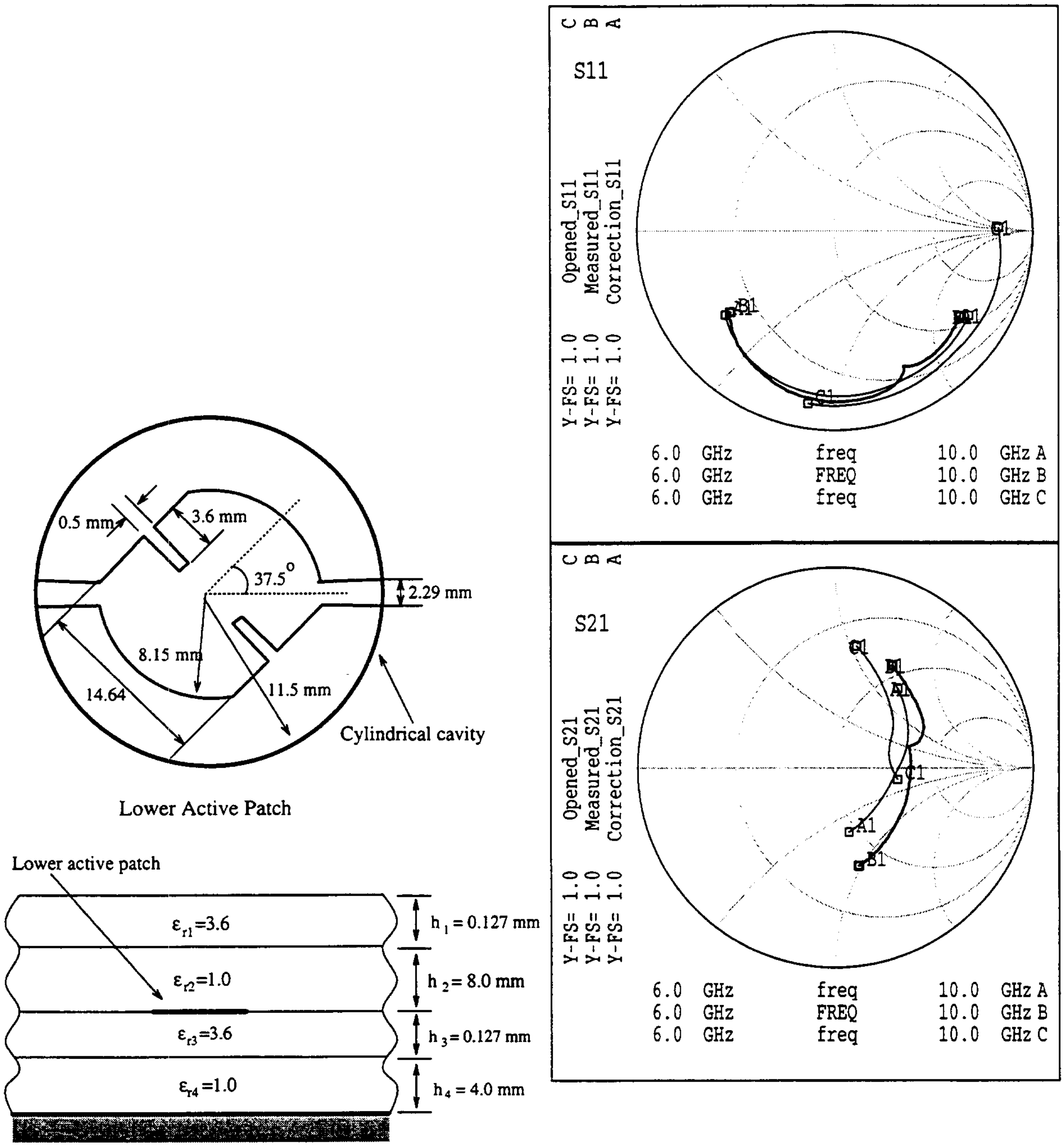

Figure 3.6: Comparison between the results obtained applying the correction, results obtained using the laterally opened model and measurements. Measured results correspond to thick line.

3.2.4 Infinite images with respect two tangent planes to cylindrical cavity

The next step is to see if more accurate results are obtained when two tangent, parallel planes to the cylindrical cavity are taken into account at the same time. In this case again, an infinite number of images with respect the two tangent planes need to be considered as shown in Fig. 3.7. The algorithm presented in the previous section can now be generalized in the following way:

$$G_{A_T}^{xx} = G_A(\rho) + \sum_{s=1}^{\infty} \cos\left[\theta_x^{(s)}\right] \left[G_A\left(\rho_a(s)\right) + G_A\left(\rho_b(s)\right)\right]$$

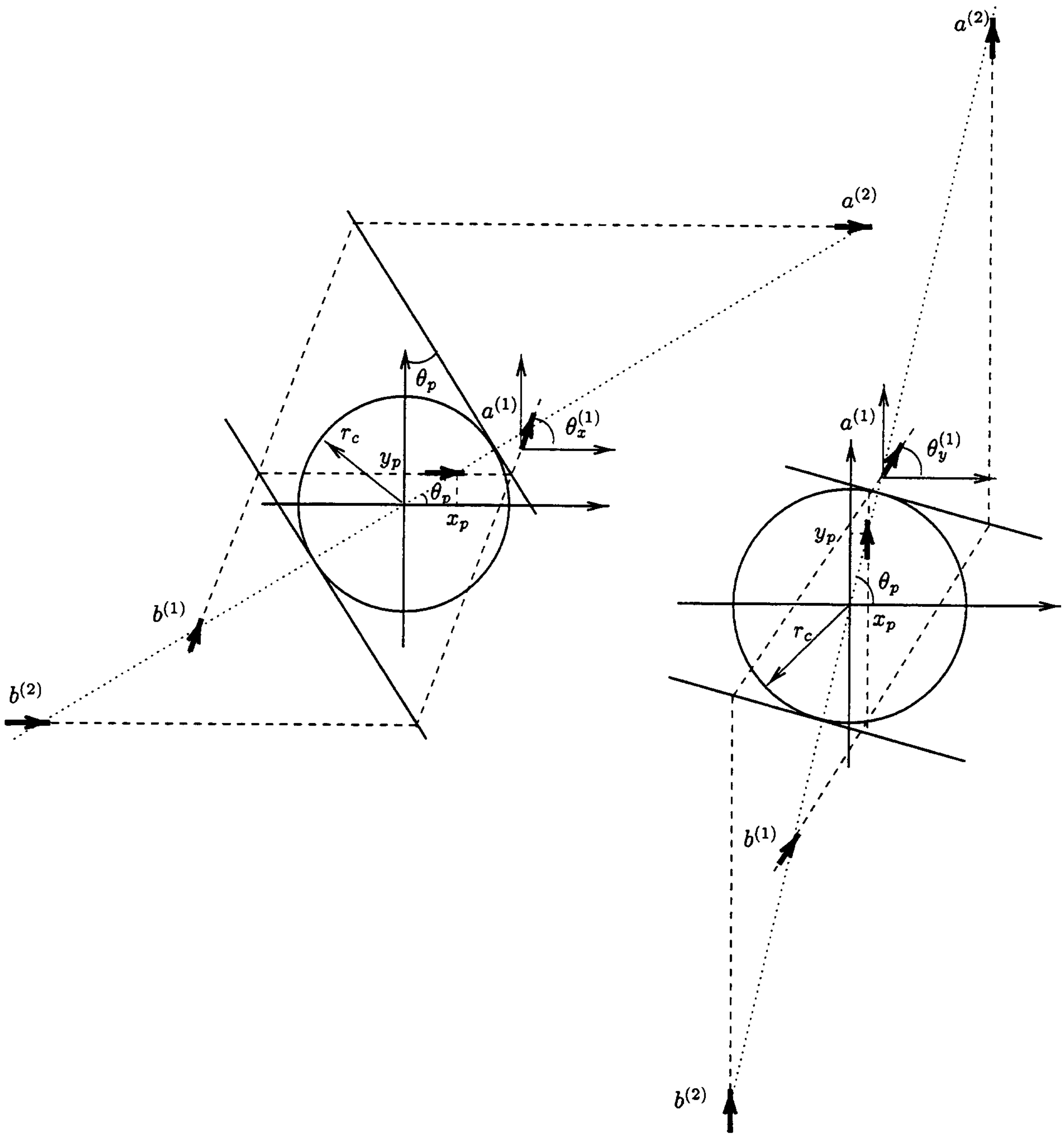

Figure 3.7: Spatial image situation when an arbitrary number of images is taken with respect the two closest parallel tangent planes to the cylindrical cavity.

$$G_{A_T}^{yx} = \sum_{s=1}^{\infty} \sin\left[\theta_x^{(s)}\right] \left[G_A\left(\rho_a(s)\right) + G_A\left(\rho_b(s)\right)\right]$$

$$G_{A_T}^{xy} = \sum_{s=1}^{\infty} \cos\left[\theta_y^{(s)}\right] \left[G_A\left(\rho_a(s)\right) + G_A\left(\rho_b(s)\right)\right]$$

$$G_{A_T}^{yy} = G_A(\rho) + \sum_{s=1}^{\infty} \sin\left[\theta_y^{(s)}\right] \left[G_A\left(\rho_a(s)\right) + G_A\left(\rho_b(s)\right)\right]$$

$$G_{v_T} = G_v(\rho) + \sum_{s=1}^{\infty}(-1)^s \left[G_v\left(\rho_a(s)\right) + G_v\left(\rho_a(s)\right)\right] \tag{3.8}$$

and according to Fig. 3.7, the distances of all the images $\rho_a(s)$, $\rho_b(s)$ to a generic observation point are found through the following recurrent relations:

$$\begin{array}{ll} \left.\begin{array}{l} r_a^{(1)} = 2\,r_c - r_p \\ r_b^{(1)} = 2\,r_c - r_p \end{array}\right\} & \text{Driven quantities} \\ r_a^{(s)} = 2\,r_c - r_b^{(s-1)} & r_b^{(s)} = 2\,r_c - r_a^{(s-1)} \\ s = 2, 3, \cdots, \infty & \\ \theta_a = \theta_p & \begin{array}{l} \theta_b = \theta_p - \pi;\ \theta_p > 0 \\ \theta_b = \theta_p + \pi;\ \theta_p < 0 \end{array} \end{array} \tag{3.9}$$

$$\begin{array}{ll} X_a^{(s)} = r_a^{(s)} \cos\left(\theta_a\right) & Y_a^{(s)} = r_a^{(s)} \sin\left(\theta_a\right) \\ X_b^{(s)} = r_b^{(s)} \cos\left(\theta_b\right) & Y_b^{(s)} = r_b^{(s)} \sin\left(\theta_b\right) \\ \rho_a(s) = \sqrt{\left(x_o - X_a^{(s)}\right)^2 - \left(y_o - Y_a^{(s)}\right)^2} & \\ \rho_b(s) = \sqrt{\left(x_o - X_b^{(s)}\right)^2 - \left(y_o - Y_b^{(s)}\right)^2} & \\ s = 1, 2, \cdots, \infty & \end{array} \tag{3.10}$$

where (x_o, y_o) are the coordinates of the observation point and the same notation as in equation (3.7) is used for the coordinates of the source point (ρ_p, θ_p). Finally, we will call $\theta_x^{(s)}$ and $\theta_y^{(s)}$ the orientation angles of the image dipoles. Straightforward geometrical considerations in Fig. 3.7 lead to the following recurrent relation for their evaluation.

$$\begin{array}{ll} \theta_x^{(1)} = 2\,\theta_p & \theta_y^{(1)} = 2\,\theta_p - \frac{\pi}{2} \\ \theta_x^{(s)} = 2\,\theta_p - \theta_x^{(s-1)} & \theta_y^{(s)} = 2\,\theta_p - \theta_y^{(s-1)} \\ s = 2, 3, \cdots, \infty & \end{array} \tag{3.11}$$

As before, in Fig. 3.8 we show the simulated results computed when this correction is applied to the conformal array lower active patch. In the same graphic we show the results when the pure laterally opened model is used and also measurements obtained when the lower active patch is backed by a cylindrical cavity and radiation is produced through a circular aperture opened at 8.0 mm distance from the lower active patch. Again, no considerable improvements are obtained.

3.2.5 Images for electric and magnetic currents

When electric and magnetic currents are considered together as it is needed in the analysis of the conformal array elementary radiator, in addition to the potentials, electric and magnetic fields Green's functions need to be evaluated. Moreover, images with respect both electric and magnetic dipoles need to be considered and the sign of the charges and orientation of the images are in both cases different [10]. In spite of this, a very compact way of writing both fields and potentials can be derived using the results in previous sections. Let G_{f_T} be a generic total electric or magnetic field Green's function produced by either electric or magnetic currents. If we consider the same structure as shown

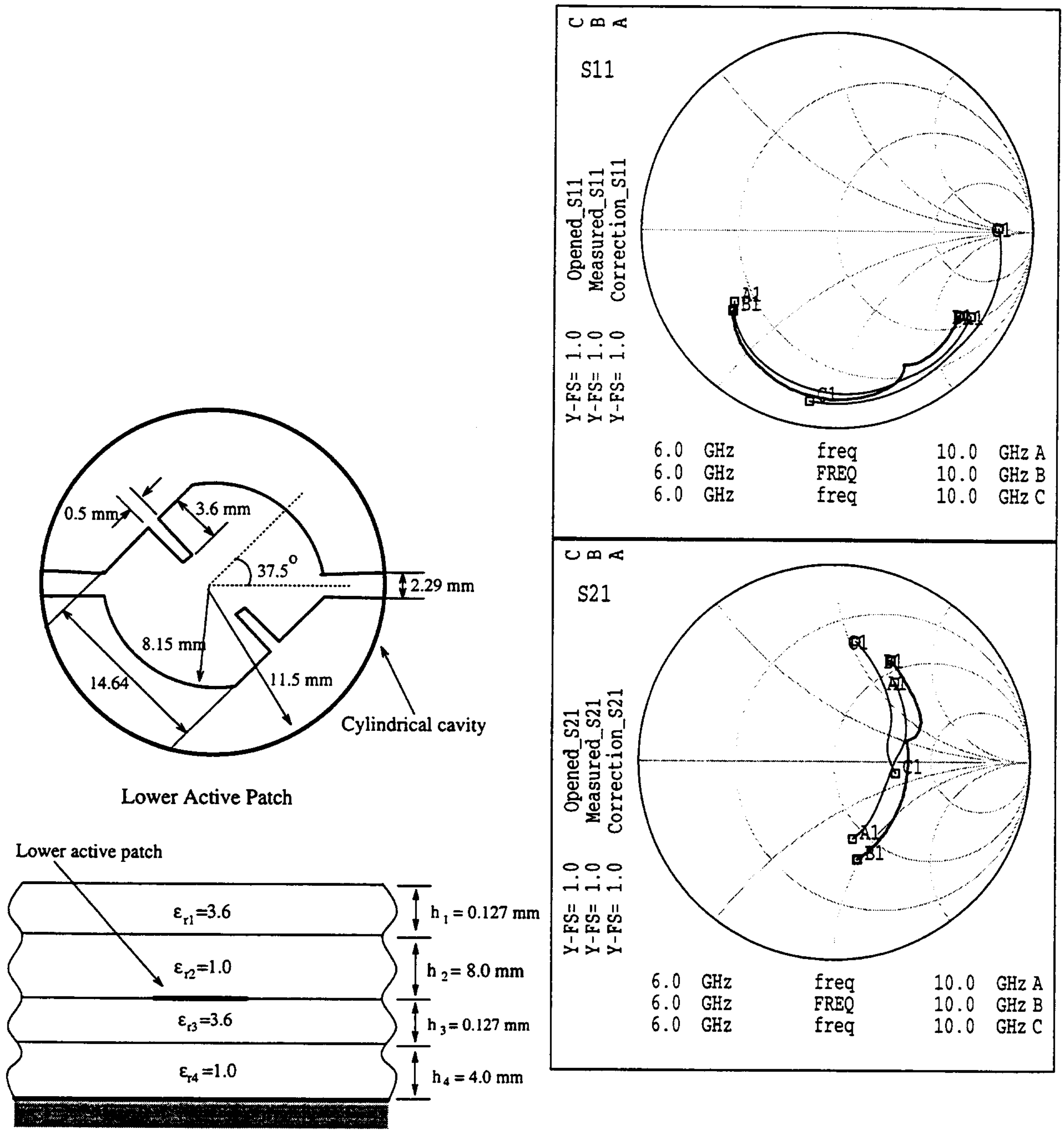

Figure 3.8: Comparison between the results obtained applying the correction, results obtained using the laterally opened model and measurements. Measured results correspond to thick line.

in Fig. 3.7, the form of the field satisfying in any case the boundary conditions at the two tangent walls shown in the figure can be written as.

$$
\begin{aligned}
G_{f_T}^{xx} &= G_f^{xx}(\rho_o,\theta_o) + \sum_{s=1}^{\infty}\Big[\cos\left(\theta_x^{(s)}\right)\left[G_f^{xx}\left(\rho_a^{(s)},\theta_a\right) + G_f^{xx}\left(\rho_b^{(s)},\theta_a\right)\right] + \\
&\quad \sin\left(\theta_x^{(s)}\right)\left[G_f^{xy}\left(\rho_a^{(s)},\theta_a\right) + G_f^{xy}\left(\rho_b^{(s)},\theta_a\right)\right]\Big] \\
G_{f_T}^{yx} &= G_f^{yx}(\rho_o,\theta_o) + \sum_{s=1}^{\infty}\Big[\cos\left(\theta_x^{(s)}\right)\left[G_f^{yx}\left(\rho_a^{(s)},\theta_a\right) + G_f^{yx}\left(\rho_b^{(s)},\theta_a\right)\right] +
\end{aligned}
$$

$$
\begin{aligned}
& \sin\left(\theta_x^{(s)}\right)\left[G_f^{yy}\left(\rho_a^{(s)},\theta_a\right)+G_f^{yy}\left(\rho_b^{(s)},\theta_a\right)\right]\Big] \\
G_{f_T}^{xy} &= G_f^{xy}\left(\rho_o,\theta_o\right)+\sum_{s=1}^{\infty}\Big[\cos\left(\theta_x^{(s)}\right)\left[G_f^{xx}\left(\rho_a^{(s)},\theta_a\right)+G_f^{xx}\left(\rho_b^{(s)},\theta_a\right)\right]+ \\
& \sin\left(\theta_x^{(s)}\right)\left[G_f^{xy}\left(\rho_a^{(s)},\theta_a\right)+G_f^{xy}\left(\rho_b^{(s)},\theta_a\right)\right]\Big] \\
G_{f_T}^{yy} &= G_f^{yy}\left(\rho_o,\theta_o\right)+\sum_{s=1}^{\infty}\Big[\cos\left(\theta_x^{(s)}\right)\left[G_f^{yx}\left(\rho_a^{(s)},\theta_a\right)+G_f^{yx}\left(\rho_b^{(s)},\theta_a\right)\right]+ \\
& \sin\left(\theta_x^{(s)}\right)\left[G_f^{yy}\left(\rho_a^{(s)},\theta_a\right)+G_f^{yy}\left(\rho_b^{(s)},\theta_a\right)\right]\Big]
\end{aligned} \tag{3.12}
$$

In the same way, let G_{sp_T} be a generic total scalar potential Green's function and G_{vp_T} a generic total vector potential Green's function produced by either electric or magnetic currents. The form of the potentials satisfying in any case the boundary conditions at the two tangent walls shown in Fig. 3.7 can be written as

$$
\begin{aligned}
G_{vp_T}^{xx} &= G_{vp}(\rho)+\sum_{s=1}^{\infty}\cos\left[\theta_x^{(s)}\right]\left[G_{vp}\left(\rho_a(s)\right)+G_{vp}\left(\rho_b(s)\right)\right] \\
G_{vp_T}^{yx} &= \sum_{s=1}^{\infty}\sin\left[\theta_x^{(s)}\right]\left[G_{vp}\left(\rho_a(s)\right)+G_{vp}\left(\rho_b(s)\right)\right] \\
G_{vp_T}^{xy} &= \sum_{s=1}^{\infty}\cos\left[\theta_y^{(s)}\right]\left[G_{vp}\left(\rho_a(s)\right)+G_{vp}\left(\rho_b(s)\right)\right] \\
G_{vp_T}^{yy} &= G_{vp}(\rho)+\sum_{s=1}^{\infty}\sin\left[\theta_y^{(s)}\right]\left[G_{vp}\left(\rho_a(s)\right)+G_{vp}\left(\rho_b(s)\right)\right] \\
G_{sp_T} &= G_{sp}(\rho)+\sum_{s=1}^{\infty}(h_o)^s\left[G_{sp}\left(\rho_a(s)\right)+G_{sp}\left(\rho_a(s)\right)\right]
\end{aligned} \tag{3.13}
$$

In above expressions, all the geometrical distances are defined in the same exact form shown in equations (3.9,3.10). As regard the orientation angles of the image dipoles $\theta_x^{(s)}$, $\theta_y^{(s)}$, they can be redefined with the following recurrent algorithm:

$$
\begin{aligned}
& \theta_x^{(0)} = 0;\ \theta_y^{(0)} = \tfrac{\pi}{2} \\
& \theta_x^{(s)} = \left[2\,\theta_p - \hat{\theta}\right] - \theta_x^{(s-1)} \\
& \theta_y^{(s)} = \left[2\,\theta_p - \hat{\theta}\right] - \theta_y^{(s-1)} \\
& s = 1, 2, \cdots, \infty
\end{aligned} \tag{3.14}
$$

where the angle $\hat{\theta}$ takes into account the actual nature of the current dipole (electric or magnetic) and the sign variable h_o the actual nature of the charge (electric or magnetic). Both variables take therefore different values for either electric or magnetic sources as shown in Table 3.1. Finally, it is

-	Electric source	Magnetic source
$\hat{\theta}$	0	π
h_o	-1	$+1$

Table 3.1: Values of $\hat{\theta}$ and h_o for both electric and magnetic sources.

interesting to notice that the angle θ_p of equations (3.12,3.13) is related with the inclination of the tangent metallic walls to the cylindrical cavity. In consequence, by selecting appropriately this angle we can use the same expressions as in (3.12,3.13) to model both the walls at the ports positions and the cylindrical cavity. The proper selection of θ_p for the two types of analysis is shown in Table 3.2. To show the applicability of the method, we present in Fig. 3.9 the results obtained for the conformal

-	θ_p
Cylindrical cavity	$\arctan\left(\frac{y_p}{x_p}\right)$
Walls at ports x=cte.	0
Walls at ports y=cte.	$\frac{\pi}{2}$

Table 3.2: Angle θ_p for different types of analysis.

array elementary radiator with both the lower active patch and the upper passive patch acting as radiating aperture.

In this case 6 images have been taken with respect two metallic walls placed at the ports positions. In the same graph we include the results computed when the laterally opened model is used and also measurements obtained when the structure is backed by a cylindrical cavity. As we see in this case the agreement between measured and simulated results is good. Finally, in Fig. 3.10 we present the results obtained when several images are taken with respect two tangent planes to the cylindrical cavity. In this case however, we clearly see numerical instabilities due to lack of precision in the modelization of the ports.

3.2.6 Imposition of boundary conditions in the image series

The series of images developed in previous sections might exhibit very slow convergence rates for certain combinations of substrates. It has been observed that this is specially true when the resulting substrate arrangement propagates surface wave modes. In this case, the radiation of a single dipole is not anymore affected only by what is happening in the vicinity of the dipole. In fact, the excitation of surfaces wave modes results in that the electromagnetic energy associated to the structure can travel long distances inside the substrates before it is attenuated. One of such a situation is shown in Fig. 3.11 where we see a printed dipole backed by two metallic walls at the ports positions. The results are computed including 2-images to account for the presence of the two metallic walls and as we observe, the model is not anymore accurate when frequency increases (transmission coefficient becomes positive at a certain frequency). In Fig. 3.12, we show the results when 20, 40 and 100 images are included in the analysis in order to increase the accuracy of the model. As shown, a ripple in the scattering parameters reveals that the series of images is converging very slowly and that even with 100-images good convergence has not yet been achieved (ripple is smaller but still present). To try to overcome this problem, it should be pointed out that there are two main characteristics in any Green's functions that must be preserved if accurate results are to be obtained, namely:

1. The singular behavior when $\rho \to 0$.

2. The boundary conditions at all interfaces.

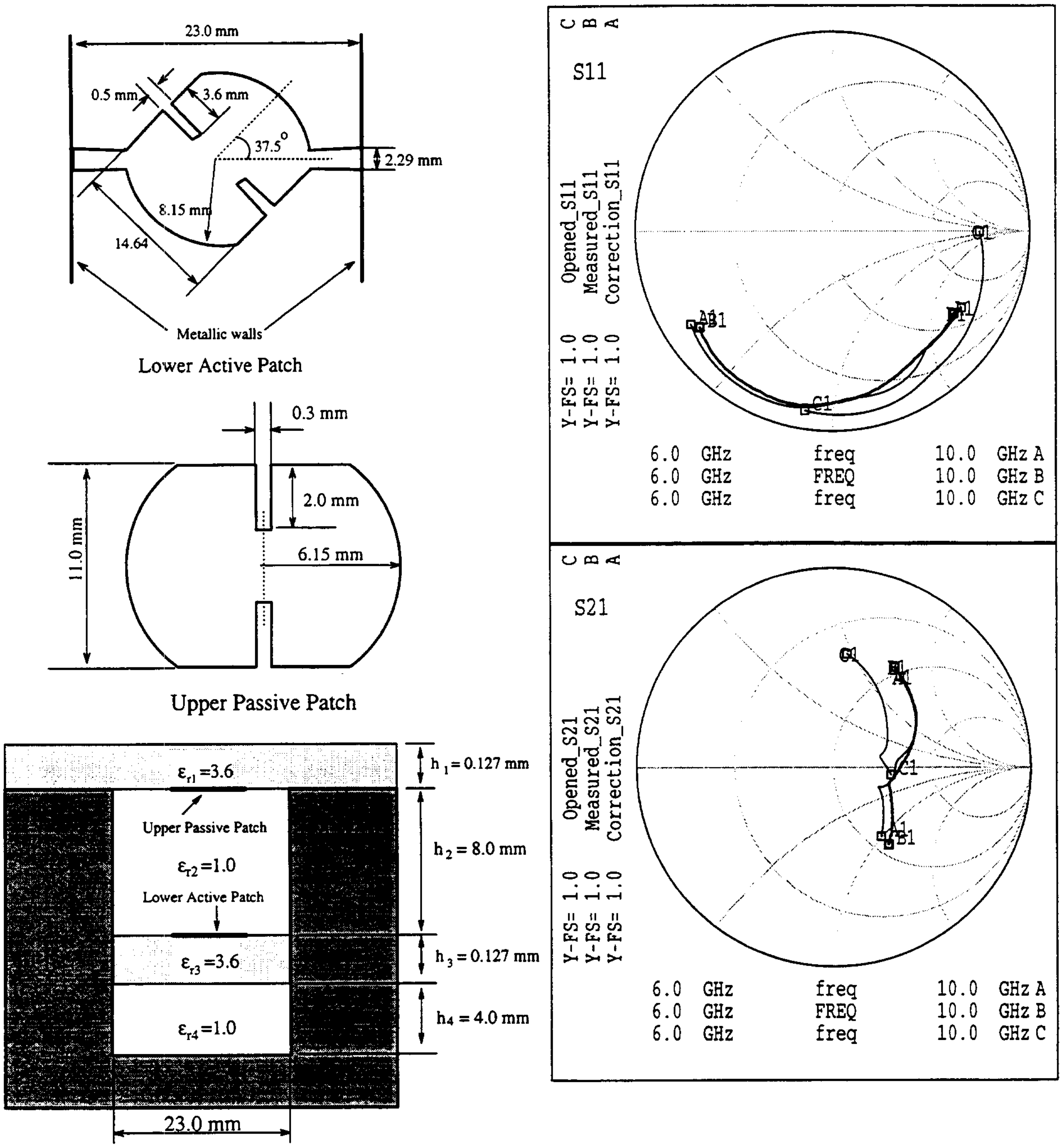

Figure 3.9: Comparison between the results obtained applying the correction, results obtained using the laterally opened model and measurements. Measured results correspond to thick line.

The singular behavior is naturally preserved in the developed series of images, because they have been constructed using standard Green's functions. What remains then, is the accurate imposition of the boundary conditions at the metallic walls. This will be done by adding the first $(n-2)$ images of the series as before, and then computing the needed strength of the last two remaining images so that the boundary conditions for the fields are strictly satisfied at the two metallic walls. Consider again the structure shown in Fig. 3.3. The total electric scalar potential in the structure is now

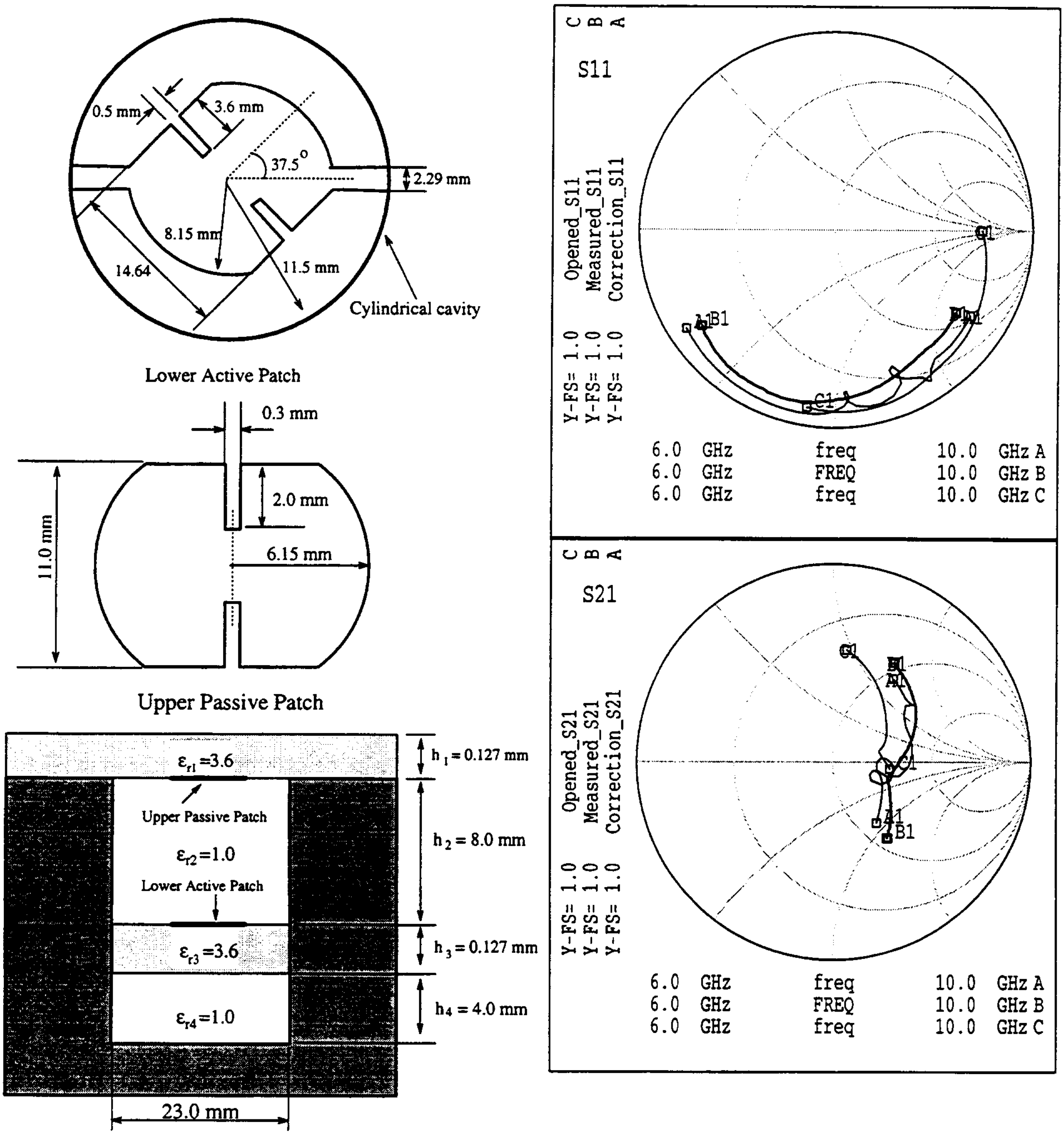

Figure 3.10: Comparison between the results obtained applying the correction, results obtained using the laterally opened model and measurements. Measured results correspond to thick line.

written as:

$$G_{v_T}(x) = G_v\left(x, x_p\right) + \sum_{s=1}^{n-1} (-1)^s \left[G_v\left(x, x_a^{(s)}\right) + G_v\left(x, x_b^{(s)}\right)\right] + q_1\, G_v\left(x, x_a^{(n)}\right) + q_2\, G_v\left(x, x_b^{(n)}\right) \quad (3.15)$$

where for instance $G_v\left(x, x_p\right)$ is the scalar potential at point (x, y) produced by a source placed at point (x_p, y_p). Since the boundary conditions for the electric field implies zero potential at the metallic walls, the additional constants q_1 and q_2 controlling the strength of the last two images will be adjusted so as to vanish the total potential at the two metallic walls. To do so we can first define

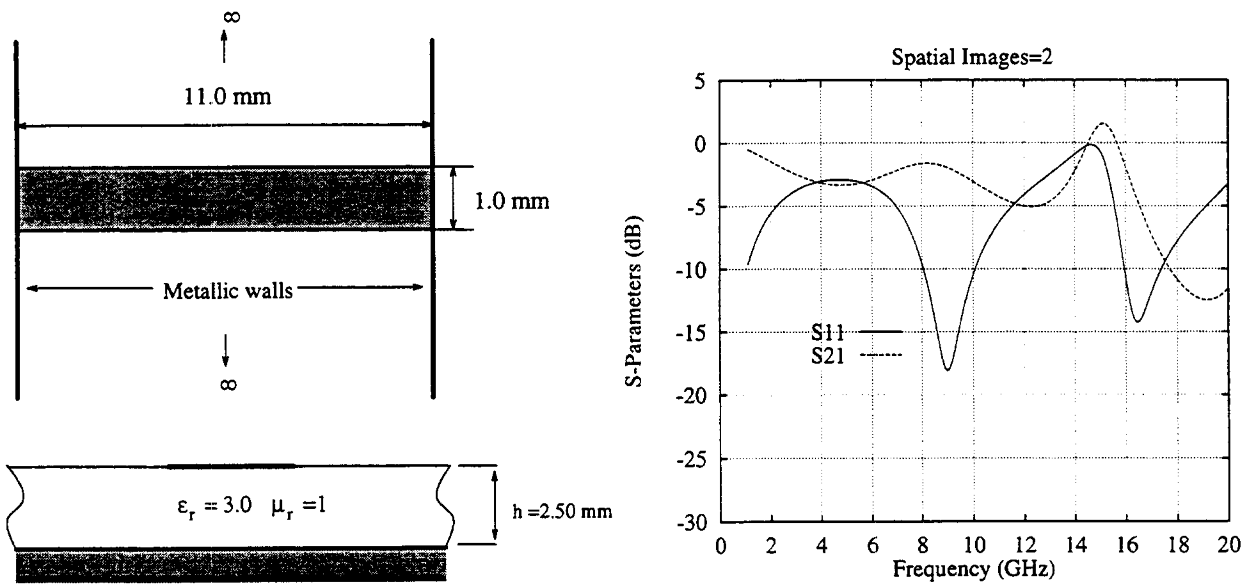

Figure 3.11: Typical results obtained with the series of images derived in previous sections for a microstrip structure, showing drop in accuracy.

the potential produced by the $(n-2)$ first images as:

$$\hat{G}_v(x) = G_v(x, x_p) + \sum_{s=1}^{n-1} (-1)^s \left[G_v\left(x, x_a^{(s)}\right) + G_v\left(x, x_b^{(s)}\right) \right] \tag{3.16}$$

and compute this potential at the two metallic walls.

$$w_1 = \hat{G}_v(x_0(1))\,;\; w_2 = \hat{G}_v(x_0(2)) \tag{3.17}$$

Next we compute the total potential produced by the two last images in the series, namely.

$$G_v^n(x) = q_1\, G_v\left(x, x_a^{(n)}\right) + q_2\, G_v\left(x, x_b^{(n)}\right) \tag{3.18}$$

Since the total potential produced by all n-images must be zero at the metallic walls, we directly write the following system of equations:

$$\begin{aligned} -w_1 &= G_v^n\left(x_0^{(1)}\right) = q_1\, G_v\left(x_0^{(1)}, x_a^{(n)}\right) + q_2\, G_v\left(x_0^{(1)}, x_b^{(n)}\right) \\ -w_2 &= G_v^n\left(x_0^{(2)}\right) = q_1\, G_v\left(x_0^{(2)}, x_a^{(n)}\right) + q_2\, G_v\left(x_0^{(2)}, x_b^{(n)}\right) \end{aligned} \tag{3.19}$$

from where we easily find the two unknowns q_1 and q_2 required to annihilate the total potential in equation (3.15) at the metallic walls:

$$q_1 = \frac{w_2\,\gamma_{12} - w_1\,\gamma_{22}}{\gamma_{11}\,\gamma_{22} - \gamma_{21}\,\gamma_{12}};\; q_2 = \frac{w_2\,\gamma_{11} - w_1\,\gamma_{21}}{\gamma_{12}\,\gamma_{21} - \gamma_{22}\,\gamma_{11}} \tag{3.20}$$

with the following redefinition of the matrix coefficients.

$$\begin{aligned} \gamma_{11} &= G_v\left(x_0(1), x_a^{(n)}\right) & \gamma_{12} &= G_v\left(x_0(1), x_b^{(n)}\right) \\ \gamma_{21} &= G_v\left(x_0(2), x_a^{(n)}\right) & \gamma_{22} &= G_v\left(x_0(2), x_b^{(n)}\right) \end{aligned} \tag{3.21}$$

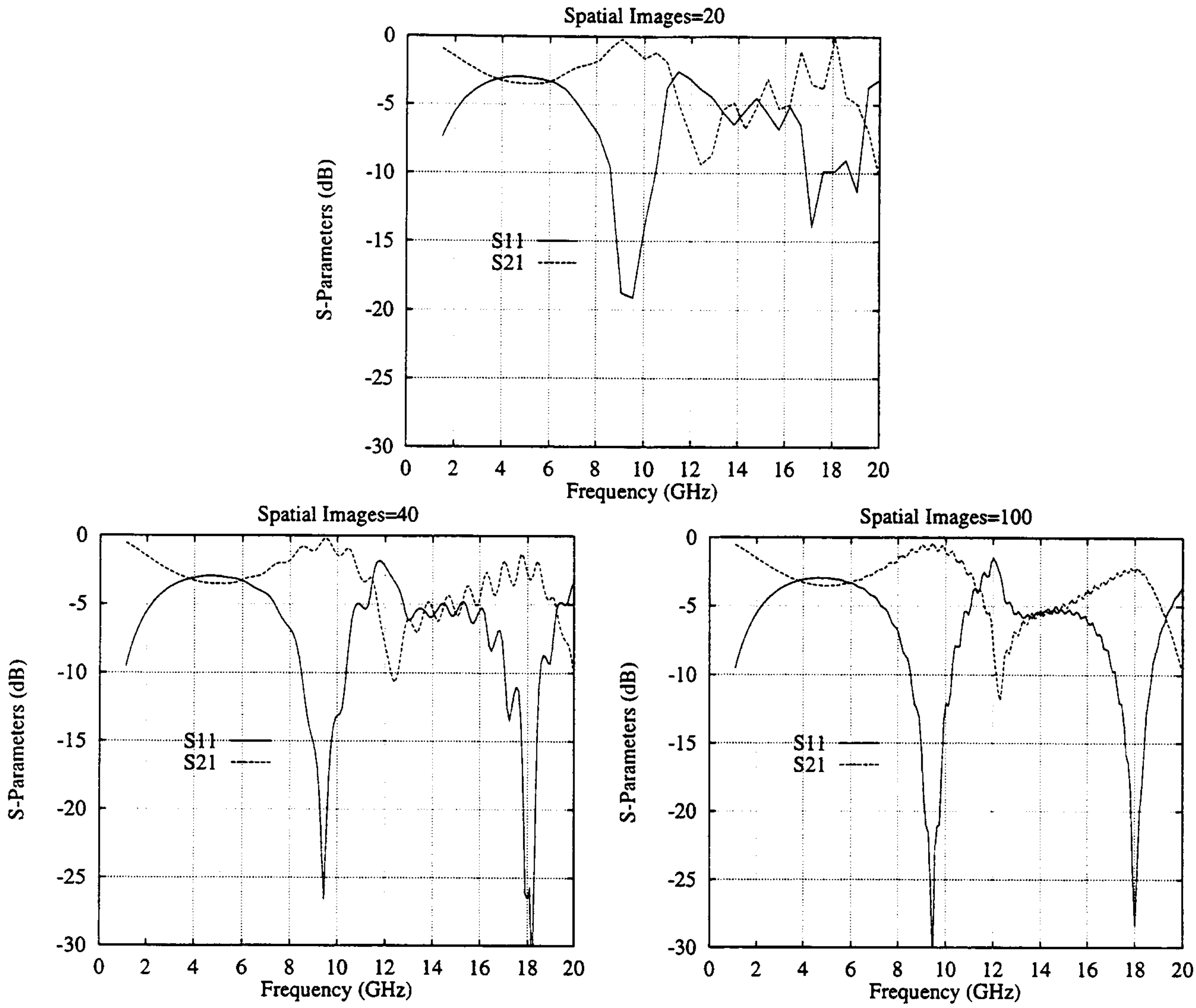

Figure 3.12: Results for the same structure as in Fig. 3.11 when more images are included in the analysis.

Fig. 3.13 shows the results obtained for the same structure as before when this algorithm is used. In the figure the results with 2 and 6 images are presented showing that the ripple has disappeared and that the convergence is good. As we can observe, by applying this technique the gain in computational effort and numerical accuracy is considerable. When magnetic currents are considered, the situation is more complicated, since now the boundary condition for the magnetic scalar potential requires the derivative with respect the normal to the metallic walls to be zero. In this case the expressions for the evaluation of the potential in equations (3.15,3.16,3.18) also apply. The only difference is in the evaluation of the unknown constants q_1 and q_2 which now must assure the total derivatives to be zero. To proceed with their evaluation, we first compute the derivative of the potential produced by the $(n-2)$ first images at the metallic walls:

$$w_1 = \frac{\hat{G}_w\left(x_0^{(1)} + \Delta x\right) - \hat{G}_w\left(x_0^{(1)}\right)}{\Delta x}; \; w_2 = \frac{\hat{G}_w\left(x_0^{(2)} + \Delta x\right) - \hat{G}_w\left(x_0^{(2)}\right)}{\Delta x} \tag{3.22}$$

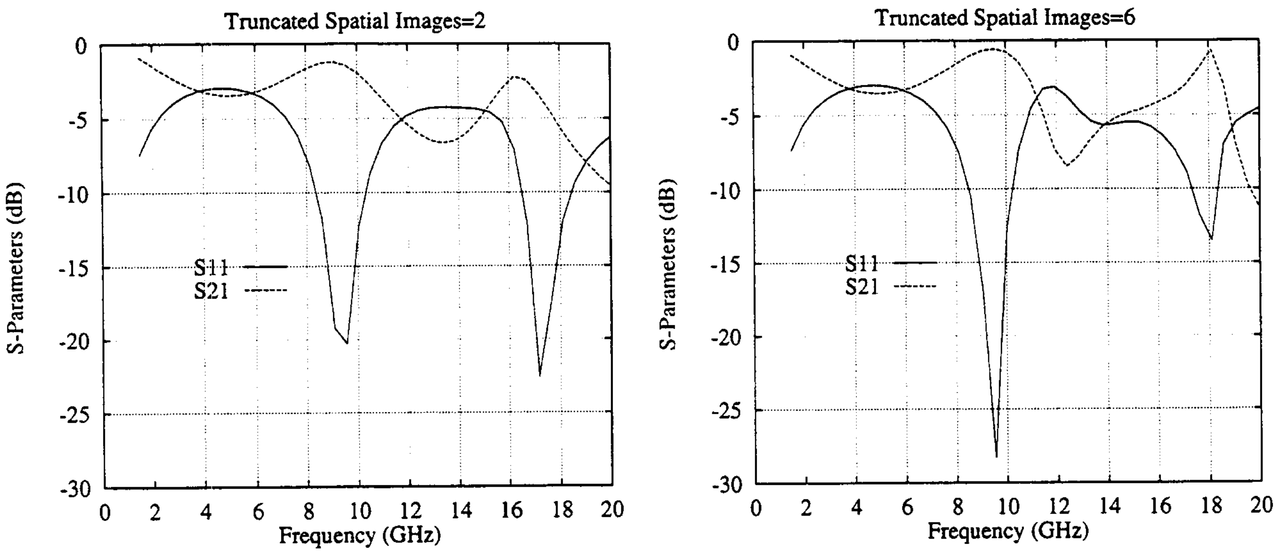

Figure 3.13: Results obtained for the same structure as in Fig. 3.11 when the last two images in the series are used to strictly impose the boundary conditions at the metallic walls.

where Δx is an arbitrary small distance. Following the same notation as before, we can now compute the derivative of the potential produced by the two last images at the metallic walls. The system of equations is obtained when we enforce these two last derivatives to exactly compensate the values w_1 and w_2 at the first and second metallic walls respectively.

$$-w_1 = \frac{G_w^n\left(x_0^{(1)} + \Delta x\right) - G_w^n\left(x_0^{(1)}\right)}{\Delta x}; \; -w_2 = \frac{G_w^n\left(x_0^{(2)} + \Delta x\right) - G_w^n\left(x_0^{(2)}\right)}{\Delta x} \tag{3.23}$$

If we introduce the definition for the potential in equation (3.18) into the system of equations formed in (3.23), the following matrix coefficients can be defined:

$$\begin{aligned} \gamma_{11} &= \frac{G_w\left(x_0^{(1)}+\Delta x, x_a^{(n)}\right) - G_w\left(x_0^{(1)}, x_a^{(n)}\right)}{\Delta x} & \gamma_{12} &= \frac{G_w\left(x_0^{(1)}+\Delta x, x_b^{(n)}\right) - G_w\left(x_0^{(1)}, x_b^{(n)}\right)}{\Delta x} \\ \gamma_{21} &= \frac{G_w\left(x_0^{(2)}+\Delta x, x_a^{(n)}\right) - G_w\left(x_0^{(2)}, x_a^{(n)}\right)}{\Delta x} & \gamma_{22} &= \frac{G_w\left(x_0^{(2)}+\Delta x, x_b^{(n)}\right) - G_w\left(x_0^{(2)}, x_b^{(n)}\right)}{\Delta x} \end{aligned} \tag{3.24}$$

so that the unknown coefficients q_1 and q_2 are computed with the same expressions as in (3.20). Finally, equation (3.15) is again reused to compute the total magnetic scalar potential Green's function. It is important to note that similar procedure is used to enforce the boundary conditions for the field Green's functions. In this case the strength of the two last images are computed so as to annihilate the required components of the field at the metallic walls (tangent components for electric fields and normal components for magnetic fields).

In Fig. 3.14 we show the results obtained when this correction is applied to the conformal array elementary radiator. In the simulation, the model corresponding to two metallic planes placed at the ports positions is used and as wee see, the results obtained are in this case good.

3.2.7 Imposition of boundary conditions for cylindrical cavity

The same idea as developed in the previous section can be used to impose the boundary conditions for the fields at a finite number of points within the cylindrical cavity wall. Following this procedure,

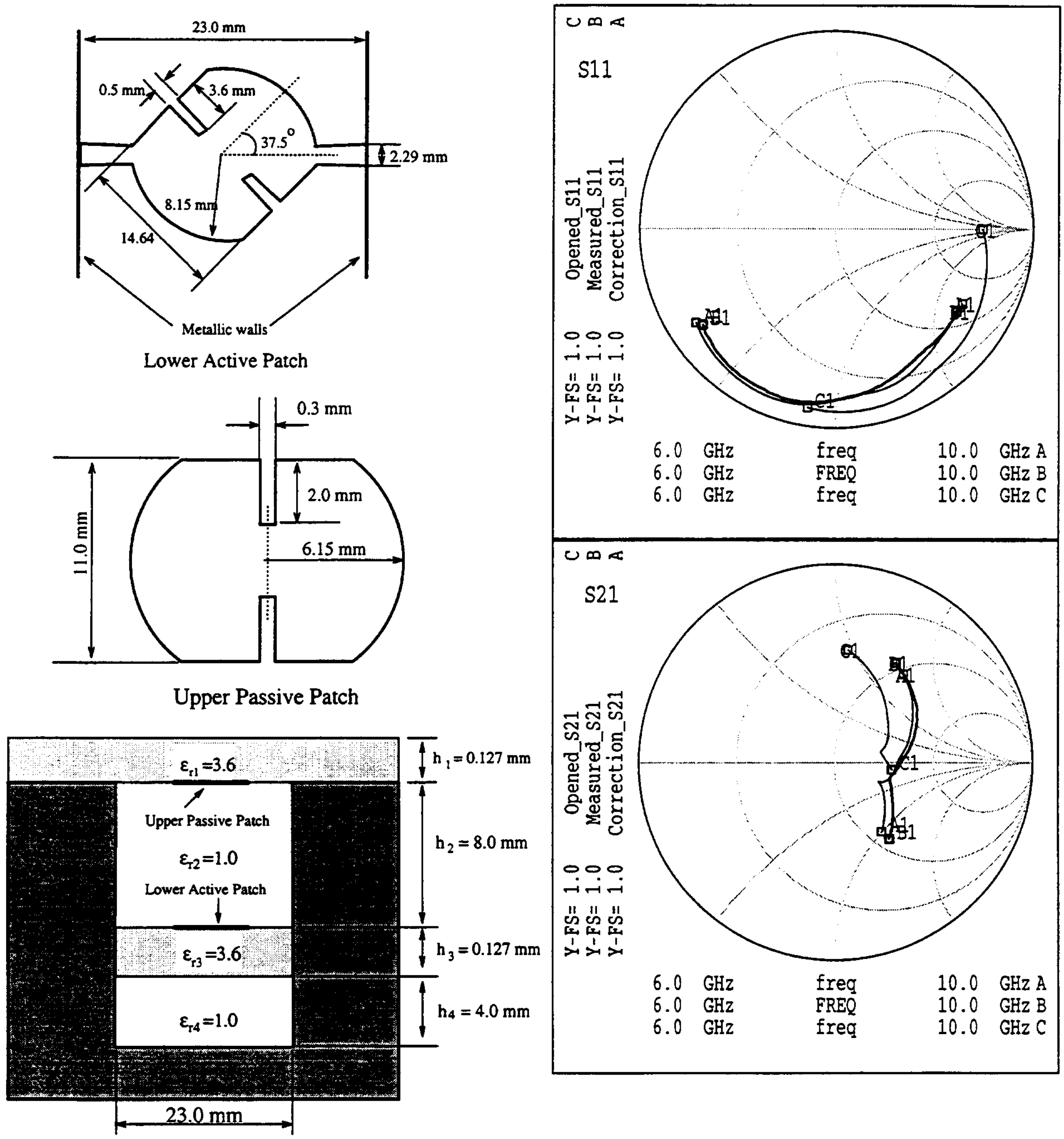

Figure 3.14: Comparison between the results obtained applying the correction, results obtained using the laterally opened model and measurements. Measured results correspond to thick line.

a certain number of images are placed strategically and the strength of all the images are computed so that the boundary conditions for the fields are strictly satisfied at a discrete set of points. Let us then consider the cylindrical cavity shown in Fig. 3.15 with an arbitrary number n of images. In the system of images shown in the figure, the total magnetic vector potential produced by an $\hat{e}_x$ directed electric dipole is written as:

$$G_{A_T}^{xx}(x,y) = G_A\left(x,y \mid x_p,y_p\right) + \sum_{k=1}^{n} q_k \cos\left[\alpha(k)\right] G_A\left(x,y \mid x_a^{(k)},y_b^{(k)}\right)$$

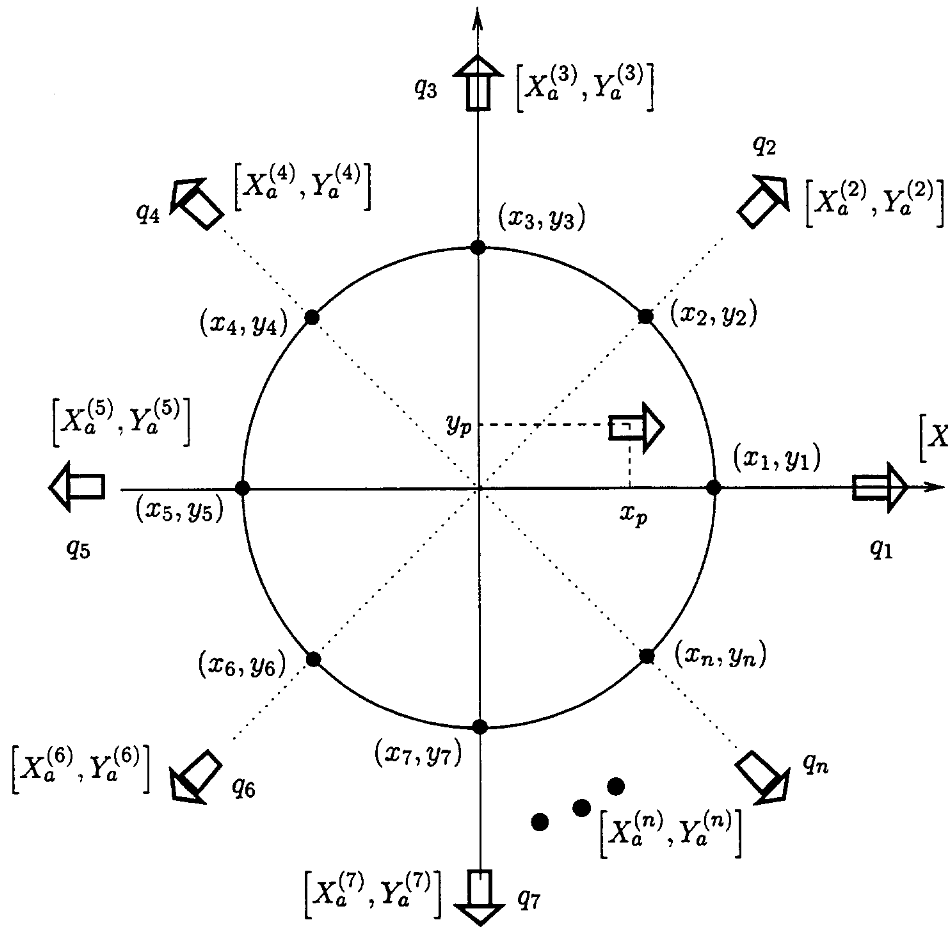

Figure 3.15: Spatial image arrangement used to try to impose the boundary conditions of the fields at a discrete set of points in the cylindrical cavity boundary.

$$G_{A_T}^{yx} = \sum_{k=1}^{n} q_k \sin[\alpha(k)] \; G_A\left(x, y \mid x_a^{(k)}, y_b^{(k)}\right) \tag{3.25}$$

where again $G_A(x, y \mid x_p, y_p)$ is the potential produced at the point (x, y) by a source placed at the point (x_p, y_p) and q_k is the set of unknown constant to be computed. Moreover, $\alpha(k)$ is the orientation angle for the k-th image and plays a similar role as the orientation angles defined in section 3.2.4. The unknown constants are computed by imposing zero tangent component of the vector potential at n-distinct points in the cylindrical cavity wall. Simple geometrical considerations translate above condition mathematically as.

$$\begin{array}{l} \sin[\alpha(i)] \; G_{A_T}^{xx}(x_i, y_i) + \cos[\alpha(i)] \; G_{A_T}^{yx}(x_i, y_i) = 0 \\ i = 1, 2, \cdots, n \end{array} \tag{3.26}$$

Introducing equation (3.25) into the boundary conditions in (3.26) and after few straightforward manipulations we obtain the following system of linear equations:

$$P^{(e)}(i) = \sum_{k=1}^{n} q_k \, P(i, k); \; i = 1, 2, \cdots, n \tag{3.27}$$

where the matrix coefficients and known term vector are given respectively by.

$$\begin{aligned} P(i,k) &= \sin\left[\alpha(i)+\alpha(k)\right]\, G_A\left(x_i,y_i \mid x_a^{(k)},y_a^{(k)}\right) \\ P^{(e)}(i) &= -\sin\left[\alpha(i)\right]\, G_A\left(x_i,y_i \mid x_p,y_p\right) \end{aligned} \tag{3.28}$$

The solution of the system of equations in (3.27,3.28) gives the unknown coefficients q_k, which are then introduced in (3.25) to find the corresponding components of the dyadic magnetic vector potential Green's functions. The Green's functions thus computed will strictly satisfy the boundary conditions, at least, at a discrete set of points around the cylindrical cavity wall.

Similar procedure is followed if an $\hat{e}_y$ directed dipole is considered. In this case, the corresponding components of the dyadic are simply written as:

$$\begin{aligned} G_{A_T}^{xy} &= \sum_{k=1}^{n} q_k \cos\left[\alpha(k)\right]\, G_A\left(x,y \mid x_a^{(k)},y_b^{(k)}\right) \\ G_{A_T}^{yy}(x,y) &= G_A\left(x,y \mid x_p,y_p\right) + \sum_{k=1}^{n} q_k \sin\left[\alpha(k)\right]\, G_A\left(x,y \mid x_a^{(k)},y_b^{(k)}\right) \end{aligned} \tag{3.29}$$

and the new unknown constants q_k are computed by imposing zero tangent components of the potential at a discrete set of points around the cylindrical cavity wall. Mathematically this is translated as.

$$\begin{aligned} &\sin\left[\alpha(i)\right]\, G_{A_T}^{xy}\left(x_i,y_i\right) + \cos\left[\alpha(i)\right]\, G_{A_T}^{yy}\left(x_i,y_i\right) = 0 \\ &i = 1,2,\cdots,n \end{aligned} \tag{3.30}$$

Again, introducing equation (3.29) into the boundary condition (3.30) a system of linear equations of the form shown in (3.27) is obtained. Now the matrix coefficients and known term vector take the following form:

$$\begin{aligned} P(i,k) &= \sin\left[\alpha(i)+\alpha(k)\right]\, G_A\left(x_i,y_i \mid x_a^{(k)},y_a^{(k)}\right) \\ P^{(e)}(i) &= -\cos\left[\alpha(i)\right]\, G_A\left(x_i,y_i \mid x_p,y_p\right) \end{aligned} \tag{3.31}$$

Finally, the same procedure can be repeated for the electric scalar potential Green's function. In this case the total potential is written as.

$$G_{v_T}(x,y) = G_v\left(x,y \mid x_p,y_p\right) + \sum_{k=1}^{n} q_k\, G_v\left(x,y \mid x_a^{(k)},y_a^{(k)}\right) \tag{3.32}$$

Now the boundary condition is simply vanishing potential at the cylindrical cavity. This condition will again be imposed at certain discrete points around the cylindrical cavity wall, namely.

$$G_{v_T}\left(x_i,y_i\right) = 0;\; i = 1,2,\cdots,n \tag{3.33}$$

Again, using equation (3.32) into the boundary conditions in (3.33) leads to the same system of linear equations in (3.27) with the following matrix coefficients and known term vector.

$$\begin{aligned} P(i,k) &= G_v\left(x_i,y_i \mid x_a^{(k)},y_a^{(k)}\right) \\ P^{(e)}(i) &= -G_v\left(x_i,y_i \mid x_p,y_p\right) \end{aligned} \tag{3.34}$$

The formulation will be completed once we define the position and orientation of the images as well as the discrete set of points where the boundary conditions are strictly imposed. The orientation angles for all the images are set following a linear rule, namely.

$$\alpha(i) = (i-1)\,\frac{2\pi}{n};\; i = 1,2,\cdots,n \tag{3.35}$$

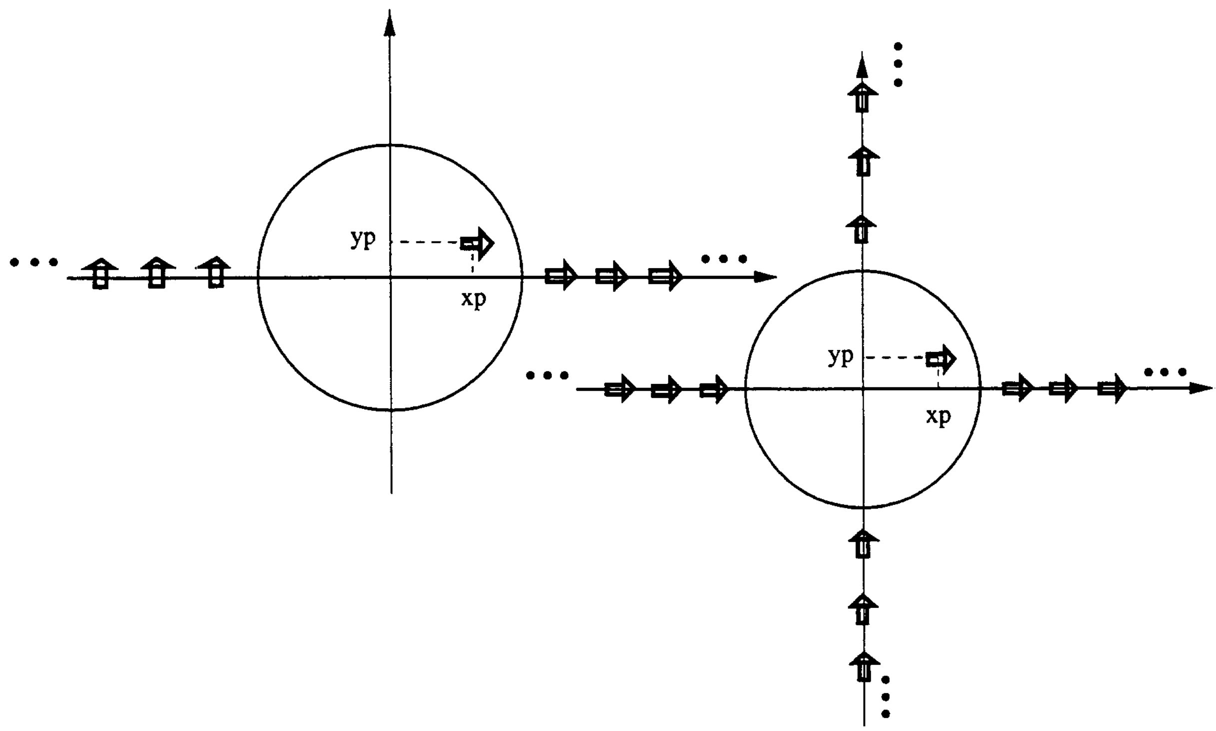

Figure 3.16: Alternative spatial image arrangements for the modelization of the cylindrical cavity.

The coordinates of all the images can now be computed as follows:

$$\begin{array}{ll} r_p = \sqrt{x_p^2 + y_p^2} & r_a = 2\,r_c - r_p \\ x_a^{(k)} = r_a \cos\left[\alpha(k)\right] & y_a^{(k)} = r_a \sin\left[\alpha(k)\right] \\ k = 1, 2, \cdots, n & \end{array} \tag{3.36}$$

where as usual (x_p, y_p) are the coordinates of the source point and r_c is the radius of the cylindrical cavity. Finally, the points where the boundary conditions are strictly imposed are computed as.

$$x_i = rc \cos\left[\alpha(i)\right]; y_i = rc \sin\left[\alpha(i)\right]; i = 1, 2, \cdots, n \tag{3.37}$$

In addition to the arrangement described above, other possible configuration of images have been tried as shown in Fig. 3.16. Unfortunately, for certain combinations of source orientations with the chosen set of points (x_i, y_i), all of them exhibited singular behaviors leading to non invertible systems of equations in (3.27).

3.3 Rigorous Green's Functions Approach

As we have seen in the previous section, there are many difficulties for an efficient implementation of the image approach, due mainly to the slow convergence rate of some of the series involved. An alternative approach can be derived by introducing the Fourier series expansion in the original Maxwell equations governing the behavior of the fields in our antenna structure. In this case, electric and magnetic fields Green's functions due to both electric and magnetic currents are easily expressed in the form of the following modal expansions

$$
\begin{aligned}
\overline{\overline{G}}_{E_J} &= \sum_m V_m(z)\, \bar{e}_m(x',y')\, \bar{e}_m(x,y) \\
\overline{\overline{G}}_{H_J} &= \sum_m I_m(z)\, \bar{e}_m(x',y')\, \bar{h}_m(x,y) \\
\overline{\overline{G}}_{E_M} &= \sum_m V_m(z)\, \bar{h}_m(x',y')\, \bar{e}_m(x,y) \\
\overline{\overline{G}}_{H_M} &= \sum_m I_m(z)\, \bar{h}_m(x',y')\, \bar{h}_m(x,y)
\end{aligned}
\tag{3.38}
$$

where the index m runs to all possible $TE_{m,n}$ and $TM_{m,n}$ modes supported by the actual cavity we are considering. As we see, the transverse dependence of the structure is represented by the e and h vector mode functions and the longitudinal dependence by the voltage and currents coefficients V_m and I_m [11]. These voltages and currents are again computed in the equivalent transmission line networks describing the geometrical dependence of the structure in the longitudinal axis and they were already derived in chapter 2. What it remains therefore, is the evaluation of the e and h vector mode functions which are dependent on the actual form of the cavity cross section. For the case of a cylindrical cavity, they can be written in analytic form as [11]

$$
\begin{aligned}
e_\rho^{TM_p} &= -\sqrt{\frac{\epsilon_m}{\pi}} \frac{J_m'\left(\frac{x_i \rho}{a}\right)}{a\, J_{m+1}(x_i)} \cos(m\,\varphi) \\
e_\varphi^{TM_p} &= \sqrt{\frac{\epsilon_m}{\pi}} \frac{m}{x_i} \frac{J_m\left(\frac{x_i \rho}{a}\right)}{\rho\, J_{m+1}(x_i)} \sin(m\,\varphi) \\
h_\rho^{TM_p} &= -\sqrt{\frac{\epsilon_m}{\pi}} \frac{m}{x_i} \frac{J_m\left(\frac{x_i \rho}{a}\right)}{\rho\, J_{m+1}(x_i)} \sin(m\,\varphi) \\
h_\varphi^{TM_p} &= -\sqrt{\frac{\epsilon_m}{\pi}} \frac{J_m'\left(\frac{x_i \rho}{a}\right)}{a\, J_{m+1}(x_i)} \cos(m\,\varphi) \\
m &= 0, 1, 2, \cdots
\end{aligned}
\tag{3.39}
$$

$$
\begin{aligned}
e_\rho^{TM_o} &= -\sqrt{\frac{2}{\pi}} \frac{J_m'\left(\frac{x_i \rho}{a}\right)}{a\, J_{m+1}(x_i)} \sin(m\,\varphi) \\
e_\varphi^{TM_o} &= -\sqrt{\frac{2}{\pi}} \frac{m}{x_i} \frac{J_m\left(\frac{x_i \rho}{a}\right)}{\rho\, J_{m+1}(x_i)} \cos(m\,\varphi) \\
h_\rho^{TM_o} &= +\sqrt{\frac{2}{\pi}} \frac{m}{x_i} \frac{J_m\left(\frac{x_i \rho}{a}\right)}{\rho\, J_{m+1}(x_i)} \cos(m\,\varphi) \\
h_\varphi^{TM_o} &= -\sqrt{\frac{2}{\pi}} \frac{J_m'\left(\frac{x_i \rho}{a}\right)}{a\, J_{m+1}(x_i)} \sin(m\,\varphi) \\
m &= 1, 2, 3, \cdots
\end{aligned}
\tag{3.40}
$$

$$
e_\rho^{TE_p} = \sqrt{\frac{\epsilon_m}{\pi}} \frac{m}{\sqrt{x_i'^2 - m^2}} \frac{J_m\left(\frac{x_i' \rho}{a}\right)}{\rho\, J_m(x_i')} \sin(m\,\varphi)
$$

$$e_{\varphi}^{TE_p} = \sqrt{\frac{\epsilon_m}{\pi}} \frac{x_i'}{\sqrt{x_i'^2 - m^2}} \frac{J_m'\left(\frac{x_i'\rho}{a}\right)}{a\, J_m\left(x_i'\right)} \cos(m\,\varphi)$$

$$h_{\rho}^{TE_p} = -\sqrt{\frac{\epsilon_m}{\pi}} \frac{x_i'}{\sqrt{x_i'^2 - m^2}} \frac{J_m'\left(\frac{x_i'\rho}{a}\right)}{a\, J_m\left(x_i'\right)} \cos(m\,\varphi)$$

$$h_{\varphi}^{TE_p} = \sqrt{\frac{\epsilon_m}{\pi}} \frac{m}{\sqrt{x_i'^2 - m^2}} \frac{J_m\left(\frac{x_i'\rho}{a}\right)}{\rho\, J_m\left(x_i'\right)} \sin(m\,\varphi)$$

$$m = 0, 1, 2, \cdots \tag{3.41}$$

$$e_{\rho}^{TE_o} = -\sqrt{\frac{2}{\pi}} \frac{m}{\sqrt{x_i'^2 - m^2}} \frac{J_m\left(\frac{x_i'\rho}{a}\right)}{\rho\, J_m\left(x_i'\right)} \cos(m\,\varphi)$$

$$e_{\varphi}^{TE_o} = \sqrt{\frac{2}{\pi}} \frac{x_i'}{\sqrt{x_i'^2 - m^2}} \frac{J_m'\left(\frac{x_i'\rho}{a}\right)}{a\, J_m\left(x_i'\right)} \sin(m\,\varphi)$$

$$h_{\rho}^{TE_o} = -\sqrt{\frac{2}{\pi}} \frac{x_i'}{\sqrt{x_i'^2 - m^2}} \frac{J_m'\left(\frac{x_i'\rho}{a}\right)}{a\, J_m\left(x_i'\right)} \sin(m\,\varphi)$$

$$h_{\varphi}^{TE_o} = -\sqrt{\frac{2}{\pi}} \frac{m}{\sqrt{x_i'^2 - m^2}} \frac{J_m\left(\frac{x_i'\rho}{a}\right)}{\rho\, J_m\left(x_i'\right)} \cos(m\,\varphi)$$

$$m = 1, 2, 3, \cdots \tag{3.42}$$

$$\begin{aligned} \epsilon_m &= 1; \ \text{if} m = 0 \\ \epsilon_m &= 2; \ \text{if} m \neq 0 \end{aligned} \tag{3.43}$$

where a is the radius of the cavity, J_m the Bessel function of order m, J_m' its first derivative, $x_i = x_{m,n}$ the n-th nonvanishing root of the m-th order Bessel function and $x_i' = x_{m,n}'$ the n-th nonvanishing root of the m-th order first derivative Bessel function. As se can clearly see from above equations, a cylindrical cavity can support four different families of modes so that in this case the index m of equation (3.38) runs to all $TM_{p_{m,n}}$, $TM_{o_{m,n}}$, $TE_{p_{m,n}}$, $TE_{o_{m,n}}$ modes. It is interesting to note that also the vector and scalar potentials Green's functions can be derived from the expressions of the field Green's functions in equation (3.38). However, in this study this is not necessary since in the integral equation formulation to be described in chapter 4 a field formulation is used to represent any coupling effect in the interior cavity region.

Equations (3.38) to (3.43) establish the rigorous formulation of the boxed Green's function in a cylindrical cavity needed in integral equation formulations for the analysis of cylindrical cavity backed antennas. However, the presence of the Bessel function and first derivative of Bessel function greatly complicates or even makes impossible any future analytical treatment on these Green's functions. The result is that the convergence acceleration of the series involved in equation (3.38) becomes a very complex task whose solution has not yet been found. It is in this point where the main approximation introduced in this study resides. The rigorous Green's functions of the cylindrical cavity shown in this section are in fact approximated by the Green's functions of an equivalent square cavity behaving as close as possible to the original cavity. The great advantage in doing this equivalence is that now the Green's functions are expressed in terms of simple trigonometric functions thus allowing complex future analytical operations. The main implication of this, is that the equivalent Green's functions can be conveniently combined with complex discretization techniques of the geometries involved (triangular cells) and still keeping good convergence rates in the associated series. For the sake of completeness we also give the analytical expressions for the vector mode functions in a rectangular cavity [11]

$$\begin{aligned}\bar{e}_{x(m,n)}^{\xi}(x,y) &= N_{e_x}^{\xi}\ \cos\left[\tfrac{m\pi}{a}(x-c)\right]\ \sin\left[\tfrac{n\pi}{b}(y-d)\right]\\ \bar{e}_{y(m,n)}^{\xi}(x,y) &= N_{e_y}^{\xi}\ \sin\left[\tfrac{m\pi}{a}(x-c)\right]\ \cos\left[\tfrac{n\pi}{b}(y-d)\right]\end{aligned} \tag{3.44}$$

$$\begin{aligned}\bar{h}_{x(m,n)}^{\xi}(x,y) &= N_{h_x}^{\xi}\ \sin\left[\tfrac{m\pi}{a}(x-c)\right]\ \cos\left[\tfrac{n\pi}{b}(y-d)\right]\\ \bar{h}_{y(m,n)}^{\xi}(x,y) &= N_{h_y}^{\xi}\ \cos\left[\tfrac{m\pi}{a}(x-c)\right]\ \sin\left[\tfrac{n\pi}{b}(y-d)\right]\end{aligned} \tag{3.45}$$

where ξ denotes the family of modes $TE_{(m,n)}$ or $TM_{(m,n)}$, a and b are the dimensions of cavity, c and d the offsets with respect the origin of coordinates and the normalization factors for both families of modes are given by:

$$\left\{\begin{aligned} N_{e_x}^{TM} &= -\frac{2}{a}\frac{m}{\sqrt{m^2\frac{b}{a}+n^2\frac{a}{b}}} \\ N_{e_y}^{TM} &= -\frac{2}{b}\frac{n}{\sqrt{m^2\frac{b}{a}+n^2\frac{a}{b}}}\end{aligned}\right. \qquad \begin{aligned} m &= 1,2,3,\cdots \\ n &= 1,2,3,\cdots\end{aligned} \tag{3.46}$$

$$\left\{\begin{aligned} N_{h_x}^{TM} &= +\frac{2}{b}\frac{n}{\sqrt{m^2\frac{b}{a}+n^2\frac{a}{b}}} \\ N_{h_y}^{TM} &= -\frac{2}{a}\frac{m}{\sqrt{m^2\frac{b}{a}+n^2\frac{a}{b}}}\end{aligned}\right. \qquad \begin{aligned} m &= 1,2,3,\cdots \\ n &= 1,2,3,\cdots\end{aligned} \tag{3.47}$$

$$\left\{\begin{aligned} N_{e_x}^{TE} &= +\frac{\sqrt{\epsilon_m\,\epsilon_n}}{b}\frac{n}{\sqrt{m^2\frac{b}{a}+n^2\frac{a}{b}}} \\ N_{e_y}^{TE} &= -\frac{\sqrt{\epsilon_m\,\epsilon_n}}{a}\frac{m}{\sqrt{m^2\frac{b}{a}+n^2\frac{a}{b}}}\end{aligned}\right. \qquad \begin{aligned} m &= 0,1,2,3,\cdots \\ n &= 0,1,2,3,\cdots \\ m &= n \neq 0\end{aligned} \tag{3.48}$$

$$\left\{\begin{aligned} N_{e_x}^{TE} &= +\frac{\sqrt{\epsilon_m\,\epsilon_n}}{a}\frac{m}{\sqrt{m^2\frac{b}{a}+n^2\frac{a}{b}}} \\ N_{e_y}^{TE} &= +\frac{\sqrt{\epsilon_m\,\epsilon_n}}{b}\frac{n}{\sqrt{m^2\frac{b}{a}+n^2\frac{a}{b}}}\end{aligned}\right. \qquad \begin{aligned} m &= 0,1,2,3,\cdots \\ n &= 0,1,2,3,\cdots \\ m &= n \neq 0\end{aligned} \tag{3.49}$$

Chapter 4

Integral Equation Formulation in Stratified Media

4.1 Introduction

The chapter is dedicated to present the integral equation formulation developed in this study and that can be used for the analysis of a general structure composed of an arbitrary number of planar printed patches and radiating slots embedded in a layered medium. The formulation is based on the Green's functions derived in previous chapters. It is shown that once the Green's functions are known, the technique can be applied indistinctly to slot and patches printed on infinite transverse substrates, backed by metallic cavities or any combination of the two.

The integral equation derived is hybrid in the sense that it combines Mixed Potential formulations (MPIE) with Fields formulations (FIE) when appropriate. In this context, the singular behavior of the Green's functions has been treated with MPIE formulations which are best suited for this purpose [12]. Whenever singularities are not found in the Green's functions, FIE formulations are used which lead to very compact algorithms for the study of arbitrary number of staked patches and slots. The only exception to this rule is for cavity backed elements which are always treated with FIE formulations. In this case, care is exercise to the convergence of the modal series involved and an asymptotic extraction procedure for convergence acceleration is presented.

Due to the complex geometries involved in the conformal array elementary radiator, a solution of the integral equation using a Galerkin Method of Moments algorithm based on triangular cells for the discretization of the antenna geometry is proposed. In this chapter we review the numerical techniques used to evaluate the matrix coefficients including the treatment of the singularities in the Green's functions. Finally, the mesh strategy based on triangular cells and developed in the present work is briefly presented. Meshes for the conformal array antenna geometry are given showing that the procedure is indeed efficient and suits well the type of structure being analyzed.

4.2 Basic Formulation

Consider a structure composed of an arbitrary number of planar printed patches and slots embedded in a multilayered medium as shown in Fig. 4.1.

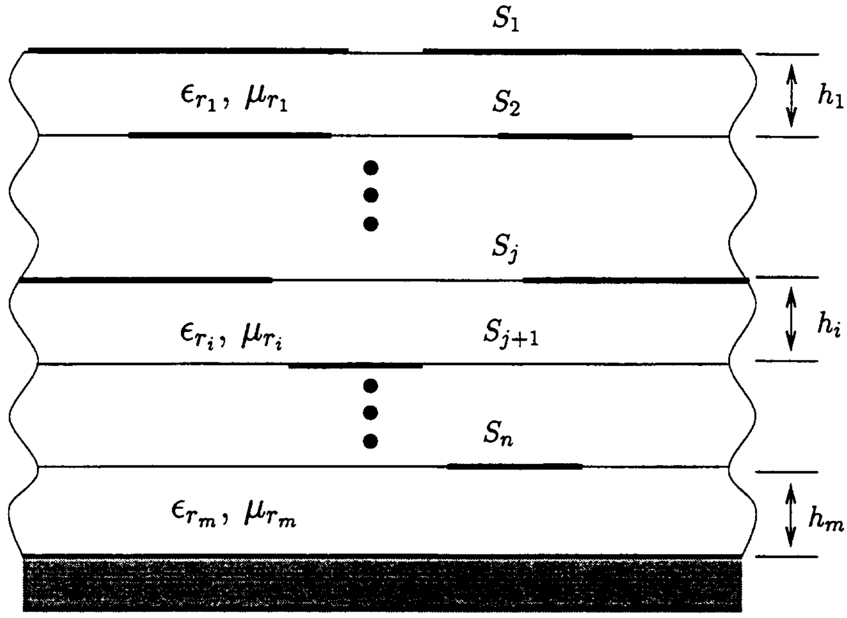

Figure 4.1: Typical layered structure composed of an arbitrary number of planar printed patches and slots.

The integral equation formulation starts with the imposition of the boundary conditions for the fields in the structure. For the structure of Fig. 4.1 we shall impose vanishing tangent electric field on the printed patches and continuity of tangent components of electric and magnetic fields on the slots. Mathematically, we can express these boundary conditions using the following notation

$$\begin{aligned} \bar{E}_T\big|_{s_r} &= 0;\ r = 1, 2, \cdots, n\ \forall\, s_r \in s_e \\ \bar{E}_T\big|_{s_r^+} &= \bar{E}_T\big|_{s_r^-};\ r = 1, 2, \cdots, n\ \forall\, s_r \in s_m \\ \bar{H}_T\big|_{s_r^+} &= \bar{H}_T\big|_{s_r^-};\ r = 1, 2, \cdots, n\ \forall\, s_r \in s_m \end{aligned} \tag{4.1}$$

where $\bar{E}_T\,|_{s_r}$ is the total tangent electric field evaluated at the interface s_r, $\bar{E}_T\,|_{s_r^+}$, $\bar{H}_T\,|_{s_r^+}$ are the total tangent fields at one side of the interface s_r, $\bar{E}_T\,|_{s_r^-}$, $\bar{H}_T\,|_{s_r^-}$ are the total tangent fields at the other side of the interface s_r, s_e has been used to denote the set of surfaces containing all printed patches (the set of electric surfaces) and s_m has been used to denote the set of surfaces containing all printed slots (the set of magnetic surfaces). In addition, in the antenna configuration we have to consider an electric field produced by the generator used to excite the structure. This additional field is called the exciting or impressed electric field and the total electric field shall therefore be expressed as the sum of the exciting electric field $\bar{E}_{(e)}$ plus all the scattered field $\bar{E}_{(scat)}$ produced by the resulting induced electric and magnetic currents on the structure. The original boundary conditions in equation (4.1) then becomes

$$\bar{E}_T\big|_{s_r} = \left[\bar{E}_{(e)} + \bar{E}_{(scat)}\right]\Big|_{s_r} = \bar{E}_{(e)} + \bar{E}^{(r)}_{(scat)} = 0;\ r = 1, 2, \cdots, n\ \forall\, s_r \in s_e \tag{4.2}$$

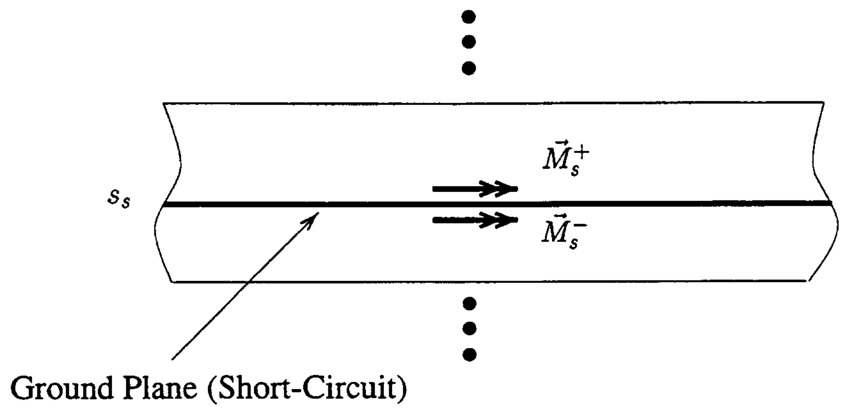

Figure 4.2: Equivalent magnetic currents resulting from the application of the surface equivalent principle to a generic slot s_s.

$$\bar{E}_{(scat)}\Big|_{s_r^+} = \bar{E}_{(scat)}\Big|_{s_r^-}; \; \bar{E}^{(r^+)}_{(scat)} = \bar{E}^{(r^-)}_{(scat)}; \; r = 1, 2, \cdots, n \; \forall \, s_r \in s_m \tag{4.3}$$

$$\bar{H}_{(scat)}\Big|_{s_r^+} = \bar{H}_{(scat)}\Big|_{s_r^-}; \; \bar{H}^{(r^+)}_{(scat)} = \bar{H}^{(r^-)}_{(scat)}; \; r = 1, 2, \cdots, n \; \forall \, s_r \in s_m \tag{4.4}$$

To easily impose above boundary conditions in the structure of Fig. 4.1 the surface equivalent principle will be systematically used in all slots [10]. Following this approach, all slots will be short-circuited by ground planes and equivalent magnetic currents are placed above and below them to preserve the original fields in the structure (Fig. 4.2). In this case, the physical mechanism governing the fields can be viewed in the following way: Once the antenna is connected to the exciting generator, the exciting electric field will induce electric currents on the printed patches $\bar{J}_s$ and equivalent magnetic currents above $\bar{M}_{s^+}$ and below $\bar{M}_{s^-}$ the slots (Fig. 4.2). These induced electric and magnetic currents are in turn the responsibles for the scattered fields. The final electric and magnetic fields thus created must satisfy the total boundary conditions in equation (4.2).

To start with the imposition of above boundary conditions, we will use the superposition integral to express the fields with the aid of the Green's functions developed in previous chapters. For example, we can express the scattered electric field produced at interface s_r by an electric current placed at interface s_s as

$$\bar{E}^{(r,s)}_{(scat)} = -j\,\omega \int_{s_s} \overline{\overline{G}}^{(r,s)}_A \cdot \bar{J}_s \, ds' + \frac{1}{j\,\omega} \int_{s_s} \left(\nabla G^{(r,s)}_v\right) \left(\nabla' \cdot \bar{J}_s\right) ds' \tag{4.5}$$

where as we see the field is expressed using its mixed potential form. Similarly, the scattered electric field produced by a magnetic current will be written as

$$\bar{E}^{(r,s)}_{(scat)} = \int_{s_s} \overline{\overline{G}}^{(r,s)}_{EM} \cdot \bar{M}_s \, ds' \tag{4.6}$$

where now the field Green's function is directly used. Using the same ideas, we can write the following relations to express the scattered magnetic field produced by electric and magnetic currents

$$\bar{H}^{(r,s)}_{(scat)} = -j\,\omega \int_{s_s} \overline{\overline{G}}^{(r,s)}_F \cdot \bar{M}_s \, ds' + \frac{1}{j\,\omega} \int_{s_s} \left(\nabla G^{(r,s)}_w\right) \left(\nabla' \cdot \bar{M}_s\right) ds' \tag{4.7}$$

$$\bar{H}^{(r,s)}_{(scat)} = \int_{S_s} \overline{\overline{G}}^{(r,s)}_{H_J} \cdot \bar{J}_s \, ds' \tag{4.8}$$

By virtue of the superposition principle, we can now compute the total scattered field produced at a generic interface s_r, by adding up the contributions of the scattered fields produced by all sources in the structure

$$\begin{aligned} \bar{E}^{(r)}_{(scat)} &= \sum_{\substack{s \\ s_s \in s_e}} \left[-j\,\omega \int_{S_s} \overline{\overline{G}}^{(r,s)}_{A} \cdot \bar{J}_s \, ds' + \frac{1}{j\,\omega} \int_{S_s} \left(\nabla G^{(r,s)}_{v} \right) (\nabla' \cdot \bar{J}_s) \, ds' \right] + \\ & \sum_{\substack{s \\ s_s \in s_m}} \int_{S_s} \overline{\overline{G}}^{(r,s)}_{E_M} \cdot \bar{M}_s \, ds' \end{aligned} \tag{4.9}$$

$$\begin{aligned} \bar{H}^{(r)}_{(scat)} &= \sum_{\substack{s \\ s_s \in s_m}} \left[-j\,\omega \int_{S_s} \overline{\overline{G}}^{(r,s)}_{F} \cdot \bar{M}_s \, ds' + \frac{1}{j\,\omega} \int_{S_s} \left(\nabla G^{(r,s)}_{w} \right) (\nabla' \cdot \bar{M}_s) \, ds' \right] + \\ & \sum_{\substack{s \\ s_s \in s_e}} \int_{S_s} \overline{\overline{G}}^{(r,s)}_{H_J} \cdot \bar{J}_s \, ds' \end{aligned} \tag{4.10}$$

The boundary condition for the electric field at the printed patches can now be easily imposed. Combining equations (4.2) and (4.9) one easily obtains

$$\begin{aligned} \bar{E}_{(e)} &= \sum_{\substack{s \\ s_s \in s_e}} \left[-j\,\omega \int_{S_s} \overline{\overline{G}}^{(r,s)}_{A} \cdot \bar{J}_s \, ds' + \frac{1}{j\,\omega} \int_{S_s} \left(\nabla G^{(r,s)}_{v} \right) (\nabla' \cdot \bar{J}_s) \, ds' \right] + \\ & \sum_{\substack{s \\ s_s \in s_m}} \int_{S_s} \overline{\overline{G}}^{(r,s)}_{E_M} \cdot \bar{M}_s \, ds' \\ & r = 1, 2, \cdots, n \ \forall s_r \in s_e \end{aligned} \tag{4.11}$$

For the imposition of the two remaining boundary conditions we must keep in mind that due to the utilization of the surface equivalence principle, ground planes are placed at all printed slots and therefore, all the interfaces associated are divided into two different regions, namely the region above and the region below the slot. Let us then take a generic slot interface s_r and compute the total scattered magnetic field above $\bar{H}^{(r^+)}_{(scat)}$ and below $\bar{H}^{(r^-)}_{(scat)}$ the interface as

$$\begin{aligned} \bar{H}^{(r^+)}_{(scat)} &= -j\,\omega \int_{S_r} \overline{\overline{G}}^{(r,r^+)}_{F} \cdot \bar{M}_{r^+} \, ds' + \frac{1}{j\,\omega} \int_{S_r} \left(\nabla G^{(r,r^+)}_{w} \right) (\nabla' \cdot \bar{M}_{r^+}) \, ds' + \\ & \sum_{\substack{s \\ s_s \in s_m^+}} \left[-j\,\omega \int_{S_s} \overline{\overline{G}}^{(r,s)}_{F} \cdot \bar{M}_s \, ds' + \frac{1}{j\,\omega} \int_{S_s} \left(\nabla G^{(r,s)}_{w} \right) (\nabla' \cdot \bar{M}_s) \, ds' \right] + \\ & \sum_{\substack{s \\ s_s \in s_e^+}} \int_{S_s} \overline{\overline{G}}^{(r,s)}_{H_J} \cdot \bar{J}_s \, ds' \end{aligned} \tag{4.12}$$

$$\begin{aligned} \bar{H}^{(r^-)}_{(scat)} &= -j\,\omega \int_{S_r} \overline{\overline{G}}^{(r,r^-)}_{F} \cdot \bar{M}_{r^-} \, ds' + \frac{1}{j\,\omega} \int_{S_r} \left(\nabla G^{(r,r^-)}_{w} \right) (\nabla' \cdot \bar{M}_{r^-}) \, ds' + \\ & \sum_{\substack{s \\ s_s \in s_m^-}} \left[-j\,\omega \int_{S_s} \overline{\overline{G}}^{(r,s)}_{F} \cdot \bar{M}_s \, ds' + \frac{1}{j\,\omega} \int_{S_s} \left(\nabla G^{(r,s)}_{w} \right) (\nabla' \cdot \bar{M}_s) \, ds' \right] + \\ & \sum_{\substack{s \\ s_s \in s_e^-}} \int_{S_s} \overline{\overline{G}}^{(r,s)}_{H_J} \cdot \bar{J}_s \, ds' \end{aligned} \tag{4.13}$$

where $\bar{M}_{r^+}$ is the magnetic current placed above the interface s_r and $\bar{M}_{r^-}$ is the magnetic current placed below the interface s_r as shown in Fig. 4.2. Moreover, the new set s_m^+ has been defined as the set containing all slots placed above the current interface s_r and consequently the set s_e^+ contains all printed patches above the current interface s_r. Following the same notation, s_m^- is the set containing all slots placed below the current interface and s_e^- is the set containing all printed patches below the current interface.

Now we are in a point where we can impose the continuity of the electric field in all slot interfaces shown in equation (4.3). To do this we will use the classical relation between the magnetic currents and the field at the aperture [10]: $\bar{M} = \hat{e}_n \times (\bar{E}_2 - \bar{E}_1)$. Applying this relation to the magnetic currents at both sides of the s_r interface shown in Fig. 4.2 we obtain

$$\begin{aligned} \bar{M}_{r^+} &= +\hat{e}_z \, E_{(scat)}^{(r^+)} \\ \bar{M}_{r^-} &= -\hat{e}_z \, E_{(scat)}^{(r^-)} \end{aligned} \tag{4.14}$$

Finally, boundary conditions in equation (4.3) combined with (4.14) suggest the following redefinition for all magnetic currents at the slot interfaces

$$\bar{M}_{r^+} = -\bar{M}_{r^-} = \bar{M}_r; \; r = 1, 2, \cdots, n \; \forall \, s_r \in s_m \tag{4.15}$$

The last boundary condition to be imposed is found in equation (4.4). If we use the intermediate results in equations (4.12,4.13) with the redefinition for the magnetic currents in equation (4.15), the boundary condition in (4.4) can be written in the following form after few straightforward manipulations

$$\begin{aligned} 0 = \; & \sum_{\substack{s \\ s_s \in s_e^+}} \int_{S_s} \overline{\overline{G}}_{HJ}^{(r,s)} \cdot \bar{J}_s \, ds' + \\ & \sum_{\substack{s \\ s_s \in s_m^+}} \left[-j\,\omega \int_{S_s} \overline{\overline{G}}_{F}^{(r,s)} \cdot \bar{M}_s \, ds' + \frac{1}{j\,\omega} \int_{S_s} \left(\nabla G_{W}^{(r,s)} \right) \left(\nabla' \cdot \bar{M}_s \right) ds' \right] + \\ & -j\,\omega \int_{S_r} \left[\overline{\overline{G}}_{F}^{(r,r^+)} + \overline{\overline{G}}_{F}^{(r,r^-)} \right] \cdot \bar{M}_r \, ds' + \frac{1}{j\,\omega} \int_{S_r} \left(\nabla \left[G_{W}^{(r,r^+)} + G_{W}^{(r,r^-)} \right] \right) \left(\nabla' \cdot \bar{M}_r \right) ds' - \\ & \sum_{\substack{s \\ s_s \in s_m^-}} \left[-j\,\omega \int_{S_s} \overline{\overline{G}}_{F}^{(r,s)} \cdot \bar{M}_s \, ds' + \frac{1}{j\,\omega} \int_{S_s} \left(\nabla G_{W}^{(r,s)} \right) \left(\nabla' \cdot \bar{M}_s \right) ds' \right] - \\ & \sum_{\substack{s \\ s_s \in s_e^-}} \int_{S_s} \overline{\overline{G}}_{HJ}^{(r,s)} \cdot \bar{J}_s \, ds' \\ & r = 1, 2, \cdots, n \; \forall \, s_r \in s_m \end{aligned} \tag{4.16}$$

Equation (4.11) and (4.16) forms the basic system of integral equations needed in the analysis of the structure shown in Fig. 4.1. An interesting aspect of the technique described arises when the Green's functions appearing in (4.11,4.16) are considered in the spectral domain. As far as equation (4.11) is concerned, all spectral domain quantities can be extracted from the equivalent transmission line network shown in Fig. 4.3a, where the short circuits are due to the application of the surface equivalent principle and are therefore placed at interfaces containing slots. We will refer to this

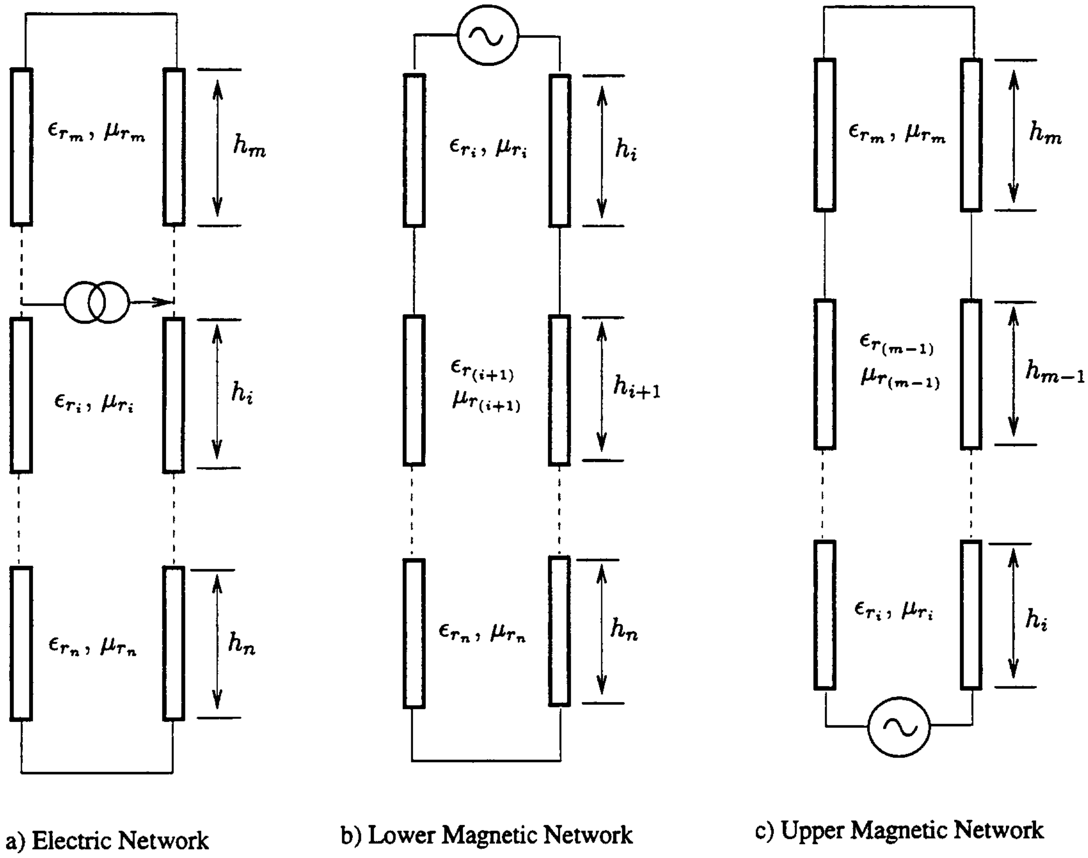

Figure 4.3: The three equivalent transmission line networks to which the analysis of the multilayered printed antenna is reduced in the spectral domain.

equivalent transmission line network as the electric network because it arises when the boundary conditions for the electric field are imposed. In a similar way, after inspection of equation (4.16) one can establish that the spectral domain Green's functions denoted as $\overline{\overline{G}}_F^{(r,r^+)}$ and $G_w^{(r,r^+)}$ can be extracted from the analysis of the equivalent transmission line network shown in Fig. 4.3b, which we call upper magnetic network. Finally, the spectral domain Green's functions associated to $\overline{\overline{G}}_F^{(r,r^-)}$ and $G_w^{(r,r^-)}$ can be extracted from the equivalent transmission line network shown in Fig. 4.3c and which will be referred as lower magnetic network. As seen, these two last equivalent networks arises from the imposition of the continuity of the magnetic field and thus we give them the names of lower and upper magnetic networks. In equation (4.16) we can further redefine the following total Green's functions

$$\begin{aligned} \overline{\overline{G}}_F^{(r,r)} &= \overline{\overline{G}}_F^{(r,r^+)} + \overline{\overline{G}}_F^{(r,r^-)} \\ G_w^{(r,r)} &= G_w^{(r,r^+)} + G_w^{(r,r^-)} \end{aligned} \tag{4.17}$$

which are simply the Green's functions sum of the Green's functions for the magnetic currents above and below the s_r interface. What it is interesting, is to note that these Green's functions can be added up at the spectral domain level. If we do so, the total spectral domain Green's functions are obtained by directly adding the currents at the generator terminals in the upper and lower magnetic networks shown in Fig. 4.3. Later, the inverse Sommerfeld transformation is applied to the sum of the currents and the total Green's functions in (4.17) are directly obtained in the spatial domain. With this simple technique all operations at the spectral domain level are reduced to the computation of the voltages and currents at all interfaces in the three equivalent transmission line networks shown in Fig. 4.3, with subsequent adding of the currents at the generator terminals for the lower and upper magnetic networks. For the sake of completeness, in Appendix A a simple iterative procedure based on network calculations is included for the analysis of the three equivalent networks when an arbitrary number of layers is considered. When the redefinitions in equation (4.17) are used inside the system of integral equations (4.11,4.16), the following final form for the integral equation formulation of the structure in Fig. 4.1 is obtained

$$\begin{aligned}
\bar{E}_{(e)} &= \sum_{\substack{s \\ s_s \in s_e}} \left[-j\,\omega \int_{S_s} \overline{\overline{G}}_A^{(r,s)} \cdot \bar{J}_s \, ds' + \frac{1}{j\,\omega} \int_{S_s} \left(\nabla G_v^{(r,s)} \right) \left(\nabla' \cdot \bar{J}_s \right) ds' \right] + \\
&\quad \sum_{\substack{s \\ s_s \in s_m}} \int_{S_s} \overline{\overline{G}}_{E_M}^{(r,s)} \cdot \bar{M}_s \, ds' \\
&\quad r = 1, 2, \cdots, n \;\forall\, s_r \in s_e
\end{aligned} \tag{4.18}$$

$$\begin{aligned}
0 &= \sum_{\substack{s \\ s_s \in s_e^+}} \int_{S_s} \overline{\overline{G}}_{H_J}^{(r,s)} \cdot \bar{J}_s \, ds' + \\
&\quad \sum_{\substack{s \\ s_s \in s_m^+}} \left[-j\,\omega \int_{S_s} \overline{\overline{G}}_F^{(r,s)} \cdot \bar{M}_s \, ds' + \frac{1}{j\,\omega} \int_{S_s} \left(\nabla G_w^{(r,s)} \right) \left(\nabla' \cdot \bar{M}_s \right) ds' \right] + \\
&\quad -j\,\omega \int_{S_r} \overline{\overline{G}}_F^{(r,r)} \cdot \bar{M}_r \, ds' + \frac{1}{j\,\omega} \int_{S_r} \left(\nabla G_w^{(r,r)} \right) \left(\nabla' \cdot \bar{M}_r \right) ds' - \\
&\quad \sum_{\substack{s \\ s_s \in s_m^-}} \left[-j\,\omega \int_{S_s} \overline{\overline{G}}_F^{(r,s)} \cdot \bar{M}_s \, ds' + \frac{1}{j\,\omega} \int_{S_s} \left(\nabla G_w^{(r,s)} \right) \left(\nabla' \cdot \bar{M}_s \right) ds' \right] - \\
&\quad \sum_{\substack{s \\ s_s \in s_e^-}} \int_{S_s} \overline{\overline{G}}_{H_J}^{(r,s)} \cdot \bar{J}_s \, ds' \\
&\quad r = 1, 2, \cdots, n \;\forall\, s_r \in s_m
\end{aligned} \tag{4.19}$$

The same procedure as the one described above is also applied if there are cavity backed printed patches or slots. The only difference is that for those elements backed by a cavity, a field formulation is always used so that the Mixed Potential terms in above formulation do not appear anymore. The theoretical developments in this case are identical as those described previously if one just substitutes equations (4.5) and (4.7) respectively by

$$\bar{E}_{(scat)}^{(r,s)} = \int_{S_s} \overline{\overline{G}}_{E_J}^{(r,s)} \cdot \bar{J}_s \, ds' \tag{4.20}$$

$$\bar{H}_{(scat)}^{(r,s)} = \int_{S_s} \overline{\overline{G}}_{H_M}^{(r,s)} \cdot \bar{M}_s \, ds' \tag{4.21}$$

and now the boxed Green's functions in equation (3.38) of chapter 3 are used instead of the Green's functions for multilayered media of infinite transverse dimensions derived in chapter 2.

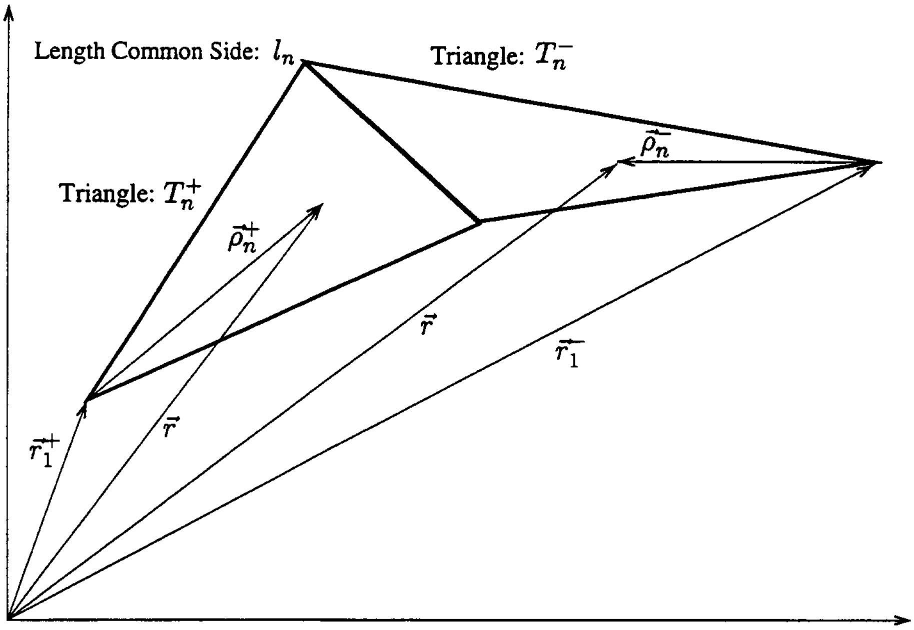

Figure 4.4: Two adjacent triangular cells defining a basis function for the MoM algorithm.

4.3 Method of Moments Algorithm

The next step in the analysis of our multilayered printed antenna is the resolution of the system of integral equations obtained in the previous section. One of the most popular techniques for solving integral equations in electromagnetics field problems is the Method of Moments (MoM) algorithm [13]. For the case of printed antennas, several variants of the MoM technique have been tried and compared in terms of computational efficiency and numerical accuracy [12]. Among all of them, we have selected for this work the so called Galerkin formulation because of its robustness and faster numerical convergence behavior that other simpler techniques (i.e. point matching, line matching).

The MoM technique starts with the expansion or the unknown electric and magnetic currents with a suitable set of basis functions. In this study, due to the complex geometrical shapes used in the conformal array elementary radiator, a triangular subdomain roof-top basis functions defined on the printed patches and slots have been selected. The definition of suitable roof-top functions based on triangular cells for the discretization of the geometries follows the work originally proposed in [14]. In this work the authors established how roof-top functions can be suitably defined on triangular cells and demonstrated that it is a good choice for the resolution of integral equations arising in the analysis of antennas and scatterers of arbitrary complex geometries.

Let us take two adjacent triangles T_n^+ and T_n^- used to discretize the geometry of the antenna as shown in Fig. 4.4. A subdomain roof-top function suitable to our purposes will be defined in the two adjacent triangles in the following form [14]

$$\bar{f}_n(\bar{r}) = \begin{cases} +\frac{l_n}{2\,A_n^+}\,\bar{\rho}_n^+; \text{ for } \bar{r} \text{ in } T_n^+ \\ -\frac{l_n}{2\,A_n^-}\,\bar{\rho}_n^-; \text{ for } \bar{r} \text{ in } T_n^+ \\ 0; \text{ Elsewhere} \end{cases} \tag{4.22}$$

where l_n is the length of the common side between the two triangles, A_n^+ is the area of the triangle T_n^+, A_n^- is the area of the triangle T_n^- and the vectors $\bar{\rho}_n^+$, $\bar{\rho}_n^-$ are the radial vectors measured from the free vertex of the triangles T_n^+ and T_n^- respectively as shown in Fig. 4.4. The main feature of the basis function defined in this way is that its normal component with respect the common edge is continuous across both triangles. If this basis function is used to discretize an unknown current, the normal component of the current will therefore be continuous across the two triangles and consequently this definition suits the need of the continuity of the currents induced in the antenna structure. In addition, another important feature of the definition in (4.22) is that the charge associated to each triangular cell is constant across the cell. Mathematically this is expressed by calculating the divergence of the basis function, which simply becomes

$$\nabla \cdot \bar{f}_n(r\bar{r}) = \begin{cases} +\frac{l_n}{A_n^+}; \text{ for } \bar{r} \text{ in } T_n^+ \\ -\frac{l_n}{A_n^-}; \text{ for } \bar{r} \text{ in } T_n^- \\ 0; \text{ Elsewhere} \end{cases} \tag{4.23}$$

Using the basis functions defined as in equations (4.22, 4.23), the unknown electric and magnetic currents induced in the antenna structure will be expanded using the following series forms

$$\begin{aligned} \bar{J}_s &= \sum_k \alpha_k^{(s)} \bar{f}_k^{(s)}(\bar{r}'); \; s = 1, 2, \cdots, n \; \forall s_s \in s_e \\ \bar{M}_s &= \sum_k \alpha_k^{(s)} \bar{f}_k^{(s)}(\bar{r}'); \; s = 1, 2, \cdots, n \; \forall s_s \in s_m \end{aligned} \tag{4.24}$$

where $\alpha_k^{(s)}$ are the unknown coefficients in the expansion and $\bar{f}_k^{(s)}$ are the roof-top functions defined in the triangular cells discretizing the geometry of the s_s interface. Introducing the form of the unknown induced electric and magnetic currents of equation (4.24) into the system of integral equations (4.18,4.19) we easily obtain

$$\begin{aligned} \bar{E}_{(e)} \;=\; & \sum_{\substack{s \\ s_s \in s_e}} \sum_k \alpha_k^{(s)} \left[-j\,\omega \int_{s_s} \overline{\overline{G}}_A^{(r,s)} \cdot \bar{f}_k^{(s)}\, ds' + \frac{1}{j\,\omega} \int_{s_s} \left(\nabla G_v^{(r,s)} \right) \left(\nabla' \cdot \bar{f}_k^{(s)} \right) ds' \right] + \\ & \sum_{\substack{s \\ s_s \in s_m}} \sum_k \alpha_k^{(s)} \int_{s_s} \overline{\overline{G}}_{E_M}^{(r,s)} \cdot \bar{f}_k^{(s)}\, ds' \\ & r = 1, 2, \cdots, n \; \forall\, s_r \in s_e \end{aligned} \tag{4.25}$$

$$\begin{aligned} 0 \;=\; & \sum_{\substack{s \\ s_s \in s_e^+}} \sum_k \alpha_k^{(s)} \int_{s_s} \overline{\overline{G}}_{H_J}^{(r,s)} \cdot \bar{f}_k^{(s)}\, ds' + \\ & \sum_{\substack{s \\ s_s \in s_m^+}} \sum_k \alpha_k^{(s)} \left[-j\,\omega \int_{s_s} \overline{\overline{G}}_F^{(r,s)} \cdot \bar{f}_k^{(s)}\, ds' + \frac{1}{j\,\omega} \int_{s_s} \left(\nabla G_w^{(r,s)} \right) \left(\nabla' \cdot \bar{f}_k^{(s)} \right) ds' \right] + \\ & \sum_k \alpha_k^{(r)} \left[-j\,\omega \int_{s_r} \overline{\overline{G}}_F^{(r,r)} \cdot \bar{f}_k^{(r)}\, ds' + \frac{1}{j\,\omega} \int_{s_r} \left(\nabla G_w^{(r,r)} \right) \left(\nabla' \cdot \bar{f}_k^{(r)} \right) ds' \right] - \\ & \sum_{\substack{s \\ s_s \in s_m^-}} \sum_k \alpha_k^{(s)} \left[-j\,\omega \int_{s_s} \overline{\overline{G}}_F^{(r,s)} \cdot \bar{f}_k^{(s)}\, ds' + \frac{1}{j\,\omega} \int_{s_s} \left(\nabla G_w^{(r,s)} \right) \left(\nabla' \cdot \bar{f}_k^{(s)} \right) ds' \right] - \end{aligned}$$

$$\sum_{\substack{s \\ s_s \in s_e^-}} \sum_k \alpha_k^{(s)} \int_{S_s} \overline{\overline{G}}_{H_J}^{(r,s)} \cdot \bar{f}_k^{(s)} \, ds'$$
$$r = 1, 2, \cdots, n \; \forall \, s_r \in s_m \tag{4.26}$$

The Galerkin procedure is now completed if we choose as testing functions the same set of functions as we used before as basis functions. Multiplying equations (4.25,4.26) by the set of testing functions $\bar{f}_i^{(r)}$ and integrating over the corresponding testing surfaces s_r, the following relations are obtained

$$\begin{aligned}
\int_{S_r} \bar{E}_{(e)} \cdot \bar{f}_i^{(r)} \, ds \;=\; & \sum_{\substack{s \\ s_s \in s_e}} \sum_k \alpha_k^{(s)} \left[-j\,\omega \int_{S_r} ds\, \bar{f}_i^{(r)} \int_{S_s} ds'\, \bar{f}_k^{(s)} \overline{\overline{G}}_A^{(r,s)} + \right. \\
& \left. \frac{1}{j\,\omega} \int_{S_r} ds \left(\nabla \cdot \bar{f}_i^{(r)} \right) \int_{S_s} ds' \left(\nabla' \cdot \bar{f}_k^{(s)} \right) G_v^{(r,s)} \right] + \\
& \sum_{\substack{s \\ s_s \in s_m}} \sum_k \alpha_k^{(s)} \int_{S_r} ds\, \bar{f}_i^{(r)} \int_{S_s} ds'\, \bar{f}_k^{(s)} \overline{\overline{G}}_{E_M}^{(r,s)} \\
& r = 1, 2, \cdots, n \; \forall \, s_r \in s_e
\end{aligned} \tag{4.27}$$

$$\begin{aligned}
0 \;=\; & \sum_{\substack{s \\ s_s \in s_e^+}} \sum_k \alpha_k^{(s)} \int_{S_r} ds\, \bar{f}_i^{(r)} \int_{S_s} ds'\, \bar{f}_k^{(s)} \overline{\overline{G}}_{H_J}^{(r,s)} + \\
& \sum_{\substack{s \\ s_s \in s_m^+}} \sum_k \alpha_k^{(s)} \left[-j\,\omega \int_{S_r} ds\, \bar{f}_i^{(r)} \int_{S_s} ds'\, \bar{f}_k^{(s)} \overline{\overline{G}}_F^{(r,s)} + \frac{1}{j\,\omega} \int_{S_r} ds \left(\nabla \cdot \bar{f}_i^{(r)} \right) \int_{S_s} ds' \left(\nabla' \cdot \bar{f}_k^{(s)} \right) G_w^{(r,s)} \right] + \\
& \sum_k \alpha_k^{(r)} \left[-j\,\omega \int_{S_r} ds\, \bar{f}_i^{(r)} \int_{S_r} ds'\, \bar{f}_k^{(r)} \overline{\overline{G}}_F^{(r,r)} + \frac{1}{j\,\omega} \int_{S_r} ds \left(\nabla \cdot \bar{f}_i^{(r)} \right) \int_{S_r} ds' \left(\nabla' \cdot \bar{f}_k^{(r)} \right) G_w^{(r,r)} \right] - \\
& \sum_{\substack{s \\ s_s \in s_m^-}} \sum_k \alpha_k^{(s)} \left[-j\,\omega \int_{S_r} ds\, \bar{f}_i^{(r)} \int_{S_s} ds'\, \bar{f}_k^{(s)} \overline{\overline{G}}_F^{(r,s)} + \frac{1}{j\,\omega} \int_{S_r} ds \left(\nabla \cdot \bar{f}_i^{(r)} \right) \int_{S_s} ds' \left(\nabla' \cdot \bar{f}_k^{(s)} \right) G_w^{(r,s)} \right] - \\
& \sum_{\substack{s \\ s_s \in s_e^-}} \sum_k \alpha_k^{(s)} \int_{S_r} ds\, \bar{f}_i^{(r)} \int_{S_s} ds'\, \bar{f}_k^{(s)} \overline{\overline{G}}_{H_J}^{(r,s)} \\
& r = 1, 2, \cdots, n \; \forall \, s_r \in s_m
\end{aligned} \tag{4.28}$$

where in addition, the surface divergence theorem has been used to transfer the gradients from the Green's functions to the testing functions, thus resulting in a more symmetric expressions in the mixed potential terms [15]. Following this procedure, the original system of integral equations has been transformed in an algebraic linear system of equations given by (4.27,4.28). In fact, in these last two equations the following scalar products can be defined

$$\begin{aligned}
P_{E_J}^{(r,s)}(i,k) \;=\; & -j\,\omega \int_{S_r} ds\, \bar{f}_i^{(r)} \int_{S_s} ds'\, \bar{f}_k^{(s)} \overline{\overline{G}}_A^{(r,s)} + \\
& \frac{1}{j\,\omega} \int_{S_r} ds \left(\nabla \cdot \bar{f}_i^{(r)} \right) \int_{S_s} ds' \left(\nabla' \cdot \bar{f}_k^{(s)} \right) G_v^{(r,s)} \\
& r = 1, 2, \cdots, n; \; \forall s_r \in s_e \\
& s = 1, 2, \cdots, n; \; \forall s_s \in s_e
\end{aligned} \tag{4.29}$$

$$
\begin{aligned}
P_{E_M}^{(r,s)}(i,k) &= \int_{s_r} ds\, \bar{f}_i^{(r)} \int_{s_s} ds'\, \bar{f}_k^{(s)}\, \overline{\overline{G}}_{E_M}^{(r,s)} \\
& \quad r = 1,2,\cdots,n;\ \forall s_r \in s_e \\
& \quad s = 1,2,\cdots,n;\ \forall s_s \in s_m
\end{aligned} \tag{4.30}
$$

$$
\begin{aligned}
P_{H_J}^{(r,s)}(i,k) &= \int_{s_r} ds\, \bar{f}_i^{(r)} \int_{s_s} ds'\, \bar{f}_k^{(s)}\, \overline{\overline{G}}_{H_J}^{(r,s)} \\
& \quad r = 1,2,\cdots,n;\ \forall s_r \in s_m \\
& \quad s = 1,2,\cdots,n;\ \forall s_s \in s_e
\end{aligned} \tag{4.31}
$$

$$
\begin{aligned}
P_{H_M}^{(r,s)}(i,k) &= -j\,\omega \int_{s_r} ds\, \bar{f}_i^{(r)} \int_{s_s} ds'\, \bar{f}_k^{(s)}\, \overline{\overline{G}}_F^{(r,s)} + \\
& \qquad \frac{1}{j\,\omega} \int_{s_r} ds\, \left(\nabla \cdot \bar{f}_i^{(r)}\right) \int_{s_s} ds'\, \left(\nabla' \cdot \bar{f}_k^{(s)}\right) G_w^{(r,s)} \\
& r = 1,2,\cdots,n;\ \forall s_r \in s_m \\
& s = 1,2,\cdots,n;\ \forall s_s \in s_m
\end{aligned} \tag{4.32}
$$

The computation of the whole matrix system (also called MoM matrix) is therefore reduced to the evaluation of only four different types of scalar products as shown in equations (4.29-4.32). In addition, the known term vector of the system can be redefined in the following form

$$
P_{(e)}^{(r)}(i) = \begin{cases} \int_{s_r} \bar{E}_{(e)} \cdot \bar{f}_i^{(r)}; & \text{if } s_r \in s_e \\ 0; & \text{if } s_r \in s_m \end{cases}
\qquad r = 1,2,\cdots,n \tag{4.33}
$$

The exact form of the linear system of equations in (4.27,4.28) depends on the number of printed patches and slots as well as on their arrangement inside the antenna structure. However, a general form of the system in matrix form can be given as follows

$$
\begin{bmatrix} \underline{P}_{(e)}^{(1)} \\ \underline{P}_{(e)}^{(2)} \\ \vdots \\ \underline{P}_{(e)}^{(n)} \end{bmatrix}
=
\begin{bmatrix} \underline{\underline{P}}^{(1,1)} & \underline{\underline{P}}^{(1,2)} & \cdots & \underline{\underline{P}}^{(1,n)} \\ \underline{\underline{P}}^{(2,1)} & \underline{\underline{P}}^{(2,2)} & \cdots & \underline{\underline{P}}^{(2,n)} \\ \vdots & \vdots & \vdots & \vdots \\ \underline{\underline{P}}^{(n,1)} & \underline{\underline{P}}^{(n,2)} & \cdots & \underline{\underline{P}}^{(n,n)} \end{bmatrix}
\cdot
\begin{bmatrix} \underline{\alpha}^{(1)} \\ \underline{\alpha}^{(2)} \\ \vdots \\ \underline{\alpha}^{(n)} \end{bmatrix} \tag{4.34}
$$

where the submatrices $\underline{\underline{P}}^{(r,s)}$ can take one of the four forms shown in equations (4.29,4.32) and the known term vectors $\underline{P}_{(e)}^{(r)}$ are defined in (4.33). Inversion of the matrix system in equation (4.34) gives as solution the unknown coefficients $\alpha_k^{(s)}$; $s = 1,2,\cdots,n$. These coefficients can now be used in the expansions of equation (4.24) to finally obtain all the induced electric and magnetic currents in the structure.

It is interesting to note that the same formulation also applies in the case of cavity backed patches or slots and the form of the resulting MoM linear system is the same as in (4.34). For those cavity backed patches or slots however, the mixed potential form of the fields is avoided and consequently the scalar products in equations (4.29) and (4.29) must be redefined in the following way

$$
\begin{aligned}
P_{E_J}^{(r,s)}(i,k) &= \int_{s_r} ds\, \bar{f}_i^{(r)} \int_{s_s} ds'\, \bar{f}_k^{(s)}\, \overline{\overline{G}}_{E_J}^{(r,s)} \\
& \quad r = 1,2,\cdots,n;\ \forall s_r \in s_e \\
& \quad s = 1,2,\cdots,n;\ \forall s_s \in s_e
\end{aligned} \tag{4.35}
$$

$$
\begin{aligned}
P_{H_M}^{(r,s)}(i,k) &= \int_{s_r} ds\, \bar{f}_i^{(r)} \int_{s_s} ds'\, \bar{f}_k^{(s)}\, \overline{\overline{G}}_{H_M}^{(r,s)} \\
& \quad r = 1,2,\cdots,n;\ \forall s_r \in s_m \\
& \quad s = 1,2,\cdots,n;\ \forall s_s \in s_m
\end{aligned} \tag{4.36}
$$

where the fields Green's functions in equation (3.38) have been used.

We also have to note that the redefinition of the Green's functions sum in equation (4.17) can not be easily performed at the spectral domain level for the magnetic currents placed at the interface between the interior cavity problem with the exterior layered media structure of infinite transverse dimensions (outside or external region). This is mainly due to the fact that the discrete spectrum of the fields in the interior cavity problem becomes suddenly continuous in the laterally opened region. To overcome this difficulty, the Green's functions sum of equation (4.17) are only defined in the spectral domain for those slot interfaces either inside a cavity or outside the cavity, but not for the interface between the two regions. The main implication of this technique is that the MoM matrices in equation (4.34) are computed separately for the inside cavity region and for the laterally opened region. Both matrices are then conveniently combined by defining an overlapping area corresponding to the magnetic currents defined on both sides of the interface separating the cavity and the non-cavity worlds. This is clearly seen in Fig. 4.5 where we show the MoM matrix for the inside and for the outside structures computed separately and then properly overlapped for the rigorous study of the transition between the two regions. The same technique can easily be extended to the study of several cavity backed to laterally opened transitions.

4.4 Overlapping Integrals Evaluation

With the integral equation formulation presented in this chapter, all the numerical effort for the analysis of a general cavity backed printed antenna is reduced to the computation of the scalar products shown in equations (4.29-4.32) and to the inversion of the linear system of equations derived in (4.34). As we see from the definition of the subsectional basis functions in equation (4.22), all scalar products are expressed in terms of four fold integrals which are extended over the triangular domains used to discretize the printed patches and slots composing the antenna geometry. In this section we present the integration techniques developed for the evaluation of the associated overlapping integrals. During the exposition we emphasize the efforts put towards an efficient implementation of the integration process for both the cavity and the laterally opened cases.

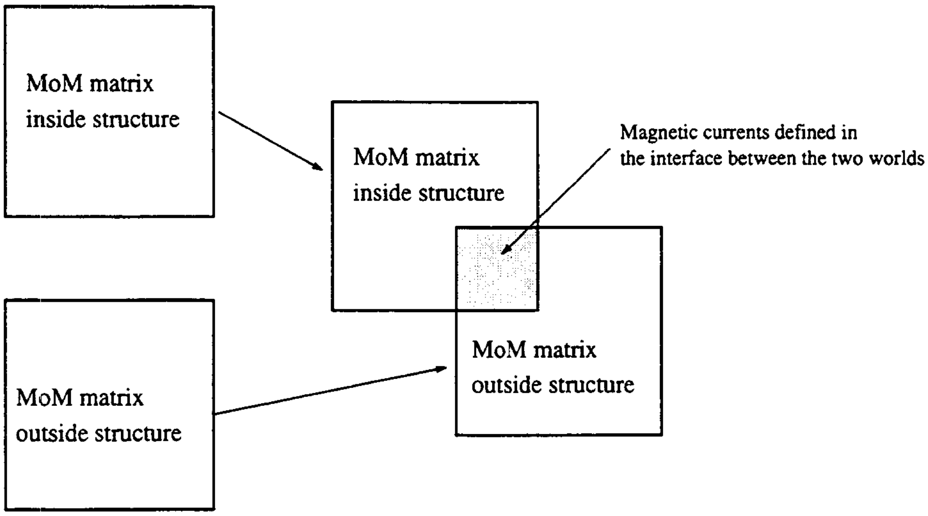

Figure 4.5: Combination of the MoM matrices for the cavity backed and for the non-cavity backed structures.

4.4.1 Laterally opened case

The first step in the numerical evaluation of the matrix coefficients in equations (4.29-4.32), is to perform the vector and dyadic operations appearing in the integrand. Note that in all cases, the matrix coefficients can easily be decomposed into the sum of four scalar integrals, namely

$$\begin{aligned} P(i,k) &= \int_{S_r} ds\, f_{x_i} \int_{S_s} ds'\, f_{x_k}\, G^{xx} + \int_{S_r} ds\, f_{x_i} \int_{S_s} ds'\, f_{y_k}\, G^{xy} + \\ & \int_{S_r} ds\, f_{y_i} \int_{S_s} ds'\, f_{x_k}\, G^{yx} + \int_{S_r} ds\, f_{y_i} \int_{S_s} ds'\, f_{y_k}\, G^{yy} \end{aligned} \tag{4.37}$$

where f_{x_i} and f_{y_i} are the x and y components of the vector basis function defined in equation (4.22) and G^{xx} is one of the components of any of the dyadic Green's functions in equations (4.29-4.32). As we see the problem is then reduced to the evaluation of several four fold integrals of scalar functions extended to triangular domains. All integrals can be recasted in the following form

$$I = \int_{T_i} dx\, dy \int_{T_k} dx'\, dy'\, F(x,y,x',y') \tag{4.38}$$

where $F(x,y,x',y')$ is any of the scalar functions in equation (4.37) and T_i, T_k two arbitrary triangular domains to which the integration is extended.

Since the direct evaluation of the four fold integral in equation (4.38) will be extremely long and complicated from the computational point of view, several tailored integration techniques specially well suited for the integration of functions on triangular domains will be used [16]. The first step in the procedure is to find a suitable transformation to convert any arbitrary triangular domain into a canonic triangular domain for which efficient integration rules can be derived. The general problem is shown in Fig. 4.6 and after few geometrical considerations we write the transformation as

$$\begin{aligned} \bar{r} &= \bar{r}_1 + u\,\bar{a} + v\,\bar{b} \\ \bar{a} &= \frac{\bar{r}_2 + \bar{r}_3}{2} - \bar{r}_1 \\ \bar{b} &= \frac{\bar{r}_2 - \bar{r}_3}{2} \end{aligned} \tag{4.39}$$

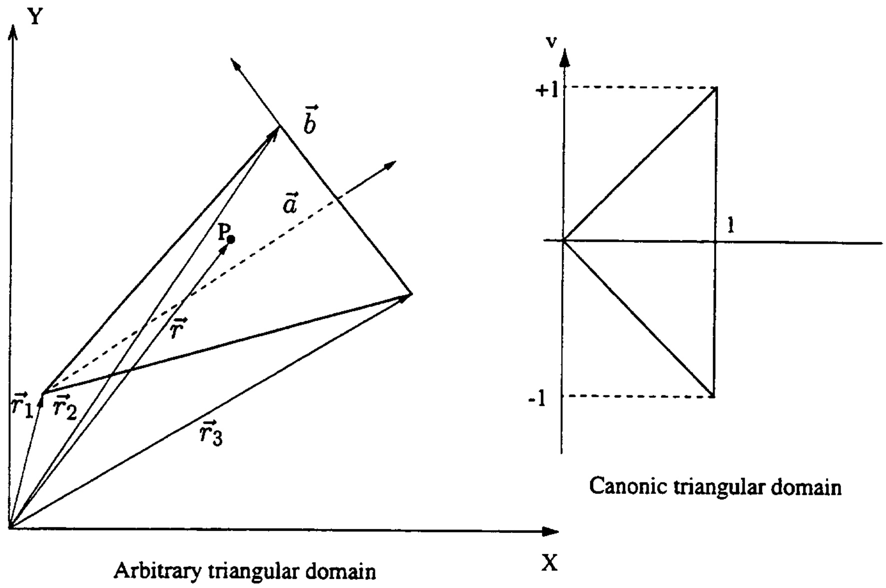

Figure 4.6: Arbitrary triangular domain and its transformation to the canonic triangular domain.

where $\bar{r}_1$, $\bar{r}_2$, $\bar{r}_3$ are the position vectors (coordinates) of the three vertexes of the original triangle, $\bar{r}$ represents the coordinates of any point in the original triangle and (u, v) are the corresponding coordinates of that point in the transformed canonic triangle of Fig. 4.6. Equation (4.39) can now be separated into its scalar components to find the final transformation between the (x, y) and (u, v) planes

$$
\begin{aligned}
x &= x_1 + u\left(\frac{x_2 + x_3}{2} - x_1\right) + v\left(\frac{x_2 - x_3}{2}\right) \\
y &= y_1 + u\left(\frac{y_2 + y_3}{2} - y_1\right) + v\left(\frac{y_2 - y_3}{2}\right)
\end{aligned}
\tag{4.40}
$$

With the aid of this transformation, the integral in equation (4.38) becomes

$$
I = A_i\, A_k \int_0^1 du \int_{-u}^{+u} dv \int_0^1 du' \int_{-u'}^{+u'} dv'\, F(u, v, u', v') \tag{4.41}
$$

where the areas of the two original triangles A_i and A_k are due to the Jacobeans of the transformations. The interesting aspect of (4.41) is that now the four fold integral is extended twice to the canonic triangular domain shown in Fig. 4.6 and specially tailored integration rules are available to perform efficiently this integration. With the proposed technique, the four fold integral in equation (4.41) is transformed into a double series of the form

$$
I = A_i\, A_k \sum_{i=1}^{N_p} \sum_{k=1}^{N_p} W_i\, W_k'\, F(u_i, v_i, u_k', v_k') \tag{4.42}
$$

where W_i, W_k' are the weights, (u_i, v_i), (u_k', v_k') the abscissas and N_p is the number of points in the corresponding integration rule. With the data available in [16] four different integration rules have been derived for an efficient integration in the canonic triangular domain of Fig. 4.6, namely a 7 points a 4 points a 3 points and a 1 point integration rules. For the sake of completeness we give in Tables 4.1, 4.2, 4.3, 4.4 the weights and abscissas for all four integration rules (note that the

-	(u_i, v_i)	W_i
1	$\left(\frac{2}{3}, 0\right)$	$\frac{270}{1200}$
2	$\left[\frac{2}{3}\left(1 - \frac{\sqrt{15}+1}{7}\right), 0\right]$	$\frac{155-\sqrt{15}}{1200}$
3	$\left[\frac{2}{3}\left(1 + \frac{\sqrt{15}+1}{14}\right), +\frac{\sqrt{15}+1}{7}\right]$	$\frac{155-\sqrt{15}}{1200}$
4	$\left[\frac{2}{3}\left(1 + \frac{\sqrt{15}+1}{14}\right), -\frac{\sqrt{15}+1}{7}\right]$	$\frac{155-\sqrt{15}}{1200}$
5	$\left[\frac{2}{3}\left(1 + \frac{\sqrt{15}-1}{7}\right), 0\right]$	$\frac{155+\sqrt{15}}{1200}$
6	$\left[\frac{2}{3}\left(1 - \frac{\sqrt{15}-1}{14}\right), +\frac{\sqrt{15}-1}{7}\right]$	$\frac{155+\sqrt{15}}{1200}$
7	$\left[\frac{2}{3}\left(1 - \frac{\sqrt{15}-1}{14}\right), -\frac{\sqrt{15}-1}{7}\right]$	$\frac{155+\sqrt{15}}{1200}$

Table 4.1: Weights and abscissas for the 7 points integration rule in the canonic triangular domain of Fig. 4.6.

-	(u_i, v_i)	W_i
1	$\left(\frac{2}{3}, 0\right)$	$\frac{3}{4}$
2	$(0, 0)$	$\frac{1}{12}$
3	$(1, 1)$	$\frac{1}{12}$
4	$(1, -1)$	$\frac{1}{12}$

Table 4.2: Weights and abscissas for the 4 points integration rule in the canonic triangular domain of Fig. 4.6.

one point integration rule is simply the rule of the triangle's barycenter). We can now use an important property of the Green's functions derived which states that the variation of the Green's functions is less abrupt when the source-spatial distance increases. The main implication of this is that when the distance between the source and observer triangles increases, less number of integration points are required to achieve the same level of accuracy. To try to exploit this feature and increase the computational efficiency of the method, we have defined an index which measures the relative distance between the source and observer triangles involved in the integral (4.38)

$$N_n = \frac{D_d}{(d_i + d_k)} \tag{4.43}$$

where D_d is the distance between the barycenters of the source and observer triangles, d_i is the radius of the circle circumscribed to the observer triangle and d_k is the radius of the circle circumscribed to the source triangle. The last step is to compute, before performing the integral, the *distance* index

-	(u_i, v_i)	W_i
1	$\left(\frac{5}{9}, \frac{1}{3}\right)$	$\frac{1}{3}$
2	$\left(\frac{5}{9}, -\frac{1}{3}\right)$	$\frac{1}{3}$
3	$\left(\frac{8}{9}, 0\right)$	$\frac{1}{3}$

Table 4.3: Weights and abscissas for the 3 points integration rule in the canonic triangular domain of Fig. 4.6.

-	(u_i, v_i)	W_i
1	$\left(\frac{2}{3},0\right)$	1

Table 4.4: Weights and abscissas for a 1 point integration rule in the canonic triangular domain of Fig. 4.6.

in equation (4.43) for each pair source-observer triangle. Then, the number of integration points is selected according to the value of the index. After some numerical tests, we established the optimum relation between the value of the *distance* index and the integration rule to be used to maintain an acceptable numerical accuracy. This relation is clearly indicated in Table 4.5. The last important

N_n	Integration Rule
≤ 2	7 points
≤ 3	4 points
≤ 4	3 points
> 4	1 point

Table 4.5: Relation between the *distance* index and the integration rule to be chosen in order to maintain good numerical accuracy.

situation not discussed yet arises when source and observer triangle coincides ($\rho \to 0$). In this case the Green's functions exhibit a singular behavior and the numerical integration presented above converge slowly and looses accuracy. Fortunately enough, those interactions susceptible of presenting singularities are formulated using the mixed potential form, and it can be shown that the potential functions exhibit only a singular behavior of the type $(1/\rho)$ when the distance ρ tends to zero. In consequence, the singularity of the Green's functions can be extracted by simply transformation of the integral extended to the observer triangle to the polar plane. Due to the Jacobean of this transformation (which is ρ), the singularity of the potential Green's functions is exactly compensated. The remaining integrals to be performed in polar coordinates therefore converge very fast, and simple Gauss-Legendre quadrature formulas with barely 3 or 4 points are enough to obtain good numerical accuracy.

The whole technique to extract the singularity is based on the integration in polar coordinates of a function in an arbitrary triangular domain as shown in Fig. 4.7. As we can see in the figure, the first step is to make an axis translation and place the origin for the polar coordinates in one of the vertex of the triangle (referred as $\bar{r}_o$ in Fig. 4.7). The transformation to the polar coordinates thus defined is given by

$$\begin{aligned} x - x_o &= \rho \cos(\varphi) \\ y - y_o &= \rho \sin(\varphi) \end{aligned} \tag{4.44}$$

whose Jacobean is indeed ρ. The integration limits φ_1 and φ_2 in the angular variable can now be easily computed as

$$\tan(\varphi_1) = \frac{y_a - y_o}{x_a - x_o}$$

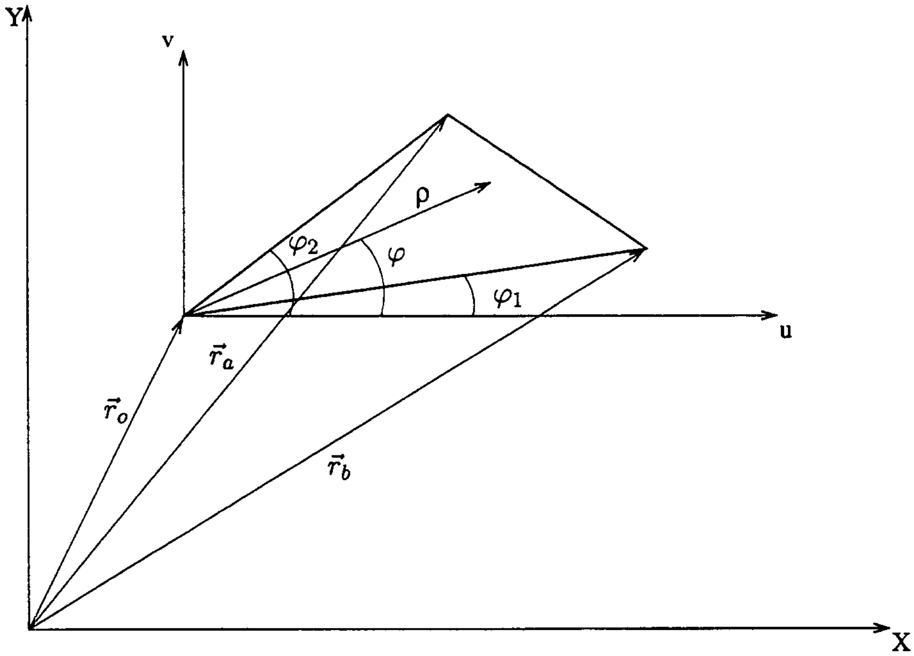

Figure 4.7: Integration in an arbitrary triangular domain using polar coordinates.

$$\tan(\varphi_2) = \frac{y_b - y_o}{x_b - x_o}$$
$$| \varphi_1 - \varphi_2 | < \pi \tag{4.45}$$

where $\bar{r}_a = (x_a; y_a)$ and $\bar{r}_b = (x_b, y_b)$ are the coordinates of the free vertexes of the triangle as shown in Fig. 4.7. As regard the integration limits in the radial variable, we first need to write the equation of the side of the triangle connecting the two free vertexes $\bar{r}_a$ and $\bar{r}_b$, namely

$$y - b = m\,(x - a)$$
$$m = \frac{y_b - y_a}{x_b - x_a}$$
$$b = y_a; \;\; a = x_a \tag{4.46}$$

Then, we must compute the intersection of this line with the following one

$$\tan(\varphi) = \frac{x - x_o}{y - y_o} \tag{4.47}$$

After few straightforward manipulations on equations (4.46,4.47) we obtain the intersection between the two lines as

$$\rho(\varphi) = \frac{m\,(x_o - x_a) - (y_o - y_a)}{\sin(\varphi) - m\,\cos(\varphi)} \tag{4.48}$$

The key step in the procedure is to note that the integral extended to the source triangle will be performed in the canonic triangular domain using the 7 points integration rule. For each source point, the observer triangle is then subdivided into three subtriangles as shown in Fig. 4.8. The origin for the polar coordinates is then translated to the source point and the above integration procedure is applied to each one of the three subtriangles. Mathematically, the whole integration process in

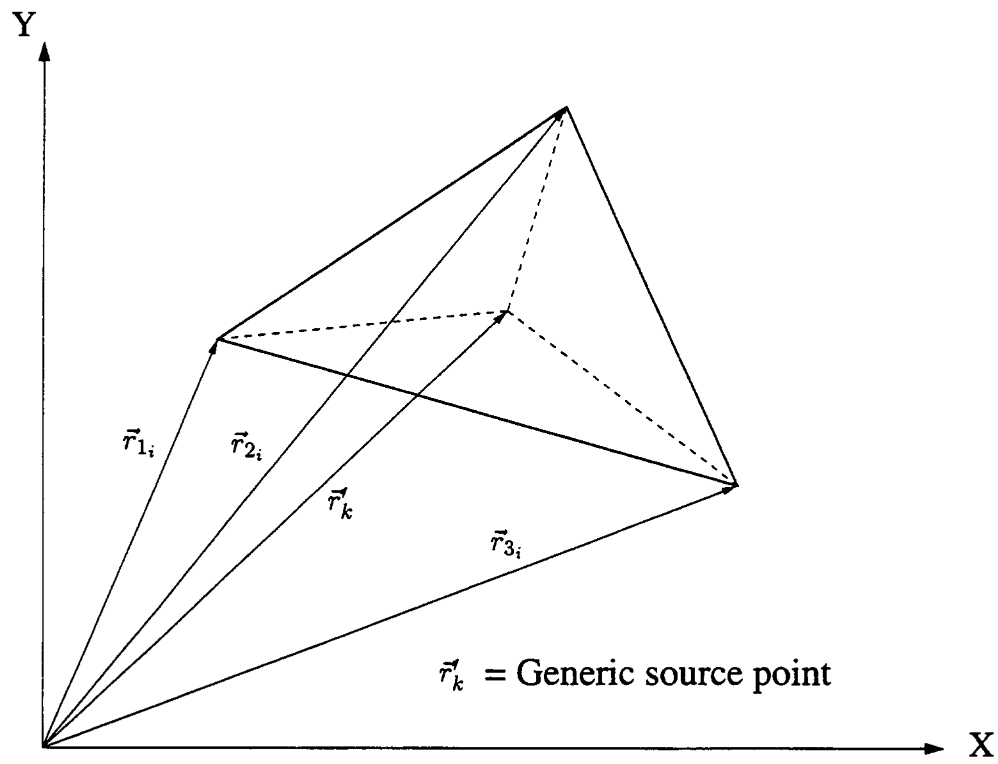

Figure 4.8: Subdivision of a generic observer triangle into the three subtriangles allowing integration using polar coordinates.

equation (4.38) can be written as

$$I = A_k \sum_{k=1}^{7} W_k' \sum_{p=1}^{3} \int_{\varphi_1(p)}^{\varphi_2(p)} d\varphi \int_0^{\rho_p(\varphi)} \rho \, d\rho \, F(\rho, \varphi, u_k', v_k') \tag{4.49}$$

and the integration limits $\varphi_1(p)$, $\varphi_2(p)$, $\rho_p(\varphi)$; $p = 1, 2, 3$ are computed with equations (4.45,4.48) by substituting the original triangle vertexes $\bar{r}_o$, $\bar{r}_a$ and $\bar{r}_b$ by the vertexes of the observer triangle in Fig. 4.8 as shown in Table 4.6 (note that r_k' denotes an arbitrary source point inside the observer triangle). Once more, we clearly see in equation (4.49) that the presence of an additional ρ in the

p	$\bar{r}_o$	$\bar{r}_a$	$\bar{r}_b$
1	$\bar{r}_k'$	$\bar{r}_{1_i}$	$\bar{r}_{3_i}$
2	$\bar{r}_k'$	$\bar{r}_{3_i}$	$\bar{r}_{2_i}$
3	$\bar{r}_k'$	$\bar{r}_{2_i}$	$\bar{r}_{1_i}$

Table 4.6: Correspondence between the vertexes of the observer triangle with the vertexes used in the polar integration. The correspondence is valid to perform the integral in the three subtriangles in which the observer triangle is subdivided.

integrand effectively cancels the singularity in the potential Green's function to be integrated.

4.4.2 Cavity backed case

For the computation of the matrix coefficients in the cavity backed case we can proceed further analytically. Introducing the boxed Green's functions derived in equation (3.38) into the scalar products definitions of equations (4.30,4.31,4.35,4.36) we obtain

$$
\begin{aligned}
&P_{E_J}^{(r,s)}(i,k) = \sum_m V_m(z) \int_{s_r} dx\, dy\, \bar{f}_i^{(r)} \cdot \bar{e}_m(x,y) \int_{s_s} dx'\, dy'\, \bar{f}_k^{(s)} \cdot \bar{e}_m(x',y') \\
&r = 1,2,\cdots,n;\ \forall s_r \in s_e \\
&s = 1,2,\cdots,n;\ \forall s_s \in s_e \\
&P_{H_J}^{(r,s)}(i,k) = \sum_m I_m(z) \int_{s_r} dx\, dy\, \bar{f}_i^{(r)} \cdot \bar{h}_m(x,y) \int_{s_s} dx'\, dy'\, \bar{f}_k^{(s)} \cdot \bar{e}_m(x',y') \\
&r = 1,2,\cdots,n;\ \forall s_r \in s_m \\
&s = 1,2,\cdots,n;\ \forall s_s \in s_e \\
&P_{E_M}^{(r,s)}(i,k) = \sum_m V_m(z) \int_{s_r} dx\, dy\, \bar{f}_i^{(r)} \cdot \bar{e}_m(x,y) \int_{s_s} dx'\, dy'\, \bar{f}_k^{(s)} \cdot \bar{h}_m(x',y') \\
&r = 1,2,\cdots,n;\ \forall s_r \in s_e \\
&s = 1,2,\cdots,n;\ \forall s_s \in s_m \\
&P_{H_M}^{(r,s)}(i,k) = \sum_m I_m(z) \int_{s_r} dx\, dy\, \bar{f}_i^{(r)} \cdot \bar{h}_m(x,y) \int_{s_s} dx'\, dy'\, \bar{f}_k^{(s)} \cdot \bar{h}_m(x',y') \\
&r = 1,2,\cdots,n;\ \forall s_r \in s_m \\
&s = 1,2,\cdots,n;\ \forall s_s \in s_m
\end{aligned}
\tag{4.50}
$$

It can be readily noticed from above equations, that all matrix coefficients are functions of only two different overlapping integrals, namely the overlapping integrals between the e and h vector mode functions with the basis functions defined in equation (4.22). We can then just consider only the following two types of integrals

$$
\begin{aligned}
&I_{fe}^{(r)}(m,i) = \int_{T_i^{(r)}} \bar{f}_i^{(r)} \cdot \bar{e}_m(x,y)\, dx\, dy \\
&r = 1,2,\cdots,n;\ \forall s_r \in s_e
\end{aligned}
\tag{4.51}
$$

$$
\begin{aligned}
&I_{fh}^{(r)}(m,i) = \int_{T_i^{(r)}} \bar{f}_i^{(r)} \cdot \bar{h}_m(x,y)\, dx\, dy \\
&r = 1,2,\cdots,n;\ \forall s_r \in s_m
\end{aligned}
\tag{4.52}
$$

where $T_i^{(r)}$ is a triangular cell discretizing the geometry of the s_r interface. Using the new overlapping integrals defined in (4.51,4.52), all matrix coefficients shown in equation (4.50) can be written as

$$
\begin{aligned}
&P_{E_J}^{(r,s)}(i,k) = \sum_m V_m(z)\, I_{fe}^{(r)}(m,i)\, I_{fe}^{(s)}(m,k) \\
&r = 1,2,\cdots,n;\ \forall s_r \in s_e \\
&s = 1,2,\cdots,n;\ \forall s_s \in s_e \\
&P_{H_J}^{(r,s)}(i,k) = \sum_m I_m(z)\, I_{fh}^{(r)}(m,i)\, I_{fe}^{(s)}(m,k)
\end{aligned}
$$

$$r = 1, 2, \cdots, n;\ \forall s_r \in s_m$$
$$s = 1, 2, \cdots, n;\ \forall s_s \in s_e$$
$$P_{E_M}^{(r,s)}(i,k) = \sum_m V_m(z)\, I_{fe}^{(r)}(m,i)\, I_{fh}^{(s)}(m,k)$$
$$r = 1, 2, \cdots, n;\ \forall s_r \in s_e$$
$$s = 1, 2, \cdots, n;\ \forall s_s \in s_m$$
$$P_{H_M}^{(r,s)}(i,k) = \sum_m I_m(z)\, I_{fh}^{(r)}(m,i)\, I_{fh}^{(s)}(m,k)$$
$$r = 1, 2, \cdots, n;\ \forall s_r \in s_m$$
$$s = 1, 2, \cdots, n;\ \forall s_s \in s_m \tag{4.53}$$

As seen, once the overlapping integrals in equations (4.51,4.52) are computed, all the MoM matrix coefficients are given in terms of the infinite series shown in (4.53). The key step therefore, is the evaluation of the overlapping integrals shown in (4.51,4.52) extended to triangular domains. Unfortunately, a numerical evaluation of these integrals demonstrated not to be feasible since when the modal index m increases, the number of integration points needed to maintain an acceptable accuracy grows exponentially. On the other hand, when the vector mode functions of the cylindrical cavity given in equations (3.39-3.42) are introduced in (4.51,4.52) an analytical treatment of the resulting integrals seems very difficult or impossible and the numerical evaluation would consume prohibitively computer resources in terms of computational time. To overcome this difficulty, in this study we have approximated the vector mode functions of the cylindrical cavity by the vector mode functions of an equivalent rectangular cavity. In this case the vector mode functions are given in equations (3.44-3.49) and an analytical treatment of the resulting integrals can be attempted. To start, let us introduce the definition of the basis functions shown in equation (4.22) into the overlapping integrals (4.51,4.52)

$$I_{fe}(m,i) = \sum_{p=1}^{2} (-1)^{p-1} \frac{li}{2\, A_i^{(p)}} \int_{T_i^{(p)}} \bar{\rho}_i^{(p)} \cdot \bar{e}_m^{(1)}(x,y)\, ds \tag{4.54}$$

$$I_{fh}(m,i) = \sum_{p=1}^{2} (-1)^{p-1} \frac{li}{2\, A_i^{(p)}} \int_{T_i^{(p)}} \bar{\rho}_i^{(p)} \cdot \bar{h}_m^{(1)}(x,y)\, ds \tag{4.55}$$

where $T_i^{(1)}$, $T_i^{(2)}$ are the two adjacent triangles forming the i-th basis function and the superscript (r) has been dropped to simplify notation. Now the analytical forms of the e and h vector mode functions in (3.44,3.45) can be introduced in (4.54,4.55). After performing the corresponding scalar products we obtain

$$I_{fe}(m,i) = \sum_{p=1}^{2} (-1)^{p-1} \frac{li}{2\, A_i^{(p)}} \left[I_{fe_x}^{(p)}(m,i) + I_{fe_y}^{(p)}(m,i) \right] \tag{4.56}$$

$$I_{fh}(m,i) = \sum_{p=1}^{2} (-1)^{p-1} \frac{li}{2\, A_i^{(p)}} \left[I_{fh_x}^{(p)}(m,i) + I_{fh_y}^{(p)}(m,i) \right] \tag{4.57}$$

where the new integrals correspond to the integrals of the x and y scalar components and are given by

$$
\begin{aligned}
I^{(p)}_{fe_x}(m,i) &= N_{e_x}(m) \int_{T_i^{(p)}} \bar{\rho}^{(p)}_{x_i} \cos\left[\frac{m\,\pi}{a}(x-c)\right] \sin\left[\frac{n\,\pi}{b}(y-d)\right] \,dx\,dy \\
I^{(p)}_{fe_y}(m,i) &= N_{e_y}(m) \int_{T_i^{(p)}} \bar{\rho}^{(p)}_{y_i} \sin\left[\frac{m\,\pi}{a}(x-c)\right] \cos\left[\frac{n\,\pi}{b}(y-d)\right] \,dx\,dy
\end{aligned}
\tag{4.58}
$$

$$
\begin{aligned}
I^{(p)}_{fh_x}(m,i) &= N_{h_x}(m) \int_{T_i^{(p)}} \bar{\rho}^{(p)}_{x_i} \sin\left[\frac{m\,\pi}{a}(x-c)\right] \cos\left[\frac{n\,\pi}{b}(y-d)\right] \,dx\,dy \\
I^{(p)}_{fh_y}(m,i) &= N_{h_y}(m) \int_{T_i^{(p)}} \bar{\rho}^{(p)}_{y_i} \cos\left[\frac{m\,\pi}{a}(x-c)\right] \sin\left[\frac{n\,\pi}{b}(y-d)\right] \,dx\,dy
\end{aligned}
\tag{4.59}
$$

The whole analytical effort must therefore be concentrated in the resolution of the following four integrals extended to arbitrary triangular domains

$$
\begin{aligned}
I^{(p)}_{cs_x}(m,i) &= \int_{T_i^{(p)}} \bar{\rho}^{(p)}_{x_i} \cos\left[\frac{m\,\pi}{a}(x-c)\right] \sin\left[\frac{n\,\pi}{b}(y-d)\right] \,dx\,dy \\
I^{(p)}_{sc_y}(m,i) &= \int_{T_i^{(p)}} \bar{\rho}^{(p)}_{y_i} \sin\left[\frac{m\,\pi}{a}(x-c)\right] \cos\left[\frac{n\,\pi}{b}(y-d)\right] \,dx\,dy \\
I^{(p)}_{sc_x}(m,i) &= \int_{T_i^{(p)}} \bar{\rho}^{(p)}_{x_i} \sin\left[\frac{m\,\pi}{a}(x-c)\right] \cos\left[\frac{n\,\pi}{b}(y-d)\right] \,dx\,dy \\
I^{(p)}_{cs_y}(m,i) &= \int_{T_i^{(p)}} \bar{\rho}^{(p)}_{y_i} \cos\left[\frac{m\,\pi}{a}(x-c)\right] \sin\left[\frac{n\,\pi}{b}(y-d)\right] \,dx\,dy
\end{aligned}
\tag{4.60}
$$

The first integral to be solved can be rewritten in the following general form

$$
I_{cs_x} = \int_T \rho_x \cos\left[e_c\,(x-g_c)\right] \sin\left[e_s\,(y-g_s)\right] \,dx\,dy \tag{4.61}
$$

Using the definition for the radial vector ρ in equation (4.22) we write

$$
I_{cs_x} = \int_T (x-x_1) \cos\left[e_c\,(x-g_c)\right] \sin\left[e_s\,(y-g_s)\right] \,dx\,dy \tag{4.62}
$$

If we now use the transformation derived in the previous section (equation (4.40)) to convert any arbitrary triangular domain into the canonic triangular domain of Fig. 4.6, above integral is written as

$$
I_{cs_x} = A_T \int_0^1 du \int_{-u}^{+u} dv\; (a_x\,u + b_x\,v) \cos\left[e_c\,(x_1 + a_x\,u + b_x\,v - g_c)\right] \sin\left[e_s\,(y_1 + a_y\,u + b_y\,v - g_s)\right] \tag{4.63}
$$

where A_T is the area of the triangle and it is due to the Jacobean of the transformation. In view of the previous expression, the total integral is written as the sum of two integrals

$$
I_{cs_x} = A_T\left[I_{cs_u} + I_{cs_v}\right] \tag{4.64}
$$

where we have defined

$$I_{cs_u} = \int_0^1 du \int_{-u}^{+u} dv\, a_x\, u\, \cos\left[e_c\left(x_1 + a_x\, u + b_x\, v - g_c\right)\right] \sin\left[e_s\left(y_1 + a_y\, u + b_y\, v - g_s\right)\right]$$
$$I_{cs_v} = \int_0^1 du \int_{-u}^{+u} dv\, b_x\, v\, \cos\left[e_c\left(x_1 + a_x\, u + b_x\, v - g_c\right)\right] \sin\left[e_s\left(y_1 + a_y\, u + b_y\, v - g_s\right)\right] \quad (4.65)$$

As a rule for the next developments, we will always use the ˆ symbol to denote quantities that depends on the outer most integration variable u. Quantities without the ˆ symbol will be true constants depending only on already known geometrical parameters. Following these rules we can now define the following auxiliary quantities

$$\begin{array}{ll} a_c = e_c & a_s = e_s \\ b_c = b_x & b_s = b_y \\ \hat{d}_c = x_1 + a_x\, u - g_c & \hat{d}_s = y_1 + a_y\, u - g_s \end{array} \quad (4.66)$$

so that the first integral in equation (4.65) is written as

$$I_{cs_u} = a_x \int_0^1 du\, u \int_{-u}^{+u} dv\, \cos\left[a_c\left(b_c\, v + \hat{d}_c\right)\right] \sin\left[a_s\left(b_s\, v + \hat{d}_s\right)\right] \quad (4.67)$$

The integral in dv can be easily performed, resulting

$$I_{cs_u} = a_x \int_0^1 du\, u\, \frac{1}{2} \left\{ \left. \frac{-\cos\left[\tilde{a}_{(-)}\, v + \hat{b}_{(-)}\right]}{\tilde{a}_{(-)}} \right|_{-u}^{+u} + \left. \frac{-\cos\left[\tilde{a}_{(+)}\, v + \hat{b}_{(+)}\right]}{\tilde{a}_{(+)}} \right|_{-u}^{+u} \right\} \quad (4.68)$$

where the new constants have been defined as

$$\begin{array}{ll} \tilde{a}_{(-)} = a_s\, b_s - a_c\, b_c & \tilde{a}_{(+)} = a_s\, b_s + a_c\, b_c \\ \hat{b}_{(-)} = \hat{d}_s\, a_s - a_c\, \hat{d}_c & \hat{b}_{(+)} = \hat{d}_s\, a_s + a_c\, \hat{d}_c \end{array} \quad (4.69)$$

To perform the integration in the outermost variable du, we must explicitly write all dependences with respect this variable. After cumbersome but straightforward manipulations, equation (4.68) becomes

$$I_{cs_u} = \frac{a_x}{2} \int_0^1 du\, u \quad \left\{ -\frac{\cos\left[\tilde{a}_{(-,+)}\, u + \tilde{h}_{(-)}\right] - \cos\left[\tilde{a}_{(-,-)}\, u + \tilde{h}_{(-)}\right]}{\tilde{a}_{(-)}} \right.$$
$$\left. - \frac{\cos\left[\tilde{a}_{(+,+)}\, u + \tilde{h}_{(+)}\right] - \cos\left[\tilde{a}_{(+,-)}\, u + \tilde{h}_{(+)}\right]}{\tilde{a}_{(+)}} \right\} \quad (4.70)$$

and the new constants are defined as

$$\begin{array}{ll} \tilde{a}_{(+,+)} = a_y\, a_s + a_x\, a_c + \tilde{a}_{(+)}; & \tilde{a}_{(+,-)} = a_y\, a_s + a_x\, a_c - \tilde{a}_{(+)} \\ \tilde{a}_{(-,+)} = a_y\, a_s - a_x\, a_c + \tilde{a}_{(-)}; & \tilde{a}_{(-,-)} = a_y\, a_s - a_x\, a_c - \tilde{a}_{(-)} \\ \tilde{h}_{(+)} = y_1\, a_s - g_s\, a_s + x_1\, a_c - g_c\, a_c; & \tilde{h}_{(-)} = y_1\, a_s - g_s\, a_s - x_1\, a_c + g_c\, a_c \end{array} \quad (4.71)$$

This last equation can be expressed as the sum of four integrals with known analytical solutions, namely

$$I_{cs_u} = \frac{a_x}{2} \quad \left\{ -\frac{1}{\tilde{a}_{(-)}} \tilde{I}_{cx}\left(1, \tilde{a}_{(-,+)}, \tilde{h}_{(-)}\right)\Big|_0^1 + \frac{1}{\tilde{a}_{(-)}} \tilde{I}_{cx}\left(1, \tilde{a}_{(-,-)}, \tilde{h}_{(-)}\right)\Big|_0^1 - \right.$$
$$\left. \frac{1}{\tilde{a}_{(+)}} \tilde{I}_{cx}\left(1, \tilde{a}_{(+,+)}, \tilde{h}_{(+)}\right)\Big|_0^1 + \frac{1}{\tilde{a}_{(+)}} \tilde{I}_{cx}\left(1, \tilde{a}_{(+,-)}, \tilde{h}_{(+)}\right)\Big|_0^1 \right\} \quad (4.72)$$

and the analytical form of the integral $\tilde{I}_{cx}$ is given in Appendix B. A similar procedure can now be applied to the solution of the second integral in equation (4.72). Defining the same constants shown in (4.66), the integral is written as

$$I_{cs_v} = b_x \int_0^1 du \int_{-u}^{+u} dv\, v \cos\left[a_c\left(b_c\, v + \hat{d}_c\right)\right] \sin\left[a_s\left(b_s\, v + \hat{d}_s\right)\right] \tag{4.73}$$

The integral in dv can now be solved analytically

$$\begin{aligned} I_{cs_v} = b_x \int_0^1 du\, \frac{1}{2} \; & \left\{ -v \frac{\cos\left[\tilde{a}_{(-)}\, v + \hat{b}_{(-)}\right]}{\tilde{a}_{(-)}}\Bigg|_{-u}^{+u} - v \frac{\cos\left[\tilde{a}_{(+)}\, v + \hat{b}_{(+)}\right]}{\tilde{a}_{(+)}}\Bigg|_{-u}^{+u} \right. \\ & \left. + \frac{\sin\left[\tilde{a}_{(-)}\, v + \hat{b}_{(-)}\right]}{\left[\tilde{a}_{(-)}\right]^2}\Bigg|_{-u}^{+u} + \frac{\sin\left[\tilde{a}_{(+)}\, v + \hat{b}_{(+)}\right]}{\left[\tilde{a}_{(+)}\right]^2}\Bigg|_{-u}^{+u} \right\} \end{aligned} \tag{4.74}$$

where all the constants are defined in equation (4.69). Again, to perform the integral in du we need to write explicitly all dependences with this variable. Using the same definitions as in (4.71) and after cumbersome but straightforward manipulations we obtain

$$\begin{aligned} I_{cs_v} = \frac{b_x}{2} \int_0^1 du \; & \left\{ -\frac{u \cos\left[\tilde{a}_{(-,+)}\, u + \tilde{h}_{(-)}\right] + u \cos\left[\tilde{a}_{(-,-)}\, u + \tilde{h}_{(-)}\right]}{\tilde{a}_{(-)}} - \frac{u \cos\left[\tilde{a}_{(+,+)}\, u + \tilde{h}_{(+)}\right] + u \cos\left[\tilde{a}_{(+,-)}\, u + \tilde{h}_{(+)}\right]}{\tilde{a}_{(+)}} \right. \\ & \left. + \frac{\sin\left[\tilde{a}_{(-,+)}\, u + \tilde{h}_{(-)}\right] - \sin\left[\tilde{a}_{(-,-)}\, u + \tilde{h}_{(-)}\right]}{\left[\tilde{a}_{(-)}\right]^2} + \frac{\sin\left[\tilde{a}_{(+,+)}\, u + \tilde{h}_{(+)}\right] - \sin\left[\tilde{a}_{(+,-)}\, u + \tilde{h}_{(+)}\right]}{\left[\tilde{a}_{(+)}\right]^2} \right\} \end{aligned} \tag{4.75}$$

and now all integrals in (4.75) can be solved analytically. Using the results of Appendix B we finally write

$$\begin{aligned} I_{cs_v} = \frac{b_x}{2} \; & \left\{ -\frac{1}{\tilde{a}_{(-)}} \left[\tilde{I}_{cx}\left(1, \tilde{a}_{(-,+)}, \tilde{h}_{(-)}\right)\Big|_0^1 + \tilde{I}_{cx}\left(1, \tilde{a}_{(-,-)}, \tilde{h}_{(-)}\right)\Big|_0^1 \right] \right. \\ & -\frac{1}{\tilde{a}_{(+)}} \left[\tilde{I}_{cx}\left(1, \tilde{a}_{(+,+)}, \tilde{h}_{(+)}\right)\Big|_0^1 + \tilde{I}_{cx}\left(1, \tilde{a}_{(+,-)}, \tilde{h}_{(+)}\right)\Big|_0^1 \right] \\ & +\frac{1}{\left[\tilde{a}_{(-)}\right]^2} \left[\tilde{I}_{s}\left(1, \tilde{a}_{(-,+)}, \tilde{h}_{(-)}\right)\Big|_0^1 - \tilde{I}_{s}\left(1, \tilde{a}_{(-,-)}, \tilde{h}_{(-)}\right)\Big|_0^1 \right] \\ & \left. +\frac{1}{\left[\tilde{a}_{(+)}\right]^2} \left[\tilde{I}_{s}\left(1, \tilde{a}_{(+,+)}, \tilde{h}_{(+)}\right)\Big|_0^1 - \tilde{I}_{s}\left(1, \tilde{a}_{(+,-)}, \tilde{h}_{(+)}\right)\Big|_0^1 \right] \right\} \end{aligned} \tag{4.76}$$

Equations (4.72,4.76) combined with the results of Appendix B give the analytical solution to the first integral in (4.60). Unfortunately, these expressions are not valid for all the values of the integrand parameters and alternative analytical solutions must be derived for these singular cases. The simplest singular case arises when $a_s = e_s = 0$ in the original equation (4.65). In this case the result of the corresponding integral is simply $I_{cs_u} = 0$. The next singular case arises when $a_c = e_c = 0$, $a_s = e_s \neq 0$. In this case the first integral in equation (4.65) becomes

$$I_{cs_u} = a_x \int_0^1 du\, u \int_{-u}^{+u} dv\, \sin\left[e_s\,(y_1 + a_y\, u + b_y\, v - g_s)\right] \tag{4.77}$$

Using the same coefficients defined in equation (4.66) we write above integral as

$$I_{cs_u} = a_x \int_0^1 du\, u \int_{-u}^{+u} dv\, \sin\left[a_s\left(b_s\, v + \hat{d}_s\right)\right] \tag{4.78}$$

The integral in dv can now be directly solved. Using the constants defined in (4.69) we write

$$I_{cs_u} = a_x \int_0^1 du\, u \left\{ \frac{-\cos\left[\tilde{a}_{(-)}\, v + .\hat{b}_{(-)}\right]}{\tilde{a}_{(-)}} \Bigg|_{-u}^{+u} \right\} \tag{4.79}$$

Again, before computing the integral in du we need to write explicitly all dependences on this variable. Using the constants defined in (4.71) we find

$$I_{cs_u} = a_x \int_0^1 du\, u \left\{ -\frac{\cos\left[\tilde{a}_{(-,+)}\, u + \tilde{h}_{(-)}\right] - \cos\left[\tilde{a}_{(-,-)}\, u + \tilde{h}_{(-)}\right]}{\tilde{a}_{(-)}} \right\} \tag{4.80}$$

The resulting expression can be solved analytically with the results of Appendix B, yielding

$$I_{cs_u} = a_x \left\{ -\frac{1}{\tilde{a}_{(-)}}\, \tilde{I}_{cx}\left(1, \tilde{a}_{(-,+)}, \tilde{h}_{(-)}\right)\Bigg|_0^1 + \frac{1}{\tilde{a}_{(-)}}\, \tilde{I}_{cx}\left(1, \tilde{a}_{(-,-)}, \tilde{h}_{(-)}\right)\Bigg|_0^1 \right\}$$
$$a_c = e_c = 0;\ a_s = e_s \neq 0;\ \tilde{a}_{(-)} \neq 0 \tag{4.81}$$

still equation (4.81) is not defined if $\tilde{a}_{(-)} = 0$. In this case however, equation (4.78) simply becomes

$$I_{cs_u} = a_x \int_0^1 du\, u \int_{-u}^{+u} dv\, \sin\left[\hat{b}_{(-)}\right] \tag{4.82}$$

Performing the integration in dv and using again the constants definitions in (4.71) we find

$$I_{cs_u} = a_x \int_0^1 2\, u^2 \sin\left[\tilde{a}_{(-,+)}\, u + \tilde{h}_{(-)}\right] du \tag{4.83}$$

and this integral can also be solved analytically. Using the results in Appendix B we simply write

$$I_{cs_u} = 2\, a_x \left\{ \tilde{I}_{sx^2}\left(1, \tilde{a}_{(-,+)}, \tilde{h}_{(-)}\right)\Big|_0^1 \right\}$$
$$a_c = e_c = 0;\ a_s = e_s \neq 0;\ \tilde{a}_{(-)} = 0 \tag{4.84}$$

Another interesting singular situation arises when $a_s = e_s \neq 0$, $a_c = e_c \neq 0$, $b_c = 0$ and $b_s = 0$. The first thing to note is that in this case $\tilde{a}_{(-)} = 0$ and $\tilde{a}_{(+)} = 0$. Also equation (4.67) now becomes

$$I_{cs_u} = a_x \int_0^1 du\, u \int_{-u}^{+u} dv\, \cos\left[a_c\, \hat{d}_c\right] \sin\left[a_s\, \hat{d}_s\right] \tag{4.85}$$

After performing integration in dv and using the constants defined in (4.66), the following integral is obtained

$$I_{cs_u} = 2\, a_x \int_0^1 du\, u^2 \cos\left[a_c\left(a_x\, u + (x_1 - g_c)\right)\right] \sin\left[a_s\left(a_y\, u + (y_1 - g_s)\right)\right] \tag{4.86}$$

and this integral can also be computed analytically. Using the results in Appendix B we simply write

$$I_{cs_u} = 2\, a_x \left\{ \tilde{I}_{scx^2}\left(a_s, a_y, (y_1 - g_s), a_c, a_x, (x_1 - g_c)\right)\Big|_0^1 \right\}$$
$$a_c = e_c \neq 0;\ a_s = e_s \neq 0;\ \tilde{a}_{(-)} = \tilde{a}_{(+)} = 0 \tag{4.87}$$

The most difficult singular cases to treat are when either $\tilde{a}_{(-)} = 0$ and $\tilde{a}_{(+)} \neq 0$ or $\tilde{a}_{(-)} \neq 0$ and $\tilde{a}_{(+)} = 0$. Starting with the first, we notice that in this case equation (4.68) is not anymore valid. Instead, we compute the integral in dv of equation (4.67) as

$$I_{cs_u} = a_x \int_0^1 du\, u\, \frac{1}{2} \left\{ \sin\left[\hat{b}_{(-)}\right]\, v\Big|_{-u}^{+u} + \frac{-\cos\left[\tilde{a}_{(+)}\, v + \hat{b}_{(+)}\right]}{\tilde{a}_{(+)}}\Bigg|_{-u}^{+u} \right\} \tag{4.88}$$

Before integrating in du we write explicitly all the dependence of the integrand with respect this variable, yielding

$$\begin{aligned} I_{cs_u} = \frac{a_x}{2} \int_0^1 du\, u \quad & \Big\{ \sin\left[\tilde{a}_{(-,+)}\, u + \tilde{h}_{(-)}\right] \\ & - \frac{\cos\left[\tilde{a}_{(+,+)}\, u + \tilde{h}_{(+)}\right] - \cos\left[\tilde{a}_{(+,-)}\, u + \tilde{h}_{(+)}\right]}{\tilde{a}_{(+)}} \Big\} \end{aligned} \tag{4.89}$$

Integration can now be performed analytically. Using the results of Appendix B we simply write

$$\begin{aligned} I_{cs_u} = \frac{a_x}{2} \quad & \Big[2\, \tilde{I}_{sx^2}\left(1, \tilde{a}_{(-,+)}, \tilde{h}_{(-)}\right)\Big|_0^1 \\ & - \frac{1}{\tilde{a}_{(+)}}\, \tilde{I}_{cx}\left(1, \tilde{a}_{(+,+)}, \tilde{h}_{(+)}\right)\Big|_0^1 + \frac{1}{\tilde{a}_{(+)}}\, \tilde{I}_{cx}\left(1, \tilde{a}_{(+,-)}, \tilde{h}_{(+)}\right)\Big|_0^1 \Big] \\ & \tilde{a}_{(+)} \neq 0;\ \tilde{a}_{(-)} = 0 \end{aligned} \tag{4.90}$$

We can also notice that the last singular case is dual to the previous one with respect the constants $\tilde{a}_{(+)}$ and $\tilde{a}_{(-)}$. We can therefore directly write

$$\begin{aligned} I_{cs_u} = \frac{a_x}{2} \quad & \Big[2\, \tilde{I}_{sx^2}\left(1, \tilde{a}_{(+,+)}, \tilde{h}_{(+)}\right)\Big|_0^1 \\ & - \frac{1}{\tilde{a}_{(-)}}\, \tilde{I}_{cx}\left(1, \tilde{a}_{(-,+)}, \tilde{h}_{(-)}\right)\Big|_0^1 + \frac{1}{\tilde{a}_{(-)}}\, \tilde{I}_{cx}\left(1, \tilde{a}_{(-,-)}, \tilde{h}_{(-)}\right)\Big|_0^1 \Big] \\ & \tilde{a}_{(+)} = 0;\ \tilde{a}_{(-)} \neq 0 \end{aligned} \tag{4.91}$$

Similar singular cases to those previously treated for the first integral in equation (4.65), must also be considered for the second integral. The simplest singular situation occurs when $a_s = e_s = 0$. In this case we simply notice $I_{cs_v} = 0$. Next we consider $a_c = e_c = 0$, $a_s = e_s \neq 0$. Under these conditions, the second integral in equation (4.65) becomes:

$$I_{cs_v} = b_x \int_0^1 du \int_{-u}^{+u} dv\, v\, \sin\left[e_s\, \left(y_1 + a_y\, u + b_y\, v - g_s\right)\right] \tag{4.92}$$

Using the same coefficients defined in equation (4.66) we write above integral as

$$I_{cs_v} = b_x \int_0^1 du \int_{-u}^{+u} dv\, v\, \sin\left[a_s\, \left(b_s\, v + \hat{d}_s\right)\right] \tag{4.93}$$

The integral in dv can now be directly solved. Using the constants defined in (4.69) we write

$$I_{cs_v} = b_x \int_0^1 du \left\{ v\, \frac{-\cos\left[\tilde{a}_{(-)}\, v + \tilde{b}_{(-)}\right]}{\tilde{a}_{(-)}}\Bigg|_{-u}^{+u} + \frac{\sin\left[\tilde{a}_{(-)}\, v + \hat{b}_{(-)}\right]}{\left[\tilde{a}_{(-)}\right]^2}\Bigg|_{-u}^{+u} \right\} \tag{4.94}$$

Again, before computing the integral in du we need to write explicitly all dependences on this variable. Using the constants defined in (4.71) we find

$$I_{cs_v} = b_x \int_0^1 du \quad \left\{ \frac{-u\,\cos\left[\tilde{a}_{(-,+)}\,u+\tilde{h}_{(-)}\right]-u\,\cos\left[\tilde{a}_{(-,-)}\,u+\tilde{h}_{(-)}\right]}{\tilde{a}_{(-)}} + \frac{\sin\left[\tilde{a}_{(-,+)}\,u+\tilde{h}_{(-)}\right]-\sin\left[\tilde{a}_{(-,-)}\,u+\tilde{h}_{(-)}\right]}{\left[\tilde{a}_{(-)}\right]^2} \right\} \tag{4.95}$$

The resulting expression can be solved analytically with the results of Appendix B, yielding

$$\begin{aligned} I_{cs_v} = b_x \quad & \left\{ -\tfrac{1}{\tilde{a}_{(-)}}\,\tilde{I}_{cx}\left(1,\tilde{a}_{(-,+)},\tilde{h}_{(-)}\right)\Big|_0^1 - \tfrac{1}{\tilde{a}_{(-)}}\,\tilde{I}_{cx}\left(1,\tilde{a}_{(-,-)},\tilde{h}_{(-)}\right)\Big|_0^1 \right. \\ & \left. + \tfrac{1}{\left[\tilde{a}_{(-)}\right]^2}\,\tilde{I}_s\left(1,\tilde{a}_{(-,+)},\tilde{h}_{(-)}\right)\Big|_0^1 - \tfrac{1}{\left[\tilde{a}_{(-)}\right]^2}\,\tilde{I}_s\left(1,\tilde{a}_{(-,-)},\tilde{h}_{(-)}\right)\Big|_0^1 \right\} \\ & a_c = e_c = 0;\ a_s = e_s \neq 0;\ \tilde{a}_{(-)} \neq 0 \end{aligned} \tag{4.96}$$

still equation (4.96) is not defined if $\tilde{a}_{(-)} = 0$. In this case however, equation (4.93) simply becomes

$$I_{cs_v} = b_x \int_0^1 du \int_{-u}^{+u} dv\, v\, \sin\left[\hat{b}_{(-)}\right] \tag{4.97}$$

Performing the integration in dv we find in this case

$$\begin{aligned} & I_{cs_v} = 0 \\ & a_c = e_c = 0;\ a_s = e_s \neq 0;\ \tilde{a}_{(-)} = 0 \end{aligned} \tag{4.98}$$

Another interesting singular situation arises when $a_s = e_s \neq 0$, $a_c = e_c \neq 0$, $b_c = 0$ and $b_s = 0$. The first thing to note is that in this case $\tilde{a}_{(-)} = 0$ and $\tilde{a}_{(+)} = 0$. Also equation (4.73) now becomes

$$I_{cs_v} = b_x \int_0^1 du \int_{-u}^{+u} dv\, v\, \cos\left[a_c\,\hat{d}_c\right]\,\sin\left[a_s\,\hat{d}_s\right] \tag{4.99}$$

After performing integration in dv we readily note that

$$\begin{aligned} & I_{cs_v} = 0 \\ & a_c = e_c \neq 0;\ a_s = e_s \neq 0;\ \tilde{a}_{(-)} = \tilde{a}_{(+)} = 0 \end{aligned} \tag{4.100}$$

Also in this case we will treat the more complicated singular cases given by the situations either $\tilde{a}_{(-)} = 0$ and $\tilde{a}_{(+)} \neq 0$ or $\tilde{a}_{(-)} \neq 0$ and $\tilde{a}_{(+)} = 0$. Starting with the first, we notice that equation (4.74) is not anymore valid. Instead, we compute the integral in dv of equation (4.73) as

$$I_{cs_v} = b_x \int_0^1 du\, \frac{1}{2} \quad \left\{ \tfrac{1}{2} v^2 \sin\left[\hat{b}_{(-)}\right]\Big|_{-u}^{+u} - v\,\frac{\cos\left[\tilde{a}_{(+)}\,v+\hat{b}_{(+)}\right]}{\tilde{a}_{(+)}}\Bigg|_{-u}^{+u} + \frac{\sin\left[\tilde{a}_{(+)}\,v+\hat{b}_{(+)}\right]}{\left[\tilde{a}_{(+)}\right]^2}\Bigg|_{-u}^{+u} \right\} \tag{4.101}$$

Before integrating in du we write explicitly all the dependence of the integrand with respect this variable, yielding

$$I_{cs_v} = \frac{b_x}{2} \int_0^1 du \quad \left\{ -\frac{u\,\cos\left[\tilde{a}_{(+,+)}\,u+\tilde{h}_{(+)}\right]+u\,\cos\left[\tilde{a}_{(+,-)}\,u+\tilde{h}_{(+)}\right]}{\tilde{a}_{(+)}} + \frac{\sin\left[\tilde{a}_{(+,+)}\,u+\tilde{h}_{(+)}\right]-\sin\left[\tilde{a}_{(+,-)}\,u+\tilde{h}_{(+)}\right]}{\left[\tilde{a}_{(+)}\right]^2} \right\} \tag{4.102}$$

Integration can now be performed analytically. Using the results of Appendix B we simply write

$$I_{cs_v} = \frac{b_x}{2} \left[-\frac{1}{\tilde{a}_{(+)}} \tilde{I}_{cx}\left(1, \tilde{a}_{(+,+)}, \tilde{h}_{(+)}\right)\Big|_0^1 - \frac{1}{\tilde{a}_{(+)}} \tilde{I}_{cx}\left(1, \tilde{a}_{(+,-)}, \tilde{h}_{(+)}\right)\Big|_0^1 \right.$$
$$\left. + \frac{1}{\left[\tilde{a}_{(+)}\right]^2} \tilde{I}_s\left(1, \tilde{a}_{(+,+)}, \tilde{h}_{(+)}\right)\Big|_0^1 - \frac{1}{\left[\tilde{a}_{(+)}\right]^2} \tilde{I}_s\left(1, \tilde{a}_{(+,-)}, \tilde{h}_{(+)}\right)\Big|_0^1 \right]$$
$$\tilde{a}_{(+)} \neq 0;\ \tilde{a}_{(-)} = 0 \tag{4.103}$$

We can also notice that the last singular case is dual to the previous one with respect the constants $\tilde{a}_{(+)}$ and $\tilde{a}_{(-)}$. We can therefore directly write

$$I_{cs_v} = \frac{b_x}{2} \left[-\frac{1}{\tilde{a}_{(-)}} \tilde{I}_{cx}\left(1, \tilde{a}_{(-,+)}, \tilde{h}_{(-)}\right)\Big|_0^1 - \frac{1}{\tilde{a}_{(-)}} \tilde{I}_{cx}\left(1, \tilde{a}_{(-,-)}, \tilde{h}_{(-)}\right)\Big|_0^1 \right.$$
$$\left. + \frac{1}{\left[\tilde{a}_{(-)}\right]^2} \tilde{I}_s\left(1, \tilde{a}_{(-,+)}, \tilde{h}_{(-)}\right)\Big|_0^1 - \frac{1}{\left[\tilde{a}_{(-)}\right]^2} \tilde{I}_s\left(1, \tilde{a}_{(-,-)}, \tilde{h}_{(-)}\right)\Big|_0^1 \right]$$
$$\tilde{a}_{(+)} = 0;\ \tilde{a}_{(-)} \neq 0 \tag{4.104}$$

This last operation completes the evaluation of the first integral in equation (4.60). Fortunately enough, the remaining three integrals can be written using the developed results for the first. Starting with the second integral in (4.60), note that after transformation to the canonic triangular domain it can be written in general form as

$$I_{sc_y} = A_T \int_0^1 du \int_{-u}^{+u} dv\, (a_y\, u + b_y\, v)\, \sin\left[e_s\, (x_1 + a_x\, u + b_x\, v - g_s)\right] \cos\left[e_c\, (y_1 + a_y\, u + b_y\, v - g_c)\right] \tag{4.105}$$

This integral has the exact same form as the one in equation (4.63) provided we interchange all variables associated to the x-axis with the variables associated to the y-axis. In Table 4.7 we show all the changes we need to make in order to compute the integral in (4.105) using the results already derived Next, the third integral in equation (4.60) is transformed into

Initial variable	Replaced by
(a_x, a_y)	(a_y, a_x)
(b_x, b_y)	(b_y, b_x)
(x_1, y_1)	(y_1, x_1)
(x_2, y_2)	(y_2, x_2)
(x_3, y_3)	(y_3, x_3)
(a, b)	(b, a)
(m, n)	(n, m)
(c, d)	(d, c)

Table 4.7: Variables correspondences needed for the evaluation of the second and fourth integrals in equation (4.63)

$$I_{sc_x} = A_T \int_0^1 du \int_{-u}^{+u} dv\, (a_y\, u + b_y\, v)\, \cos\left[e_c\, (x_1 + a_x\, u + b_x\, v - g_c)\right] \sin\left[e_s\, (y_1 + a_y\, u + b_y\, v - g_s)\right] \tag{4.106}$$

We can see that this integral in the same as the one shown in equation (4.63) if we just change the multiplicative factors a_x and b_x of the term $(a_x\, u + b_x\, v)$ by the factors a_y and b_y, thus obtaining the new term $(a_y\, u + b_y\, v)$ appearing in (4.106). Once this change is made, the same expressions as obtained before can be used. Finally, the fourth integral in equation (4.60) becomes

$$I_{cs_y} = A_T \int_0^1 du \int_{-u}^{+u} dv\, (a_x\, u + b_x\, v)\, \sin\left[e_s\, (x_1 + a_x\, u + b_x\, v - g_s)\right] \cos\left[e_c\, (y_1 + a_y\, u + b_y\, v - g_c)\right] \tag{4.107}$$

which as seen, it is equal to (4.106) if we use the same variables correspondences as in Table 4.7.

Once the basic integrals in (4.60) are computed, they can be used inside (4.59,4.58,4.57,4.56) to evaluate the final overlapping integrals between the basis functions and the modes of the cavity. The MoM matrix coefficients are then computed by using these overlapping integrals inside the series shown in equation (4.53). The point that remains to be discussed is therefore the convergence behavior of these series. In the next section we address this problem and develop a technique to try to accelerate the series convergence rates.

4.5 Asymptotic Extraction Procedure

Even though all the analytical effort derived up to now, when there are printed patches or slots backed by a cavity, the final matrix coefficients are given by the infinite series in (4.53) which must be summed up numerically. Usually, the resulting series exhibit a relatively slow convergence behavior and it would be therefore desirable to find a technique to try to accelerate the convergence. For this purpose, in this section we describe a frequency extraction technique based on extracting the asymptotic parts of the resulting summations and which was first proposed in [17]. The original method in [17] however, was applied only to the case of electric currents and in this study it is extended to account for the presence of both electric and magnetic interactions.

To start, first note that any MoM matrix coefficients inside a cavity shown in equation (4.53) can be rewritten in the following more general form

$$P(i,k) = \sum_m t_m(r,s)\, I_{fm}(m,i)\, I_{fm}(m,k) \tag{4.108}$$

where I_{fm} is an overlapping integral of the type studied in the previous section and $t_m(r,s)$ is a voltage or current coefficient computed in any of the equivalent transmission line networks shown in Fig. 4.3 (spectral domain quantity). Moreover $t_m(r,s)$ indicates that the current or voltage is measured at an interface s_r when the exciting generator has been placed at an interface s_s.

The first step in the formulation is to add and subtract to (4.108) the asymptotic term of the spectral domain quantity $t_m(r,s)$ when the order of the mode m tends to infinity ($m \to \infty$).

$$P(i,k) = \sum_m \left[t_m(r,s) - t_{m_0}(r,s)\right] I_{fm}(m,i)\, I_{fm}(m,k) + P_0(i,k) \tag{4.109}$$

where t_{m_0} is the asymptotic part of t_m and we have defined

$$P_0(i,k) = \sum_m t_{m_0}(r,s)\, I_{fm}(m,i)\, I_{fm}(m,k) \tag{4.110}$$

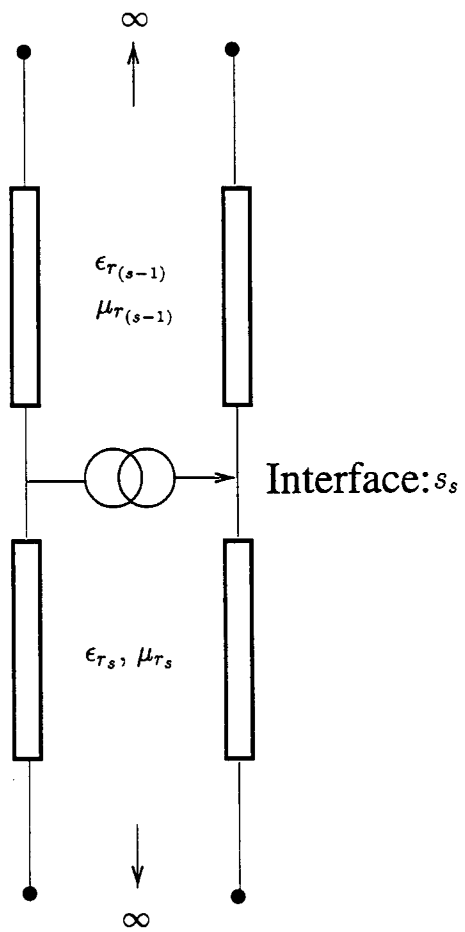

Figure 4.9: Equivalent transmission line network for electric sources in the asymptotic limiting case $m \to \infty$.

Note that if the source and observer points are at different interfaces, when $m \to \infty$ the energy excited by the source can never reach the observer interface s_r because the corresponding mode is *infinitely* below cut-off. In this case, no matter the nature of the source and observer, the interaction between them (for the asymptotic term) is negligible and we directly write

$$t_{m_0}(r,s) = 0; \ \forall r \neq s \tag{4.111}$$

What remains to be done, is to evaluate the asymptotic coefficients t_{m_0} when source and observer are at the same interface ($r = s$). In this case however, we shall consider two different situations, namely when source and observer are of electric type and when they are of magnetic type. Starting with the electric type case, we notice that for the asymptotic limiting case ($m \to \infty$) the equivalent transmission line network of electric type in Fig. 4.3 is reduced to the network shown in Fig. 4.9. The spectral quantity of interest in this case is the voltage at the generator terminals which is directly computed in the network of Fig. 4.9 as

$$t_{m_0}(s,s) = \frac{Z_{Cm}^{(s)}\, Z_{Cm}^{(s-1)}}{Z_{Cm}^{(s)} + Z_{Cm}^{(s-1)}}$$
$$s = 1, 2, \cdots, n; \ \forall s \in s_e \tag{4.112}$$

where $Z_{c_m}^{(s)}$ is the characteristic impedance of the transmission line placed below the interface s_s and $Z_{c_m}^{(s-1)}$ is the characteristic impedance of the transmission line placed above the interface s_s as shown in Fig. 4.1. It is now convenient to write the explicit forms of the characteristic impedances for both $TE_{m,n}$ and $TM_{m,n}$, namely

$$
\begin{aligned}
Z_{c_m}^{(s)TE} &= \frac{\omega\, \mu_0\, \mu_r^{(s)}}{\sqrt{k_0^2\, \epsilon_r^{(s)}\, \mu_r^{(s)} - (\frac{m\,\pi}{a})^2 - (\frac{n\,\pi}{b})^2}} \\
Z_{c_m}^{(s)TM} &= \frac{\sqrt{k_0^2\, \epsilon_r^{(s)}\, \mu_r^{(s)} - (\frac{m\,\pi}{a})^2 - (\frac{n\,\pi}{b})^2}}{\omega\, \epsilon_0\, \epsilon_r^{(s)}}
\end{aligned} \tag{4.113}
$$

For the asymptotic limiting case $m \to \infty$ above impedances become

$$
\begin{aligned}
Z_{c_m}^{(s)TE} &= \frac{\omega\, \mu_0\, \mu_r^{(s)}}{-j\, \sqrt{(\frac{m\,\pi}{a})^2 + (\frac{n\,\pi}{b})^2}} \\
Z_{c_m}^{(s)TM} &= \frac{-j\, \sqrt{(\frac{m\,\pi}{a})^2 + (\frac{n\,\pi}{b})^2}}{\omega\, \epsilon_0\, \epsilon_r^{(s)}}
\end{aligned} \tag{4.114}
$$

In above characteristic impedances we can define a frequency independent quantity, namely

$$
Q_s^{(m,n)} = \sqrt{\left(\frac{m\,\pi}{a}\right)^2 + \left(\frac{n\,\pi}{b}\right)^2} \tag{4.115}
$$

so that finally

$$
\begin{aligned}
Z_{c_m}^{(s)TE} &= \frac{j\, \omega\, \mu_0\, \mu_r^{(s)}}{Q_s^{(m,n)}} \\
Z_{c_m}^{(s)TM} &= \frac{Q_s^{(m,n)}}{j\, \omega\, \epsilon_0\, \epsilon_r^{(s)}}
\end{aligned} \tag{4.116}
$$

Upon using these last forms of the characteristic impedances in the asymptotic expression of the spectral coefficients in equation (4.108), we obtain for both TE and TM modes

$$
\begin{aligned}
t_{m_0}^T M(s,s) &= \frac{j\, \omega\, \mu_0}{Q_s^{(m,n)}}\, M(s) \\
t_{m_0}^T E(s,s) &= \frac{Q_s^{(m,n)}}{j\, \omega\, \epsilon_0\, E(s)} \\
s &= 1, 2, \cdots, n;\ \forall s_s \in s_e
\end{aligned} \tag{4.117}
$$

where the new constants have been defined as

$$
\begin{aligned}
M(s) &= \frac{\mu_r^{(s)}\, \mu_r^{(s-1)}}{\mu_r^{(s)} + \mu_r^{(s-1)}} \\
E(s) &= \epsilon_r^{(s)} + \epsilon_r^{(s-1)}
\end{aligned} \tag{4.118}
$$

Next, if we introduce equation (4.117) into the asymptotic matrix coefficients shown in (4.110) the following expressions are obtained for both TE and TM modes

$$
\begin{aligned}
P_0^{TE}(i,k) &= \sum_m \frac{1}{Q_s^{(m,n)}}\, I_{fm}^{TE}(m,i)\, I_{fm}^{TE}(m,k) \\
P_0^{TM}(i,k) &= \sum_m Q_s^{(m,n)}\, I_{fm}^{TM}(m,i)\, I_{fm}^{TM}(m,k)
\end{aligned} \tag{4.119}
$$

where I_{fm}^{TE} and I_{fm}^{TM} are the overlapping integrals between the basis functions with the $TE_{m,n}$ and $TM_{m,n}$ modal sets respectively. The interesting feature of equation (4.119) is that all quantities depend only on geometrical parameters of the antenna and are therefore frequency independent. Consequently, the series in (4.119) are computed only once for a given geometry and are not recomputed for each point in frequency. Once they are summed up, the total asymptotic matrix coefficients in equation (4.110) are evaluated by applying superposition on the coefficients obtained under TE and TM waves. After straightforward manipulations we obtain

$$P_0(i,k) = j\, d_n^{(s)TE}\, P_0^{TE}(i,k) + \frac{1}{j\, d_n^{(s)TM}}\, P_0^{TM}(i,k) \tag{4.120}$$

where the new constants have been defined as

$$\begin{aligned} d_n^{(s)TE} &= \omega\, \mu_0\, M(s) \\ d_n^{(s)TM} &= \omega\, \epsilon_0\, E(s) \end{aligned} \tag{4.121}$$

Substituting equation (4.120) into (4.109) the final MoM matrix coefficients are obtained, this time frequency dependent. It is important to note however, that since the asymptotic term is extracted in (4.109) the resulting series will converge much faster than the original series. All computational effort is therefore reduced to the evaluation of the series in (4.119) (frequency independent) with subsequent evaluation of the series in (4.109) (frequency dependent but with better convergence behavior). To illustrate the procedure we show in Fig. 4.10 a typical convergence plot obtained for the static series in (4.119). Fig. 4.11 shows a tyical plot for the dynamic part in (4.109) for the same structure.

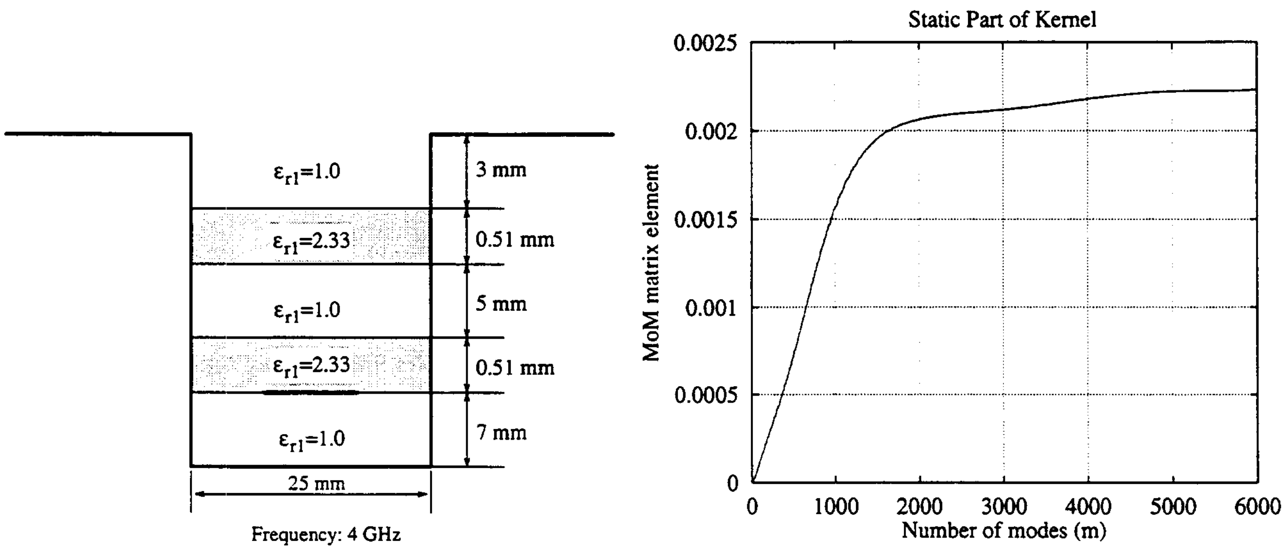

Figure 4.10: Convergence behavior of the static part of the kernel for the structure shown

As we see more modes are needed to sum the static part, but the computational effort is done only once for a given geometry and it is not repeated for each subsequent frequency point. The result is a considerable reduction in computational time for the analysis of the antenna over a wide frequency range.

The last step to complete the procedure, is to repeat the analysis when source and observer points are at the same interface and they are of magnetic type. In the asymptotic limiting case ($m \to \infty$)

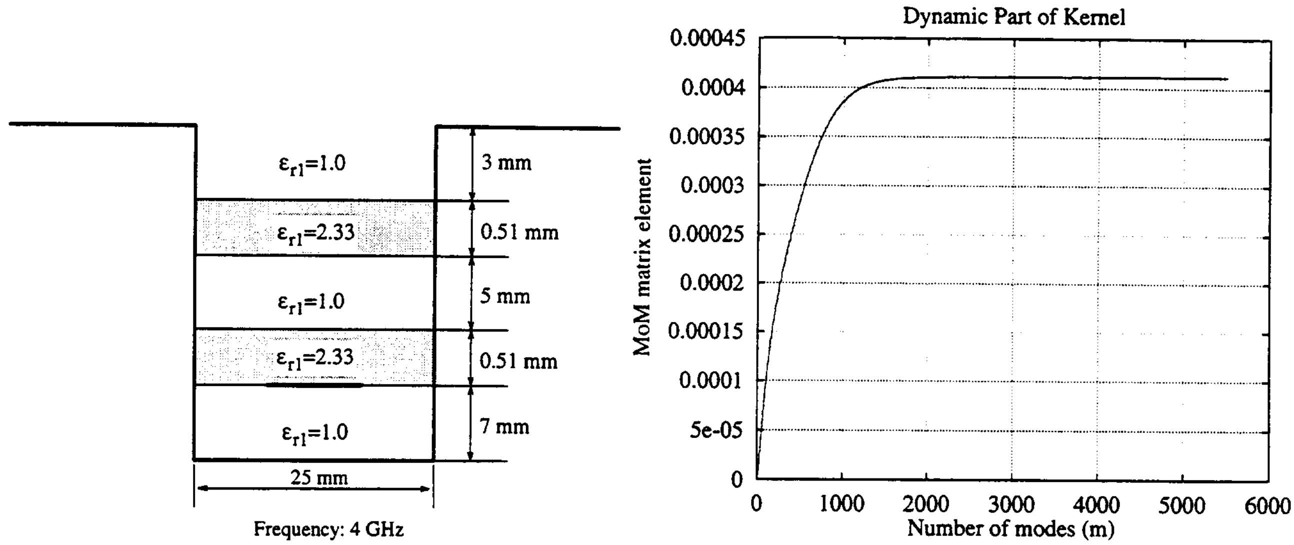

Figure 4.11: Convergence behavior of the dynamic part of the kernel for the structure shown

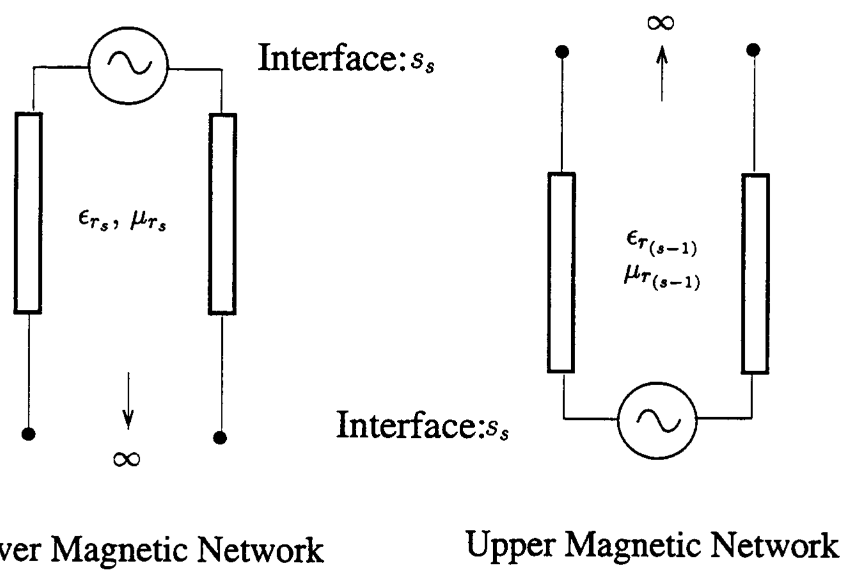

Figure 4.12: Equivalent transmission line networks for magnetic sources in the asymptotic limiting case $m \to \infty$.

the equivalent transmission line networks of upper and lower magnetic types in Fig. 4.3 are reduced to the networks shown in Fig. 4.12. If the Green's function sum defined in equation (4.17) is computed at the spectral domain level, then the total asymptotic spectral coefficient t_{m_0} will be computed by adding the currents at the generator terminals in the upper and lower magnetic networks shown in Fig. 4.12. We therefore simply write

$$t_{m_0}(s,s) = \frac{1}{Z_{Cm}^{(s)}} + \frac{1}{Z_{Cm}^{(s-1)}}$$
$$s = 1, 2, \cdots, n; \ \forall s_s \in s_m \tag{4.122}$$

Using the definitions for the asymptotic characteristic impedances in (4.116), above equation is transformed for both TE and TM modes as

$$t_{m_0}^{TE}(s,s) = \frac{Q_s^{(m,n)}}{j\, d_n^{(s)TE}}$$
$$t_{m_0}^{TM}(s,s) = \frac{j\, d_n^{(s)TM}}{Q_s^{(m,n)}} \tag{4.123}$$

where in addition, the same definitions in equations (4.118,4.121) have again been used. Introducing equation (4.123) into (4.110) the asymptotic matrix coefficients for TE and TM waves become

$$P_0^{TE}(i,k) = \sum_m Q_s^{(m,n)}\, I_{fm}^{TE}(m,i)\, I_{fm}^{TE}(m,k)$$
$$P_0^{TM}(i,k) = \sum_m \frac{1}{Q_s^{(m,n)}}\, I_{fm}^{TM}(m,i)\, I_{fm}^{TM}(m,k) \tag{4.124}$$

and the total asymptotic matrix coefficients expressed as the superposition of TE and TM cases

$$P_0(i,k) = \frac{1}{j\, d_n^{(s)TE}}\, P_0^{TE}(i,k) + j\, d_n^{(s)TM}\, P_0^{TM}(i,k) \tag{4.125}$$

The same considerations as before also applies to the frequency independent series in (4.124). Finally, with equation (4.125) the total MoM matrix coefficients can be computed for the magnetic case by direct application of equation (4.109). There is however, a special case that must be treated separately. This corresponds to the case when the magnetic currents are placed at the top aperture of the cavity. As we discussed in section 4.2, in this case the Green's functions for the magnetic currents defined above and below the aperture are not combined at the spectral domain level. The main implication of this is that the asymptotic spectral coefficients t_{m_0} are only defined with the lower magnetic network of Fig. 4.3 so that instead of equation (4.122) we need to write

$$t_{m_0}(r,s) = \frac{1}{Z_{c_m}^{(s)}} \tag{4.126}$$

where as seen, the asymptotic spectral coefficients depend only on the characteristic impedances of the transmission line below the top interface. If we repeat the same process as before, we can notice that the same expressions as derived in equations (4.123,4.124,4.125,4.121) can still be used provided the constants in (4.118) are redefined as

$$M(s) = \mu_r^{(s)}$$
$$E(s) = \epsilon_r^{(s)} \tag{4.127}$$

4.6 Meshing Strategy

The integral equation formulation for the analysis of arbitrary cavity backed antennas derived in this chapter is based on the availability of efficient meshing techniques that can effectively discretize an arbitrary planar geometry using triangular cells. On the other hand, the complex geometrical shapes used in the conformal array elementary radiator results in that the meshing procedure can be a very complex task. In this work a dedicated meshing strategy based on triangular domains has been developed for both the lower and the active patch shown in Fig. 1.1. For this purpose, structural meshes have been first developed for a number of simpler objects like rectangles, sectors, arcs, triangles and junctions to cite a few. Then, the complex geometrical shapes are decomposed into a number of these simpler objects and finally the meshes of all simpler objects are combined to produce the global mesh for the whole complex geometry.

This modular way of producing the meshes of the antenna geometry has shown to be very convenient since then, specific parts of the geometry can be treated separately for instance to refine selectively the mesh. The technique has been used successfully in the case of the conformal array elementary radiator where the meshes have been refined around the ridges opened in the circular patches as shown in Fig. 1.1. In chapter 6 we show that this has important influence on the quality of the simulated results, since a finer mesh is required around the ridges to properly model the strong variation of the currents in these areas.

In this section, to verify the meshing strategy developed, we present some typical examples of meshes obtained for the conformal array elementary radiator. In Fig. 4.13 a classical mesh for the lower active patch with two ports is presented. Fig. 4.14 shows the mesh of the upper passive

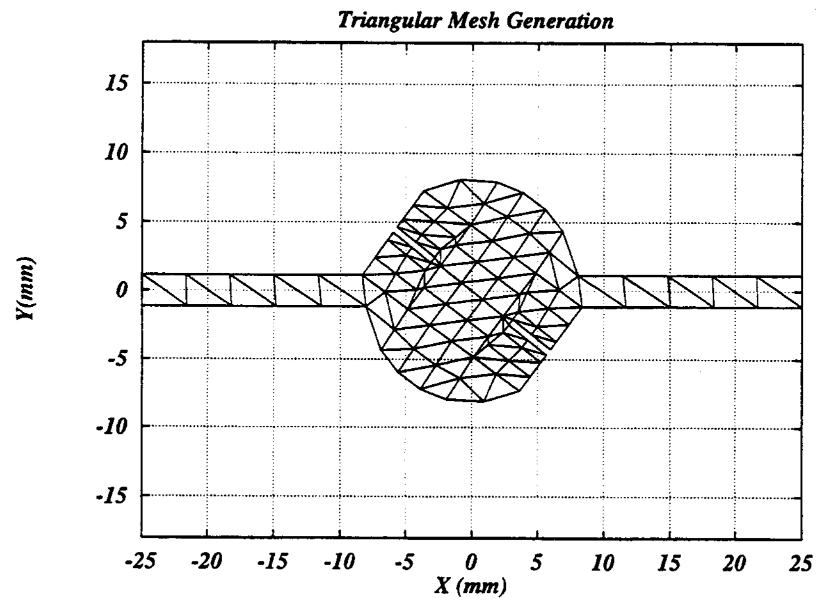

Figure 4.13: Mesh for the conformal array lower active patch as obtained with the proposed approach.

patch when it is acting as the upper radiating aperture. We clearly see that in this case the part of the circuit meshed is the one corresponding to the air gap where the equivalent magnetic currents are placed. In addition, Fig. 4.15 shows the mesh for the upper passive patch when it is acting as a true electric patch outside the metallic cavity. Finally, we also show in Fig. 4.16 a typical mesh of the lower active patch for the configuration with only one port. It is also important to note that an additional difficulty arises if one tries to mesh the lower active patch with an arbitrary angle between the axis of the patch and the lateral cuts (angle φ in Fig. 1.1). In fact, the decomposition of the lower active patch into simpler objects must be different depending on the value of this angle. To

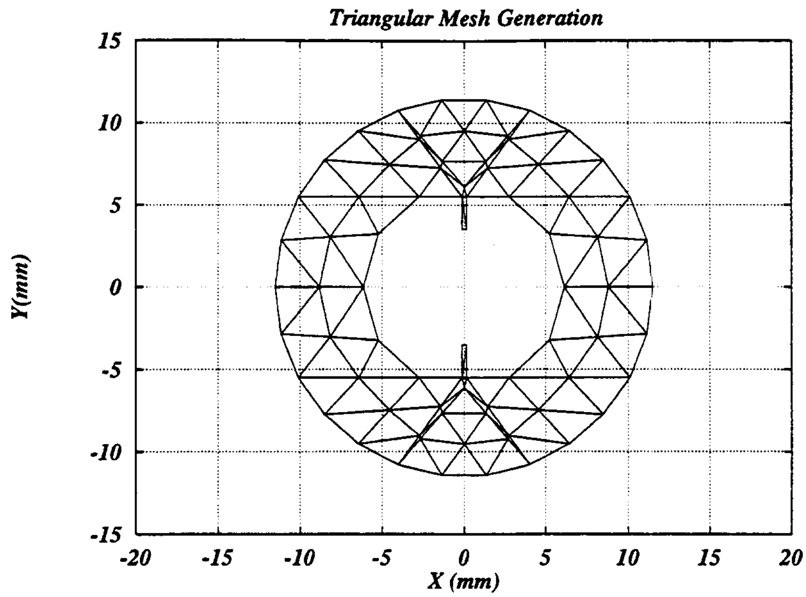

Figure 4.14: Typical mesh for the conformal array upper passive patch when it is acting as radiating aperture.

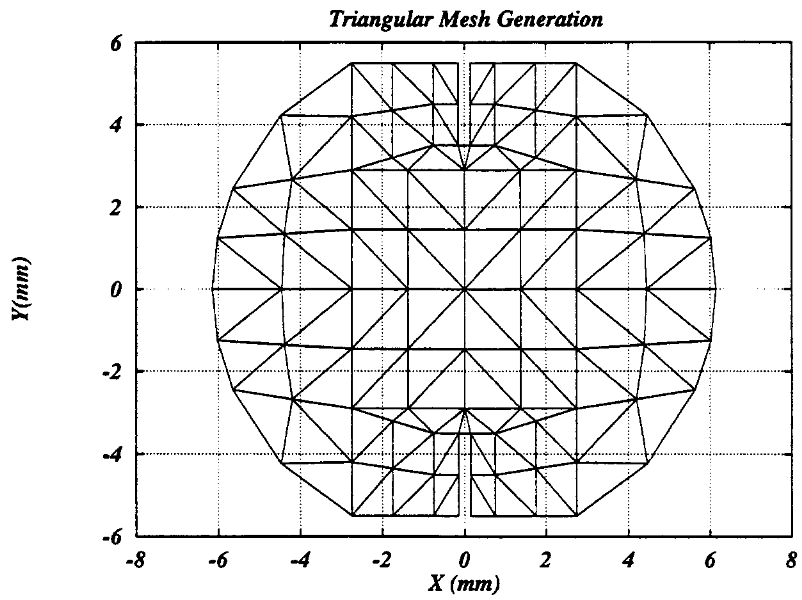

Figure 4.15: Typical mesh for the conformal array upper passive patch when it is acting as a true electric patch.

overcome this problem, five different models have been derived during the decomposition of the lower active patch into simpler objects. Once the angle is specified, the most suitable model is selected, the geometry is decomposed into simpler objects according to the corresponding model and the mesh is thus computed. To show the validity of this approach, we present in Fig. 4.17 and Fig. 4.18 the meshes computed for two different patch angles. As seen, the meshes obtained are well structured in all cases and they can effectively be used with the integral equation formulation derived in this chapter.

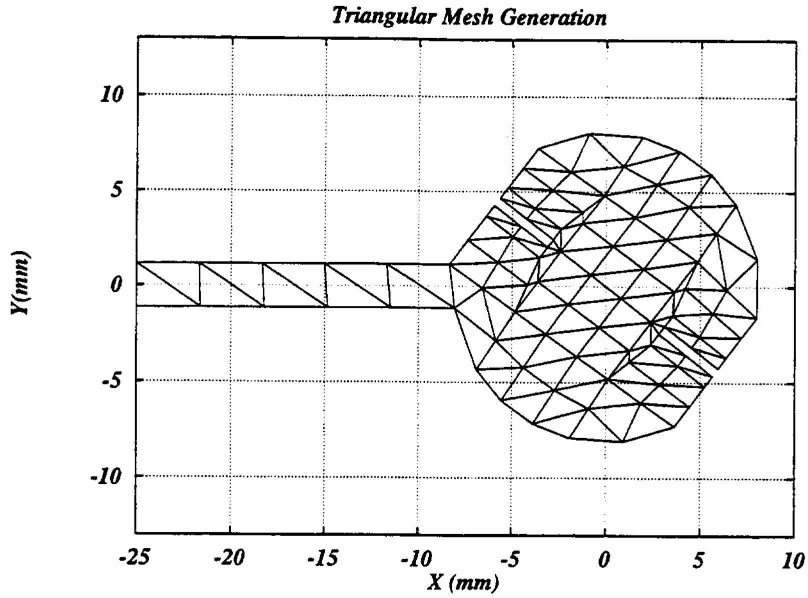

Figure 4.16: Typical mesh for the conformal array lower active patch when only one input port is considered.

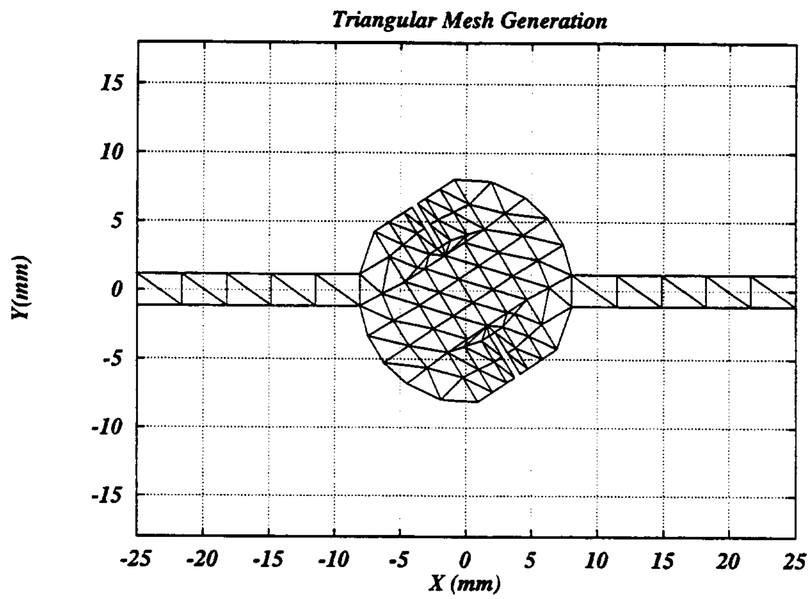

Figure 4.17: Computed mesh for the lower active patch with an angle $\varphi = 57.5^o$

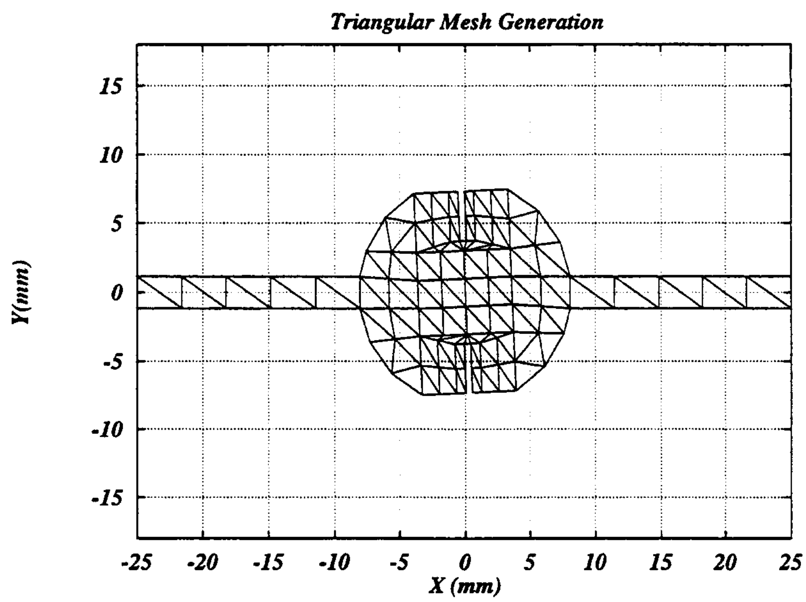

Figure 4.18: Computed mesh for the lower active patch with an angle $\varphi = 87.5^o$

Chapter 5

Electrical Characteristics Computations

5.1 Introduction

The last step in the analysis of the antenna structure is the computation of the electrical characteristics that are of interest from the engineering point of view. Once the integral equation formulated in chapter 4 is solved with the Method of Moments (MoM) algorithm, all induced electric and magnetic currents in the structure are known. In this chapter we detail how to use this information to compute the final electrical behavior of the antenna, namely the input impedance or full scattering parameters in the case of the two ports structure and the far field radiated by the structure.

5.2 Scattering Parameters

The computation of the scattering parameters of the antenna will be accomplished using the well known *delta* gap model presented for instance in [18]. Consider a general structure with an arbitrary number of ports n as shown in Fig. 5.1. To extract the scattering parameters of this structure we can place an exciting generator at a generic port s as shown in Fig. 5.1 and load all other ports with the characteristic impedance of reference Z_c. Following the *delta* gap model [17], a voltage V_q constant

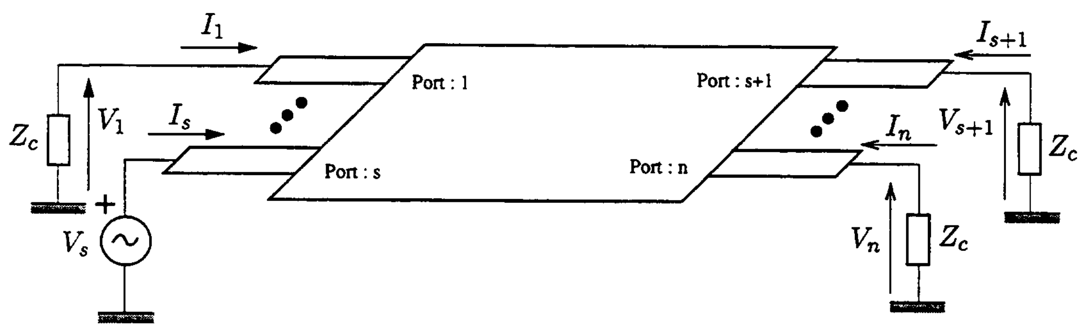

Figure 5.1: General multiport network with the exciting generator placed at port s and all other ports loaded with the characteristic impedance.

along the width of the line is assumed to be applied to each port. This is equivalent to consider an impressed or exciting field at each port $\bar{E}_{(e)}^{(q)}$ produced by the voltage V_q, and the total impressed or exciting field $\bar{E}_{(e)}$ of equation (4.18) will be expressed as the sum of the impressed fields at all ports

$$\bar{E}_{(e)} = \sum_{q=1}^{n} \bar{E}_{(e)}^{(q)} \tag{5.1}$$

What we need to do therefore, is to compute the impressed fields at all ports of the structure, so that with equation (5.1) the final known term vector of the MoM system given in (4.33) can be evaluated. To start let us note that the voltage V_q considered constant along the width of the port, will produce an impressed field at this port which can be written with the following *dirac*-delta expression

$$\bar{E}_{(e)}^{(q)} = -V_q\, \delta\left(\bar{r} - \bar{r}_q\right)\, \hat{e}_q;\; 1 \leq q \leq n \tag{5.2}$$

where $\bar{r}_q$ is the position vector of the q-th port and $\hat{e}_q$ is the unit vector indicating the orientation of the port. For all ports connected to the characteristic impedance, the boundary condition imposed by the loads requires the following redefinition of the exciting electric field

$$\bar{E}_{(e)}^{(r)} = I_r\, Z_c\, \delta\left(\bar{r} - \bar{r}_r\right)\, \hat{e}_r \left\{ \begin{array}{c} 1 \leq r \leq n \\ r \neq s \end{array} \right. \tag{5.3}$$

and I_r is the current flowing at the r-th port as shown in Fig. 5.1. This current can be computed through integration along the port width of the current density induced at the port position, namely

$$I_r = \int_{w_r} \bar{J}_r(\bar{r}')|_{\bar{r}'=\bar{r}_r} \cdot \hat{e}_r\, dr';\; 1 \leq r \leq n \tag{5.4}$$

where w_r has been used to denote the width of the r-th port. Using the expansion of the electric current density in equation (4.24), the total induced current at the r-th port is written as

$$I_r = \sum_k \alpha_k\, \gamma_k^{(r)};\; 1 \leq r \leq n \tag{5.5}$$

where the following γ coefficients have been defined

$$\gamma_k^{(r)} = \int_{w_r} \bar{f}_k\left(\bar{r}'\right)|_{\bar{r}'=\bar{r}_r} \cdot \hat{e}_r\, dr';\; 1 \leq r \leq n \tag{5.6}$$

It is interesting to note that using the definition for the vector mode functions $\bar{f}_k$ given in equation (4.22) above γ coefficients can be easily evaluated analytically. With the currents flowing at the ports expressed as in equation (5.5), the final exciting field for those ports connected to the loads is written as (equation (5.3))

$$\bar{E}_{(e)}^{(r)} = \sum_k \alpha_k\, \gamma_k^{(r)} Z_c\, \delta\left(\bar{r} - \bar{r}_r\right)\, \hat{e}_r \left\{ \begin{array}{c} 1 \leq r \leq n \\ r \neq s \end{array} \right. \tag{5.7}$$

The last impressed field to be computed is the one associated to the port where the generator is placed (s-th port). In this case we take the voltage V_s applied as exciting voltage. Therefore, using directly equation (5.2) we write

$$\bar{E}_{(e)}^{(s)} = -V_s\, \delta\left(\bar{r} - \bar{r}_s\right)\, \hat{e}_s \tag{5.8}$$

Once all the impressed fields at the ports are known, they can be used in equation (5.1) to finally write the known term vector of the MoM system given in (4.33) as

$$P_{(e)} = V_s \int_{w_s} \delta(\bar{r} - \bar{r}_s)\, \hat{e}_s \cdot \bar{f}_i(\bar{r})\, dr - \sum_{\substack{r=1 \\ r \neq s}}^{n} \sum_k \alpha_k\, \gamma_k^{(r)}\, Z_c \int_{w_r} \delta(\bar{r} - \bar{r}_r)\, \hat{e}_r \cdot \bar{f}_i(\bar{r})\, dr \tag{5.9}$$

But the integrals in equation (5.9) can again be expressed as a function of the γ coefficients defined in (5.6). We can then write

$$P_{(e)} = V_s\, \gamma_i^{(s)} - \sum_{\substack{r=1 \\ r \neq s}}^{n} \sum_k \alpha_k\, \gamma_k^{(r)}\, Z_c\, \gamma_i^{(r)} \tag{5.10}$$

It is interesting to observe that in the known term vector of equation (5.10) there is one part depending on the unknown coefficients α_k. In consequence, this part is moved to the right hand side of the MoM system and is therefore absorbed in the system matrix. The true known term vector of the system is consequently composed of only the part of equation (5.10) independent on the unknown α_k coefficients. After all these manipulations, the final general form for the MoM system structure given in equation (4.34) is transformed into the following one

$$\begin{bmatrix} \underline{\gamma}^{(s)} \\ \underline{0} \\ \vdots \\ \underline{0} \end{bmatrix} = \begin{bmatrix} \left(\underline{\underline{P}}^{(1,1)} + \sum_{\substack{r=1 \\ r \neq s}}^{n} \underline{\gamma}^{(r)}\, Z_c\, \underline{\gamma}^{(r)T} \right) & \underline{\underline{P}}^{(1,2)} & \dots & \underline{\underline{P}}^{(1,n)} \\ \underline{\underline{P}}^{(2,1)} & \underline{\underline{P}}^{(2,2)} & \dots & \underline{\underline{P}}^{(2,n)} \\ \vdots & \vdots & \vdots & \vdots \\ \underline{\underline{P}}^{(n,1)} & \underline{\underline{P}}^{(n,2)} & \dots & \underline{\underline{P}}^{(n,n)} \end{bmatrix} \cdot \begin{bmatrix} \frac{\underline{\alpha}^{(1)}}{V_s} \\ \frac{\underline{\alpha}^{(2)}}{V_s} \\ \vdots \\ \frac{\underline{\alpha}^{(n)}}{V_s} \end{bmatrix} \tag{5.11}$$

where for clarity, it has been assumed that all ports are attached to the first printed patch of the antenna and all equations of the system have been divided by the exciting voltage V_s. Also, $\underline{\gamma}^{(r)T}$ denotes the transpose of the corresponding γ vector defined in equation (5.6). The input impedance can now be defined as the ratio between the applied voltage V_s and the induced current I_s at the point of excitation. Using equation (5.4) together with the expansion of the current density in (4.24) for the computation of the current, and again the γ coefficients definition in (5.6), the input impedance at the excitation port simply becomes

$$Z_{in} = \frac{V_s}{I_s} = \frac{1}{\sum_k \frac{\alpha_k}{V_s} \gamma_k^{(s)}} \tag{5.12}$$

where $\frac{\alpha_k}{V_s}$ is directly the vector of solutions computed by inverting the system of linear equations shown in (5.11). The computation of the rest of the scattering matrix is accomplished by first evaluating all the trans-admittances to all other ports

$$Y_{tran}^{(r)} = \frac{I_r}{V_s} = \sum_k \frac{\alpha_k}{V_s} \gamma_k^{(r)} \tag{5.13}$$

then, by use of simple network relations [19]

$$\begin{aligned} S_{r,s} &= \frac{Z_{in} - Z_c}{Z_{in} + Z_c};\ r = s \\ S_{r,s} &= \frac{2\, Z_c\, Y_{tran}^{(r)}\, Z_{in}}{Z_c + Z_{in}} \begin{cases} 1 \leq r \leq n \\ r \neq s \end{cases} \end{aligned} \tag{5.14}$$

Finally, the whole process is repeated but placing the exciting generator at all ports consecutively $1 \leq s \leq n$, thus completing the evaluation of all S-parameters of the structure. The last point that remains to be discussed, is the evaluation of the γ coefficients defined in equation (5.6). To do so, we must notice that in order to allow current flowing through the ports, half roof-top functions must be defined along the widths of all ports as shown in Fig. 5.2. Physically, the amplitudes of these half

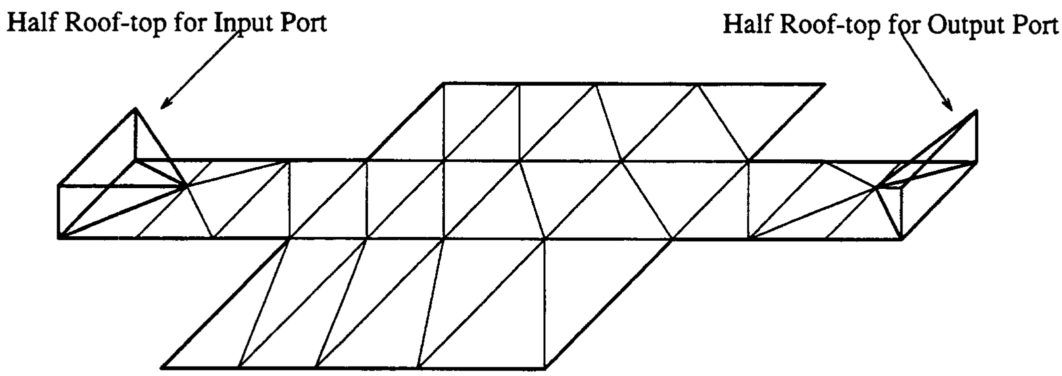

Figure 5.2: General printed circuit showing the defined half roof-top functions at the ports to allow current flowing.

roof-top functions represent the current induced at the ports positions. To compute the γ coefficients in equation (5.6), we first introduce the expression of the vector basis functions defined in (4.22), thus obtaining

$$\gamma_k^{(r)} = \frac{l_k}{2\,A_k} \int_{w_r} \left[\bar{\rho}_k|_{\bar{r}=\bar{r}_r} \cdot \hat{e}_r \right] dr \tag{5.15}$$

The first thing to notice is that the resulting integral is zero for all triangular domains not containing the point $\bar{r}_r$. Also, we remark that only the half roof-top functions defined at the r-th port will both contain the point $\bar{r}_r$ and at this point the radial vector $\bar{\rho}|_{\bar{r}=\bar{r}_r}$ will not vanish. The situation is shown in Fig. 5.3 where we show a half roof-top attached to the r-th port and the radial vector $\bar{\rho}$ evaluated at the point $\bar{r}_r$. As we see from the figure the scalar product $\left[\bar{\rho}_k|_{\bar{r}=\bar{r}_r} \cdot \hat{e}_r \right]$ is the height of the triangle

$$\left[\bar{\rho}_k|_{\bar{r}=\bar{r}_r} \cdot \hat{e}_r \right] = h_k; \; \forall k \in \text{Half roof-top attached to r-th port} \tag{5.16}$$

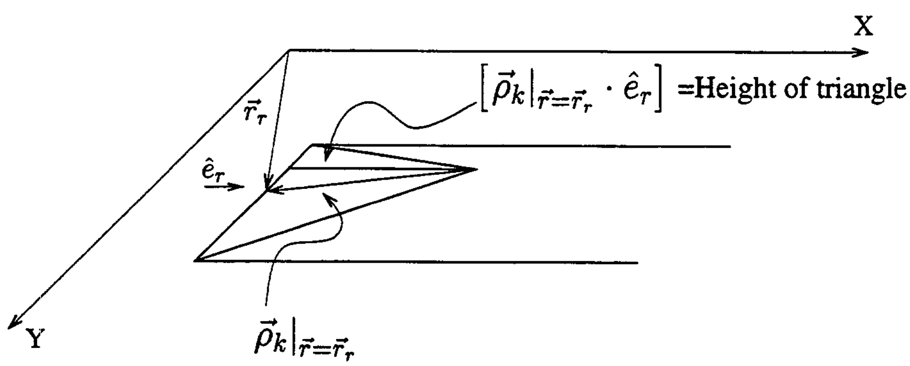

Figure 5.3: Geometry used to compute the *gamma* coefficients associated to half roof-top functions.

Upon using equation (5.16) into (5.15) we finally obtain

$$\gamma_k^{(r)} = \frac{l_k}{2\,A_k}\,h_k \int_{w_r} dr = w_r;\ \forall k \in \text{Half roof-top attached to r-th port} \tag{5.17}$$

where w_r is the width of the r-th port. This last result is summarized in the following equation where we give the value of the γ coefficients at a generic port r.

$$\gamma_k^{(r)} = \begin{cases} w_r; & \forall k \in \text{Half roof-top attached to r-th port} \\ 0; & \text{Rest of } k \end{cases} \tag{5.18}$$

It should be pointed out that with the proposed approach, any number of half roof-top functions can be defined along the width of each port to accurately model the transverse dependence of the currents along the lines acting as ports.

5.3 Radiation Characteristics

One of the most interesting electrical parameters of an antenna is the far field radiated by the structure. With this information, we can study for instance how does the antenna radiate, including the directivity of the antenna and the polarization of the radiated signal. Once the electric and magnetic currents induced in the structure are computed with the integral equation technique derived in chapter 4, the total radiated field can be computed by using the superposition integrals in (4.5,4.6,4.7,4.8). The main difficulty in using these equations however, is the evaluation of the associated Green's functions derived in chapter 2 in the far field region $\rho \to \infty$. Indeed, numerically it is not possible to compute the Sommerfeld integrals when $\rho \to \infty$. To overcome this difficulty we shall first develop alternative asymptotic expressions for the Green's functions valid in the far field region ($\rho \to \infty$). Once the new expressions for the Green's functions are known, they can be introduced in equations (4.5,4.6,4.7,4.8) where the usual far field approximations will, in addition, be applied [10]. From this point, standard evaluation of the so-called radiation integral leads directly to the computation of the far field radiated by the antenna.

5.3.1 Asymptotic form of Green's functions

In this section we are interested in evaluating an asymptotic form for a general spatial domain Green's function when $\rho \to \infty$. To start let us consider the spectral domain counterpart $\tilde{G}$ and note that spectral and spatial domains are linked by the classical double Fourier spatial transformation given by

$$G(x, y, z) = \frac{1}{2\pi} \int_{-\infty}^{+\infty} \int_{-\infty}^{+\infty} dk_x\, dk_y\, \tilde{G}(k_x, k_y, z)\, \exp(j\,k_x\,x)\, \exp(j\,k_y\,y) \tag{5.19}$$

Since we are studying the radiation characteristics of structures, we will assume that the spectral domain Green's function dependence on the coordinate z is that of a pure spherical wave traveling in the upper semi-infinite free space, namely

$$\tilde{G}(k_x, k_y, z) = \tilde{g}(k_x, k_y)\, \exp(-j\,\beta\,z) \tag{5.20}$$

where β is the propagation constant along the longitudinal axis of the structure and it was defined in (2.5). Now, we can make a change to polar spectral coordinates as follows

$$k_x = k_\rho \cos(k_\varphi)$$
$$k_y = k_\rho \sin(k_\varphi) \tag{5.21}$$

so that the double Fourier transformation in (5.19) becomes

$$G(x,y,z) = \frac{1}{2\pi}\int_0^{2\pi} dk_\varphi \int_0^\infty dk_\rho\, k_\rho\, \tilde{g}\, \exp(-j\,\beta\, z)\, \exp\left[j\, (k_\rho \cos(k_\varphi)\, x + k_\rho \sin(k_\varphi)\, y)\right] \tag{5.22}$$

Next, we further transform the resulting integral to polar spatial coordinates

$$x = \rho \cos(\varphi)$$
$$y = \rho \sin(\varphi) \tag{5.23}$$

so that we easily write (5.22) as

$$G(x,y,z) = \frac{1}{2\pi}\int_0^{2\pi} dk_\varphi \int_0^\infty dk_\rho\, k_\rho\, \tilde{g}\, \exp(-j\,\beta\, z)\, \exp\left[j\, k_\rho\, \rho\, (\cos(k_\varphi)\, \cos(\varphi) + \sin(k_\varphi)\, \sin(\varphi))\right] \tag{5.24}$$

which using the expression for the cosine of the difference between two angles and reversing the order of the integration, becomes

$$G(x,y,z) = \frac{1}{2\pi}\int_0^\infty dk_\rho\, k_\rho\, \exp(-j\,\beta\, z) \int_0^{2\pi} dk_\varphi\, \tilde{g}\, \exp\left[j\, k_\rho\, \rho \cos(k_\varphi - \varphi)\right] \tag{5.25}$$

In this expression, the inner integral can be evaluated using the Debye's Saddle point formula. Indeed, it can be demonstrated that if $k_\rho\, \rho \to \infty$, then the function to be integrated exhibits a saddle point in $k_\varphi = \varphi$. In this case, practically all the contribution to the value of the integral is due to the saddle point so that we can approximate the whole integral by the value of the function at the saddle point

$$G(x,y,z) = \frac{1}{2\pi}\int_0^\infty dk_\rho\, k_\rho\, \exp(-j\,\beta\, z)\sqrt{\frac{2\pi}{j\, k_\rho\, \rho}}\, \tilde{g}\, \exp(j\, k_\rho\, \rho)$$
$$k_\rho\, \rho \to \infty \tag{5.26}$$

Now, to the remaining integral we apply the following change of variable

$$k_\rho = k_0 \sin(w) \tag{5.27}$$

To do so, first note that β is also function of k_ρ. Using the definition in equation (2.5) and applying the change of variable in (5.27) we obtain

$$\beta = \sqrt{k_0^2 - k_0^2 \sin^2(w)} = k_0 \cos(w) \tag{5.28}$$

so that equation (5.26) becomes

$$G(x,y,z) = \frac{1}{2\pi}\int_0^\infty \sqrt{\frac{2\pi\, k_0 \sin(w)}{j\, \rho}}\, \tilde{g}\, k_0 \cos(w)\, \exp\left[j\, k_0\, (\rho \sin(w) - z \cos(w))\right] dw$$
$$k_\rho\, \rho \to \infty \tag{5.29}$$

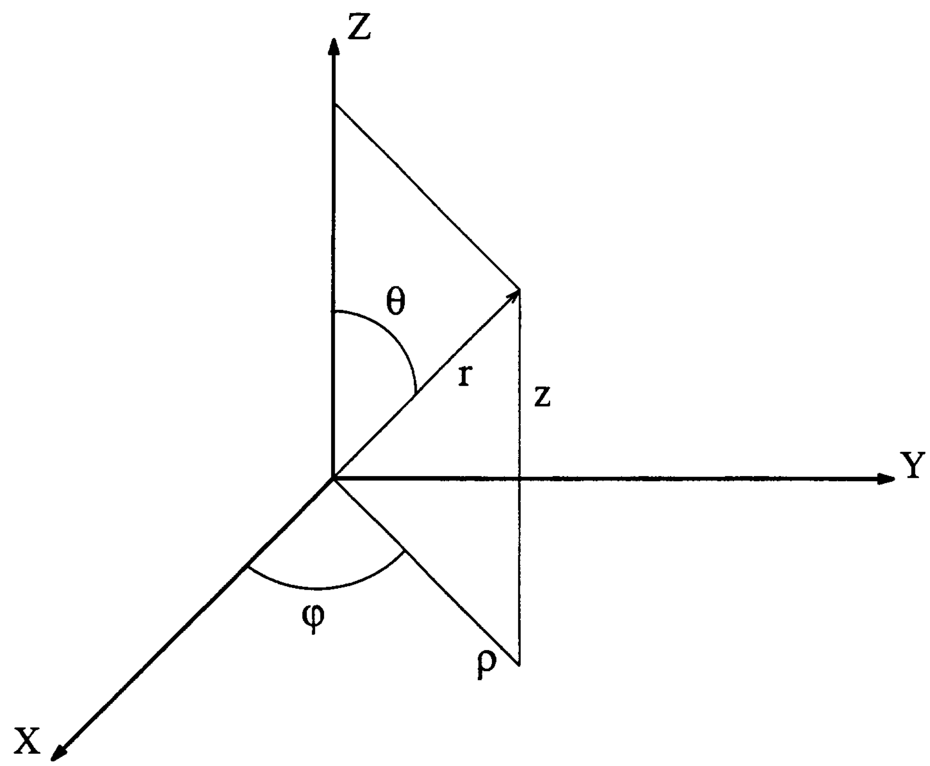

Figure 5.4: Standard cylindrical and spherical coordinate systems relations.

It is now convenient to change the (ρ, φ, z) coordinates of the cylindrical coordinate system, to the standard spherical coordinate system (r, θ, φ) (see Fig. 5.4). Equation (5.29) then becomes

$$\begin{aligned}
&G(x,y,z) = \frac{1}{2\pi} \int_0^{\infty} \sqrt{\frac{2\pi k_0 \sin(w)}{j\, r \sin(\theta)}}\, \tilde{g}\, k_0 \cos(w) \exp\left[j\, k_0\, r \left(\sin(\theta) \sin(w) - \cos(\theta) \cos(w)\right)\right] dw \\
&k_\rho\, \rho \to \infty
\end{aligned} \tag{5.30}$$

$$\begin{aligned}
&G(x,y,z) = \frac{1}{2\pi} \int_0^{\infty} \sqrt{\frac{2\pi k_0 \sin(w)}{j\, r \sin(\theta)}}\, \tilde{g}\, k_0 \cos(w) \exp\left[-j\, k_0\, r \cos(w+\theta)\right] dw \\
&k_\rho\, \rho \to \infty
\end{aligned} \tag{5.31}$$

This last integral can again be solved analytically using the Debye's saddle point integration formula. In fact, it can be demonstrated that when $k_0\, r \to \infty$ then the resulting function to be integrated exhibits a saddle point at $w = -\theta$. Again, it is this saddle point that contributes mainly to the value of the integral. The integral is then computed by simple evaluation of the function at the saddle point

$$\begin{aligned}
&G(x,y,z) = \frac{1}{2\pi} \sqrt{\frac{-2\pi k_0}{j\, r}} \sqrt{\frac{2\pi}{-j\, k_0\, r}}\, \tilde{g}\, k_0 \cos(\theta) \exp\left(-j\, k_0\, r\right) \\
&k_\rho\, \rho \to \infty \\
&k_0\, r \to \infty
\end{aligned} \tag{5.32}$$

which can be written in its final form as

$$\begin{aligned}
&G(x,y,z) = j\,k_0\,\cos(\theta)\,\tilde{g}(k_x,k_y)\,\frac{\exp(-j\,k_0\,r)}{r} \\
&k_\rho\,\rho \to \infty \\
&k_0\,r \to \infty
\end{aligned} \tag{5.33}$$

Finally, it is interesting to see what are the values of the spectral domain variables k_x and k_y when all the above transformations are applied. First, compute equation (5.21) in the saddle point $k_\varphi = \varphi$

$$\begin{aligned}
k_x &= k_\rho\,\cos(\varphi) \\
k_y &= k_\rho\,\sin(\varphi)
\end{aligned} \tag{5.34}$$

Next use the change of variables in (5.27)

$$\begin{aligned}
k_x &= k_0\,\sin(w)\,\cos(\varphi) \\
k_y &= k_0\,\sin(w)\,\sin(\varphi)
\end{aligned} \tag{5.35}$$

Finally, compute the resulting expression in the saddle point $w = -\theta$

$$\begin{aligned}
k_x &= -k_0\,\sin(\theta)\,\cos(\varphi) \\
k_y &= -k_0\,\sin(\theta)\,\sin(\varphi)
\end{aligned} \tag{5.36}$$

Note also that using (5.36), the radial spectral variable k_ρ is written as

$$k_\rho = k_0\,\sin(\theta) \tag{5.37}$$

As we can see in equation (5.33), the spatial domain Green's function is expressed as a function of its spectral domain counterpart evaluated at the points (k_x, k_y) given by equations (5.36,5.37). In addition, the spectral domain Green's function $\tilde{g}$ is evaluated at the top interface of the layered structure as required by the $\exp(-j\,\beta\,z)$ dependence shown in (5.20). The asymptotic form of the Green's function derived in (5.33) is suitable to be used inside the superposition integrals of equations (4.5,4.6,4.7,4.8) for the computation of the radiated far field of the antenna structure.

5.3.2 Radiation integral evaluation

In this section we detail how to compute the far field radiated by a planar printed antenna composed of an arbitrary number of printed patches and slots embedded in a multilayered medium. We will consider the radiation from electric and magnetic currents separately and then the total radiated field will be computed as the superposition of the two previous cases.

Starting with the electric case, we can use equation (4.5) to compute the total electric field radiated by all the printed patches in the antenna structure as

$$\bar{E} = -j\,\omega \sum_{\substack{s \\ s_s \in s_e}} \int_{S_s} \overline{\overline{G}}_A^{(s)} \cdot \bar{J}_s\,ds' \tag{5.38}$$

where $G_A^{(s)}$ is the magnetic vector potential dyadic Green's function produced by the electric source s evaluated asymptotically in the far field region as described in the previous section. We can also notice that the contributions of the electric scalar potential G_v have been neglected in the far field region, because it contains dependences of the type $(1/r^2)$ in front of the $(1/r)$ dependence of $\overline{\overline{G}}_A$ [10]. Using the form of the dyadic in equation (2.6), we can write (5.38) as

$$\bar{E} = -j\,\omega \sum_{\substack{s \\ s_s \in s_e}} \bar{A}^{(s)} \tag{5.39}$$

where the new vectors have been defined as

$$\bar{A}^{(s)} = \int_{S_s} G_A^{(s)}\, \bar{J}_s\, ds' \tag{5.40}$$

The next step is to use in above equation the asymptotic form of the spatial Green's function derived in (5.33)

$$\bar{A}^{(s)} = j\,k_0\, \cos\theta\, \tilde{g}_A^{(s)}(k_x, k_y) \int_{S_s} \frac{\exp(-j\,k_0\,R)}{R}\, \bar{J}_s\, ds' \tag{5.41}$$

where $\tilde{g}_A^{(s)}$ is the magnetic vector potential spectral Green's function produced by the source s evaluated at the points given by equations (5.36,5.36) and at the top interface of the layered structure as discussed in the previous section. Moreover, R has been used to denote the distance between the source and observer points. In the far field region we can introduce in (5.41) the approximation of parallel rays and write [10] (see Fig. 5.5)

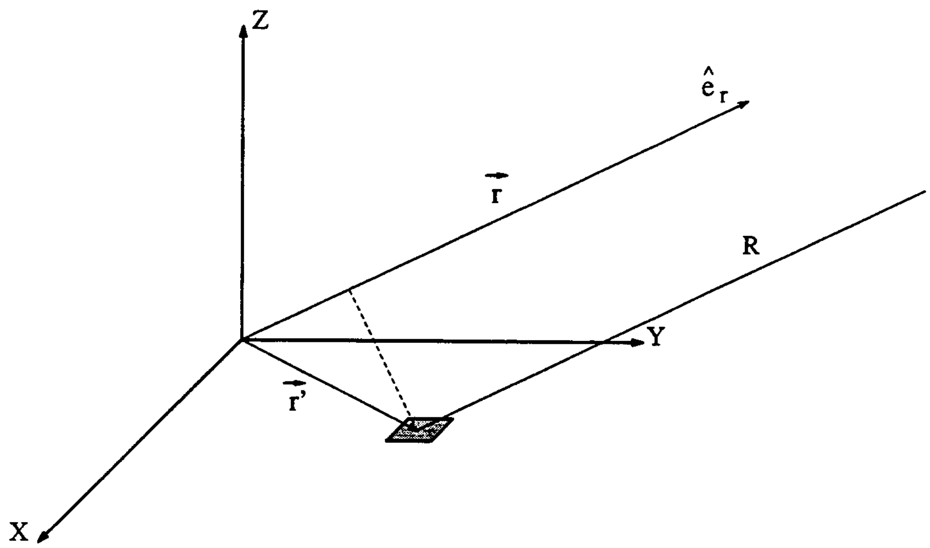

Figure 5.5: Standard far field approximation for source and observer position vectors.

$$\bar{A}^{(s)} = j\,k_0\, \cos\theta\, \tilde{g}_A^{(s)}(k_x, k_y)\, \frac{\exp(-j\,k_0\,r)}{r} \int_{S_s} \exp(+j\,k_0\,\bar{r}' \cdot \hat{e}_r)\, \bar{J}_s\, ds' \tag{5.42}$$

with the usual vector identity [10]

$$\bar{r}' \cdot \hat{e}_r = x'\, \sin\theta\, \cos\varphi + y'\, \sin\theta\, \sin\varphi + z'\, cos\theta \tag{5.43}$$

In this last equation we can define the radiation vector as

$$\bar{N}^{(s)} = \int_{S_s} \exp(+j\,k_0\,\bar{r}' \cdot \hat{e}_r)\, \bar{J}_s\, ds' \tag{5.44}$$

For the evaluation of the radiation vector, we must first introduce in equation (5.44) the expansion of the electric currents given in (4.24), thus obtaining

$$\bar{N}^{(s)} = \sum_k \alpha_k^{(s)} \int_{S_s} \exp(+j\, k_0\, \bar{r}' \cdot \hat{e}_r)\, \bar{f}_k^{(s)}(\bar{r}')\, ds' \tag{5.45}$$

where $\alpha_k^{(s)}$ are the coefficients of the expansion computed through the solution of the MoM system. If we now use the definition of the vector basis functions given in (4.22), above equation becomes

$$\bar{N}^{(s)} = \sum_k \alpha_k^{(s)} \sum_{m=1}^{2} (-1)^{m-1} \frac{l_k}{2\, A_k^{(m)}} \int_{T_k^{(m)}} \bar{\rho}_k^{(m)} \exp(+j\, k_0\, \bar{r}' \cdot \hat{e}_r)\, ds' \tag{5.46}$$

and $T_k^{(1)}$, $T_k^{(2)}$ are the two triangles where the k-th basis function is defined. Note that from equation (5.46), it is simple to evaluate numerically the rectangular components of the radiation vector defined as

$$\begin{aligned} N_x^{(s)} &= \sum_k \alpha_k^{(s)} \sum_{m=1}^{2} (-1)^{m-1} \frac{l_k}{2\, A_k^{(m)}} \int_{T_k^{(m)}} \rho_{x_k}^{(m)} \exp(+j\, k_0\, \bar{r}' \cdot \hat{e}_r)\, ds' \\ N_y^{(s)} &= \sum_k \alpha_k^{(s)} \sum_{m=1}^{2} (-1)^{m-1} \frac{l_k}{2\, A_k^{(m)}} \int_{T_k^{(m)}} \rho_{y_k}^{(m)} \exp(+j\, k_0\, \bar{r}' \cdot \hat{e}_r)\, ds' \end{aligned} \tag{5.47}$$

With the integration techniques extended to triangular domains developed in chapter 4, the integrals in (5.47) are easily evaluated. Moreover, it has been observer that the integration rule of only one point suffices for an accurate evaluation of (5.47). Once the rectangular components of the radiation vector are evaluated, the spherical components can easily be obtained through the classical rectangular to spherical transformation

$$\begin{aligned} N_\theta^{(s)} &= \cos\theta\, \sin\varphi\, N_x^{(s)} + \cos\theta\, \sin\varphi\, N_y^{(s)} \\ N_\varphi^{(s)} &= -\sin\varphi\, N_x^{(s)} + \cos\varphi\, N_y^{(s)} \end{aligned} \tag{5.48}$$

The spherical components of the total radiated far field are now computed by combining equations (5.39,5.42,5.44, 5.47,5.48)

$$\begin{aligned} E_\theta &= \omega\, k_0\, \cos\theta\, \frac{\exp(-j\, k_0\, r)}{r} \sum_{\substack{s \\ s_s \in s_e}} \tilde{g}_A^{(s)}(k_x, k_y)\, N_\theta^{(s)} \\ E_\varphi &= \omega\, k_0\, \cos\theta\, \frac{\exp(-j\, k_0\, r)}{r} \sum_{\substack{s \\ s_s \in s_e}} \tilde{g}_A^{(s)}(k_x, k_y)\, N_\varphi^{(s)} \end{aligned} \tag{5.49}$$

For the case of planar slots, the radiated far field is computed following a dual procedure than the one described above. In this case equation (4.7) is used to compute the total magnetic field radiated by the printed slots as

$$\bar{H} = -j\, \omega \sum_{\substack{s \\ s_s \in s_m}} \int_{S_s} \overline{\overline{G}}_F^{(s)} \cdot \bar{M}_s\, ds' \tag{5.50}$$

where again the contributions of the magnetic scalar potential G_w are neglected. In an exact parallel way as before, we can now write above equation as

$$\bar{H} = -j\, \omega \sum_{\substack{s \\ s_s \in s_m}} \bar{F}^{(s)} \tag{5.51}$$

with the definition of the following vectors

$$\bar{F}^{(s)} = \int_{S_s} G_F^{(s)} \bar{M}_s \, ds' \tag{5.52}$$

Introducing the asymptotic form of the spatial Green's function we write

$$\bar{F}^{(s)} = j\, k_0\, \cos\theta\, \tilde{g}_F^{(s)}(k_x, k_y)\, \frac{\exp(-j\, k_0\, r)}{r} \int_{S_s} \exp(+j\, k_0\, \bar{r}' \cdot \hat{e}_r)\, \bar{M}_s \, ds' \tag{5.53}$$

from where the radiation vector for magnetic currents can be defined as

$$\bar{L}^{(s)} = \int_{S_s} \exp(+j\, k_0\, \bar{r}' \cdot \hat{e}_r)\, \bar{M}_s \, ds' \tag{5.54}$$

Again, equation (5.54) is evaluated numerically on the triangular domains with the one point rule developed in chapter 4. Once it is computed, the total radiated magnetic field is obtained as

$$\begin{aligned} H_\theta &= \omega\, k_0\, \cos\theta\, \frac{\exp(-j\, k_0\, r)}{r} \sum_{\substack{s \\ s_s \in s_m}} \tilde{g}_F^{(s)}(k_x, k_y)\, L_\theta^{(s)} \\ H_\varphi &= \omega\, k_0\, \cos\theta\, \frac{\exp(-j\, k_0\, r)}{r} \sum_{\substack{s \\ s_s \in s_m}} \tilde{g}_F^{(s)}(k_x, k_y)\, L_\varphi^{(s)} \end{aligned} \tag{5.55}$$

To further compute the radiated electric field, we can use the well known relations between electric and magnetic fields in the far field region [10]

$$\begin{aligned} E_\theta &= +\eta\, H_\varphi \\ E_\varphi &= -\eta\, H_\theta \end{aligned} \tag{5.56}$$

where η is the characteristic impedance in free space

$$\eta = \sqrt{\frac{\mu_0}{\epsilon_0}} \tag{5.57}$$

we then obtain the radiated far field as

$$\begin{aligned} E_\theta &= +\cos\theta\, \frac{1}{4\pi\, k_0}\, \frac{\exp(-j\, k_0\, r)}{r} \sum_{\substack{s \\ s_s \in s_m}} \tilde{g}_F^{(s)}(k_x, k_y)\, L_\varphi^{(s)} \\ E_\varphi &= -\cos\theta\, \frac{1}{4\pi\, k_0}\, \frac{\exp(-j\, k_0\, r)}{r} \sum_{\substack{s \\ s_s \in s_m}} \tilde{g}_F^{(s)}(k_x, k_y)\, L_\theta^{(s)} \end{aligned} \tag{5.58}$$

Finally, for a complex antenna structure containing both printed patches and slots, we compute the total radiated electric field by using superposition on equations (5.49,5.58). After some simple manipulations we obtain

$$\begin{aligned} E_\theta = \cos\theta\, \frac{1}{4\pi\, k_0}\, \frac{\exp(-j\, k_0\, r)}{r} \Bigg\{ &\eta \sum_{\substack{s \\ s_s \in s_e}} \tilde{g}_A^{(s)}(k_x, k_y)\, N_\theta^{(s)} \\ &+ \sum_{\substack{s \\ s_s \in s_m}} \tilde{g}_F^{(s)}(k_x, k_y)\, L_\varphi^{(s)} \Bigg\} \end{aligned}$$

$$E_\varphi = \cos\theta \, \frac{1}{4\pi k_0} \, \frac{\exp(-j\,k_0\,r)}{r} \left\{ \eta \sum_{\substack{s \\ s_s \in s_e}} \tilde{g}_A^{(s)}(k_x, k_y)\, N_\varphi^{(s)} - \sum_{\substack{s \\ s_s \in s_m}} \tilde{g}_F^{(s)}(k_x, k_y)\, L_\theta^{(s)} \right\} \tag{5.59}$$

5.3.3 Polarization and axial ratio

Once the total far field radiated by the antenna structure is computed, the polarization and axial ratio of the radiated wave can be derived using standard techniques. First note that the total radiated field computed in the previous section has the following general form

$$\bar{E} = E_\theta\, \hat{e}_\theta + E_\varphi\, \hat{e}_\varphi \tag{5.60}$$

where in general, the spherical components E_θ, E_φ are complex numbers (phasors) and it is assumed that the radial component in the far field region is negligible ($E_r = 0$). If real an imaginary parts are separated in equation (5.60), the following expression is obtained for the radiated far field

$$\bar{E} = \bar{E}^{(r)} + j\,\bar{E}^{(i)} \tag{5.61}$$

where the real and imaginary vectors have been defined as

$$\begin{aligned} \bar{E}^{(r)} &= E_\theta^{(r)}\, \hat{e}_\theta + E_\varphi^{(r)}\, \hat{e}_\varphi \\ \bar{E}^{(i)} &= E_\theta^{(i)}\, \hat{e}_\theta + E_\varphi^{(i)}\, \hat{e}_\varphi \end{aligned} \tag{5.62}$$

and $E_\theta^{(r)}$, $E_\varphi^{(r)}$, $E_\theta^{(i)}$, $E_\varphi^{(i)}$ are the real and imaginary parts of the vector components in equation (5.60). Since we are considering time harmonic fields, we can introduce the time dependence of the fields as

$$\bar{E} = \bar{E}^{(r)}\, \cos\omega t - \bar{E}^{(i)}\, \sin\omega t \tag{5.63}$$

Next, we can compute the time instant τ_1 where above field is maximum or minimum, namely

$$\tan(2\,\omega\,\tau_1) = \frac{2\,\bar{E}^{(r)} \cdot \bar{E}^{(i)}}{|\bar{E}^{(i)}|^2 - |\bar{E}^{(r)}|^2} \tag{5.64}$$

In addition, the time instant where the field is minimum or maximum is simply

$$\omega\,\tau_2 = \omega\,\tau_1 + \frac{\pi}{2} \tag{5.65}$$

If we introduce $t = \tau_1$ and $t = \tau_2$ into the expression of the field given in equation (5.63), the values $\bar{E}_1$, $\bar{E}_2$ at the major (minor) and minor (major) semiaxis of the polarization ellipse are thus computed. The axial ratio of the radiated wave is then written as

$$\begin{aligned} A_r &= \frac{|\bar{E}_1|}{|\bar{E}_2|};\ \text{if } |\bar{E}_1| > |\bar{E}_2| \\ A_r &= \frac{|\bar{E}_2|}{|\bar{E}_1|};\ \text{if } |\bar{E}_2| > |\bar{E}_1| \end{aligned} \tag{5.66}$$

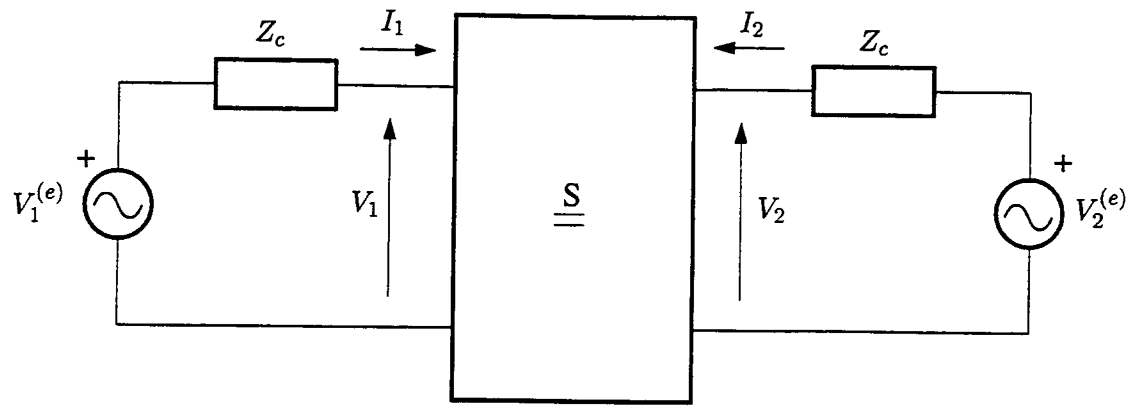

Figure 5.6: General two ports network with excitation on both ports ready for the de-embedding process.

Finally, note that $A_r = 1$ indicates circular polatization while $A_r \to \infty$ reveals linear polarization of the radiated waves.

5.4 Ports De-embedding

When the antenna structure contains more than one port, it would be nice to be able to compute the radiation characteristics when known established excitations are applied to all the ports at the same time. This would be useful for instance in dual polarization antennas with two points of excitation. In this case we might be interested in computing the radiation characteristics of the structure for different values of the voltages (module and phase) applied to each port. In the case of the conformal array antenna, a series feeding network is sometimes used to adjust the phases in the different elements of the array. In this case the lower active patch shown in Fig. 1.1 contains two excitation feeding points and it will be useful to know the radiation characteristics of the structure under different values of the voltages applied to both ports. This process is called ports de-embedding and in this section the analysis for a two ports structure will be detailed. At the end of the section we will generalize the results obtained for structures with arbitrary number of ports.

Consider the two ports network shown in Fig. 5.6 characterized by the scattering parameters as computed in section 5.2. As seen, two generators $V_1^{(e)}$ and $V_2^{(e)}$ are applied to ports (1) and (2) respectively. What we want to do is to compute the radiated far field of the structure under this situation. The first thing to do is to apply superposition on the generators and consider first the generator $V_1^{(e)}$ exciting the structure when the second generator is short-circuited. Then we reverse the process and consider the generator $V_2^{(e)}$ exciting the structure when the first generator is short-circuited. Let us now suppose that when $V_1^{(e)}$ is exciting the structure alone, the resulting induced current is $\bar{J}_{s_1}$ and when $V_2^{(e)}$ is exciting the structure alone, the resulting induced current is $\bar{J}_{s_2}$. The total current $\bar{J}_s$ that will radiate and therefore will contribute to the radiation characteristics of the structure is obtained, applying superposition, as

$$\bar{J}_s = \bar{J}_{s_1} + \bar{J}_{s_2} \tag{5.67}$$

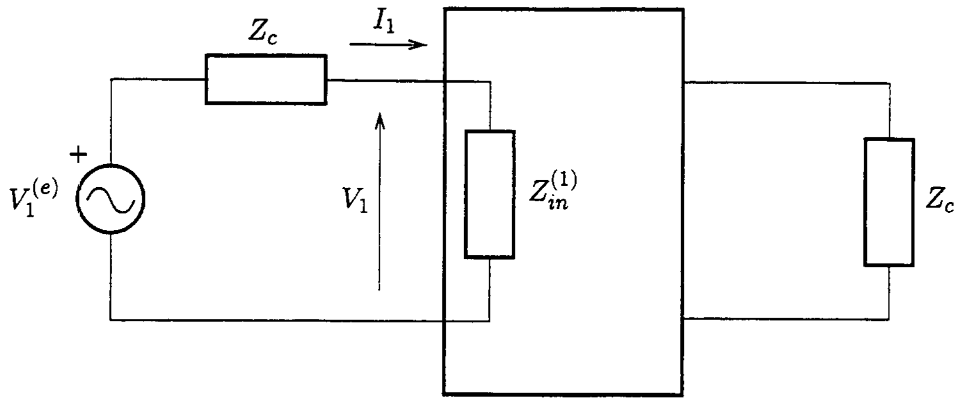

Figure 5.7: Same two ports network as in Fig. 5.6 with the generator at port (2) short-circuited.

where, if using the expansion for the currents in equation (4.24) we can write

$$
\begin{aligned}
\bar{J}_{s_1} &= \sum_k \alpha_k^{(1)} \bar{f}_k(\bar{r}') \\
\bar{J}_{s_2} &= \sum_k \alpha_k^{(2)} \bar{f}_k(\bar{r}')
\end{aligned}
\tag{5.68}
$$

and $\alpha_k^{(1)}$ is the unknown coefficients of the expansion when the generator is at port (1), and $\alpha_k^{(2)}$ when the generator is at port (2). Moreover, as seen in the final MoM matrix system formulated in equation (5.11), what we obtain from the solution of the MoM system of linear equations is not directly the unknown coefficients $\alpha_k^{(1)}$ and $\alpha_k^{(2)}$ but rather

$$
\begin{aligned}
\hat{\alpha}_k^{(1)} &= \frac{\alpha_k^{(1)}}{V_1} \\
\hat{\alpha}_k^{(2)} &= \frac{\alpha_k^{(2)}}{V_2}
\end{aligned}
\tag{5.69}
$$

where V_1 and V_2 are the voltages directly applied to both ports and are therefore different from the generator voltages $V_1^{(e)}$ and $V_2^{(e)}$ as shown in Fig. 5.6. Introducing equation (5.69) into the expansions (5.68) we easily obtain

$$
\begin{aligned}
\bar{J}_{s_1} &= V_1 \sum_k \alpha_k^{(1)} \bar{f}_k(\bar{r}') \\
\bar{J}_{s_2} &= V_2 \sum_k \alpha_k^{(2)} \bar{f}_k(\bar{r}')
\end{aligned}
\tag{5.70}
$$

Consequently, the only thing that need to be done is the evaluation of the voltages V_1 and V_2 as a function of the generator voltages $V_1^{(e)}$, $V_2^{(e)}$. To start we consider the generator $V_1^{(e)}$ exciting port (1) with the second generator short-circuited as shown in Fig. 5.7. In these conditions the computation of the voltage V_1 is extremely simple

$$
V_1 = V_1^{(e)} \frac{Z_{in}^{(1)}}{Z_c + Z_{in}^{(1)}}
\tag{5.71}
$$

where $Z_{in}^{(1)}$ is the input impedance computed in equation (5.12) when the generator is placed at port (1). If we repeat the process shown in section 5.2 but placing the generator $V_2^{(e)}$ at port (2), we obtain an input impedance $Z_{in}^{(2)}$ so that

$$V_2 = V_2^{(e)} \frac{Z_{in}^{(2)}}{Z_c + Z_{in}^{(2)}} \tag{5.72}$$

Using equations (5.72,5.71,5.70, 5.69) we can finally compute the total current density in (5.67) as

$$\bar{J}_s = V_1^{(e)} \frac{Z_{in}^{(1)}}{Z_c + Z_{in}^{(1)}} \sum_k \hat{\alpha_k}^{(1)} \bar{f}_k(\bar{r}') + V_2^{(e)} \frac{Z_{in}^{(2)}}{Z_c + Z_{in}^{(2)}} \sum_k \hat{\alpha_k}^{(2)} \bar{f}_k(\bar{r}') \tag{5.73}$$

Note now that expression (5.73) can be easily generalized for the case of an antenna containing an arbitrary number of ports n. In this case se write

$$\bar{J}_s = \sum_k \left[\sum_{r=1}^{n} V_r^{(e)} \frac{Z_{in}^{(r)}}{Z_c + Z_{in}^{(r)}} \hat{\alpha}_k^{(r)} \right] \bar{f}_k(\bar{r}') \tag{5.74}$$

where as we have seen, $V_r^{(e)}$ is the voltage of the generator connected to the r-th port, $Z_{in}^{(r)}$ is the input impedance obtained following the procedure described in section 5.2 when the generator is placed at the r-th port and $\bar{\alpha_k}^{(r)}$ are the MoM system vector of solutions shown in equation (5.11). Finally, the radiation characteristics computations considering the de-embedding of the ports are obtained by following the procedure described in section 5.3.2 applied to the current density computed in equation (5.74).

Chapter 6

Results

6.1 Introduction

Using the integral equation technique described in this document, a software tool has been developed for the analysis of the conformal array elementary radiator whose basic structure is shown in Fig. 1.1 and 1.2. In this chapter we present some results obtained with the developed software and we compare them with measurements obtained on real manufactured hardware. The conformal array elementary radiator is investigated both with and without the cylindrical cavity walls and measurements in both configurations are presented. For the non-cavity case, comparisons and validation test cases are also included using the HP-MOMENTUM commercial software package.

6.2 Laterally Open Case

The first structure to be investigated is the conformal array elementary radiator considering only the lower active patch in the two ports version (see Fig. 1.2), and printed on a microstrip substrate with theoretically infinite transverse dimensions. Two experimental bread-boards have been prepared under this configuration. The first one printed on a low dielectric constant and relatively thick substrate (RT/Duroid 5870; $\epsilon_r = 2.33$, $h = 1.57mm$) and the second one printed on a high dielectric constant and relatively thin substrate (RT/Duroid 6010; $\epsilon_r = 10.5$, $h = 0.635mm$). In Fig. 6.1 we show the measured and simulated results for the first substrate and in Fig. 6.2 for the second one. As we can see from the results, there are some differences between measured and simulated behavior specially as frequency increases, where some measured resonances are not predicted by the software tool. In order to try to isolate the causes of these differences, a parametric study, both numerically and geometrically, was launched. The results of the study determined that the differences are due to the strong variations of the currents induced around the ridges of the patch. In fact, to properly model these currents, a finer mesh density is required in the neighboring areas around the ridges. After introducing the mesh ridge refinement technique described in section 4.6, new simulated results were obtained and they are shown in Fig. 6.3 and 6.4. As seen, measured and simulated results are now in good agreement even in the high frequency region, and all measured resonances are correctly predicted in the simulations. Using the mesh selective refinement technique, we are able to obtain accurate results without increasing largerly the total number of cells (and therefore of unknowns) in

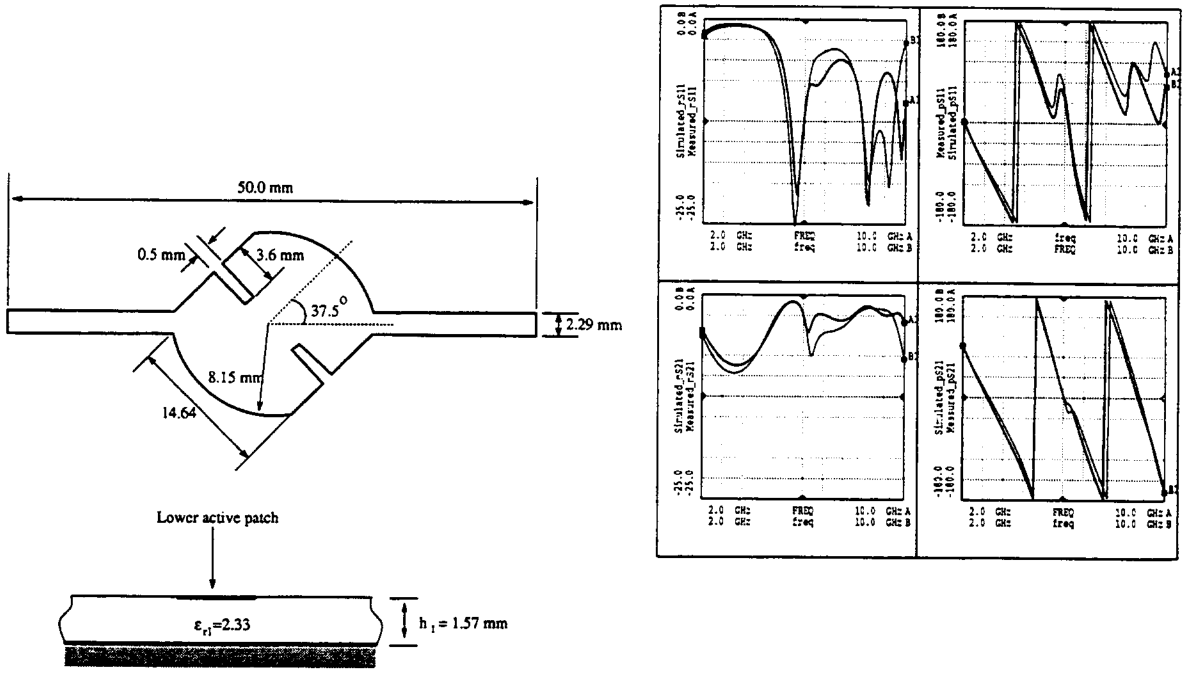

Figure 6.1: Measured versus simulated results for the structure shown when no mesh refinement is applied. Measured results are indicated with thick line.

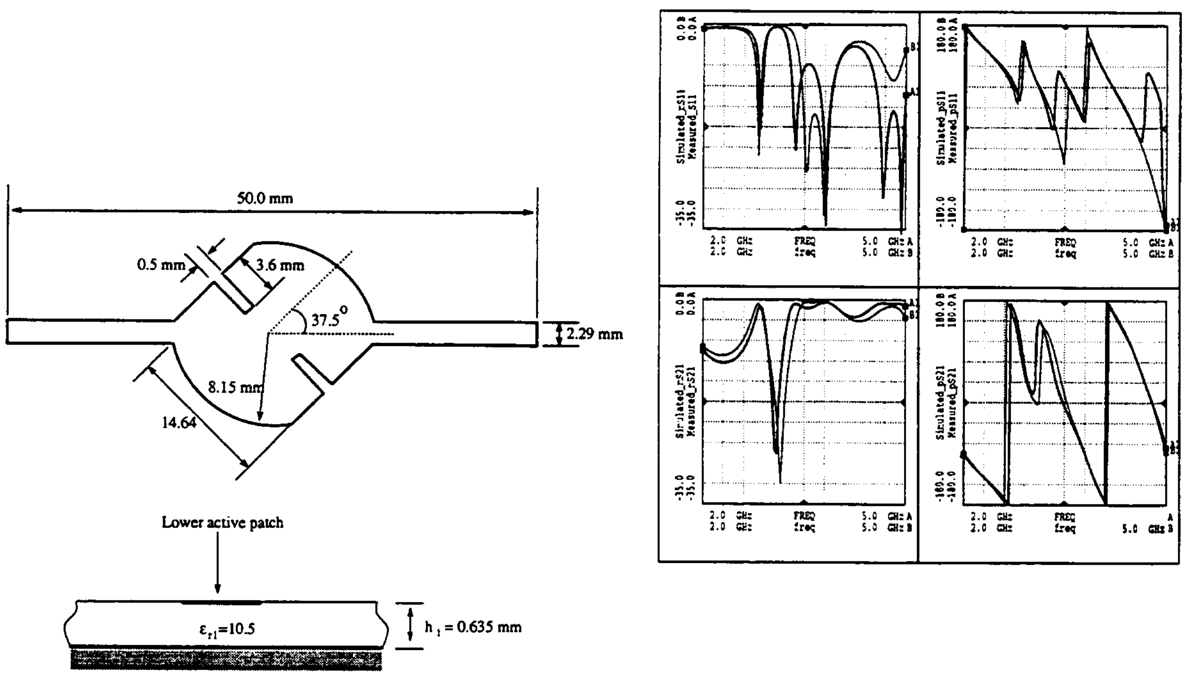

Figure 6.2: Measured versus simulated results for the structure shown when no mesh refinement is applied. Measured results are indicated with thick line.

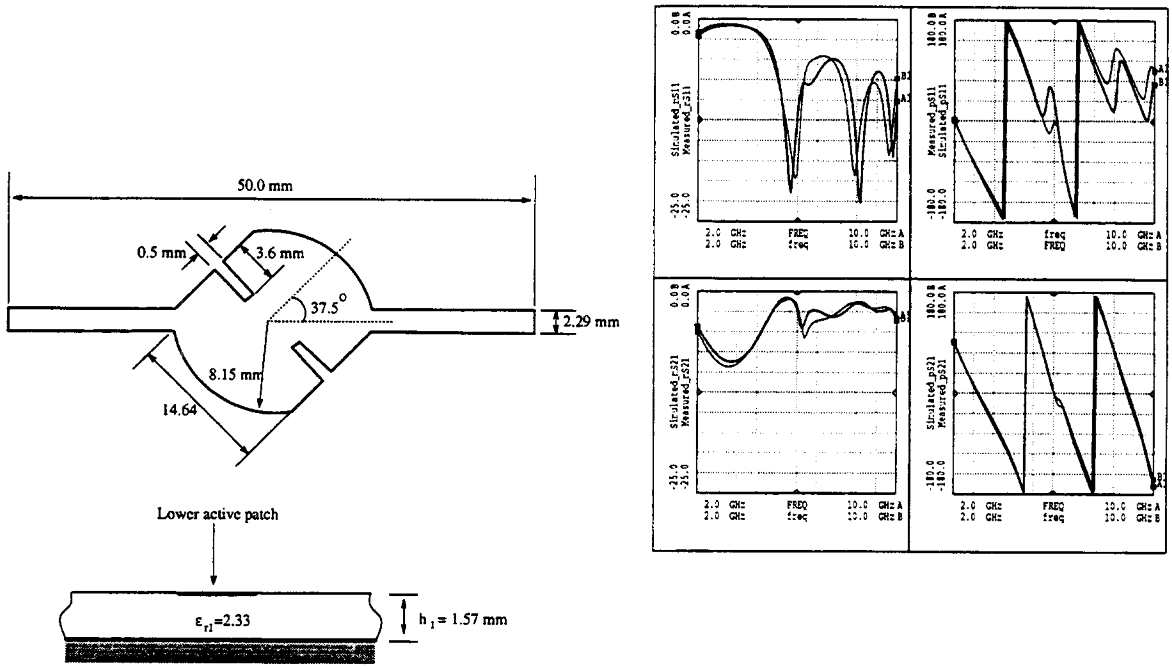

Figure 6.3: Measured versus simulated results for the structure shown when the mesh refinement is applied to the ridge area of the patch. Measured results are indicated with thick line.

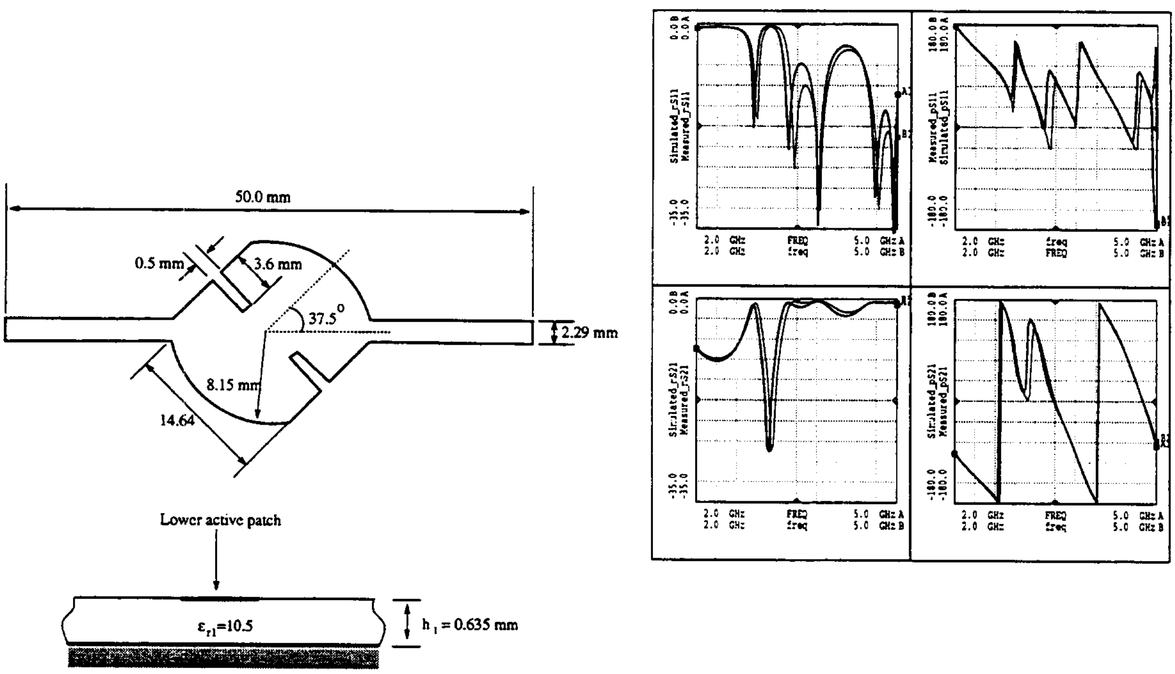

Figure 6.4: Measured versus simulated results for the structure shown when the mesh refinement is applied to the ridge area of the patch. Measured results are indicated with thick line.

the problem. The software takes only 6 seconds per frequency point to analyze the whole structure on an HP712/80 work-station.

Using the HP-MOMEMTUM commercial package, the software developed has also been validated if the lower active patch is considered with only one port. In Fig. 6.5 we present the results obtained for a typical case with both softwares, showing an excellent agreement. Finally, we also used

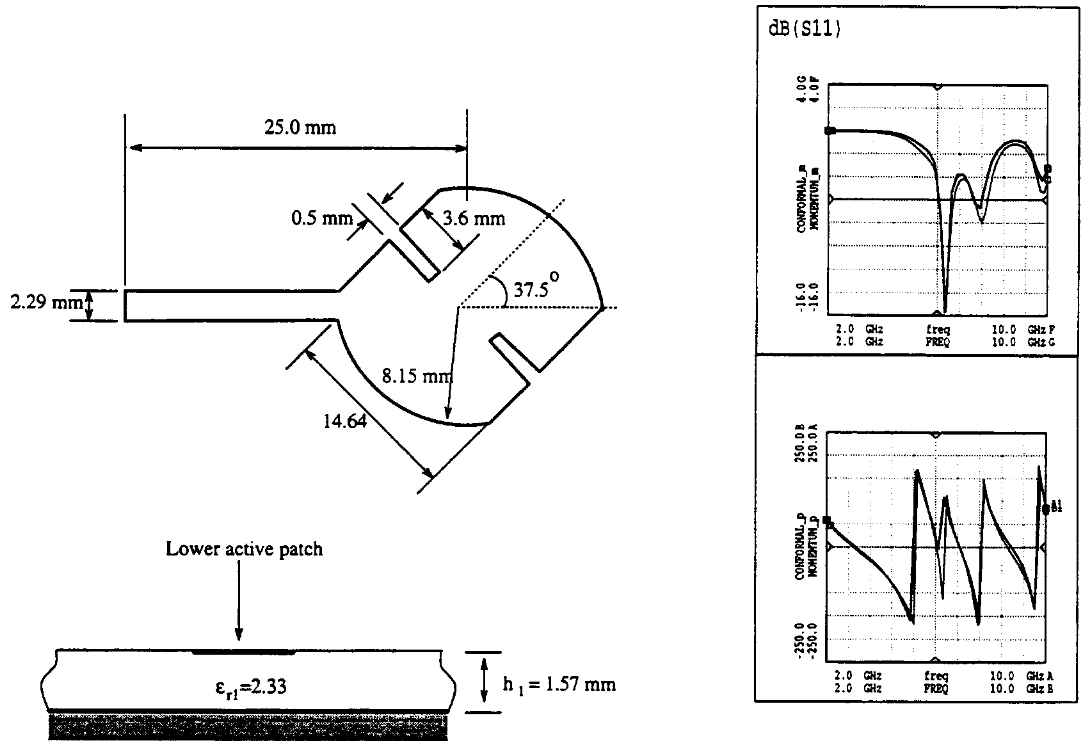

Figure 6.5: Comparison between results obtained with our software and with HP-MOMENTUM for the elementary radiator in the one port configuration as shown in the figure. HP-MOMEMTUM results are indicated with thick line.

HP-MOMENTUM to validate the software when the upper passive patch is placed inside the antenna. In this analysis the upper passive patch is considered as an aperture opened on the top ground plane as shown in Fig. 1.2. Fig. 6.6 presents the results obtained with both softwares exhibiting again good concordance. In this case the software took 25 seconds per frequency point to analyze the whole structure in the same HP712/80 work-station.

6.3 Cavity Backed Case

The software developed has also been validated when the conformal array elementary radiator is backed in its final metallic cylindrical cavity. It is interesting to note that in this case the Green's functions of the cylindrical cavity have been approximated by the Green's functions of an equivalent rectangular cavity, and it is important to establish the level of accuracy that can be attained when such approximation is introduced in the analysis.

In Fig. 6.7 we show the measured and simulated results when the lower active patch is backed

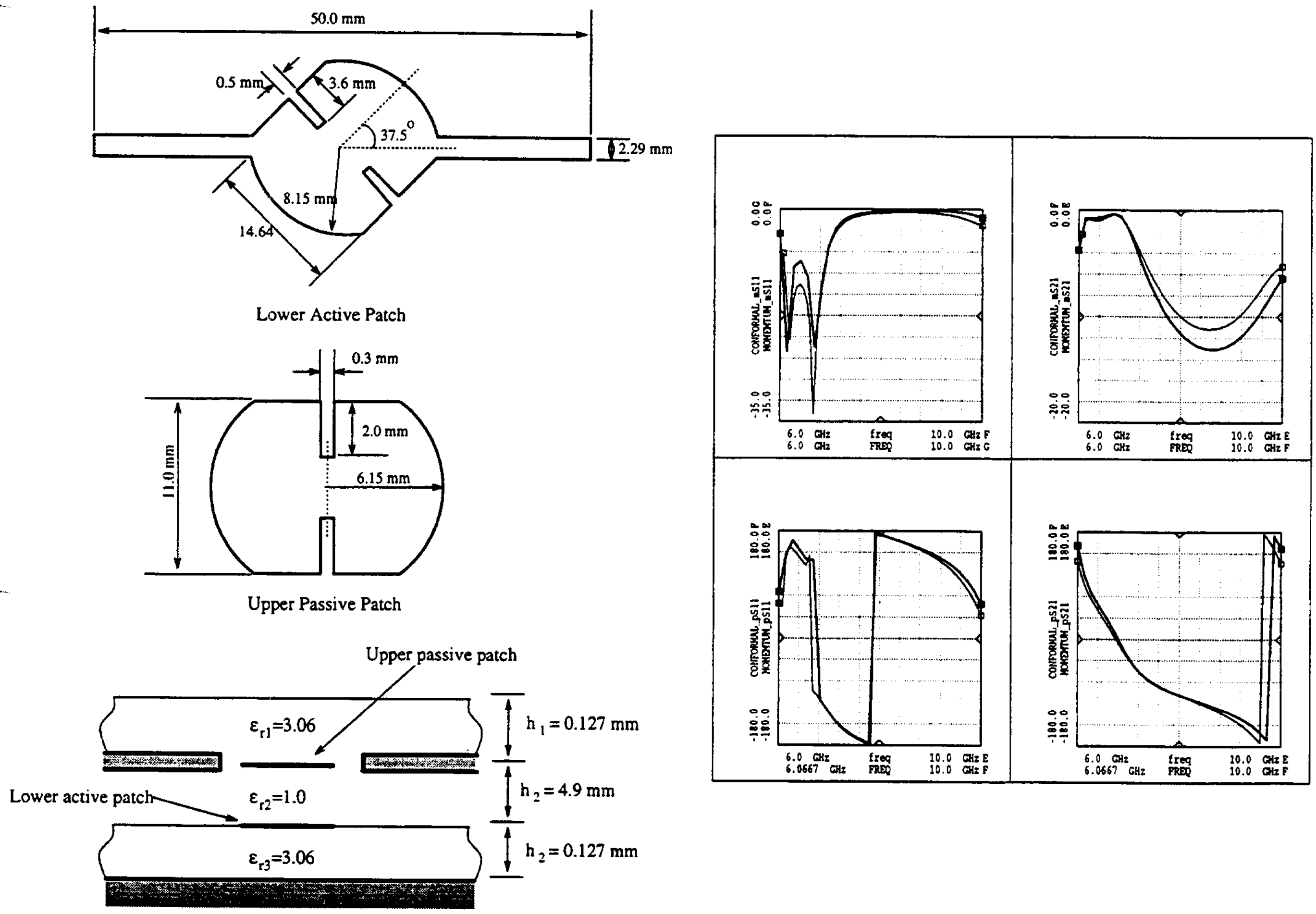

Figure 6.6: Comparison between results obtained with our software and with `HP-MOMEMTUM` for the structure shown. `HP-MOMEMTUM` results are indicated with thick line.

by the metallic cavity and radiation is produced through a circular aperture opened on top of the cavity. In the same graphics we also show the results obtained for this structure when the lateral cylindrical metallic walls are removed. As we can see from the results, the correction introduced by considering the Green's functions of an equivalent rectangular cavity represents a considerably improvement with respect the results obtained in the laterally opened case. In Fig. 6.8 we present the results when the structure is influenced with the upper passive patch. In this case, the upper passive patch is placed on top of the structure and it is therefore modeled as an aperture opened at the cavity. As we can see, the simulated results follow correctly the measured influence of the upper passive patch in the whole structure. Again, the *cavity backed* results are considerably better than the results obtained when the structure is considered *laterally opened.*

The last interesting result that we present in this chapter is to see what happens when the upper passive patch is printed on the other side of the substrate and it is therefore placed outside the cavity (see Fig. 1.2). In this case, radiation is produced through a circular aperture opened on top of the cavity and coupled to the upper passive patch placed outside. Since the substrates used to print the patches are relatively thin, essentially the same measured results as before are obtained in this case. As regard the simulated results, this represents a very different situation from the numerical point of

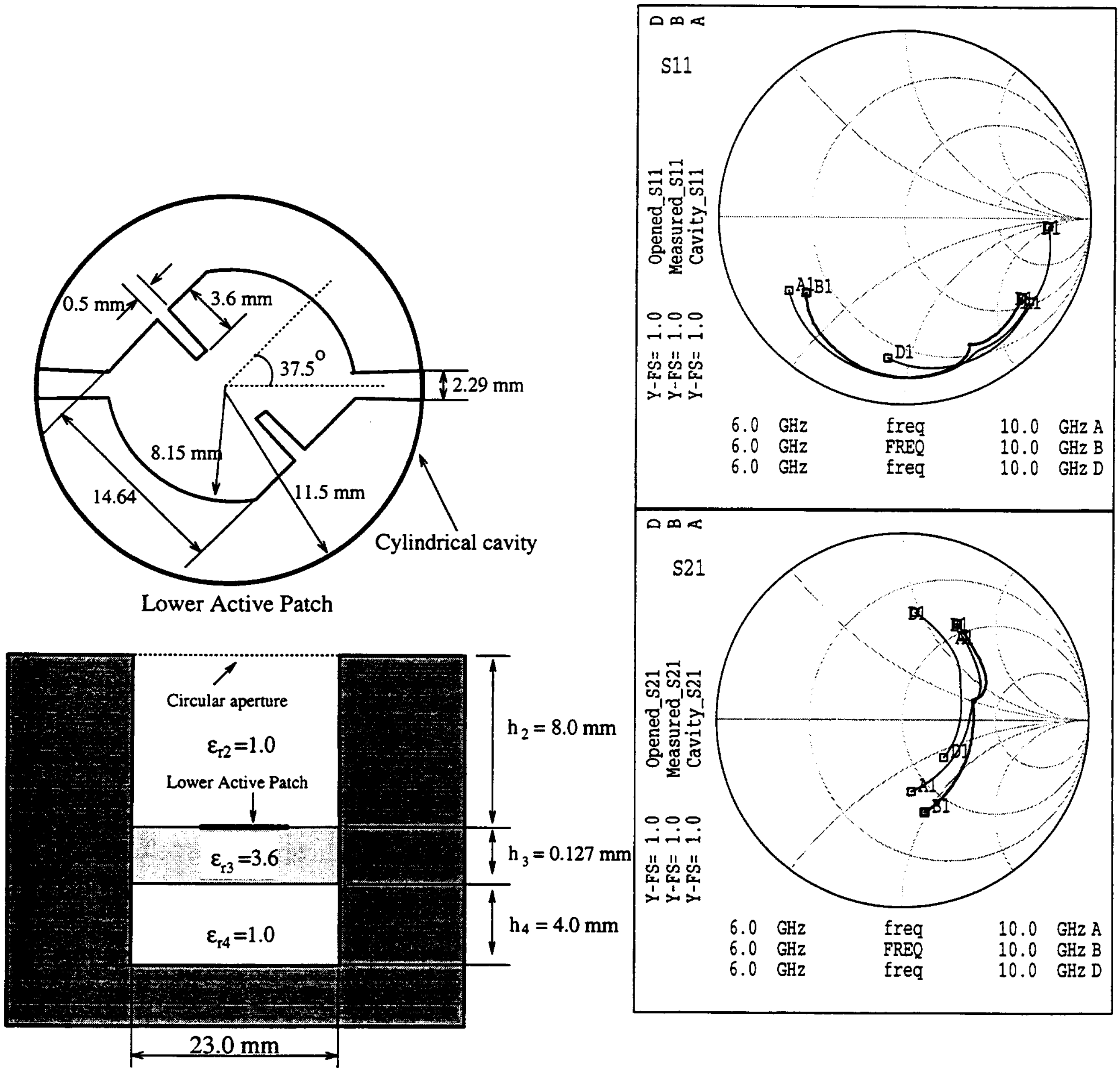

Figure 6.7: Measured versus simulated results for the cavity backed structure shown. Results obtained with the laterally opened model are also included. Measured results correspond to thick line.

view. In fact now, the global MoM matrix is considerably greater than before and new interactions from the circular aperture and the upper patch need to be evaluated. In spite of this, the results presented in Fig. 6.9 indicates that the analysis is also accurate and that it predicts small changes in the final electrical performance of the structure as also shown by the measured results. To give an idea of the computational time for cavity backed structures, the software spends an initial 10 minutes to perform all the frequency independent calculations plus 2 minutes per each additional frequency point for the analysis of the structure in Fig. 6.9. It should be pointed out however, that the computational time is strongly dependent on the total number of cells (mesh density) used to discretize the patches geometries. The data given in this section is to be applied to structures which

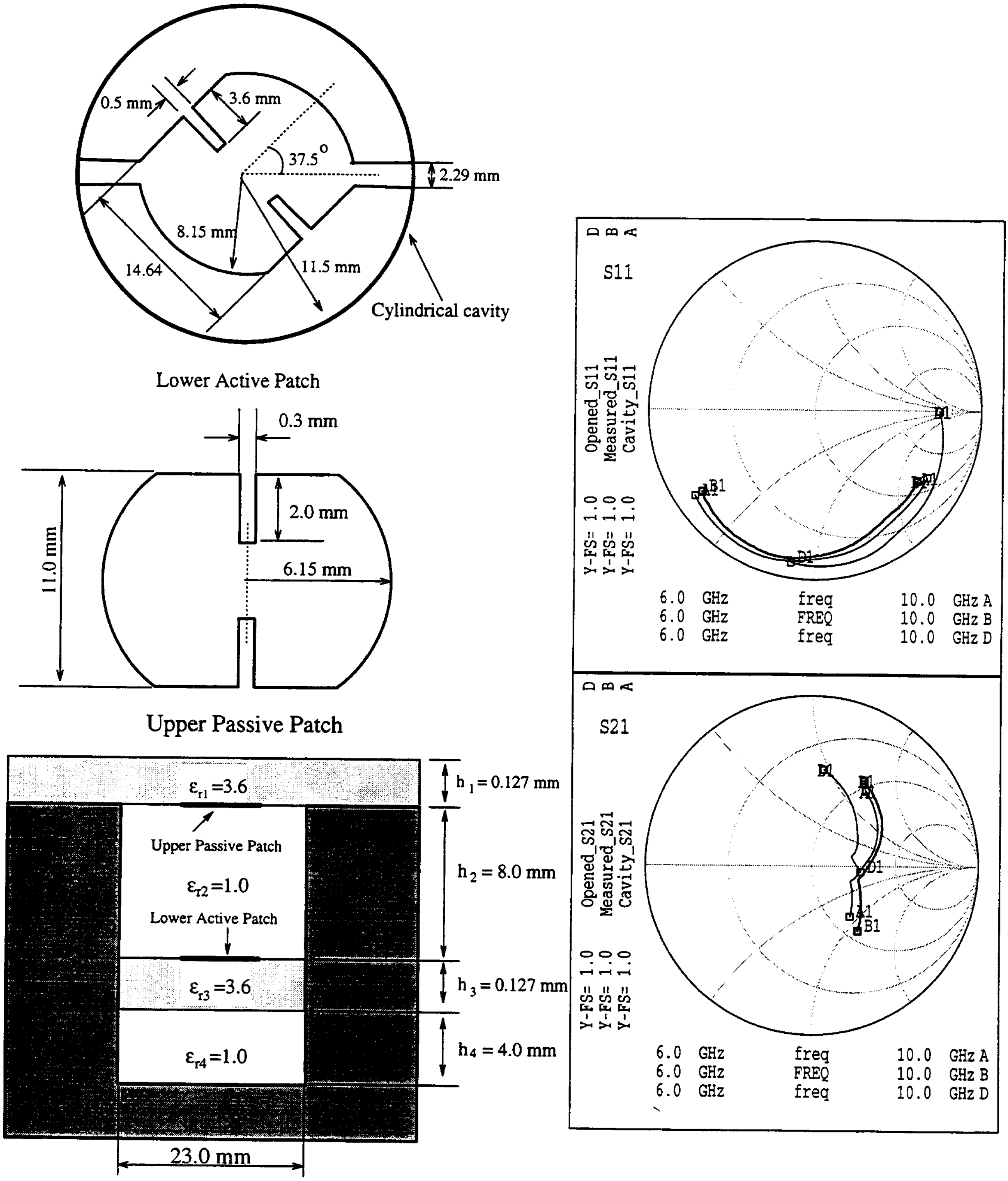

Figure 6.8: Measured versus simulated results for the cavity backed structure shown. Results obtained with the laterally opened model are also included. Measured results correspond to thick line.

have been optimized to give enough accurate results with a minimum of mesh density.

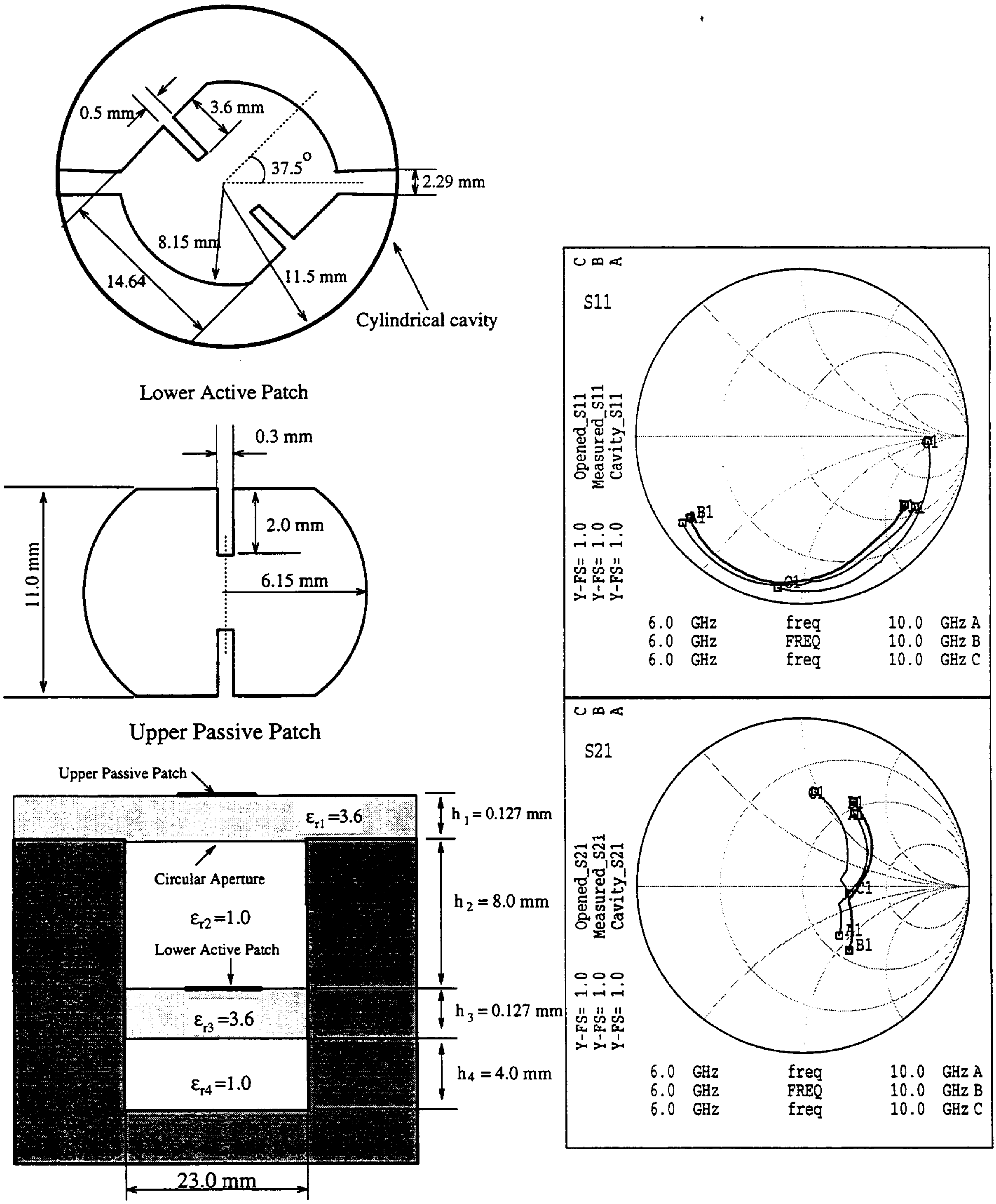

Figure 6.9: Measured versus simulated results for the cavity backed structure shown. Results obtained with the laterally opened model are also included. Measured results corresponds to thick line.

6.4 Alcatel Antenna Test

In this section we are going to further exploit the computational capabilities of the developed software. For this purpose, the goal is to find the theoretical electrical characteristics of the conformal array elementary radiator slightly modified as shown in Fig. 6.10. As seen, the antenna structure to be analyzed is essentially composed of the two basic elementary radiator patches but now, the ridges have been removed from the structure and in addition, the upper passive patch is rotated with respect the feeding axis of the lower active patch. For the analysis of this structure, new meshing subroutines were incorporated to both allow a rotational angle of the upper passive patch with respect the lower active patch axis and to allow the generation of the meshes for the patches without ridges. In order to perform a detailed investigation on the structure, first the modified elementary radiator was studied when the upper passive patch is placed at the cavity's top aperture (structure shown in Fig. 6.10a). Using this configuration the structure was investigated with and without cavity walls so that the influence of the lateral metallic walls could be evaluated. Finally, the upper passive patch is placed out of the cavity printed on the top side of the substrate (structure shown in Fig. 6.10b). This last structure has been investigated backed by the cavity in order to establish the differences due to a change in the position of the upper passive patch with respect the cavity's top aperture.

The meshes used in the analysis of the first configuration, for both the lower active patch and upper radiating aperture are shown in Fig. 6.11 and 6.12. In Fig. 6.13 we present the input impedance in Smith chart when no lateral walls are considered. Moreover, Fig. 6.14 shows the module and phase of the input reflection coefficient of the antenna for the same case. The electrical characterization of the structure is now completed by giving some data concerning the radiation properties of the antenna, including polarization and pattern features. In Fig. 6.15 the axial ratio of the antenna in the broadside direction as a function of the frequency is presented. Finally, Fig. 6.16, 6.17 and 6.18 give the E and H plane radiation patterns of the antenna at three different frequencies, namely 7 GHz, 7.5 GHz and 8 GHz. As it can be noticed, in the graphics the two components E_θ and E_φ of the radiated far-field are plotted in each principal plane.

For comparison purposes we now give the same results as before but when the lateral cavity walls are included in the analysis. Fig. 6.19 shows the input impedance of the antenna in Smith chart for the cavity backed case and in Fig. 6.20 we present the module and phase of the input reflection coefficient. As it can be seen from the results, all the basic resonances appearing in the laterally opened case (Fig. 6.14) are also present in the cavity backed model. The only remarkable difference is in the coupling coefficients between the resonances. This clearly indicates that the main influence of the lateral cavity walls is the modification of the amount of coupling going to the basic resonances. Fig. 6.21 shows the axial ratio of the antenna when lateral cavity walls are included in the analysis. As seen, the first peak around 7 GHz shown in Fig. 6.15 is now more abrupt. On the contrary, the second peak has not been essentially modified and it is still placed around 8.5 GHz as shown in both Fig. 6.15 and 6.21. Finally, we present in Fig. 6.22, 6.23 and 6.24 the E and H plane radiation patterns of the structure (both field components) at the frequencies 7 GHz, 7.5 GHz and 8 GHz respectively. The radiated far-field in the cavity backed model is essentially the same as in the laterally opened case. The only significant difference is in the level of the cross polarization components in each principal plane.

As the last study, we wanted to see the effects in the electrical performances of the antenna when the upper patch is placed outside the cavity and it is therefore printed on the top side of the substrate. The mesh of the upper passive patch used in this computation is shown in Fig. 6.25. In Fig. 6.26 we show the input impedance in Smith chart for the cavity backed case and in Fig. 6.27 the module and phase of the input reflection coefficient. Moreover, the axial ratio in the broadside direction versus frequency is shown in Fig. 6.28. Finally, the E and H plane radiation patterns for the same frequencies as before are presented in Fig. 6.29, 6.30 and 6.31. Comparing the results in Fig. 6.19-i6.24 with the results in Fig. 6.26-6.31 we readily notice that the electrical characteristics of the antenna have not been essentially modified by printing the upper patch on the top side of the substrate. This is mainly because the substrate is very thin to substantially change the electromagnetic behavior of the structure. From the computational point of view, however, it is far more efficient the analysis of the first configuration because in this case, the relevant unknowns of the problem are placed at only two interfaces (lower patch, radiating aperture) and not at three interfaces as it is the case in the last example treated (lower patch, radiating aperture, upper patch).

6.5 Conclusions

In this document we have presented all the techniques developed under the ESA/ESTEC contract No. 11698/95/NL/SB for the analysis of the conformal array elementary radiator. First, the Green's functions for layered media of infinite transverse dimensions have been developed. In order to account for the presence of the lateral cylindrical cavity walls, the Green's functions derived have been used with the spatial images technique. Several spatial images arrangements have been discussed and the limitations and problems encountered have been outlined. Due to the slow convergence behavior of the series involved for certain layered geometries, a reliable implementation of this technique was found to be very arduous. An alternative formulation based on the rigorous cavity backed Green's functions have been derived and the complete rigorous formulation for a cylindrical cavity has been presented. The analytical complexity of the resulting modal functions in the cylindrical cavity case, furnished the introduction of an equivalent rectangular cavity behaving as close as possible to the real cylindrical cavity. The simplification in the modal expansions used, allows further analytical treatment which leads to efficient techniques for the analysis of the structures under study.

Once the Green's functions are derived, they are used inside an integral equation formulation which has been developed for the analysis of a general antenna structure composed of an arbitrary number of planar printed patches and slots. The integral equation derived is solved with a Galerkin Method of Moments algorithm formulated with subsectional basis functions defined on triangular cells for the discretization of the geometries involved. The use of triangular cells in the MoM formulation was suggested by the rather complex geometrical shapes of the patches used in the conformal array elementary radiator and a meshing strategy based on decomposing the whole structure in simpler objects has been developed. The whole technique has been validated and simulated results have been compared with measurements on real manufactured hardware, for both the laterally opened and for the cavity backed cases. The results have shown that the achieved accuracy in all cases is good, and that the approximation introduced in the cavity backed case leads to enough accurate results for engineering purposes. In addition, data concerning the computational time needed to analyze several test cases has been given indicating good computational time performance. Consequently, the associated software has shown to be a valuable engineering tool for the analysis and design of this type of antennas.

6.6 Acknowledgments

The authors would like to thanks P. Otero for his help with the practical aspects of this project and many discussions. Thanks are also due to O. Staub and J-F Zurcher for their help during the manufacturing and measuring phases of the hardware used in validating the software.

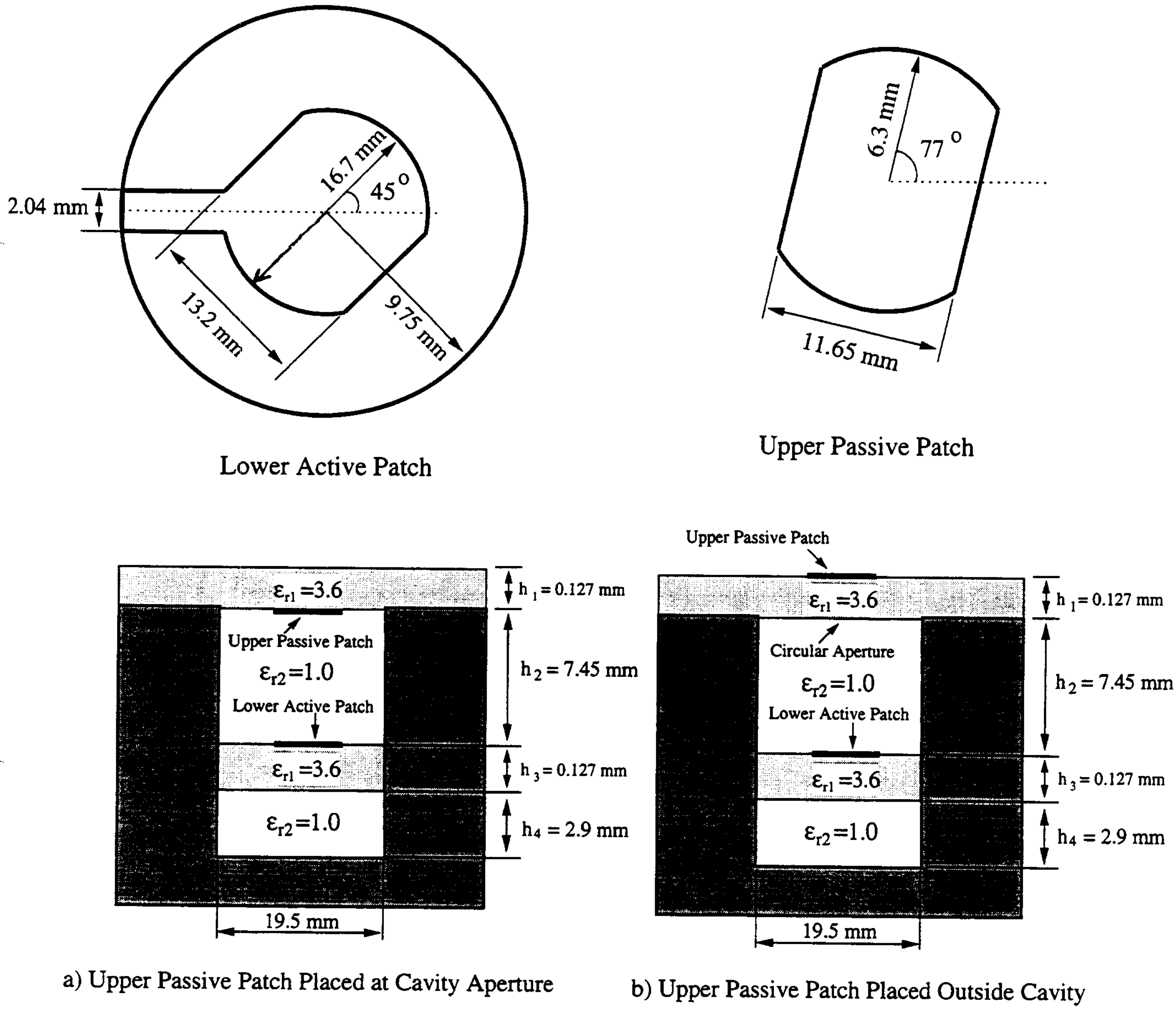

Figure 6.10: Basic antenna structure proposed by Alcatel as antenna test.

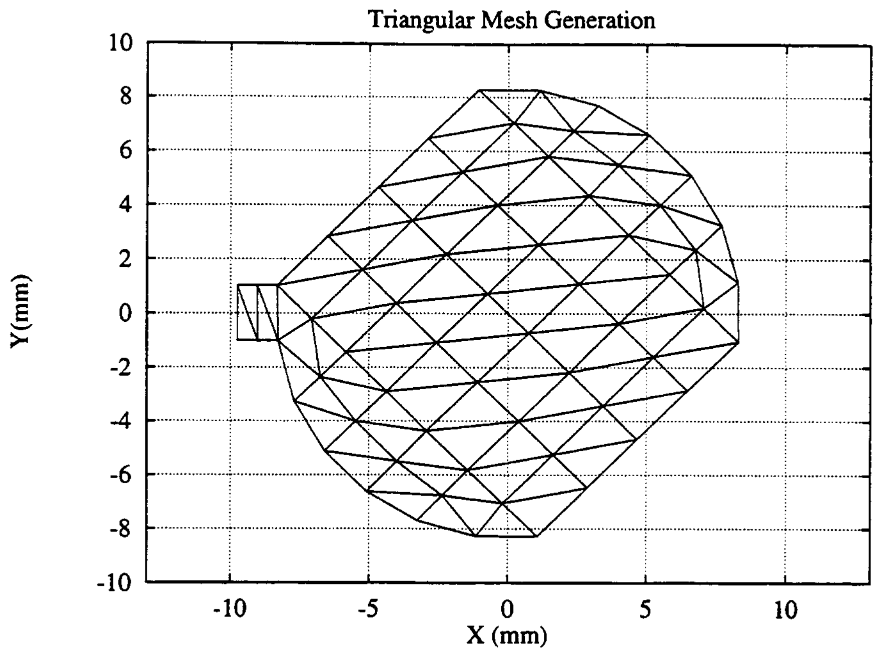

Figure 6.11: Mesh for the lower active patch used in the computations of this section.

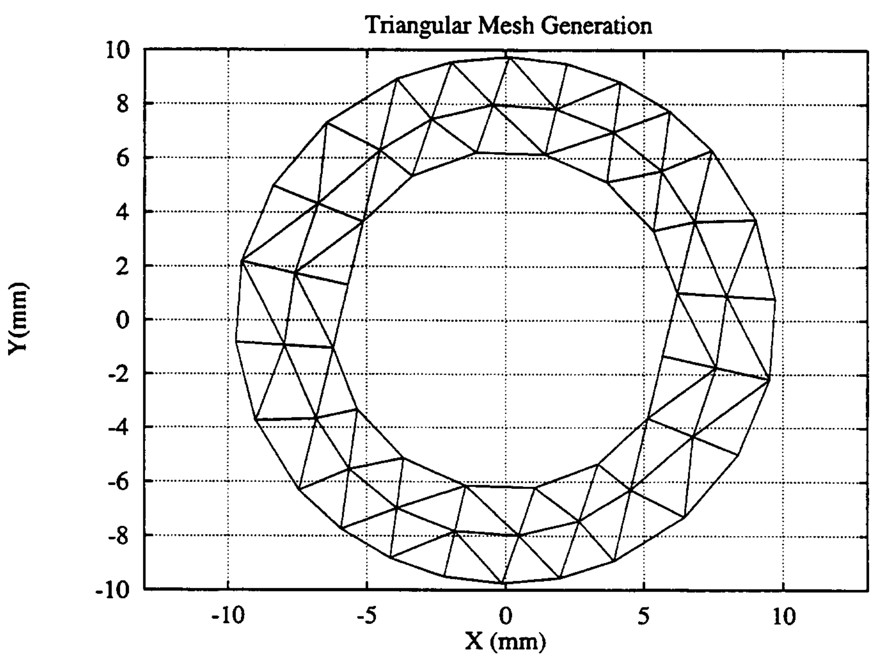

Figure 6.12: Mesh for the upper passive patch when it is acting as a radiating aperture, used in the computations of this section.

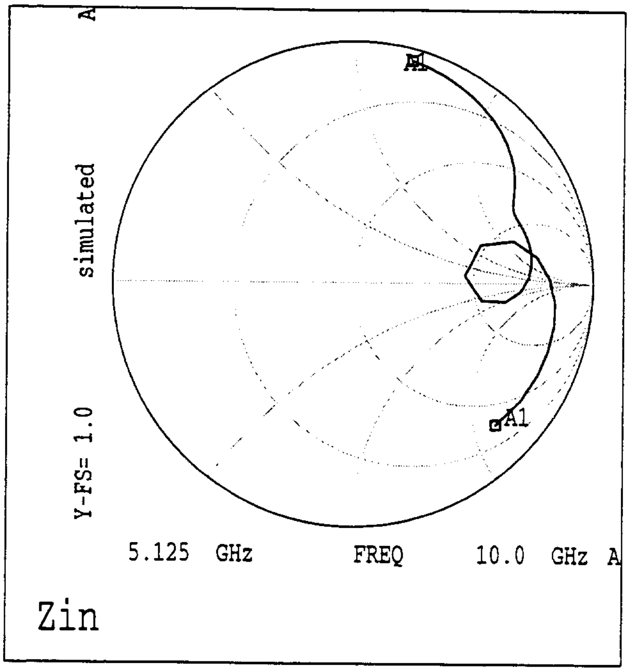

Figure 6.13: Input impedance of the Alcatel antenna test. Upper passive patch is placed at the top aperture (Fig. 6.10a). Analysis without lateral walls.

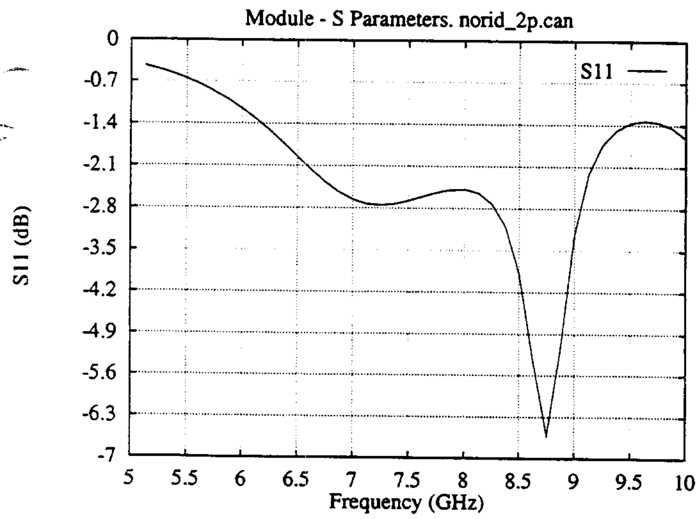

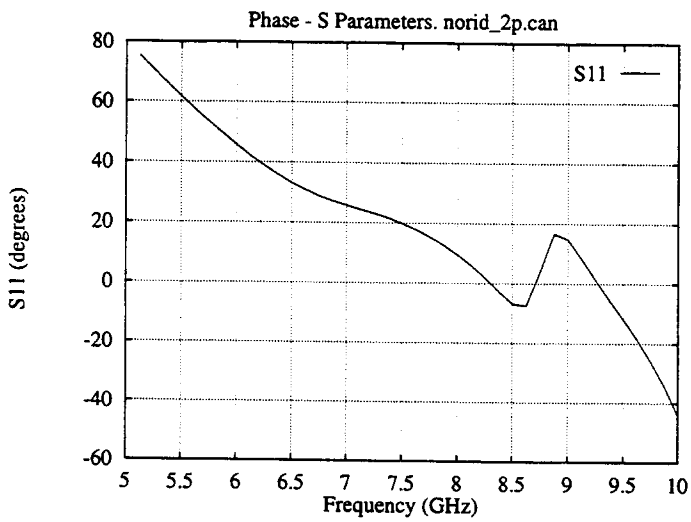

Figure 6.14: Module and phase of the input reflection coefficient for the Alcatel antenna test. Upper passive patch is placed at the top aperture (Fig 6.10a). Analysis without lateral walls.

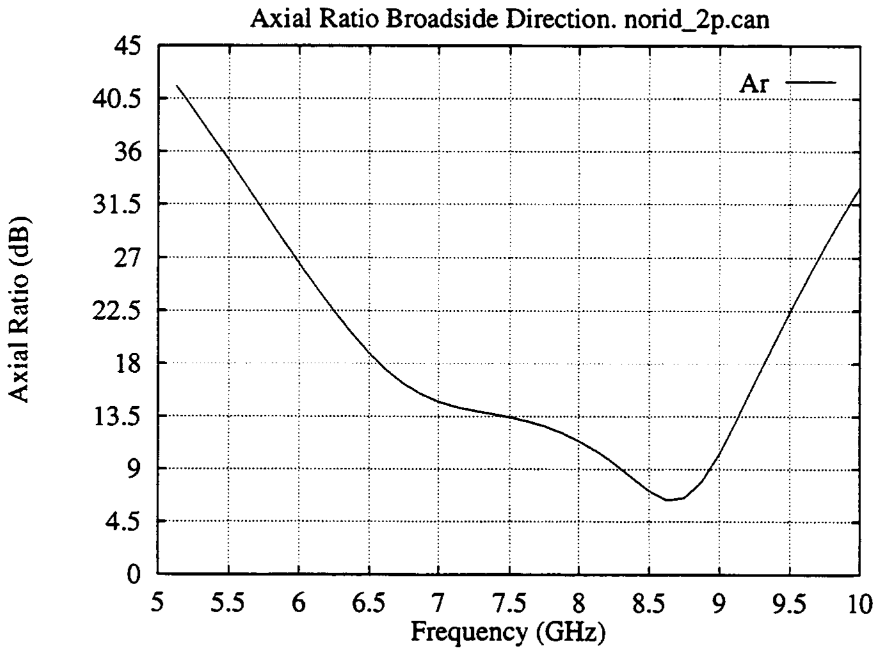

Figure 6.15: Axial ratio in broadside direction versus frequency. Upper passive patch is placed at the top aperture (Fig 6.10a). Analysis without walls.

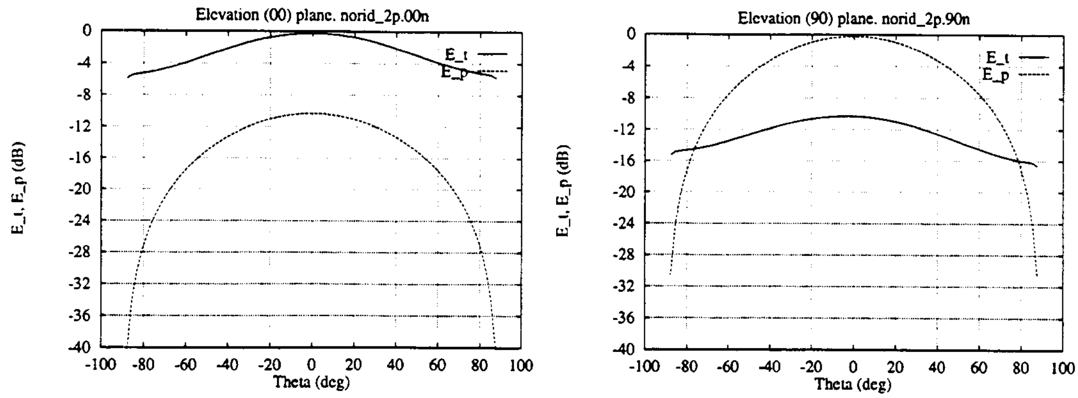

Figure 6.16: Co and Cross polar components of the radiated far-field in the principal E and H planes. Frequency of the analysis: f_0 = 7 GHz. Upper passive patch is placed at the top aperture (Fig 6.10a). Analysis without walls.

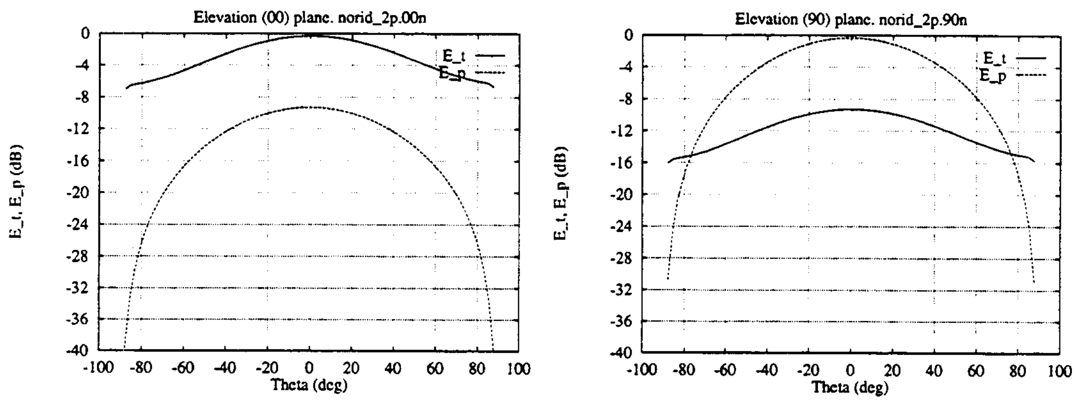

Figure 6.17: Co and Cross polar components of the radiated far-field in the principal E and H planes. Frequency of the analysis: f_0 = 7.5 GHz. Upper passive patch is placed at the top aperture (Fig 6.10a). Analysis without walls.

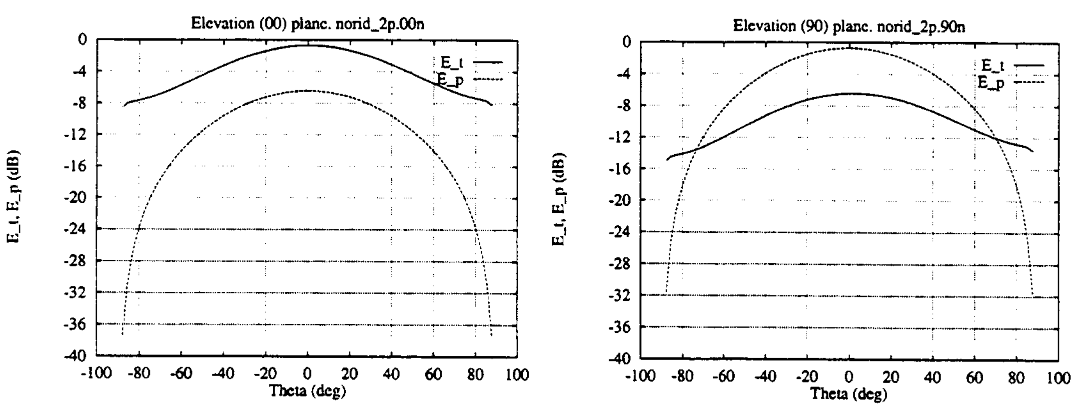

Figure 6.18: Co and Cross polar components of the radiated far-field in the principal E and H planes. Frequency of the analysis: f_0 = 8 GHz. Upper passive patch is placed at the top aperture (Fig 6.10a). Analysis without walls.

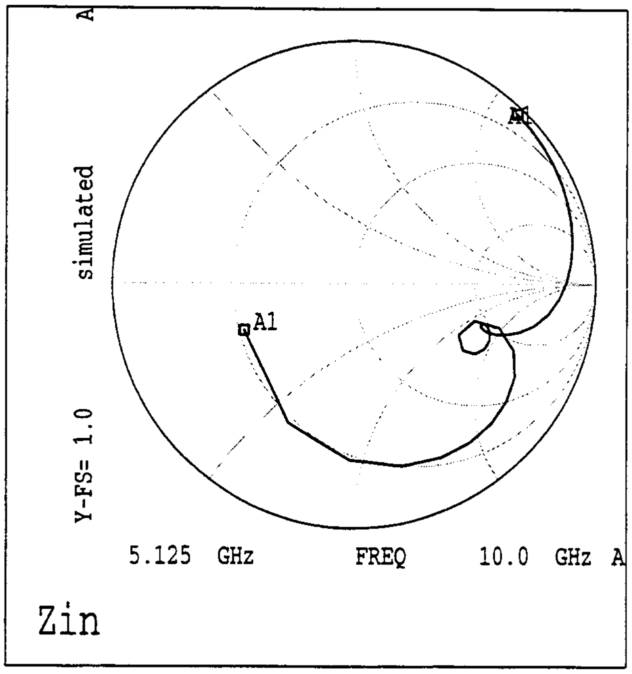

Figure 6.19: Input impedance of the Alcatel antenna test. Upper passive patch is placed at the top aperture (Fig 6.10a). Analysis with lateral cavity walls.

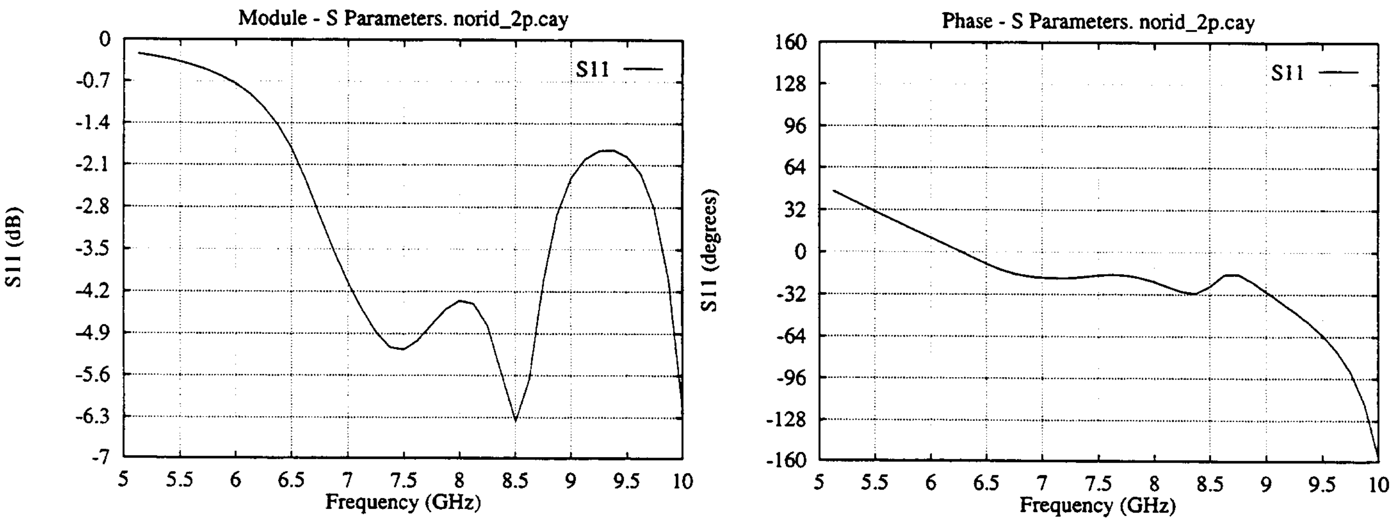

Figure 6.20: Module and phase of the input reflection coefficient of the Alcatel antenna test. Upper passive patch is placed at the top aperture (Fig 6.10a). Analysis with lateral cavity walls.

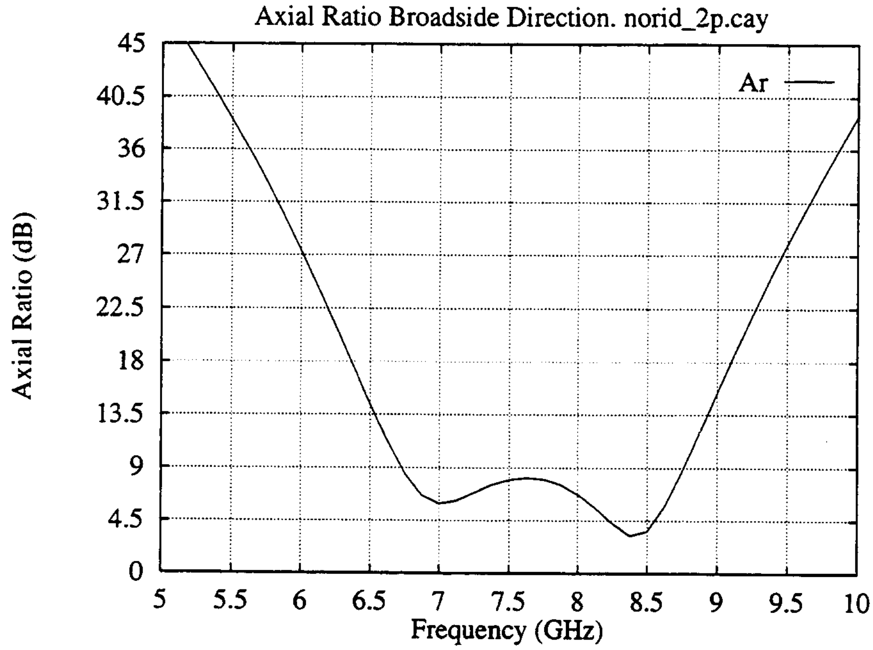

Figure 6.21: Axial ratio in broadside direction versus frequency. Upper passive patch is placed at the top aperture (Fig 6.10a). Analysis with lateral cavity walls.

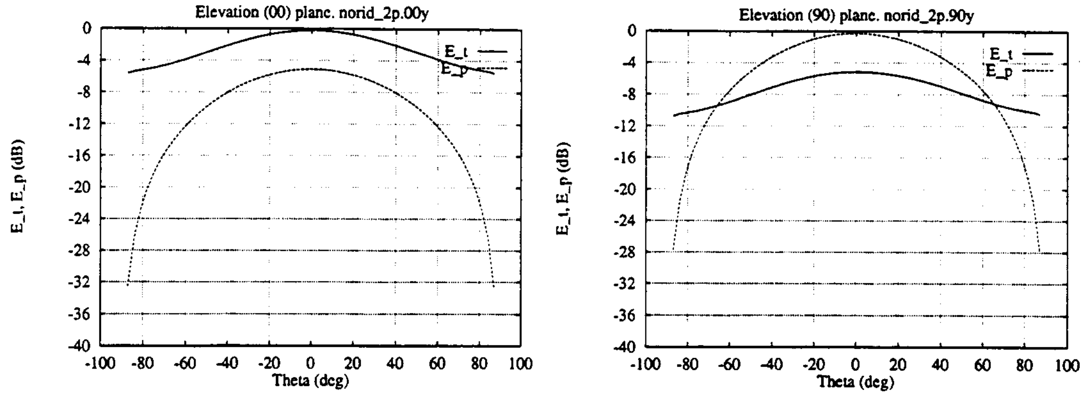

Figure 6.22: Co and Cross polar components of the radiated far-field in the principal E and H planes. Frequency of the analysis: f_0 = 7 GHz. Upper passive patch is placed at the top aperture (Fig 6.10a). Analysis with cavity walls.

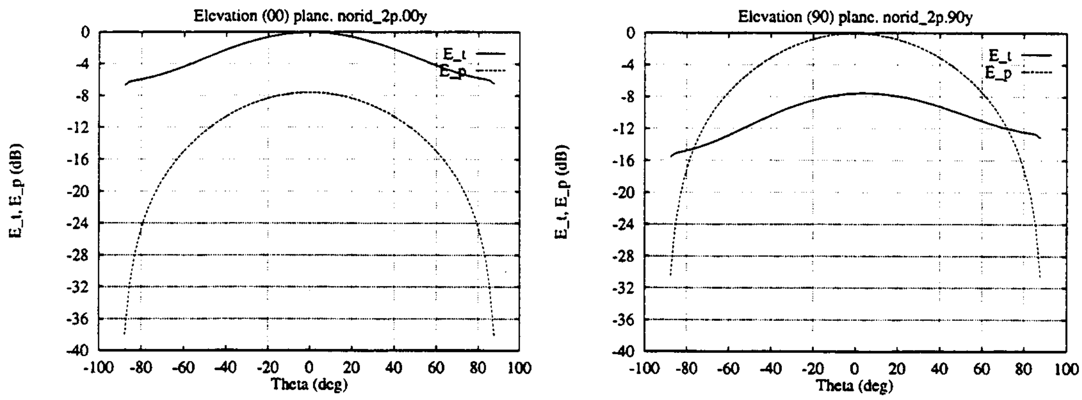

Figure 6.23: Co and Cross polar components of the radiated far-field in the principal E and H planes. Frequency of the analysis: f_0 = 7.5 GHz. Upper passive patch is placed at the top aperture (Fig 6.10a). Analysis with cavity walls.

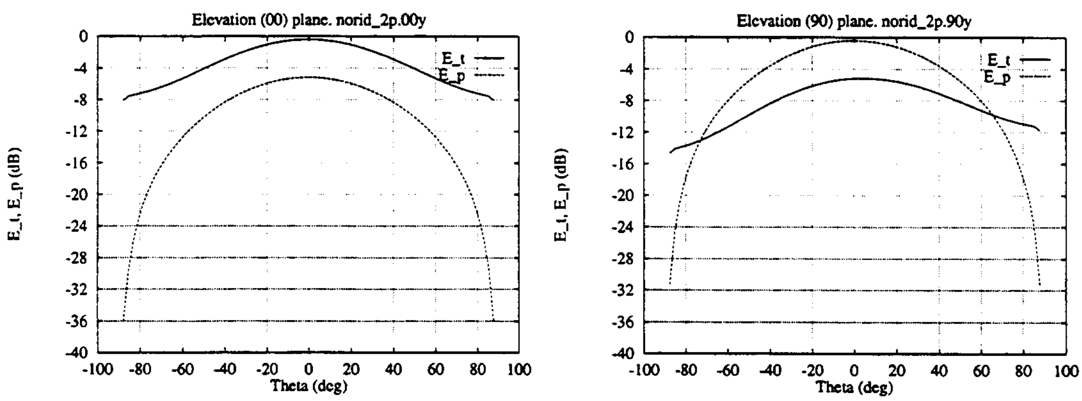

Figure 6.24: Co and Cross polar components of the radiated far-field in the principal E and H planes. Frequency of the analysis: f_0 = 8 GHz. Upper passive patch is placed at the top aperture (Fig 6.10a). Analysis with cavity walls.

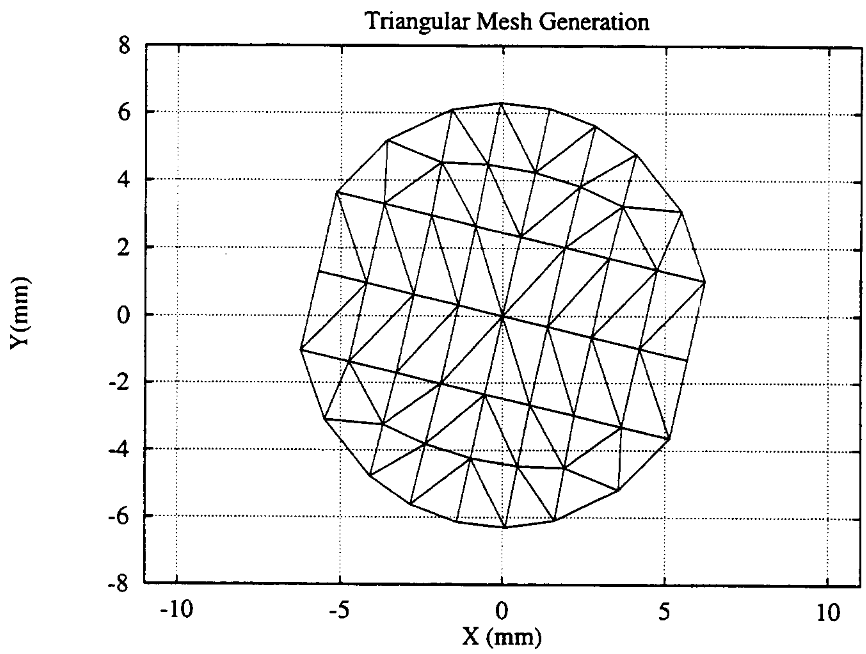

Figure 6.25: Mesh for the upper passive patch when it is placed outside the cavity, therefore printed on the top side of the substrate (structure shown in Fig 6.10b).

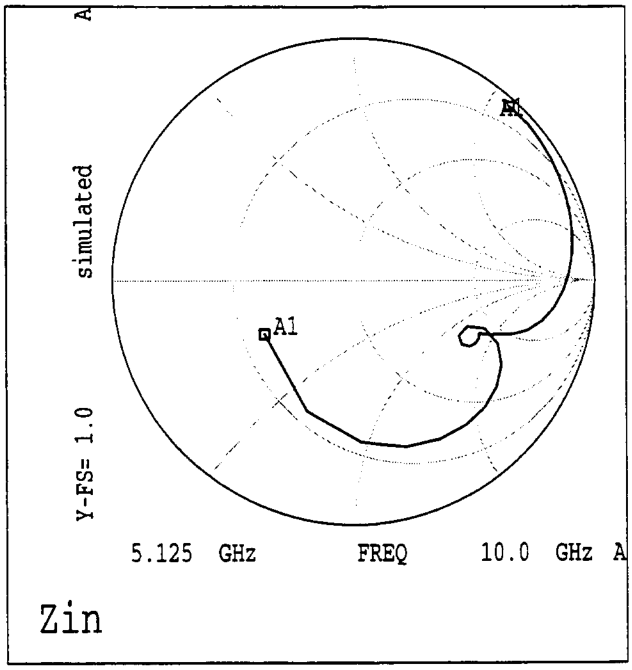

Figure 6.26: Input impedance of the Alcatel antenna test. Upper passive patch is placed outside the cavity (Fig 6.10b). Analysis with lateral cavity walls.

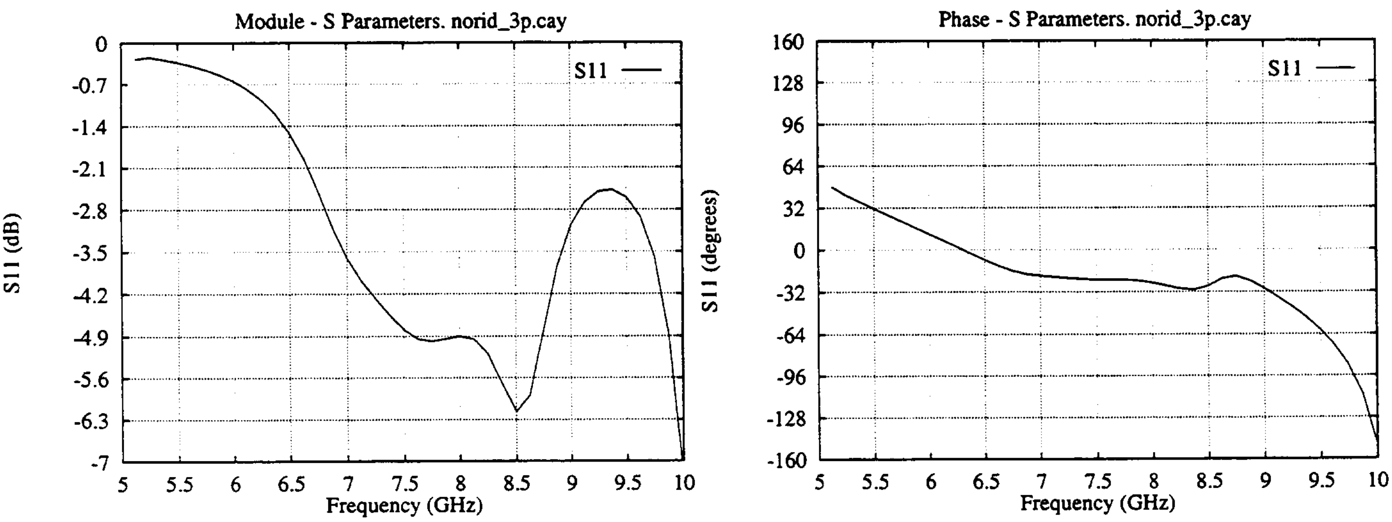

Figure 6.27: Module and phase of the input reflection coefficient for the Alcatel antenna test. Upper passive patch is placed outside the cavity (Fig 6.10b). Analysis with lateral cavity walls.

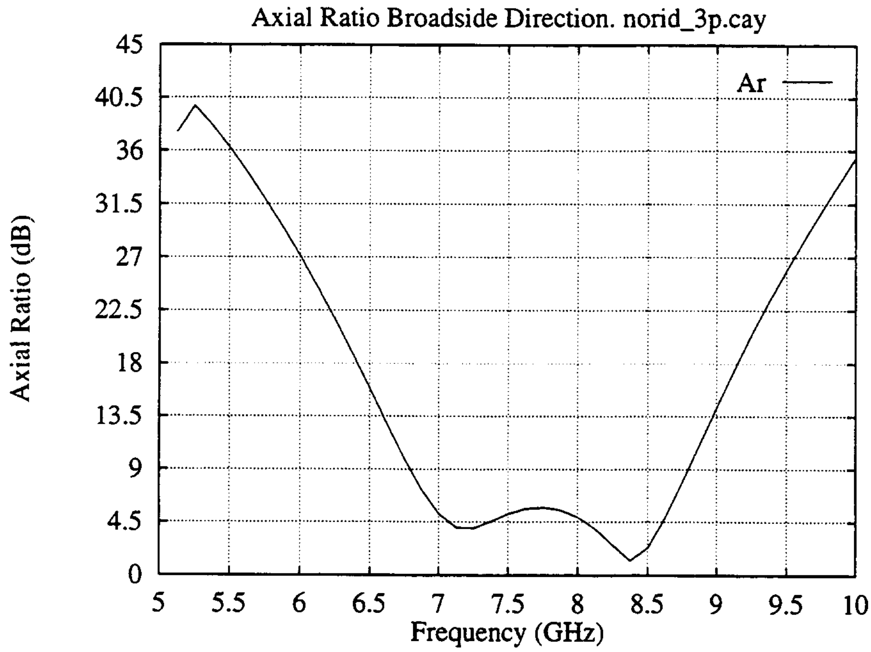

Figure 6.28: Axial ratio in broadside direction versus frequency. Upper passive patch is placed outside the cavity (Fig 6.10b). Analysis with lateral cavity walls.

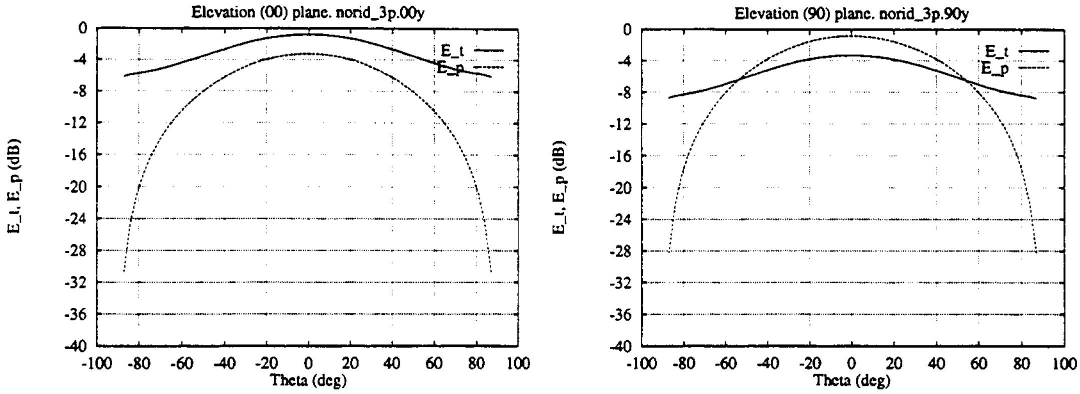

Figure 6.29: Co and Cross polar components of the radiated far-field in the principal E and H planes. Frequency of the analysis: f_0 = 7 GHz. Upper passive patch is placed outside the cavity (Fig 6.10b). Analysis with lateral cavity walls.

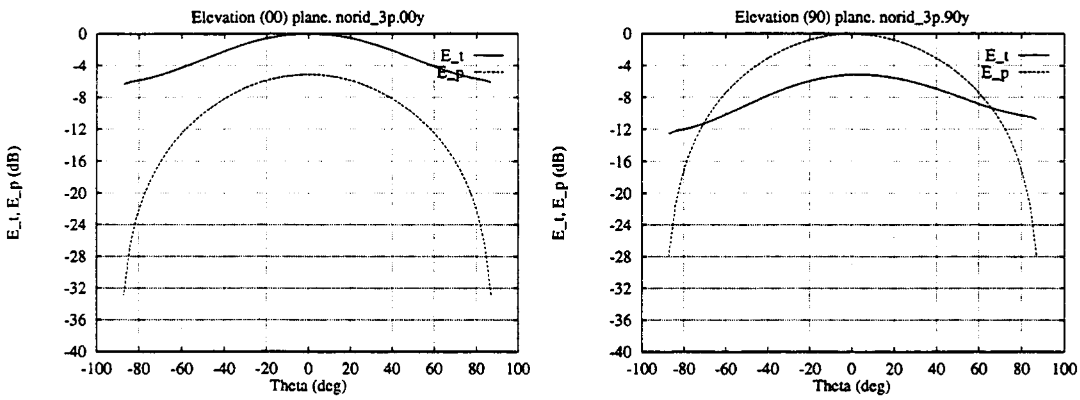

Figure 6.30: Co and Cross polar components of the radiated far-field in the principal E and H planes. Frequency of the analysis: f_0 = 7.5 GHz. Upper passive patch is placed outside the cavity (Fig 6.10b). Analysis with lateral cavity walls.

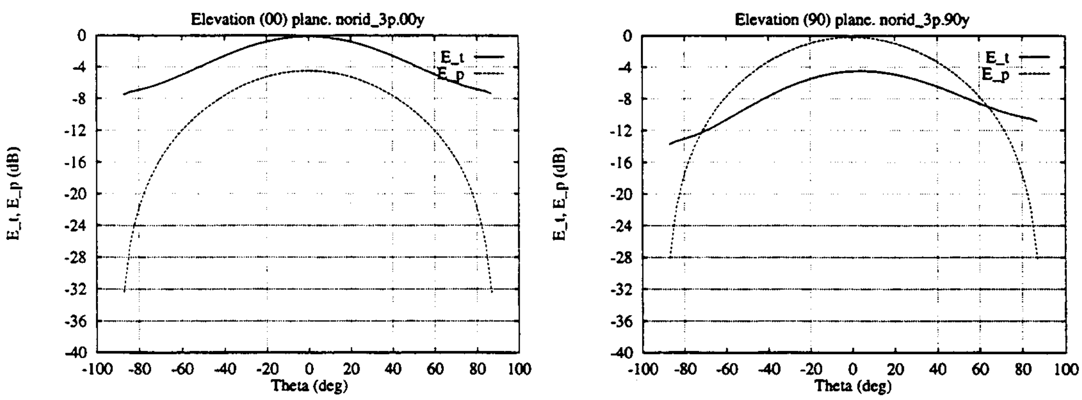

Figure 6.31: Co and Cross polar components of the radiated far-field in the principal E and H planes. Frequency of the analysis: f_0 = 8 GHz. Upper passive patch is placed outside the cavity (Fig 6.10b). Analysis with lateral cavity walls.

Appendix A

Equivalent Transmission Line Networks

It is well known that the longitudinal dependence of a multilayered printed antenna can be reduced to the evaluation of the voltages and currents on equivalent transmission line networks [5], [20]. For a general multilayered antenna composed of an arbitrary number of planar printed patches and slots as shown in Fig. 4.1, there are three different equivalent transmission line networks which must be analyzed, namely the electric network, the lower magnetic network and the upper magnetic network (see Figure A.1). In this appendix we show a simple iterative procedure to compute the voltages and currents at all interfaces in the three networks of Figure A.1. The method is based on replacing each transmission line section of length l_i by an equivalent two ports impedance network (Figure A.2), where

$$\left\{ \begin{array}{l} Z_a^{(i)} = +j\, Z_{c_i} \tan\left(\beta_i \frac{l_i}{2}\right) \\ Z_b^{(i)} = -j\, Z_{c_i} \csc\left(\beta_i\, l_i\right) \end{array} \right. \tag{A.1}$$

$$\left\{ \begin{array}{l} Z_{11}^{(i)} = Z_{22}^{(i)} = Z_a^{(i)} + Z_b^{(i)} \\ Z_{12}^{(i)} = Z_{21}^{(i)} = Z_b^{(i)} \end{array} \right. \tag{A.2}$$

β_i is the propagation constant of the i-th transmission line and Z_{c_i} its characteristic impedance. With this transformation, the analysis in all cases is reduced to simple network theory rather than to transmission line theory.

A.1 Electric Network

For the electric network of Figure A.1 we can first compute the input impedance at the first interface

$$Z_{p_u} = \left\{ \begin{array}{ll} j\, Z_{c_{p_u}} \tan\left(\beta_{p_u}\, h_{p_u}\right) & \text{Upper limit is short-circuit} \\ Z_{c_{p_u}} & \text{Upper limit goes to infinity} \end{array} \right. \tag{A.3}$$

then compute all other input impedances up to the position of the generator.

$$Z_i = Z_{c_i} \frac{Z_{i-1} + j\, Z_{c_i} \tan\left(\beta_i\, h_i\right)}{Z_{c_i} + j\, Z_{i-1} \tan\left(\beta_i\, h_i\right)};\; i = p_u + 1, p_u + 2, \cdots, p_s - 1 \tag{A.4}$$

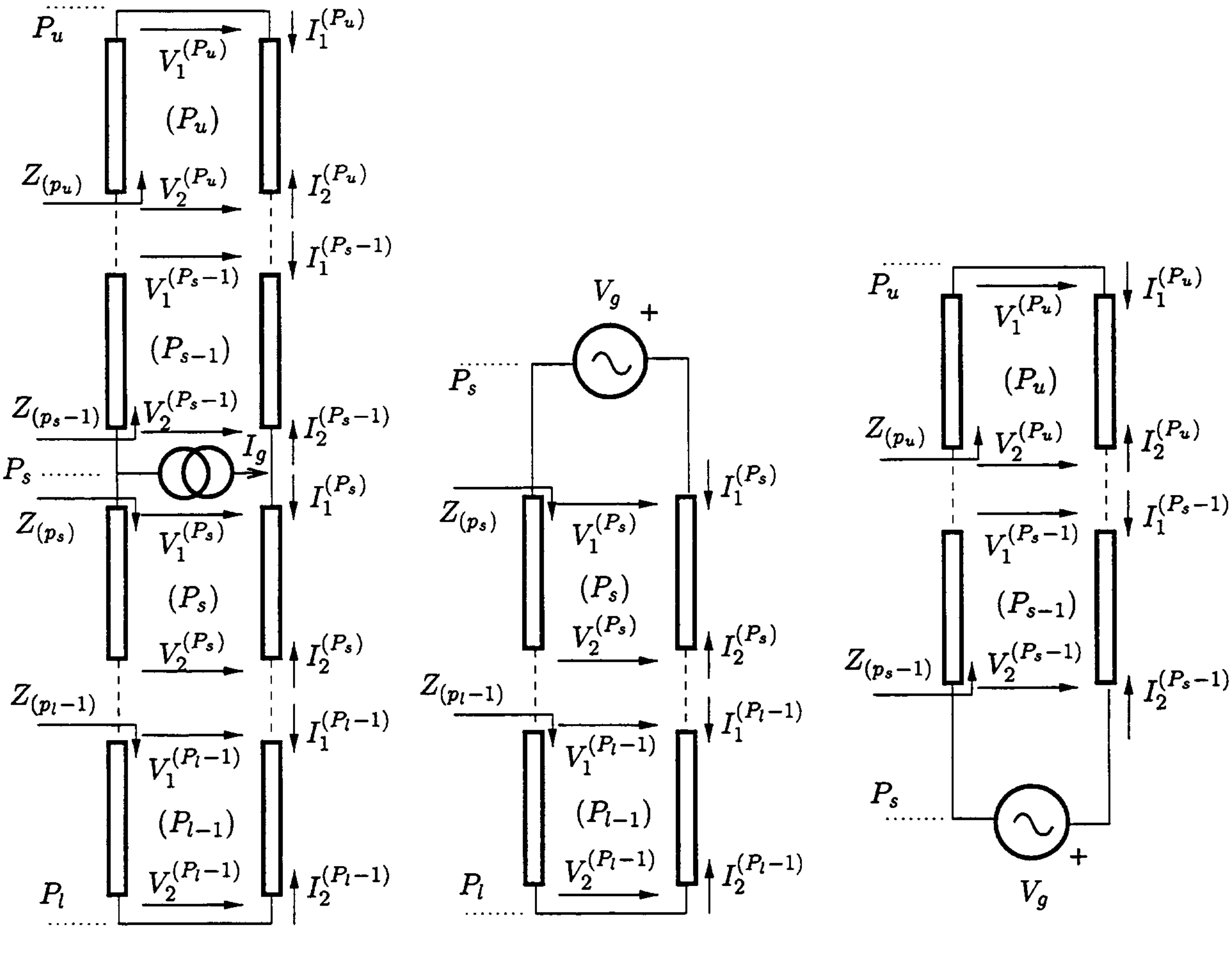

a) Electric network b) Lower magnetic network c) Upper magnetic network

Figure A.1: The three equivalent transmission line networks to which the analysis of any multilayered printed antenna is reduced in the spectral domain.

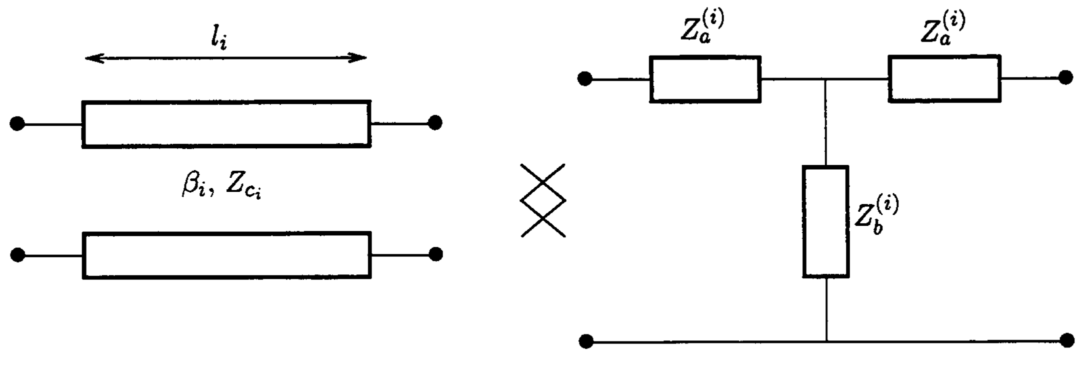

Figure A.2: Equivalent network of a section of transmission line of length l_i.

With these impedances it is simple to compute the voltages and currents at the generator terminals, namely

$$\begin{cases} V_2^{(p_s-1)} = I_g \frac{Z_{p_s-1} Z_{p_s}}{Z_{p_s-1}+Z_{p_s}} \\ V_1^{(p_s)} = V_2^{(p_s-1)} \\ I_2^{(p_s-1)} = I_g \frac{Z_{p_s}}{Z_{p_s-1}+Z_{p_s}} \\ I_1^{(p_s)} = I_g \frac{Z_{p_s-1}}{Z_{p_s-1}+Z_{p_s}} \end{cases} \tag{A.5}$$

All other voltages and currents above the generator are now easily computed by applying the transformation in equations (A.1,A.2)

$$\left\{\begin{array}{l} I_1^{(i)} = \frac{V_2^{(i)} - Z_{22}^{(i)} I_2^{(i)}}{Z_{21}^{(i)}} \\ V_1^{(i)} = Z_{11}^{(i)} I_1^{(i)} + Z_{12}^{(i)} I_2^{(i)} \\ \\ V_2^{(i-1)} = +V_1^{(i)} \\ I_2^{(i-1)} = -I_1^{(i)} \end{array}\right. \qquad i = p_s - 1, p_s - 2, \cdots, p_u + 1 \tag{A.6}$$

For the top interface we must check if the first transmission line is extended or not to infinity

$$\begin{array}{l} V_1^{(p_u)} = 0 \\ I_1^{(p_u)} = \left\{\begin{array}{ll} -\frac{Z_{12}^{(p_u)}}{Z_{11}^{(p_u)}} I_2^{(p_u)} & \text{Top interface is a short-circuit} \\ 0 & \text{Top interface placed at infinity} \end{array}\right. \end{array} \tag{A.7}$$

For the part of the network below the generator we can proceed in the same manner. Firts compute the input impedance at the last interface

$$Z_{p_l-1} = \left\{\begin{array}{ll} j\, Z_{c_{p_l-1}} \tan\left(\beta_{p_l-1}\, h_{p_l-1}\right) & \text{Lower limit is short-circuit} \\ Z_{c_{p_l-1}} & \text{Lower limit goes to infinity} \end{array}\right. \tag{A.8}$$

then compute all other input impedances up to generator

$$Z_i = Z_{c_i} \frac{Z_{i+1} + j\, Z_{c_i} \tan\left(\beta_i\, h_i\right)}{Z_{c_i} + j\, Z_{i+1} \tan\left(\beta_i\, h_i\right)}; \; i = p_l - 2, p_l - 3, \cdots, p_s \tag{A.9}$$

The voltages and currents in all interfaces below the generator are then computed simply as

$$\left\{\begin{array}{l} I_2^{(i)} = \frac{V_1^{(i)} - Z_{11}^{(i)} I_1^{(i)}}{Z_{12}^{(i)}} \\ V_2^{(i)} = Z_{21}^{(i)} I_1^{(i)} + Z_{22}^{(i)} I_2^{(i)} \\ \\ V_1^{(i+1)} = +V_2^{(i)} \\ I_1^{(i+1)} = -I_2^{(i)} \end{array}\right. \qquad i = p_s, p_s + 1, \cdots, p_l - 2 \tag{A.10}$$

For the bottom interface we must also check if the associated transmission line is extended or not to infinity

$$\begin{array}{l} V_2^{(p_l-1)} = 0 \\ I_2^{(p_l-1)} = \left\{\begin{array}{ll} -\frac{Z_{21}^{(p_l-1)}}{Z_{22}^{(p_l-1)}} I_1^{(p_l-1)} & \text{Bottom interface is a short-circuit} \\ 0 & \text{Bottom interface placed at infinity} \end{array}\right. \end{array} \tag{A.11}$$

As seen in Figure A.1, p_s is the interface where the current generator is placed, p_u is the interface corresponding to the top (upper) short-circuit, p_l is the interface corresponding to the bottom (lower) short-circuit and I_g is the strength of the current generator of excitation.

A.2 Lower Magnetic Network

For the lower magnetic network of Figure A.1 we start by computing the input impedance at the last interface

$$Z_{p_l-1} = \begin{cases} j\, Z_{c_{p_l-1}} \tan\left(\beta_{p_l-1}\, h_{p_l-1}\right) & \text{Lower limit is short-circuit} \\ Z_{c_{p_l-1}} & \text{Lower limit goes to infinity} \end{cases} \tag{A.12}$$

As before, the input impedances in all other interfaces simply become

$$Z_i = Z_{c_i} \frac{Z_{i+1} + j\, Z_{c_i} \tan\left(\beta_i\, h_i\right)}{Z_{c_i} + j\, Z_{i+1} \tan\left(\beta_i\, h_i\right)};\; i = p_l - 2, p_l - 3, \cdots, p_s \tag{A.13}$$

Now the voltage and current at the generator terminals are written as

$$\begin{cases} V_1^{(p_s)} = V_g \\ I_1^{(p_s)} = \frac{V_g}{Z_{p_s}} \end{cases} \tag{A.14}$$

Using again the transformation given in (A.1,A.2) we compute the voltages and currents in all other interfaces as

$$\begin{cases} I_2^{(i)} = \frac{V_1^{(i)} - Z_{11}^{(i)} I_1^{(i)}}{Z_{12}^{(i)}} \\ V_2^{(i)} = Z_{21}^{(i)} I_1^{(i)} + Z_{22}^{(i)} I_2^{(i)} \\ & i = p_s, p_s + 1, \cdots, p_l - 2 \\ V_1^{(i+1)} = +V_2^{(i)} \\ I_1^{(i+1)} = -I_2^{(i)} \end{cases} \tag{A.15}$$

For the last interface we check if the associated transmission line is extended or not up to infinity

$$\begin{aligned} V_2^{(p_l-1)} &= 0 \\ I_2^{(p_l-1)} &= \begin{cases} -\frac{Z_{21}^{(p_l-1)}}{Z_{22}^{(p_l-1)}} I_1^{(p_l-1)} & \text{Bottom interface is a short-circuit} \\ 0 & \text{Bottom interface placed at infinity} \end{cases} \end{aligned} \tag{A.16}$$

As before, p_s is the interface where the voltage generator is placed, p_l the order of the bottom (lower) interface and V_g the strength of the voltage generator of excitation.

A.3 Upper Magnetic Network

For the upper magnetic network of Figure A.1 we start by computing the input impedance at the first interface

$$Z_{p_u} = \begin{cases} j\, Z_{c_{p_u}} \tan\left(\beta_{p_u}\, h_{p_u}\right) & \text{Upper limit is short-circuit} \\ Z_{c_{p_u}} & \text{Upper limit goes to infinity} \end{cases} \tag{A.17}$$

The input impedances in all other interfaces can be written as

$$Z_i = Z_{c_i} \frac{Z_{i-1} + j\, Z_{c_i} \tan\left(\beta_i\, h_i\right)}{Z_{c_i} + j\, Z_{i-1} \tan\left(\beta_i\, h_i\right)};\; i = p_u + 1, p_u + 2, \cdots, p_s - 1 \tag{A.18}$$

The voltage and currents at the generator terminals now become

$$\begin{cases} V_2^{(p_s-1)} = V_g \\ I_2^{(p_s-1)} = \frac{V_g}{Z_{p_s-1}} \end{cases} \tag{A.19}$$

Finally, the voltages and currents at all other interfaces are written as

$$\left\{\begin{array}{l} I_1^{(i)} = \frac{V_2^{(i)} - Z_{22}^{(i)} I_2^{(i)}}{Z_{21}^{(i)}} \\ V_1^{(i)} = Z_{11}^{(i)} I_1^{(i)} + Z_{12}^{(i)} I_2^{(i)} \\ \\ V_2^{(i-1)} = +V_1^{(i)} \\ I_2^{(i-1)} = -I_1^{(i)} \end{array}\right. \qquad i = p_s - 1, p_s - 2, \cdots, p_u + 1 \tag{A.20}$$

For the first interface we check if the associated transmission line is extended or not up to infinity

$$\begin{array}{l} V_1^{(p_u)} = 0 \\ I_1^{(p_u)} = \left\{\begin{array}{ll} -\frac{Z_{12}^{(p_u)}}{Z_{11}^{(p_u)}} I_2^{(p_u)} & \text{Top interface is a short-circuit} \\ 0 & \text{Top interface placed at infinity} \end{array}\right. \end{array} \tag{A.21}$$

and again, p_s is the interface position of the voltage generator, p_u the order of the top (upper) interface and V_g the strength of the voltage generator of excitation.

Appendix B

Analytical Primitives

In this appendix we give the analytical expressions for the primitives needed in the evaluation of the overlapping integrals between the modal functions of the cavity box and the triangular cells used in the discretization of the antenna geometry. These primitives complete the analytical treatment for the integral equation formulation of cavity backed antennas given in chapter 4, section 4.4.2.

$$\tilde{I}_{cx}(a_c, b_c, d_c)\Big|_l^u = \int_l^u x \cos\left[a_c\left(b_c\, x + d_c\right)\right] dx =$$
$$u\,\frac{\sin\left[a_c\left(b_c\, u + d_c\right)\right]}{a_c\, b_c} - l\,\frac{\sin\left[a_c\left(b_c\, l + d_c\right)\right]}{a_c\, b_c} + \frac{\cos\left[a_c\left(b_c\, u + d_c\right)\right]}{(a_c\, b_c)^2} - \frac{\cos\left[a_c\left(b_c\, l + d_c\right)\right]}{(a_c\, b_c)^2} \tag{B.1}$$

Two singular cases must be treated in equation (B.1), namely

$$\tilde{I}_{cx}(0, b_c, d_c)\Big|_l^u = \frac{u^2 - l^2}{2}$$
$$\tilde{I}_{cx}(a_c, 0, d_c)\Big|_l^u = \cos(a_c\, d_c)\,\frac{u^2 - l^2}{2} \tag{B.2}$$

Next compute the integral

$$\tilde{I}_s(a_s, b_s, d_s)\Big|_l^u = \int_l^u \sin\left[a_s\left(b_s\, x + d_s\right)\right] dx = -\frac{\cos\left[a_s\left(b_s\, u + d_s\right)\right]}{a_s\, b_s} + \frac{\cos\left[a_s\left(b_s\, l + d_s\right)\right]}{a_s\, b_s} \tag{B.3}$$

Two singular cases must be treated in equation (B.3), namely

$$\tilde{I}_s(0, b_s, d_s)\Big|_l^u = 0$$
$$\tilde{I}_s(a_s, 0, d_s)\Big|_l^u = \sin(a_s\, d_s)\,(u - l) \tag{B.4}$$

Next compute

$$\tilde{I}_{sx^2}(a_s, b_s, d_s)\Big|_l^u = \int_l^u x^2 \sin\left[a_s\left(b_s\, x + d_s\right)\right] dx =$$
$$-\frac{u^2 \cos\left[a_s\left(b_s\, u + d_s\right)\right]}{a_s\, b_s} + \frac{l^2 \cos\left[a_s\left(b_s\, l + d_s\right)\right]}{a_s\, b_s} + \frac{2\,u \sin\left[a_s\left(b_s\, u + d_s\right)\right]}{(a_s\, b_s)^2} - \frac{2\,l \sin\left[a_s\left(b_s\, l + d_s\right)\right]}{(a_s\, b_s)^2}$$
$$+\frac{2 \cos\left[a_s\left(b_s\, u + d_s\right)\right]}{(a_s\, b_s)^3} - \frac{2 \cos\left[a_s\left(b_s\, l + d_s\right)\right]}{(a_s\, b_s)^3} \tag{B.5}$$

The two singular situations in (B.5) lead to

$$\tilde{I}_{sx^2}(0, b_s, d_s)\Big|_l^u = 0$$
$$\tilde{I}_{sx^2}(a_s, 0, d_s)\Big|_l^u = \sin(a_s\, d_s)\,\frac{u^3 - l^3}{3} \tag{B.6}$$

Finally we also need to compute the following integral

$$\tilde{I}_{scx^2}\left(a_s, b_s, d_s, a_c, b_c, d_c\right)\Big|_l^u = \int_l^u x^2 \sin\left[a_s\left(b_s\,x + d_s\right)\right]\,\cos\left[a_c\left(b_c\,x + d_c\right)\right]\,dx \tag{B.7}$$

If we integrate this expression by parts, the remaining integrals can be either evaluated directly or expressed as combination of integrals of the type shown in equation (B.1). After some straightforward manipulations we obtain

$$\begin{aligned}
&\tilde{I}_{scx^2}\left(a_s, b_s, d_s, a_c, b_c, d_c\right)\Big|_l^u = \\
&-\frac{u^2 \cos\left[\tilde{a}_{(-)}\,u + \tilde{b}_{(-)}\right]}{2\,\tilde{a}_{(-)}} + \frac{l^2 \cos\left[\tilde{a}_{(-)}\,l + \tilde{b}_{(-)}\right]}{2\,\tilde{a}_{(-)}} - \frac{u^2 \cos\left[\tilde{a}_{(+)}\,u + \tilde{b}_{(+)}\right]}{2\,\tilde{a}_{(+)}} + \frac{l^2 \cos\left[\tilde{a}_{(+)}\,l + \tilde{b}_{(+)}\right]}{2\,\tilde{a}_{(+)}} \\
&+\frac{1}{\tilde{a}_{(-)}}\,\tilde{I}_{cx}\left(1, \tilde{a}_{(-)}, \tilde{b}_{(-)}\right)\Big|_l^u + \frac{1}{\tilde{a}_{(+)}}\,\tilde{I}_{cx}\left(1, \tilde{a}_{(+)}, \tilde{b}_{(+)}\right)\Big|_l^u
\end{aligned} \tag{B.8}$$

where the following constants have been defined

$$\begin{aligned}
\tilde{a}_{(-)} &= a_s\,b_s - a_c\,b_c \\
\tilde{a}_{(+)} &= a_s\,b_s + a_c\,b_c \\
\tilde{b}_{(-)} &= d_s\,a_s - a_c\,d_c \\
\tilde{b}_{(+)} &= d_s\,a_s + a_c\,d_c
\end{aligned} \tag{B.9}$$

There are now certain singular situations to be treated in equation (B.8). For the simplest cases we can directly write

$$\begin{aligned}
&\tilde{I}_{scx^2}\left(0, b_s, d_s, a_c, b_c, d_c\right)\Big|_l^u = 0 \\
&\tilde{I}_{scx^2}\left(a_s, b_s, d_s, 0, b_c, d_c\right)\Big|_l^u = \tilde{I}_{sx^2}\left(1, \tilde{a}_{(-)}, \tilde{b}_{(-)}\right)\Big|_l^u \\
&\tilde{I}_{scx^2}\left(a_s, 0, d_s, a_c, 0, d_c\right)\Big|_l^u = \sin(a_s\,d_s)\,\cos(a_c\,d_c)\,\frac{u^3 - l^3}{2}
\end{aligned} \tag{B.10}$$

where $\tilde{I}_{sx^2}$ is defined in equation (B.5). Next, for the more complex singular situation: $\tilde{a}_{(-)} = 0$, $\tilde{a}_{(+)} \neq 0$, we find

$$\begin{aligned}
&\tilde{I}_{scx^2}\left(a_s, b_s, d_s, a_c, b_c, d_c\right)\Big|_l^u = \\
&+\frac{u^3 \sin\left[\tilde{b}_{(-)}\right]}{6} - \frac{l^3 \sin\left[\tilde{b}_{(-)}\right]}{6} - \frac{u^2 \cos\left[\tilde{a}_{(+)}\,u + \tilde{b}_{(+)}\right]}{2\,\tilde{a}_{(+)}} + \frac{l^2 \cos\left[\tilde{a}_{(+)}\,l + \tilde{b}_{(+)}\right]}{2\,\tilde{a}_{(+)}} \\
&+\frac{1}{\tilde{a}_{(+)}}\,\tilde{I}_{cx}\left(1, \tilde{a}_{(+)}, \tilde{b}_{(+)}\right)\Big|_l^u \\
&\tilde{a}_{(-)} = 0;\ \tilde{a}_{(+)} \neq 0
\end{aligned} \tag{B.11}$$

Finally, for the dual singular case: $\tilde{a}_{(+)} = 0$, $\tilde{a}_{(-)} \neq 0$, we simply write

$$\begin{aligned}
&\tilde{I}_{scx^2}\left(a_s, b_s, d_s, a_c, b_c, d_c\right)\Big|_l^u = \\
&+\frac{u^3 \sin\left[\tilde{b}_{(+)}\right]}{6} - \frac{l^3 \sin\left[\tilde{b}_{(+)}\right]}{6} - \frac{u^2 \cos\left[\tilde{a}_{(-)}\,u + \tilde{b}_{(-)}\right]}{2\,\tilde{a}_{(-)}} + \frac{l^2 \cos\left[\tilde{a}_{(-)}\,l + \tilde{b}_{(-)}\right]}{2\,\tilde{a}_{(-)}} \\
&+\frac{1}{\tilde{a}_{(-)}}\,\tilde{I}_{cx}\left(1, \tilde{a}_{(-)}, \tilde{b}_{(-)}\right)\Big|_l^u \\
&\tilde{a}_{(+)} = 0;\ \tilde{a}_{(-)} \neq 0
\end{aligned} \tag{B.12}$$

thus completing all the operations needed for the evaluation of the overlapping integrals in the cavity backed situation.

Bibliography

[1] I. J. Bahl and P. Bhartia (1994) "Microstrip Antenna". *Artech House.* Canton Street, Norwood, MA 02062.

[2] P. Bhartia, K. V. S. Rao and R. S. Tomar (1990) "Millimeter-Wave Microstrip and Printed Circuit Antennas". *Artech House.* Canton Street, Norwood, MA 02062.

[3] Juan R. Mosig and F. E. Gardiol (1983) "Analytical and Numerical Techniques in the Green's Function Treatment of Microstrip Antennas and Scatterers". *IEE Proceedings.* Vol. 130, Pt. H, No. 2, March 1983, pp.175-182.

[4] L. B. Felsen and N. Marcuvitz (1994) "Radiation and Scattering of Waves". *IEEE Press.* New York.

[5] Krzysztof A. Michalski and Juan R. Mosig (1997). "Multilayered Media Green's Functions in Integral Equation Formulations". *IEEE Transactions on Antennas and propagation.* Vol. 45, No. 3, March 1997, pp.508-519.

[6] Juan R. Mosig (1989) "Integral Equation Technique". Chapter 3 in "Numerical Techniques for Microwave and Millimeter-Wave Passive Structures". Edited by Tatsuo Itho. *Wiley Interscience Publication.* New York.

[7] J. A. Stratton (1941) "Electromagnetic Theory". *McGraw-Hill.* New york.

[8] Juan R. Mosig and Tapan K. Sarkar (1986) "Comparison of Quasi-Static and Exact Electromagnetic Fields from a Horizontal Electric Dipole Above a Lossy Dielectric Backed by an Imperfect Ground Plane". *IEEE Transactions on Microwave Theory and Techniques.* Vol. 34, No. 4, April 1986, pp. 379-387.

[9] Phillipe Gay-Balmaz (1996) "Sructures 3-D Planaires en Milieux Stratifiés: Fonctions de Green et application à des antennes incluant des parois verticales". *PhD dissertation.* École Polytechnique Fédérale de Lausanne.

[10] Constantine A. Balanis (1982) "Antenna Theory Analysis and Design". *John Wiley and Sons.* New York.

[11] N. Marcuvitz (1950) "Waveguide Handbook". *Boston Technical Publishers, Inc.* USA.

[12] Juan R. Mosig (1988) "Arbitrarily Shaped Microstrip Structures and Their Analysis with a Mixed Potential Integral Equation". *IEEE Transactions of Microwave Theory and Techniques.* Vol. 36, No. 2, February 1988, pp. 314-323.

[13] R. F. Harrington (1993) "Field Computation by Moment Methods". *IEEE Press.* New York.

[14] Sadasiva M. Rao, Donald R. Wilton and Allen W. Glisson (1982) "Electromagnetic Scattering by Surfaces of Arbitrary Shape". *IEEE Transactions on Antennas and Popagation.* Vol. AP-30, No. 3, May 1982, pp. 409-418

[15] Chen-To Tai (1993) "Dyadic Green Functions in Electromagnetic Theory". *IEEE Press.* New York.

[16] Milton Abramowitz and Irene A. Stegun (1964) "Handbook of Mathematical Functions". *Dover Publications, inc.* New York.

[17] Georges V. Eleftheriades, Juan R. Mosig and M. Gugliemi (1996). "A Fast integral Equation Technique for Shielded Planar Circuits Defined on Nonuniform Meshes". *IEEE Transactions on Microwave theory and Techniques.* Vol. 44, No. 12, December 1996, pp. 2293-2296.

[18] Georges V. Eleftheriades and Juan R. Mosig (1996). "On the Network Characterization of Planar Passive Circuits Using the Method of Moments". *IEEE Transactions on Microwave Theory and Techniques.* Vol. 44, No. 2, March 1996, pp. 438-445.

[19] G. Matthaei, L. Young and E. M. T. Jones (1980). "Microwave Filters, impedance-Matching Networks, and Coupling Structures". *Artech House.* Denham, MA.

[20] Sheng-Gen Pan and Ingo Wolff (1994). "Scalarization of dyadic Spectral Green's Functions and Network Formalism for Three-Dimensional Full-Wave Analysis of Planar Lines and Antennas". *IEEE Transactions on Microwave Theory and Techniques.* Vol. 42, No. 11, November 1994, pp. 2118-2127.

CONFORMAL ARRAY

CHAPTER 6

ACTIVE SUB-ASSEMBLY
ARCHITECTURES AND EXPECTED PERFORMANCES

(WP 2400)

Reproduction interdite © ALCATEL ESPACE Reproduction forbidden

CONFORMAL ARRAY ANTENNA

Estec Contract 11698/95/NL/SB

DATE :	ED/REV :	
30/10/96	1/-	

Titre / Title

CHAPTER 6 (WP 2400)

ACTIVE SUB-ASSEMBLY

ARCHITECTURES AND EXPECTED PERFORMANCES

Rédigé par / Written by	Responsabilité / responsibility	Date	Signature
T.ADAM	Engineer	30/11/96	
Vérifié par / Verified by			
B.COGO	In charge of advanced repeaters activity-repeater product line	30/11/96	p.o. Rogn
Approbation / Approved			
G.CAILLE	Technical Manager of the contract	3/12/96	

ALCATEL TELECOM

Reproduction interdite © ALCATEL ESPACE Reproduction forbidden

SUMMARY

Reproduction interdite © ALCATEL ESPACE Reproduction forbidden

1. Introduction

According to the specifications presented in Chapter 4 §2, the purpose of this document is to propose a detailed electrical diagram of the active sub-assembly, a technology for each device and an evaluation of mass, volume and power consumption.

2. Overall architecture

Because the more stringent specification is DC power consumption, the first idea is to divide the required gain between MMIC module and a supplementary pre-amplifier, localised at the beginning of the RF chain, just behind the QPSK modulators.

In this configuration, decreasing the gain of each MMIC module, we can reduce its power DC consumption. Then, the overall power DC consumption, including the consumption of one MMIC module multiplied by 24 but only the one of a pre-amplifier multiplied by 3, should be minimized.

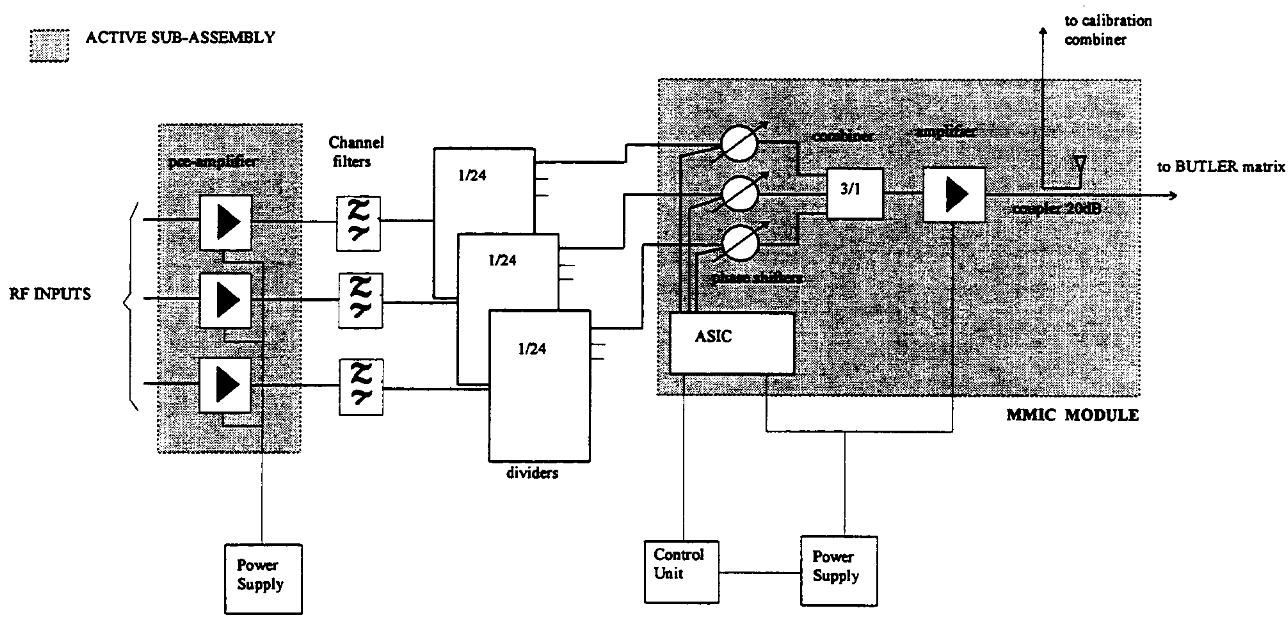

figure1 : Electrical diagram of the active sub-assembly in its context

On this first figure, the active sub-assembly appears consequently divided into two entities. The first one is a pre-amplifier containing three amplifiers working respectively at the frequencies of the three channels: 8.1, 8.2, 8.3GHz. The second one called "MMIC module" contains three phase shifters driven by an ASIC (located into the module), one combiner 3 to 1 delivering a three tone signal from the three channels, one high-linearity amplifier providing the specified linearity and a 20dB coupler delivering a calibration signal.

3. Amplifier Chain performances

3.1. Precision about active sub-assembly specifications: linearity consideration

Our goal is to express C/I3 specification with three-tone RF signal in terms of C/I3 specification with two-tone excitation, which is commonly used in RF design.

- In three-tone mode, third-order products at $(f_i+f_j-f_k)$ are 6dB above their counterparts at $(2f_i\pm f_j)$
  This result can be deduced from a simple computation using a power series model of the non-linearity.
  $I_D=a_0+a_1V+a_2V^2+a_3V^3+\ldots$ if $V=V_1+V_2+V_3$
  Development of $(V_1+V_2+V_3)^3$, where V_1, V_2, V_3 are waves at same power level, gives terms $3V_i^2V_j$ (like with two-tone excitation) and $6V_iV_jV_k$, corresponding respectively at frequency $(2f_i\pm f_j)$ and $(f_i+f_j-f_k)$, where i,j,k are any value between 1 and 3. The 6/3 waves level ratio squared gives power level ratio between IM products at $(2f_i\pm f_j)$ and $(f_i+f_j-f_k)$
  If p_2=IMP3 power spectral density at $(2f_i\pm f_j)$
  p_3=IMP3 power spectral density at $(f_i+f_j-f_k)$ $\boxed{p_3=4p_2}$

- For the given frequency plan f_1=8.1, f_2=8.2, f_3=8.3GHz, the spectral occupancy of three-tone third-order intermod products spurring in DSN band, is presented in figure 2:

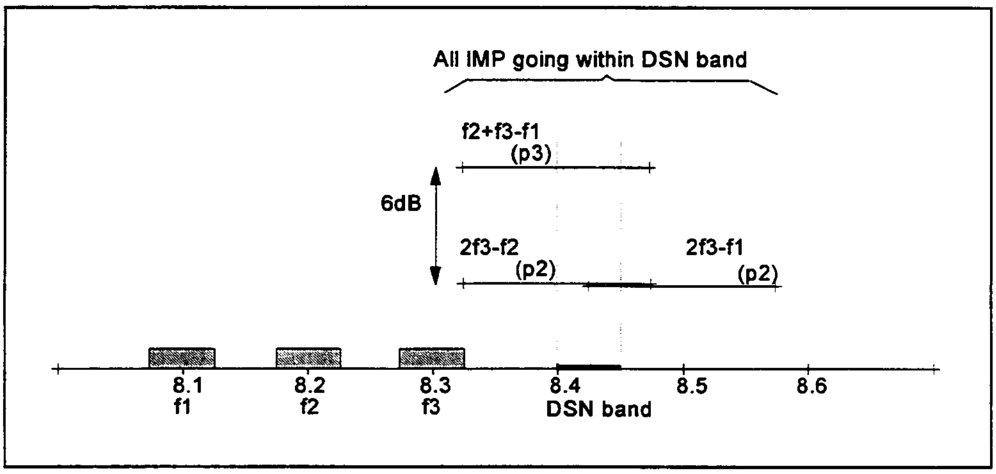

figure2: Spurious in DSN band

❐ Assuming that IMP power spectral density is constant in its band, we can compute equivalent power spectral density in DSN band:

$2f_3\text{-}f_2$: $p_2/3$
$2f_3\text{-}f_1$: $p_2/6$
$f_2+f_3\text{-}f_1$: $p_3/3=$ $4p_2/3$
Total IMP3 power in DSN band = $11p_2/6$

Thus, from this approached computation, we conclude that:
Σ three-tone IMP3 ≅ one two-tone IMP3 + 3dB

$\Rightarrow$ $\boxed{C/I3_{\text{two-tone}} \cong C/I3_{\text{three-tone}}+3dB}$

$\Rightarrow$ Required C/I3 with two-tone excitation : 31dB (28+3)

3.2 A strategy to design

For the amplifier, the most realistic technological choice, with a launching scheduled after year 2000, is to use transistor with high electronic mobility, like PHEMT acronym of Pseudomorphic High Electronic Mobility Transistor.

This type of structure, based on the properties of two-dimensional electronic moving, provides two main improvements:
- a higher gain per stage (≥12dB) provided by the increase of the maximum oscillation frequency,
- a higher Power added efficiency (PAE) at 1dB compression in part for the same reason and also because of the intrinsic efficiency improvement.

With a necessary active gain roughly estimated greater than 48dB (according to Sub-assemblies specifications Chapter 4 §2), the more secure structure is: five stages + variable attenuator for tuning precisely the overall required gain (common commercial value, largely compliant for our application, is 20dB).

In introduction to the optimisation problem of the sharing-out stages among MMIC Modules and pre-amplifier to perform the lowest DC consumption, we clarify two points of strategy:
- First, we make work the pre-amplifier near to 1dB compression point (namely with a small backoff guaranteeing the output power required and minimising unsuitable effects like widening of channel spectrum),
- Secondly, the amplifier in the MMIC Module must be designed with the convenient backoff to perform the required linearity.

Reproduction interdite © ALCATEL ESPACE Reproduction forbidden

3.3 Optimisation sharing out stages among MMIC pre-amplifier and MMIC Module

Because four stages will probably be sufficient to perform the necessary gain, taking into account technological improvements in next years, and because the possible fifth stage is a low-level amplifier consuming less than 100mW, to optimise sharing out stages among pre-amplifier and MMIC Module, we need to compute three cases: 1-/-3 meaning one stage in the pre-amplifier and three stages in the MMIC Module and with the same notations : 2-/-2 and 3-/-1.

Three constraints have been taken in account:

- a backoff of 1.5dB from 1dB compression point for the pre-amplifier output power,
- required linearity for the MMIC Module,
- required pre-amplifier output power with losses and gain worst case (temperature drift + flatness).

We obtain, with computation extrapolated from measurement data from other studies, the following figure:

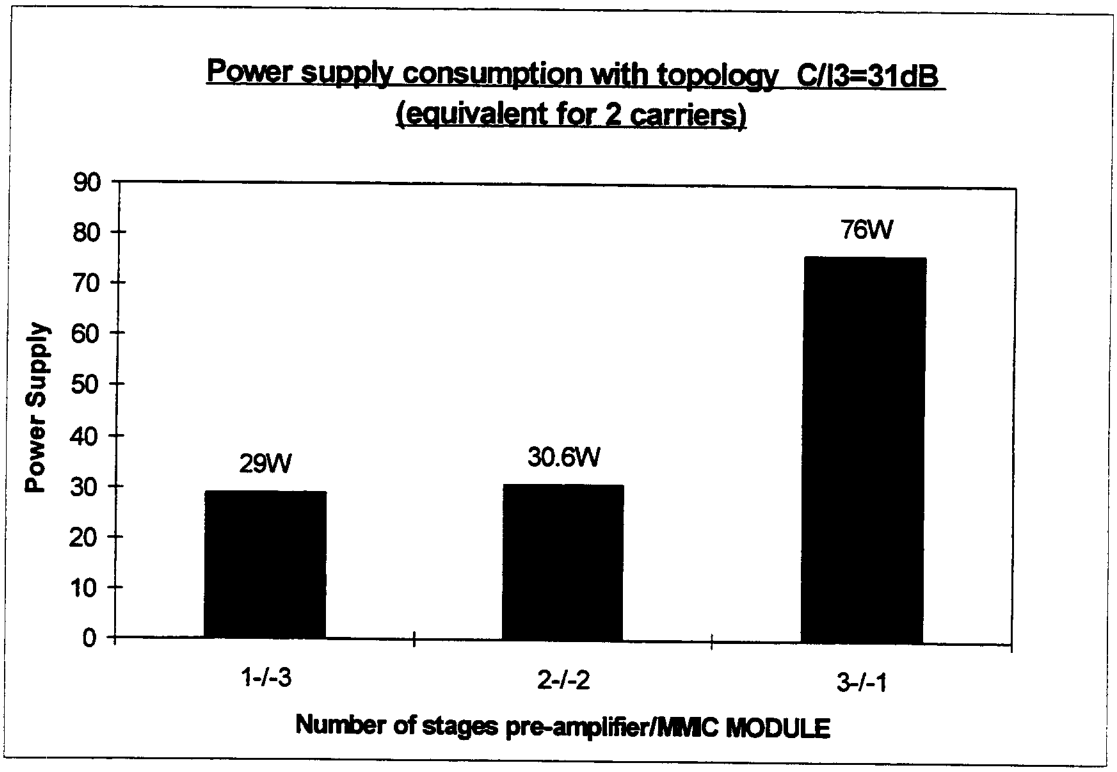

Those results show very close consumption values between 1-/-3 and 2-/-2 distribution. Then, two others criteria have been retained to involve the final choice: 2-/-2, which performs:

- better temperature stability avoiding temperature compensation (if difference 5°C maximum between modules)
- better sharing out gain between pre-amplifier and modules minimizing dispersion effects.

Reproduction interdite © ALCATEL ESPACE Reproduction forbidden

3.4. Minimum gain and pre-amplifier output power to perform

We can now precisely compute the minimum gain to perform the required output power.

REQUIRED GAIN (see in "Chapter4 Sub-Assemblies specifications" §2, specification 2.c	35.5 dB
Maximal insertion losses through phase shifters:	9 dB
Insertion losses through combiner 3/1:	5.2 dB
Overall provision for flatness and temperature drift:	1 dB

Minimal gain to perform: 50.7 dB

The overall provision for flatness and temperature drift is computed in the worst case at 45°C with 12dB minimal gain guaranteed at ambient temperature for each module with a 0.04dB/°C slope on 20°C range, we obtain 0.8dB + 0.2dB maximal ripple in each 50MHz channel.

Insertion losses through combiners have been computed assuming a theoretical loss 10Log3 plus 0.4dB for ohmic losses.

Secondly, we compute the minimal output power pre-amplifier to perform the required MMIC Module output power for each channel in the worst case:

⇨ worst case losses for various components
⇨ minimal gain

REQUIRED OUTPUT POWER PER CHANNEL :	19 dBm
MMIC amplifier nominal gain (at 25°C) :	- 24 dB
Maximal insertion losses through phase shifters :	+ 9 dB
Insertion losses through combiner 3/1 :	+ 5.2 dB
Overall provision for flatness and temperature drift :	+ 1 dB
Dividers and cables overall insertion loss :	+15.8 dB
Channel filter loss :	+ 0.7 dB

Minimal pre-amplifier output power to perform : 26.7 dBm

(all supplementary data referring to "Chapter 4 Sub-Assemblies specifications" § 2 specification 2.c)

3.5. Detailed electrical diagram of the active sub-assembly

According to the previous data, we can precisely detail the structure of each module and check all intermediate power levels at each input and output device.

Reproduction interdite © ALCATEL ESPACE Reproduction forbidden

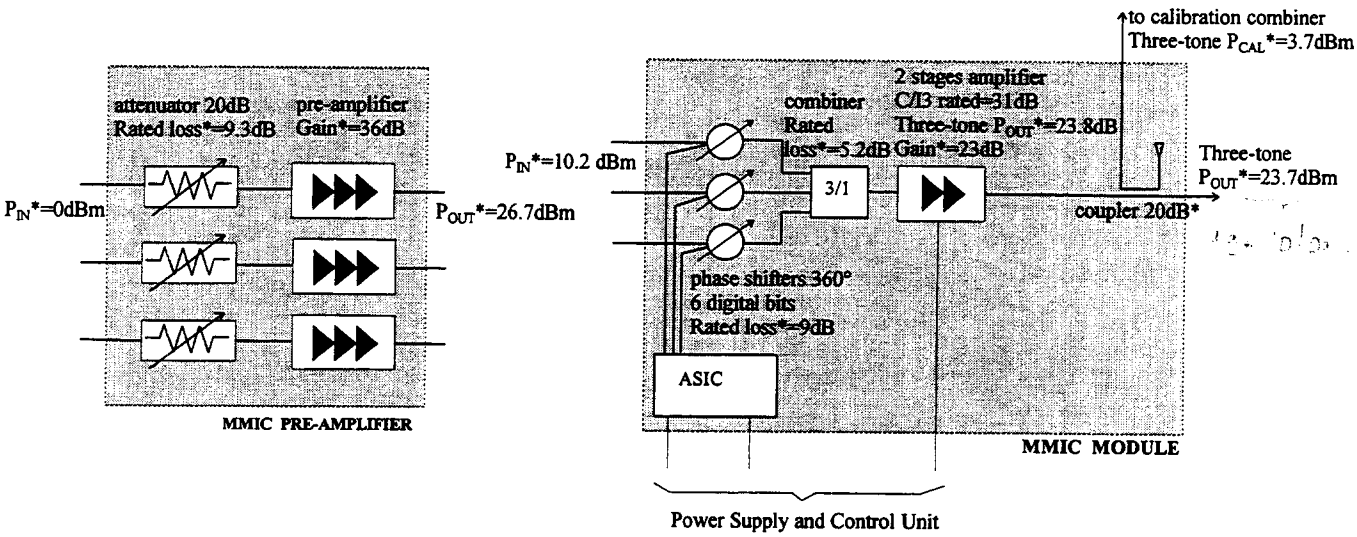

* All worst case values at 45°C

4. MMIC amplifier expected performances

Now, we can indicate all the expected parameters for the different devices.

Carriers : 8.1 8.2 8.3	Pre-amplifier 3 stages	MMIC MODULE 2 stages
Gain (dB) @	36	24
Frequency band	50MHz respectively centered at 8.1 8.2 8.3 GHz	250 MHz [8.075 ; 8.325] GHz
Gain flatness (dB)	<<0.1 p-p	<<0.1p-p within each 50MHz channel
Nominal output power (dBm) with worst case losses	26.7 max. single tone	23.7 Three-tone delivered
Single tone Output Power at 1dB compression (dBm)	28.3	28
Nominal PAE (%)	37	20
C/I3 at nominal output power	>20	31.6
IP3 (dBm)	32.6 (not critical)	34.8
Time delay variation (ns)	<<1	<<1
Output and Input return loss (dB)	>15	>15
DC Power consumption at nominal output power (W)	1.25	1.1
DC Power consumption without RF (W)	0.7	0.95
Temperature range of the baseplate (°C)	NA	[-5, 45°C]
Gain variation versus Temperature (dB/°C)	<0.06 (not critical)	<0.04

Reproduction interdite © ALCATEL ESPACE Reproduction forbidden

5. Combiner expected performances

Parameters	Expected values
Frequency range	8 - 8.4 GHz
Insertion loss	5.2 dB
Insertion loss variation into 50Mhz band centered at 8.1 8.2 8.3 GHz	<< 0.1 dB
Input and Output return loss	>18 dB
Delay time variation	<< 1 ns
DC Power consumption (W)	NA (passive circuit)
Temperature range of the baseplate	[-5;45°]C
Technology	Microstrip

6. Phase shifters expected performances

Parameters	Expected values
Number of bits	6
Frequency band	8 - 8.4 GHz
Insertion loss	9 dB max
Flatness	<<0.1 dB p-p
Insertion loss variation over all 64 phase states	-0.5dB +0.5dB
RMS Insertion loss variation over all 64 phase states	<0.4dB
Insertion loss with 5°C temperature drift and scattering between 24 modules	<0.1dB p-p
RMS Insertion loss with 5°C temperature drift and scattering between 24 modules	<0.05 dB
Input and Output return loss (dB)	>18
DC Power consumption (W)	negligible
Worst case Phase control	< 8° over all the 64 states
RMS Phase control	< 3° over all the 64 states
IP3	>40 dBm
Input power at 1° phase shift and 0.1 dB compression	22dBm
Temperature range (°C)	[-5°C, 40°C]
Delay time variation	<<1 ns
Switching speed	20 ns
Technology	MESFET 0.5µm

Reproduction interdite © ALCATEL ESPACE Reproduction forbidden

7. Coupler expected performances

Parameters	Expected values
Frequency range	8 - 8.4 GHz
Nominal coupling	20 dB
Directivity	17 dB
Insertion loss variation into 50Mhz band centered at 8.1 8.2 8.3 GHz	<0.1 dB
Input and Output return loss	>18 dB
DC Power consumption (W)	NA (passive circuit)
Temperature range of the baseplate	[-5;45°]C
Technology	Microstrip

8. Overall expected performances

Board 1/2

Carriers : 8.1 8.2 8.3	Pre-amplifier 3 stages + attenuators	MMIC MODULE 2 stages amplifiers+phase shifters+combiner+ ASIC	Whole active sub-assembly expected values	Compliance
Gain	26.7dB	8.8dB at 45°C	35.5dB	OK
Frequency band	50MHz	250 MHz [8.075 ; 8.325] GHz	-	OK
Gain flatness	<0.1 dB p-p	<0.1 dB p-p within each 50MHz channel	<0.2 dB p-p	OK
Phase control	NA	over 360° with 5.625° resolution (6 bits)	over 360° with 5.625° resolution (6 bits)	OK
Worst case Phase control over all 64 phase states	NA	8°	8°	OK
RMS phase control over all 64 phase states	NA	<3°	<3°	OK
Insertion loss variation over all 64 phase states	NA	+/- 0.5dB	+/- 0.5dB	OK
RMS Insertion loss variation over all 64 phase statse	NA	<0.4dB	<0.4dB	OK
Insertion loss with 5°C temperature drift and scattering between 24 modules	NA	0.4 dB p-p	0.4 dB p-p	OK
RMS gain variation with 5°C temperature drift and scattering between 24 modules	NA	0.3 dB	0.3 dB	OK

Reproduction interdite © ALCATEL ESPACE Reproduction forbidden

Board 2/2

Carriers : 8.1 8.2 8.3	Pre-amplifier 3 stages + attenuators	MMIC MODULE 2 stages amplifiers+phase shifters+combiner+ ASIC	Whole active sub-assembly expected values	Compliance
Nominal output power with worst case losses	26.7 dBm max.single tone	23.7 dBm Three tone delivered	23.7 dBm Three tones delivered	OK
C/I3 at nominal output power	>20 dB	31.6 dB	31.6 dB	OK
Time delay variation	<1 ns	<1 ns	<2 ns	OK
Input and output return loss	>15 dB	>15 dB	>15 dB	OK
DC Power consumption at nominal output power	1.25 W	1.1 W	<30.6 W (ASIC included)	OK
DC Power consumption without RF	0.7 W	0.95 W	25.1 W	OK
Nominal PAE	38%	20%	18.5%	OK
Temperature range	NA	[-5, 45°C]	-	OK
Gain variation versus Temperature	<0.06 dB/°C (not critical)	<0.04 dB/°C	-	OK

9. Expected mechanical data (included preliminary interface control data)

Parameters of each quadri-module	Expected values
Size	120*60*15 mm
Weight	< 240 g
RF connectors	Inputs: 12 female SMA Outputs: 8 female SMA
Digitals signals and power supply connector (1 per group of 4 modules)	CANNON [15/25/37]P female TBD
Technology	Multichip module based on cofired alumina

A preliminary interface control drawing is given in the following figure, according to integration possibilities of the multilayer structure:

Reproduction interdite © ALCATEL ESPACE Reproduction forbidden

ACTIVE MODULE PACKAGE (FOUR ACTIVE MODULE TO BE MULTIPLY BY 6)
(all dimensions given in mm) With connector CANNON 25P

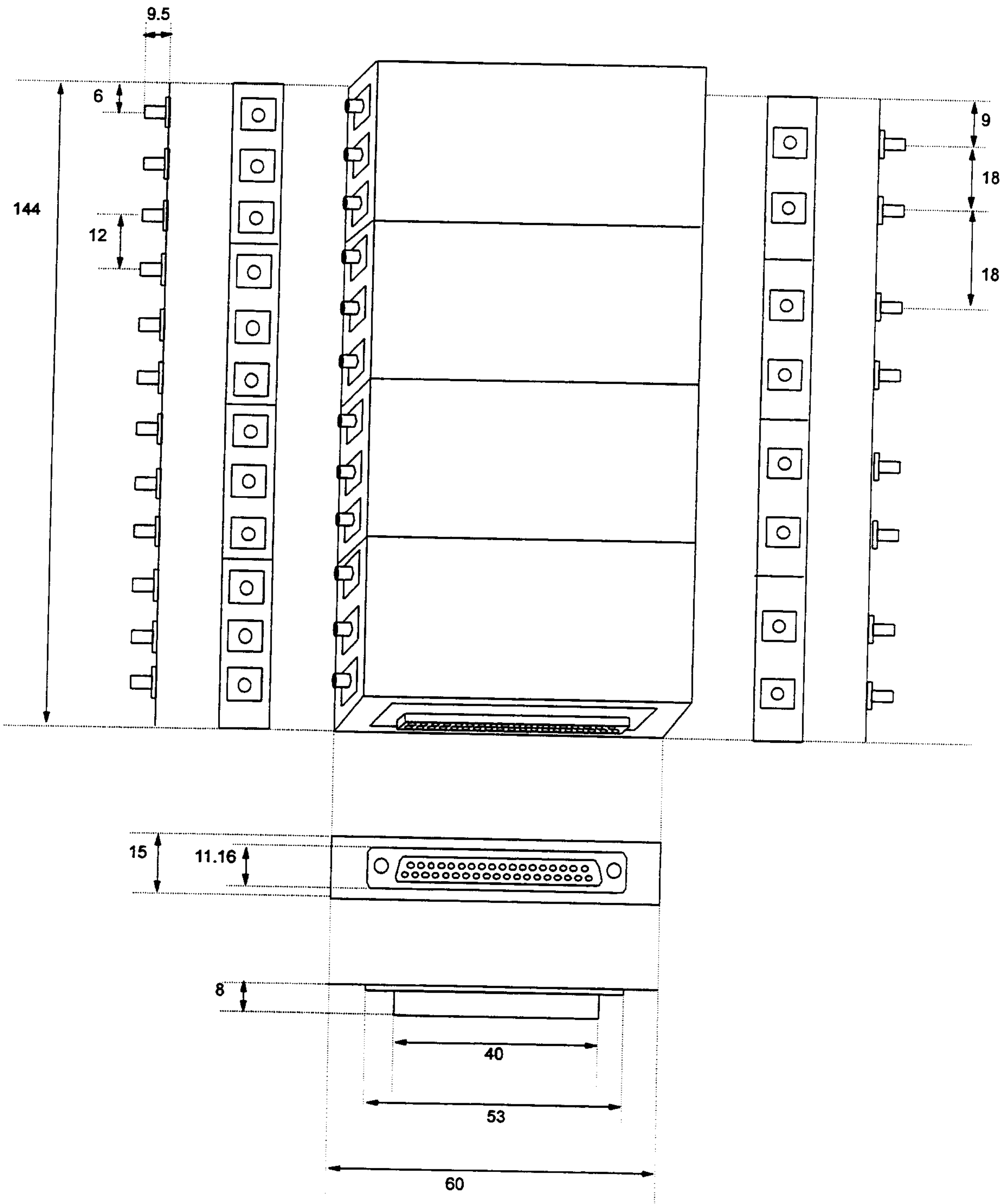

Reproduction interdite © ALCATEL ESPACE Reproduction forbidden

CONFORMAL ARRAY

CHAPTER 7

RADIATING SURFACE

(WP 2200)

Reproduction interdite © ALCATEL ESPACE Reproduction forbidden

The information contained in this document is proprietary to ALCATEL ESPACE and shall not be disclosed by the recipient to third persons without the written consent of the company

ALCATEL TELECOM	CONFORMAL ARRAY ANTENNA	ESTEC CONTRACT 11698/95/NL/SB		
		AES 97 01290 / ASP 023		
		DATE : 15/02/97	ED/REV 1/-	1

CHAPTER 7

Titre / Title
RADIATING SURFACE **(WP 2200)**

Rédigé par / Written by	*Responsabilité / Responsibility*	*Date*	*Signature*
VOURCH Eric	Antenna Study Engineer	15/02/97	
Approbation / Approved			
CAILLE Gérard	Technical Manager of the study	15/2/97	
DURET Gilles	Head of Antenna Department	15/2/97	

Les informations contenues dans ce document demeurent propriété exclusive d'ALCATEL ESPACE et ne doivent pas être divulguées par le destinataire à des tiers sans l'accord écrit de la société.

The information contained in this document is proprietary to ALCATEL ESPACE and shall not be disclosed by the recipient to third persons without the written consent of the company

PROJECT DIFFUSION LIST

COMPANY	DEPARTMENT	DIF.	RECEIVER NAME
ALCATEL Espace	ASP		G. DURET
			G. CAILLE
			F. CROQ
			E. VOURCH
			P. BOSSHARD
	DTT		J. OSTER
ESA/ESTEC			G. VAN DOOREN (5 ex.)
CASA	Div. Espacio		M.J. MARTIN (3 ex.)
EPFL	LEMA		J. MOSIG
			A. ALVAREZ

Les informations contenues dans ce document demeurent propriété exclusive d'ALCATEL ESPACE et ne doivent pas être divulguées par le destinataire à des tiers sans l'accord écrit de la société.

ENREGISTREMENT DES EVOLUTIONS / CHANGE RECORD

ED/REV.	DATE	AUTORISATION AUTHORIZATION	DESCRIPTION DES EVOLUTIONS CHANGE RECORD	REDACTEUR AUTHOR
1/-	15/02/97		Final issue including ESA comments	E. VOURCH

The information contained in this document is proprietary to ALCATEL ESPACE. It shall not be disclosed by the recipient to third persons without the written consent of the company

Les informations contenues dans ce document demeurent propriété exclusive d'ALCATEL ESPACE et ne doivent pas être divulguées par le destinataire à des tiers sans l'accord écrit de la société.

The ...mation contained in this document is proprietary to ALCATEL ESPACE. ...all not be disclosed by the recipient to third persons without the written consent of the company

Les in... ...ons contenues dans ce document demeurent propriété exclusive d'ALC... ESPACE et ne doivent pas être divulguées par le destinataire à des tiers sans l'accord écrit de la société.

TABLE OF CONTENTS

The information contained in this document is proprietary to ALCATEL ESPACE and shall not be disclosed by the recipient to third persons without the written consent of the company

Les informations contenues dans ce document demeurent propriété exclusive d'ALCATEL ESPACE et ne doivent pas être divulguées par le destinataire à des tiers sans l'accord écrit de la société.

I INTRODUCTION

The preliminary trade-off (WP 1200) had led to the choice of a semi-active conformal array. The antenna is composed of 24 folded subarrays of 6 elementary radiators.

We have theoretically demonstrated that this antenna is able to comply with all the ESA specifications.

The objectives of this work package (WP 2200) consist in:

- manufacturing a single subarray
(choice of the elementary radiator, the suited repartitor...)
- proving that the radiated characteristics of the subarray permits to comply with the specifications of the whole antenna (EIRP, axial ratio, return loss, bandwidth, mass...)

The information contained in this document is proprietary to ALCATEL ESPACE and shall not be disclosed by the recipient to third persons without the written consent of the company

Les informations contenues dans ce document demeurent propriété exclusive d'ALCATEL ESPACE et ne doivent pas être divulguées par le destinataire à des tiers sans l'accord écrit de la société.

II THEORETICAL PERFORMANCES OF THE SUBARRAY

II-1 OUTPUTS OF PRELIMINARY TRADE-OFF

The profile of the subarray is the output of WP 1200: the subarray is constituted by 5 elementary radiators tilted from 25° to the revolution axis of the antenna and one radiator (the closest to nadir) tilted from 35° (fig. II-1-1).

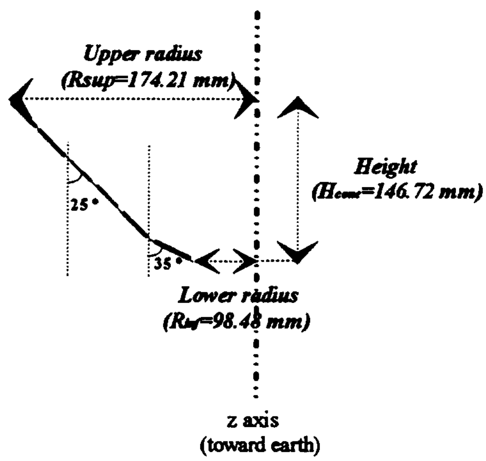

Fig. II-1-1: Profile of the subarray

The spacing between the elementary radiators is equal to 0.75 λ (27.42 mm).

**** the elementary radiator***

The elementary radiator is a double stacked patch in cavity (figure II-1-2). It has been developed during a previous study in the same bandwidth (8-8.4 GHz). This geometry is particularly interesting because coupling is highly reduced and mass minimized. Moreover, it provides good circular polarisation with only single port feeding. The electrical characteristics are summarised in the above figures (II-1-3 to II-1-5). For the theoretical results, the diagram will be fitted by a cosine function, without cross polarisation, as shown in figure II-1-3.

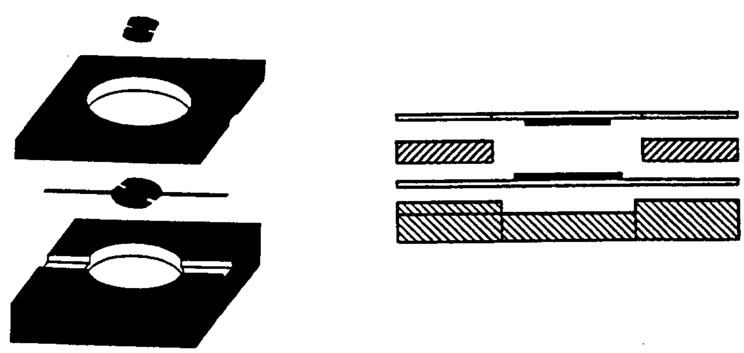

Fig. II-1-2: Elementary radiator geometry

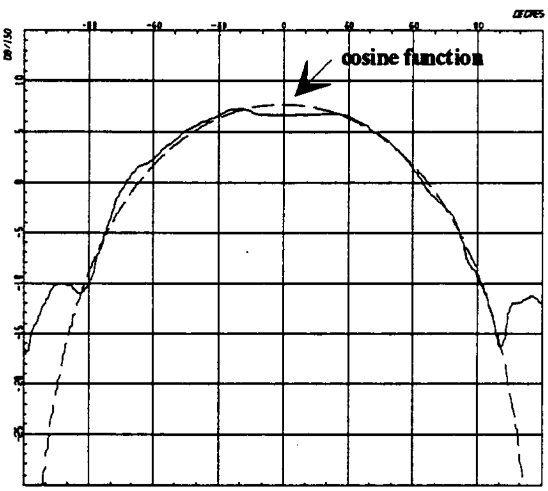

Fig. II-1-3: Radiated patterns of the Elementary Radiator at 8.2 GHz

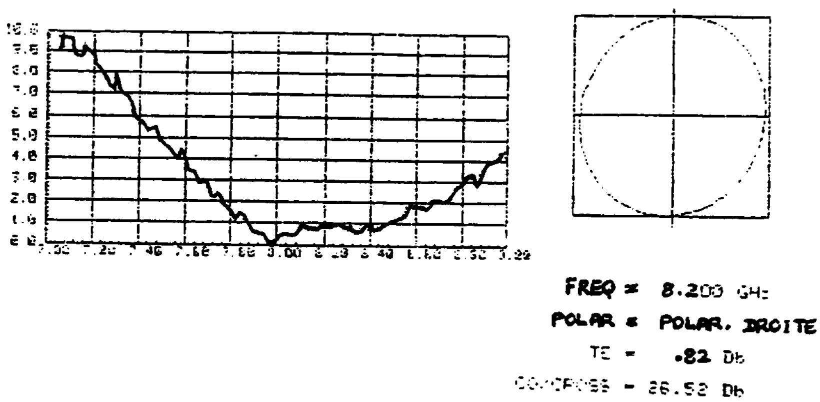

Fig. II-1-4: Axial ratio in the whole bandwidth

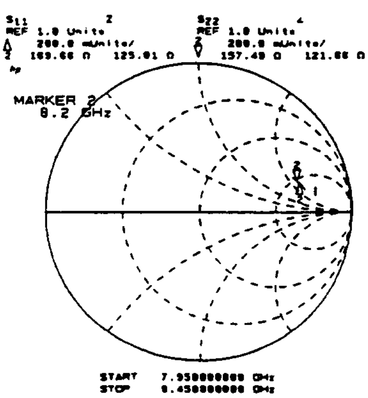

Fig. II-1-5: Input impedance in the bandwidth

The information contained in this document is proprietary to ALCATEL ESPACE and shall not be disclosed by the recipient to third persons without the written consent of the company

Les informations contenues dans ce document demeurent propriété exclusive d'ALCATEL ESPACE et ne doivent pas être divulguées par le destinataire à des tiers sans l'accord écrit de la société.

The information contained in this document is proprietary to ALCATEL ESPACE and shall not be disclosed by the recipient to third persons without the written consent of the company

**** the optimised excitations***

The optimised excitations were the following:

ER number	α_i	A_i*(in dB)*	ϕ_i*(in degrees)*
1	35	-0.27 dB	-116°
2	25	-0.23 dB	-80°
3	25	-0.13 dB	0°
4	25	0 dB	-25°
5	25	-0.27 dB	32°
6	25	-0.23 dB	-10°

The profile has been optimised with the condition $\alpha_1 \geq \alpha_2 \geq \alpha_3 \geq \alpha_4 \geq \alpha_5 \geq \alpha_6$ in order to reduce the electromagnetic coupling between elementary radiators. The amplitude excitations are quasi equal. It seems to be a little bit too restrictive but it can be explained by the constraints in a bandwidth of 5%.

In fact, all the line lengths for feeding the elementary radiators must be more or less equivalent. For example, let's take two accesses with 5 mm differences: if we suppose that the phase excitations at 8.2 GHz are respectively ϕ_1 and ϕ_2, a relative difference of 49° will be obtained in reason of the access line differences at 8.1 GHz. That's why, great attention must be observed in the design of the repartitor.

The radiated pattern of the theoretical subarray is given in figure II-1-8. The shape of the subarray is not exactly included in the mask. In order to understand the reason, it is necessary to draw (see figure II-1-6) what we can called the "transfer function" of the conical array (i.e. the difference between the directivity of the whole antenna and the directivity of a single subarray).

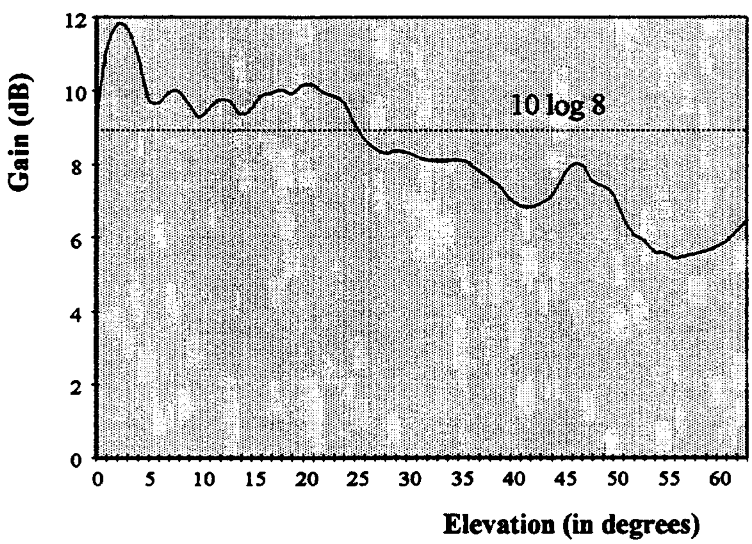

Fig. II-1-6: Transfer function of a conical array of 24 subarrays

Les informations contenues dans ce document demeurent propriété exclusive d'ALCATEL ESPACE et ne doivent pas être divulguées par le destinataire à des tiers sans l'accord écrit de la société.

The information contained in this document is proprietary to ALCATEL ESPACE and shall not be disclosed by the recipient to third persons without the written consent of the company
Les informations contenues dans ce document demeurent propriété exclusive d'ALCATEL ESPACE et ne doivent pas être divulguées par le destinataire à des tiers sans l'accord écrit de la société.

The analysis of figure II-1-6 shows that a conformal array could not be treated like a planar array; it means that azimuth and elevation are not separable.

In fact, we can distinguish three parts in the figure:

- the nadir, which is a particular case in a semi-active conical antenna: we have demonstrated in annexe 2 of WP1200 report that the level obtained by the whole antenna is equal to the sum of the level of a single subarray and 10 log (N_B) where N_B is the number of Butler matrixes in the whole antenna. The EIRP specification of ESA at nadir is 7.8 dB min and 9.8 dB max (if we assume 1 dB loss in the subarray). The minimum level of a single subarray at the nadir is equal to 7.8 - 10 log 8=-1.23 dB.
- low elevation (until 25 °): it can be observed that the transfer function is higher than 10 log 8. It is normal because for low elevation energy could be distributed on more than eight subarrays.
-high elevation (after 25° until 62.3°): higher the elevation is, lower the transfer level will be. So for the specification of a minimum directivity of 21 dBi for maximal elevation (1 dB loss included in the specification), the level of a single subarray must be 21 - 10 log 8 +2 # 14 dBi.

In order to understand what happened as soon as the elevation vary, the power obtained at the output of the Butlers (for an input of 1 on each input) is proposed above (fig. II-1-7):

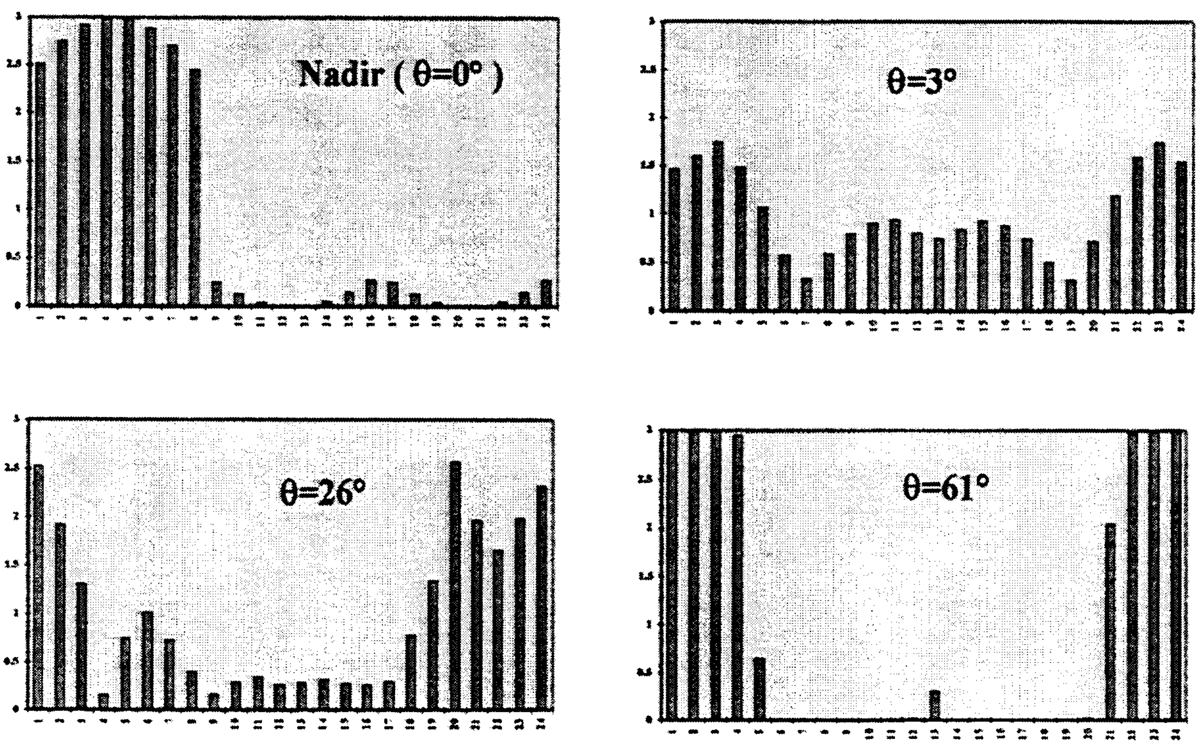

Fig. II-1-7: Output level of the subarray in function of elevation (input power of 1 on each input)

The information contained in this document is proprietary to ALCATEL ESPACE and shall not be disclosed by the recipient to third persons without the written consent of the company

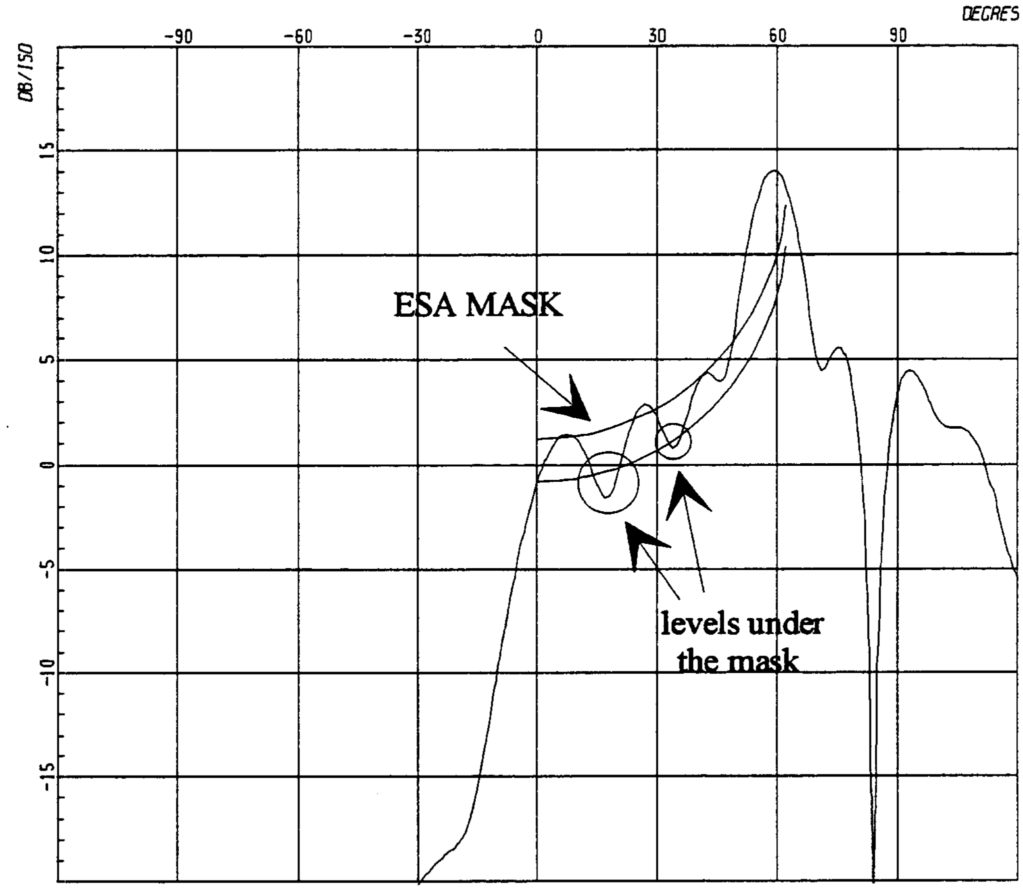

Fig. II-1-8: Theoretical radiated pattern of a single subarray

II-2 SIMULATED RESULTS WITH ACADEMY

The simulation of an equi-amplitude parallel repartitor with ACADEMY is not an easy work. The constraints of small size and equal line lengths leads to some discontinuities not easy to simulate with a "circuit software" (cross, tees, bend, meander...). The minimum line length will be the one of the farest radiator which is a drawback in terms of ohmic losses. No electromagnetic coupling is taken into account in the analysis which could be insufficient with such complex repartitor.

**** the printed circuit***

The geometry of the printed circuits is proposed in figure II-2-1. Quasi equal length are obtained for the 6 radiators; that's why extra lines are needed for the two central radiators. The phase excitations are given by the sum of the phase shift induced by the lines length and the elementary radiator rotation.

Les informations contenues dans ce document demeurent propriété exclusive d'ALCATEL ESPACE et ne doivent pas être divulgées par le destinataire à des tiers sans l'accord écrit de la société.

The information contained in this document is proprietary to ALCATEL ESPACE and shall not be disclosed by the recipient to third persons without the written consent of the company

Les informations contenues dans ce document demeurent propriété exclusive d'ALCATEL ESPACE et ne doivent pas être divulguées par le destinataire à des tiers sans l'accord écrit de la société.

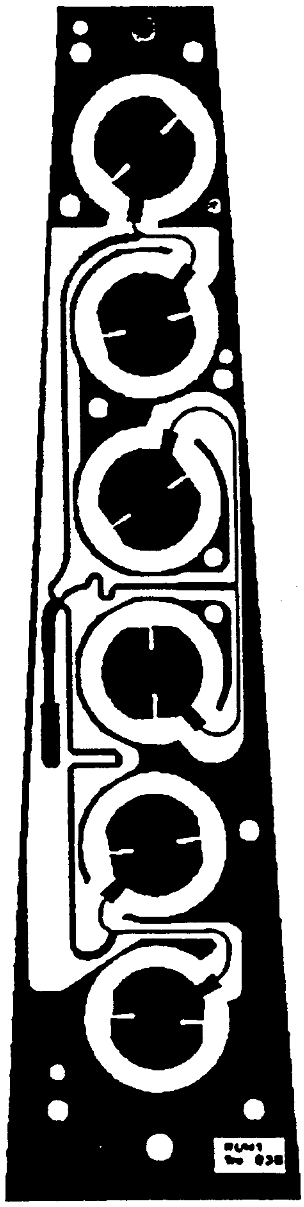

Fig. II-2-1: the parallel repartitor

*** the simulated excitations on the whole bandwidth**

The excitations (for both amplitude and phase) are given in figure II-2-2 and II-2-3. We can noticed that the dynamic range of the amplitude is included in a 1 dB range on the whole bandwidth whereas a good phase dispersion on the bandwidth is obtained for quasi all the radiators...except perhaps the radiator number 6 located in the superior cone tip (the one fartest to nadir).

The reason is quasi simple to understand: if we look at the dispersion of the patch just at the bottom (number 5), the phase dispersion is low so the length from the feeding to the input of the patch is quasi equal to the reference (patch number 3); this length is inferior and it induces phase dispersion. The phenomenon is the same for the radiators number 1 and 2 but lower visible.

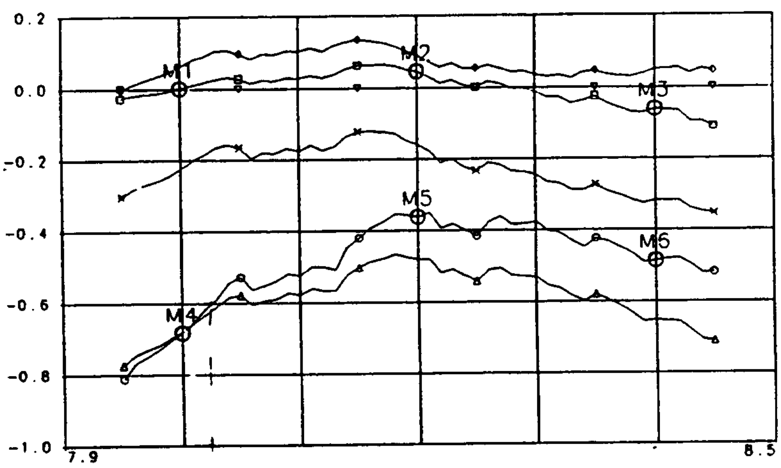

Fig. II-2-2: Amplitude simulated distribution along the subarray

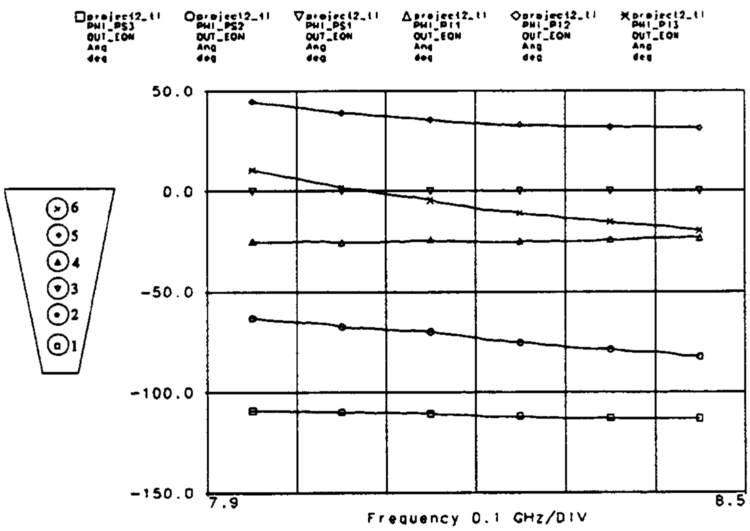

Fig. II-2-3: Phase simulated distribution along the subarray

The information contained in this document is proprietary to ALCATEL ESPACE and shall not be disclosed by the recipient to third persons without the written consent of the company
Les informations contenues dans ce document demeurent propriété exclusive d'ALCATEL ESPACE et ne doivent pas être divulguées par le destinataire à des tiers sans l'accord écrit de la société.

The information contained in this document is proprietary to ALCATEL ESPACE and shall not be disclosed by the recipient to third persons without the written consent of the company

Les informations contenues dans ce document demeurent propriété exclusive d'ALCATEL ESPACE et ne doivent pas être divulguées par le destinataire à des tiers sans l'accord écrit de la société.

Performance of the antenna on the whole bandwidth

The radiated power of the overall antenna, <u>for one channel</u>, at 8.2 GHz, is proposed in figure II-2-4 with a radiated power of -0.77 dBW. The ESA mask is drawn with a margin of 1 dB which corresponds to the antenna budget loss (see WP 1200 - page 3-15). It shows that this subarray permits to comply with the EIRP specifications. The compliance has been proved on the whole bandwidth by using the dispersions of the excitations (for both modulus and phasis) found by Academy.

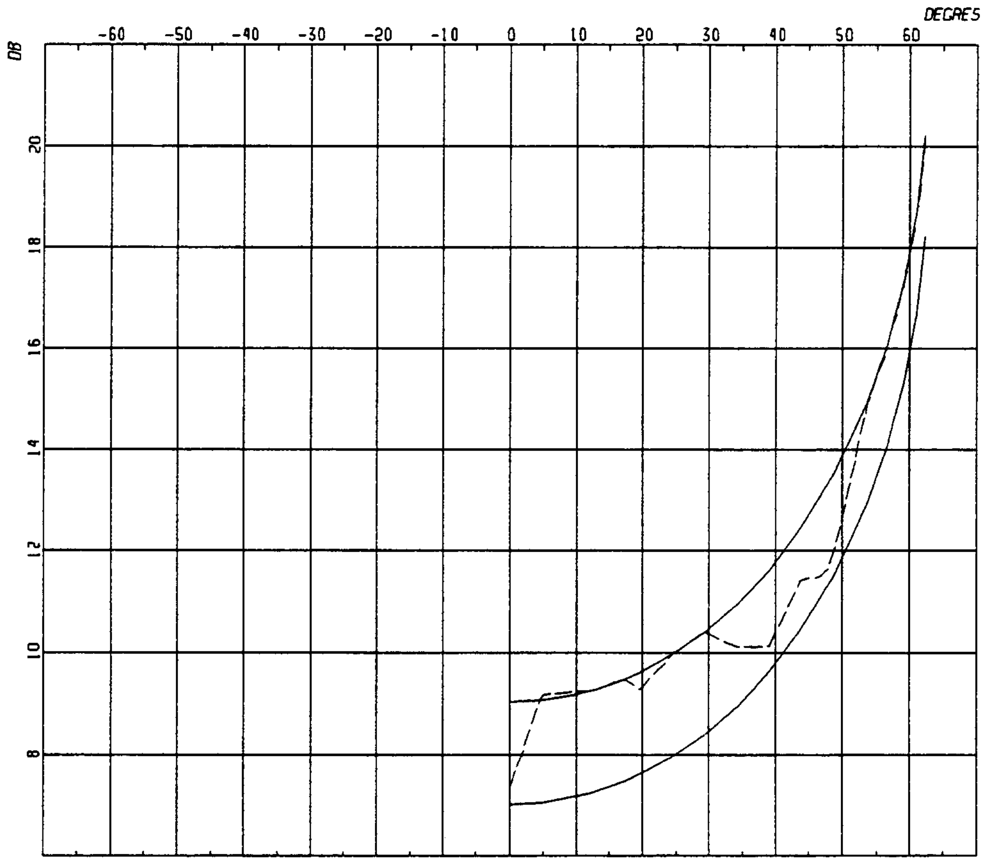

Fig. II-2-4: Simulated EIRP of the whole antenna at 8.2 GHz

The information contained in this document is proprietary to ALCATEL ESPACE and shall not be disclosed by the recipient to third persons without the written consent of the company

Les informations contenues dans ce document demeurent propriété exclusive d'ALCATEL ESPACE et ne doivent pas être divulguées par le destinataire à des tiers sans l'accord écrit de la société.

III MEASUREMENT OF THE SUBARRAY : FIRST RUN

III-1 MANUFACTURING OF THE SUBARRAY

The repartitor simulated by Academy is printed in stripline technology. Some rules for manufacturing must be respected (minimum width between lines and walls...); it implies that a minimum azimuth spacing of 29 mm is taken in the first crown of the conical array instead of 28 mm as suggested in the preliminary trade-off. The incidence in the whole antenna is to enlarge a little the upper radius (about 2 mm). The new configuration of the antenna is proposed in figure III-1-1.

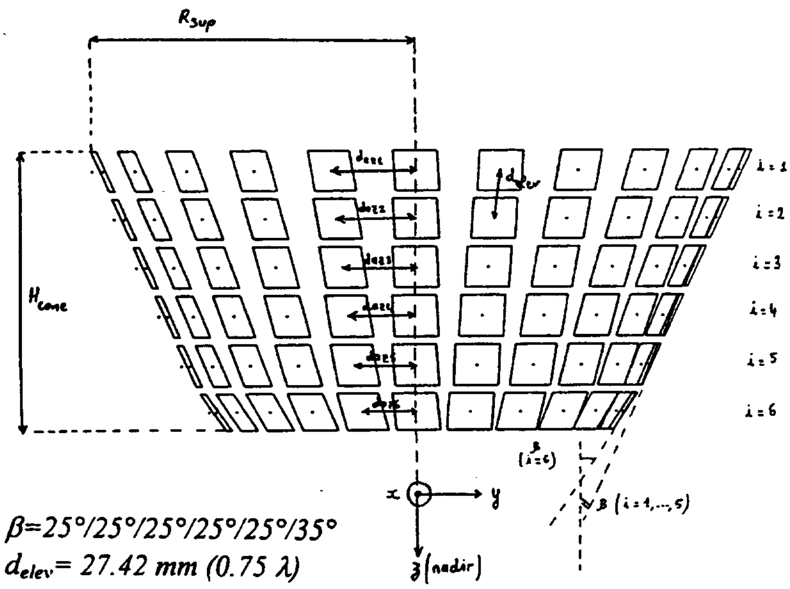

β=25°/25°/25°/25°/25°/35°
d_{elev}= 27.42 mm (0.75 λ)
d_{az1}= 44.80 mm (1.23 λ)
d_{az2}= 41.75 mm (1.14 λ)
d_{az3}= 38.70 mm (1.06 λ)
d_{az4}= 35.65 mm (0.98 λ)
d_{az5}= 32.60 mm (0.89 λ)
d_{az6}= 29.00 mm (0.79 λ)

H_{cone}= 146.72 mm
R_{sup}= 175.94 mm
N_{tot}= 24
N_{ER}= 6
N_B = 8
N=3

Fig. III-1-1: New configuration of the conical antenna (azimuth spacing=29 mm)

A picture of the subarray is presented in figure III-1-2. It permits to see the different part of the subarray: coaxial to stripline transition, printed circuits, cavity and upper patch.

Les info. contenues dans ce document demeurent propriété exclusive d'ALC SPACE et ne doiv. s être divulguées par le destinataire à des tiers sans l'accord écrit de la dé.
The ation contained in this document is proprietary to ALCATEL ESPA hall not be d. ed by the recipient to third persons without the written consent of the c y

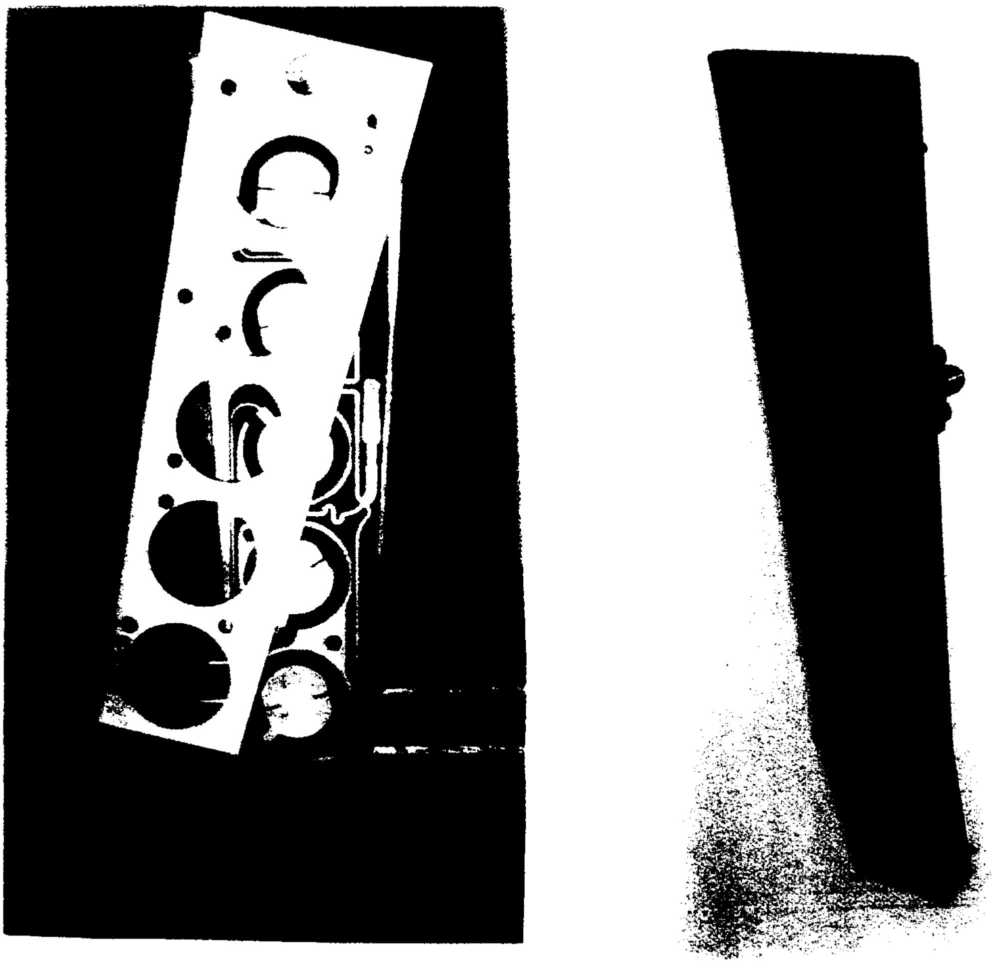

Fig. III-1-2: the subarray

The information contained in this document is proprietary to ALCATEL ESPACE and shall not be disclosed by the recipient to third persons without the written consent of the company
Les informations contenues dans ce document demeurent propriété exclusive d'ALCATEL ESPACE et ne doivent pas être divulguées par le destinataire à des tiers sans l'accord écrit de la société.

III-2 COMPARISON BETWEEN THEORY AND EXPERIMENT

III-2-1 THE ANECHOIC CHAMBERS

For the measurement, the far field distance is equal to $2D^2/\lambda$, where D represents the largest dimension of the antenna. For the Conformal Array subarray, D#4λ which gives 32 λ as minimum length to be in far field condition. The reference marks are described in figure III-2-1. The reference mark for computation is not the same than for measurement. It can be explained by the necessity to have the maximum radiation in the θ=0° axis for the precision of measurements.

(Xc, Yc, Zc) : Computation reference

(Xm, Ym, Zm) : Measurement reference

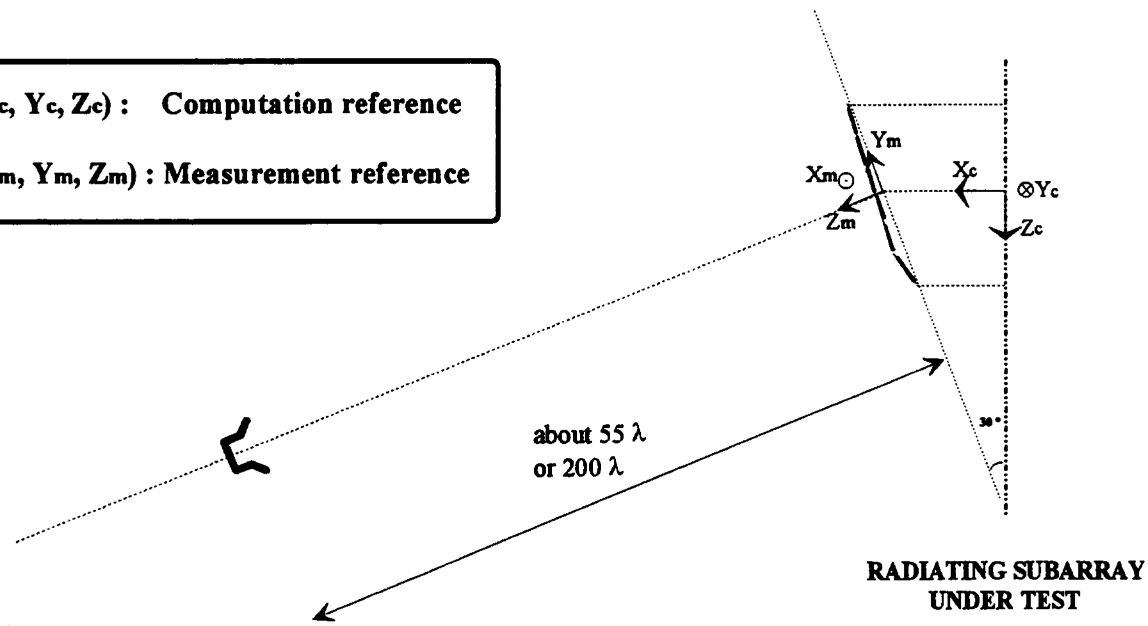

Fig. III-2-1: References

Two anechoic chambers will be used in function of their disponibility. In the first one, the subarray under test will be located at 55 λ of the feed corn. In the second one, it will be located at 200 λ of the feed corn. A software will recomputed the measurement at a distance of 1000 λ.

III-2-2 THE FIRST RUN

The first run has been measured in the 55 λ anechoic chamber. The field is re-computed in sufficient far-field conditions. The comparison between theory and experiment is proposed in fig. III-2-2.

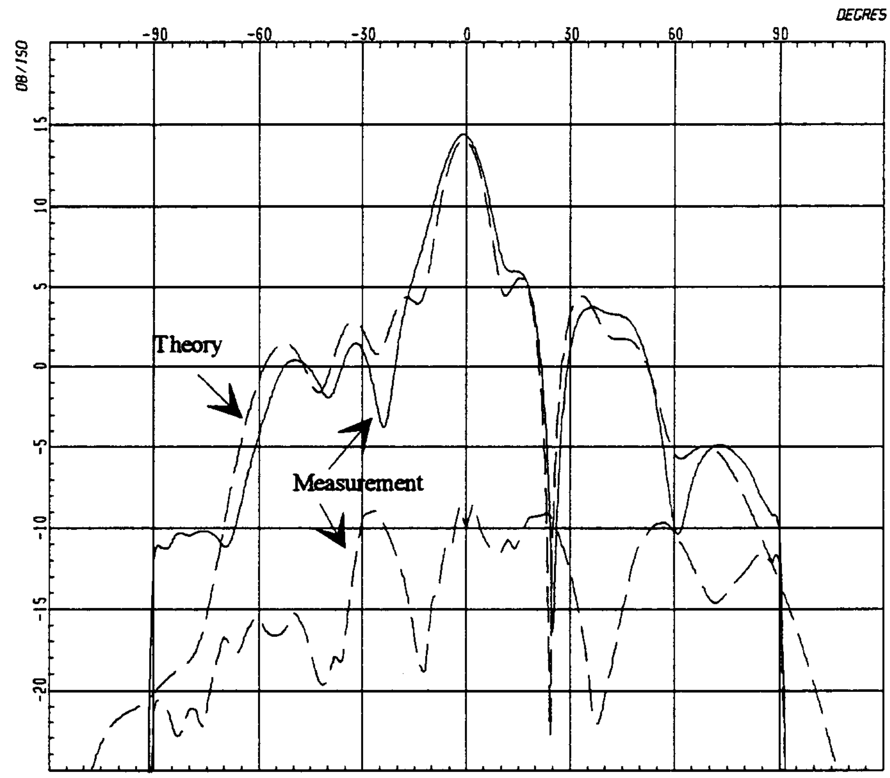

Fig. III-2-2: First run: theoretical / measured patterns

The compliance of the results with the theoretical prediction is unacceptable: some unexpected levels for both co and cross polarisations are observed.

One of the possible reason for explaining the differences can be the non accuracy of the simulations: the printed circuits includes a lot of discontinuities (the input cross, meanders, tees, bends...) and no electromagnetic coupling between elements is taken into account. The coaxial to stripline transition is not taken into account in the analysis. It means that Academy software is insufficient to accurately simulate the subarray.

Some parts of the repartitor can be simulated on Momentum software, included in Academy 6.0. The theoretical principle of Momentum is based on the Integral Equation technique solved by a Method of Moments. The coupling between the printed circuits could then be taken into account. This simulation is time consuming for good accuracy of the results: a meshing of 30

The ...mation contained in this document is proprietary to ALCATEL ESPACE. ...all not be disclosed by the recipient to third persons without the written consent of the company
Les in...ons contenues dans ce document demeurent propriété exclusive d'ALC... ESPACE et ne doivent pas être divulguées par le destinataire à des tiers sans l'accord écrit de la société.

cells by guided wavelength must be respected and meshing must be very fine at the discontinuities in order to let the maximum of freedom degrees to the current lines.

One of the first critical point seems to be the input cross. The Momentum meshing and the results of simulation are presented in figure III-2-3 and III-2-4.

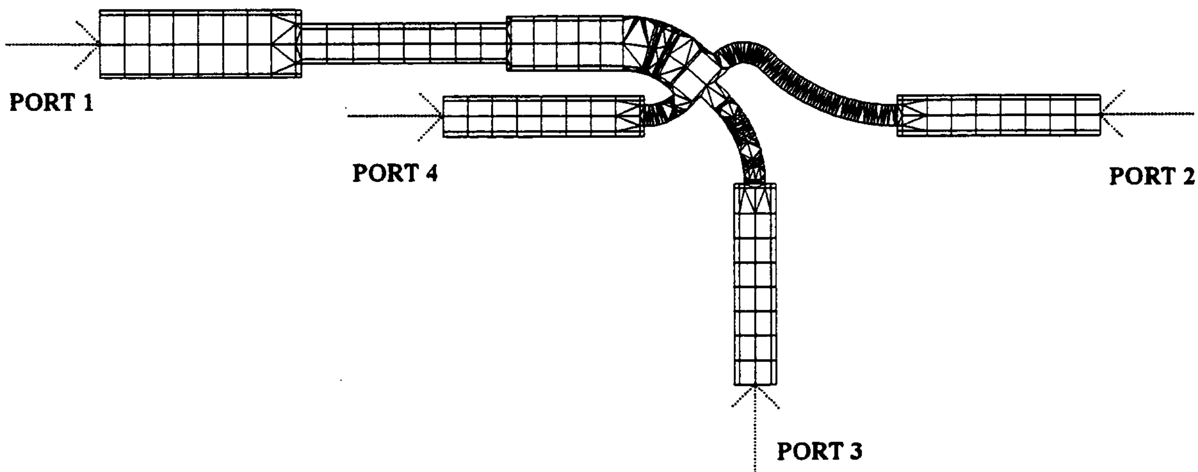

Fig. III-2-3: Meshing of the input cross

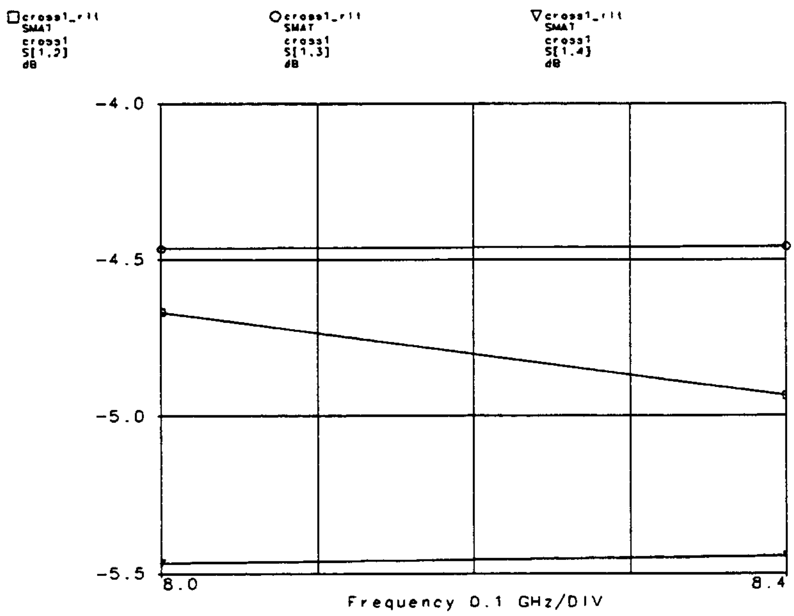

Fig. III-2-4: Scattering parameters of the cross

The Momentum simulation of the input cross shows clearly that energy is not equallly distributed between the 6 radiators: 1 dB difference is observed between the two central radiators (number 3 and 4) and the radiators 1 and 2. The same simulation with Academy gives an equi-amplitude distribution between the three accesses. It confirms that Academy is not too accurate for simulating the Conformal Array repartitor.

The information contained in this document is proprietary to ALCATEL ESPACE and shall not be disclosed by the recipient to third persons without the written consent of the company

Les informations contenues dans ce document demeurent propriété exclusive d'ALCATEL ESPACE et ne doivent pas être divulguées par le destinataire à des tiers sans l'accord écrit de la société.

The information contained in this document is proprietary to ALCATEL ESPACE and shall not be disclosed by the recipient to third persons without the written consent of the company

The analysis of the whole repartitor is presented in figure III-2-5 and III-2-6 (meshing + comparison between Momentum and Measurement). The conclusions of this analysis is that Momentum gives better results than Academy but don't take into account all the coupling phenomenon of the repartitor.

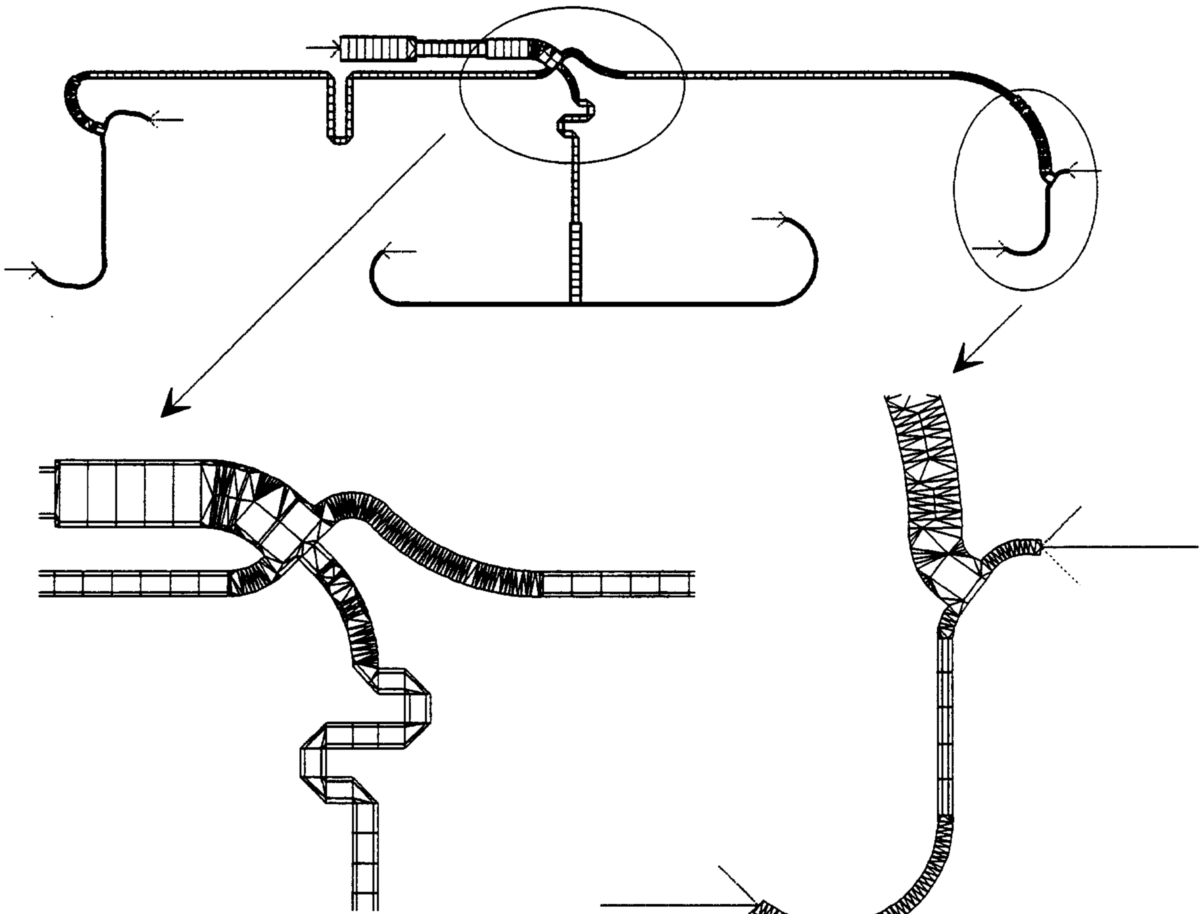

Fig. III-2-5: Meshing of the whole repartitor

Les informations contenues dans ce document demeurent propriété exclusive d'ALCATEL ESPACE et ne doivent pas être divulguées par le destinataire à des tiers sans l'accord écrit de la société.

The information contained in this document is proprietary to ALCATEL ESPACE and shall not be disclosed by the recipient to third persons without the written consent of the company

Les informations contenues dans ce document demeurent propriété exclusive d'ALCATEL ESPACE et ne doivent pas être divulguées par le destinataire à des tiers sans l'accord écrit de la société.

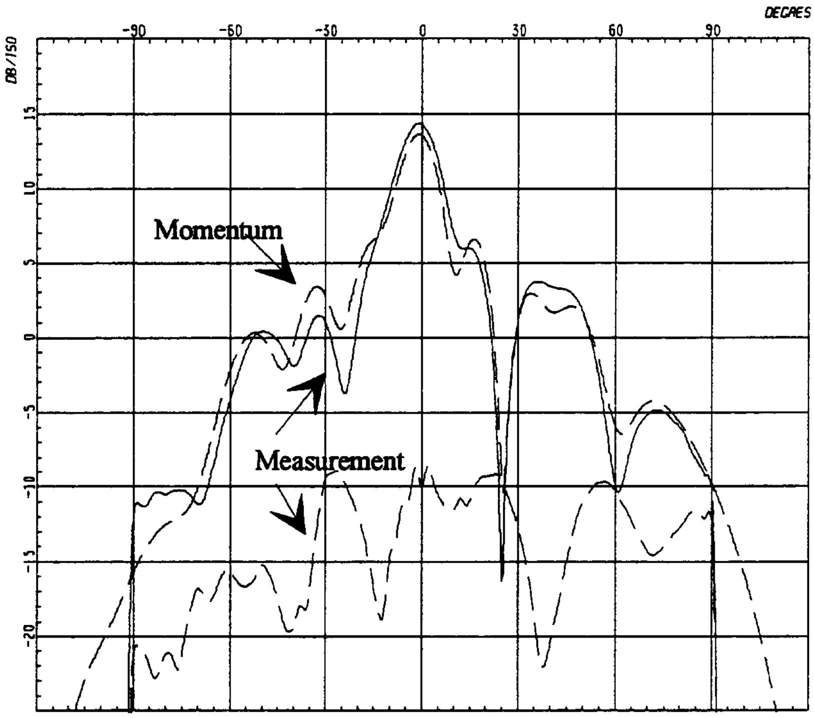

Fig. III-2-6: Comparison between Momentum /Measurement

Apparently, the accurate simulation of this repartitor is a very hard work. That's why, the best way for analysing the problems is to recompute the excitations from the measurement; it is done by an inverse Fourier Transform in a specific software developed in Alcatel during previous contract: this software is called SPDRI.

The results of this analysis are reported in the table here above:

ER number	Academy a_i	Academy ϕ_i	SPDRI a_i	SPDRI ϕ_i
1	-0.27 dB	-116°	-2.66 dB	-109°
2	-0.23 dB	-80°	-1.64 dB	-81°
3	-0.13 dB	0°	0 dB	-13°
4	0 dB	-25°	-0.22 dB	-13°
5	-0.27 dB	32°	-2.99 dB	37°
6	-0.23 dB	-10°	-4.35 dB	-23°

The analysis of this table permits to show that the main problem is the amplitude distribution. In fact, the excitations dynamic is greater than 4 dB instead of 0.3 dB -theoretically expected- whereas the phase distribution is well simulated because 13° difference between expected results and measured ones are obtained. The radiated pattern computed with the excitations found by SPDRI gives good agreement with measurement (see figure III-2-7)

The ...ation contained in this document is proprietary to ALCATEL ESPACE ...ll not be di...sed by the recipient to third persons without the written consent of the com...

Les in...ns contenues dans ce document demeurent propriété exclusive d'ALC... ESPACE et ne d... pas être divulguées par le destinataire à des tiers sans l'accord écrit de l... ...iété.

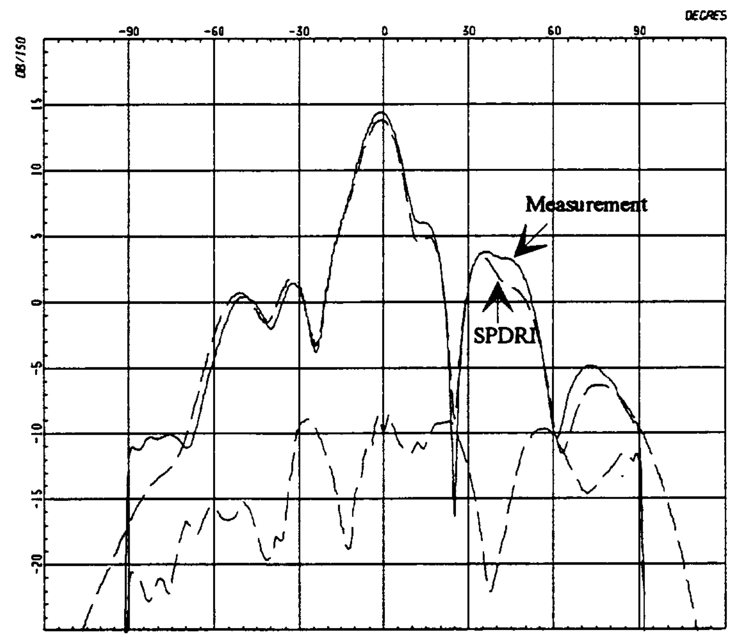

Fig. III-2-7:Comparison between the pattern found by SPDRI and the measurement

It leads to the following logic for the development of the subarray: considering that the amplitude given by SPDRI is the one of the subarray and try to find a compliant phase excitation over the subarray in order to be compliant.

It is evident that a few runs will be necessary to be fully compliant with the specifications.

IV PERFORMANCES ON THE WHOLE BANDWIDTH

IV-1-1 FROM THE FIRST RUN TO THE FINAL ONE

The excitations which permit to be compliant with ESA specifications, including the amplitude distribution found by SPDRI software, is contained in the following table:

ER number	α_i	A_i*(in dB)*	ϕ_i*(in degrees)*
1	35	-2.66 dB	-111°
2	25	-1.64 dB	-79°
3	25	0 dB	0°
4	25	-0.22 dB	-31°
5	25	-2.99 dB	26°
6	25	-4.35 dB	-10°

Phase only optimisation

The amplitude are similar than the one found by SPDRI; concerning the phases the higher phase difference is obtained for the radiator number 4 with a difference of +18°. This new excitations gives the radiated pattern of figure IV-1-1. Comparison with theoretical estimations are proposed here above.

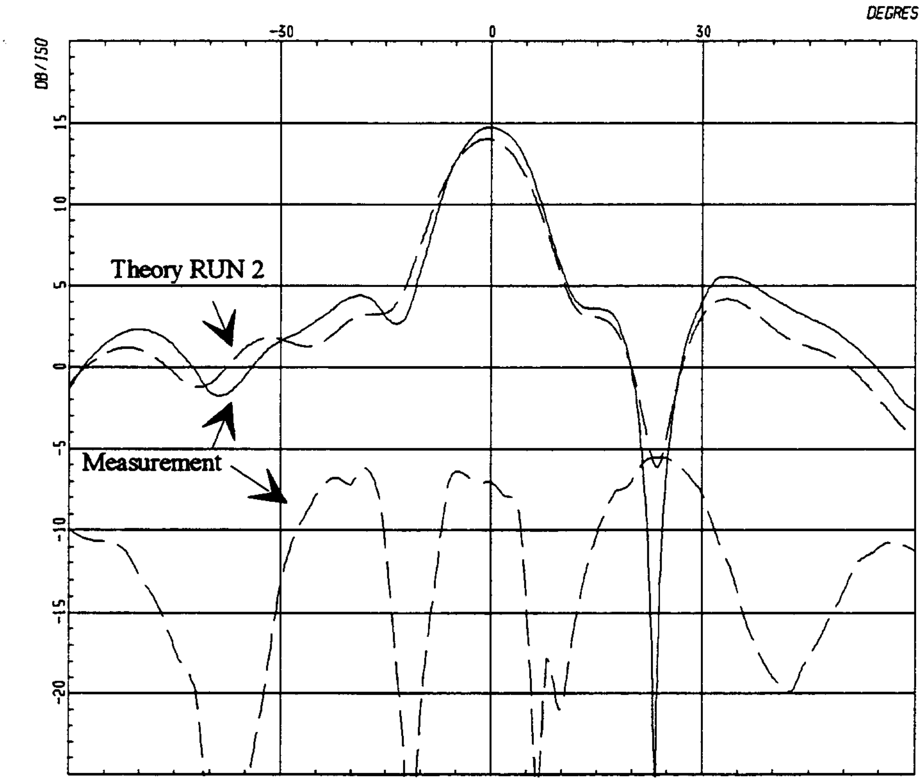

Fig. IV-1-1: Radiated pattern of RUN 2

This new pattern permits to be *quasi compliant* for EIRP specification at 8.2 GHz (see figure IV-1-2).

The ... mation contained in this document is proprietary to ALCATEL ESPACE ... nall not be disclosed by the recipient to third persons without the written consent of the company
Les in... ons contenues dans ce document demeurent propriété exclusive d'ALC... ESPACE et ne doivent pas être divulguées par le destinataire à des tiers sans l'accord écrit de la société.

The in...mation contained in this document is proprietary to ALCATEL ESPACE a... shall not be disclosed by the recipient to third persons without the written consent of the company

Les info... ...ions contenues dans ce document demeurent propriété exclusive d'ALCA... ESPACE et ne doivent pas être divulguées par le destinataire à des tiers sans l'accord écrit de la société.

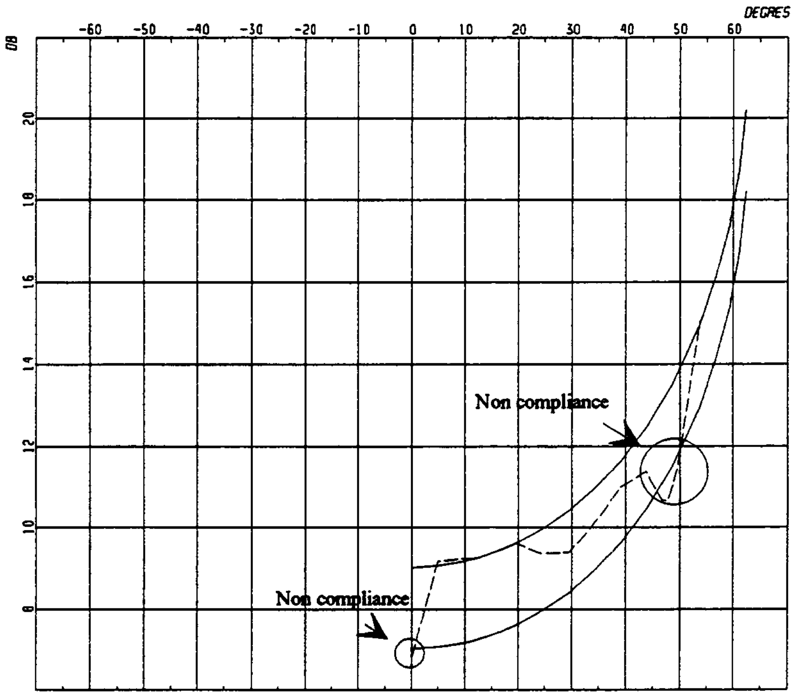

Fig. IV-1-2: EIRP simulation for RUN 2

The comparison is better than RUN 1. It is interesting to analyse the results of SPDRI by comparing the predicted results to the ones of SPDRI. These results are reported in the following table:

ER number	THEORY a_i	THEORY ϕ_i	SPDRI a_i	SPDRI ϕ_i
1	-2.66 dB	-111°	-3.72 dB	-115°
2	-1.64 dB	-79°	-2.52 dB	-81°
3	0 dB	0°	0 dB	0°
4	-0.22 dB	-31°	-3.10 dB	-32°
5	-2.99 dB	26°	-1.39 dB	25°
6	-4.35 dB	-10°	-4.13 dB	-2°

It is interesting to notice that the maximum phase difference is now lower than 8° (obtained for the radiator number 6). Moreover, the amplitude distribution is considerably modified. It can be explained by the fact that the feeding line of 142 Ω is not very well matched to the input impedance of the radiator. It permits to define another logic for the following runs: try to modify a minimum number of radiator excitations.

One of the important problem of this subarray concerns the cross polarisation level. The axial ratio of the antenna is drawn versus elevation angle at 8.3 GHz (worst case) in figure IV-1-3.

The information contained in this document is proprietary to ALCATEL ESPACE and shall not be disclosed by the recipient to third persons without the written consent of the company

Les informations contenues dans ce document demeurent propriété exclusive d'ALCATEL ESPACE et ne doivent pas être divulguées par le destinataire à des tiers sans l'accord écrit de la société.

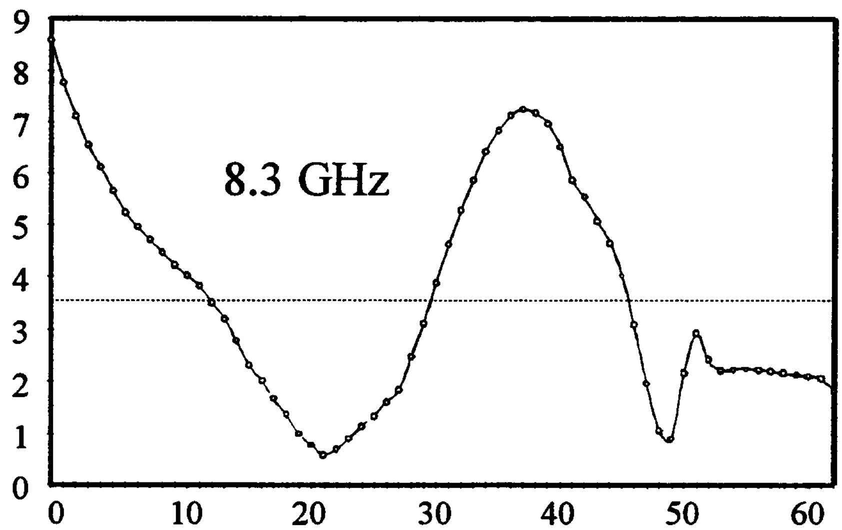

Fig. IV-1-3: Axial ratio of the subarray at 8.3 GHz

The specification of 3.5 dB for the whole range of elevation angle is not reached. At the nadir, an axial ratio just lower than 9 dB is obtained...It is unacceptable because it corresponds to an isolation of 7 dB between the co-polarisation and the cross-polarisation.

The main reason for bad cross-polarisation level is certainly the effects of the coaxial to stripline input transition. That's why a new design of the repartitor is proposed by isolating the excitations from the rest of the printed circuits. Figure IV-1-4 illustrates the new design of the repartitor by comparison to the previous one. A quarter wavelength connection to the mass can be previewed to confine the current lines at the level of the transition and the printed lines are distant from the transition.

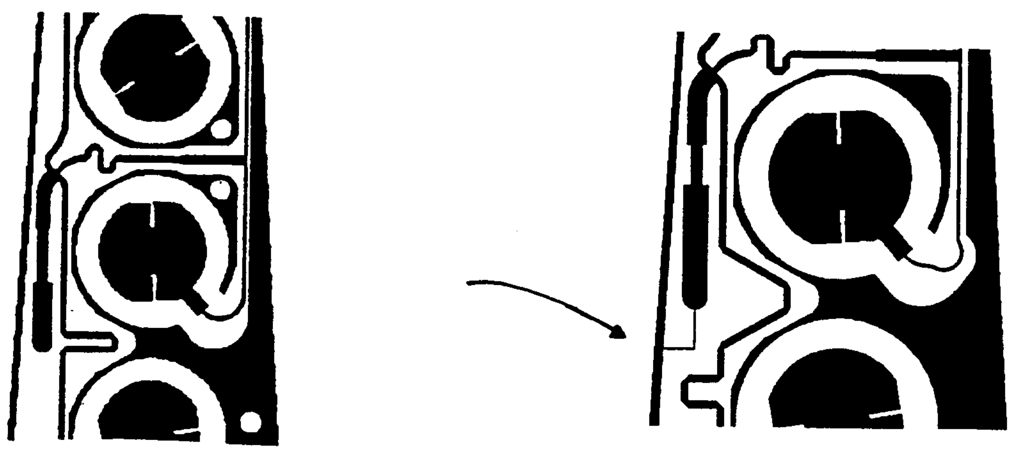

Fig. IV-1-4: Modification of the repartitor for RUN 3

The information contained in this document is proprietary to ALCATEL ESPACE and shall not be disclosed by the recipient to third persons without the written consent of the company
Les informations contenues dans ce document demeurent propriété exclusive d'ALCATEL ESPACE et ne doivent pas être divulguées par le destinataire à des tiers sans l'accord écrit de la société.

The excitations which permit to be compliant with ESA specifications, including the amplitude distribution found by SPDRI software during RUN 2, are contained in the following table:

ER number	α_i	A_i*(in dB)*	ϕ_i*(in degrees)*
1	35	-3.72 dB	-115°
2	25	-2.52 dB	-81°
3	25	0 dB	0°
4	25	-3.10 dB	-32°
5	25	-1.39 dB	25°
6	25	-4.13 dB	-17°

Only one radiator has changed: the number 6 in which a phase difference of -15° is achieved. The radiated pattern is proposed in figure IV-1-5 and this new excitations permits to be compliant with ESA EIRP requirements on the whole bandwidth (see figure IV-1-6) -except from the level at the nadir which 0.2 dB under specification at 8.2 GHz and 0.3 dB at 8.3 GHz).

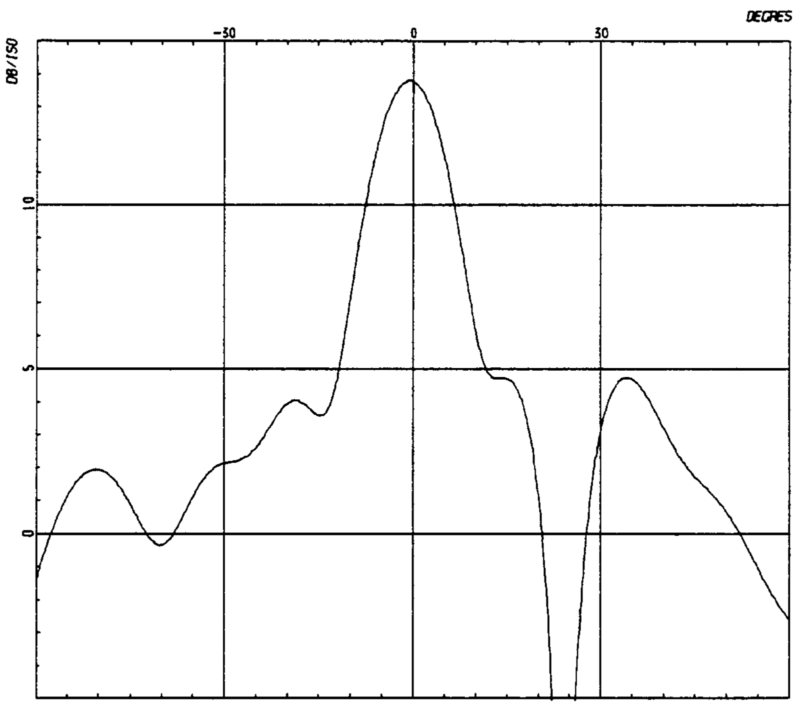

Fig. IV-1-5: Radiated pattern at 8.2 GHz for RUN 3 (Theory)

The information contained in this document is proprietary to ALCATEL ESPACE and shall not be disclosed by the recipient to third persons without the written consent of the company

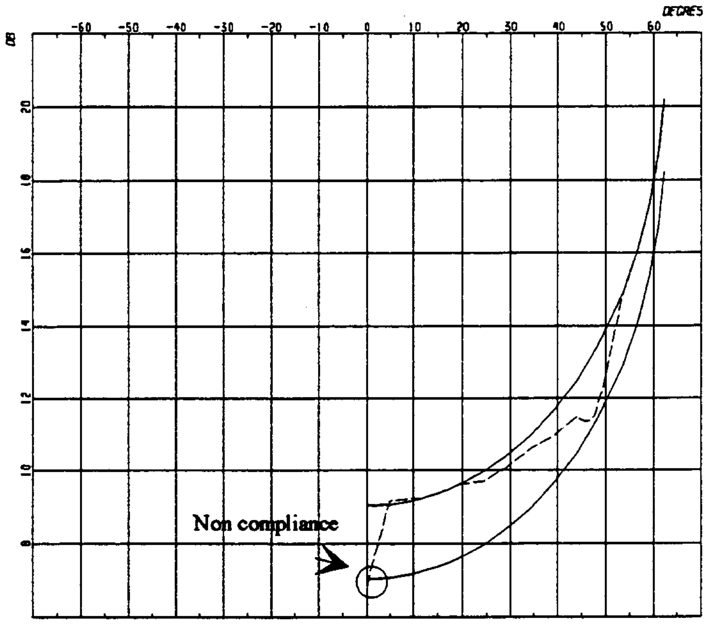

Fig. IV-1-6: EIRP simulation for RUN 3 at 8.2 GHz (Theory)

The measurement of RUN 3 is compared with the theoretical estimations in figure IV-1-7. A good agreement between measured and expected results is obtained. The level of cross-polarisation is better than for RUN 2 (fig. IV-1-7 compared to fig. IV-1-1).

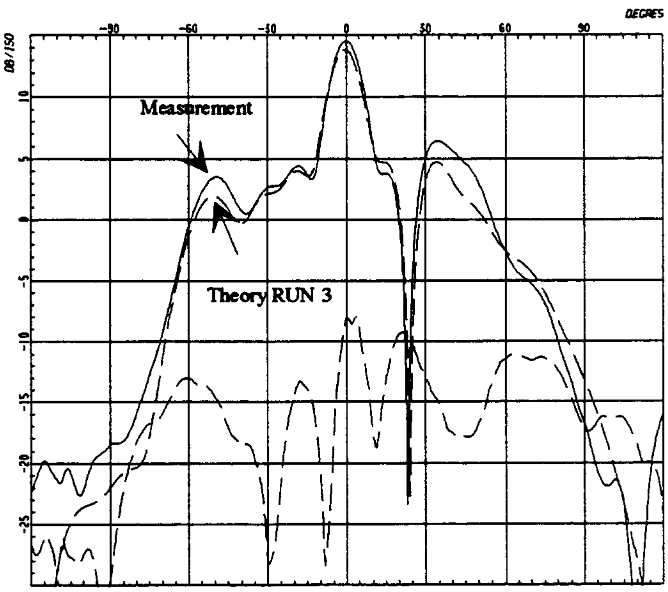

Fig. IV-1-7: Comparison between theory and measurement for RUN 3

Les informations contenues dans ce document demeurent propriété exclusive d'ALCATEL ESPACE et ne doivent pas être divulguées par le destinataire à des tiers sans l'accord écrit de la société.

The information contained in this document is proprietary to ALCATEL ESPACE and shall not be disclosed by the recipient to third persons without the written consent of the company

Les informations contenues dans ce document demeurent propriété exclusive d'ALCATEL ESPACE et ne doivent pas être divulguées par le destinataire à des tiers sans l'accord écrit de la société.

It is also interesting to analyse the results of SPDRI by comparing the predicted results to the ones of SPDRI. These results are reported in the following table:

ER number	THEORY a_i	THEORY ϕ_i	SPDRI a_i	SPDRI ϕ_i
1	-3.72 dB	-115°	-4.06 dB	-122°
2	-2.52 dB	-81°	-2.56 dB	-88°
3	0 dB	0°	0 dB	0°
4	-3.10 dB	-32°	-3.23 dB	-35°
5	-1.39 dB	25°	-0.73 dB	27°
6	-4.13 dB	-17°	-3.82 dB	-15°

It can be noticed that the amplitude distribution has not considerably changed and the phase distribution is near than the one predicted. The compliance of the radiated characteristics of the subarray will be detailed in the next part of the chapter. This third run will be the final one for the design of the subarray.

IV-2 FINAL SUBARRAY PERFORMANCES

The final repartitor is presented in figure IV-2-1.

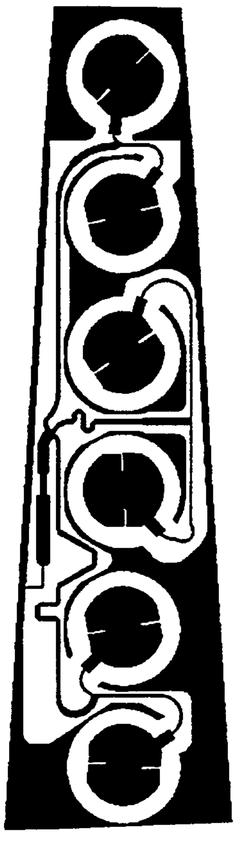

Fig. IV-2-1: Final repartitor

The information contained in this document is proprietary to ALCATEL ESPACE and shall not be disclosed by the recipient to third persons without the written consent of the company

*** return loss**

The return loss of the subarray is presented in figure IV-2-2. It is fully compliant with the specifications on the whole bandwidth (14 dB for the whole bandwidth)

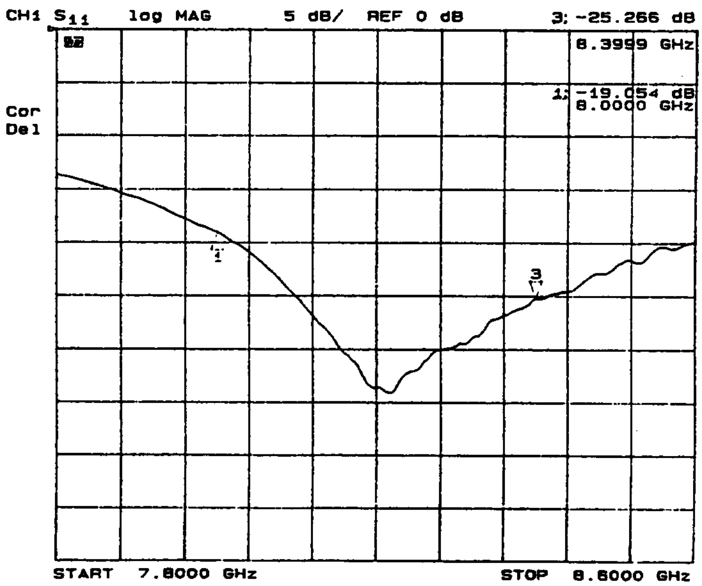

Fig. IV-2-2: Return loss of the subarray on the whole bandwidth

*** radiated patterns**

The radiated patterns of the subarray are presented for 8.1 GHz, 8.2 GHz and 8.3 GHz in figure IV-2-3, 4 and 5. A good level of cross polarisation is obtained on the bandwidth.

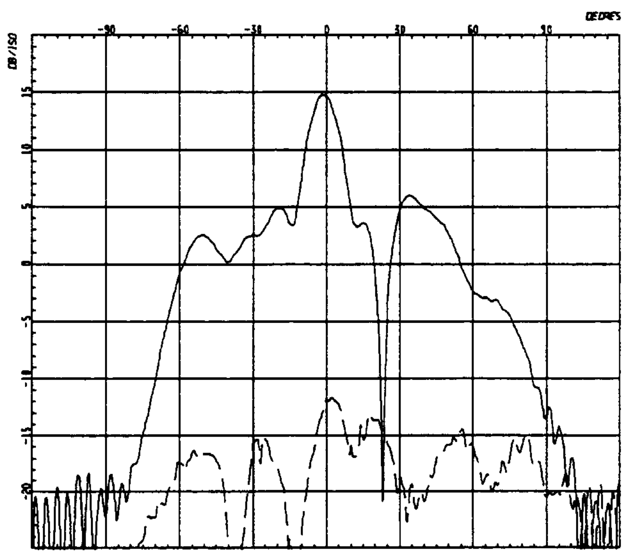

Fig. IV-2-3:Radiated patterns at 8.1 GHz

Les informations contenues dans ce document demeurent propriété exclusive d'ALCATEL ESPACE et ne doivent pas être divulguées par le destinataire à des tiers sans l'accord écrit de la société.

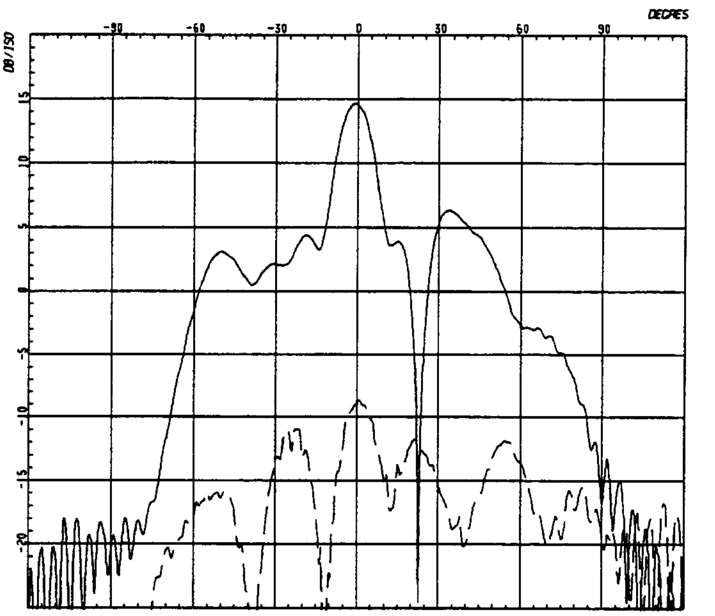

Fig. IV-2-4:Radiated patterns at 8.2 GHz

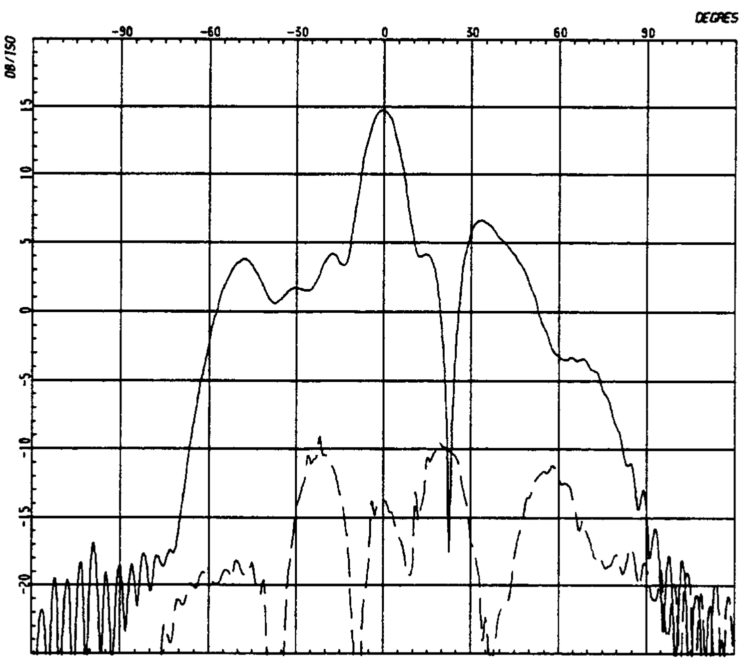

Fig. IV-2-5:Radiated patterns at 8.3 GHz

The information contained in this document is proprietary to ALCATEL ESPACE and shall not be disclosed by the recipient to third persons without the written consent of the company

Les informations contenues dans ce document demeurent propriété exclusive d'ALCATEL ESPACE et ne doivent pas être divulguées par le destinataire à des tiers sans l'accord écrit de la société.

The information contained in this document is proprietary to ALCATEL ESPACE and shall not be disclosed by the recipient to third persons without the written consent of the company

Les informations contenues dans ce document demeurent propriété exclusive d'ALCATEL ESPACE et ne doivent pas être divulguées par le destinataire à des tiers sans l'accord écrit de la société.

Axial Ratio

The axial ratio of the subarray is determined by the following formula:

$$A.R\ (\text{in dB}) = 20 \log ((ISOL-1)/(ISOL+1))$$

where ISOL= CO/CROSS (in amplitude value)

The axial ratio is drawn in function of the elevation angle theta in figure IV-2-6.

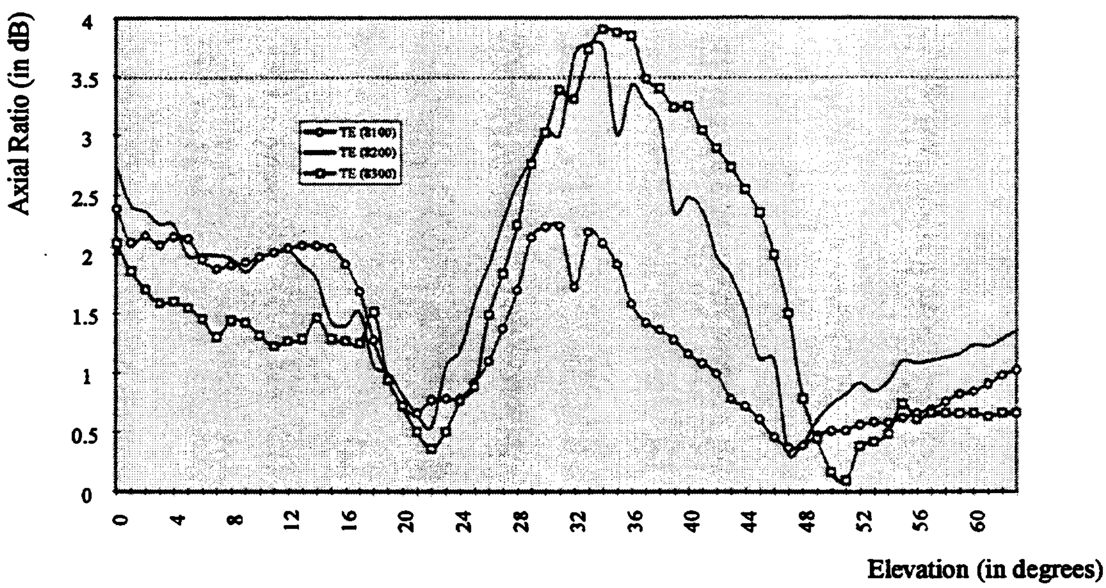

Fig. IV-2-6:Axial ratio on the bandwidth

The specification (see chapter 4) is 3.5 dB on the full range of elevation and for the whole bandwidth (dotted line in the figure). We can see that a short non compliance at 8.2 and 8.3 GHz for angles round 30° is observed. But, it will be without effects on the ESA requirements of 3.5 dB for the overall antenna on the whole bandwidth (see next part).

The information contained in this document is proprietary to ALCATEL ESPACE and shall not be disclosed by the recipient to third persons without the written consent of the company

*** Gain**

The measured gain is presented in figure IV-2-7. It is compliant with the loss budget of chapter 3 (page 3-15). The total losses (ohmic+VSWR) are equal to -0.78 dB at 8.1 GHz, -0.73 dB at 8.2 GHz and -0.76 dB at 8.3 GHz.

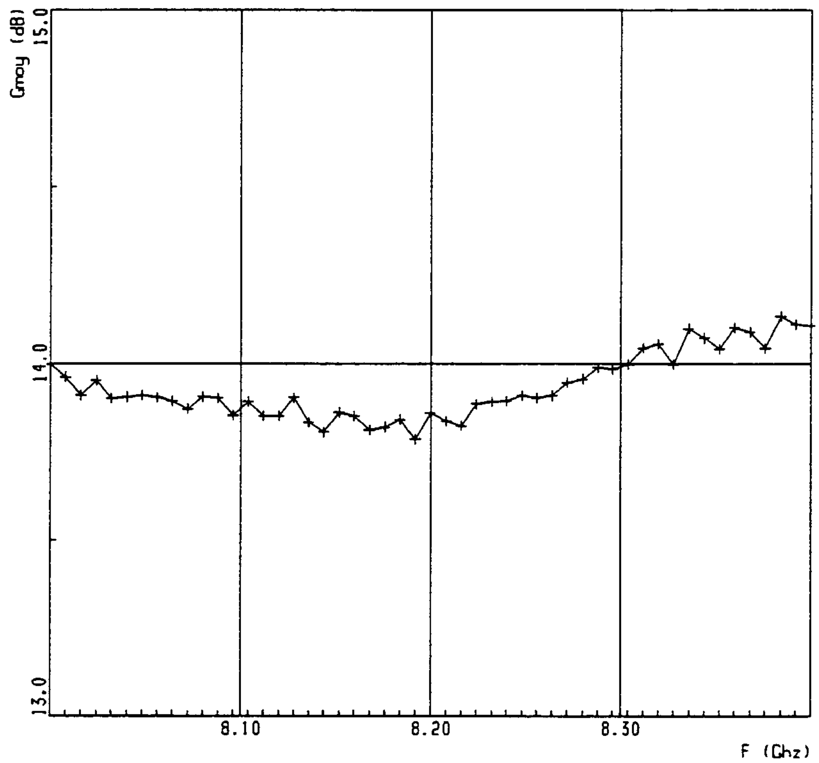

Fig. IV-2-7:Gain of the subarray

*** Mass**

The mass of the subarray is actually 130 g instead of 90 g specified. The specification was based on a previous subarray of 4 patches. In spite of this non compliance on the mass of the subarray, the final mass of the breadboard had been estimated round 7 Kg instead of 10 Kg specified by ESA.

We are actually trying to reduce the mass of the subarray by 30 or 40 g in order to design a more attractive antenna mechanically and thermally compliant with the mission (40 g saved in a subarray will induce a little less than 1 Kg saved on the final breadboard...which is not negligible).

Les informations contenues dans ce document demeurent propriété exclusive d'ALCATEL ESPACE et ne doivent pas être divulguées par le destinataire à des tiers sans l'accord écrit de la société.

IV-3 THE WHOLE ANTENNA PERFORMANCES

*** Radiated power**

The radiated power obtained with an input power of -0.77 dBW is presented in figure IV-3-1 for 8.1 GHz, 8.2 GHz and 8.3 GHz. The characteristics are drawn increasing the ESA mask with 1 dB loss. In this 1 dB, 0.2 dB is included as the loss in the bandwidth; that's why, the radiated power could be consider compliant at 8.1 and 8.2 GHz but not at 8.3 GHz (nadir level and 45 to 50° elevation levels).

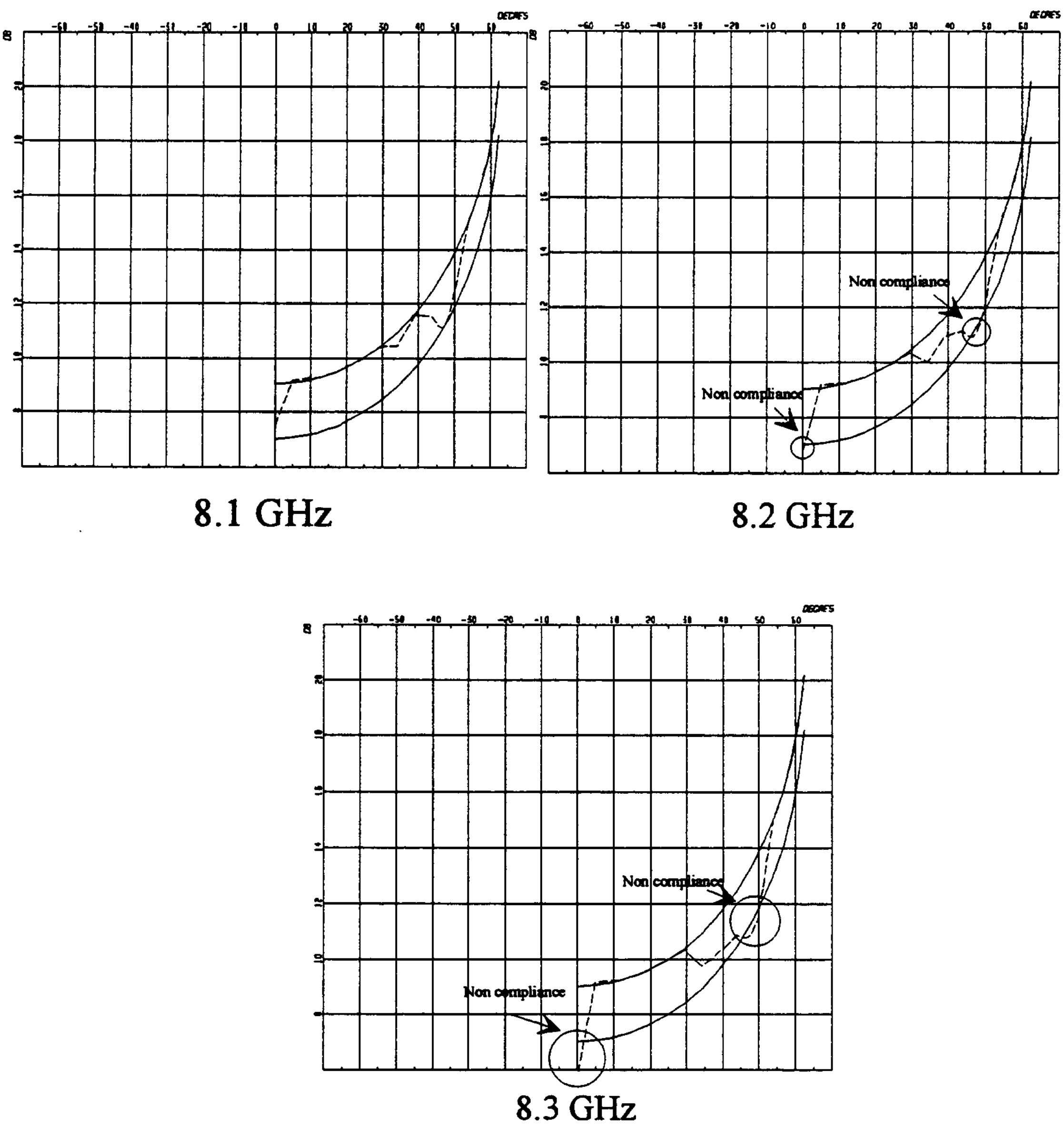

Fig. IV-3-1: EIRP of the antenna with 25°/25°/25°/25°/25°/35° profile at 8.1 GHz, 8.2 GHz and 8.3 GHz

The information contained in this document is proprietary to ALCATEL ESPACE and shall not be disclosed by the recipient to third persons without the written consent of the company

Les informations contenues dans ce document demeurent propriété exclusive d'ALCATEL ESPACE et ne doivent pas être divulguées par le destinataire à des tiers sans l'accord écrit de la société.

The information contained in this document is proprietary to ALCATEL ESPACE and shall not be disclosed by the recipient to third persons without the written consent of the company

Les informations contenues dans ce document demeurent propriété exclusive d'ALCATEL ESPACE et ne doivent pas être divulguées par le destinataire à des tiers sans l'accord écrit de la société.

For being fully compliant, the idea consists in tilting the subarray by 1° more. It means that the profile of the subarray becomes 26°/26°/26°/26°/26°/36°. Very low incidence is obtained on the antenna new geometrical characteristics: increase of upper radius, decrease of height of the conical array (see figure IV-3-2).

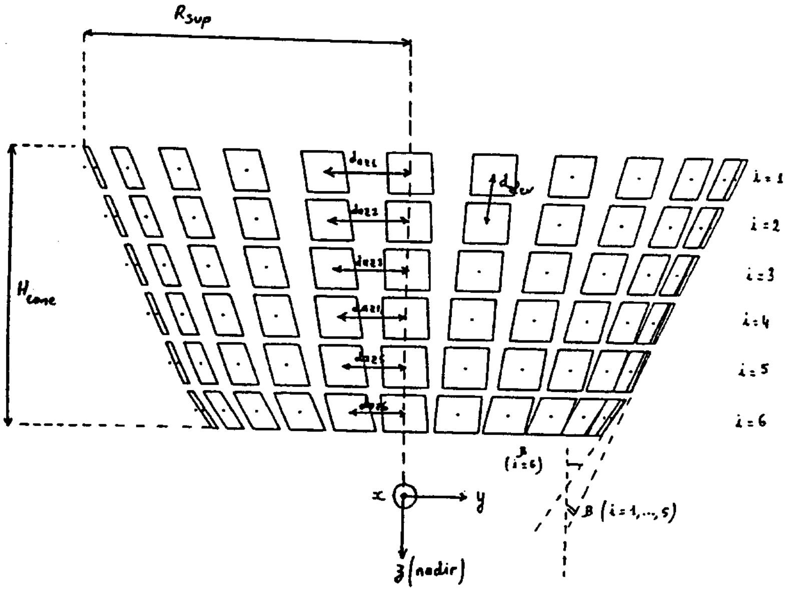

H_{cone}= 145.41 mm
R_{sup}= 178.30 mm
N_{tot}= 24
N_{ER}= 6
N_B = 8
N=3
β=26°/26°/26°/26°/26°/36°
d_{elev}= 27.42 mm (0.75 λ)
d_{az1}= 45.36 mm (1.24 λ)
d_{az2}= 42.20 mm (1.15 λ)
d_{az3}= 39.03 mm (1.07 λ)
d_{az4}= 35.87 mm (0.98 λ)
d_{az5}= 32.70 mm (0.89 λ)
d_{az6}= 29.00 mm (0.79 λ)

Fig. IV-3-2: Final geometrical characteristics of the antenna

The obtained radiated power with this new profile becomes fully compliant on the whole bandwidth as shown in figure IV-3-3.

The information contained in this document is proprietary to ALCATEL ESPACE and shall not be disclosed by the recipient to third persons without the written consent of the company

Les informations contenues dans ce document demeurent propriété exclusive d'ALCATEL ESPACE et ne doivent pas être divulguées par le destinataire à des tiers sans l'accord écrit de la société.

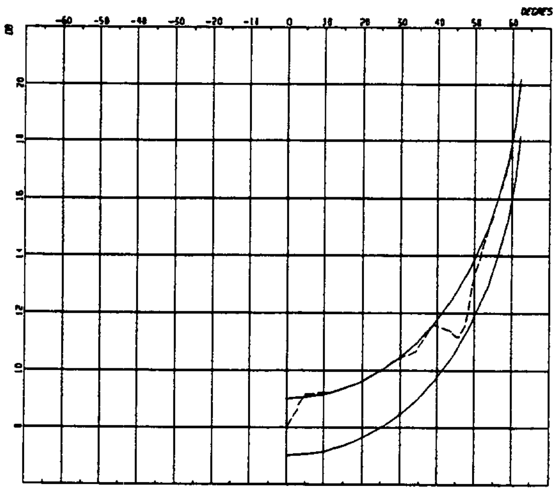

8.1 GHz

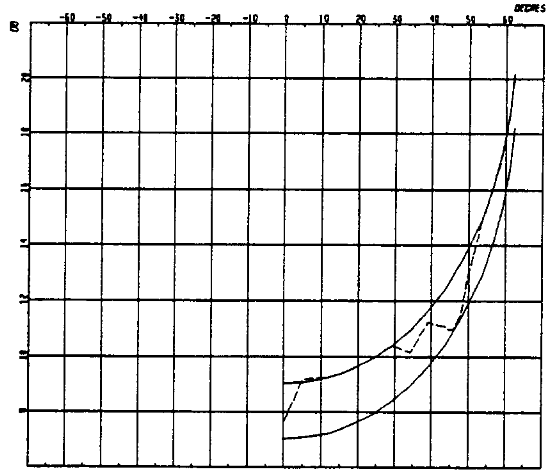

8.2 GHz

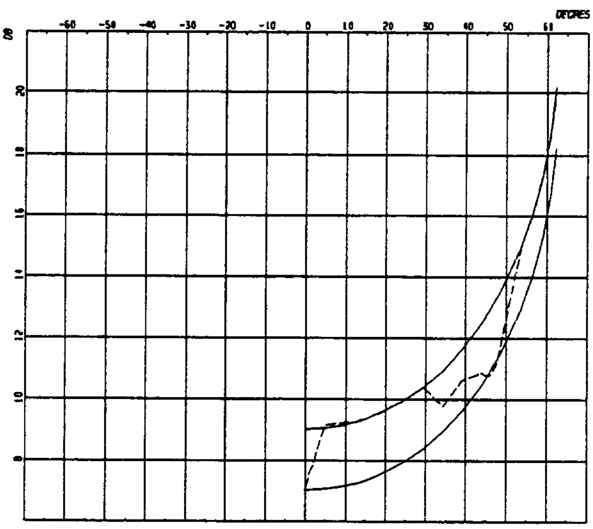

8.3 GHz

Fig. IV-3-3: EIRP of the antenna with 26°/26°/26°/26°/26°/36° profile

*** *Axial ratio***

The axial ratio of the whole antenna is presented in figure IV-3-4. It is under the 3.5 dB specified by ESA for the whole bandwidth. The maximal value of axial ratio is 2.64 dB at 8.3 GHz.

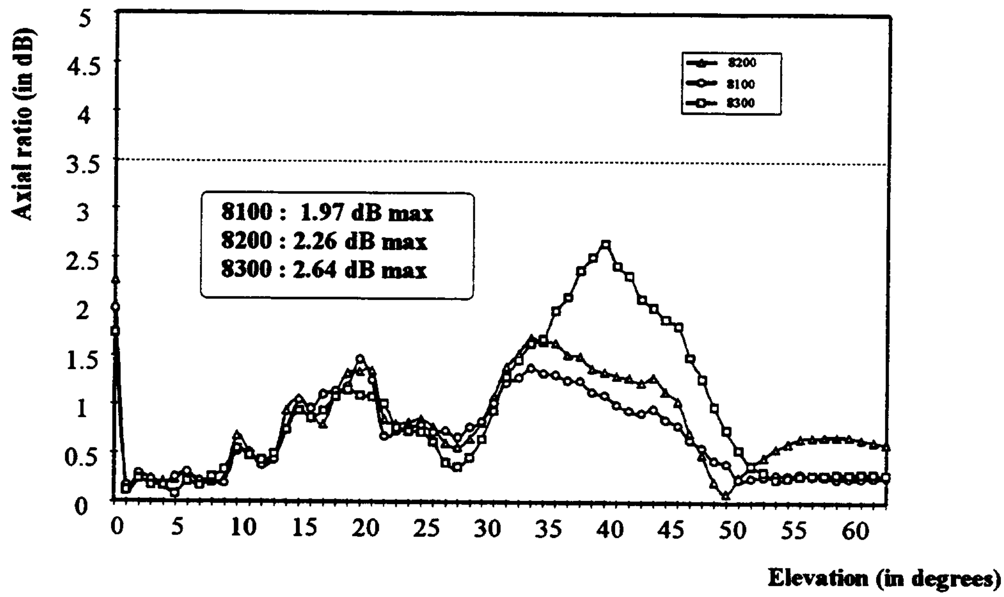

Fig. IV-3-4: Axial ratio of the whole antenna

We can observed that the axial ratio of the whole antenna is lower than the axial ratio of the single subarray except at the nadir (see the comparison in figure IV-3-5 at 8.2 GHz).

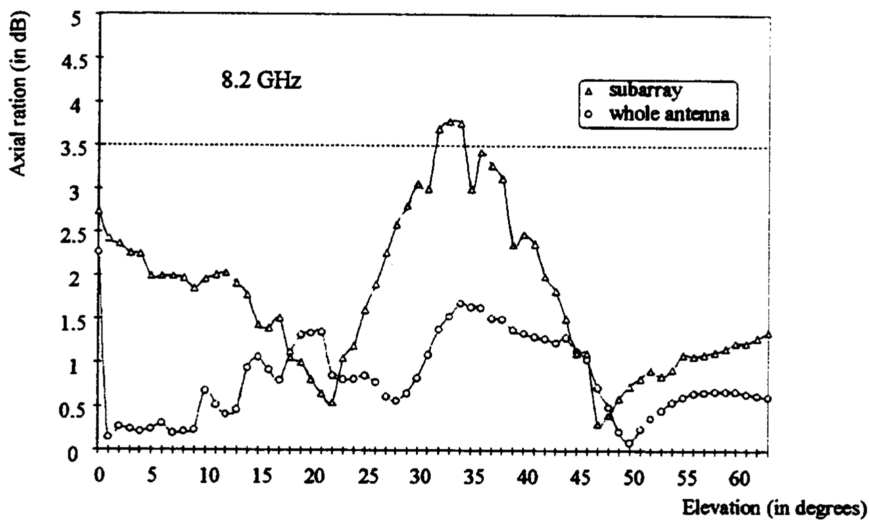

Fig. IV-3-5: Comparison between the axial ratio of a single subarray and the axial ratio of the whole antenna at 8.2 GHz

The information contained in this document is proprietary to ALCATEL ESPACE and shall not be disclosed by the recipient to third persons without the written consent of the company

Les info...ions contenues dans ce document demeurent propriété exclusive d'ALCATEL ESPACE et ne doivent pas être divulguées par le destinataire à des tiers sans l'accord écrit de la société.

Radiated patterns

The radiated patterns of the whole antenna could be obtained by SYCOB software if no coupling between subarray is considered. Figure IV-3-6 to IV-3-8 represents the directivity of the antenna at 8.1 GHz, 8.2 GHz and 8.3 GHz for three elevations (0°, 30° and 60°). For real gain observed on earth, ohmic + VSWR losses, and isoflux attenuation for each elevation must be take off to the directivity.

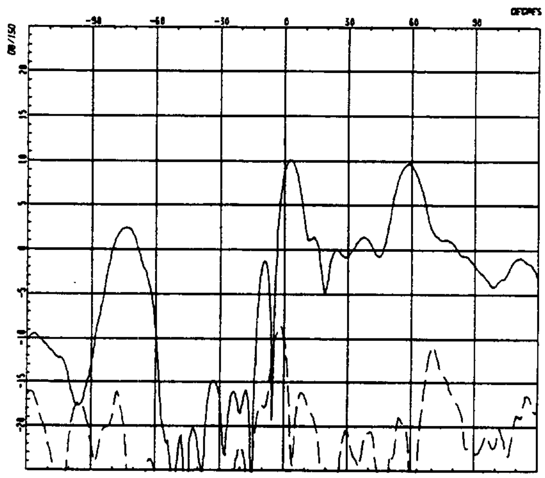

θ=0°

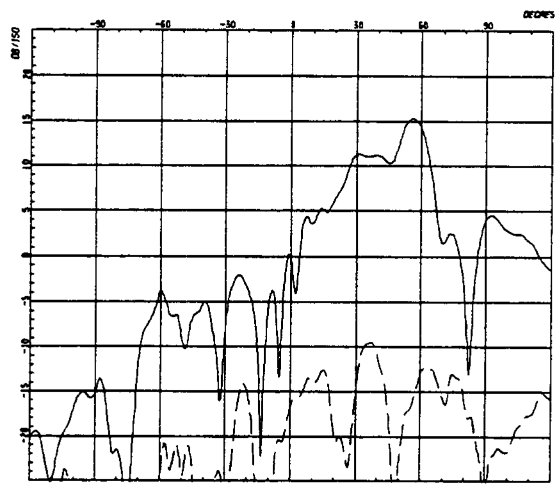

θ=30°

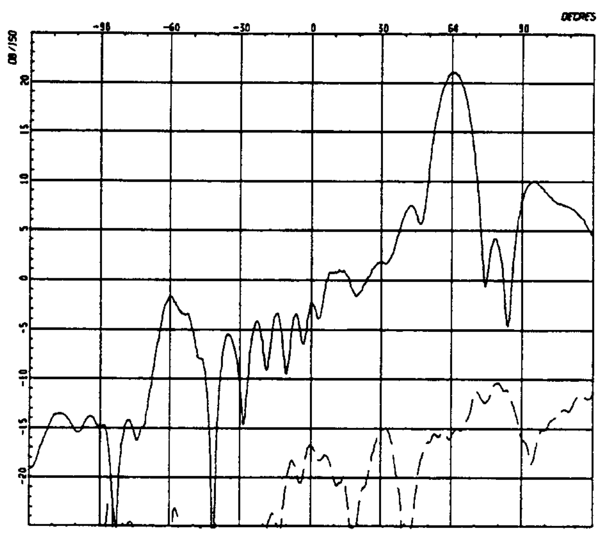

θ=60°

Fig. IV-3-6: Radiated patterns at 8.1 GHz for 0°, 30° and 60°

The information contained in this document is proprietary to ALCATEL ESPACE and shall not be disclosed by the recipient to third persons without the written consent of the company

Les informations contenues dans ce document demeurent propriété exclusive d'ALCATEL ESPACE et ne doivent pas être divulguées par le destinataire à des tiers sans l'accord écrit de la société.

The information contained in this document is proprietary to ALCATEL ESPACE and shall not be disclosed by the recipient to third persons without the written consent of the company

Les informations contenues dans ce document demeurent propriété exclusive d'ALCATEL ESPACE et ne doivent pas être divulguées par le destinataire à des tiers sans l'accord écrit de la société.

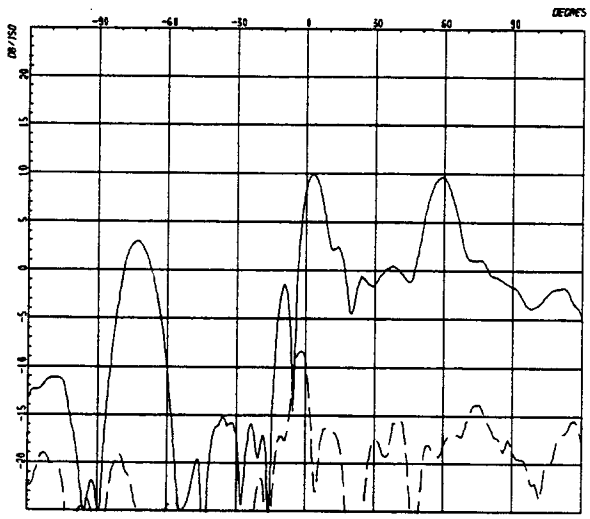

θ=0°

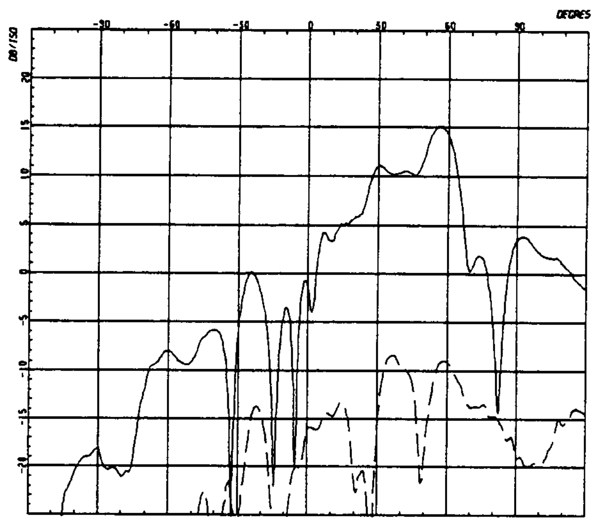

θ=30°

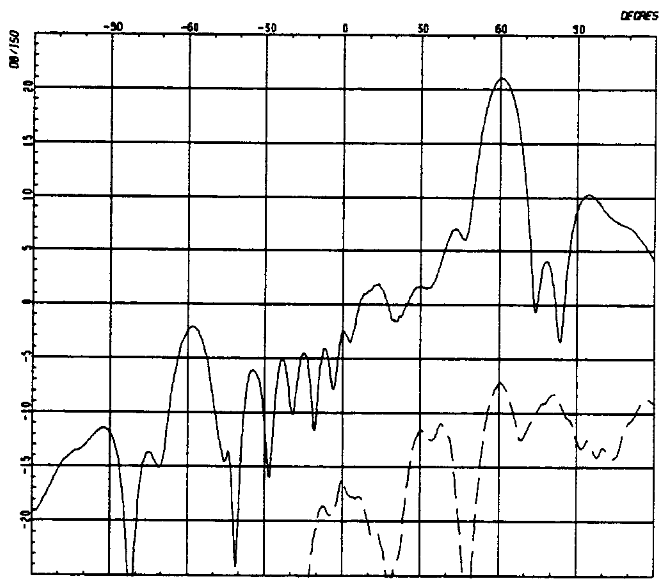

θ=60°

Fig. IV-3-7: Radiated patterns at 8.2 GHz for 0°, 30° and 60°

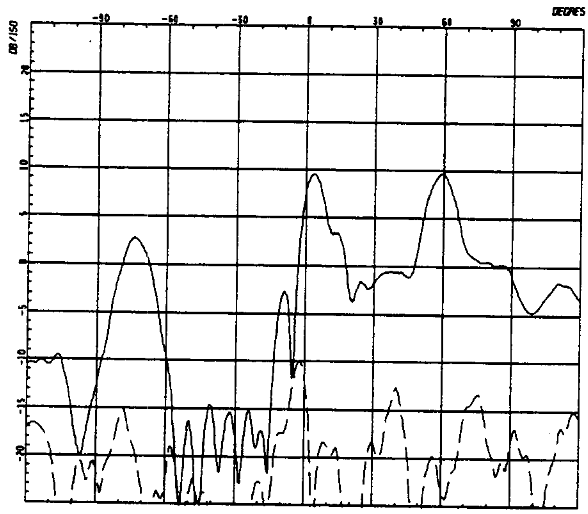

θ=0°

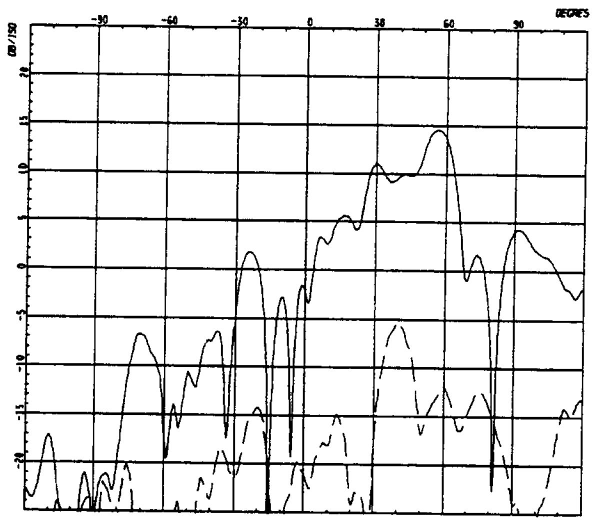

θ=30°

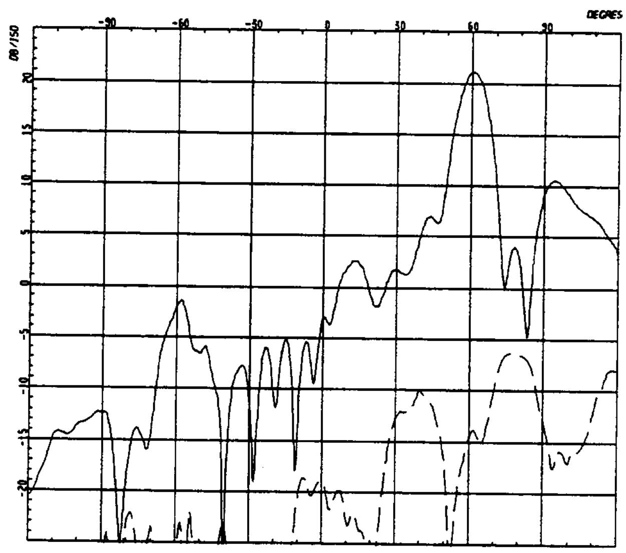

θ=60°

Fig. IV-3-8: Radiated patterns at 8.3 GHz for 0°, 30° and 60°

The information contained in this document is proprietary to ALCATEL ESPACE and shall not be disclosed by the recipient to third persons without the written consent of the company

Les informations contenues dans ce document demeurent propriété exclusive d'ALCATEL ESPACE et ne doivent pas être divulguées par le destinataire à des tiers sans l'accord écrit de la société.

V TABLE OF COMPLIANCE

REQUIREMENT	8.1 GHz	8.2 GHz	8.3 GHz	Compliance on the whole bandwidth
RETURN LOSS < -14 dB	-26 dB	-33 dB	-28 dB	C
AXIAL RATIO < 3.5 dB *subarray*	2.38 dB max	3.75 dB max	3.85 dB max	QC
AXIAL RATIO < 3.5 dB *whole antenna*	1.97 dB max	2.26 dB max	2.64 dB max	C
Gain (62.3°) > 20.05 dBi	20.15 dBi	20.23 dBi	20.24 dBi	C
losses < 0.95 dB	0.78 dB	0.73 dB	0.76 dB	C
Radiated Power < -0.77 dBW	-0.77 dBW	-0.77 dBW	-0.77 dBW	C
SUBARRAY MASS < 90 g	130 g	130 g	130 g	to be optimized with antenna structure

VI CONCLUSIONS

The feasibility of a 6 patches subarray feeding by a parallel repartitor had been demonstrated. The realisation of such a repartitor is a complex work because no software is actually able to give accurate results. That's why a few runs are necessary to obtain the final configuration.

This subarray is broadband (400 MHz at X-Band), small size (which permits to reduce the final mass of the breadboard) and fully compliant with the specification of ESA in terms of axial ratio, return loss and radiated power.

The information contained in this document is proprietary to ALCATEL ESPACE and shall not be disclosed by the recipient to third persons without the written consent of the company

Les informations contenues dans ce document demeurent propriété exclusive d'ALCATEL ESPACE et ne doivent pas être divulguées par le destinataire à des tiers sans l'accord écrit de la société.

CONFORMAL ARRAY

CHAPTER 8

ELECTRICAL DESIGN OF

PASSIVE BEAM FORMING NETWORK

(WP 2300)

Reproduction interdite © ALCATEL ESPACE Reproduction forbidden

CASA

CONSTRUCCIONES AERONAUTICAS, S.A.

DIVISION ESPACIO
SPACE DIVISION

Registro Mercanti id - Tomo 139 - Folio 36 - Hoja nº 4813 - Inscripción 1 7/3/1923 - Núm. Identificación Fiscal A-28-006104

Nº : CAS-COA-TNO-0004

Título / Title

ELECTRICAL DESIGN OF PASSIVE BEAM FORMING NETWORK

Conformal Array Antenna

Edición / Issue:	1
Fecha / Date:	18.12.96
Nº de Páginas / No. of pages:	52 + Annex
Clase / Class:	
Categoría / Category:	

Preparado por / Prepared by	F. MONJAS D. GARCIA M.J. MARTIN
Revisado por / Revised by	
Aprobado por / Approved by	M.J. MARTIN

J M-1

LISTA DE DISTRIBUCION
(DISTRIBUTION LIST)

NORMAL ⊗ **CONFIDENCIAL**

INTERNA (Internal)			EXTERNA (External)		
DPT.	NOMBRE (Name)	Nº Copias	CIA.	NOMBRE (Name)	Nº COPIAS
	J. NAVARRO	1	ESTEC	G. VAN DOOREN	5
	R. JIMENEZ	1			
	R. BALANZA	1	ALCATEL	G. CAILLE	3
	C. MONTESANO	1		E. VOURCH	--
	M.J. MARTIN	3			
	ARCHIVO	ORIGINAL			

Registro Mercantil de Madrid - - Folio 36 - Hoja nº 4813 - Inscripción 1ª fecha 27/3/1 ...n. Identificación Fiscal A-28-006104

ESTADO DE LAS EDICIONES
ISSUE - RECORD

Nº de Edición Issue Number	Incorporación de las Modificaciones Incorporation of Change Proposals	Impacto sobre el producto Impact on the product
Issue: 01 **Date:** 18.12.96 **Pages:** 52 + Annex	Initial issue.	

Registro Mercantil de Madrid - . - Folio 36 - Hoja nº 4813 - Inscripción 1ª fecha 27/3/1: .. Identificación Fiscal A-28-006104

REPERTORIO DE MODIFICACIONES
CHANGE - RECORD

Nº	Fecha Date	Pag. afectadas Changed Pag.	Descripción del cambio Description of Change	Impacto sobre el producto Impact on the product

Registro Mercantil de Madrid - Tomo 139 - F - Hoja nº 4813 - Inscripción 1ª fecha 27/3/1923 - Núm. I .ación Fiscal A-28-006104

LIST OF CONTENTS

Registro Mercantil de Madrid - Tomo 139 - Folio 36 - Hoja nº 4813 - Inscripción 1ª fecha 27/3/1923 - Núm. Identificación Fiscal A-28-006104

Mod M-11

APPLICABLE DOCUMENTS A.D.[X]

[1] ***"Preliminary Design Review of the Conformal Array Antenna"***
ALCATEL presentation hand-out, ESTEC, 26.06.96.

[2] ***"Subassemblies Specifications"***
Conformal Array Antenna, AES 96-29460/ASP-394, 14.10.96

It contains:

- *"Specifications for the passive BFN (dividers, cables, measurements of the whole BFN"*, Conformal Array Antenna. AES 96-29460/ASP-394, 19.09.96.
- *"Specifications for the active modules and preamplifier of a flight type antenna"*, Conformal Array Antenna, AES 96-29461/ASP-395, 16.09.96.
- *"Specifications for 3 x 3 Butler matrices", Conformal Array Antenna, AES-96-0602/ASP-025, 13.09.96.*
- *"Specifications for the DSN Band rejection filters"*, Conformal Array Antenna. AES 96-32058/ASP-139, 11.09.96.

[3] ***"Remarks about time - delays"***
E-mail. G. Caille, 24.11.96.

[4] ***"Clarification about 'Group Delay Variation' specification"***, AES 96-32061/ASP-441, 05.12.96.

Registro Mercantil de Madrid - Tomo 139 - Folio 36 - Hoja nº 4813 - Inscripción 1ª fecha 27/3/1923 - Núm. Identificación Fiscal A-28-006104

Mod M-11

REFERENCE DOCUMENTS R.D.[X]

[1] ***"Multiple Beams from Linear Arrays"***
Shelton, J.P., Kelleher, K.S.
IRE Trans on AP March 1961, pp. 154-161.

[2] ***"Six Port Couplers for Generalized Butler Like Matrices"***
Roederer, A., García, Q., Hernanz, M.L., Martín, C.
ESA Workshop on Advanced BFN, November 1991.

[3] ***"Electrical Design of DSN-band rejection filters"***
CAS-CAA-TNO-0005, December 1996.

[4] ***"Conformal Array Antenna Design"***
CAS-CAA-TNO-0001, December 1996.

[5] ***"Alcatel presentation hand-out, 2nd Conformal Array Antenna Progress Meeting"***
Lausanne, 09.10.96.

[6] ***"Thermal Design and Analysis"***
CAS-CAA-TNO-0003, December 1996.

[7] ***"Microwave Design System"***
Hewlett Packard.

Registro Mercantil de Madrid - Tomo 139 - Folio 36 - Hoja nº 4813 - Inscripción 1ª fecha 27/3/1923 - Núm. Identificación Fiscal A-28-006104

Mod M-11

Registro Mercantil de Madrid - Tomo 139 - Folio 36 - Hoja nº 4813 - Inscripción 1ª fecha 27/3/1923 - Núm. Identificación Fiscal A-28-006104

Mod M-11

0. INTRODUCTION

This document reports the electrical design of the passive Beam Forming Network of the Conformal Array antenna designed by Alcatel, A.D.[1], as result of a trade-off to select the suitable antenna system for the proposed Earth observation mission in LEO orbit. Conclusion of above system analysis is the semi-active antenna whose block diagram is illustrated in figure 1.

A representative breadboard model of the complete Conformal Array Antenna will be manufactured and tested at RF level only, based on a simpler system where only one of the three simultaneous beam be active. The BB-Antenna block diagram is presented in figure 2.

This paper deals with the detailed RF design of the passive BFN which excludes the pre-amplifiers and channel filters, as they are not part of the BB-antenna, with interface at the input port of the dividers (fig. 2). It also excludes the design of the active modules composed of the variable phase shifters plus amplifier control subassembly.

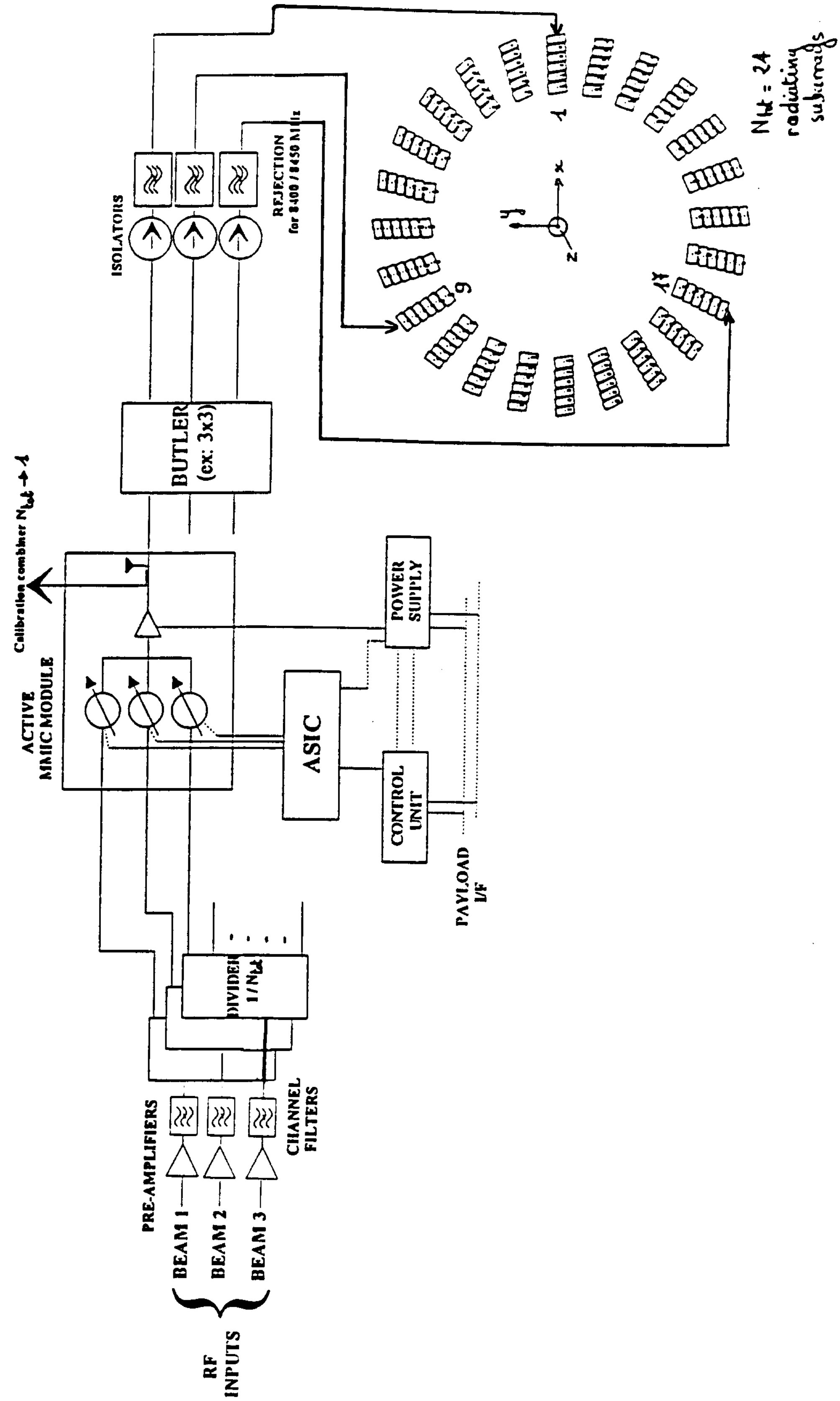

Fig. 1 : Semi-active antenna architecture for a flight-type full antenna. Alcatel design (AES 96-29460 / ASP-394)

Registro Mercantil de Madrid - Tomo 139 - Folio 36 - Hoja nº 4813 - Inscripción 1ª fecha 27/3/19.. - Núm Identificación Fiscal A-28-006104

Mod M-11

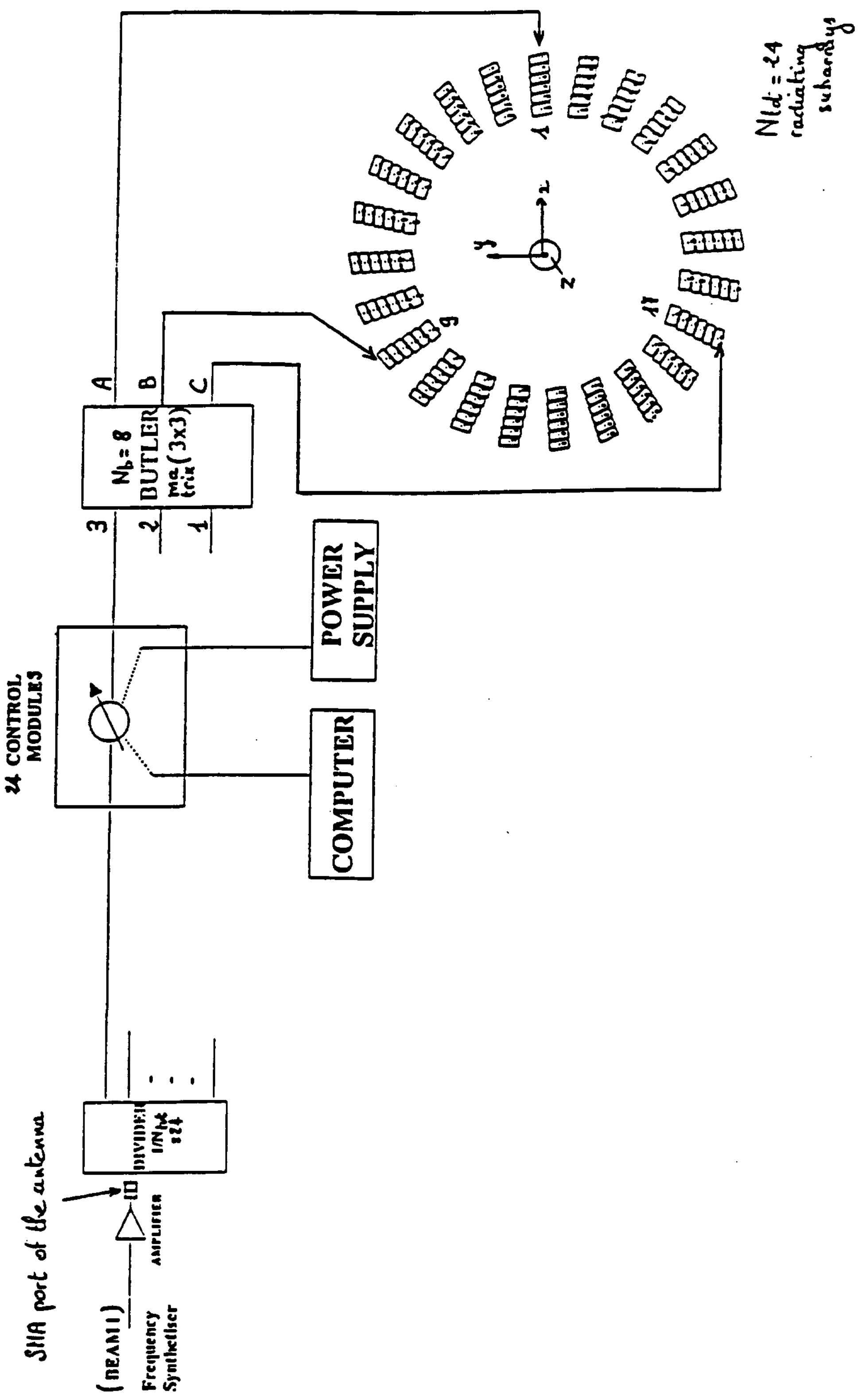

Fig. 2 : Architecture of the "one simultaneous channel" breadboard, the three channels are measured one after each other through the same BFN.

Alcatel Design (AES 96-29460 / ASP-394)

Registro Mercantil de Madrid · 139 · Folio 36 · Hoja nº 4813 · Inscripción 1ª fecha 27/3/.. · Núm. Identificación Fiscal A-28-006104
Mod M-11

Registro Mercantil de Madrid - Tomo 139 - Folio 36 - Hoja nº 4813 - Inscripción 1ª fecha 27/3/1923 - Núm. Identificación Fiscal A-28-006104

1. REQUIREMENTS

A summary of RF requirements for each section of the passive BFN is herebelow listed. These specifications have been established by the antenna system responsible in A.D.[2]. Electrical design shall be aimed to meet all the requirements.

The frequency band is defined 8025-8400 mHz, with three 50 MHz channels centered at 8100, 8200 and 8300 MHz respectively.

1.1. "IN FRONT" OF ACTIVE MODULES

It applies to the part of the BFN which takes place before the active modules of the antenna (figures 1/2), this is, the set composed by the dividers plus coaxial cables.

A distinction is made between the complete flight antenna with three channel-BFN and the breadboard antenna with only one channel BFN.

The 3:1 combiner is not included in these specifications.

- **Matching:** Input and outputs return loss
  < -18 dB, whole BW.
- **Insertion loss:** < 2 dB flight antenna
  < 2.5 dB BB antenna: longer cables are allowed.
- **Amplitude unbalance at a given frequency:**
  < 0.2 dB peak-peak
- **Phase unbalance at a given frequency:**
  < 50° peak-peak
- **Amplitude variation within each channel:**
  < 0.2 dB peak-peak
- **Group delay variation within each channel:**
  < 2 ns peak-peak.

Note: Group delay variation is specified < 2 ns within 50 MHz channel bandwidth, A.D.[3,4], for the complete antenna.

Mod M-11

1.2. BFN "AFTER" ACTIVE MODULES

It applies to the part of the BFN that takes place after the active modules of the antenna (figures 1/2), excluding the DSN-band rejection filters bank, design which is reported separately in R.D.[1].

This BFN section is composed of the Butler matrices plus cables subassembly. In particular, Butler matrices have a dedicated section within this document and the requirements document, A.D.[2].

- **Matching:** Input and outputs return loss
  < -18 dB, whole BW.
- **Insertion loss:** < 1.1 dB flight antenna (including matrices)
  < 1.6 dB BB antenna (including matrices): longer cables are allowed.
- **Amplitude unbalance at a given frequency for any path:**
  < 0.4 dB peak-peak flight antenna.
  < 0.6 dB peak-peak BB antenna.
- **Phase unbalance at a given frequency for any path:**
  < 5° peak-peak flight antenna
  < 10° peak-peak BB antenna
- **Amplitude variation within each channel:**
  < 0.5 dB peak-peak
- **Group delay variation within each channel:**
  < 6 ns peak-peak.

Note: Group delay variation is specified < 2 ns within 50 MHz channel bandwidth, A.D.[3,4], for the complete antenna.

Registro Mercantil de Madrid - Tomo 139 - Folio 36 - Hoja nº 4813 - Inscripción 1ª fecha 27/3/1923 - Núm. Identificación Fiscal A-28-006104

Mod. M-11

Registro Mercantil de Madrid - Tomo 139 - Folio 36 - Hoja nº 4813 - Inscripción 1ª fecha 27/3/1923 - Núm. Identificación Fiscal A-28-006104

1.3. BUTLER MATRIX

System studies carried out during the project have demonstarted the advantages of using 3×3 Butler matrices instead of either 2×2 or 4×4 hybrid modules composed of conventional 90° or 180° hybrids AD[2]. In the following paragraphs a brief summary and comment on the specifications of such modules will be done.

An initial description of the operation of a 3×3 junction for multiple beam antenna systems was addressed in RD[1], where the symmetry of operation of the device was detailed. A functional device fullfilling the phase and amplitude characteristics was first described in RD[2], where two different designs were included, both of them working at L-band, made in microstrip technology.

Basically, the 3×3 Butler device is a matched six port hybrid coupler with 1/3 power division from one port to other three and 120° phase shift between two of them and a reference output, being all input and output ports isolated among them. The scheme of the element is sketched in figure1.3.1: following the figure, ports 1,2,3 are isolated as well as ports A,B,C, and transmission paths exist between 123 and ABC, with reference output phase in the port located in the symmetry plane (e.g., 1A is the reference and 1B, 1C are shifted 120°).

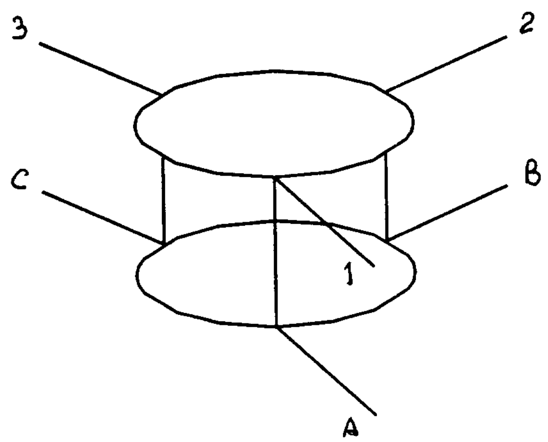

Figure 1.3.1.- Sketch of the 3×3 hybrid coupler

Mod M-11

Nevertheless, system analysis requirements for the transmission phases of the Butler matrices differ from those indicated in previous paragraph for the 3×3 hybrid coupler.

- The **phase distribution** required for the Butler Matrix is listed in table 1.3.1 below.

Table 1.3.1

PORTS	A	B	C
1	φ	φ	φ
2	φ	φ+120	φ-120
3	φ	φ-120	φ+120

In order to comply with the phase distribution, the hybrid coupler is modified by inserting additional transmision lines with electrical lengths of 120° at two ports, as sketched in figure 1.3.2 below.

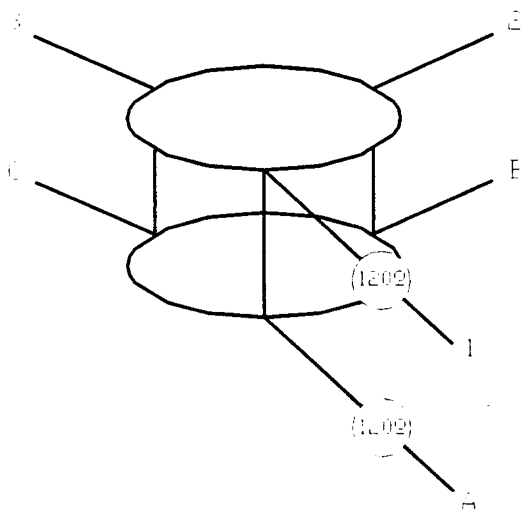

Figure 1.3.2.- Modified 3×3 hybrid coupler for Butler Matrix

Registro Mercantil de Madrid - Tomo 139 - Folio 36 - Hoja nº 4813 - Inscripción 1ª fecha 27/3/1923 - Núm. Identificación Fiscal A-28-006104

Mod M-11

Registro Mercantil de Madrid - Tomo 139 - Folio 36 - Hoja nº 4813 - Inscripción 1ª fecha 27/3/1923 - Núm. Identificación Fiscal A-28-006104

The conformal array antenna requires 8 of these devices to be manufactured with a minimum error between them.

- **Amplitude unbalance** between the 9 paths of each matrix and over the complete series must be in a ±0.2dB range at each frequency within the whole bandwidth with respect to the mean insertion loss, defined as

$$\bar{L} = \frac{\Sigma L_n}{N_b}$$

where L_n es the insertion loss averaged over the 9 paths of matrix *i* and N_b is the number of matrices. Since this can only be determined once the 8 matrices are manufactured, in the design stages we have proceed applying this restriction to L_n defined as:

$$L_n = \frac{\Sigma S_{ij}}{9}$$

and the dispersion within each channel is given, in dB by:

$$d_j = S_{j1} - L_n$$

- Within each channel, the **variation of the 9 transmission path amplitudes** must be lower than 0.4dB (pk-pk) and the variation vs. frequency of the 9 paths, also within each channel, must be lower than 0.4dB (pk-pk).

- **Losses** associated to each matrix transmission path must be lower than 0.8dB.

- Within each channel, the **variation of the group delay** for each path must be lower than (TBD) for the 8 delivered matrices: lower than 2 ns at complete antenna level.

- The reference **insertion phase φ** is defined when input port 1 is excited, and the error for each matrix at a given frequency must be no more than ±5° over the bandwidth, and the variation of the reference phase over the 8 matrices must be lower than 50° peak to peak.

Mod M 11

- **Impedance matching** better than 14 and 18dB are required respectively at the input and outputs ports of the Butler matrices.

This specification list must be maintained in a temperature range of -50ºC to +50ºC.

Finally, the preferred technology for the realization of the matrices is microstrip in order to maintain the coherence with the remaining parts of the system (SSPAs, power dividers, etc,..).

Registro Mercantil de Madrid - Tomo 139 - Folio 36 - Hoja nº 4813 - Inscripción 1ª fecha 27/3/1923 - Núm. Identificación Fiscal A-28-006104

Mod. M-11

2. ELECTRICAL DESIGN

The antenna system has been designed by Alcatel, A.D.[1], during the first phase of the Conformal Array Antenna project. Antenna architecture is presented as introduction of the document, being the frame where the electrical design of the antenna Beam Forming Network is made.

RF solutions for each passive device involved in the BFN are hereafter described, filters excluded, R.D.[1].

Once that antenna architecture and basic desing of components is known, the complete antenna is created in a 3-D assembly, R.D.[2], which allows to determine the cables length, antenna mass & loss budgets, volume, interfaces, etc.

Figure 2.1 shows a general view of the whole system.

Registro Mercantil de Madrid - Tomo 139 - Folio 36 - Hoja nº 4813 - Inscripción 1ª fecha 27/3/1923 - Núm. Identificación Fiscal A-28-006104

Mod M-11

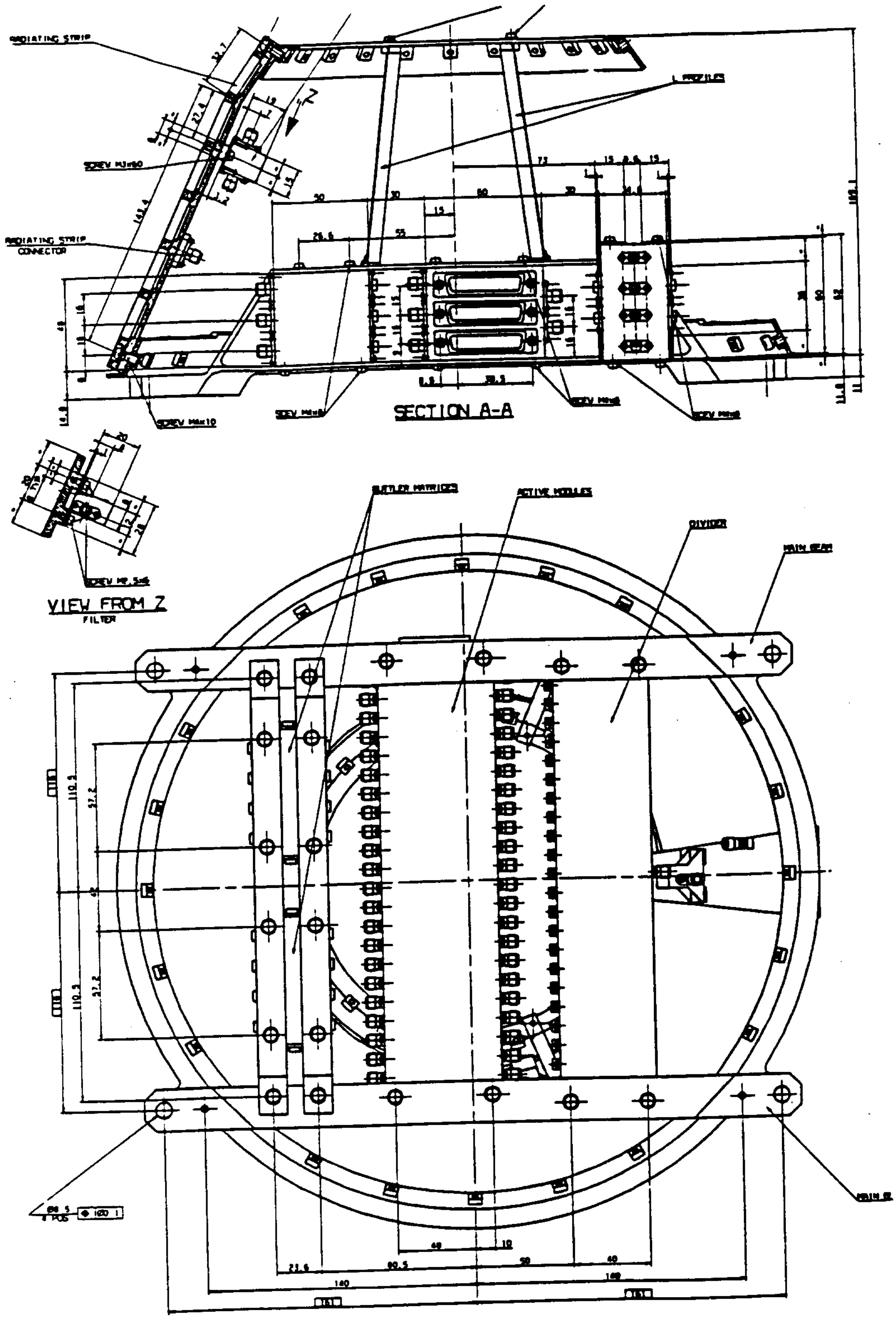

Fig. 2.1 : Complete Conformal Array Antenna - Flight Type.

3-D model from R.D.[2]

Registro Mercantil de Madrid - Tomo 139 - Folio 36 - Hoja nº 4813 - Inscripción 1ª fecha 27/3/1923 - Núm. Identificación Fiscal A-28-006104

Mod. M-11

Registro Mercantil de Madrid 139 - Folio 36 - Hoja nº 4813 - Inscripción 1ª fecha 27/ - Núm. Identificación Fiscal A-28-006104

2.1. SIGNAL DIVIDER 1:24

Baseline design of the signal divider is based on a chain of two-way Wilkinson dividers, of the uncompensated type, as shown in figure.

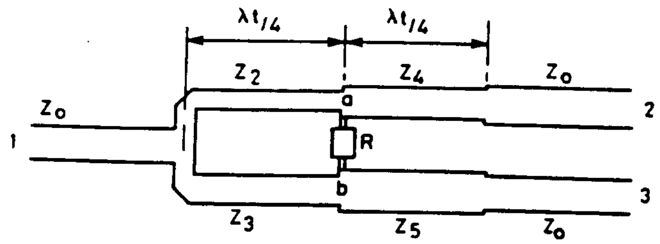

Fig. 2.1.1 : Two-way Wilkinson Divider

The topology is fully-parallel due to bandwidth requirements. With a correct choosing of line impedances, power entering port 1 will make voltages at points a and b to be equal, and the resistor will not absorb any power. The isolation between output ports is high and the reflection looking into any port low. The only disadvantage of these power dividers (compared to the simple T-junction splitters) is the need to include an additional component: the resistor, but this element is essential to get good output match. Another kind of dividers such as branch-line couplers or hybrid rings could be used with similar good performances, but their use is unadvisable because they require larger surface areas to be implemented and so introduce additional losses.

The number of outputs ports (24) is not a power of two so two kinds of Wilkinson dividers must be designed:

- Equal-power divider.
- Unequal-power divider, with power ratio 2/3:1/3. This element is the most prone to amplitude unbalances and mismatches.

The reference impedance line has 50 **Ω**, compromise between losses and width (which implies coupling and room problems).

Mod M-11

The design does not take advantage of the possibility to decompose the 1:24 divider into smaller dividers, to save mass and to avoid possible problems related to the connection and soldering than this would imply. Nevertheless, testing of the 1:24 divider performances could lead to use this technique (for example, to divide the problem in one 1:3 input splitter and three 1:8 output splitters).

Classical microstrip lines are used to implement the divider. The substrate used has the following characteristics:

Height	:	0.6 mm
Er	:	2.94
tg δ	:	$2.5\ 10^{-3}$
Metallization thickness	:	35 μm

A layout of the printed circuit can be seen on the figure below.

General dimensions are (circuit with enclosure): (251,5 x 66,8 x 16 mm). Separation between output ports is 10 mm.

Registro Mercantil de Madrid - ... 139 - Folio 36 - Hoja nº 4813 - Inscripción 1ª fecha 27/3/1923 - Núm. Identificación Fiscal A-28-006104

Mod M-11

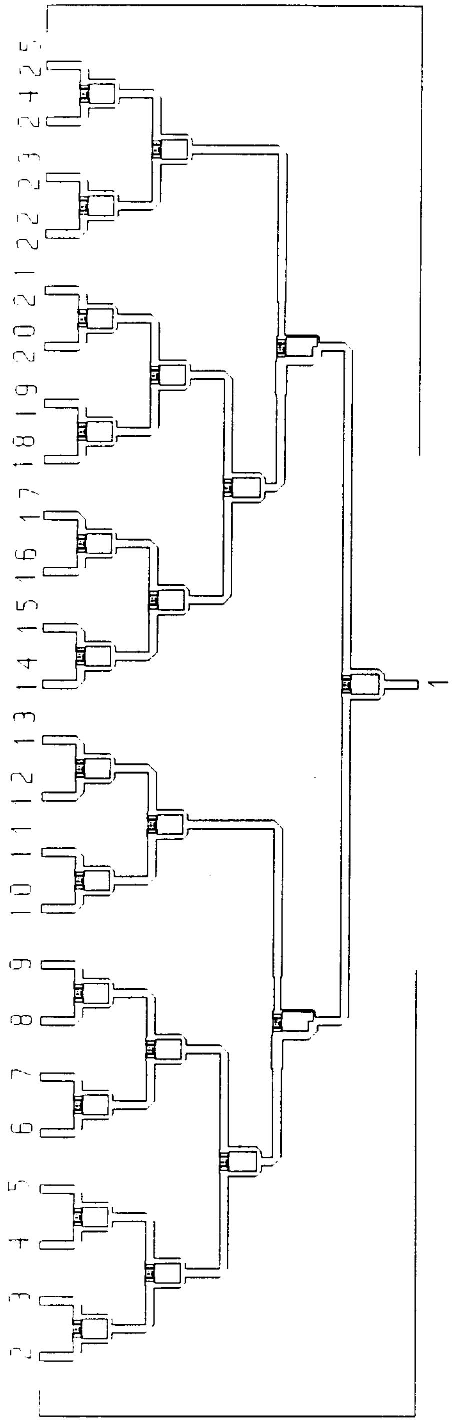

Fig. 2.1.2 : Layout of 1:24 signal divider

Registro Mercantil de Madrid - Tomo 139 - Folio 36 - Hoja nº 4813 - Inscripción 1ª fecha 27/3/1923 - Núm. Identificación Fiscal A-28-006104

Mod. M-11

Super Compact software has been used to simulate the divider. All straight sections of transmission lines, mitred bends, T-junctions and step-in-widths have been considered. Resistors are modelled as ideal components until reliable data about parasitics is got. Coupling effect between parallel lines has not been taken into account as the separation between them is well enough (higher than two line widths).

The following figures represent electrical performances provided by the 1:24 divider. Note that in the figures containing transmission responses, only two output ports (and not the 24 existent) are represented. This is caused by the fact that only two different ports are present in the design:

Port 2 represents actual ports : 2, 3, 4, 5, 6, 7, 8, 9, 14, 15, 16, 17, 18, 19, 20 and 21.

Port 3 represents actual ports : 10, 11, 12, 13, 22, 23, 24 and 25.

Registro Mercantil de Madrid - Tomo 139 - Folio 36 - Hoja nº 4813 - Inscripción 1ª fecha 27/3/1923 - Núm. Identificación Fiscal A-28-006104

Mod M-11

Mod M-11 Registro Mercantil de Madrid 139 · Folio 36 · Hoja nº 4813 · Inscripción 1ª fecha 27 · Núm. Identificación Fiscal A-28-006104

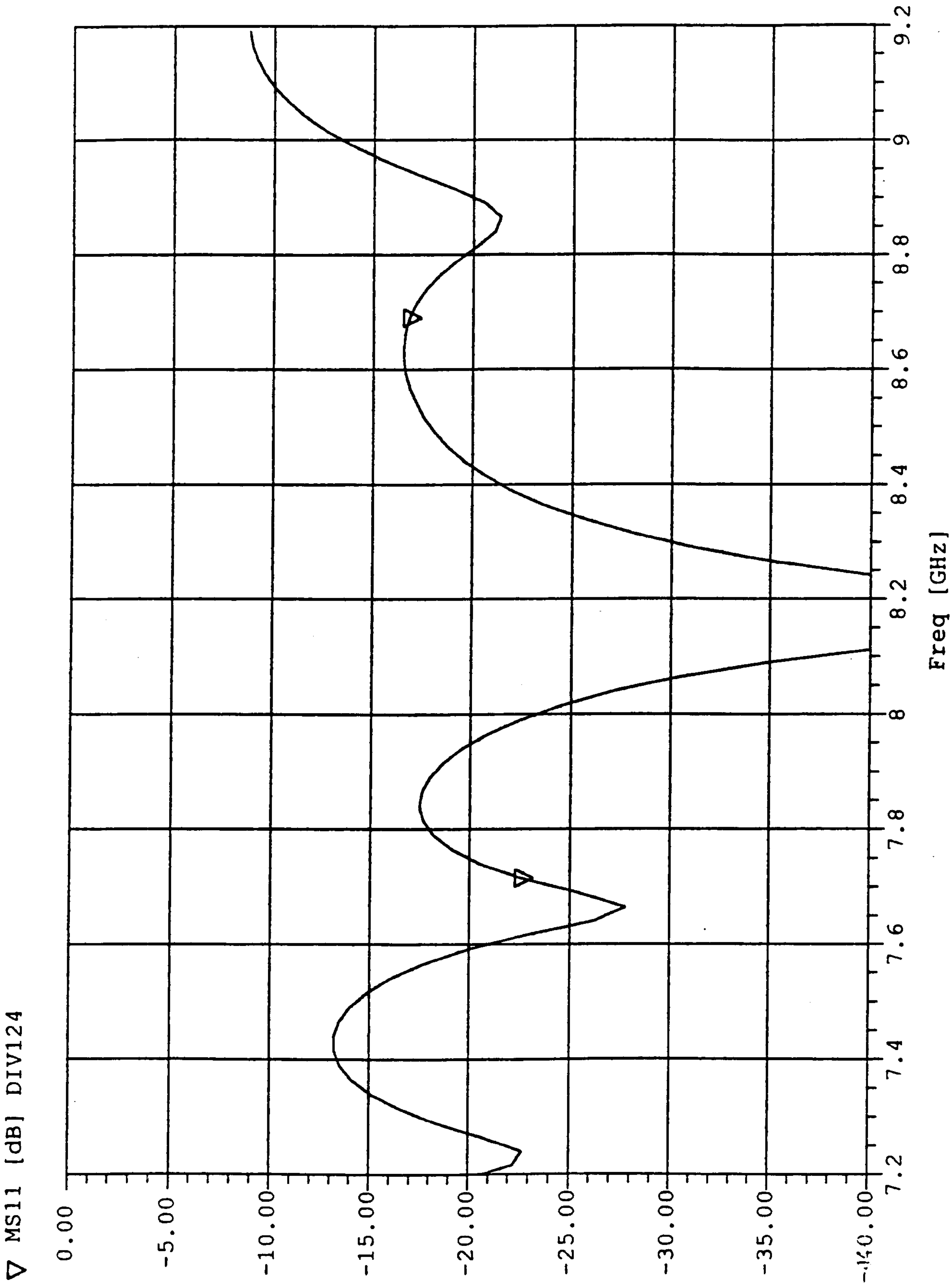

Fig. 2.1.3 : Input return loss

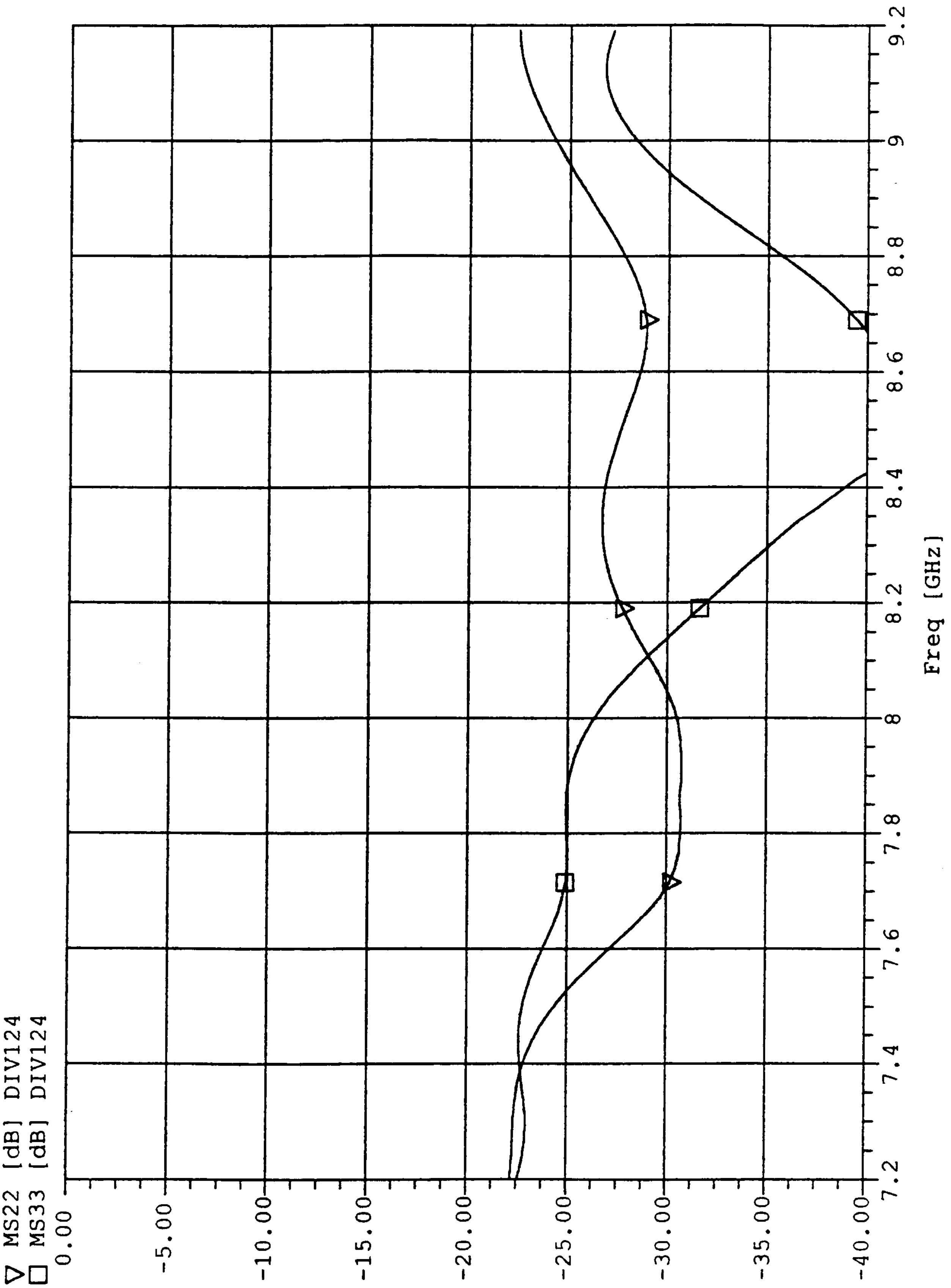

Fig. 2.1.4 : Output return loss

Mod M-11 Registro Mercantil de Madrid 139 - Folio 36 - Hoja nº 4813 - Inscripción 1ª fecha 27. - Núm. Identificación Fiscal A-28-006104

Mod M:11 Registro Mercantil de Madrid - ?:39 - Folio 36 - Hoja nº 4813 - Inscripción 1ª fecha 27/. - Núm. Identificación Fiscal A-28-006104

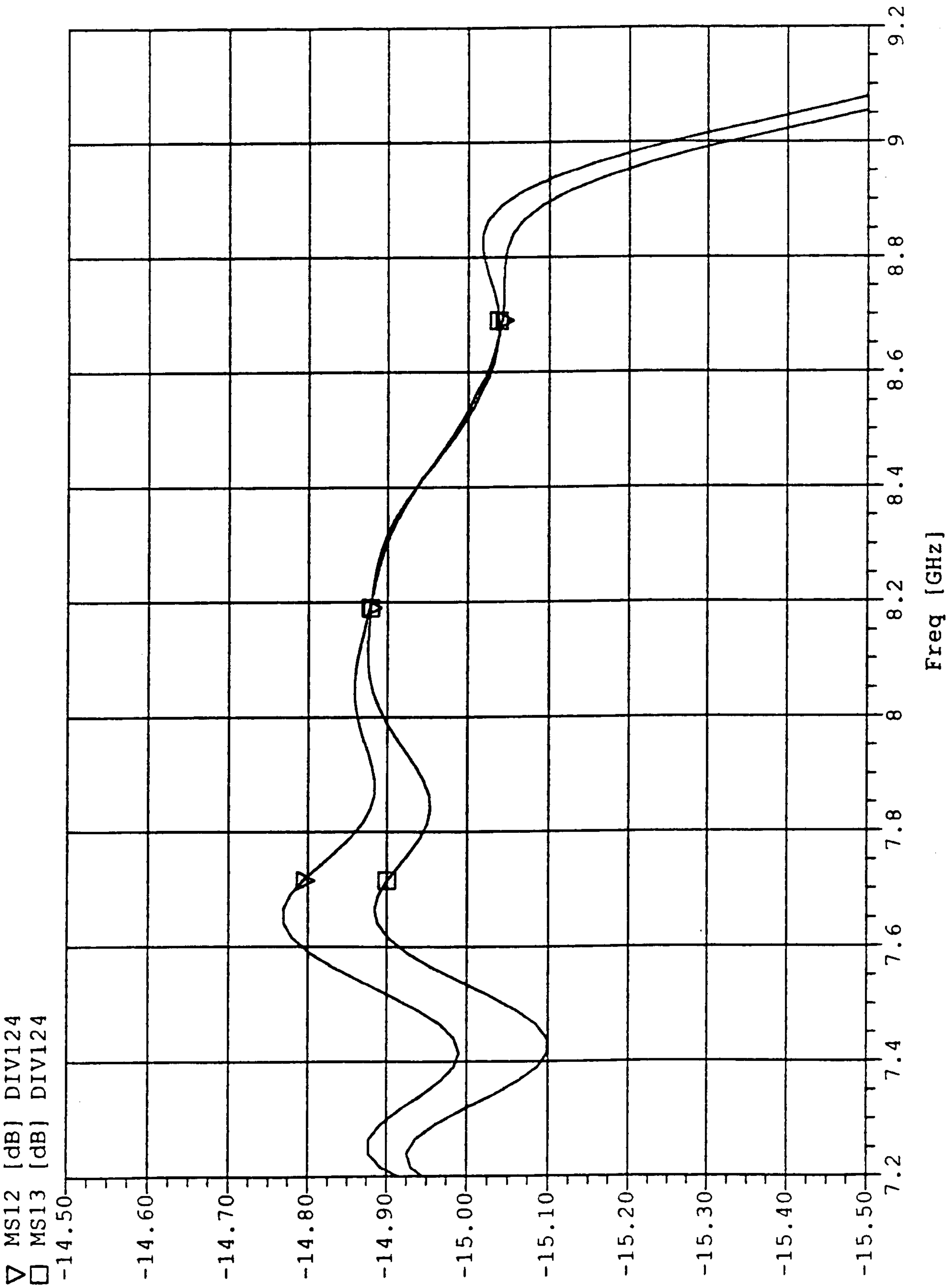

Fig. 2.1.5 : Transmission parameters (amplitude)

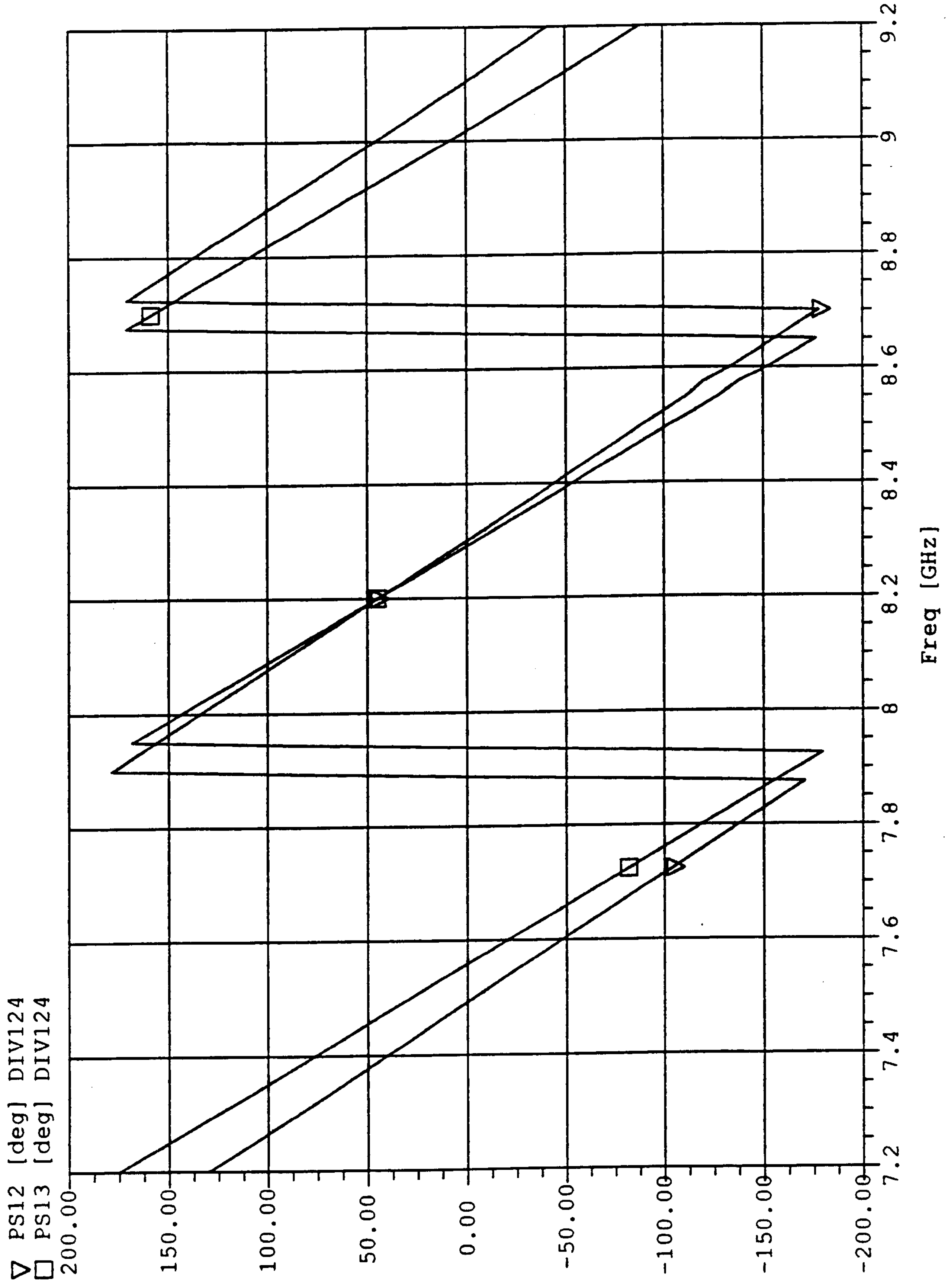

Fig. 2.1.6 : Transmission parameters (phase)

Mod M-11 Registro Mercantil de Madrid - 9 - Folio 36 - Hoja nº 4813 - Inscripción 1ª fecha 27/3/ Núm. Identificación Fiscal A-28-006104

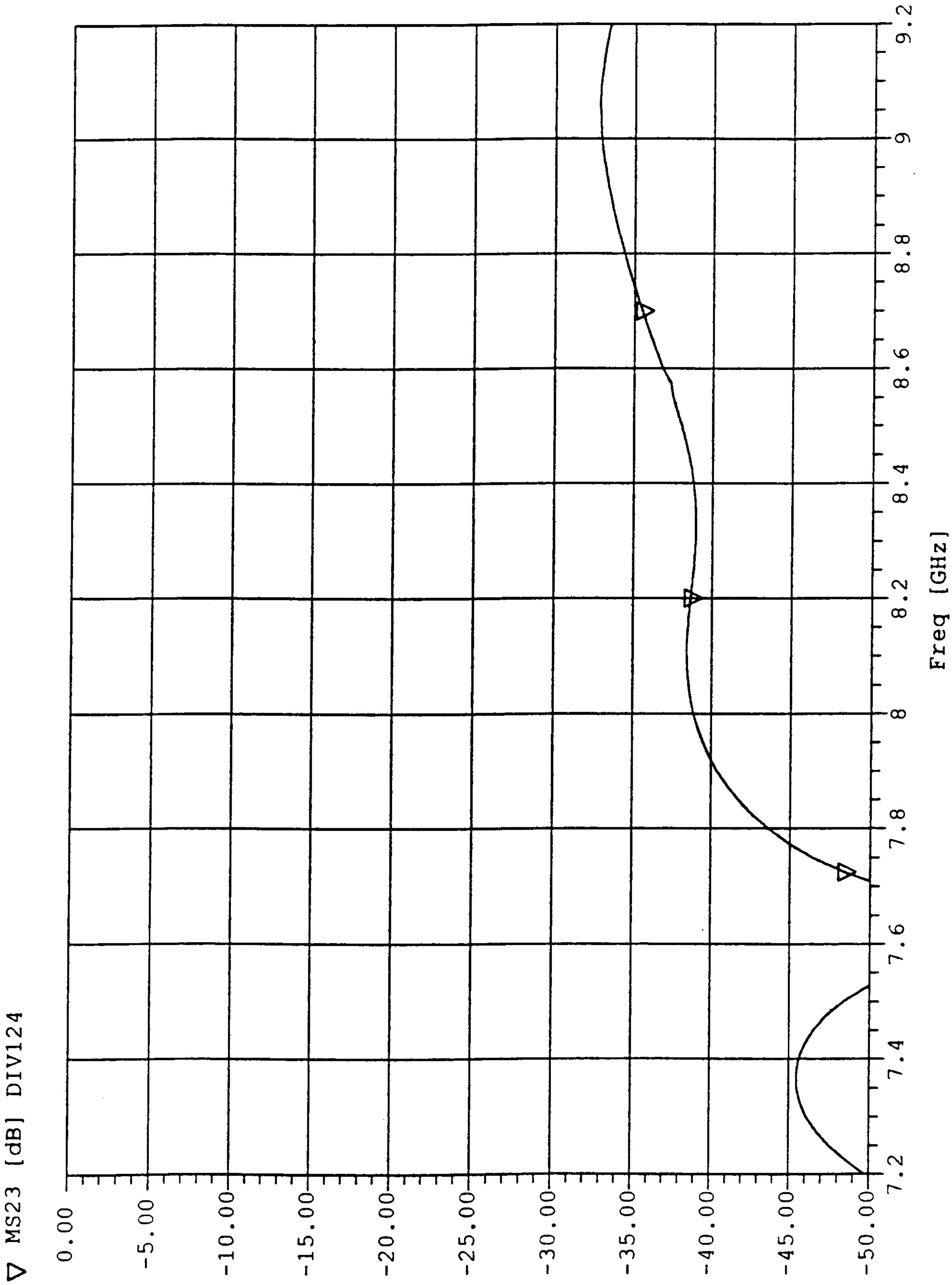

Fig. 2.1.7 : Isolation between ports

Mod M-11 Registro Mercantil de Madrid -]19 - Folio 36 - Hoja nº 4813 - Inscripción 1ª fecha 27/3] Núm. Identificación Fiscal A-28-006104

Mod M-11 Registro Mercantil de Madrid - 39 - Folio 36 - Hoja nº 4813 - Inscripción 1ª fecha 27/3 Núm. Identificación Fiscal A-28-006104

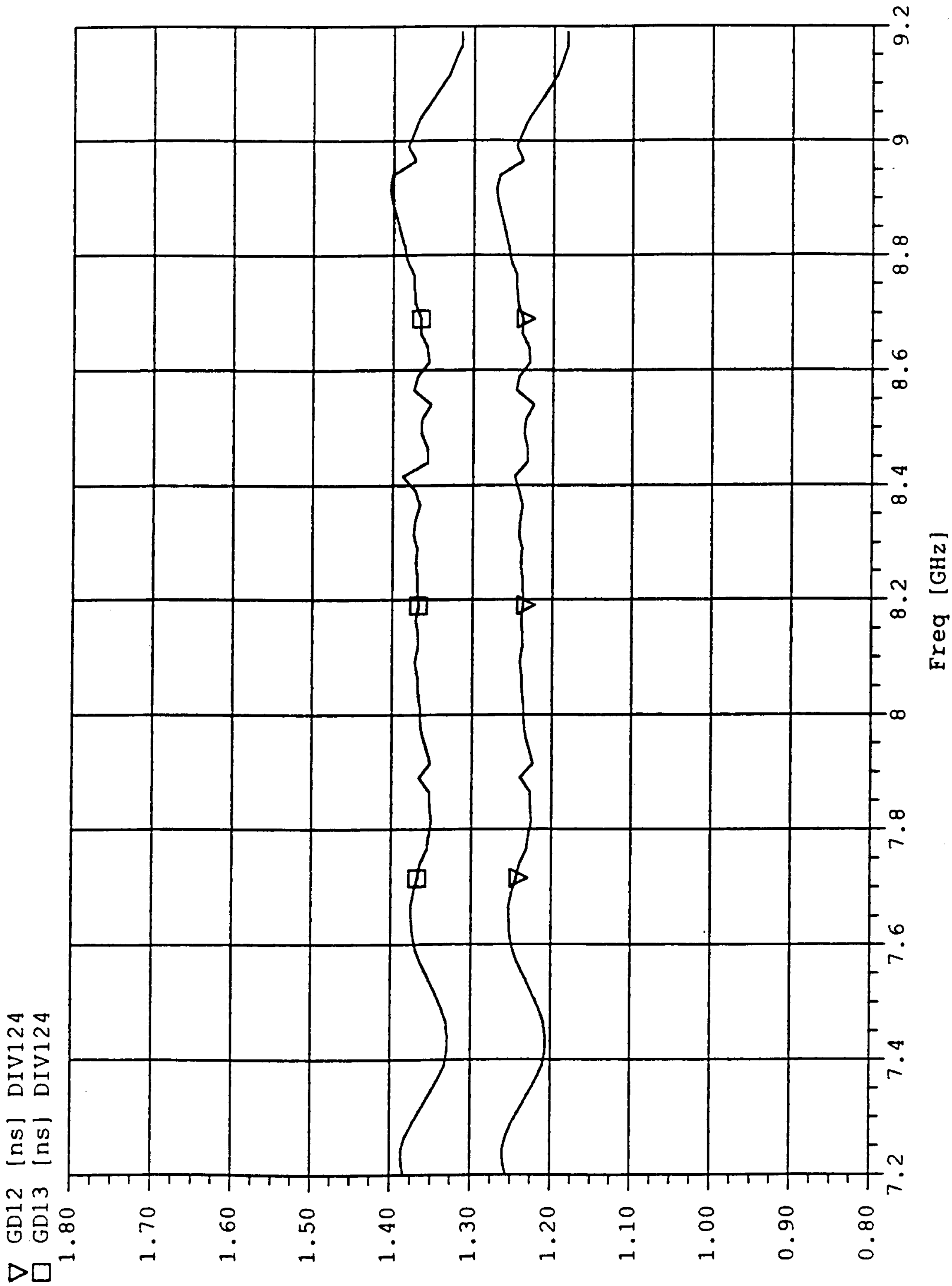

Fig. 2.1.8 : Absolute group delay

The main performances are summarized in the following table, and the worst case value in the band (8,025 - 8,4 GHz) is presented:

Parameter	Worst Case Value
Input return loss	-21,4 dB
Output return loss	-26,7 dB
Amplitude unbalance (at a given frequency)	0,03 dB
Phase unbalance (at a given frequency)	9.4°
Amplitude variation (within 50 MHz channel)	0,02 dB
Group delay variation (within 50 MHz channel)	3 ps
Insertion losses	1,04 dB

Registro Mercantil de Madrid - Tomo 139 - Folio 36 - Hoja nº 4813 - Inscripción 1ª fecha 27/3/1923 - Núm. Identificación Fiscal A-28-006104

Mod. M-11

Registro Mercantil de Madrid - Tomo 139 - Folio 36 - Hoja nº 4813 - Inscripción 1ª fecha 27/3/1923 - Núm. Identificación Fiscal A-28-006104

Mod M-11

2.2. CABLES

In agreement with the antenna assembly design, R.D.[2] illustrated in figure 2.1, the interconnecting RF cables have been selected with the objectives of:

- Low insertion losses.
- Low weight.
- Curvature compatible with handling capabilities required for BFN assembly according to R.D.[2].
- Length adjust and trimming capabilities, before and during integration process.

All these objectives are met by KMW RG402/U cable, with nominal 50/50/200 mm length at the connection of dividers - active modules / active modules - Butler matrices / Butler matrices - rejection filters respectively.

These cables are ended by:

- SUHNER 23 SMA-50-0-11 or similar connector at one end.
- SUHNER 71Z-03-16 or similar connector at the other end, with easy trimming at this point during integration.

Main selected cable characteristics are:

- 1.32 dB/m insertion losses at 8.4 GHz.
- 0.035 Kg/m.
- 4.76 mm bending radius.
- 12.7 mm flexing radius.

Translated to the 50 mm and 200 mm sections, this means:

Insertion Losses:

- 50 mm cable	0.066 dB
- 200 mm cable	0.264 dB

Amplitude Unbalance:

- Cable length error 0.00132 dB/mm
- Over complete bandwidth 0.04 dB

Phase Unbalance:

- Cable length error 9.9°/mm
- Over complete bandwidth 0.45° (linear performance)

Registro Mercantil de Madrid - Tomo 139 - Folio 36 - Hoja nº 4813 - Inscripción 1ª fecha 27/3/1923 - Núm. Identificación Fiscal A-28-006104

Mod M-11

Registro Mercantil de Madrid - Tomo 139 - Folio 36 - Hoja nº 4813 - Inscripción 1ª fecha 27/3/1923 - Núm. Identificación Fiscal A-28-006104

2.3. BUTLER MATRIX

2.3.1. Initial Considerations

Figure 2.3.1 is a more detailed scheme of the Butler Matrix based on the 6 ports hybrid coupler. The characteristic impedance of all the transmission lines is Z_0 (50**Ω**). In principle, the hybrid coupler transmission line lengths must be those sketched in the figure ($\lambda/3$ and $\lambda/12$, with λ corresponding to the guided wavelength), although some modifications in length are allowed maintaining (ideally) the performances: any of the $\lambda/3$ lines can be increased by λ, and any of the $\lambda/12$ can be increased by $\lambda/2$ maintaining phase and amplitude relations at the design frequency. This is an important feature since, as will be shown later, some of the designs which have been considered had some dimensioning constraints which are solved by adding line sections where apropriate.

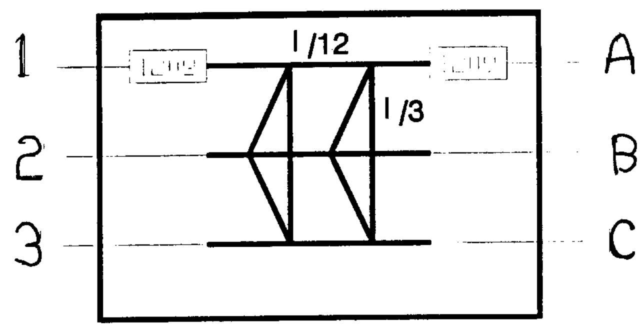

Figure 2.3.1.

Nevertheless, it must be noticed that although the insertion of line sections does not affect the results at the design frequency, the performances within the frequency band are seriously degraded by dispersion due to line length. The results which are shown below correspond to ideal lossless transmission lines following the scheme shown before. Graphics correspond to the 3×3 hybrid coupler (not the complete Butler Matrix).

As conclusion from this first analysis, provided the analysis was carried out for lossless ideal transmission lines independently of the technology considered, the 3×3 directional coupler shows a narrowband response, even for the shortest line lengths. The combination of long ($\lambda/3$) and short ($\lambda/12$) transmission lines does not help to obtain a frequency independent device.

Mod M-11

LINE LENGTHS OF 120° AND 30°

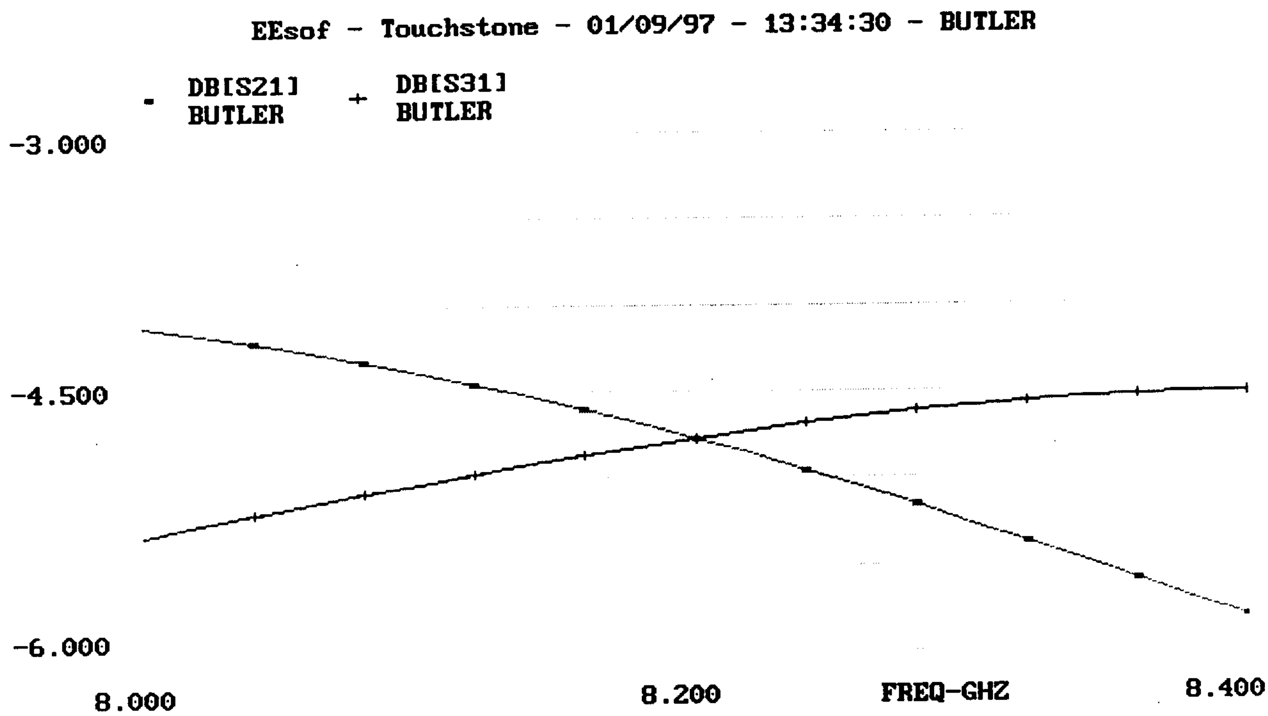

Figure 2.3.2 .- Transmission coefficients of 3x3 ideal 30/120

Registro Mercantil de Madrid - Tomo 139 - Folio 36 - Hoja nº 4813 - Inscripción 1ª fecha 27/3/1923 - Núm. Identificación Fiscal A-28-006104

Mod. M-11

LINE LENGTHS OF 120+360° AND 30°

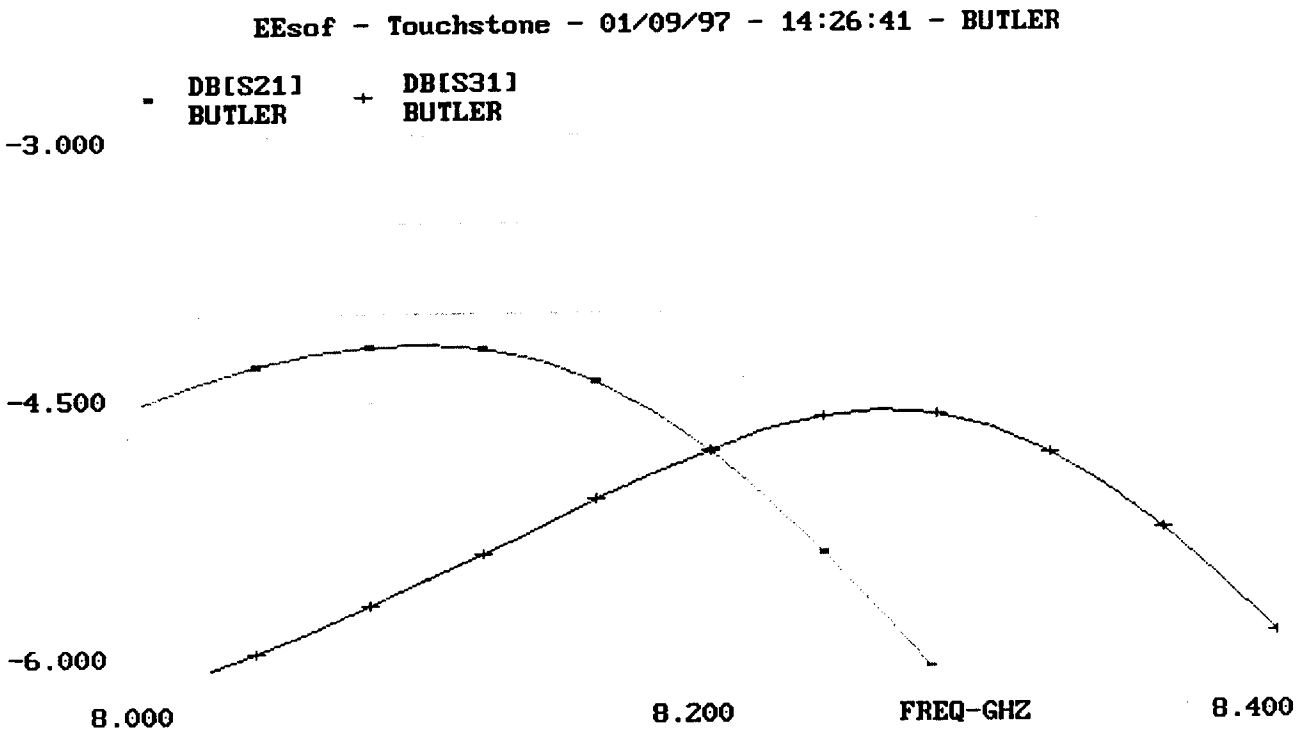

Figure 2.3.3.- Transmission coefficients of 3x3 ideal 30/480

Registro Mercantil de Madrid - Tomo 139 - Folio 36 - Hoja nº 4813 - Inscripción 1ª fecha 27/3/1923 - Núm. Identificación Fiscal A-28-006104

Mod M-11

LINE LENGTHS OF 120° AND 30+180°

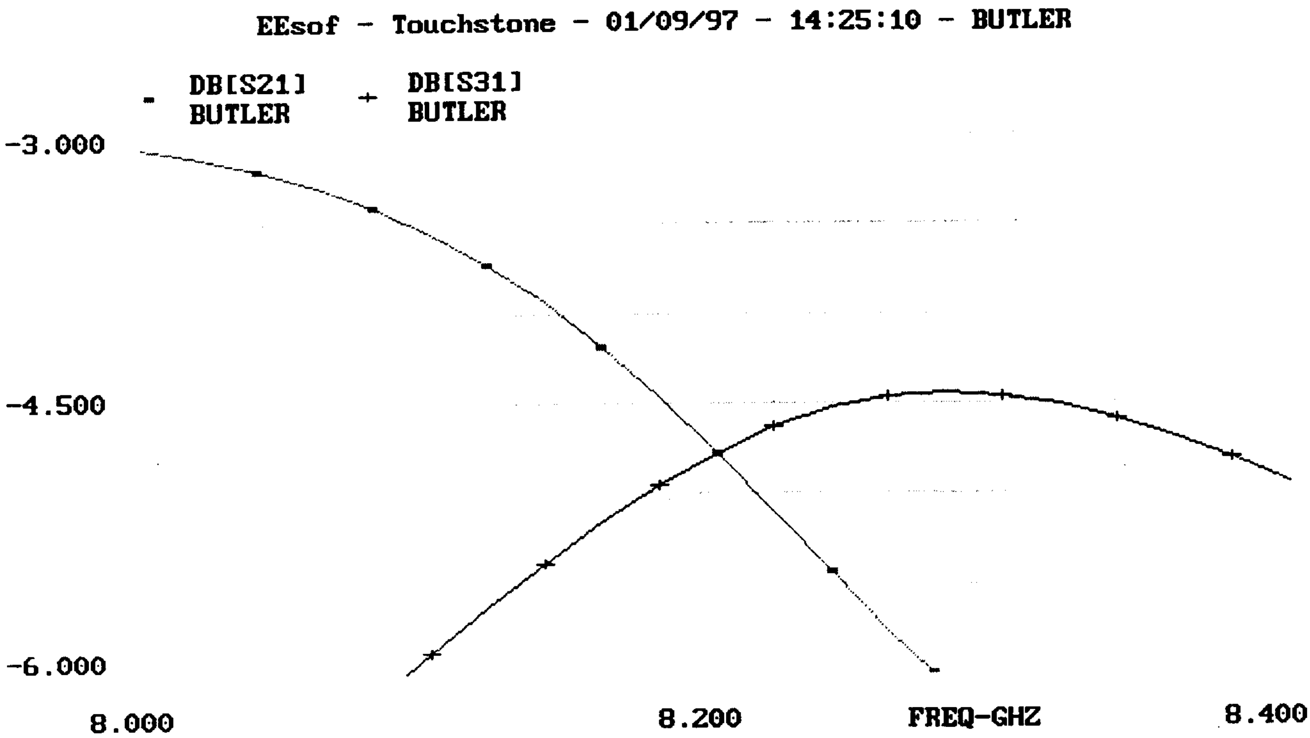

Figure 2.3.4.- Transmission coefficients of 3x3 ideal 210/120

Registro Mercantil de Madrid - Tomo 139 - Folio 36 - Hoja nº 4813 - Inscripción 1ª fecha 27/3/1923 - Núm. Identificación Fiscal A-28-006104

Mod M-11

Registro Mercantil de Madrid - Tomo 139 - Folio 36 - Hoja nº 4813 - Inscripción 1ª fecha 27/3/1923 - Núm. Identificación Fiscal A-28-006104

LINE LENGTHS OF 120+360° AND 30+180°

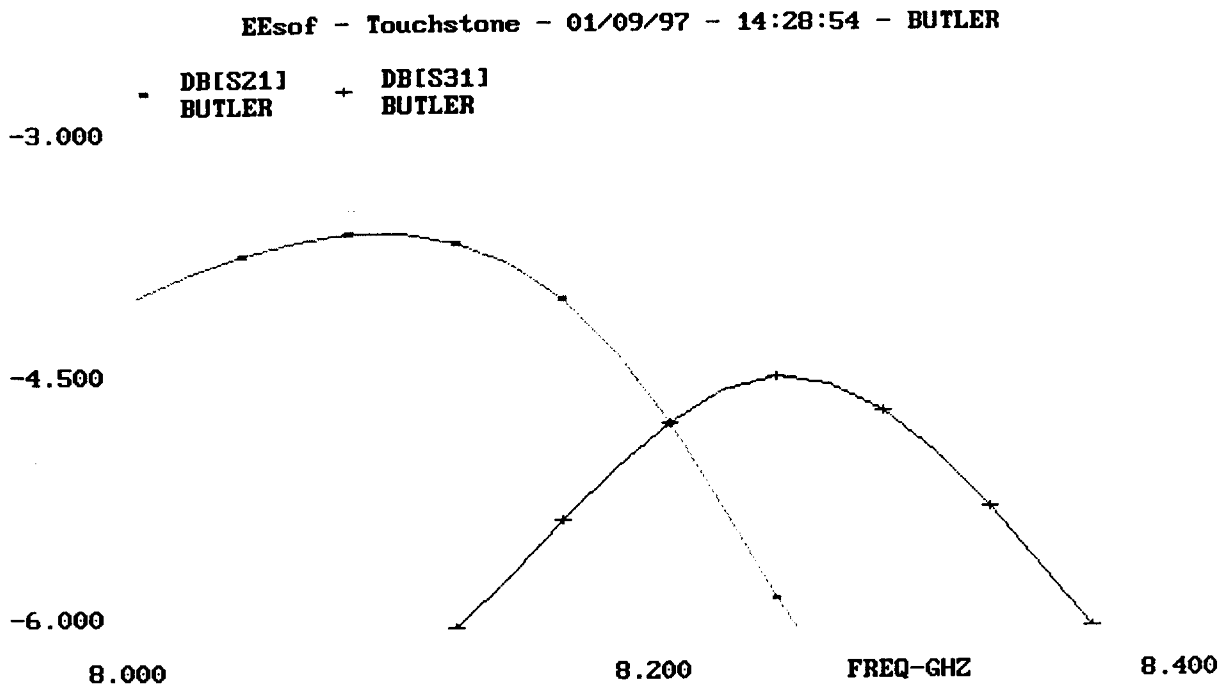

Figure 2.3.5.- Transmission coefficients of 3x3 ideal 210/480

Mod M-11

Registro Mercantil de Madrid - Tomo 139 - Folio 36 - Hoja nº 4813 - Inscripción 1ª fecha 27/3/1923 - Núm. Identificación Fiscal A-28-006104

Mod M-11

2.3.2. Electrical Design

For the implementation of the Butler matrices several options have been considered. In first place, those already proved in R.D.[2], consisting on a 3D configuration on two layers, where the $\lambda/3$ transmission lines are photoetched and connected by 50Ω coaxial transmission lines of 30° electrical length.

A second option consists of to concentrical configurations where the inner ring was occupied by $\lambda/3$ lines and the outer was occupied by $\lambda/3+\lambda$ lines, connected by the $7\lambda/12$ microstrip transmission line.

Several alternatives have been also considered to reduce the size of the device, particularly those based on slotlines as connection between two microstrip layers where the $\lambda/3$ lines where photoetched, and finally a printed version based on brach line couplers, which has also shown promising results. In the next paragraphs the work carried out on these developments will be described.

FIRST CONFIGURATION

The first option is based on the original configuration described in R.D.[2]. It is the most direct implementation of the scheme which was shown in preceeding section. An sketch of the connection between both layers is shown in figure 2.3.6.

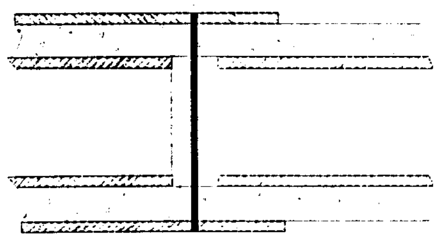

Figure 2.3.6.- Coaxial connection between microstrip layers

Each of the printed board layers of the 3×3 coupler has the basic shape shown in figure 2.3.7. The microstriplines, which originally are 50Ω, are optimized using a CAD program R.D.[7] to obtain a flat response over the complete bandwidth. The final Butler Matrix device includes additional transmission lines at the inputs and outputs in order to properly adjust the transmission phases of the device.

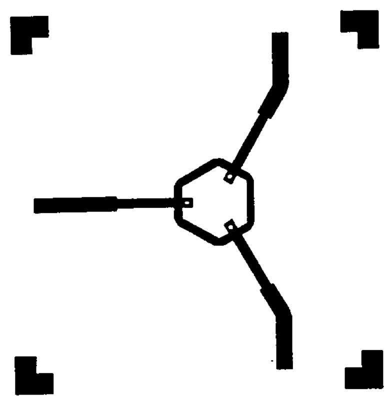

Figure 2.3.7.- Layout of a layer of the 3×3 coupler

This configuration has been optimised for both $\lambda/12$ and $\lambda+\lambda/12$ coaxial transmission lines, leading to different transmission line widths. Following the theoretical results corresponding to the ideal elements, shown in the initial considerations, the longer lines give place to a narrower input impedance match, while the shorter coaxial gives simulated results which are compliant with the specification. Detailed results will be given in the performances section.

Registro Mercantil de Madrid - Tomo 139 - Folio 36 - Hoja nº 4813 - Inscripción 1ª fecha 27/3/1923 - Núm. Identificación Fiscal A-28-006104

Mod. M-11

Registro Mercantil de Madrid - Tomo 139 - Folio 36 - Hoja nº 4813 - Inscripción 1ª fecha 27/3/1923 - Núm. Identificación Fiscal A-28-006104

Mod. M-11

SECOND CONFIGURATION

The second configuration analysed is the planar concentric configuration whose basic layout is sketched in figure 2.3.8. The outer ring is composed of transmission lines of length $4\lambda/3$, which are connected through $7\lambda/12$ transmission lines to the $\lambda/3$ inner ring. The connecting lines have been chosen of that length in order to reduce the posibble coupling between the transmission lines of each level; it must be borne in mind that the low ϵ of the substrate gives place both to wide line widths and possible high coupling between them.

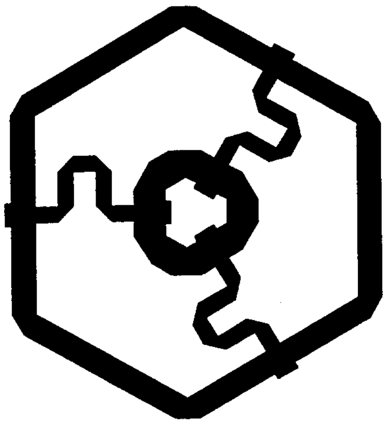

Figure 2.3.8.- Planar 'anular' 6 port coupler

Apart from the electrical performances, which simulation reveales to be not compliant with the requirements, one point which causes some concerns on this configuration is the difficult assembly and connection to the coaxial input/output ports, particularly cumbersome for the lines coming from the inner ring (figure 2.3.9). The configuration has been analysed and optimised and, finally, rejected.

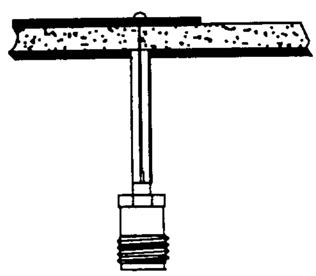

Figure 2.3.9.- Coaxial connection of the anular matriz

THIRD CONFIGURATION

Clearly, the optimum solution should be a planar or quasiplanar configuration in which preferrably there should not be either any coaxial soldering nor 'through' coaxial assemblies. It has been considered that a slotline connecting two layers of microstrip lines could provide the required performances. The slotline length should take the role of the coaxial lines, being of $\lambda/12$ electrical length. In fact, instead of a simple slotline, the configuration should make use of a sandwiched-slotline supported by both microstrip layers. Figure 2.3.10 shows a section view of the device.

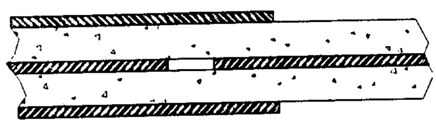

Figure 2.3.10.- Section view of the planar slot 6 port coupler

Each level made in microstrip should resemble those of the coaxial configuration sketched before, and should include a transition from microstrip to sandwiched slotline. The room required by these transitions were problematic in the original configuration with $\lambda/3$ microstrip transmision lines, so that the microstrip line lengths were increased in λ, giving the configuration sketched in figure 2.3.11.

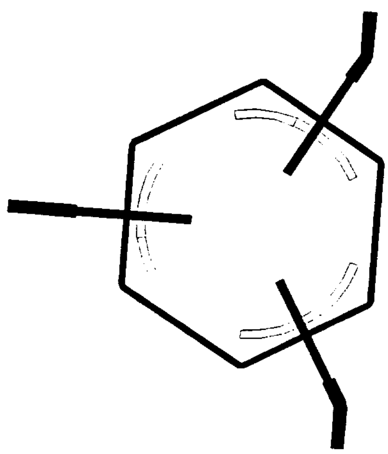

Figure 2.3.11.- Slotline planar 6 port coupler configuration

Registro Mercantil de Madrid - Tomo 139 - Folio 36 - Hoja nº 4813 - Inscripción 1ª fecha 27/3/1923 - Núm. Identificación Fiscal A-28-006104

Mod. M-11

Registro Mercantil de Madrid - Tomo 139 - Folio 36 - Hoja nº 4813 - Inscripción 1ª fecha 27/3/1923 - Núm. Identificación Fiscal A-28-006104

The theoretical analysis with ideal transmission lines reveals again a narrower bandwidth impedance match than the first configuration, but the design is more compact than any of the rest, and simulation results may be considered promising. The design has also been optimized using CAD, including a transition from slotline to microstrip.

The transition was optimised and compared to the coaxial line transmission considered in the first design approach.

FOURTH CONFIGURATION

The last configuration considered for the 6 port coupler is based on the classical branch line couplers extensively used in microstrip and waveguide technology as quadrature hybrids. However, in order the device to work properly, there must be included trasnmission lines in a different level connecting edge ports. Following the scheme sketched in figure 2.3.12 below, a connection is required between cross junction in port 3 with that of port 2, and the same occurs between ports 5 and 6. This transmission line must be of $4\lambda/3$ in order to be feasible the physical connection. In principle the first approach consists of making such transitions in coaxial line, although is considered the possibility of a printed transmission line on a layer below the branch line, connected with pins through the substrate.

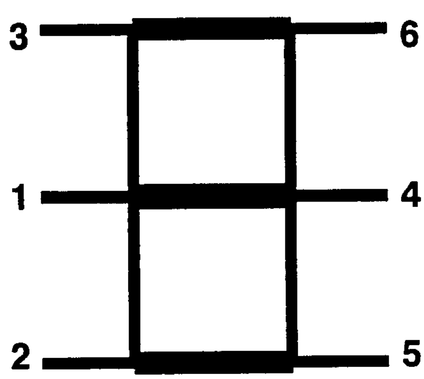

Figure 2.3.12.- 3×3 branch line coupler (the coaxial conection of 3-2 and 6-5 is not shown)

Mod M-11

BASELINE DESIGN

The results obtained from all the simulations carried out up to now show that the first coaxial approach is the more adjusted one to the electrical requirements. The complete Butler matrix based on this coupler includes the input transmission lines required to fit the phase distribution following specifications.

Breadboarding of these elements is under way, Figure 2.3.13.

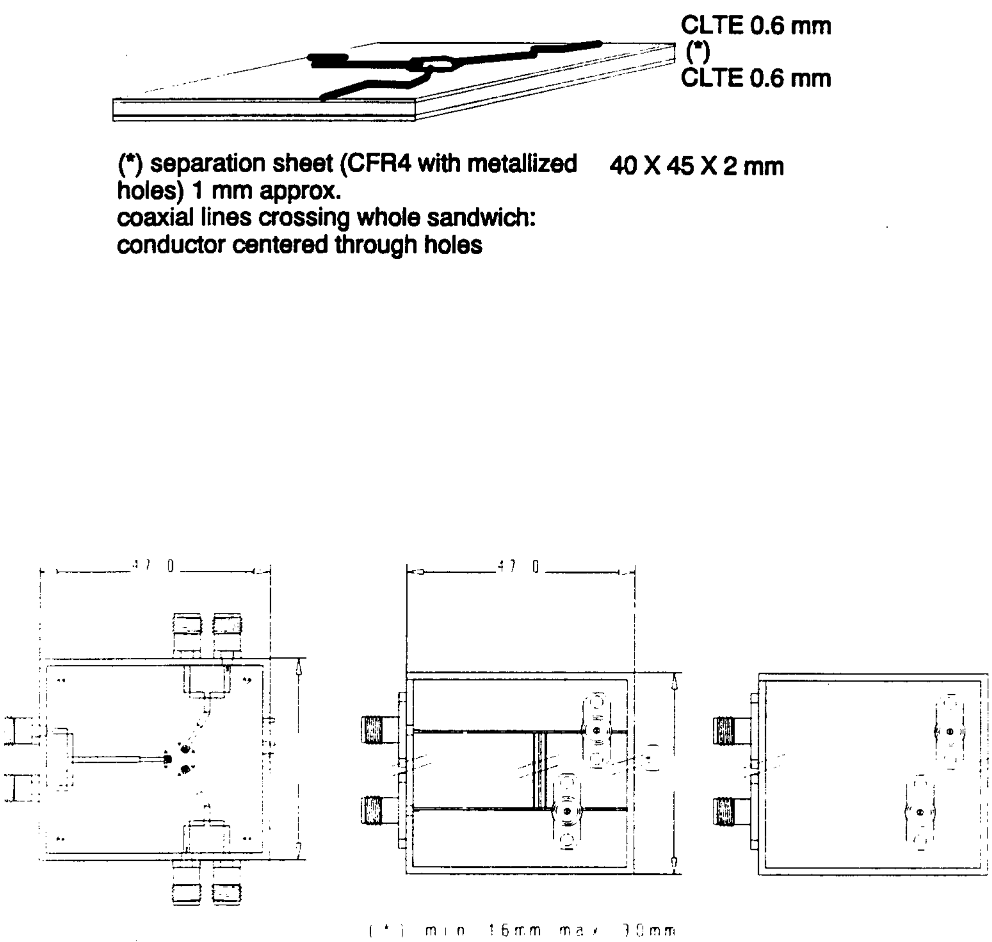

Figure 2.3.13.- Layout of the Butler Matrix Baseline

Registro Mercantil de Madrid - Tomo 139 - Folio 36 - Hoja nº 4813 - Inscripción 1ª fecha 27/3/1923 - Núm. Identificación Fiscal A-28-006104

Mod M-11

2.3.3. Substrate Selection

Taken into account the frequency band, and in order to have components which can be handled (not miniature), the permittivity of the substrate should not be higher than 3 or 4, and based on temperature range considerations, the quite vast list of possible material choices is reduced to DUROID 6002 from ROGERS, CLTE from ARLON for its low variation of dielectric constant with temperature. AR320 from ARLON is also considered but only for initial samples.

The thickness of the material has been selected according to considerations of low radiation from discontinuities, regardless the devices are shielded or not in a metallic enclosure. For the Conformal Antenna operational frequencies this criterium has lead us to a substrate thickness of about 0.5 mm for a material with ϵ close to 3 as the ones above presented.

Registro Mercantil de Madrid - Tomo 139 - Folio 36 - Hoja nº 4813 - Inscripción 1ª fecha 27/3/1923 - Núm. Identificación Fiscal A-28-006104

Mod. M-11

2.3.4. Electrical Performances

BUTLER MATRIX WITH COAXIAL (λ/12) CONNECTION (BASELINE)

Summary of electrical characteristics

	Channel 1	Channel 2	Channel 3	Whole band
Amplitude unbalance	±0.15dB	±0.2dB	±0.25dB	±0.25dB
Phase unbalance (pk-pk)	-3.5°/1.5°	-1.3°/0.1°	-2.2°/2.1°	-4.3°/3.9°
Amplitude variation vs frequency	0.05dB	0.05dB	0.05dB	0.15dB
Group delay variation	0ns	0.01ns	0.01ns	0.05ns
Matching ports	< -18.0	<-21	<-23	<-17.5
Overall loss				<-0.4 dB (λ/12 lines)

a) Input match, transmission coefficients and mean insertion loss vs frequency

FREQ	dB(S11)	dB(S33)	dB(S41)	dB(S51)	dB(S61)	avgIL	dB(S43)	dB(S53)	dB(S63)
8.000E+09	-17.190	-16.357	-5.077	-5.128	-5.204	-5.157	-5.204	-5.204	-5.189
8.025E+09	-18.017	-17.064	-5.032	-5.123	-5.198	-5.139	-5.198	-5.198	-5.144
8.050E+09	-18.917	-17.818	-4.992	-5.120	-5.194	-5.123	-5.194	-5.194	-5.103
8.075E+09	-19.896	-18.622	-4.955	-5.119	-5.192	-5.109	-5.192	-5.192	-5.064
8.100E+09	-20.964	-19.477	-4.921	-5.120	-5.191	-5.097	-5.191	-5.191	-5.029
8.125E+09	-22.120	-20.376	-4.891	-5.122	-5.191	-5.088	-5.191	-5.191	-4.997
8.150E+09	-23.355	-21.307	-4.863	-5.126	-5.194	-5.080	-5.194	-5.194	-4.968
8.175E+09	-24.620	-22.241	-4.839	-5.132	-5.198	-5.075	-5.198	-5.198	-4.943
8.200E+09	-25.800	-23.122	-4.819	-5.139	-5.204	-5.072	-5.204	-5.204	-4.920
8.225E+09	-26.679	-23.865	-4.801	-5.148	-5.211	-5.071	-5.211	-5.211	-4.901
8.250E+09	-26.993	-24.358	-4.786	-5.158	-5.220	-5.073	-5.220	-5.220	-4.884
8.275E+09	-26.630	-24.505	-4.774	-5.170	-5.231	-5.076	-5.231	-5.231	-4.870
8.300E+09	-25.749	-24.281	-4.765	-5.184	-5.243	-5.081	-5.243	-5.243	-4.859
8.325E+09	-24.615	-23.744	-4.759	-5.199	-5.257	-5.088	-5.257	-5.257	-4.850
8.350E+09	-23.426	-23.004	-4.755	-5.215	-5.272	-5.097	-5.272	-5.272	-4.844
8.375E+09	-22.280	-22.164	-4.753	-5.233	-5.289	-5.108	-5.289	-5.289	-4.840
8.400E+09	-21.216	-21.298	-4.754	-5.253	-5.308	-5.120	-5.308	-5.308	-4.838

Registro Mercantil de Madrid - Tomo 139 - Folio 36 - Hoja nº 4813 - Inscripción 1ª fecha 27/3/1923 - Núm. Identificación Fiscal A-28-006104

Mod M-11

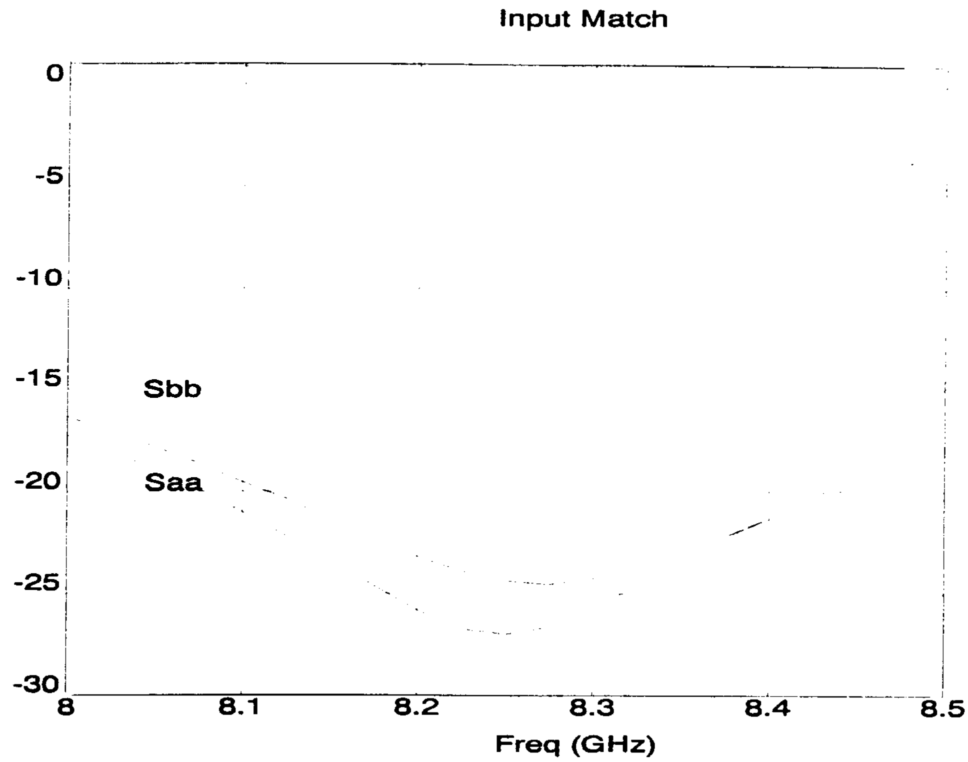

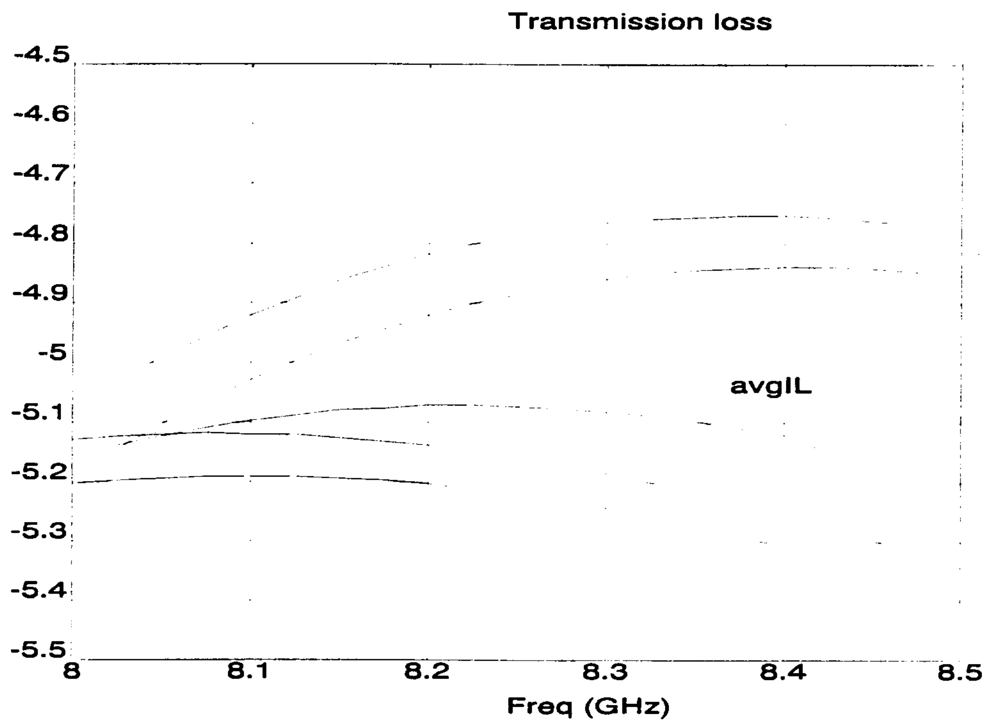

Registro Mercantil de Madrid - Tomo 139 - Folio 36 - Hoja nº 4813 - Inscripción 1ª fecha 27/3/1923 - Núm. Identificación Fiscal A-28-006104

Mod M-11

b) Losses and amplitude dispersion wrt mean insertion loss vs. frequency

FREQ	dB(Loss)	Disp1	Disp2	Disp3	Disp4
8.000E+09	-0.386	0.081	0.029	-0.032	-0.047
8.025E+09	-0.367	0.106	0.016	-0.006	-0.060
8.050E+09	-0.351	0.131	0.002	0.020	-0.071
8.075E+09	-0.337	0.154	-0.011	0.044	-0.083
8.100E+09	-0.325	0.176	-0.023	0.068	-0.094
8.125E+09	-0.315	0.197	-0.035	0.090	-0.104
8.150E+09	-0.307	0.217	-0.046	0.112	-0.114
8.175E+09	-0.302	0.236	-0.056	0.132	-0.123
8.200E+09	-0.298	0.254	-0.067	0.152	-0.131
8.225E+09	-0.297	0.270	-0.076	0.171	-0.140
8.250E+09	-0.298	0.286	-0.086	0.189	-0.148
8.275E+09	-0.300	0.301	-0.094	0.206	-0.155
8.300E+09	-0.305	0.316	-0.103	0.222	-0.162
8.325E+09	-0.312	0.329	-0.111	0.238	-0.169
8.350E+09	-0.320	0.342	-0.118	0.253	-0.175
8.375E+09	-0.330	0.354	-0.126	0.268	-0.181
8.400E+09	-0.342	0.366	-0.132	0.282	-0.187

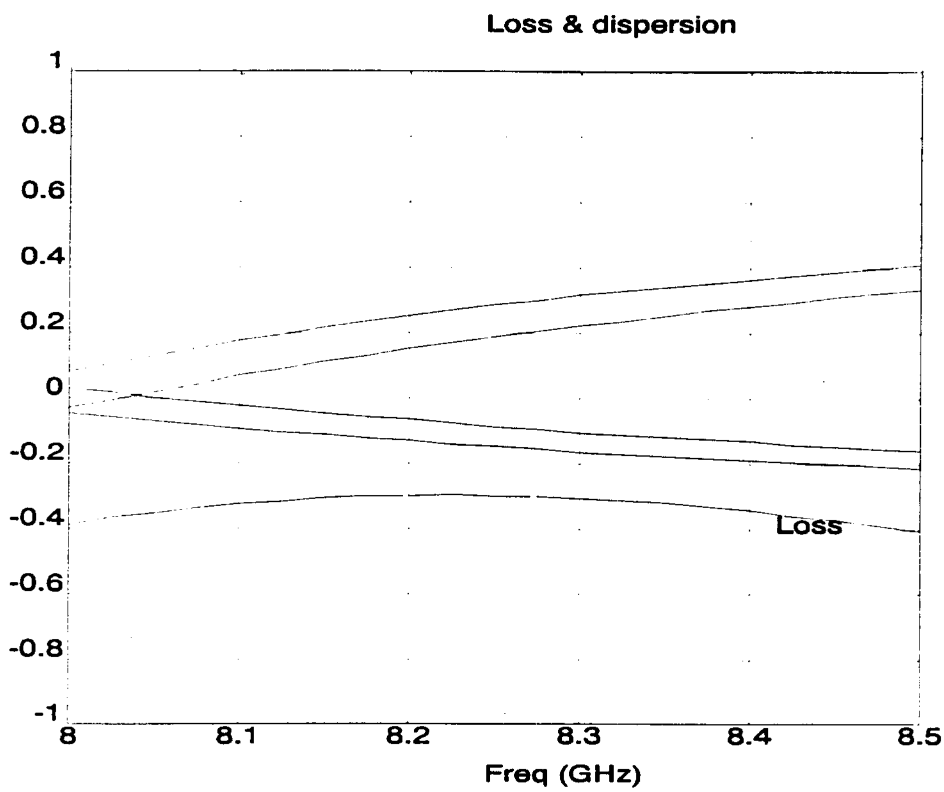

Registro Mercantil de Madrid - Tomo 139 - Folio 36 - Hoja nº 4813 - Inscripción 1ª fecha 27/3/1923 - Núm. Identificación Fiscal A-28-006104

Mod. M-11

c) Phase Differences between ports vs. frequency

FREQ	Dfi1	Dfi2	Dfi3	Dfi4	Dfi5	Dfi6	Dfi7	Dfi8
8.000E+09	-124.732	117.473	117.473	-124.732	532.9E-15	1.072E-12	596.8E-15	0.594
8.025E+09	-124.231	117.827	117.827	-124.231	-56.84E-15	-625.2E-15	-234.4E-15	0.382
8.050E+09	-123.729	118.183	118.183	-123.729	-454.7E-15	142.1E-15	227.3E-15	0.170
8.075E+09	-123.224	118.540	118.540	-123.224	-78.15E-15	966.3E-15	255.7E-15	-0.039
8.100E+09	-122.716	118.898	118.898	-122.716	-1.008E-12	49.73E-15	-355.2E-15	-0.247
8.125E+09	-122.205	119.257	119.257	-122.205	-170.5E-15	-14.21E-15	461.8E-15	-0.451
8.150E+09	-121.689	119.617	119.617	-121.689	-589.7E-15	618.1E-15	675.0E-15	-0.652
8.175E+09	-121.168	119.978	119.978	-121.168	-56.84E-15	682.1E-15	1.726E-12	-0.849
8.200E+09	-120.642	120.340	120.340	-120.642	-397.9E-15	-476.0E-15	-1.399E-12	-1.041
8.225E+09	-120.110	120.703	120.703	-120.110	369.4E-15	-298.4E-15	284.2E-15	-1.228
8.250E+09	-119.571	121.067	121.067	-119.571	287.7E-15	-504.4E-15	-1.151E-12	-1.409
8.275E+09	-119.025	121.432	121.432	-119.025	-557.7E-15	841.9E-15	110.1E-15	-1.584
8.300E+09	-118.472	121.798	121.798	-118.472	-451.1E-15	-159.8E-15	-888.1E-15	-1.753
8.325E+09	-117.910	122.164	122.164	-117.910	170.5E-15	-891.7E-15	-810.0E-15	-1.914
8.350E+09	-117.341	122.532	122.532	-117.341	-934.3E-15	671.4E-15	-298.4E-15	-2.068
8.375E+09	-116.762	122.899	122.899	-116.762	412.1E-15	1.065E-12	213.1E-15	-2.215
8.400E+09	-116.175	123.268	123.268	-116.175	319.7E-15	-46.18E-15	39.07E-15	-2.353

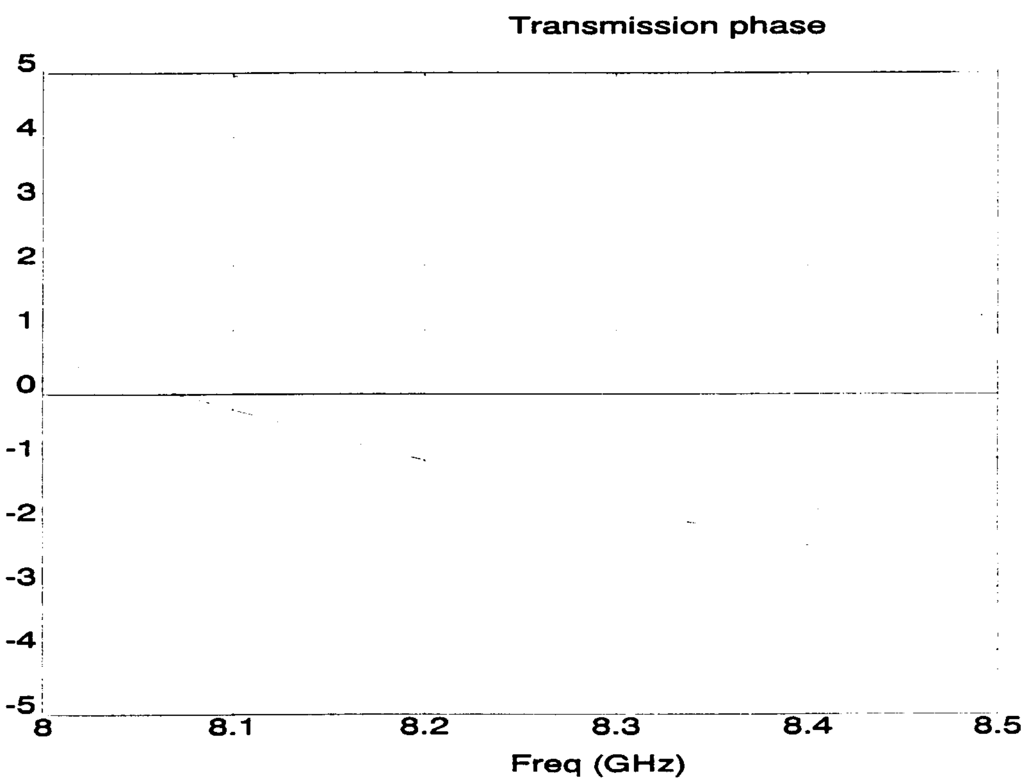

Registro Mercantil de Madrid - Tomo 139 - Folio 36 - Hoja nº 4813 - Inscripción 1ª fecha 27/3/1923 - Núm. Identificación Fiscal A-28-006104

Mod M-11

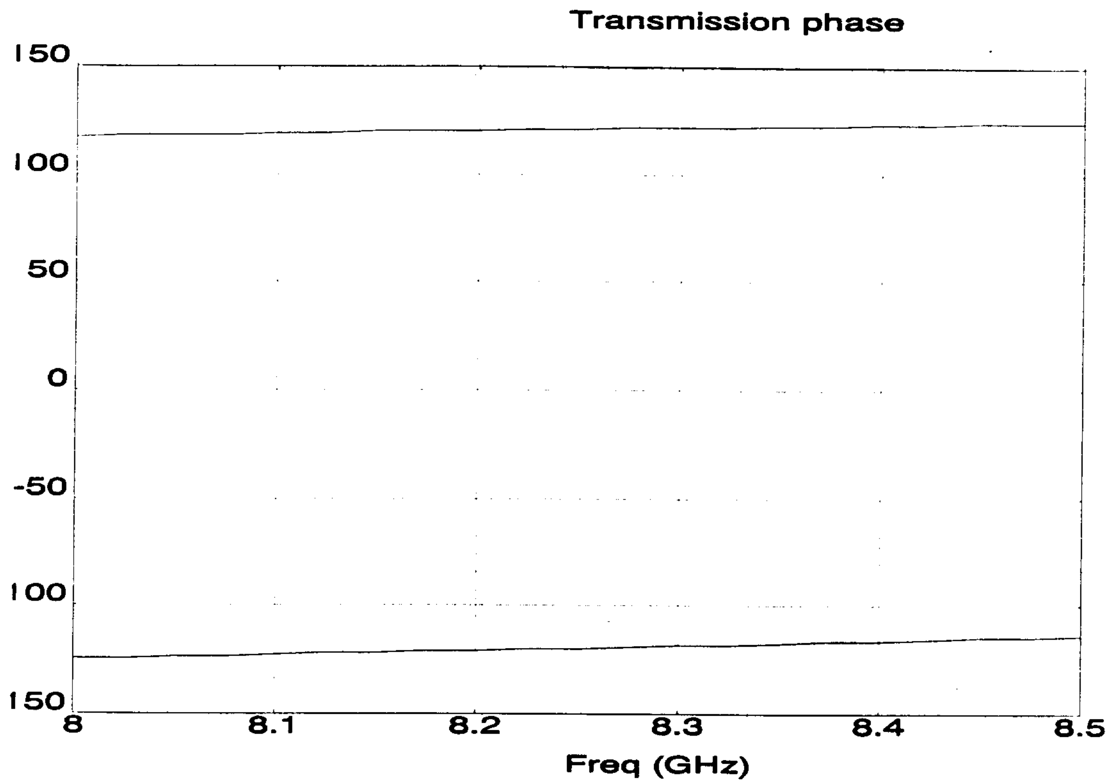

d) Time delay variation was computed from transmission phase data. Absolute dispersion is better than 0.3ns over the complete bandwidth, and the variation is lower than 0.05ns also over the complete bandwidth.

Registro Mercantil de Madrid - Tomo 139 - Folio 36 - Hoja nº 4813 - Inscripción 1ª fecha 27/3/1923 - Núm. Identificación Fiscal A-28-006104

Mod. M-11

Registro Mercantil de Madrid - Tomo 139 - Folio 36 - Hoja nº 4813 - Inscripción 1ª fecha 27/3/1923 - Núm. Identificación Fiscal A-28-006104

BRANCH LINE BUTLER MATRIX WITH COAXIAL (λ/3+λ) CONNECTION

(FOURTH CONFIGURATION - BACK UP)

Summary of electrical characteristics

	Channel 1	Channel 2	Channel 3	Whole band
Amplitude unbalance	±0.25dB	±0.15dB	±0.2dB	±0.25dB
Phase unbalance (pk-pk)	-2°/2.5°	-2.5°/2°	-3°/2°	-11.9°/11°
Amplitude variation vs frequency	0.24dB	0.05dB	0.15dB	0.24dB
Matching ports	< -11	<-16	<-16.5	<-11
Overall loss				< 0.6dB

Mod. M-11

a) **Input match, transmission coefficients and mean insertion loss vs frequency**

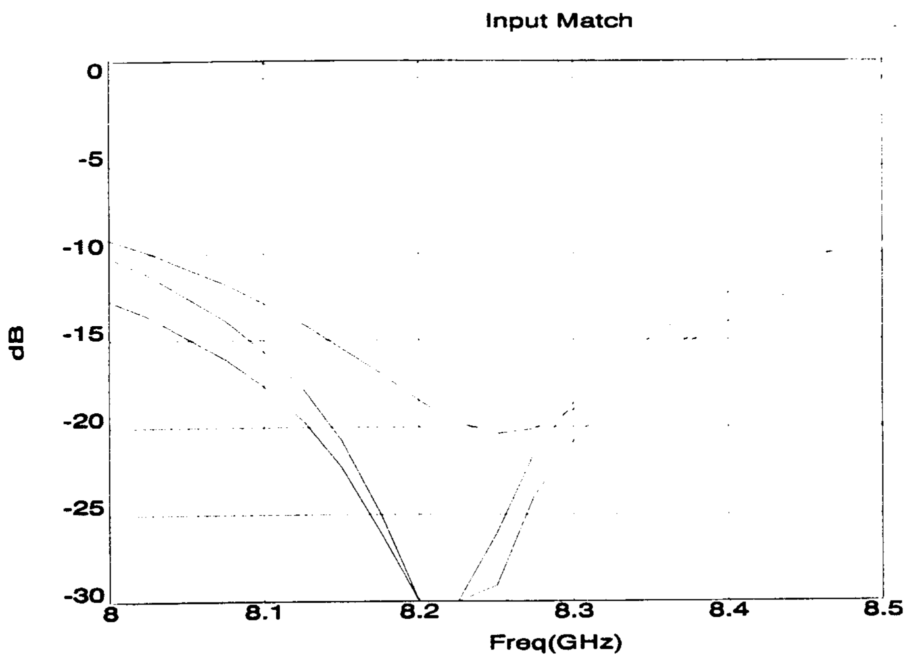

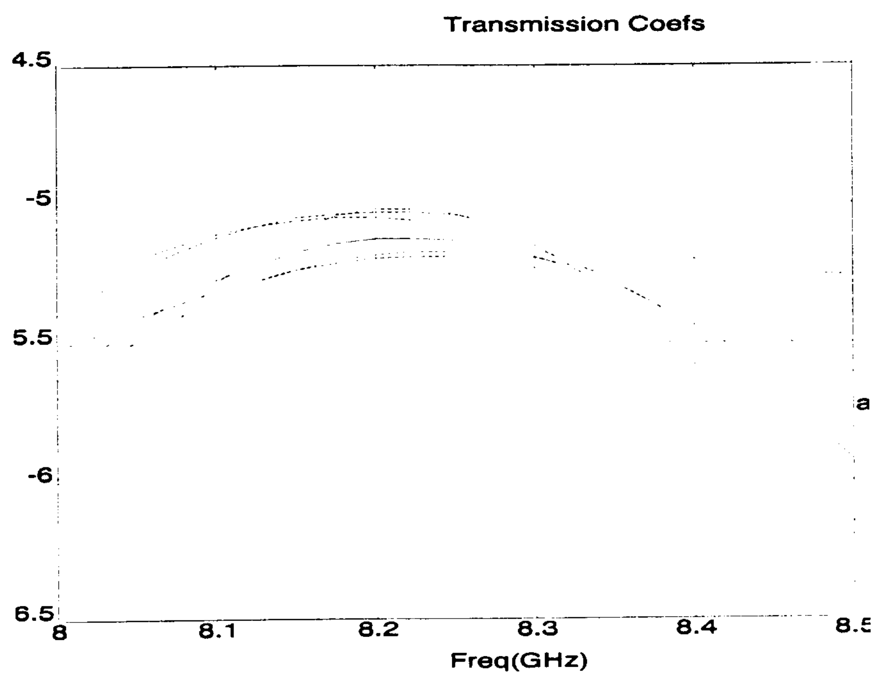

Registro Mercantil de Madrid - Tomo 139 - Folio 36 - Hoja nº 4813 - Inscripción 1ª fecha 27/3/1923 - Núm. Identificación Fiscal A-28-006104

Mod. M-11

b) **Transmission losses and amplitude dispersion wrt mean insertion loss vs. frequency**

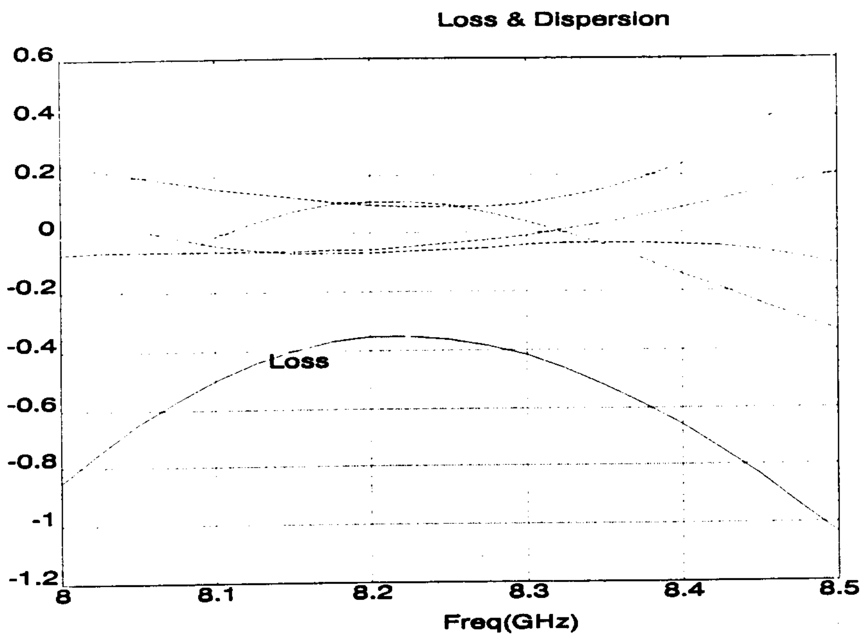

c) **Phase Differences between ports vs. frequency**

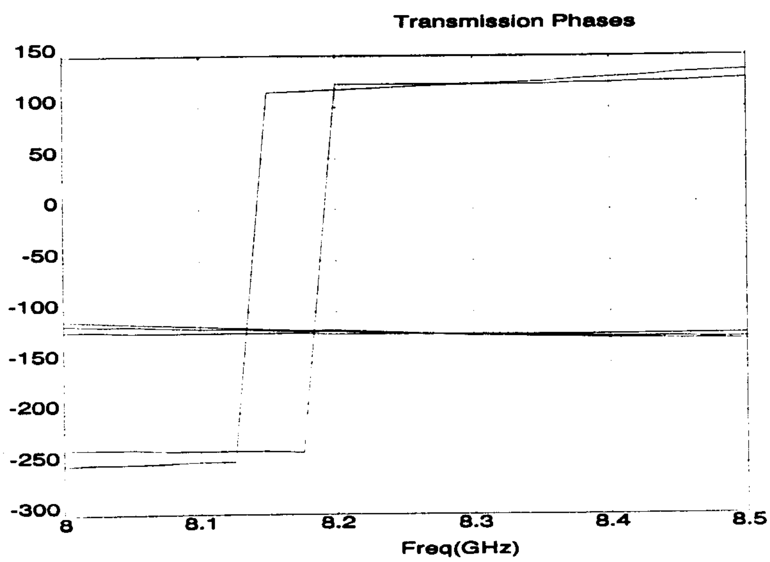

Registro Mercantil de Madrid - Tomo 139 - Folio 36 - Hoja nº 4813 - Inscripción 1ª fecha 27/3/1923 - Núm. Identificación Fiscal A-28-006104

Mod M-11

Registro Mercantil de Madrid - Tomo 139 - Folio 36 - Hoja nº 4813 - Inscripción 1ª fecha 27/3/1923 - Núm. Identificación Fiscal A-28-006104

Mod. M-11

2.4. LOSS BUDGET

Taking into account the electrical characteristics of each component as shown in this document, the loss budget of the passive Beam Forming Network of the Conformal Array Antenna is established as follows:

Divider 1:24	-1.1 dB
Coaxial cable (50 mm)	-0.07
Coaxial cable (50 mm)	-0.06
Butler matrix	-0.6 dB
Coaxial cable (200 mm)	-0.26
Isolator (if necessary)	-0.3 dB
Rejection filter	-1.2 dB
Total loss	**-3.6 dB**

Added to the RF performances of the active modules and radiating panel, A.D.[1,2], the power dissipation map results:

Input Data:

- Antenna block diagram, A.D. [1,2]
- Insertion losses of the passive BFN.
- Insertion losses of the active modules: 1.1 w/module, R.D.[3].
- Insertion losses of the radiating columns: -1.0 dB, A.D.[1].
- Active module gain: 8.8 dB, R.D.[3].
- Preamplifiers design: RF power at antenna I/F, 26.0 dBm per beam, R.D.[3], A.D.[2].
- Cables length, R.D.[2].

Dissipated power on flight antenna:

- 3 divider box: 270 mW
- 50 mm (72) connecting cables: 5 mw/cable.
- 24 complete active modules box: 26.4 w.
- 50 mm (24) connecting cables: 2 mw/cable.
- 8 Butler matrices sub-assembly: 320 mw.
- 200 mm (24) connecting cables: 5 mw/cable.
- 8 isolator + rejection filters subassembly: 15 mw/isol. + filter.
- 24 radiating columns: 13 mw/column.

The highest dissipation is produced at the active modules, being the dimensioning section for the thermal design, R.D. [4]. In the BB antenna case this dissipation is reduced in one third to 8 w approximately.

Registro Mercantil de Madrid - Tomo 139 - Folio 36 - Hoja nº 4813 - Inscripción 1ª fecha 27/3/1923 - Núm. Identificación Fiscal A-28-006104

Mod. M-11

Registro Mercantil de Madrid - Tomo 139 - Folio 36 - Hoja nº 4813 - Inscripción 1ª fecha 27/3/1923 - Núm. Identificación Fiscal A-28-006104

Mod M-11

2.5. CRITICAL ITEMS

Signal Divider

Computer model for the 1:24 signal divider meets all the specifications. However, manufacturing tolerances, unaccuracies in the model, parasitics effects, etc. can lead to deviations in the performances. To find out which parameters are most important in the design a simple sensitivity analysis has been performed, studying the basic unit of the design: a 2-way Wilkinson power divider.

The main conclusions can be written in the form of this table:

Parameter	Spec. affected	Requirement
Tolerance in line widths	Amplitude unbalance	< 30 μm
Tolerance in line lengths ($\lambda/4$ transformers)	$\lvert S_{11}\rvert$	± 5 % (± 0,3 mm)
Resistor values tolerances	$\lvert S_{22}\rvert$	10%
Resistor parasitics	$\lvert S_{22}\rvert$	C < 0,12 pF L < 0,5 nH
Resistor attachment to the lines (soldering, bonding, epoxy)	$\lvert S_{22}\rvert$	Repetitivity

As can be seen, the most stringent requirement is the one concerning line width tolerance, related to the specification of amplitude unbalance (the most difficult to meet).

The rest of the parameters affecting $\lvert S_{11}\rvert$ and $\lvert S_{22}\rvert$ can be tuned in subsequent design iterations, except possibly those concerning parasitics effects of the resistors (that are difficult to characterize). Resistor values tolerances refer mainly to those nearer to the output ports.

Butler Matrices

Since the analysis carried are based on CAD simulations, it is evident that the critical aspects which may arise are associated to components not modelled, particularly the transitions to cable for the baseline design.

On the other hand, manufacturing and assembly are also points to take into account in these printed components. Undergoing breadboards measurements (Annex 1) are aimed to the detailed definition of the $\lambda/12$ coaxial line physical implementation: the pursued matrix assembly is illustrated in the exploded view of figure 2.5.1.

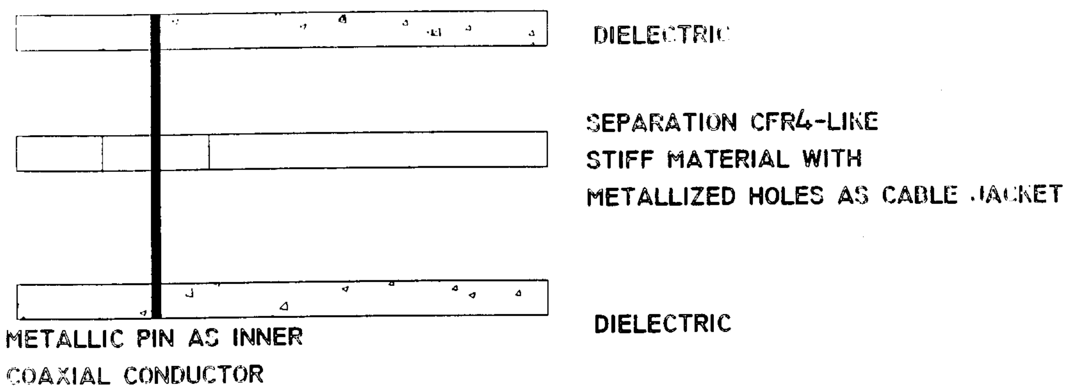

Fig. 2.5.1 : Butler matrix sandwich exploded view

The Butler matrices will be enclosed in metallic boxes and coaxial connectors will be assembled on these boxes. In this way, the expected low radiation from the devices due to the substrate choice, will be minimized to be EM compatible with the remaining parts of the electronic system.

<u>BFN Assembly</u>

No major critical points are detected at complete BFN assembly level.

Registro Mercantil de Madrid - Tomo 139 - Folio 36 - Hoja nº 4813 - Inscripción 1ª fecha 27/3/1923 - Núm. Identificación Fiscal A-28-006104

Mod. M-11

3. COMPLIANCE MATRIX

Comparison of performances after RF design versus requirements are herein summarized in compliance matrix format.

Signal divider and Butler matrices are evaluated separately (based on simulations) and altogether with cables in the form of Sub-BFN as defined in the requirements document, "in front" and "after" active modules respectively.

No differences are made between flight and BB antenna given that no major increase in cables length is foreseen for the BreadBoard and because of the low losses of the selected coaxial cables.

PARAMETER	SIGNAL DIVIDER	"IN FRONT" SUB-BFN			BUTLER MATRIX	"AFTER" SUB-BFN		
	p	R	P	STATUS	P	R	P	STATUS
MATCHING	< -20	< -18 dB	< -20	C	< 18.0 dB	< -18 dB	< -18.0	MC (1)
INSERTION LOSS	< 1.15	< 2 dB	< 1.2	C	< 0.6 dB	< 1.1 dB	< 1.0	C
Amplitude unbalance (at a given frequency)	< 0.05	< 0.2 dB peak-peak	< 0.05	C	± 0.25 dB	< 0.4 dB peak-peak	< 0.4	C
Phase unbalance (at a given frequency)	< 10°	< 50° peak-peak	< 10°	C	- 4.5° + 4.0°	< 5° peak-peak	< 5°	C (2)
Amplitude variation (within 50 MHz channel)	< 0.05	< 0.2 dB peak-peak	< 0.1	C	0.05 dB	< 0.5 dB peak-peak	< 0.1	C
Group delay variation (within 50 MHz channel)	< 0.01	< 2 ns complete antenna	< 0.01	C	< 0.05 ns	< 2 ns complete antenna	< 0.1	C

R-Requirement
P-Performances
C-Compliant
MC-Marginal Compliance

(1) Minimum margin 0 at lower frequency (8025 Mhz)
(2) Tolerance impossed to cables length: ± 0.07 mm

Table 3.1 : Compliance Matrix

Registro Mercantil de Madrid - Tomo 139 - Folio 36 - Hoja nº 4813 - Inscripción 1ª fecha 27/3/1923 - Núm. Identificación Fiscal A-28-006104

Mod M-11